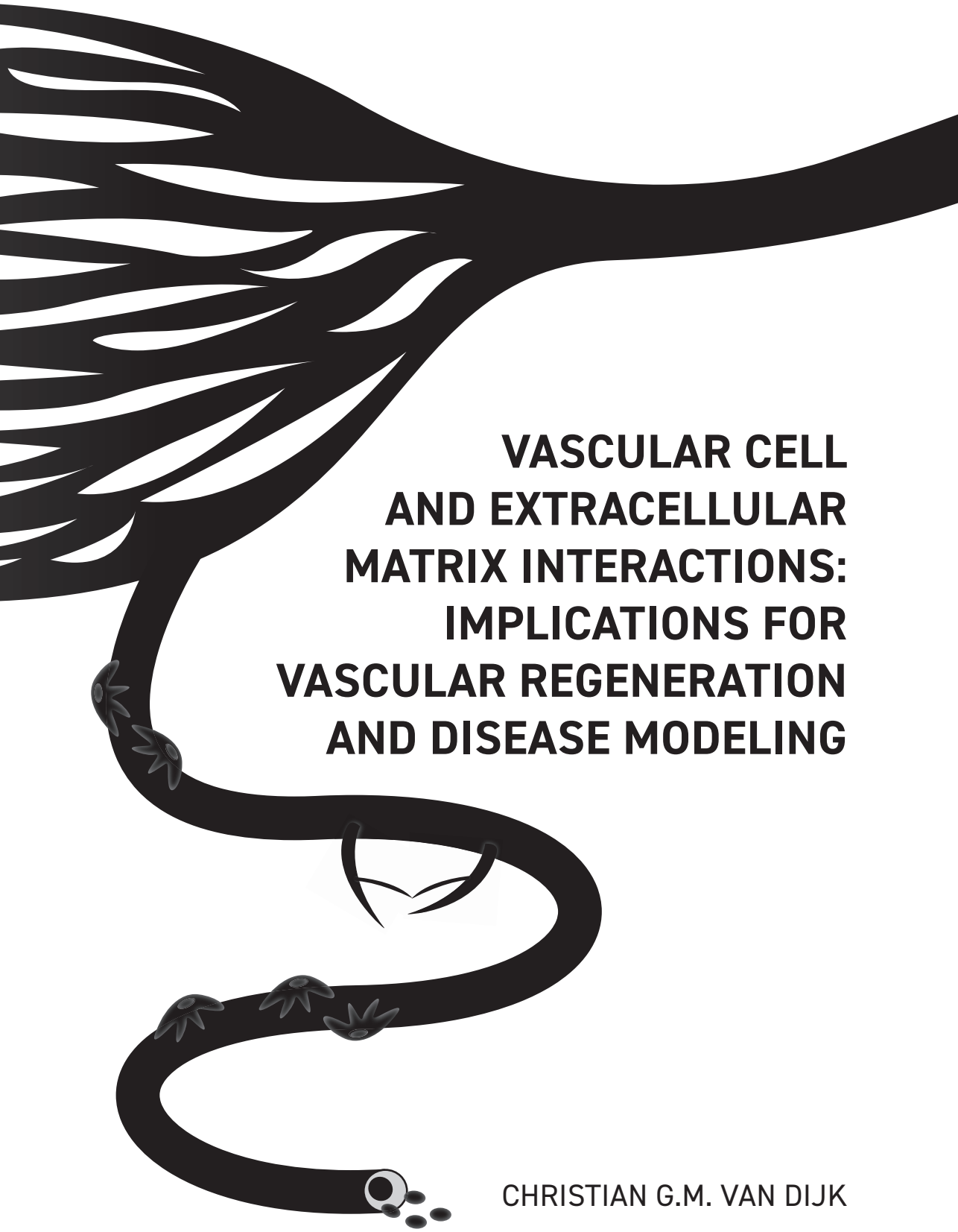

VASCULAR CELL AND EXTRACELLULAR MATRIX INTERACTIONS: IMPLICATIONS FOR VASCULAR REGENERATION AND DISEASE MODELING

CHRISTIAN G.M. VAN DIJK

Vascular cell and extracellular matrix interactions: Implications for vascular regeneration and disease modeling

Christian Gerardus Marinus van Dijk

Vascular cell and extracellular matrix interactions: Implications for vascular regeneration and disease modeling

ISBN: 978-94-6423-234-9

Printed by: ProefschriftMaken – www.proefschriftmaken.nl
Cover design: ProefschriftOntwerp – Bregje Jaspers

Financial support by the Dutch Heart Foundation for the publication of this thesis is gratefully acknowledged.

Vascular cell and extracellular matrix interactions: Implications for vascular regeneration and disease modeling

Vasculaire cel en extracellulaire matrix interacties: Implicaties voor vasculaire regeneratie en ziektemodellering

(met een samenvatting in het Nederlands)

Proefschrift

ter verkrijging van de graad van doctor aan de Universiteit Utrecht
op gezag van de rector magnificus, prof.dr. H.R.B.M. Kummeling,
ingevolge het besluit van het college voor promoties
in het openbaar te verdedigen op

dinsdag 22 juni 2021 des middags te 12.15 uur

door

Christian Gerardus Marinus van Dijk

geboren op 4 februari 1988
te Oosterhout

Promotor:

Prof. dr. M.C. Verhaar

Copromotor:

Dr. K.L. Cheng

Table of contents

Chapter 1

Introduction and outline of this thesis

The efficacy of regenerative medicine applications such as implanted tissue engineered constructs, relies on a functional, circulatory vascular system to provide sufficient nutrient and oxygen to the organ cells. This vascular system is very complex with multiple cell types that interact with the surrounding tissue including the extracellular matrix (ECM), and responds to prevalent biomechanical forces. In this thesis we studied vascular cell interactions with their ECM environment in vascular development, regeneration, and response to renal and cardiovascular disease. Current vascular studies that focus on vascular cell interactions or vascular interaction with their environment use simplified culture models or animal models. However, these *in vitro* and *in* vivo models are often limited in their ability to mimic the complexity of the vasculature or limited in human relevance, respectively [1-3]. A better understanding of EC/pericyte interaction and vascular cell/ECM interactions in development and disease conditions is essential to develop more advanced *in vitro* vessel-on-a-chip models that more fully mimic the human vasculature in anatomy and response to human diseases. This combined with the identification of critical pathways in vascular regulation and regeneration, will provide novel leads for vascular regenerative strategies.

In this chapter, we will first discuss the basic function and structure of blood vessels, focusing on the interaction of the endothelial cells (ECs) and the surrounding environment, in particular mural cells and the vascular basement membrane, and the different molecular mechanisms that are involved in vascular growth and regeneration. In particular, we will focus on the vascular circulatory network in development and the contribution of different vascular components to warrant vascular stability in health and disease, including kidney disease and diastolic heart failure. We discuss how critical steps in these regulatory mechanisms could provide interesting leads for the development of new therapies that aim at protecting or restoring the (micro)vasculature, or could be translated into new strategies for regenerative purposes. We will also discuss how our in-depth understanding of the (micro)vascular compartment can and has been successfully implemented in the development of more advanced vessel-on-a-chip devices.

Understanding the basic function and structure of blood vessels

The majority of tissues in the body rely on blood vessels to supply the cells with oxygen, nutrients and removal of waste products to meet their metabolic demand. Blood vessels are located in a range of 100 to 200 μm from the individual cells allowing optimal oxygen diffusion [4]. In addition, blood vessels offer a pathway for circulating cells to conduct immune surveillance throughout the body. During embryogenic development as well as during adult life, the vascular system is required to remain highly dynamic to cope with changes in the

human body as tissues continue to adapt during development as well as in pathological conditions such as scarring and tumor formation during adult life.

The extensive vascular circulatory network consists of arteries, capillaries and veins. Three histological regions can be identified, each with distinct characteristics. Starting from the lumen, the tunica intima contains a layer endothelial cells (ECs) supported by a basement membrane (BM) (or basal lamina) [5]. Perivascular cell, so-called pericytes, provide additional support and strength to the endothelium. The tunica media contains smooth muscle cells (SMC) and elastic ECM components. This layer is more organized in larger arteries, matching its specific function. The outer layer, tunica adventitia, contains mainly ECM components. In large arteries, this also contains the vaso vasorum, a network of blood vessels, which supplies the vascular wall with oxygen and nutrients [6]. Arteries that feed the heart contain more elastic membranes to cope with the high mechanical forces derived from high local blood pressures compared to the more muscular arteries, which main function is rapid regulation of blood (re)distribution over the vascular tree [5]. Bifurcations from the main arteries such as the femoralis or carotid branch off into vessels with a smaller diameter and less elastic and muscular layers, which include arterioles and precapillary arterioles that precede a dense network of capillaries. This microvascular bed lacks SMC but are supported instead by pericytes. The small diameter (<10 μm [7]) and the absence of multiple elastic and muscular layers allows diffusion of oxygen and nutrients to the surrounding tissue. The endothelium forms a continuous layer of ECs that provides a tight (endothelial) barrier composed of densely packed interacting cell-junction proteins that provides the connection between individual ECs. This barrier is maintained by pericytes that provide essential biological signals to the endothelium and together with the ECs create a suitable ECM environment to preserve vessel stability. Fluids and small solutes are able to pass through via this endothelial barrier via the cell junctions (paracellular permeability) and is actively adapted to changing conditions [8,9]. Similarly circulating cells can transmigrate by loosening EC contacts and interact with these junction proteins for para-vascular immune surveillance and repair [10]. In contrast, macro molecules (e.g. lipids) pass through the endothelial barrier by transcytosis, a process that requires receptor binding and trafficking of these molecules in vesicles across the endothelium (transcellular permeability) [11]. The endothelium in more specialized tissue such as the kidney and liver contains fenestrae and sinusoids, respectively. These intracellular pores enable the more efficient exchange of endocrine solutes and water [12]. Transition from capillaries into post-capillary venules and veins is marked with a gradual return of the tunica media and tunica adventitia. Veins in the lower limbs of the body contains additional uni-directional valves to prevent the accumulation of blood due to the low blood flow [5].

The general structure of vessel segments in the vascular tree is thus composed of (1) a layer of ECs, (2) supporting mural cells (either pericytes or SMC) and (3) additional ECM components. Due to the essential functions performed by blood vessels in the human body, the biological pathways that control vascular response in both health and disease has been widely studied.

Key molecular mechanisms of vascular development

New blood vessels develop through two different process, vasculogenesis and angiogenesis. *De novo* blood vessel formation by vasculogenesis is mostly restricted to embryonic development. Mesodermal derived endothelial precursor cells (angioblasts) are activated upon stimulation by the two main drivers of this process; fibroblast growth factor (FGF) and vascular endothelial growth factor (VEGF) [13,14] and form blood islands in collaborations with hematopoietic cells. The fusion of multiple blood islands results in a primary capillary plexus, a pre-mature *de novo* blood vessel [15]. Hypoxia driven angiogenesis then continues to drive the development of a circulatory vascular bed from this primary vascular plexus. Unlike vasculogenesis, angiogenesis occurs both during embryonic development and adulthood, with tissue adaptation and remodeling, wound healing and pathological conditions such as tumor formation as exemplary conditions in which angiogenesis is activated in the adult state [16]. The process can be divided in intussusceptive and sprouting angiogenesis [17,18]. Intussusceptive angiogenesis was first observed in 1986 [19], and is characterized by transluminal pillars that fuse together to form new blood vessels [18]. Changes in hemodynamic forces directly affect this process [18]. The observation of sprouting angiogenesis was first described in tumor development [4,20,21], and the process is defined by the formation of neovessels by the phenotypical adaptation of quiescent ECs into tip and stalk cells. Although complex interactions between pericytes and ECs also occur in vasculogenesis [22], the multiple steps during sprouting angiogenesis are better studied and provide a good understanding of the complex, molecular interactions that are required to achieve the balance between ECs, pericytes and ECM proteins, necessary for neovessel stabilization.

During the sprouting process, previously quiescent blood vessels sense secreted factors such as VEGF and FGF secreted by the surrounding hypoxic tissue. In response, ECs become activated and secrete angiopoietin 2 (Angpt2) and matrix metalloproteinases (MMPs). Pericytes detach from the ECs in response to Angpt2 and the BM is degraded by the MMPs [23,24]. The surrounding ECM environment is further remodeled by MMPs, releasing ECM bound pro-angiogenic factors. Endothelial junctions such as vascular endothelial cadherin (VE-cadherin) are rearranged as a direct result of the VEGF and Notch signaling pathway to

permit migration away from the pre-existing endothelial monolayer [25]. One EC is selected as tip cell and leads the sprout towards the gradient of pro-angiogenic factors via integrin binding to the ECM [26]. Proliferating ECs behind this tip cell, so-called stalk cells, elongate and form a lumen which remains connected to the circulatory vasculature [17,24]. This is followed by blood perfusion and initiation of the biomechanical response mechanisms that aid vascular maturation. In contrast, non-perfused vessels lacking this stimulus fail to maturate and eventually regress [17,27]. Signaling molecules such as platelet derived growth factor B (PDGFB), transforming growth factor β (TGFβ), Notch and Angpt1 promote pericyte coverage of ECs and aid the maturation of the newly formed vessel. The introduction of blood flow and pericyte coverage both stimulate junction formation between ECs and trigger vascular barrier maturation in neovessels [17,24,28]. For example, pericyte derived Angpt1 activates the endothelial tyrosine kinase receptor (Tie2). Via PI3K and Akt, Rac1 GTPase is stimulated. This leads to deactivation of RhoA GTPase and accumulation of VE-cadherin, increasing the endothelial barrier function [28].

Notch, VEGF, Angpt, TGFβ, PDGFB and Wnt signaling pathways orchestrate the communication between tip and stalk cell and EC and pericyte. Interaction between these pathways are pivotal for angiogenesis [24]. For example, Notch ligand DLL4 downregulates VEGF receptor 2 (VEGFR2) but upregulates VEGFR1 (or FLT1) in stalk cells. FLT1 act as VEGF decoy receptor which makes stalk cells less sensitive to sprouting while preserving their capacity for proliferation, elongation and lumen formation [29]. Angpt1 and -2 are both ligands of the Tie2 receptor and act as a signaling pathway with a dual function: Angpt1 stimulates ECs quiescence and pericytes coverage and is thus considered anti-angiogenic whereas Angpt2 antagonizes this function and therefore stimulates angiogenesis [23].

In vivo studies greatly contributed to further unraveling the pivotal role of various signaling pathways in angiogenesis. Endothelial specific PDGFB null mice demonstrated the importance of the PDGF signaling pathway and the essential role of pericytes in capillary stabilization. In PDGFB null mice, newly formed sprouts were unstable and prone to regression and showed microvascular leakage resulting in severe vascular defects in retina, placenta and heart [30,31]. Additionally, both general and endothelial specific Notch1 deficiency in mice results in embryonic lethality marked by vascular defects in the placenta and yolk sac [32,33]. Notch1 deficient ECs form a primary capillary plexus but fail to induce the formation of a mature vascular network [33]. Mouse knockout models of TGFβ [34], TGFβ receptor ALK5 [35] and TGFβ downstream factor Smad5 [36] showed similar vascular defects and are embryonically lethal.

Among the various signaling pathways orchestrating vascular development and growth, signaling of the Wnt pathways in ECs has been demonstrated to be crucial [37]. With a total

of 18 Wnt ligands, 10 Frizzled (Fzd) receptors and multiple co-receptors, this signaling pathway plays a prominent role in embryonic development [38-40]. Wnt ligands bind to transmembrane receptor Fzd, initiating β-catenin dependent (canonical) or β-catenin independent (non-canonical) intracellular signaling. Upon activation of Fzd receptor, intracellular Dishevelled (DVL) is phosphorylated, followed by either canonical β-catenin stabilization, or non-canonical Wnt/Ca^{2+} activation and Wnt/Planar cell polarity (PCP) signaling [41]. Several studies illustrated the pivotal role of Wnt signaling in angiogenesis. Fzd4 knockout mice showed severe vascular defects in the retina hampering the blood retina barrier integrity [42,43]. Furthermore, Fzd4 plays a role in arterial formation and organization via the non-canonical Wnt/PCP pathway, but its contribution is restricted to smaller arteries and do not affect large arteries [44]. Similar, Fzd7 deficient mice show vascular defects in the retina [45]. Fzd7 activated canonical Wnt pathway controls the Notch pathway during postnatal angiogenesis [45]. In contrast, deletion of murine Fzd5 results in embryonic lethality after 10.75 days due to vascular defects in the yolk sac and placenta [46]. A conditional knockout murine model using Sox2-cre to overcome *in utero* lethality, illustrates a key role of Fzd5 in eye development [47]. Furthermore, Fzd5 plays a role in zebrafish eye development via the canonical Wnt11/β-catenin signaling [48]. In contrast, Fzd5 does not seem to regulate the Wnt/β-catenin pathway in murine eye development, suggesting a species dependent function [49]. Activation of the non-canonical Protein Kinase C (PKC) pathway by Fzd5/Wnt5a suggest that the same Fzd receptor can activate different Wnt pathways [49,50]. Recent literature identified multiple variants of Fzd5 involved in ocular coloboma [51], an ocular malformation that is caused by defects during embryogenesis [52]. Fzd5 involvement in vascular and ocular defects in embryogenesis in combination with evidence for Fzd5 mediated endothelial growth [46], suggest that Fzd5 can be an important regulator of angiogenesis. The exact type of Wnt signaling pathway and molecular actions involved requires in depth evaluation. In this thesis, we investigated the mechanisms behind the pro-angiogenic role of Fzd5 (**Chapter 2**).

Key mechanisms that define vascular stability

Vascular stability is determined by the state of the endothelial barrier [53], EC/pericyte interaction and the ECM composition of the BM laid down by this interaction which provide biological cues to the endothelium to maintain this barrier. Cardiovascular diseases can affect vascular stability by pathological remodeling of these vascular components and by obstructing these pathways. In this chapter we delve deeper in the pathways involved in endothelial barrier establishment and maintenance, EC/pericyte interactions and the contribution of ECM to vascular stability.

Mechanisms that define endothelial barrier function

Microvascular leakage is a major vascular complication and is mainly the consequence of impaired pericyte coverage. Matured, quiescent endothelium acquires and maintains a barrier function between the blood circulation and surrounding tissue. Distinct vascular barriers in specific tissues such as the brain, retina and placenta are marked by a high prevalence of pericytes supporting the ECs [54]. Pericyte deficient mice illustrated the essential role of pericytes in blood-brain-barrier (BBB) integrity during embryogenesis and the active regulation of the BBB by this cell type [55,56]. The majority of vascular barrier research focused on the BBB acknowledges the essential role of adherens junctions (AJ), gap junctions (GJ) and tight junctions (TJ) between ECs. Connexin 43 (Cx43) is a GJ present between ECs, which is also present in peg and socket connections between ECs and pericytes and is responsible for para-cellular communication [57]. CX43 deficient mice and mice with diabetes-induced inhibition of CX43 expression exhibit acellular capillaries and vascular cell apoptosis in the retina [58]. TJs may consist of multiple adhesive proteins including claudin, occludin and junctional adhesion molecules, and are intracellularly-linked to the actin cytoskeleton via zonula occludens (ZO-1, -2, -3). AJ proteins such as Neural-cadherin (N-cadherin) and VE-cadherin are essential in barrier integrity regulation and communication, with N-cadherin being a main factor in pericyte/EC interaction that is abundantly present in peg and socket connections [59]. Several factors, including VEGF, induce VE-cadherin phosphorylation and increase vascular permeability. VE-cadherin also interacts with the cytoskeleton and regulates cell polarity. Recent years, endothelial genes cingulin like 1 (CGNL1) and CKLF like MARVEL transmembrane domain containing 3 and -4 (CMTM3 and -4) demonstrated a regulatory role in angiogenesis [60-62]. These molecules mediate vascular barrier integrity and vascular sprouting via VE-cadherin stabilization and VE-cadherin turnover [60-62].

The endothelial barrier is partially altered during leukocyte diapedesis in response to inflammation. Circulating immune cells first encounter the endothelium upon inflammatory activation [10]. Activated ECs in inflamed tissue increase expression of selectins (P- and E-selectin) and adhesion molecules (ICAM and VCAM) in response to pro-inflammatory factors such as tumor necrosis factor α (TNFα) [63]. Ligands such as VLA4 and LFA1 on the leukocyte surface adhere to the endothelium, resulting in leukocyte rolling and crawling to endothelial exit sites. These exit sites are located between ECs, and are marked by the opening of endothelial junctions (including VE-cadherin) in response to activation by leucocytes. Endothelial adhesion molecules cluster at these exit sites and aid in leukocyte diapedesis. As a result, leukocytes can transmigrate the endothelial and cross the pericyte and BM layer to enter the inflamed tissue [10].

Pathways of pericyte and endothelial cell interaction

A common regulator in the previously discussed vascular functions are pericytes. Pericytes are first discovered in 1873 by Benjamin Rouget, and were labelled pericytes by Zimmerman according to their perivascular location [64,65]. Over the last 40 years, researchers slowly elucidated the origin of pericytes and their role regarding the vasculature. The pericyte is defined as a cell embedded within the vascular BM [66]. Multiple molecular markers can be used to identify this cell type, but the majority of markers are also expressed by SMCs and fibroblasts. Although some markers such as PDGFRβ and NG2 are commonly used, a pericyte specific marker does not exists and the combined use of identification markers with the perivascular location is still considered the most optimal way to identify this cell type [54]. Anatomically, pericytes wrap their cell bodies perpendicularly around the endothelium. Since pericytes contain a lot of cytoplasm, one pericyte can cover and interact with multiple ECs although this is tissue specific. For example in skeletal muscle, a single pericyte can be in contact and support up to 100 ECs, whereas pericytes in the brain or retina are more abundantly present, and multiple pericytes can cover one capillary in a ratio of 1:1-3 (pericyte: EC) [54,67]. Overall pericyte density correlates positively with barrier formation, EC turnover, and blood pressure [54,67]. In addition to their critical role in vascular development and vascular barrier maintenance by stimulating EC junctions, additional functions can be assigned to this cell type. For example, although leukocyte diapedesis is mostly described as a complex interaction between leukocytes and EC, pericytes can also aid in this process [68,69]. NG2 positive pericytes can attract circulating leukocytes via ICAM1 and chemoattractant MIF in response to inflammatory cues [69]. Furthermore, similarly to SMC and other cells of the mesenchymal lineage, pericytes have the ability to contract via proteins such as desmin and vimentin. In combination with the pericyte's perpendicular orientation around blood vessels and their presence at locations of transition from arterioles to capillaries, these findings indicate that pericytes can act as important regulator of microvascular flow by operating as pre-capillary sphincters [66,70-72].

Multiple studies have so far indicated that pericyte dysfunction plays a major role in the onset and progression of vascular related diseases. For example, studies have demonstrated a role for pericytes in renal capillary rarefaction and proximal tubule injury [73]. At the same time, pericytes have also been identified as a putative pool of mesenchymal stem cells (MSCs) [74] and may be used as therapeutic strategy in regenerative medicine. The field of pericyte research is rapidly evolving, and in recent years, new discoveries have greatly improved our understanding of the role of pericytes in disease onset and progression as well as deepened our perception of their therapeutic potential. In **Chapter 3,** the contribution of pericytes in health and disease are reviewed. **Chapter 3** emphasizes the role of pericytes in diabetic

retinopathy and the loss of pericyte/EC crosstalk in the breakdown of the BBB. Furthermore, we explore pericyte dysfunction as a driver of fibrosis with emphasize on chronic kidney disease (CKD). We also discuss pericyte use in future cell-based regenerative strategies. Combined, **chapter 3** lists our current knowledge about this versatile cell type, offering a more in-depth understanding of pericytes and their potential.

Both pericytes and endothelium are essential in angiogenesis and capillary homeostasis, and a well-orchestrated cross talk between these two cell types is vital for neovessel growth and survival. To elucidate their interaction, **Chapter 4** describes the adaptation in the pericyte transcriptome in absence or presence of microvascular ECs. Transcriptomic analysis of pericytes in presence or absence of microvascular endothelium demonstrate pericyte upregulation of *Gli1* mRNA compared to pericytes co-cultured with microvascular ECs [75]. Gli1 positive pericytes are described to detach from renal capillaries after acute kidney injury, resulting is loss of vascular support by these pericytes resulting in capillary rarefaction [73]. Furthermore, Gli1 positive MSCs play a role in bone marrow fibrosis, suggesting a pivotal role of hedgehog Gli1 signaling in fibrosis [76]. Since pericytes cultured in the presence of ECs express less *Gli1* mRNA in our transcriptome analysis, these findings imply that pericytes in close contact with ECs are more mature associate Gli1 expression to a more progenitor like pericyte population [75].

Contribution of the extracellular matrix on the stability of the (micro)vasculature and impact of cardiovascular disease

The ECM is secreted by all cells and provides tissue strength and support for cell anchorage. It consists of 2 forms; (i) BM and (ii) interstitial matrix [77,78]. The BM separates endothelium and epithelial cells from stroma and is produced by all cell types involved. Interstitial matrix is primarily produced by stromal cells and is less compact and more porous compared to the BM [79]. ECM can be divided in multiple subclasses; (i) glycoproteins, (ii) proteoglycans (including glycosaminoglycans; GAGs) and (iii) more fibrous proteins like collagens and elastin. ECM binding proteins such as ECM regulators and secreted factors are key for ECM homeostasis and are therefore also classified as ECM proteins [80-83]. Cells can both use the ECM as a migration barrier or as a migration track and provide anchorage points for cell type specific integrins, contributing to the physical stability of cells and tissues [79]. A fully functional ECM also contains biochemical properties. ECM fibers act as a growth factor and chemokine reservoir by binding, for example, TGFβ. Cell secreted TGFβ binds to latent transforming growth factor binding proteins (LTBPs) and latency associated peptide (LAP), creating a larger protein complex which requires disruption for TGFβ activation [84]. Multiple

ECM components are involved in the bioavailability and storage of TGFβ including LTBPs, fibrillins (FBNs) and elastin microfibril interface proteins (EMILINs), emphasizing the complex, highly orchestrated and dynamic function of the ECM.

ECM also directly influence cell behavior as seen in blood vessel formation. During normal blood vessel homeostasis, ECs and pericytes are embedded in laminin rich BM. After BM disruption in response to pro-angiogenic signal, ECs are exposed to the collagen type I rich interstitial matrix. Microvascular ECs cultured on collagen type I ECM showed increased Src and Rho activity leading to disrupted VE-cadherin junctions and increased stress fibers resulting in morphological adaptation of ECs such as network formation [85,86]. Pericyte recruitment to the new capillary sprouts leads to secretion and local accumulation of ECM components including laminin isoforms [87]. After the BM is established, maturation of the newly formed vessels occurs and ECs shift their phenotype away from active sprouting and angiogenesis towards quiescence and barrier function maintenance. Microvascular ECs cultured on laminin-111 ECM do not activate Src and Rho and trigger no morphological adaptation in ECs [85], highlighting the important role of different ECM proteins in blood vessel homeostasis [86].

Integrin binding to ECM substrates in ECs triggers recruitment of multi-protein complexes under the membrane called focal adhesions (FA) consisting of paxillin, vinculin and talin. The precise composition of these integrins and FA complexes, is highly variable and dependent on the type of ECM. FAs are attached to actin fibers and signal to the nucleus via activated Rho GTPases. This is a classic example of outside-in signaling, a cascade of actions from integrins via downstream kinases and actin cytoskeleton to the nucleus. Vice versa, inside-out signaling occurs when intracellular signals are transmitted to the outside of the cells and influence the affinity of integrins resulting in regulation of integrin adhesion [88].

Using integrin signaling, cells are able to sense the different forces in the ECM and tissue and respond accordingly to the mechanical ques, a process known as mechano-sensing. ECM stiffness can regulate cell fate on gene expression regulatory level. For example, different ECM elasticities can direct MSC differentiation toward different lineages [89]. Epithelial cells and SMC cultured on ECM coated acrylamide gels with different elastic moduli, have an increased cyclin D expression, suggesting a role of matrix stiffness in cell proliferation [90]. Furthermore, SMC increase FA formation and actin stress fibers when cultured on stiff matrices, suggesting that ECM properties can influence e.g. SMC cell migration by affecting Rho GTPase mediated contractility [91].

Although only a few examples were highlighted, the influence of the complex and dynamic ECM on vascular cell migration, proliferation, adhesion and fate in embryonic development is

widely acknowledged. The importance of this ECM vascular cell interaction is further highlighted in developmental disorders and progressive fibrosis where the balance of ECM composition is shifted towards a pathological phenotype.

For example, elastic protein FBN1 is widely distributed in the human embryo [92]. Point mutations in FBN1 results in Marfan syndrome (MFS), an inherited disorder of connective tissue [93]. Mice studies with a heterozygous FBN1 mutations showed accelerated vascular ageing and leads to aortic manifestations resembling MFS [94]. Elastic protein EMILIN1 contains a specific domain for integrin adhesion and is therefore important for cell-ECM interaction [95]. EMILIN1 deficient mice demonstrate aortic valve abnormalities and structural and functional defects in the lymph vasculature [96,97]. Proteomic analysis of aortic valves from EMILIN1 deficient aged mice further showed a decrease in LTBP3 and fibulin 5 levels, both proteins known to interact with TGFβ [98]. These data suggest that EMILIN1-TGFβ interactions influence multiple ECM proteins and protein network and may contribute to aortic valve disease progression.
In this thesis we demonstrate that elastic proteins EMILIN1 and FBN1 are prominent proteins in both renal and vascular tissue during development. **Chapter 5** (kidney) and **Chapter 6** (renal arteries) provide a human ECM catalogue of proteins in a quiescent, mature state versus an active, development state and investigate their roles in renal epithelial and EC fate [99,100].
Previous examples demonstrate the delicate balance in vascular cell response that is defined by the ECM composition and elucidates the critical function of specific ECM proteins. In disease conditions where ECM turnover is affected, excess deposition and accumulation of ECM proteins, leads to progressive fibrosis and could lead to loss of organ function. Focusing on only cardiac and renal fibrosis, different subtypes can be identified. Cardiac fibrosis can be divided in three classes based on their etiology; i) reactive, interstitial fibrosis, ii) replacement or scarring fibrosis, and iii) infiltrative interstitial fibrosis [101]. Renal fibrosis can be divided in three types, including tubulointerstitial, glomerulosclerosis and the vasculature fibrosis [102,103]. During fibrosis, activated myofibroblasts mainly secrete collagen type I and III, two fibrillar collagen types that are abundantly present in interstitial tissue [77]. The origin of myofibroblasts is not clear since multiple studies identified different cell types as myofibroblasts source. Mack *et al.* provided an overview of myofibroblast sources and their contribution to renal fibrosis [104]. They demonstrated, using lineage tracing experiments, that resident fibroblast and pericyte contribute to the majority of myofibroblasts [104-106]. As described earlier, Gli1+ pericytes also contribute to renal and bone marrow fibrosis [73,76]. Myofibroblasts can also emerge from ECs via endothelial to mesenchymal transition

(EndoMT) in both renal and cardiac fibrosis [107,108]. This suggests that there is not one specific myofibroblast progenitor cell, possibly due to a large variations in local triggers that could induce fibrosis. Indeed, the list of fibrotic triggers is extensive and the composition of these depends on each specific disease etiology. However, members of the TGFβ superfamily have often shown to take central stage, including in cardiac and renal fibrosis, as critical molecular regulators of e.g. myofibroblast activation [109-111].

The ECM of the basement membrane experiences constant remodeling of its fibrous network. As observed in angiogenesis, breakdown of the interstitial ECM by MMPs is essential for tip cell migration. MMPs and their antagonists, the tissue inhibitors of metalloproteinases (TIMP), are the main proteases responsible for ECM turnover [112]. Multiple MMPs are identified and can be subdivided in multiple classes, including membrane bound MMPs, gelatinases and collagenases, all responsible for degradation of specific ECM substrates. Since fibrosis is seen as the disbalance between ECM deposition (collagen type I accumulation) and ECM degradation (MMP activity), it has been hypothesized that MMP levels should be low in pro-fibrotic conditions. However, MMPs have been observed to be highly expressed in multiple forms of fibrosis, postulating a key role in its pathophysiology [113]. MMPs have both a stimulatory and inhibiting role in fibrogenesis [114]. This can be further elucidated by the fibrotic response observed in for example, myocardial infarction (MI). In the immediate response to the ischemic myocardium, the ECM is degraded and fiber cross-linking is reduced. The degraded ECM allows infiltration of inflammatory cell, which also produce MMPs [112,115]. This results in proliferation and maturation of (myo)fibroblasts and the subsequent excess accumulation of ECM proteins [112]. Although MMPs and TIMPs are tightly regulated at the site of proteolytic targets [116] and local protein levels may deviate from the concentrations at a systemic level, MMP and TIMP plasma protein levels are widely used as biomarkers for cardiac and renal fibrosis progression. TIMP1 plasma levels have shown to be predictive of left ventricle (LV) dysfunction [117]. Multiple TIMPs and MMPs are described useful fibrotic biomarkers in patients with heart failure [112,118-120], lung fibrosis [113,121] and CKD [122]. However, systemic MMP and TIMP plasma levels may fail to resemble the physical, dynamic levels in the affected tissue. In line with other cardiac pathologies, left ventricle diastolic dysfunction (LVDD) is characterized with progressive fibrosis, suggesting a prominent role for MMPs and TIMPs. The pathophysiology of LVDD and the relation with heart failure with preserved ejection fraction (HFpEF) will be further elucidated in the next paragraph. Since LVDD and HFpEF are increasingly recognized as a major cardiac pathology, MMP and TIMP dynamics could provide a potential prognostic tool. In **Chapter 7** we conducted a meta-analysis to investigate cardiac MMP and TIMP levels in different LVDD and HFpEF animals models. This systematic review provides a critical overview of the published

data concerning cardiac ECM dynamics and can be further used to critically evaluate MMPs and TIMPs as prognostic markers for diastolic dysfunction.

Impact of heart failure with preserved ejection fraction on the stability of the cardiac vasculature

LVDD is the result of impaired relaxation of the LV and increased chamber stiffness [123]. LVDD can remain latent or be accompanied by heart failure (HF) symptoms and result in heart failure with preserved ejection fraction (HFpEF) [124]. Worldwide, there are 26 million HF patients defining HF as a global pandemic [125]. Approximately 5.8 million HF patients are registered in America and these numbers will increase to an estimated 8.4 million HF patients in 2030 [126]. The prevalence of HFpEF is around 50% of all HF patients [127-129], with a two-times higher prevalence in women [130,131]. The current paradigm of HFpEF, as stated by Paulus and Tschöpe, describes HFpEF as a systemic disease with multiple co-morbidities leading to diastolic dysfunction and renal dysfunction with microvascular dysfunction playing a central role [132]. A combination of metabolic co-morbidities, such as obesity, and hypertension affect both the heart and kidney and are considered causative factors in the so-called cardio-renal metabolic syndrome (CRMS) [133]. These co-morbidities contribute to a systemic pro-inflammatory state resulting in chronic inflamed coronary microvascular endothelium, and microvascular dysfunction [134]. This subsequently results in reduced endothelial derived nitric oxide bioavailability and protein kinase G (PKG) activity in cardiomyocytes. Low PKG levels lead to cardiac hypertrophy due to hypo-phosphorylated titin in cardiomyocytes. Increase in stiffness in cardiomyocytes and interstitial fibrosis further contribute to diastolic LV stiffness, dysfunction and subsequently heart failure development [132]. Moreover, CKD plays a key role in the development of HFpEF [135,136]. Renal dysfunction leads to an activated systemic inflammatory state via a disbalance in circulating factors including uremic toxins [137]. This also leads to microvascular dysfunction and subsequent cardiomyocyte stiffening and interstitial fibrosis, underlining the important renal-cardiac connection in heart failure [135].

The distinct pathophysiological differences between HFpEF and heart failure with reduced ejection fraction (HFrEF) require a different therapeutic approach [138]. Known therapeutic strategies such as angiotensin-converting enzyme inhibitors and β-blockers that are beneficial for HFrEF patients fail to be efficient for HFpEF patients [139], who are currently only treated for their underlying co-morbidities. A better understanding of cell-cell and cell-ECM interaction in HFpEF patients would aid in improving potential diagnostic and therapeutic strategies. Animal models provide an ideal alternative for adequately controlled studies focusing on (multiple) co-morbidities associated with HFpEF provided that they are well validated. Animal

models should mimic clinical relevant characteristics and preferably develop HFpEF spontaneously without surgical interventions. In **chapter 8** we present a rodent model of CRMS sharing characteristics with human HFpEF patients. These obese diabetic Zucker fatty/Spontaneously hypertensive (ZSF1) rats have multiple metabolic risk factors and can be studied during early onset of the disease as well as disease progression. Furthermore, ZSF1 rats demonstrate renal and cardiac microvascular fibrotic responses. Further studies using this ZSF1 obese rat model will enhance our understanding of CRMS/HFpEF disease onset and progression.

Current vascular clinical applications

Intervention in angiogenic pathways can be used as a strategy to restrain the progression of several types of diseases in which excessive vascularization contribute the pathogenesis. There are important advances made over the last decades in anti-angiogenic therapies targeting mainly cancer and ocular disease [140]. Whereas anti-angiogenic therapeutics targeting of the VEGF pathway have shown in multiple studies to repress abnormal tumor angiogenesis, the use of more sophisticated combination therapies are more recently investigated to shift the abnormal tumor vasculature to a more normalized vascular bed to improve the targeting of cancer cells [141,142]. On the hand, the use of pro-angiogenic factors in clinical trials were applied in the late 90's of the last century. Most applications focused on the use of FGF2 and VEGF as a therapy to reduce loss of cardiac microvasculature at infarct border sites to alleviate damage by myocardial ischemia and restore perfusion in coronary artery disease [143-147]. Recently the Angpt-Tie pathway emerged as a promising vascular therapy target in diverse pathologies. Several compounds that target Angpt2 or Tie2 by inhibiting their function have already used in clinical phase I and II trials and show promising results [148]. Although the use of Angpt1 protein as a drug target seems to be effective in preclinical trials, clinical use of Angpt1 mimetics needs more investigation [148]. Current development of drugs targeting the Angpt-Tie pathway mainly focused on inhibiting the function of Angpt2. However, as the balance in Angpt2/Angpt1 ratio greatly impact vascular stability, targeting the Angpt1-Tie2 pathway has also been suggested to be a relevant strategy for vascular restoration after (ischemic) disease [148]. Despite these developments, identification of new therapeutic targets could further advance these efforts.

Although pharmaceutical induction of *in situ* vascular restoration of the compromised vascular bed is highly feasible for the microvasculature, *in situ* restoration is far more difficult to achieve for macrovessels. For patients with CAD or CKD patients that require vascular access for hemodialysis, macrovascular replacement by surgery using either fully synthetic polymer

based scaffold grafts or by scaffold grafts that are either cellularized *ex vivo* or *in* situ (also known as tissue engineered vascular grafts (TEVGs), are considered a more feasible approach. In recent years, great progress has been made in creating complex TEVGs due to the recent innovations in the field of tissue engineering and regenerative medicine [149,150]. On the other hand, acellular synthetic scaffold that are biofunctionalized with vascular cell-derived ECM from Humacyte showed promising results in clinical trials to improve vascular access for hemodialysis patients [151] and peripheral arterial disease [152]. Moreover, *in situ* endogenous vascular tissue formation in bioabsorbable scaffold grafts was observed in clinical trials two years after implantation [153]. Compared to the *in situ* approach of implanting bare scaffolds for local cell recruitment, TEVGs has its limitations regarding the use of additional cells and growth factors in addition to the time consuming process of *ex vivo* tissue culture [154]. Nevertheless, it provides a more controlled environment to guide the growth and morphology of the generated vascular tissue. For both the *in situ* and *ex vivo* cellularization approach, a more in depth understanding of the required ECM environment, is critical for successful vascular tissue growth.

Advanced human microvasculature models based on incorporation of multiple vascular compartments and flow perfusion

The molecular mechanisms that regulate vascular behavior are extremely complex. To improve the translation of *in vitro* and *in vivo* findings towards clinical implementation, this complexity needs to be incorporated in the study design. Animal models offer a complete vascular circulation that can be combined with (systematic) disease conditions, but often lack the direct relevance to the human condition that is provided by the study of human cells. Currently, many research groups focus on designing assays that mimic the complex human vasculature *in vitro* to study vascular biology in both healthy and diseased conditions. In contrast to traditional 2D cell culture, microfluidic approaches and on-a-chip models offer the possibility to study the vascular response to flow-induced mechanical stimulation. Novel technologies and applications of material such as soft lithography and bioprinting have facilitated the development of such perfused *in vitro* models. To mimic the native complex microvascular bed and increase vascular stability in these systems, pericytes are critical to incorporate. Multiple studies confirmed the beneficial role of pericytes in reducing the vascular permeability using several advanced vascular microfluidic models. In particular, spatiotemporal quantification or observations of dextran diffusion support the constructive role of pericyte in endothelial barrier function and thus (micro)vascular stability [155-159].

Moreover, the BM should be incorporated to provide biochemical and biomechanical vascular stabilizing cues to the cells. This can be achieved by using ECM based hydrogels loaded with

vital BM components or by creating an environment to induce BM secretion by the incorporated vascular cells. For the latter, co-culture of both ECs and mural cells in vascular microfluidic models have shown to already contribute to the production of BM proteins such as collagen type IV and laminin [156,160]. For the majority of vascular microfluidic device collagen type I gel is used to support their vascular structures, with differences in approaches in which the channel fully is completely encased by collagen [157,160,161] or is partially in contact with collagen, with the rest of the endothelium growing on top of a plastic or an elastic surface [155,156,162].

In addition to BM stimulation, perfusion of the artificial blood vessel(s) is also important for many critical vascular regulatory mechanisms, such as e.g. pathways that stimulate strengthening of cell-cell junction and thus improves the vascular barrier property [163,164]. The effect of biomechanical cues provided to the vascular cells, including as shear stress, strain, (ECM) stiffness and the effect of geometry can all be assessed using microfluidic models [165]. Perfusion of an artificial endothelial channel also allows circulating cells to interact with the vascular wall. For example, many previous studies used vascular microfluidic devices to study cancer metastasis or leukocyte transmigration across the vascular wall in response to inflammation [166-171].

The infinite possibility in further adapting microfluidic design can be used to mimic (part of) complex tissues to study their interaction with the vasculature, thus creating vascularized organ-on-a-chip models. For example, structures such as the BBB can be studied using microfluidics as well as complex vascular interactions with organ cells, such as the interaction between epithelial cells from the intestine or kidney and the vasculature [162,172-174]. Production of microfluidic devices for high throughput studies have resulted in successful companies such as AIM Biotech and Mimetas [155,167]. However, although many studies successfully created interesting models for vasculature/vascularized organ-on-a-chip solutions, many of these still fail to fully capture the high complexity of the native situation. In particular, the design of a vascular model that can incorporate the correct dimensions, mechanical cues and ECM components in combination with culturing multiple vascular cell types has thus far remained a considerable challenge. In **chapter 9** we describe the design and validation of a novel human vascular microfluidic device that attempt to create a more advanced perfused vessel on a chip device. The easily fabricated device offer live fluorescent cell imaging over time, and offers multiple endothelial neovessels on one chip with pericytes support in a full 3D ECM matrix that can be subjected to hemodynamic stimulation with circulating immune cells. This unique in house developed system shall provide a useful platform to study vascular response to e.g. inflammation and pathological changes in mechanical cues in a highly controlled manner.

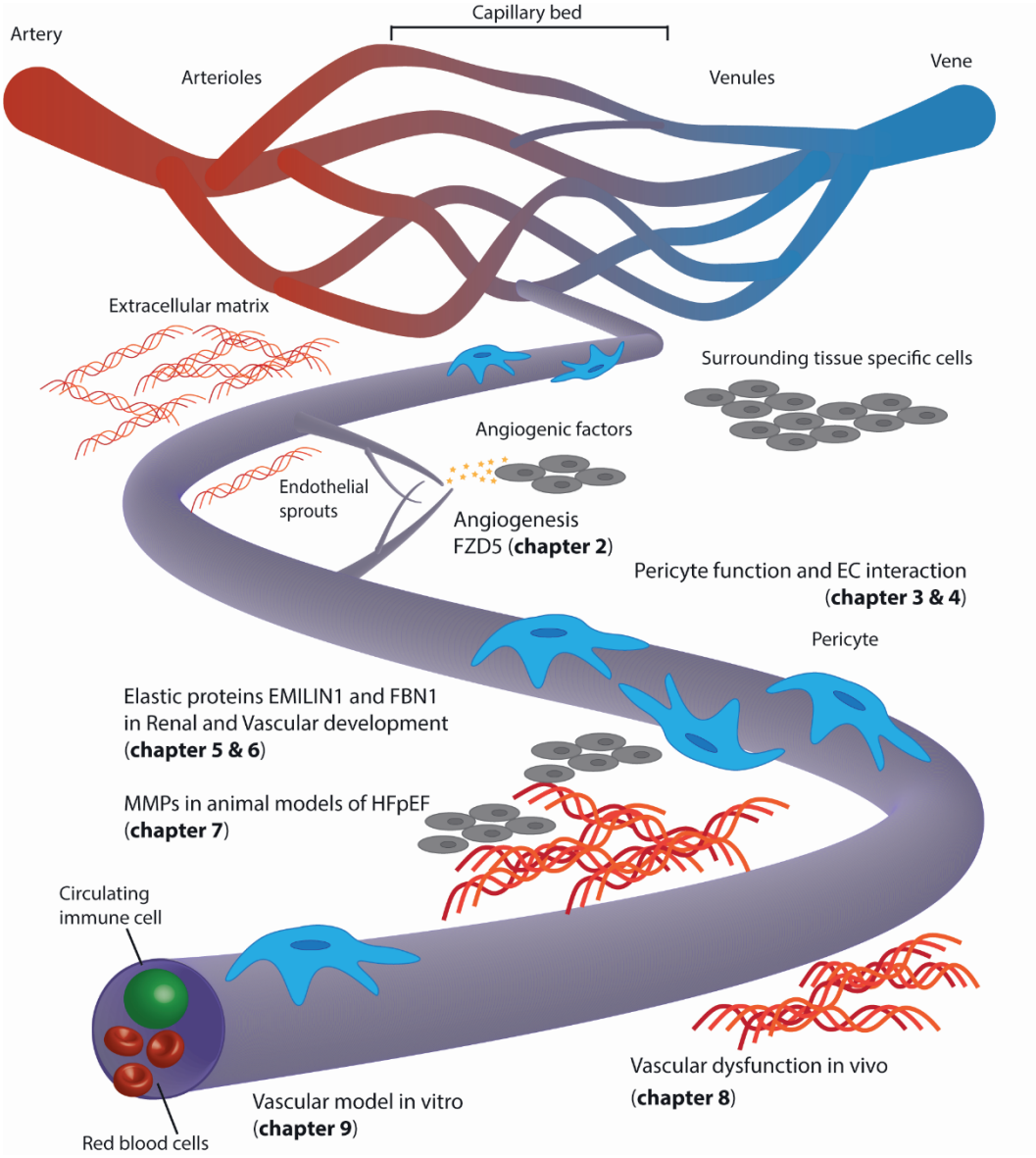

Figure 1. Schematic overview of the vasculature and the chapters described in this thesis.

Thesis outline

Regenerative applications such as tissue engineering rely on a functional, circulatory vascular system to provide sufficient nutrient and oxygen to cells. However, the vasculature is a very complex system with multiple cell types that interact with the surrounding tissue, and responds to prevalent biomechanical forces and the ECM (Figure 1). **The aim of this thesis is to study vascular cell interactions with their environment, in particular the ECM, in development, regeneration, and response to disease.** A better understanding of EC/pericyte interaction and vascular cell/ECM interactions in development, health and disease is essential to develop better in vitro models that mimic the vasculature for human vessel-on-a-chip studies and will provide new leads for vascular regenerative strategies. **Chapter 1** introduced some of the complex mechanisms of ECs and pericytes interaction and touched upon the essential role of ECM, the contribution of microvascular dysfunction in disease and provided a brief introduction into human *in vitro* vascular models.

In **Chapter 2**, we further describe the pro-angiogenic role of FZD5. This endothelial receptor of the Wnt pathway is involved in endothelial tubule formation, cell cycle progression and migration. Endothelial loss of FZD5 results in transcription of Angpt2 and VEGFR1 via PKC/Ets.

In **Chapter 3 and 4** the important roles of pericytes in health and disease are examined. **Chapter 3** touches upon the different functions of pericytes in supporting the microvasculature and the multipotent role in both normal homeostasis and vascular diseases. Furthermore, we elaborate on the use of pericytes as therapeutic target in future cell-based regenerative strategies. In **Chapter 4**, differences in the transcriptome of pericytes cultured in presence and absence of microvascular ECs are analyzed. This transcriptome study reveals the major impact of ECs on pericytes, regulating proliferation, maturation and repression of ECM production.

In **Chapter 5 and 6** we compare the proteome of fetal and mature renal ECM. In **Chapter 5**, samples of healthy human kidney are enriched for ECM proteins and analyzed using LC-MS/MS. Enriched in developing kidneys, EMILIN1 is identified as an important regulator of renal epithelial cell adhesion via a unique *in vitro* assay to assess secreted cell-derived ECM. In **Chapter 6,** using a comparable approach, EMILIN1 and FBN1 are enriched in renal arteries during development and transcriptomic analysis in ECs cultured on EMILIN1 and FBN1 deficient ECM reveals a potential role of these elastic proteins in the endothelial regenerative response.

Chapter 7 describe ECM regulators MMP and TIMP in animal models of diastolic dysfunction. Using a systematic approach, multiple studies of animal diastolic dysfunction with accompanied cardiac fibrosis are reviewed and analyzed for MMP and TIMP levels as dynamic regulators of the ECM.

In **Chapter 8**, the microvascular fibrotic responses in a rat model of HFpEF is described. These ZSF1 obese rats share characteristics with the human cardio-renal metabolic syndrome, a major driver behind HFpEF progression. Both the cardiac and renal microvasculature are hampered in ZSF1 obese rats,

Chapter 9 describes the design and validation of a novel vascular microfluidic device that mimics the complex vasculature. This *in vitro* model enables the co-culture of multiple vascular cells types in a 3D ECM environment while being perfused. The flexibility of this model allows research of specific cell-cell and cell-ECM interactions in a complex *in vitro* system.

To conclude, in **Chapter 10,** we discuss the findings described in this thesis and elaborate on implementing these finding for future regenerative strategies and *in vitro* models.

References

1. Stryker ZI, Rajabi M, Davis PJ, Mousa SA: Evaluation of Angiogenesis Assays. *Biomedicines* **2019,** 7:37
2. Moleiro AF, Conceicao G, Leite-Moreira AF, Rocha-Sousa A: A Critical Analysis of the Available In Vitro and Ex Vivo Methods to Study Retinal Angiogenesis. *J Ophthalmol* **2017,** 2017:3034953
3. Tahergorabi Z, Khazaei M: A Review on Angiogenesis and Its Assays. *Iranian Journal of Basic Medical Sciences* **2011,** 15:1110-1126
4. Carmeliet P, Jain R: Angiogenesis in cancer and other diseases. *Nature* **2000,** 407:249-257
5. Pugsley MK, Tabrizchi R: The vascular system An overview of structure and function. *Journal of Pharmacological and Toxicological Methods* **2000,** 44:333-340
6. Mulligan-Kehoe MJ, Simons M: Vasa vasorum in normal and diseased arteries. *Circulation* **2014,** 129:2557-2566
7. Doerschuk CM, Beyers N, Coxson HO, Wiggs B, Hogg JC: Comparison of neutrophil and capillary diameters and their relation to neutrophil sequestration in the lung. *J Appl Physiol* **1993,** 74:3040-3045
8. Gunzel D, Yu AS: Claudins and the modulation of tight junction permeability. *Physiol Rev* **2013,** 93:525-569
9. Yazdani S, Jaldin-Fincati JR, Pereira RVS, Klip A: Endothelial cell barriers: Transport of molecules between blood and tissues. *Traffic* **2019,** 20:390-403
10. Vestweber D: How leukocytes cross the vascular endothelium. *Nature Reviews* **2015,** 15:692-704
11. Tjakra M, Wang Y, Vania V, Hou Z, Durkan C, Wang N, Wang G: Overview of Crosstalk Between Multiple Factor of Transcytosis in Blood Brain Barrier. *Front Neurosci* **2019,** 13:1436
12. Takakura Y, Mahato RI, Hashida M: Extravasation of macromolecules. *Advanced Drug Delivery Reviews* **1998,** 34:93-108
13. Risau W, Flamme I: Vasculogenesis. *Annu. Rev. Cell Dev. Biol.* **1995,** 11:73-91
14. Poole TJ, Finkelstein EB, Cox CM: The role of FGF and VEGF in angioblast induction and migration during vascular development. *Developmental Dynamics* **2001,** 220:1-17
15. Goldie LC, Nix MK, Hirschi KK: Embryonic vasculogenesis and hematopoietic specification. *Organogenesis* **2008,** 4:257-263
16. Mentzer SJ, Konerding MA: Intussusceptive angiogenesis: expansion and remodeling of microvascular networks. *Angiogenesis* **2014,** 17:499-509
17. Potente M, Gerhardt H, Carmeliet P: Basic and therapeutic aspects of angiogenesis. *Cell* **2011,** 146:873-887
18. Makanya AN, Hlushchuk R, Djonov VG: Intussusceptive angiogenesis and its role in vascular morphogenesis, patterning, and remodeling. *Angiogenesis* **2009,** 12:113-123
19. Caduff JH, Fischer LC, Burri PH: Scanning electron microscope study of the developing microvasculature in the postnatal rat lung. *Anat Rec* **1986,** 216:154-164
20. Goldmann E: The growth of malignant disease in man and the lower animals, with special reference to the vascular system. *Proc R Soc Med* **1908,** 1:1-13
21. Algire GH, Chalkley HW, Earle WE, Legallais FY, Park HD, Shelton E, Schilling EL: Vascular reactions of normal and malignant tissues in vivo. Vascular reactions of mice to fibroblasts treated in vitro with methylcholanthrene. *J Natl Cancer Inst* **1950,** 11:555-580
22. Payne LB, Tewari B, Dunkenberger L, Bond S, Savelli A, Darden J, Zhao H, Powell M, Oestreich K, Sontheimer H, Dal-Pra S, Chappell JC: Pericytes Directly communicate with Emerging Endothelial Cells During Vasculogenesis. **2020,**
23. Augustin HG, Koh GY, Thurston G, Alitalo K: Control of vascular morphogenesis and homeostasis through the angiopoietin-Tie system. *Nat Rev Mol Cell Biol* **2009,** 10:165-177
24. Carmeliet P, Jain RK: Molecular mechanisms and clinical applications of angiogenesis. *Nature* **2011,** 473:298-307
25. Bentley K, Franco CA, Philippides A, Blanco R, Dierkes M, Gebala V, Stanchi F, Jones M, Aspalter IM, Cagna G, Westrom S, Claesson-Welsh L, Vestweber D, Gerhardt H: The role of differential VE-cadherin dynamics in cell rearrangement during angiogenesis. *Nat Cell Biol* **2014,** 16:309-321
26. Gerhardt H: VEGF and endothelial guidance in angiogenic sprouting. *Organogenesis* **2008,** 4:241-246
27. Franco CA, Jones ML, Bernabeu MO, Geudens I, Mathivet T, Rosa A, Lopes FM, Lima AP, Ragab A, Collins RT, Phng LK, Coveney PV, Gerhardt H: Dynamic endothelial cell rearrangements drive developmental vessel regression. *PLoS Biol* **2015,** 13:e1002125

28. Milam KE, Parikh SM: The angiopoietin-Tie2 signaling axis in the vascular leakage of systemic inflammation. *Tissue Barriers* **2015,** 3:e957508
29. Blanco R, Gerhardt H: VEGF and Notch in tip and stalk cell selection. *Cold Spring Harb Perspect Med* **2013,** 3:a006569
30. Bjarnegard M, Enge M, Norlin J, Gustafsdottir S, Fredriksson S, Abramsson A, Takemoto M, Gustafsson E, Fassler R, Betsholtz C: Endothelium-specific ablation of PDGFB leads to pericyte loss and glomerular, cardiac and placental abnormalities. *Development* **2004,** 131:1847-1857
31. Enge M, Bjarnegard M, Gerhardt H, Gustafsson E, Kalen M, Asker N, Hammes HP, Shani M, Fassler R, Betsholtz C: Endothelium-specific platelet-derived growth factor-B ablation mimics diabetic retinopathy. *EMBO Journal* **2002,** 21:4307-4316
32. Swiatek PJ, Lindsell CE, Del Amo FF, Weinmaster G, Gridley T: Notch1 is essential for postimplantation development in mice. *Genes & Development* **1994,** 8:707-719
33. Limbourg FP, Takeshita K, Radtke F, Bronson RT, Chin MT, Liao JK: Essential role of endothelial Notch1 in angiogenesis. *Circulation* **2005,** 111:1826-1832
34. Dickson MC, Martin JS, Cousins FM, Kulkarni AB, Karlsson S, Akhurst RJ: Defective haematopoiesis and vasculogenesis in transforming growth factor B1 knock out mice. *Development* **1995,** 1221:1845-1854
35. Larsson A, Goumans MJ, Jansson Sjostrand L, van Rooijen MA, Ward D, Leveen P, Xu X, Ten Dijke P, Mummery CL, Karlsson S: Abnormal angiogenesis but intact hematopoietic potential in TGF-B type I receptor-deficient mice. *EMBO Journal* **2001,** 20:1663-1673
36. Chang H, Huylebroeck D, Verschueren K, Guo Q, Matzuk M, Zwijsen A: Smad5 knockout mice die at mid-gestation due to multiple embryonic and extraembryonic defect. *Development* **1999,** 126:1631-1642
37. Tsaousi A, Mill C, George SJ: The Wnt pathways in vascular disease: lessons from vascular development. *Curr Opin Lipidol* **2011,** 22:350-357
38. Wiese KE, Nusse R, van Amerongen R: Wnt signalling: conquering complexity. *Development* **2018,** 145:
39. Clevers H: Wnt/beta-catenin signaling in development and disease. *Cell* **2006,** 127:469-480
40. Wang Y, Chang H, Rattner A, Nathans J: Frizzled Receptors in Development and Disease. *Curr Top Dev Biol* **2016,** 117:113-139
41. Niehrs C: The complex world of WNT receptor signalling. *Nat Rev Mol Cell Biol* **2012,** 13:767-779
42. Wang Y, Rattner A, Zhou Y, Williams J, Smallwood PM, Nathans J: Norrin/Frizzled4 signaling in retinal vascular development and blood brain barrier plasticity. *Cell* **2012,** 151:1332-1344
43. Paes KT, Wang E, Henze K, Vogel P, Read R, Suwanichkul A, Kirkpatrick LL, Potter D, Newhouse MM, Rice DS: Frizzled 4 is required for retinal angiogenesis and maintenance of the blood-retina barrier. *Invest Ophthalmol Vis Sci* **2011,** 52:6452-6461
44. Descamps B, Sewduth R, Ferreira Tojais N, Jaspard B, Reynaud A, Sohet F, Lacolley P, Allieres C, Lamaziere JM, Moreau C, Dufourcq P, Couffinhal T, Duplaa C: Frizzled 4 regulates arterial network organization through noncanonical Wnt/planar cell polarity signaling. *Circ Res* **2012,** 110:47-58
45. Peghaire C, Bats ML, Sewduth R, Jeanningros S, Jaspard B, Couffinhal T, Duplaa C, Dufourcq P: Fzd7 (Frizzled-7) Expressed by Endothelial Cells Controls Blood Vessel Formation Through Wnt/beta-Catenin Canonical Signaling. *Arterioscler Thromb Vasc Biol* **2016,** 36:2369-2380
46. Ishikawa TO, Tamai Y, Zorn AM, Yoshida H, Seldin MF, Nishikawa S, Taketo MM: Mouse Wnt receptor gene Fzd5 is essential for yolk sac and placental angiogenesis. *Development* **2001,** 128:22-33
47. Liu C, Nathans J: An essential role for frizzled 5 in mammalian ocular development. *Development* **2008,** 135:3567-3576
48. Cavodeassi F, Carreira-Barbosa F, Young RM, Concha ML, Allende ML, Houart C, Tada M, Wilson SW: Early stages of zebrafish eye formation require the coordinated activity of Wnt11, Fz5, and the Wnt/beta-catenin pathway. *Neuron* **2005,** 47:43-56
49. Burns CJ, Zhang J, Brown EC, Van Bibber AM, Van Es J, Clevers H, Ishikawa TO, Taketo MM, Vetter ML, Fuhrmann S: Investigation of Frizzled-5 during embryonic neural development in mouse. *Dev Dyn* **2008,** 237:1614-1626
50. Weeraratna AT, Jiang Y, Hostetter G, Rosenblatt K, Duray P, Bittner M, Trent JM: Wnt5a signaling directly affects cell motility and invasion of metastatic melanoma. *Cancer Cell* **2002,** 1:279-288
51. Aubert-Mucca M, Pernin-Grandjean J, Marchasson S, Gaston V, Habib C, Meunier I, Sigaudy S, Kaplan J, Roche O, Denis D, Bitoun P, Haye D, Verloes A, Calvas P, Chassaing N,

Plaisancie J: Confirmation of FZD5 implication in a cohort of 50 patients with ocular coloboma. *Eur J Hum Genet* **2020,**

52. Gregory-Evans CY, Williams MJ, Halford S, Gregory-Evans K: Ocular coloboma: a reassessment in the age of molecular neuroscience. *J Med Genet* **2004,** 41:881-891
53. Schwartz MA, Vestweber D, Simons M: A unifying concept in vascular health and disease. *Science* **2018,** 360:270-271
54. Armulik A, Genove G, Betsholtz C: Pericytes: developmental, physiological, and pathological perspectives, problems, and promises. *Dev Cell* **2011,** 21:193-215
55. Armulik A, Genove G, Mae M, Nisancioglu MH, Wallgard E, Niaudet C, He L, Norlin J, Lindblom P, Strittmatter K, Johansson BR, Betsholtz C: Pericytes regulate the blood-brain barrier. *Nature* **2010,** 468:557-561
56. Daneman R, Zhou L, Kebede AA, Barres BA: Pericytes are required for blood-brain barrier integrity during embryogenesis. *Nature Letter Research* **2010,** 468:562-566
57. Okamoto T, Usuda H, Tanaka T, Wada K, Shimaoka M: The Functional Implications of Endothelial Gap Junctions and Cellular Mechanics in Vascular Angiogenesis. *Cancers (Basel)* **2019,** 11:
58. Bobbie MW, Roy S, Trudeau K, Munger SJ, Simon AM, Roy S: Reduced connexin 43 expression and its effect on the development of vascular lesions in retinas of diabetic mice. *Invest Ophthalmol Vis Sci* **2010,** 51:3758-3763
59. Winkler EA, Bell RD, Zlokovic BV: Central nervous system pericytes in health and disease. *Nat Neurosci* **2011,** 14:1398-1405
60. Chrifi I, Hermkens D, Brandt MM, van Dijk CGM, Burgisser PE, Haasdijk R, Pei J, van de Kamp EHM, Zhu C, Blonden L, Kros JM, Duncker DJ, Duckers HJ, Cheng C: Cgnl1, an endothelial junction complex protein, regulates GTPase mediated angiogenesis. *Cardiovasc Res* **2017,** 113:1776-1788
61. Chrifi I, Louzao-Martinez L, Brandt M, van Dijk CGM, Burgisser P, Zhu C, Kros JM, Duncker DJ, Cheng C: CMTM3 (CKLF-Like Marvel Transmembrane Domain 3) Mediates Angiogenesis by Regulating Cell Surface Availability of VE-Cadherin in Endothelial Adherens Junctions. *Arterioscler Thromb Vasc Biol* **2017,** 37:1098-1114
62. Chrifi I, Louzao-Martinez L, Brandt MM, van Dijk CGM, Burgisser PE, Zhu C, Kros JM, Verhaar MC, Duncker DJ, Cheng C: CMTM4 regulates angiogenesis by promoting cell surface recycling of VE-cadherin to endothelial adherens junctions. *Angiogenesis* **2019,** 22:75-93
63. Zhang H, Park Y, Wu J, Chen X, Lee S, Yang J, Dellsperger KC, Zhang C: Role of TNF-alpha in vascular dysfunction. *Clin Sci (Lond)* **2009,** 116:219-230
64. Rouget C: Memoire sur le developement, la structure et les proprietes physiologiques des capillaries sanguins et lymphatiques. *Arch Physiol Norm Path* **1873,** 5:603-663
65. Zimmerman K: Der feinere bau der blutkapillaren. *Z Anat Entwicklungsgesch* **1923,** 68:29-109
66. Hirschi KK, D'Amore PA: Pericytes in the microvasculature. *Cardiovascular Research* **1996,** 32:687-698
67. Sims DE: The pericyte -- a review. *Tissue Cell.* **1986,** 18:153-174
68. Ayres-Sander CE, Lauridsen H, Maier CL, Sava P, Pober JS, Gonzalez AL: Transendothelial migration enables subsequent transmigration of neutrophils through underlying pericytes. *PLoS One* **2013,** 8:e60025
69. Stark K, Eckart A, Haidari S, Tirniceriu A, Lorenz M, von Bruhl ML, Gartner F, Khandoga AG, Legate KR, Pless R, Hepper I, Lauber K, Walzog B, Massberg S: Capillary and arteriolar pericytes attract innate leukocytes exiting through venules and 'instruct' them with pattern-recognition and motility programs. *Nat Immunol* **2013,** 14:41-51
70. Allt G, Lawrenson J: Pericytes: Cell Biology and Pathology. *Cells Tissues Organs* **2001,** 169:1-11
71. Itoh Y, Suzuki N: Control of brain capillary blood flow. *J Cereb Blood Flow Metab* **2012,** 32:1167-1176
72. Grubb S, Cai C, Hald BO, Khennouf L, Murmu RP, Jensen AGK, Fordsmann J, Zambach S, Lauritzen M: Precapillary sphincters maintain perfusion in the cerebral cortex. *Nat Commun* **2020,** 11:395
73. Kramann R, Wongboonsin J, Chang-Panesso M, Machado FG, Humphreys BD: Gli1(+) Pericyte Loss Induces Capillary Rarefaction and Proximal Tubular Injury. *J Am Soc Nephrol* **2017,** 28:776-784
74. Crisan M, Yap S, Casteilla L, Chen CW, Corselli M, Park TS, Andriolo G, Sun B, Zheng B, Zhang L, Norotte C, Teng PN, Traas J, Schugar R, Deasy BM, Badylak S, Buhring HJ, Giacobino JP, Lazzari L, Huard J, Peault B: A perivascular origin for mesenchymal stem cells in multiple human organs. *Cell Stem Cell* **2008,** 3:301-313

75. Brandt MM, van Dijk CGM, Maringanti R, Chrifi I, Kramann R, Verhaar MC, Duncker DJ, Mokry M, Cheng C: Transcriptome analysis reveals microvascular endothelial cell-dependent pericyte differentiation. *Sci Rep* **2019,** 9:15586
76. Schneider RK, Mullally A, Dugourd A, Peisker F, Hoogenboezem R, Van Strien PMH, Bindels EM, Heckl D, Busche G, Fleck D, Muller-Newen G, Wongboonsin J, Ventura Ferreira M, Puelles VG, Saez-Rodriguez J, Ebert BL, Humphreys BD, Kramann R: Gli1(+) Mesenchymal Stromal Cells Are a Key Driver of Bone Marrow Fibrosis and an Important Cellular Therapeutic Target. *Cell Stem Cell* **2017,** 20:785-800 e788
77. Theocharis AD, Skandalis SS, Gialeli C, Karamanos NK: Extracellular matrix structure. *Adv Drug Deliv Rev* **2016,** 97:4-27
78. Marchand M, Monnot C, Muller L, Germain S: Extracellular matrix scaffolding in angiogenesis and capillary homeostasis. *Semin Cell Dev Biol* **2019,** 89:147-156
79. Lu P, Weaver VM, Werb Z: The extracellular matrix: a dynamic niche in cancer progression. *J Cell Biol* **2012,** 196:395-406
80. Hynes RO, Naba A: Overview of the matrisome--an inventory of extracellular matrix constituents and functions. *Cold Spring Harb Perspect Biol* **2012,** 4:a004903
81. Naba A, Clauser KR, Ding H, Whittaker CA, Carr SA, Hynes RO: The extracellular matrix: Tools and insights for the "omics" era. *Matrix Biol* **2016,** 49:10-24
82. Naba A, Clauser KR, Hoersch S, Liu H, Carr SA, Hynes RO: The matrisome: in silico definition and in vivo characterization by proteomics of normal and tumor extracellular matrices. *Mol Cell Proteomics* **2012,** 11:M111 014647
83. Naba A, Hoersch S, Hynes RO: Towards definition of an ECM parts list: an advance on GO categories. *Matrix Biol* **2012,** 31:371-372
84. ten Dijke P, Arthur HM: Extracellular control of TGFbeta signalling in vascular development and disease. *Nat Rev Mol Cell Biol* **2007,** 8:857-869
85. Liu Y, Senger DR: Matrix-specific activation of Src and Rho initiates capillary morphogenesis of endothelial cells. *FASEB J* **2004,** 18:457-468
86. Senger DR, Davis GE: Angiogenesis. *Cold Spring Harb Perspect Biol* **2011,** 3:a005090
87. Stratman AN, Malotte KM, Mahan RD, Davis MJ, Davis GE: Pericyte recruitment during vasculogenic tube assembly stimulates endothelial basement membrane matrix formation. *Blood* **2009,** 114:5091-5101
88. Kim C, Ye F, Ginsberg MH: Regulation of integrin activation. *Annu Rev Cell Dev Biol* **2011,** 27:321-345
89. Engler AJ, Sen S, Sweeney HL, Discher DE: Matrix elasticity directs stem cell lineage specification. *Cell* **2006,** 126:677-689
90. Klein EA, Yin L, Kothapalli D, Castagnino P, Byfield FJ, Xu T, Levental I, Hawthorne E, Janmey PA, Assoian RK: Cell-cycle control by physiological matrix elasticity and in vivo tissue stiffening. *Curr Biol* **2009,** 19:1511-1518
91. Peyton SR, Putnam AJ: Extracellular matrix rigidity governs smooth muscle cell motility in a biphasic fashion. *J Cell Physiol* **2005,** 204:198-209
92. Quandamatteo F, Reinhardt DP, Charbonneau NL, Pophal G, Sakai LY, Herken R: Fibrillin-1 and Fibrillin-2 in human embryonic and early fetal development. *Matrix Biology* **2002,** 21:637-646
93. Sakai LY, Keene DR, Renard M, De Backer J: FBN1: The disease-causing gene for Marfan syndrome and other genetic disorders. *Gene* **2016,** 591:279-291
94. Mariko B, Pezet M, Escoubet B, Bouillot S, Andrieu JP, Starcher B, Quaglino D, Jacob MP, Huber P, Ramirez F, Faury G: Fibrillin-1 genetic deficiency leads to pathological ageing of arteries in mice. *J Pathol* **2011,** 224:33-44
95. Capuano A, Fogolari F, Bucciotti F, Spessotto P, Nicolosi PA, Mucignat MT, Cervi M, Esposito G, Colombatti A, Doliana R: The alpha4beta1/EMILIN1 interaction discloses a novel and unique integrin-ligand type of engagement. *Matrix Biol* **2018,** 66:50-66
96. Danussi C, Spessotto P, Petrucco A, Wassermann B, Sabatelli P, Montesi M, Doliana R, Bressan GM, Colombatti A: Emilin1 deficiency causes structural and functional defects of lymphatic vasculature. *Mol Cell Biol* **2008,** 28:4026-4039
97. Munjal C, Opoka AM, Osinska H, James JF, Bressan GM, Hinton RB: TGF-B mediates early angiogenesis and latent fibrosis in an Emilin1-deficient mouse model of aortic valve disease. *Dis Model Mech* **2014,** 7:987-996
98. Angel PM, Narmoneva DA, Sewell-Loftin MK, Munjal C, Dupuis L, Landis BJ, Jegga A, Kern CB, Merryman WD, Baldwin HS, Bressan GM, Hinton RB: Proteomic Alterations Associated with Biomechanical Dysfunction are Early Processes in the Emilin1 Deficient Mouse Model of Aortic Valve Disease. *Ann Biomed Eng* **2017,** 45:2548-2562

99. Louzao-Martinez L, van Dijk CGM, Xu YJ, Korn A, Bekker NJ, Brouwhuis R, Nicese MN, Demmers JAA, Goumans M-JTH, Masereeuw R, Duncker DJ, Verhaar MC, Cheng C: A proteome comparison between human fetal and mature renal extracellular matrix identifies EMILIN1 as a regulator of renal epithelial cell adhesion. *Matrix Biology Plus* **2019,** 4:
100. van Dijk CGM, Louzao-Martinez L, van Mulligen E, Boermans B, Demmers JAA, van den Bosch TPP, Goumans MJ, Duncker DJ, Verhaar MC, Cheng C: Extracellular Matrix Analysis of Human Renal Arteries in Both Quiescent and Active Vascular State. *Int J Mol Sci* **2020,** 21:
101. Mewton N, Liu CY, Croisille P, Bluemke D, Lima JA: Assessment of myocardial fibrosis with cardiovascular magnetic resonance. *J Am Coll Cardiol* **2011,** 57:891-903
102. Bulow RD, Boor P: Extracellular Matrix in Kidney Fibrosis: More Than Just a Scaffold. *J Histochem Cytochem* **2019,** 67:643-661
103. Genovese F, Manresa AA, Leeming DJ, Karsdal MA, Boor P: The extracellular matrix in the kidney: a source of novel non-invasive biomarkers of kidney fibrosis? *Fibrogenesis & Tissue Repair* **2014,** 7:4
104. Mack M, Yanagita M: Origin of myofibroblasts and cellular events triggering fibrosis. *Kidney Int* **2015,** 87:297-307
105. Humphreys BD, Lin SL, Kobayashi A, Hudson TE, Nowlin BT, Bonventre JV, Valerius MT, McMahon AP, Duffield JS: Fate tracing reveals the pericyte and not epithelial origin of myofibroblasts in kidney fibrosis. *Am J Pathol* **2010,** 176:85-97
106. LeBleu VS, Taduri G, O'Connell J, Teng Y, Cooke VG, Woda C, Sugimoto H, Kalluri R: Origin and function of myofibroblasts in kidney fibrosis. *Nat Med* **2013,** 19:1047-1053
107. Zeisberg EM, Potenta SE, Sugimoto H, Zeisberg M, Kalluri R: Fibroblasts in kidney fibrosis emerge via endothelial-to-mesenchymal transition. *J Am Soc Nephrol* **2008,** 19:2282-2287
108. Zeisberg EM, Tarnavski O, Zeisberg M, Dorfman AL, McMullen JR, Gustafsson E, Chandraker A, Yuan X, Pu WT, Roberts AB, Neilson EG, Sayegh MH, Izumo S, Kalluri R: Endothelial-to-mesenchymal transition contributes to cardiac fibrosis. *Nat Med* **2007,** 13:952-961
109. Chen L, Yang T, Lu DW, Zhao H, Feng YL, Chen H, Chen DQ, Vaziri ND, Zhao YY: Central role of dysregulation of TGF-beta/Smad in CKD progression and potential targets of its treatment. *Biomed Pharmacother* **2018,** 101:670-681
110. Hanna A, Frangogiannis NG: The Role of the TGF-beta Superfamily in Myocardial Infarction. *Front Cardiovasc Med* **2019,** 6:140
111. Wu J, Jackson-Weaver O, Xu J: The TGFbeta superfamily in cardiac dysfunction. *Acta Biochim Biophys Sin (Shanghai)* **2018,** 50:323-335
112. Moore L, Fan D, Basu R, Kandalam V, Kassiri Z: Tissue inhibitor of metalloproteinases (TIMPs) in heart failure. *Heart Failure Reviews* **2011,** 17:693-706
113. Pardo A, Cabrera S, Maldonado M, Selman M: Role of matrix metalloproteinases in the pathogenesis of idiopathic pulmonary fibrosis. *Respir Res* **2016,** 17:23
114. Giannandrea M, Parks WC: Diverse functions of matrix metalloproteinases during fibrosis. *Dis Model Mech* **2014,** 7:193-203
115. Webb CS, Bonnema DD, Ahmed SH, Leonardi AH, McClure CD, Clark LL, Stroud RE, Corn WC, Finklea L, Zile MR, Spinale FG: Specific temporal profile of matrix metalloproteinase release occurs in patients after myocardial infarction: relation to left ventricular remodeling. *Circulation* **2006,** 114:1020-1027
116. Spinale FG: Myocardial matrix remodeling and the matrix metalloproteinases: influence on cardiac form and function. *Physiol Rev* **2007,** 87:1285-1342
117. Lindsay MM, Maxwell P, Dunn FG: TIMP-1: a marker of left ventricular diastolic dysfunction and fibrosis in hypertension. *Hypertension* **2002,** 40:136-141
118. Ngu JM, Teng G, Meijndert HC, Mewhort HE, Turnbull JD, Stetler-Stevenson WG, Fedak PW: Human cardiac fibroblast extracellular matrix remodeling: dual effects of tissue inhibitor of metalloproteinase-2. *Cardiovasc Pathol* **2014,** 23:335-343
119. DeLeon-Pennell KY, Meschiari CA, Jung M, Lindsey ML: Matrix Metalloproteinases in Myocardial Infarction and Heart Failure. *Prog Mol Biol Transl Sci* **2017,** 147:75-100
120. Zachariah JP, Colan SD, Lang P, Triedman JK, Alexander ME, Walsh EP, Berul CI, Cecchin F: Circulating matrix metalloproteinases in adolescents with hypertrophic cardiomyopathy and ventricular arrhythmia. *Circ Heart Fail* **2012,** 5:462-466
121. Corbel M, Boichot E, Lagente V: Role of gelatinases MMP-2 and MMP-9 in tissue remodeling following acute lung injury. *Brazilian Journal of Medical and Biological Research* **2000,** 33:749-754
122. Kobusiak-Prokopowicz M, Krzysztofik J, Kaaz K, Jolda-Mydlowska B, Mysiak A: MMP-2 and TIMP-2 in Patients with Heart Failure and Chronic Kidney Disease. *Open Med (Wars)* **2018,** 13:237-246

123. Nagueh SF, Smiseth OA, Appleton CP, Byrd BF, 3rd, Dokainish H, Edvardsen T, Flachskampf FA, Gillebert TC, Klein AL, Lancellotti P, Marino P, Oh JK, Alexandru Popescu B, Waggoner AD, Houston T, Oslo N, Phoenix A, Nashville T, Hamilton OC, Uppsala S, Ghent, Liege B, Cleveland O, Novara I, Rochester M, Bucharest R, St. Louis M: Recommendations for the Evaluation of Left Ventricular Diastolic Function by Echocardiography: An Update from the American Society of Echocardiography and the European Association of Cardiovascular Imaging. *Eur Heart J Cardiovasc Imaging* **2016,** 17:1321-1360
124. Guan Z, Liu S, Wang Y, Meng P, Zheng X, Jia D, Yang J, Ma C: Left ventricular systolic dysfunction potentially contributes to the symptoms in heart failure with preserved ejection fraction. *Echocardiography* **2019,** 36:1825-1833
125. Ponikowski P, Anker SD, AlHabib KF, Cowie MR, Force TL, Hu S, Jaarsma T, Krum H, Rastogi V, Rohde LE, Samal UC, Shimokawa H, Budi Siswanto B, Sliwa K, Filippatos G: Heart failure: preventing disease and death worldwide. *ESC Heart Fail* **2014,** 1:4-25
126. Heidenreich PA, Albert NM, Allen LA, Bluemke DA, Butler J, Fonarow GC, Ikonomidis JS, Khavjou O, Konstam MA, Maddox TM, Nichol G, Pham M, Pina IL, Trogdon JG, American Heart Association Advocacy Coordinating C, Council on Arteriosclerosis T, Vascular B, Council on Cardiovascular R, Intervention, Council on Clinical C, Council on E, Prevention, Stroke C: Forecasting the impact of heart failure in the United States: a policy statement from the American Heart Association. *Circ Heart Fail* **2013,** 6:606-619
127. Dunlay SM, Roger VL, Redfield MM: Epidemiology of heart failure with preserved ejection fraction. *Nat Rev Cardiol* **2017,** 14:591-602
128. Devereux RB, Roman MJ, Liu JE, Welty TK, Lee ET, Rodeheffer R, Fabsitz RR, Howard BV: Congestive heart failure despite normal left ventricular systolic function in a population-based sample: the strong heart study. *Am J Cardiol* **2000,** 86:1090-1096
129. Sacha Bhatia R, Tu JV, Lee DS, Austin PS, Fang J, Haouzi A, Gong Y, Liu PP: Outcome of heart failure with preserved ejection fraction in a population-based study. *N Engl J Med.* **2006,** 355:260-269
130. Scantlebury DC, Borlaug BA: Why are women more likely than men to develop heart failure with preserved ejection fraction? *Curr Opin Cardiol* **2011,** 26:562-568
131. Dewan P, Rorth R, Raparelli V, Campbell RT, Shen L, Jhund PS, Petrie MC, Anand IS, Carson PE, Desai AS, Granger CB, Kober L, Komajda M, McKelvie RS, O'Meara E, Pfeffer MA, Pitt B, Solomon SD, Swedberg K, Zile MR, McMurray JJV: Sex-related differences in heart failure with preserved ejection fraction. *Circ Heart Fail* **2019,** 12:e006539
132. Paulus WJ, Tschope C: A novel paradigm for heart failure with preserved ejection fraction: comorbidities drive myocardial dysfunction and remodeling through coronary microvascular endothelial inflammation. *J Am Coll Cardiol* **2013,** 62:263-271
133. Whaley-Connell A, Sowers JR: Basic science: Pathophysiology: the cardiorenal metabolic syndrome. *J Am Soc Hypertens* **2014,** 8:604-606
134. Franssen C, Chen S, Unger A, Korkmaz HI, De Keulenaer GW, Tschope C, Leite-Moreira AF, Musters R, Niessen HW, Linke WA, Paulus WJ, Hamdani N: Myocardial Microvascular Inflammatory Endothelial Activation in Heart Failure With Preserved Ejection Fraction. *JACC Heart Fail* **2016,** 4:312-324
135. Ter Maaten JM, Damman K, Verhaar MC, Paulus WJ, Duncker DJ, Cheng C, van Heerebeek L, Hillege HL, Lam CS, Navis G, Voors AA: Connecting heart failure with preserved ejection fraction and renal dysfunction: the role of endothelial dysfunction and inflammation. *Eur J Heart Fail* **2016,** 18:588-598
136. van de Wouw J, Broekhuizen M, Sorop O, Joles JA, Verhaar MC, Duncker DJ, Danser AHJ, Merkus D: Chronic Kidney Disease as a Risk Factor for Heart Failure With Preserved Ejection Fraction: A Focus on Microcirculatory Factors and Therapeutic Targets. *Front Physiol* **2019,** 10:1108
137. Brunet P, Gondouin B, Duval-Sabatier A, Dou L, Cerini C, Dignat-George F, Jourde-Chiche N, Argiles A, Burtey S: Does uremia cause vascular dysfunction? *Kidney Blood Press Res* **2011,** 34:284-290
138. Borlaug BA, Paulus WJ: Heart failure with preserved ejection fraction: pathophysiology, diagnosis, and treatment. *Eur Heart J* **2011,** 32:670-679
139. Henning RJ: Diagnosis and treatment of heart failure with preserved left ventricular ejection fraction. *World J Cardiol* **2020,** 12:7-25
140. Rust R, Gantner C, Schwab ME: Pro- and antiangiogenic therapies: current status and clinical implications. *FASEB J* **2019,** 33:34-48
141. Goel S, Duda DG, Xu L, Munn LL, Boucher Y, Fukumura D, Jain RK: Normalization of the vasculature for treatment of cancer and other diseases. *Physiol Rev* **2011,** 91:1071-1121

142. Jaszai J, Schmidt MHH: Trends and Challenges in Tumor Anti-Angiogenic Therapies. *Cells* **2019,** 8:
143. Ng YS, D'Amore PA: Therapeutic angiogenesis for cardiovascular disease. *Curr Control Trials Cardiovasc Med* **2001,** 2:278-285
144. Schumacher B, Pecher P, von Specht BU, Stegmann T: Induction of neoangiogenesis in ischemic myocardium by human growth factors, first clinical results of a new treatment of coronary heart disease. *Circulation* **1998,** 97:645-650
145. Laham RJ, Rezaee M, Post M, Novicki D, Sellke FW, Pearlman JD, Simons M, Hung D: Intrapericardial delivery of fibroblast growth factor -2 induces neovascularization in a porcine model of chronic myocardial ischemia. *The Journal of Pharmacology and Experimental Therapeutics* **2000,** 202:795-802
146. Losordo DW, Vale PR, Symes JF, Dunnington CH, Esakof DD, Maysky M, Ashare AB, Lathi K, Isner JM: Gene therapy for myocardial angiogenesis, initial clinical results with direct myocardial injection of phVEGF165 as sole therapy for myocardical ischemia. *Circulation* **1998,** 98:2800-2804
147. Rosengart TK, Lee LY, Patel SR, Kligfield PD, Okin PM, Hackett NR, O.W. I, Crystal RG: Six-month assessment of a phase I trial of angiogenic gene therapy for the treatment of coronary artery disease using direct intramyocardial administration of an adenovirus vector expressing the VEGF121 cDNA. *Annals of Surgery* **1999,** 230:466-472
148. Saharinen P, Eklund L, Alitalo K: Therapeutic targeting of the angiopoietin-TIE pathway. *Nat Rev Drug Discov* **2017,** 16:635-661
149. Chandra P, Atala A: Engineering blood vessels and vascularized tissues: technology trends and potential clinical applications. *Clin Sci (Lond)* **2019,** 133:1115-1135
150. Niklason LE, Lawson JH: Bioengineered human blood vessels. *Science* **2020,** 370:
151. Lawson JH, Glickman MH, Ilzecki M, Jakimowicz T, Jaroszynski A, Peden EK, Pilgrim AJ, Prichard HL, Guziewicz M, Przywara S, Szmidt J, Turek J, Witkiewicz W, Zapotoczny N, Zubilewicz T, Niklason LE: Bioengineered human acellular vessels for dialysis access in patients with end-stage renal disease: two phase 2 single-arm trials. *The Lancet* **2016,** 387:2026-2034
152. Gutowski P, Gage SM, Guziewicz M, Ilzecki M, Kazimierczak A, Kirkton RD, Niklason LE, Pilgrim A, Prichard HL, Przywara S, Samad R, Tente B, Turek J, Witkiewicz W, Zapotoczny N, Zubilewicz T, Lawson JH: Arterial reconstruction with human bioengineered acellular blood vessels in patients with peripheral arterial disease. *J Vasc Surg* **2020,** 72:1247-1258
153. Bockeria L, Carrel T, Lemaire A, Makarenko V, Kim A, Shatalov K, Cox M, Svanidze O: Total cavopulmonary connection with a new restorative vascular graft: results at 2 years. *J Thorac Dis* **2020,** 12:4168-4173
154. Ong CS, Zhou X, Huang CY, Fukunishi T, Zhang H, Hibino N: Tissue engineered vascular grafts: current state of the field. *Expert Rev Med Devices* **2017,** 14:383-392
155. van Duinen V, van den Heuvel A, Trietsch SJ, Lanz HL, van Gils JM, van Zonneveld AJ, Vulto P, Hankemeier T: 96 perfusable blood vessels to study vascular permeability in vitro. *Sci Rep* **2017,** 7:18071
156. Yamamoto K, Tanimura K, Watanabe M, Sano H, Uwamori H, Mabuchi Y, Matsuzaki Y, Chung S, Kamm RD, Tanishita K, Sudo R: Construction of Continuous Capillary Networks Stabilized by Pericyte-like Perivascular Cells. *Tissue Eng Part A* **2019,** 25:499-510
157. Alimperti S, Mirabella T, Bajaj V, Polacheck W, Pirone DM, Duffield J, Eyckmans J, Assoian RK, Chen CS: Three-dimensional biomimetic vascular model reveals a RhoA, Rac1, and N-cadherin balance in mural cell-endothelial cell-regulated barrier function. *Proc Natl Acad Sci U S A* **2017,** 114:8758-8763
158. Kim S, Chung M, Ahn J, Lee S, Jeon NL: Interstitial flow regulates the angiogenic response and phenotype of endothelial cells in a 3D culture model. *Lab Chip* **2016,** 16:4189-4199
159. Zheng Y, Chen J, Craven M, Choi NW, Totorica S, Diaz-Santana A, Kermani P, Hempstead B, Fischbach-Teschl C, Lopez JA, Stroock AD: In vitro microvessels for the study of angiogenesis and thrombosis. *Proc Natl Acad Sci U S A* **2012,** 109:9342-9347
160. Kim J, Chung M, Kim S, Jo DH, Kim JH, Jeon NL: Engineering of a Biomimetic Pericyte-Covered 3D Microvascular Network. *PLoS One* **2015,** 10:e0133880
161. Herland A, van der Meer AD, FitzGerald EA, Park TE, Sleeboom JJ, Ingber DE: Distinct Contributions of Astrocytes and Pericytes to Neuroinflammation Identified in a 3D Human Blood-Brain Barrier on a Chip. *PLoS One* **2016,** 11:e0150360
162. Bang S, Lee SR, Ko J, Son K, Tahk D, Ahn J, Im C, Jeon NL: A Low Permeability Microfluidic Blood-Brain Barrier Platform with Direct Contact between Perfusable Vascular Network and Astrocytes. *Sci Rep* **2017,** 7:8083

163. Davies PF, Zilberberg J, Helmke BP: Spatial microstimuli in endothelial mechanosignaling. *Circ Res* **2003,** 92:359-370
164. Lu D, Kassab GS: Role of shear stress and stretch in vascular mechanobiology. *J R Soc Interface* **2011,** 8:1379-1385
165. Gray KM, Stroka KM: Vascular endothelial cell mechanosensing: New insights gained from biomimetic microfluidic models. *Semin Cell Dev Biol* **2017,** 71:106-117
166. Zhang Q, Liu T, Qin J: A microfluidic-based device for study of transendothelial invasion of tumor aggregates in realtime. *Lab Chip* **2012,** 12:2837-2842
167. Zervantonakis IK, Hughes-Alford SK, Charest JL, Condeelis JS, Gertler FB, Kamm RD: Three-dimensional microfluidic model for tumor cell intravasation and endothelial barrier function. *Proc Natl Acad Sci U S A* **2012,** 109:13515-13520
168. Chen MB, Whisler JA, Jeon JS, Kamm RD: Mechanisms of tumor cell extravasation in an in vitro microvascular network platform. *Integr Biol (Camb)* **2013,** 5:1262-1271
169. Edwards EE, Thomas SN: P-Selectin and ICAM-1 synergy in mediating THP-1 monocyte adhesion in hemodynamic flow is length dependent. *Integr Biol (Camb)* **2017,** 9:313-327
170. Wu X, Newbold MA, Haynes CL: Recapitulation of in vivo-like neutrophil transendothelial migration using a microfluidic platform. *Analyst* **2015,** 140:5055-5064
171. Han S, Yan JJ, Shin Y, Jeon JJ, Won J, Jeong HE, Kamm RD, Kim YJ, Chung S: A versatile assay for monitoring in vivo-like transendothelial migration of neutrophils. *Lab Chip* **2012,** 12:3861-3865
172. Kim HJ, Ingber DE: Gut-on-a-Chip microenvironment induces human intestinal cells to undergo villus differentiation. *Integr Biol (Camb)* **2013,** 5:1130-1140
173. Bein A, Shin W, Jalili-Firoozinezhad S, Park MH, Sontheimer-Phelps A, Tovaglieri A, Chalkiadaki A, Kim HJ, Ingber DE: Microfluidic Organ-on-a-Chip Models of Human Intestine. *Cell Mol Gastroenterol Hepatol* **2018,** 5:659-668
174. Campisi M, Shin Y, Osaki T, Hajal C, Chiono V, Kamm RD: 3D self-organized microvascular model of the human blood-brain barrier with endothelial cells, pericytes and astrocytes. *Biomaterials* **2018,** 180:117-129

Chapter 2

Endothelial loss of Fzd5 stimulates PKC/Ets1-mediated transcription of Angpt2 and VEGFR1

Maarten M. Brandt, Christian G.M. van Dijk, Ihsan Chrifi, Heleen M. Kool, Petra Burgisser, Laura Louzao-Martinez, Jiayi Pei, Robbert J. Rottier, Marianne C. Verhaar, Dirk J. Duncker, Caroline Cheng

Angiogenesis, 2018 Nov;21(4):805-821

Abstract

Formation of a functional vascular system is essential and its formation is a highly regulated process initiated during embryogenesis, which continues to play important roles throughout life in both health and disease. In previous studies, Fzd5 was shown to be critically involved in this process and here we investigated the molecular mechanism by which endothelial loss of this receptor attenuates angiogenesis.

Using short interference RNA mediated loss of function assays, the function and mechanism of signaling via Fzd5 was studied in human endothelial cells (ECs). Our findings indicate that Fzd5 signaling promotes neovessel formation *in vitro* in a collagen matrix based 3D co-culture of primary vascular cells. Silencing of Fzd5 reduced EC proliferation, as a result of G_0/G_1 cell cycle arrest, and decreased cell migration. Furthermore, Fzd5 knockdown resulted in enhanced expression of the factors Angpt2 and VEGFR1, which are mainly known for their destabilizing effects on the vasculature. In Fzd5 silenced ECs, Angpt2 and VEGFR1 upregulation was induced by enhanced PKC signaling, without the involvement of canonical Wnt signaling, non-canonical Wnt/Ca^{2+} mediated activation of NFAT, and non-canonical Wnt/PCP mediated activation of JNK. We demonstrated that PKC induced transcription of Angpt2 and VEGFR1 involved the transcription factor Ets1.

The current study demonstrates a pro-angiogenic role of Fzd5, which was shown to be involved in endothelial tubule formation, cell cycle progression and migration, and partly does so by repression of PKC/Ets1 mediated transcription of VEGFR1 and Angt2.

Introduction

New formation of blood vessels from pre-existing vessels, a process called angiogenesis, is a critical step in embryogenesis and continues to play important roles throughout life in both health and disease [1]. It is a dynamic process that is tightly regulated by a diverse range of signal transduction cascades and imbalances in these pathways can be a causative or a progressive factor in many diseases [2].

Multiple studies suggest an important role for endothelial signal transduction via Frizzled (Fzd) receptors in angiogenesis [3-5]. The Fzd receptors belong to a family of 10 transmembrane receptors (Fzd1-10), which can initiate Fzd/Wnt canonical and non-canonical signaling upon binding with one of the 19 soluble Wnt ligands. Canonical Wnt signaling depends on Fzd receptor and LRP 5/6 co-activation, initiating Disheveled (DVL) to stabilize β-catenin, followed by β-catenin-mediated transcriptional regulation [6-8]. In contrast, non-canonical Wnt signaling also involves Dvl, but proceeds via Wnt/Ca^{2+} mediated-activation of Nuclear factor of activated T-cells (NFAT) or Wnt/Planar Cell Polarity (PCP) mediated activation of c-JUN N-terminal Kinase (JNK) [6]. A potential link between Fzd5 and angiogenesis was previously demonstrated in Fzd5 full knockout mice [5]. Fzd5 silencing induced *in utero* death at approximately E10.5, which was associated with vascular defects in the placenta and yolk sac. Furthermore, isolated endothelial cells (ECs) from Fzd5 deficient mice showed a reduction in cell proliferation, which is crucial for neo vessel formation. These findings suggest that Fzd5 can be an important regulator of angiogenesis. However, the exact type of endothelial Fzd5/Wnt signaling and the downstream molecular mechanism causal to the poor vascular phenotype in absence of this receptor requires further in depth evaluation.

Here we studied the angiogenic potential of Fzd5 and investigated the signaling pathways that are mediated by Fzd5/Wnt signaling in human ECs. Our findings indicate that Wnt5a, which is endogenously expressed in ECs, binds and signals via Fzd5, but in absence of this receptor triggers a poor angiogenic phenotype via an alternative signaling route. We demonstrated that Fzd5 is essential for neovessel formation *in vitro* in a collagen matrix based 3D co-culture of primary human vascular cells. Silencing of Fzd5 reduced EC proliferation as a result of G_0/G_1 cell cycle arrest and decreased cell migration capacity. Furthermore, Fzd5 knockdown resulted in enhanced expression of the factors Angiopoietin 2 (Angpt2) and Fms Related Tyrosine Kinase 1 (VEGFR1), which are mainly known for their destabilizing effects on the vasculature [9-11]. In Fzd5 silenced ECs, Angpt2 and VEGFR1 upregulation was induced by enhanced Protein Kinase C (PKC) signaling, without the involvement of canonical Wnt signaling, non-canonical Wnt/Ca^{2+} mediated activation of NFAT, and non-canonical Wnt/PCP mediated activation of JNK. Further downstream, PKC induced transcription of Angpt2 and VEGFR1 involved the transcription factor Protein C-Ets-1 (Ets1), as knockdown of both Fzd5

and Ets1 resulted in a marked repression of Angpt2 and VEGFR1 expression levels. In addition, silencing of Ets1 partially restored the impaired endothelial tubule formation capacity of Fzd5 silenced ECs.

Methods

Cell culture

Human Umbilical Vein Endothelial Cells (HUVECs; Lonza) and Human Brain Vascular Pericytes (Sciencell) were cultured on gelatin coated plates in EGM-2 medium (EBM-2 medium supplemented with EGM-2 bullet kit; Lonza, and 100U/ml penicillin/streptomycin; Lonza) and DMEM (supplemented with 100U/ml penicillin/streptomycin; Lonza, and 10% FCS; Lonza) respectively, in 5% CO_2 at 37 ˚C. The experiments were performed with cells at passage 3-5. Lentivirus green fluorescent protein (GFP) transduced HUVECs and lentivirus discosoma sp. red fluorescent protein (dsRED) transduced pericytes were used at passage 5-7. HUVECs and GFP-labeled HUVECs were used from 6 different batches derived from pooled donors. Pericytes and dsRED-labeled pericytes were used from 8 different batches derived from single donors. Fzd5, Ets1, and Wnt5a knockdown in HUVECs was achieved by cell transfection of a pool containing 4 targeting short interference RNA (siRNA) sequences, whereas PKC isoforms where knocked down with individual siRNA strands (Dharmacon), all in a final concentration of 100nM. Control cells were either untreated or transfected with a pool of 4 non-targeting siRNA sequences (Dharmacon) in a final concentration of 100nM. Target sequences are listed in Table 1. Inhibition of GSK3β, NFAT, JNK, and PKC activation was achieved with 20μM LiCl (Sigma), 1μM Cyclosporine A (CsA; Sigma), 20μM SP600125 (Sigma), and 5, 10 and 20nM staurosporine (CST) respectively. Phosphatase activity was inhibited with 50nM Calyculin A. Free Ca^{2+} induced activation of NFAT-mediated transcription was achieved with 10μM A23187. In experiments involving a serum starvation step, the cells were cultured for 24 hours in EBM-2.

Quantitative PCR and Western blot analysis

Total RNA was isolated using RNA mini kit (Bioline) and reversed transcribed into cDNA using iScript cDNA synthesis kit (Bioline). Gene expression was assessed by qPCR using SensiFast SYBR & Fluorecein kit (Bioline) and primers as listed in Table 2. Expression levels are relative to the housekeeping gene β-actin. For assessment of protein levels, cells were lysed in cold NP-40 lysis buffer (150 mM NaCl, 1.0% NP-40, 50 mM Tris, pH 8.0)

Table 1. siRNA sequences used in cell culture.

Target gene	*Target sequence*
Non-targeting	UGGUUUACAUGUCGACUAA
	UGGUUUACAUGUUGUGUGA
	UGGUUUACAUGUUUUCUGA
	UGGUUUACAUGUUUUCCUA
Fzd5	GCAUUGUGGUGGCCUGCUA
	GCACAUGCCCAACCAGUUC
	AAAUCACGGUGCCCAUGUG
	GAUCCGCAUCGGCAUCUUC
Ets1	AUAGAGAGCUACGAUAGUU
	GAAAUGAUGUCUCAAGCAU
	GUGAAACCAUAUCAAGUUA
	CAGAAUGACUACUUUGCUA
Wnt5a	GCCAAGGGCUCCUACGAGA
	GUUCAGAUGUCAGAAGUAU
	CAUCAAAGAAUGCCAGUAU
	GAAACUGUGCCACUUGUAU
PKCα	UAAGGAACCACAAGCAGUA
PKCδ	CCAUGUAUCCUGAGUGGAA
PKCε	GUGGAGACCUCAUGUUUCA
PKCη	GCACCUGUGUCGUCCAUAA

supplemented with 1 mM β-glycerolphosphate, 1 mM PMSF, 10 mM NaF, 1 mM NaOV, and protease inhibitor cocktail (Roche). Total protein concentration was quantified by Pierce® BCA Protein Assay Kit (Thermo Scientific) as a loading control. Lysates were denaturated in Laemmli buffer (60 mM Tris pH 6.8, 2% SDS, 10% glycerol, 5% β-mercaptoethanol, 0.01% bromophenol blue) at 90°C for 5 min followed by electrophoresis on a 10% SDS-page gel (Biorad). Subsequently, proteins were transferred to a nitrocellulose membrane (Pierce) and incubated for 1 hour in PBS with 5% non-fat milk, followed by incubation with rabbit anti-Fzd5 (Milipore), goat anti-β-actin (Abcam), rabbit anti-β-catenin, anti-non-phospho β-catenin and phospho-β-catenin (CST, validated in Supplemental Figure 3A), rabbit anti-Angpt2 (Abcam), rabbit anti-JNK and phospho-JNK (CST, validated in Supplemental Figure 4C), rabbit anti-JUN and phospho-JUN (CST, validated in Supplemental Figure 4C), rabbit anti-Wnt5a (CST) rabbit anti-Dvl2 (CST) according to manufacturer's description. Protein bands were visualized with the Li-Cor detection system (Westburg). Levels of secreted VEGFR1 in cultured medium were assessed 72 hours post transfection using a VEGFR1 ELISA kit (R&D systems).

Table 2. Primer sequences used for (q)PCR.

Gene	*Sense primer sequence*	*Antisense primer sequence*
Fzd1	GCCCTCCTACCTCAACTACCA	ACTGACCAAATGCCAATCCA
Fzd2	GCTTCCACCTTCTTCACTGTC	GCAGCCCTCCTTCTTGGT
Fzd3	CTTCCCTGTCGTAGGCTGTGT	GGGCTCCTTCAGTTGGTTCT
Fzd4	ATGAACTGACTGGCTTGTGCT	TGTCTTTGTCCCATCCTTTTG
Fzd5	TACCCAGCCTGTCGCTAAAC	AAAACCGTCCAAAGATAAACTGC
Fzd6	GCGGAGTGAAGGAAGGATTAG	TGAACAAGCAGAGATGTGGAA
Fzd7	CGCCTCTGTTCGTCTACCTCT	CTTGGTGCCGTCGTGTTT
Fzd8	GCCTATGGTGAGCGTGTCC	CTGGCTGAAAAAGGGGTTGT
Fzd9	CTGGTGCTGGGCAGTAGTTT	GCCAGAAGTCCATGTTGAGG
Fzd10	CCTTCATCCTCTCGGGCTTC	AGGCGTTCGTAAAAGTAGCAG
Wnt1	CAACAGCAGTGGCCGATGGTGG	CGGCCTGCCTCGTTGTTGTGAAG
Wnt2	GTCATGAACCAGGATGGCACA	TGTGTGCACATCCAGAGCTTC
Wnt2b	AAGATGGTGCCAACTTCACCG	CTGCCTTCTTGGGGGCTTTGC
Wnt3	GAGAGCCTCCCCGTCCACAG	CTGCCAGGAGTGTATTCGCATC
Wnt3a	CAGGAACTACGTGGAGATCATG	CCATCCCACCAAACTCGATGTC
Wnt4	GCTCTGACAACATCGCCTAC	CTTCTCTCCCGCACATCC
Wnt5a	GACCTGGTCTACATCGACCCC	GCAGCACCAGTGGAACTTGCA
Wnt5b	TGAAGGAGAAGTACGACAGC	CTCTTGAACTGGTTGTAGCC
Wnt6	TTATGGACCCTACCAGCAT	ATGTCCTGTTGCAGGATG
Wnt7a	GCCGTTCACGTGGAGCCTGTGCGTGC	AGCATCCTGCCAGGGAGCCCGCAGCT
Wnt7b	GATTCGGCCGCTGGAACTGCTC	TGGCCCACCTCGCGGAACTTAG
Wnt8a	CTGGTCAGTGAACAATTTCC	GTAGCACTTCTCAGCCTGTT
Wnt8b	GTCTTTTCACCTGTGTCCTC	AGGCTGCAGTTTCTAGTCAG
Wnt10a	CTGTTCTTCCTACTGCTGCT	ACACACACCTCCATCTGC
Wnt10b	GCACCACAGCGCCATCCTCAAG	GGGGTCTCGCTCACAGAAGTCAGGA
Wnt11	CACTGAACCAGACGCAACAC	CCTCTCTCCAGGTCAAGCAAA
Wnt14	ACAAGTATGAGACGGCACTC	AGAAGCTAGGCGAGTCATC
Wnt15	TGAAACTGCGCTATGACTC	GTGAGTCCTCCATGTACACC
Wnt16	GAGAGATGGAACTGCATGAT	GATGGGGAAATCTAGGAACT
Axin2	TTGAATGAAGAAGAGGAGTGGA	TCGGGAAATGAGGTAGAGACA
Ccnd1	GTCCATGCGGAAGATCGTCG	TCTCCTTCATCTTAGAGGCCACG
C-myc	CACAGCAAACCTCCTCACAG	CGCCTCTTGACATTCTCCTC
Angpt1	GCTGAACGGTCACACAGAGA	CTTTCCCCCTCAAAGAAAGC
Angpt2	TTATCACAGCACCAGCAAGC	TTCGCGAGAACAAATGTGAG
VEGFa	AAGGAGGAGGGCAGAATCAT	ATCTGCATGGTGATGTTGGA
VEGFR2	AGCGATGGCCTCTTCTGTAA	ACACGACTCCATGTTGGTCA
VEGFR1	TGTCAATGTGAAACCCCAGA	GTCACACCTTGCTCCGGAAT
DSCR1	GAGGACGCATTCCAAATCAT	AGTCCCAAATGTCCTTGTGC

TF	TACTTGGCACGGGTCTTCTC	TGTCCGAGGTTTGTCTCCA
Ets1	GGAGCAGCCAGTCATCTTTC	GGTCCCGCACATAGTCCTT
PKCα	CGACTGGGAAAAACTGGAGA	ACTGGGGGTTGACATACGAG
PKCδ	ATTGCCGACTTTGGGATGT	TGAAGAAGGGGTGGATTTTG
PKCε	AAGCCACCCTTCAAACCAC	GGCATCAGGTCTTCACCAAA
PKCη	TCCCACACAAGTTCAGCATC	CCCAATCCCATTTCCTTCTT
MMP1	GATTCGGGGAGAAGTGATGTT	CGGGTAGAAGGGATTTGTG
β-actin	TCCCTGGAGAAGAGCTACGA	AGCACTGTGTTGGCGTACAG

3D analysis of endothelial tubule formation

Twenty-four hours post siRNA transfection, GFP-labeled HUVECs were harvested and suspended with non-transfected dsRED-labeled pericytes in collagen as previously described by Stratman and colleagues [12]. In summary, HUVECs and pericytes were mixed in a 5:1 ratio in EBM-2 supplemented with Ascorbic Acid, Fibroblast Growth Factor, and 2% FCS from the EGM-2 bullet kit. Additionally, C-X-C motif chemokine 12, Interleukin 3, and Stem Cell Factor were added in a concentration of 800ng/ml (R&D systems). The cell mixture was suspended in bovine collagen (Gibco) with a final concentration of 2mg/ml and pipetted in a 96 wells plate. One hour of incubation in 5% CO_2 at 37 ˚C was followed by the addition of 100 µl of the adjusted EBM-2 medium on the collagen gels. The addition of recombinant human Angpt2 and VEGFR1 (R&D systems) was done 24 hours post seeding in the collagen matrix, both in a final concentration of 1000ng/ml. Forty-eight hours and 120 hours post seeding, these co-cultures were imaged by fluorescence microscopy, followed by analysis of the number of junctions, the number of tubules, and the tubule length using AngioSys. At least 3 technical replicates were averaged per condition per independent replicate.

Migration assay

Twenty-four hours post siRNA transfection, HUVECs were plated at a density of 0.5 x 10^5 cells/well in an Oris™ Universal Cell migration Assembly Kit (Platypus Technologies) derived 96 well plate with cell seeding stoppers. Twenty-four hours post sub culturing, the cell stoppers were removed and cells were allowed to migrate into the cell free region for 16 hours in 5% CO_2 at 37 ˚C. Subsequently, the cells were washed in PBS and stained by Calcein-AM followed by visualization using fluorescence microscopy. Wells in which cell seeding stoppers were not removed were used as a negative control. Results were analyzed by Clemex. At least 3 technical replicates were averaged per condition per independent replicate.

Intracellular immunofluorescent staining

Forty-eight hours post siRNA transfection, HUVECs were seeded on gelatin coated glass coverslips in 12 wells plates at a density of 0.5 x 10^5 cells/well (sub-confluent) and 3.5 x 10^5 cells/well (confluent). Subsequently, cells adhered for 24 hours followed by fixation for 15 min in 4% paraformaldehyde and blocking for 60 min in PBS with 5% bovine serum albumin (Sigma) and 0.3% Triton X-100 (Sigma). After blocking, coverslips were placed on droplets PBS with 1% BSA and 0.3% Triton X-100 containing rabbit anti-β-catenin antibody (CST) for 16 hours in a humidified environment at 4°C. Thereafter, coverslips were incubated on PBS with 1% BSA and 0.3% Triton X-100 containing an Alexa Fluor 594-labeled secondary antibody (Invitrogen) and phalloidin-rhodamin (Invitrogen) for 1 hour at room temperature, finally followed by mounting the stained coverslips on vectashield with DAPI (Brunschwig). Coverslips were imaged by confocal microscopy.

Proliferation, cell cycle assay and apoptosis

Twenty-four hours post siRNA transfection, HUVECs were seeded in 6 wells plates at a density of 0.5 x 10^5 cells/well. To study the effect of Fzd5 knockdown on proliferation, HUVECs were harvested 24 hours, 48 hours, and 72 hours post sub culturing and counted by flow cytometry. For analysis of cell cycle progression, cells were harvested 48h post sub culturing and fixated in 70% ethanol for 60 minutes on ice. Subsequently, cells were stained with PI and treated with RNAse (Sigma) for 30 minutes at 37 ˚C and analyzed by flow cytometry. Apoptosis was studied 72 hours after transfection using an *in situ* cell death detection kit (Roche) as described by manufacturer on 4% PFA fixated cells.

Wnt5a adenovirus preparation, transduction and stimulation

Recombinant adenoviruses were produced using the Gateway pAd/CMV/V5DEST vector and ViraPowerTM Adenoviral Expression System (Invitrogen), according to manufacturer's instructions. Briefly, the Wnt5a expression cassette was cloned from the pENTR^{TM} 221 Wnt5a entry vector (Invitrogen) into pAd/CMV/V5-DEST expression vector (Invitrogen) via the LR-reaction II (Invitrogen). After verification by DNA sequencing, the pAd/CMV plasmids were linearized by Pac1 restriction and subsequently transfected with Lipofectamine 2000 (Invitrogen) in 293A cells. Infected cells were harvested by the time 80% of the cells detached from plates followed by isolation of viral particles from crude viral lysate. HeLa cells were used to produce Wnt5a (or dsRED, referred to as adSHAM) by transduction with a calculated 5 viral particles per cell. Forty-eight hours post transduction, HeLa cells were cultured for 24 hours on EBM-2, which eventually was used to stimulate serum-starved endothelium for 3 hours.

Statistical analysis

For each experiment, N represents the number of independent replicates. Statistical analysis was performed by GraphPad Prism using one-way ANOVA followed by post hoc Tukey's test, unless stated otherwise. Results are expressed as mean ± SEM. Significance was assigned when $P<0.05$ (two-tailed).

Results

Fzd5 siRNA induces a specific knockdown of endothelial Fzd5

The function of Fzd5 was studied *in vitro* using siRNA mediated silencing in HUVECs, which were shown to express all Fzd receptors other than Fzd10 (Supplemental Figure 1A), and Wnt2b, 3, 4, 5a, and 11 (Supplemental Figure 1B). Both qPCR and Western blot analysis confirmed a significant loss of Fzd5 expression in cells treated with an siRNA pool specific for Fzd5, compared to untreated control cells and cells treated with a pool of non-targeting siRNA, referred to as siSHAM (Supplemental Figure 1C,D). Although Fzd receptors share highly similar domains, knockdown of Fzd5 was specific. None of the other Fzd receptors were differentially expressed after treatment with Fzd5 siRNA, other than Fzd5 (Supplemental Figure 1C).

Wnt5a signals via endothelial Fzd5

Previous studies listed Wnt5a and Secreted Frizzled-Related Protein 2 (SFRP2) as most likely candidates to activate Fzd5-mediated signaling in ECs [13-15]. In contrast to SFRP2 [16], Wnt5a is endogenously expressed by HUVECs (Supplemental Figure 1B). To address the potential signal capacities of this endogenously expressed Wnt5a as ligand for Fzd5, HeLa cells were transduced with an adenoviral overexpression plasmid for Wnt5a to produce cultured medium containing high levels of this Wnt ligand. HeLa cells were selected for this purpose over HUVECs as these cells were shown to have a more refined machinery to produce and secrete functional Wnt5a than HUVECs, as illustrated by enhanced mRNA expression of Wntless (WLS) and Porcupine (PORCN) (data not shown). Transduction with this overexpression vector (adWnt5a) led to a significant upregulation of Wnt5a compared to dsRED control transduced cells (adSHAM) (Figure 1A). To assess whether Fzd5 was involved in transducing the signal of Wnt5a, cultured medium from transduced HeLa cells was applied to serum starved HUVECs after which Dvl activation was monitored. Western blot analysis showed that Wnt5a strongly induced Dvl phosphorylation in untreated or non-targeting siRNA treated HUVECs, however this effect was blocked in absence of Fzd5 (Figure 1B), confirming the importance of endothelial Fzd5 in transducing Wnt5a signaling.

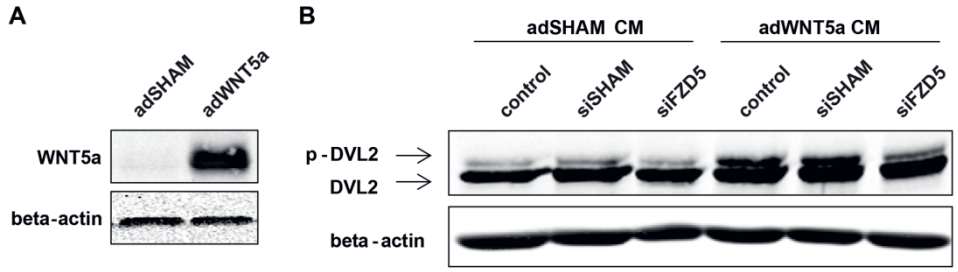

Figure 1. Wnt5a induced Fzd5-mediated DVL activation in HUVECs. (A) Representative Western blot of adenoviral-based Wnt5a overexpression in HeLa cells, 72 hours post transduction. N=4. **(B)** Representative Western blot of Dvl and phosphorylated Dvl in HUVECs after 3 hours stimulation with cultured medium (CM) from HeLa cells overexpressing dsRED or Wnt5a, 72 hours post siRNA transfection in HUVECs. N=6

Fzd5 expression is essential for endothelial proliferation, migration, and tubule formation

The angiogenic capacities of these Fzd5 silenced HUVECs were evaluated in a well-validated *in vitro* 3D angiogenesis assay developed for studying formation of micro-capillary structures [12]. In this assay, HUVECs with GFP marker expression and dsRED-labeled pericytes directly interact in a collagen type I matrix environment, resulting in EC sprouting, tubule formation, and neovessel stabilization as a result of perivascular recruitment of pericytes. At day 5 post-seeding, well-defined, micro-capillaries with pericyte coverage can be observed. Imaging and quantification of the vascular structures was conducted at day 2 and 5. Endothelial knockdown of Fzd5 strongly impaired endothelial tubule formation (Figure 2A). Quantification revealed a significant reduction in the total tubule length, the number of endothelial junctions, and the number of endothelial tubules, both after 2 and 5 days (Figure 2B). To get a better insight in the causative factor for this poor vascular phenotype, the migration and proliferation capacities of Fzd5 silenced ECs were studied. A plug-in migration assay was performed to analyze the effects of Fzd5 knockdown on endothelial mobility. Knockdown of Fzd5 significantly inhibited the migration of ECs towards the open cell-devoid area compared to untreated and non-targeting siRNA treated ECs (Figure 3A,B). In addition, knockdown of Fzd5 significantly reduced cell numbers compared to control and siSHAM condition (Figure 3C). To clarify whether this was a result of impaired cell proliferation or increased apoptosis, cell cycle progression was analyzed in a cell-cycle assay in which total DNA was stained with PI, followed by flow cytometry. A strong increase of cells in the G_0/G_1 phase of the cell-cycle was observed after knockdown of Fzd5, indicative of a cell cycle arrest (Figure 3D,E). For apoptosis analysis, a terminal deoxynucleotidyl transferase dUTP nick end labeling (TUNEL) based detection staining was used. Although seeded in similar densities, Fzd5 knockdown led to a significant reduction of nuclei per image field.

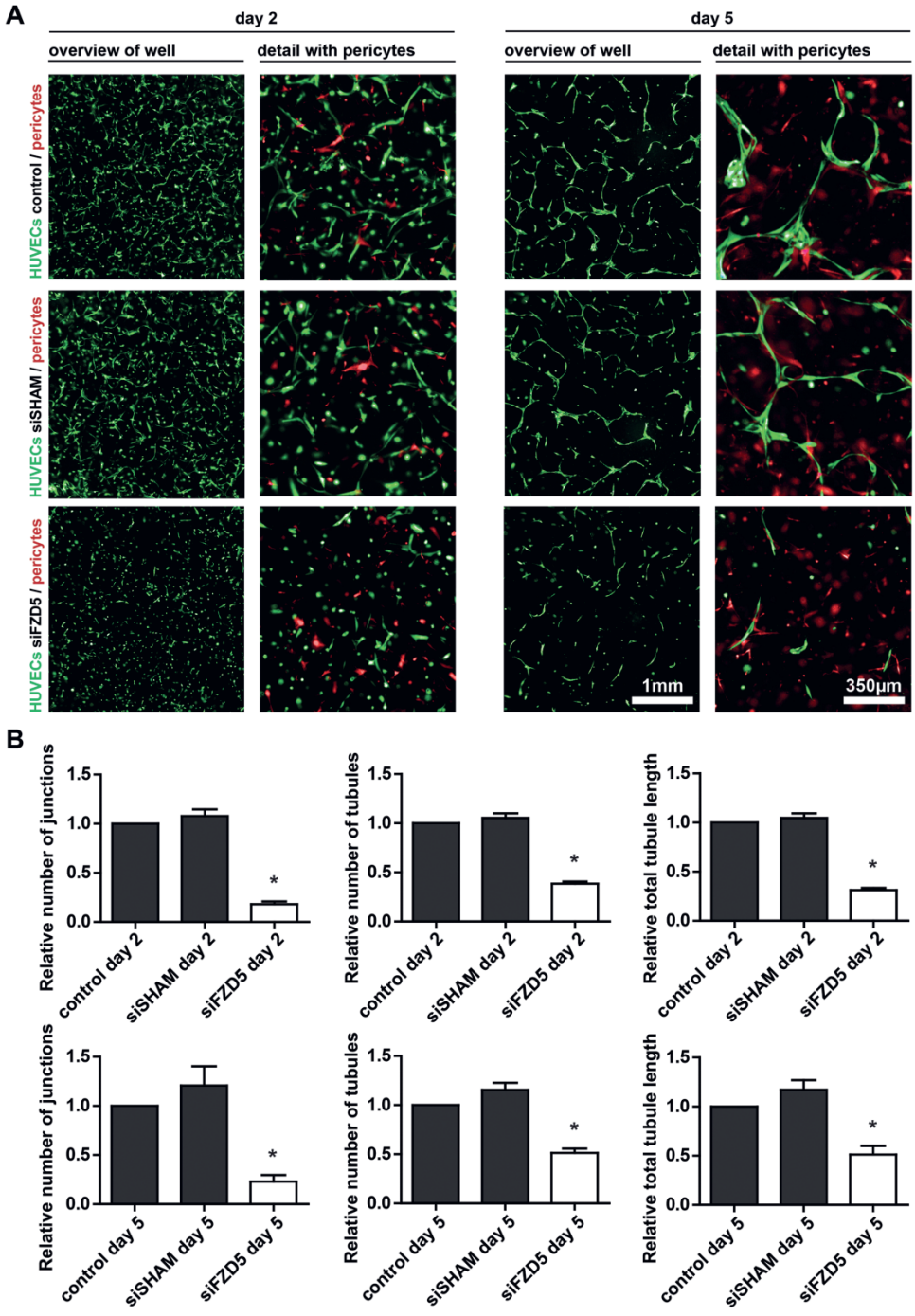

Figure 2. Fzd5 expression is crucial for vascular formation *in vitro*. (A) Representative fluorescent microscope images of GFP-labeled HUVECs (green) in co-culture with dsRED-labeled pericytes (red) in

◄a 3D collagen matrix during vascular formation. Shown are the results at day 2 and 5 of non-transfected control, siSHAM, and siFzd5 conditions. Scale bar in the left columns represents 1mm. Scale bar in the right columns represents 350 µm. **(B)** Bar graphs show the quantified results of the co-culture assay. Shown are the total tubule length, and the number of endothelial junctions and tubules relative to the control conditions, both after 2 days and 5 days. N=4, *P<0.05 compared to control and siSHAM condition.

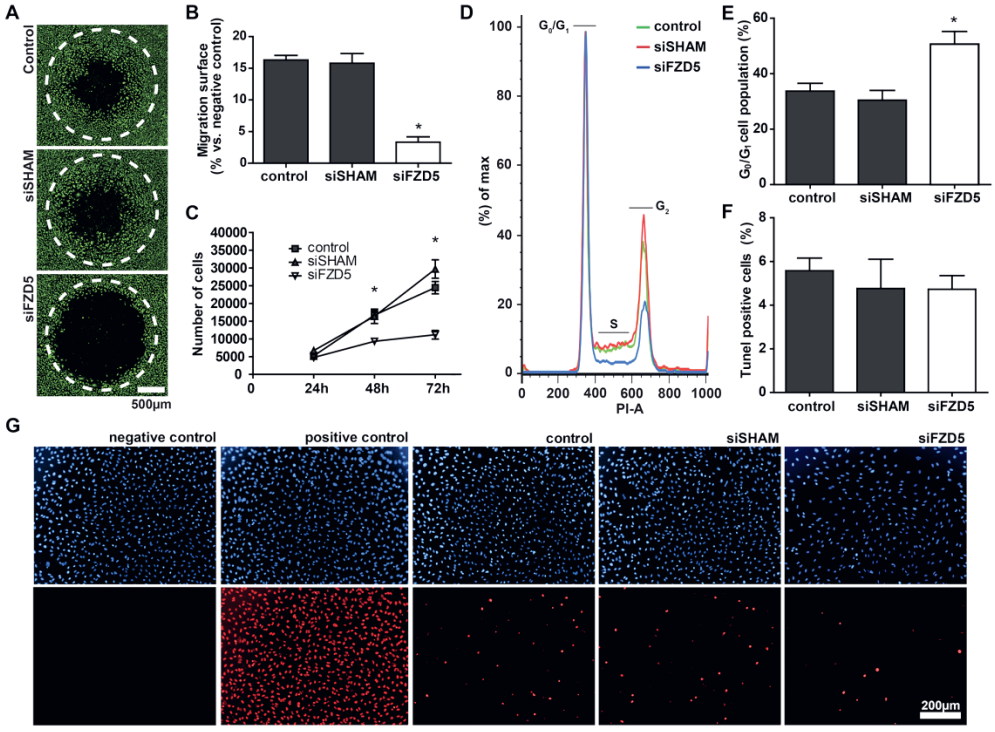

Figure 3. Endothelial knockdown of Fzd5 significantly inhibited EC migration and proliferation, but had no effect on apoptosis. (A) Representative fluorescent microscope images of Calcein-AM labeled HUVECs (green) in a plug-stopper based migration assay. Shown are the results of 16 hours of migration of non-transfected control, siSHAM, and siFzd5 conditions. Scale bar represents 500 µm. Open migration areas produced by the plug-stopper before initiation of the assay are indicated by dotted lines. **(B)** Bar graph shows the quantified results of migration assay. Shown are the percentages of surface area within the dotted circle covered by HUVECs after 16 hours of migration. N=4, *P<0.05 compared to control and siSHAM condition. **(C)** ECs expansion at 24 hours, 48 hours, and 72 hours post seeding in similar densities, as quantified by flow cytometry. N=3, *P<0.05 compared to control and siSHAM condition (two-way ANOVA followed by Bonferroni post hoc test). **(D)** Representative histogram of flow cytometric analysis of PI based DNA staining showing the distribution of cells over the cell-cycle in the different groups at 48 hours post transfection. **(E)** Quantified results of cell-cycle analysis. Percentage of cells in G_0/G_1 phase is shown. N=3, *P<0.05 compared to control and siSHAM condition. **(F)** Quantified results of TUNEL staining. Percentage TUNEL positive cells of total number of cell is shown, 72 hours post-

◄transfection of control, siSHAM, and siFzd5 conditions. N=3, no significance. **(G)** Representative fluorescent microscope images of DAPI bases nuclei staining in HUVECs (blue, upper row) and TUNEL staining of the same cells (red, lower row). Positive control was treated with DNAse solution. Scale bar represents 200 µm.

However, the relative number of TUNEL positive nuclei in the Fzd5 knockdown condition was similar when compared to control and siSHAM condition, showing that the reduction of ECs in the Fzd5 knockdown condition is not related to increased apoptosis (Figure 3F,G).

Loss of Fzd5 does not interfere with endogenous canonical Wnt signaling

To further dissect the molecular mechanism of endothelial Fzd5 signaling in angiogenesis, known Fzd/Wnt signaling pathways were studied. Downstream Fzd signaling occurs via the canonical Wnt signaling pathway, also known as the Wnt/β-catenin pathway, or by the less well described non-canonical Wnt signaling pathways. Activation of canonical Wnt signaling is characterized by an accumulation of cytoplasmic β-catenin, eventually resulting in nuclear translocation and subsequent expression of β-catenin dependent target genes. To evaluate the effect of Fzd5 knockdown on the canonical Wnt signaling pathway, total levels of β-catenin, as well as phospho-β-catenin (ser33/37/thr41) and non phospho-β-catenin (active) were examined 24h, 48h and 72h post transfection by Western blot. Ser33/37/thr41 phosphorylation is induced by GSK3β and primes β-catenin for subsequent degradation, and could be indicative for a reduced activity of canonical Wnt signaling. Total β-catenin, as well as non phospho-β-catenin (active) levels were unaffected by Fzd5 silencing, and no phospho-β-catenin (ser33/37/thr41) was observed in all conditions (Figure 4A,B), even though the antibody was capable of detecting GSK3β-induced β-catenin phosphorylation (Figure 4C). Furthermore, expression levels of previously described endothelial target genes of β-catenin were studied using qPCR, but no differences were observed in the expression of Axin2, Ccnd1 and C-myc after knockdown of Fzd5 (Figure 4D). An immunofluorescent staining, validated to detect cellular distribution of β-catenin (Supplemental Figure 3B), was also performed on transfected ECs, as stable total levels of β-catenin found by Western blot did not deviate between cytoplasmic- or nuclear localized β- catenin. In line with the other experiments focusing on β-catenin-mediated signaling, no differences in β-catenin localization were observed after knockdown of Fzd5, both in confluent and sub confluent cells (Figure 4E and 4F, respectively).

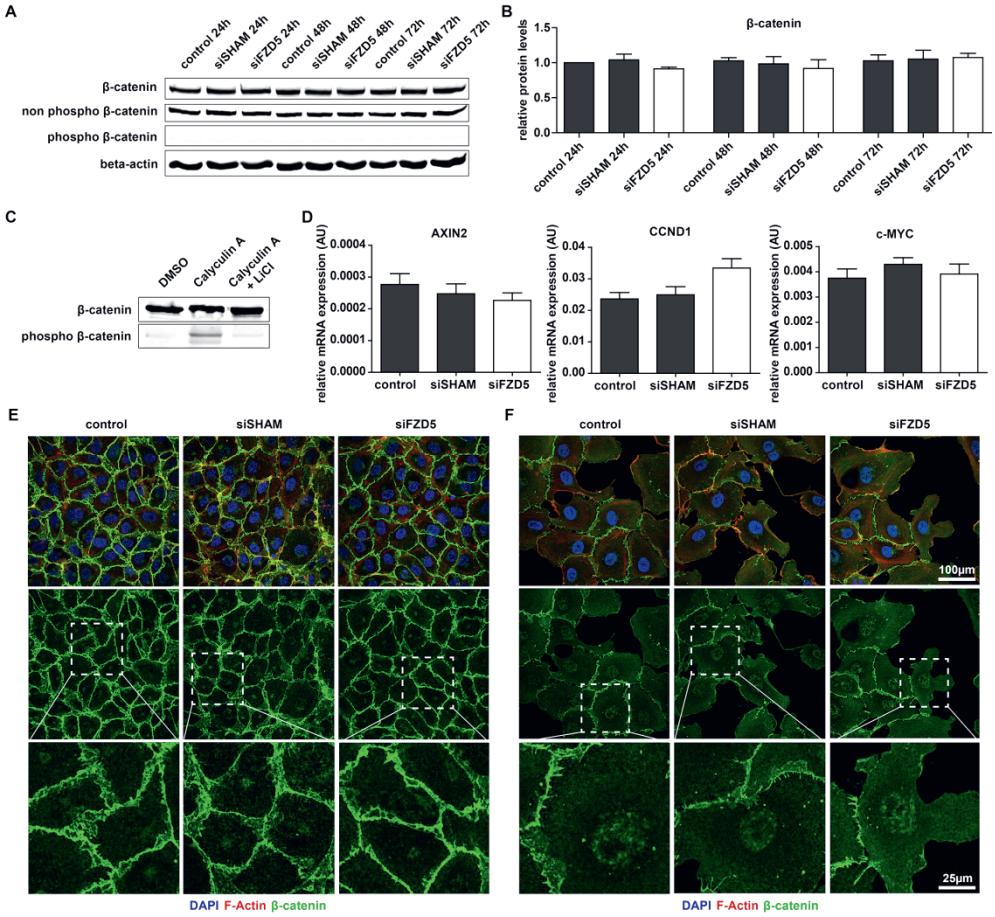

Figure 4. Fzd5 knockdown did not affect the canonical Wnt signaling pathway in ECs. (A) Representative Western blot result of total levels of β-catenin, non phospho-β-catenin, phospho-β-catenin (ser33/37/thr41), and β-actin loading control, at different time points post-transfection. **(B)** Quantified results of β-catenin Western blot. Shown are β-catenin levels relative to β-actin loading control. N=3, no significance. **(C)** Western blot result of total levels of β-catenin and phospho-β-catenin in response to treatment with the phosphatase inhibitor Calyculin A (50nM) with and without a 30 minute pre-treatment of the GSK3β inhibitor LiCl (20mM). **(D)** QPCR analysis of the mRNA expression levels of β-catenin target genes Axin2, Cyclin D1 (Ccnd1) and C-myc in the different conditions 72 hours post transfection. N=4, no significance. **(E)** Immunofluorescent staining β-catenin (green), F-actin (red), and DAPI (blue) in confluent and sub-confluent **(F)** HUVECs after knockdown of Fzd5. N=3.

Fzd5 knockdown induces the expression of several (anti-) angiogenic factors

To further elucidate the anti-angiogenic phenotype observed after Fzd5 knockdown, expression levels of several important regulators of angiogenesis were analyzed. In contrast to what was previously reported [17], our findings in HUVECs indicate that expression of

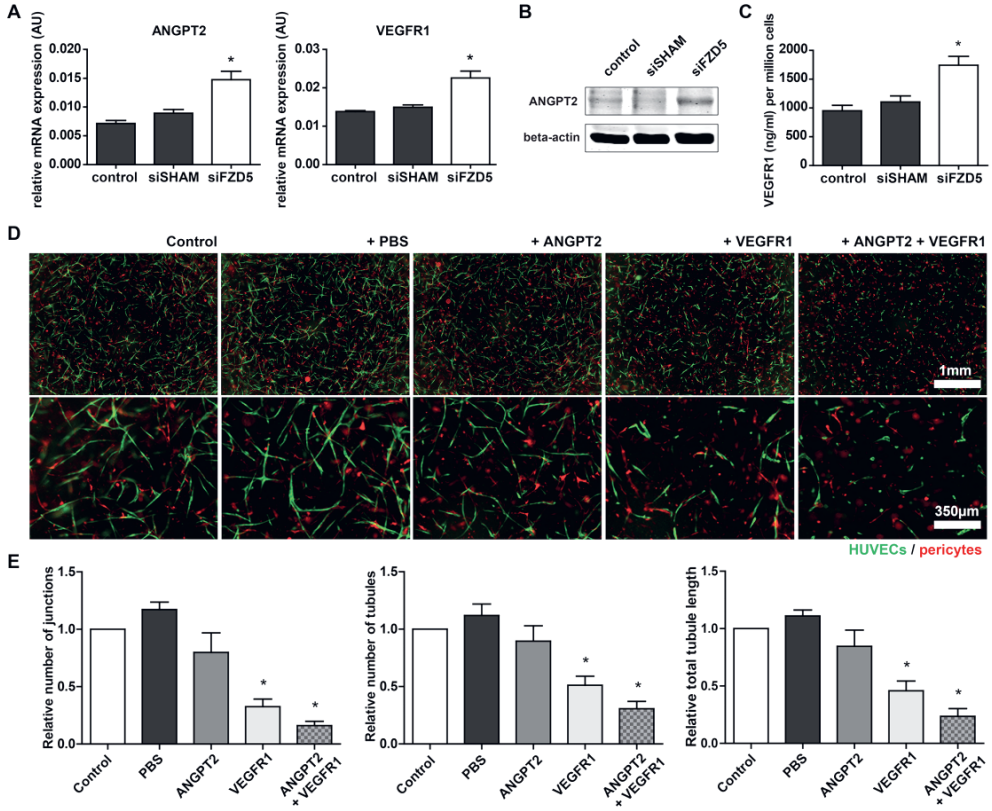

Figure 5. Fzd5 knockdown led to increased expression of vascular regression associated genes VEGFR1 and Angpt2. (A) QPCR results of expression levels of Angpt2 and VEGFR1 in the different conditions 72 hours post transfection. N=11, *P<0.05 compared to control and siSHAM condition. **(B)** Representative Western blot results of Angpt2 expression levels in the different conditions 72 hours post transfection. N=3. **(C)** Enzyme-linked immuno sorbent assay based quantification of secreted VEGFR1 levels in cultured endothelial medium 72h post transfection. N=8, *P<0.05 compared to control and siSHAM condition. **(D)** Representative fluorescent microscope images of GFP-labeled HUVECs (green) in co-culture with dsRED-labeled pericytes (red) in a 3D collagen matrix during vascular formation. Shown are the results at day 5 of an untreated control, and after stimulation with PBS, Angpt2 (1000 ng/ml), VEGFR1 (1000 ng/ml), and Angpt2 + VEGFR1 (1000 ng/ml both). Scale bar in the upper row represent 1mm, in the bottom row 350 µm. **(E)** Bar graphs show the quantified results of the co-culture assay. Shown are the total tubule length, and the number of endothelial junctions and tubules after 5 days. N=4, *P<0.05 compared to control and siSHAM condition.

tissue factor (TF) is not positively regulated by Fzd5 signaling, as Fzd5 knockdown did not attenuate TF expression. In fact, TF was slightly upregulated in Fzd5 silenced HUVECs compared to untreated control cells, yet was statistically equal to non-targeting siRNA treated HUVECs (Supplemental Figure 2). Interestingly, Vascular Endothelial Growth Factor A (VEGFA) decoy receptor VEGFR1, and the vascular destabilizing factor Angpt2 were significantly upregulated at both mRNA and protein level in HUVECs treated with Fzd5 siRNA when compared to untreated or non-targeting siRNA treated HUVECs (Figure 5A-C). Expression levels of VEGF receptor 2, VEGFA, as well as Angpt1 remained unaffected in absence of Fzd5 (Supplemental Figure 2). In line with previous findings of Lobov *et al.*, combined addition of VEGFR1 and Angpt2 in the 3D co-culture system completely attenuated endothelial tubule formation (Figure 5D,E) [9].

Knockdown of a Fzd receptor could not only attenuate signal transduction, but due to impaired inhibitory crosstalk between the individual pathways, or via alternative receptor binding by the Wnt ligand could also have a stimulatory effect [18,19]. Since Fzd5 knockdown had no effect on the canonical Wnt signaling pathway, the described non-canonical Wnt/Ca^{2+} and PCP pathways were studied for their potential role in the upregulation of Angpt2 and VEGFR1. Activation of the Wnt/Ca^{2+} pathway could induce VEGFR1 and Angpt2 transcription, as stimulation of the Wnt/Ca^{2+} pathway leads to free Ca^{2+}-induced activation of Calcineurin, which in turn could promote NFAT-mediated transcription by dephosphorylating NFAT [6]. The mRNA expression level of Down Syndrome Critical Region 1 (DSCR1) was evaluated to assess the potential link between Fzd5 knockdown and NFAT activation, as DSCR1 is a profound target gene of NFAT, involved in a feedback loop to fine-tune NFAT-mediated transcription [20,21]. However, no correlation between endothelial knockdown of Fzd5 and DSCR1 upregulation was observed (Figure 6A). The involvement of NFAT-mediated transcription was also evaluated by pharmacological inhibition of the Wnt/Ca^{2+} signaling cascade using the Calcineurin inhibitor Cyclosporine A (CsA). The effectiveness of CsA (1 µM) was confirmed by its ability to inhibit calcium ionophore (A23187) induced transcription of DSCR1 as a result of free Ca^{2+}-mediated NFAT activation in ECs (Figure 6A). In line with the absence of DSCR1 upregulation in the Fzd5 knockdown condition, the upregulation of VEGFR1 and Angpt2 could not be linked to an increase of NFAT-mediated transcription in the Fzd5 knockdown condition, as CsA stimulation failed to reduce Angpt2 and VEGFR1 upregulation in Fzd5 silenced cells (Figure 6B). Besides activation of the Wnt/Ca^{2+} pathway, the PCP pathway could also stimulate the expression of VEGFR1 and Angpt2 via activation of the Wnt/PCP signaling cascade linked to downstream JNK-induced transcriptional activation of c-JUN [22,23]. Activation of JNK/c-JUN-mediated transcription involves

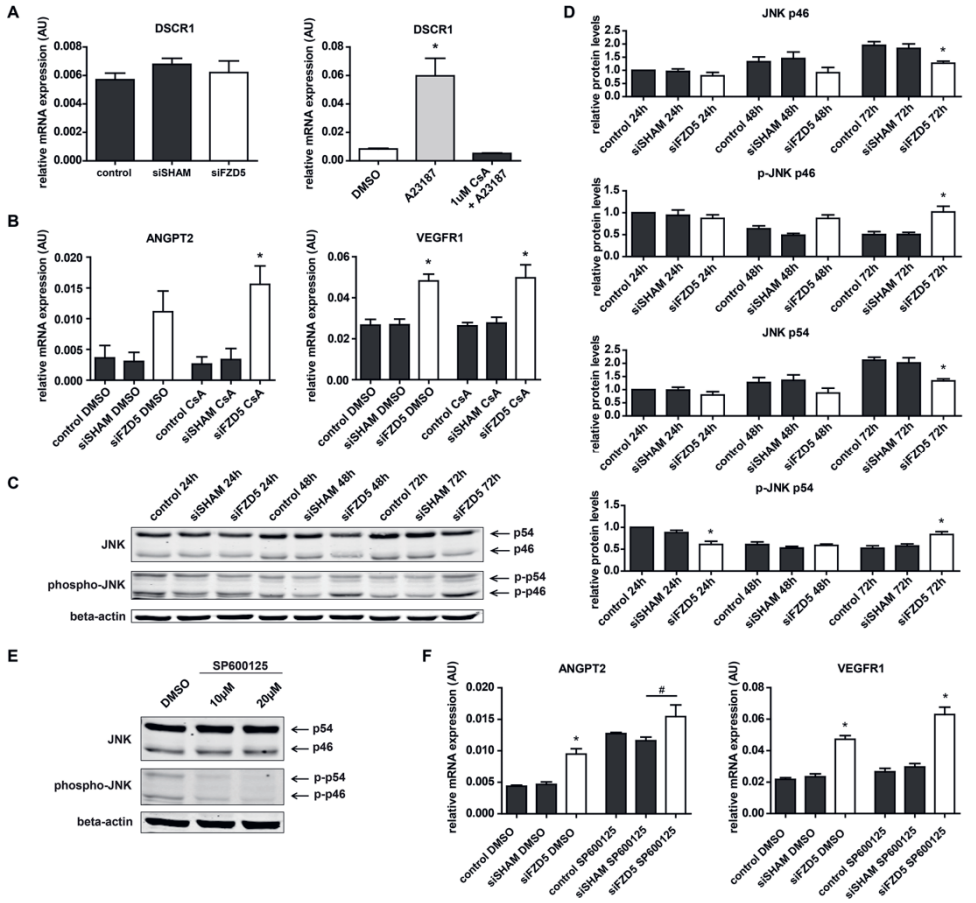

Figure 6. Fzd5 knockdown led to increased expression of vascular regression associated genes VEGFR1 and Angpt2, independent of the non-canonical Wnt/Ca^{2+} and PCP pathways. (A) QPCR results of NFAT target gene Dscr1 in the different conditions 72 hours post transfection and in response to ionophore A23187 (10 μM) induced Ca^{2+} flux, with and without NFAT inhibitor Cyclosporin A (CsA) (1 μM). N=5, *P<0.05 compared to control and siSHAM condition, and DMSO treated and CsA + A23187 treated ECs respectively. **(B)** Angpt2 and VEGFR1 mRNA expression levels in HUVECs in response to CsA, supplemented 48 hours post transfection. N=4, *P<0.05 compared to control and siSHAM condition (two-way ANOVA followed by Bonferroni post hoc test). **(C)** Representative Western blot of total JNK, phospho-JNK, and β-actin levels at different time points post-transfection. **(D)** Quantified results of JNK and phospho-JNK Western blot. Shown are individual (phospho) JNK isoform (p46 and p54) levels relative to β-actin loading control. N=6, *P<0.05 compared to control and siSHAM condition within 1 time comparison (24, 48 or 72 hours). **(E)** Western blot of total JNK, phospho-JNK, and β-actin levels in response to different concentrations of JNK inhibitor SP600125 after 1 hour. **(F)** QPCR analysis showing the effect of SP600125, supplemented 48 hours post transfection, on VEGFR1 and Angpt2 mRNA levels in the different conditions. N=4, *P<0.05 compared to control and siSHAM condition, #P<0.05 as indicated in graph (two-way ANOVA followed by Bonferroni post hoc test).

phosphorylation of JNK, which was slightly increased both 48h and 72h post transfection (Figure 6C,D). JNK-mediated phosphorylation of c-JUN however was not observed (Supplemental Figure 4A,B). Since JNK is a kinase with a broad spectrum of downstream substrates [24], the JNK inhibitor SP600125 was used to block activation of JNK to define whether the enhanced phosphorylation of JNK played a role in the upregulation of VEGFR1 and Angpt2. The effectiveness of SP600125 (20 μM) was confirmed by its ability to inhibit JNK phosphorylation in ECs (Figure 6E). Treatment of HUVECs with SP600125 did not diminish Fzd5 silencing-induced upregulation of VEGFR1 and Angpt2 (Figure 6F). In contrast, SP600125 treatment rather induced a general upregulation of Angpt2, indicating that activation of JNK was not causally related to the Fzd5 knockdown-mediated upregulation of both genes.

Angpt2 and VEGFR1 upregulation is mediated via PKC and Ets1

Previously it was demonstrated that Wnt signal transduction could also involve PKC [25-27]. PKCs are part of a kinase family with a diverse range of potential downstream targets. To verify whether Fzd5 knockdown-induced upregulation of VEGFR1 and Angpt2 depended on activation of PKC, HUVECs were treated with the PKC inhibitor Staurosporine in the concentration range of 5 nM to 20 nM, as not all different PKC family members are equally inhibited at similar concentrations. Interestingly, both Angpt2 and VEGFR1 overexpression induced by Fzd5 knockdown was dose dependently reduced by PKC inhibition compared to control and siSHAM condition (Supplemental Figure 5A). Since HUVECs express multiple PKC isoforms [28,29], PKC expression was knocked down by siRNA to interrogate which isoform mediated the observed upregulation of Angpt2 and VEGFR1. Individual PKC isoform knockdown only had a minor effect on the Fzd5 knockdown-induced overexpression of the anti-angiogenic factors, whereas combined knockdown of the novel PKCs (nPKCs) completely attenuated the upregulation of Angpt2 and VEGFR1 (Figure 7A, Supplemental Figure 5B).

PKC signaling can induce elevated synthesis of the transcription factor Ets1 [30,31], which has binding sites in the promoter regions of both Angpt2 and VEGFR1 [32,33]. Ets1 was significantly upregulated in absence of Fzd5, which was orchestrated by PKC (Supplemental Figure 5C). Involvement of Ets1 in transcriptional regulation of Angpt2 and VEGFR1 was evaluated in the Fzd5 knockdown condition using a double knockdown of both Fzd5 and Ets1. Knockdown of Ets1 alone had no effect on the expression of VEGFR1 and Angpt2 compared to control and siSHAM condition, indicating no active transcription regulation of these two genes by Ets1 in control conditions. However, knockdown of Ets1 in Fzd5-silenced HUVECs fully inhibited upregulation of Angpt2 and partially inhibited the upregulation of VEGFR1

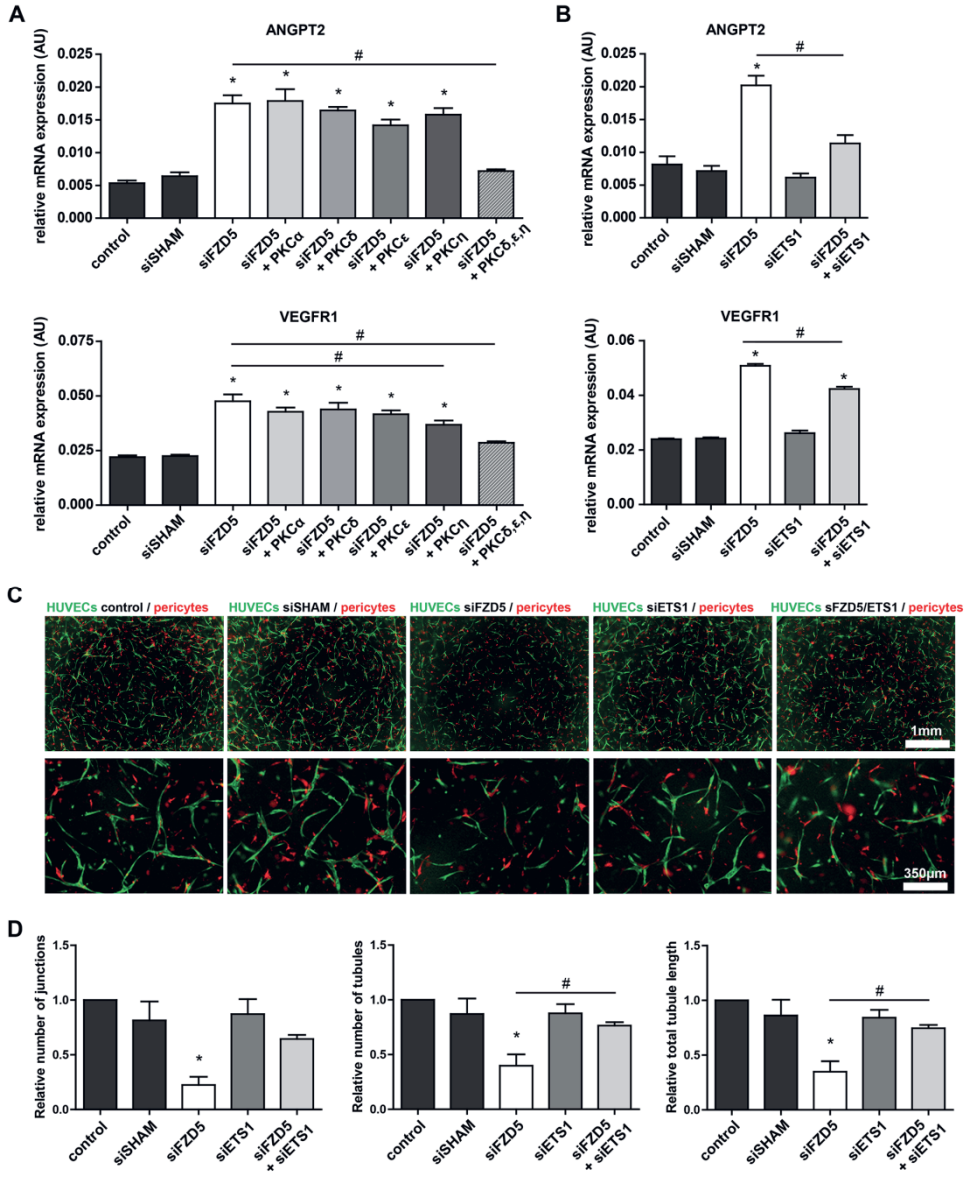

Figure 7. Fzd5 knockdown induced upregulation of Angpt2 and VEGFR1 expression is mediated via enhanced PKC and Ets1 signaling. (A) QPCR results showing expression levels of Angpt2 and VEGFR1 in HUVECs after knockdown of Fzd5 alone, in combination with different PKC isoforms, and in combination with all novel PKC isoforms (PKCδ,ε,η), 48 hours post transfection. N=4, *P<0.05 compared to control and siSHAM condition, #P<0.05 as indicated in graph. **(B)** QPCR results of Angpt2 and VEGFR1 expression in HUVECs, 72 hours post transfection, with and without knockdown of transcription factor Ets1, a downstream target of PKC. N=4, *P<0.05 compared to control and siSHAM condition, #P<0.05 as indicated in graph. **(C)** Representative fluorescent microscope images of GFP-labeled HUVECs

◄(green) in co-culture with dsRED-labeled pericytes (red) in a 3D collagen matrix during vascular formation. Shown are the results at day 5 of non-transfected control, siSHAM, siFzd5, siEts1 and the combined knockdown of Fzd5 and Ets1. Scale bar in the upper row represent 1 mm, in the bottom row 350 µm. **(D)** Bar graphs show the quantified results of the co-culture assay. Shown are the total tubule length, and the number of endothelial junctions and tubules after 5 days. N=6, *P<0.05 compared to control and siSHAM condition, #P<0.05 as indicated in graph.

when compared to Fzd5-silenced controls (Figure 7B). The involvement of Ets1-induced transcription was further substantiated by a similar Ets1 dependent upregulation of Matrix metalloproteinase 1 (MMP1), a verified endothelial target gene of Ets1 (Supplemental Figure 6A,B) [34]. To evaluate if the anti-angiogenic phenotype of Fzd5 silencing observed in the 3D angiogenesis co-culture assay was mediated via this pathway, Ets1 was silenced in GFP-labeled HUVECs. Analysis of the 3D co-culture results demonstrated that inhibition of Ets1 in the Fzd5 knockdown condition partly rescued the Fzd5 knockdown mediated reduction of endothelial tubule formation (Figure 7C-D).

Discussion

The main findings of the current study are: (1) Endothelial Fzd5 expression is essential for vascular formation, as shown in a 3D co-culture assay. (2) Fzd5 silencing inhibits EC proliferation and migration. (3) Endothelial loss of Fzd5 expression does not interfere with endogenous canonical Wnt signaling. (4) Fzd5 knockdown leads to increased expression of vascular regression associated factors VEGFR1 and Angpt2, independent of both the non-canonical Wnt/Ca^{2+}-mediated activation of NFAT and PCP-mediated activation JNK. (5) Inhibition of nPKC signaling, as well as knockdown of the PKC target Ets1 suppressed the upregulation of VEGFR1 and Angpt2 in absence of Fzd5. The Ets1 knockdown intervention also partially rescued the Fzd5 knockdown-induced inhibitory effect on new vessel formation.

Previously it was reported that Fzd5 is indispensable for murine embryogenesis [5]. Fzd5 knockout embryos died *in utero* from severe defects in yolk sac and placenta vascularization. Using trophoblast specific Fzd5 knockout mice, Lu and co-workers reported that the observed phenotype in the Fzd5 full knockout placenta was partly initiated by a defect in chorionic branching morphogenesis [35]. As defective branching morphogenesis of the chorion of these mice resulted in a smaller placental labyrinth layer compared to wild-type littermates, it remained difficult to distinguish whether the placental defects observed in the Fzd5 full knockout mice were indeed vascular related, or the outcome of proportional growth limitations resulting from the reduced villous volume. In our study, we demonstrated that endothelial

knockdown of Fzd5 *in vitro* leads to a severe reduction in vascular tubule formation in a 3D co-culture model, thereby providing evidence for the direct role of Fzd5 in new vessel growth.

The most detailed described Fzd/Wnt signaling cascade is the canonical or ß-catenin dependent pathway. Without stimulation of the canonical pathway, ß-catenin is degraded by a destruction complex consisting of Axin, Glycogen Synthase Kinase 3ß, Adenomatous Polyposis Coli, and Casein Kinase 1α. Upon binding of Wnt ligands to a Fzd receptor in the presence of the co-receptor Lrp5 or Lrp6, a conformation change in Lrp extracts Axin away from the destruction complex, leading to an increase in intracellular ß-catenin levels. When translocated into the nucleus, ß-catenin binds to the TCF/Lef complex and promotes the expression of ß-catenin target genes [6-8]. Knockdown of a Fzd receptor could both have an inhibiting effect on this pathway, due to a reduction in receptors capable of transducing a signal for downstream signaling cascade activation, and an activating effect, either due to impaired inhibitory crosstalk between the individual pathways or via alternative receptor binding by the Wnt ligand [18-19]. Involvement of Fzd5 in this canonical pathway appears to be tissue dependent. Steinhart *et al.* recently demonstrated that canonical Wnt signaling via Fzd5 was involved in pancreatic tumor growth and Caricasole *et al.* reported enhanced ß-catenin mediated signaling upon Wnt7a interaction with both Fzd5 and Lrp6 in the rat pheochromocytoma cell line PC12 [36,37]. In the mouse optic vesicle however, no evidence suggest that Fzd5 activates or suppresses canonical Wnt signaling [38,39]. Our analysis of endogenous canonical Fzd/Wnt signaling suggests that Fzd5 is not involved in Wnt ß-catenin signaling in ECs.

In contrast to the ß-catenin target genes, expression levels of Angpt2 and VEGFR1 were significantly upregulated in HUVECs with suppressed Fzd5 expression. Angpt2 on itself is known to have a positive effect on neovessel formation, as it is involved in pericyte detachment and destabilization of the endothelium to potentiate the actions of pro-angiogenic factors [40,41]. However, in absence of VEGFA, or in the presence of an increased expression of VEGFR1, a decoy receptor for VEGFA, Angpt2 is known to induce vascular regression [9-11]. Both Angpt2 and VEGFR1 are potential downstream target genes of the non-canonical Fzd/Wnt signaling pathways. Upon stimulation of the Fzd/Wnt/Ca^{2+} pathway, activation of phospholipase C leads to cleavage of the membrane component PIP2 into DAG and IP3. When IP3 binds its receptor on the endoplasmic reticulum, Ca^{2+} is released in the cytosol, activating the transcription factor NFAT via Calcineurin [6]. In recent studies, VEGFR1 and Angpt2 were shown to be transcriptional targets of NFAT [42,43]. Like Angpt2 and VEGFR1, the endogenous NFAT inhibitor DSCR1 is also a verified target of the transcription factor

NFAT [20,21], yet our data showed that the expression level of DSCR1 remained stable after knockdown of Fzd5. More important, our experiments demonstrated that inhibition of NFAT activation with CsA after endothelial knockdown of Fzd5 did not inhibit the upregulation of Angpt2 and VEGFR1, suggesting that it was unlikely that the enhanced transcription of these anti-angiogenic factors was mediated by enhanced activity of NFAT. Alternatively, stimulation of the Fzd/Wnt/PCP pathway could also induce the transcription of VEGFR1 and Angpt2 via GTPase mediated activation of JNK, which eventually activates c-JUN based transcription [6]. Multiple studies provided evidence for transcriptional regulation of VEGFR1 and Angpt2 either by c-JUN alone, or by the transcription complex AP-1 involving c-JUN [22,23]. Our data indicated that Fzd5 knockdown led to an increase in JNK phosphorylation, but no increase in c-JUN phosphorylation was observed. In addition, inhibition of JNK activity with SP600125 ruled out the involvement of the PCP-JNK signal transduction axis as causal factor for the enhanced expression of vascular regression associated factors Angpt2 and VEGFR1 in ECs with Fzd5 knockdown, as upregulation of these factors remained evident. In future studies however, it remains of interest to further dissect the relevance of this altered JNK signaling in absence of Fzd5.

Multiple reports have previously suggested a role for PKC involvement in Fzd/Wnt signaling [25-27]. Staurosporine, as well as siRNA-mediated knockdown of nPKCs inhibited the upregulation of Angpt2 and VEGFR1 in HUVECs with suppressed expression of Fzd5, indicating the involvement of PKC signaling in the transcriptional regulation of these genes in Fzd5 silenced ECs. The promoter regions of both Angpt2 and VEGFR1 contain binding sites of the transcription factor Ets1 [32,33], which was shown by our data to be PKC dependently upregulated in absence of Fzd5. Our results demonstrate the involvement of enhanced Ets1 mediated transcription of these two genes in Fzd5 silenced ECs, as Ets1 knockdown resulted in a marked repression of Angpt2 and VEGFR1 expression levels. Another validated endothelial target of PKC/Ets1-mediated transcription MMP1, which like Angpt2 and VEGFR1 was previously shown to be involved in vascular regression [34], was also upregulated via Ets1 in absence of Fzd5. The involvement of Ets1 was further validated using the 3D co-culture model, in which Ets1 knockdown in Fzd5 silenced ECs partially rescued the inhibitory effect on new vessel formation that was observed in Fzd5 silenced conditions. These results indicate a repressing function on PKC/Ets1 signaling by Fzd5 in ECs, leading to reduced expression of vascular regression associated factors Angpt2 and VEGFR1.

In this study the effect of Fzd5 knockdown on the different Fzd/Wnt signaling routes was studied without the addition of exogenous Wnt factors. HUVECs secrete Wnt factors

themselves, amongst which the typical canonical factor Wnt3 and non-canonical factor Wnt5a. Knockdown of endothelial Fzd5 led to functional defects, as well as differential expression of important genes in the angiogenic process, indicating that lack of Fzd5 interferes with endogenous Fzd/Wnt signaling. The nature of this endogenous signaling in absence of Fzd5 was shaped by the finding that combined knockdown of Fzd5 and endogenous Wnt5a significantly suppressed Angpt2 and VEGFR1 upregulation (Supplemental Figure 7).

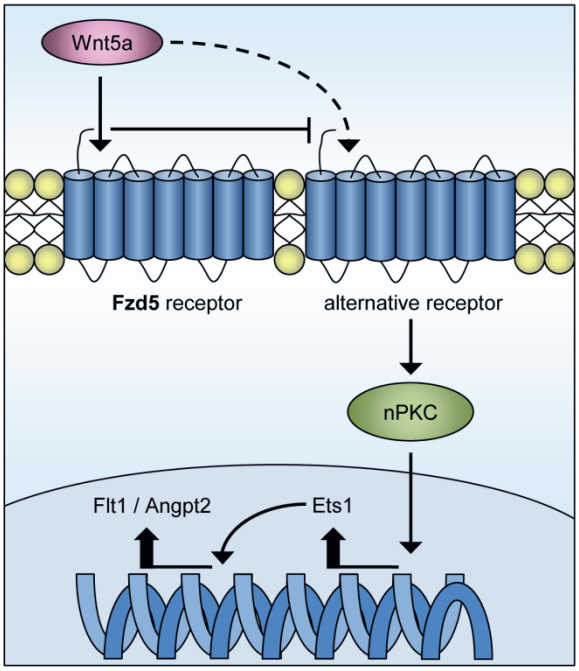

Figure 8. Schematic representation of the proposed model of signaling via Fzd5 in ECs. Our data provide evidence for a new proposed model of signaling in ECs in absence of Fzd5 in which knockdown of this receptor provokes its ligand Wnt5a to signal via an alternative receptor, thereby triggering the activation of nPKC/Ets1-mediated transcription of vascular regression associated factors, amongst which VEGFR1 and Angpt2.

It was previously demonstrated that Wnt factors induce signaling via a variety of Fzd and non-Fzd receptors, and that binding selectivity is receptor context dependent [13,44]. As suppression of endogenous Wnt5a signaling partially rescued the Fzd5 knockdown induced upregulation of Angpt2 and VEGFR1, our data suggest that endothelial knockdown of Fzd5 provokes its ligand Wnt5a to signal via an alternative receptor, thereby triggering the activation of the observed PKC/Ets1-mediated transcription (Figure 8). Although our experiments demonstrate that this alternative signaling route via PKC and Ets1 plays an important role in the poor angiogenic phenotype in absence of Fzd5, the relative contribution of suppressed Fzd5 signaling itself to this phenomenon is yet to be determined. Future studies should also aim to identify the unknown alternative Wnt5a receptor.

The aim of this study was to explore the involvement of Fzd5 in vascular and perivascular biology, which might eventually serve as a foundation for future therapeutic strategies, e.g. in modulating tumor vasculature. A recent genome-wide CRISPR-Cas9 study demonstrated that Fzd5 is a potential druggable target in specific subtypes of pancreatic tumors [36]. Signaling via Fzd5 in these tumor cells was shown to be crucial in β-catenin mediated proliferation and treatment of these pancreatic adenocarcinoma cells with Fzd5 antibodies led to inhibited cell growth, both *in vitro* and in xenograft models *in vivo*. Although these pancreatic adenocarcinoma tumors are not excessively vascularized, they were previously shown to depend on angiogenesis for growth [45,46]. Our data demonstrate the importance of Fzd5 in ECs during angiogenesis and might imply that targeting the Fzd5 in these types of tumors not only affects the pancreatic adenocarcinoma cells, but could in addition potentially result in beneficial suppression of tumor vascularization.

In conclusion, the current study provides evidence for an important role of endothelial Fzd5 in angiogenesis, thereby providing novel insights in the molecular mechanism causal to the poor angiogenic phenotype in absence of this receptor.

References

1. Potente M, Gerhardt H, Carmeliet P: Basic and therapeutic aspects of angiogenesis. *Cell* **2011**, 146:873-887.
2. Carmeliet P: Angiogenesis in health and disease. *Nat Med* **2003**, 9:653-660.
3. Paes KT, Wang E, Henze K, Vogel P, Read R, Suwanichkul A, Kirkpatrick LL, Potter D, Newhouse MM, Rice DS: Frizzled 4 is required for retinal angiogenesis and maintenance of the blood-retina barrier. *Invest Ophthalmol Vis Sci* **2011**, 52:6452-6461.
4. Peghaire C, Bats ML, Sewduth R, Jeanningros S, Jaspard B, Couffinhal T, Duplaa C, Dufourcq P: Fzd7 (Frizzled-7) Expressed by Endothelial Cells Controls Blood Vessel Formation Through Wnt/beta-Catenin Canonical Signaling. *Arterioscler Thromb Vasc Biol* **2016**, 36:2369-2380.
5. Ishikawa T, Tamai Y, Zorn AM, Yoshida H, Seldin MF, Nishikawa S, Taketo MM: Mouse Wnt receptor gene Fzd5 is essential for yolk sac and placental angiogenesis. *Development* **2001**, 128:25-33.
6. Niehrs C: The complex world of Wnt receptor signalling. *Nat Rev Mol Cell Biol* **2012**, 13:767-779.
7. MacDonald BT, Tamai K, He X: Wnt/beta-catenin signaling: components, mechanisms, and diseases. *Dev Cell* **2009**, 17:9-26.
8. Clever, H: Wnt/beta-catenin signaling in development and disease. *Cell* **2006**, 127: 469-480.
9. Lobov IB, Brooks PC, Lang RA: Angiopoietin-2 displays VEGF-dependent modulation of capillary structure and endothelial cell survival in vivo. *Proc Natl Acad Sci U S A* **2002**, 99:11205-11210.
10. Zygmunt T, Gay CM, Blondelle J, Singh MK, Flaherty KM, Means PC, Herwig L, Krudewig A, Belting HG, Affolter M, Epstein JA, Torres-Vazquez J: Semaphorin-PlexinD1 signaling limits angiogenic potential via the VEGF decoy receptor sVEGFR1. *Dev Cell* **2011**, 21:301-314.
11. Hanahan D: Signaling vascular morphogenesis and maintenance. *Science* **1997**, 277:48-50.
12. Stratman AN, Malotte KM, Mahan RD, Davis MJ, Davis GE: Pericyte recruitment during vasculogenic tube assembly stimulates endothelial basement membrane matrix formation. *Blood* **2009**, 114:5091-5101.
13. Dijksterhuis JP, Baljinnyam B, Stanger K, Sercan HO, Ji Y, Andres O, Rubin JS, Hannoush RN, Schulte G: Systematic mapping of Wnt-Fzd protein interactions reveals functional selectivity by distinct Wnt-Fzd pairs. *J Biol Chem* **2015**, 290:6789-6798.
14. He X, Saint-Jeannet JP, Wang Y, Nathans J, Dawid I, Varmus H: A member of the Frizzled protein family mediating axis induction by Wnt-5A. *Science* **1997**, 275:1652-1654.
15. Peterson YK, Nasarre P, Bonilla IV, Hilliard E, Samples J, Morinelli TA, Hill EG, Klauber-DeMore N: Frizzled-5: a high affinity receptor for secreted frizzled-related protein-2 activation of nuclear factor of activated T-cells c3 signaling to promote angiogenesis. *Angiogenesis* **2017**, 20:615-628.
16. Goodwin AM, Sullivan KM, D'Amore PA: Cultured endothelial cells display endogenous activation of the canonical Wnt signaling pathway and express multiple ligands, receptors, and secreted modulators of Wnt signaling. *Dev Dyn* **2006**, 235:3110-3120.
17. Arderiu G, Espinosa S, Pena E, Aledo R, Badimon L: Monocyte-secreted Wnt5a interacts with Fzd5 in microvascular endothelial cells and induces angiogenesis through tissue factor signaling. *J Mol Cell Biol* **2014**, 6:380-393.
18. Topol L, Jiang X, Choi H, Garrett-Beal L, Carolan PJ, Yang Y: Wnt-5a inhibits the canonical Wnt pathway by promoting GSK-3-independent beta-catenin degradation. *J Cell Biol* **2003**, 162: 899-908.
19. Flentke GR, Garic A, Hernandez M, Smith SM: CaMKII represses transcriptionally active beta-catenin to mediate acute ethanol neurodegeneration and can phosphorylate beta-catenin. *J Neurochem* **2014**, 128: 523-535.
20. Minami T, Horiuchi K, Miura M, Abid MR, Takabe W, Noguchi N, Kohro T, Ge X, Aburatani H, Hamakubo T, Kodama T, Aird WC: Vascular endothelial growth factor- and thrombin-induced termination factor, Down syndrome critical region-1, attenuates endothelial cell proliferation and angiogenesis. *J Biol Chem* **2004**, 279:50537-50554.

21. Lange AW, Molkentin JD, Yutzey KE: DSCR1 gene expression is dependent on NFATc1 during cardiac valve formation and colocalizes with anomalous organ development in trisomy 16 mice. *Dev Biol* **2004**, 266:346-360.
22. Ye FC, Blackbourn DJ, Mengel M, Xie JP, Qian LW, Greene W, Yeh IT, Graham D, Gao SJ: Kaposi's sarcoma-associated herpesvirus promotes angiogenesis by inducing angiopoietin-2 expression via AP-1 and Ets1. *J Virol* **2007**, 81:3980-3991.
23. Salomonsson L, Svensson L, Pettersson S, Wiklund O, Ohlsson BG: Oxidised LDL decreases VEGFR-1 expression in human monocyte-derived macrophages. *Atherosclerosis* **2003**, 169:259-267.
24. Bogoyevitch MA, Kobe B: Uses for JNK: the many and varied substrates of the c-Jun N-terminal kinases. *Microbiol Mol Biol Rev* **2006**, 70:1061-1095.
25. Liu A, Chen S, Cai S, Dong L, Liu L, Yang Y, Guo F, Lu X, He H, Chen Q, Hu S, Qiu H: Wnt5a through noncanonical Wnt/JNK or Wnt/PKC signaling contributes to the differentiation of mesenchymal stem cells into type II alveolar epithelial cells in vitro. *PLoS One* **2014**, 9:e90229.
26. Sheldahl LC, Park M, Malbon CC, Moon RT: Protein kinase C is differentially stimulated by Wnt and Frizzled homologs in a G-protein-dependent manner. *Curr Biol* **1999**, 9:695-698.
27. Kinoshita N, Iioka H, Miyakoshi A, Ueno N: PKC delta is essential for Dishevelled function in a noncanonical Wnt pathway that regulates Xenopus convergent extension movements. *Genes Dev* **2003**, 17:1663-1676.
28. Lorenzi O, Frieden M, Villemin P, Fournier M, Foti M, Vischer UM: Protein kinase C-delta mediates von Willebrand factor secretion from endothelial cells in response to vascular endothelial growth factor (VEGF) but not histamine. *J Thromb Haemost* **2008**, 6:1962-1969.
29. Gliki G, Abu-Ghazaleh R, Jezequel S, Wheeler-Jones C, Zachary I: Vascular endothelial growth factor-induced prostacyclin production is mediated by a protein kinase C (PKC)-dependent activation of extracellular signal-regulated protein kinases 1 and 2 involving PKC-delta and by mobilization of intracellular Ca2+. *Biochem J* **2001**, 353:503-512.
30. Naito S, Shimizu S, Maeda S, Wang J, Paul R, Fagin JA: Ets-1 is an early response gene activated by ET-1 and PDGF-BB in vascular smooth muscle cells. *Am J Physiol* **1998**, 274:C472-480.
31. Lindemann RK, Ballschmieter P, Nordheim A, Dittmer J: Transforming growth factor beta regulates parathyroid hormone-related protein expression in MDA-MB-231 breast cancer cells through a novel Smad/Ets synergism. *J Biol Chem* **2001**, 276:46661-46670.
32. Wakiya K, Begue A, Stehelin D, Shibuya M: A cAMP response element and an Ets motif are involved in the transcriptional regulation of flt-1 tyrosine kinase (vascular endothelial growth factor receptor 1) gene. *J Biol Chem* **1996**, 271:30823-30828.
33. Hegen A, Koidl S, Weindel K, Marme D, Augustin HG, Fiedler U: Expression of angiopoietin-2 in endothelial cells is controlled by positive and negative regulatory promoter elements. *Arterioscler Thromb Vasc Biol* **2004**, 24:1803-1809.
34. Naito S, Shimizu S, Matsuu M, Nakashima M, Nakayama T, Yamashita S, Sekine I: Ets-1 upregulates matrix metalloproteinase-1 expression through extracellular matrix adhesion in vascular endothelial cells. *Biochem Biophys Res Commun* **2002**, 291:130-138.
35. Lu J, Zhang S, Nakano H, Simmons DG, Wang S, Kong S, Wang Q, Shen L, Tu Z, Wang W, Wang B, Wang H, Wang Y, van Es JH, Clevers H, Leone G, Cross JC, Wang H: A positive feedback loop involving Gcm1 and Fzd5 directs chorionic branching morphogenesis in the placenta. *PLoS Biol* **2013**, 11:e1001536.
36. Steinhart Z, Pavlovic Z, Chandrashekhar M, Hart T, Wang X, Zhang X, Robitaille M, Brown KR, Jaksani S, Overmeer R, Boj SF, Adams J, Pan J, Clevers H, Sidhu S, Moffat J, Angers S: Genome-wide CRISPR screens reveal a Wnt-Fzd5 signaling circuit as a druggable vulnerability of RNF43-mutant pancreatic tumors. *Nat Med* **2017**, 23:60-68.
37. Caricasole A, Ferraro T, Iacovelli L, Barletta E, Caruso A, Melchiorri D, Terstappen GC, Nicoletti F: Functional characterization of Wnt7A signaling in PC12 cells: interaction with A Fzd5 x LRP6 receptor complex and modulation by Dickkopf proteins. *J Biol Chem* **2003**, 278:37024-37031.

38. Burns CJ, Zhang J, Brown EC, Van Bibber AM, Van Es J, Clevers H, Ishikawa TO, Taketo MM, Vetter ML, Fuhrmann S: Investigation of Frizzled-5 during embryonic neural development in mouse. *Dev Dyn* **2008**, 237:1614-1626.
39. Maretto S, Cordenonsi M, Dupont S, Braghetta P, Broccoli V, Hassan AB, Volpin D, Bressan GM, Piccolo S: Mapping Wnt/beta-catenin signaling during mouse development and in colorectal tumors. *Proc Natl Acad Sci U S A* **2003**, 100:3299-3304.
40. Rennel ES, Regula JT, Harper SJ, Thomas M, Klei, C, Bates DO: A human neutralizing antibody specific to Ang-2 inhibits ocular angiogenesis. *Microcirculation* **2011**, 18:598-607.
41. White RR, Shan S, Rusconi CP, Shetty G, Dewhirst MW, Kontos CD, Sullenger BA: Inhibition of rat corneal angiogenesis by a nuclease-resistant RNA aptamer specific for angiopoietin-2. *Proc Natl Acad Sci U S A* **2003**, 100:5028-5033.
42. Stefater JA 3rd, Lewkowich I, Rao S, Mariggi G, Carpenter AC, Burr AR, Fan J, Ajima R, Molkentin JD, Williams BO, Wills-Karp M, Pollard JW, Yamaguchi T, Ferrara N, Gerhardt H, Lang RA: Regulation of angiogenesis by a non-canonical Wnt-VEGFR1 pathway in myeloid cells. *Nature* **2011**, 474:511-515.
43. Minami T, Jiang S, Schadler K, Suehiro J, Osawa T, Oike Y, Miura M, Naito M, Kodama T, Ryeom S: The calcineurin-NFAT-angiopoietin-2 signaling axis in lung endothelium is critical for the establishment of lung metastases. *Cell Rep* **2013**, 4:709-723.
44. Van Amerongen R, Mikels A, Nusse R: Alternative Wnt signaling is initiated by distinct receptors. *Sci Signal* **2008**, 1:re9.
45. Hotz HG, Gill PS, Masood R, Hotz B, Buhr HJ, Foitzik T, Hines OJ, Reber HA: Specific targeting of tumor vasculature by diphtheria toxin-vascular endothelial growth factor fusion protein reduces angiogenesis and growth of pancreatic cancer. *J Gastrointest Surg* **2002**, 6:159-166.
46. Hotz HG, Reber HA, Hotz B, Sanghavi PC, Yu T, Foitzik T, Buhr HJ, Hines OJ: Angiogenesis inhibitor TNP-470 reduces human pancreatic cancer growth. *J Gastrointest Surg* **2001**, 5:131-138.

Supplemental Data

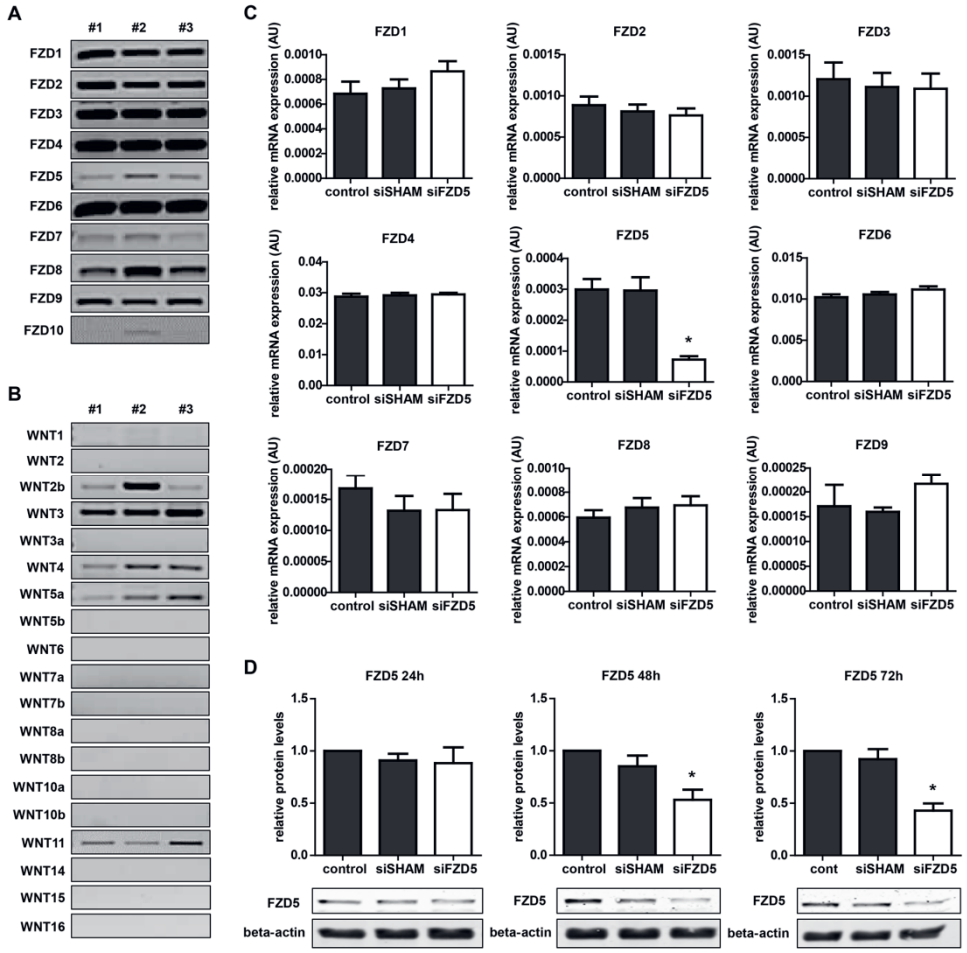

Supplemental Figure 1. Fzd5 siRNA induced a significant and specific knockdown of Fzd5. (A) PCR results showing expression levels of Fzd receptors in HUVECs. N=3 (#1-3 indicate these replicates). **(B)** PCR results showing expression levels of Wnt ligands in HUVECs. N=3 (#1-3 indicate these replicates). **(C)** QPCR results of expression levels of all Fzd receptors expressed in HUVECs (Fzd1-9) in the different conditions 20 hours post transfection. N=7, *P<0.05 compared to control and siSHAM condition. **(D)** Representative Western blot of Fzd5 and β-actin levels 72 hours post transfection. N=5.

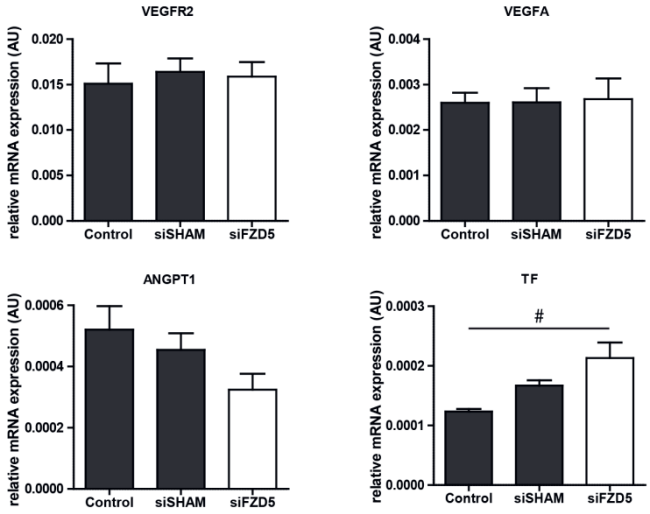

Supplemental Figure 2. Effect of Fzd5 knockdown on important angiogenic regulators. qPCR results showing expression levels of VEGFR2, VEGFA, Angpt1 and TF in the different conditions 72 hours post transfection. N=5, #P<0.05 compared to untreated control condition.

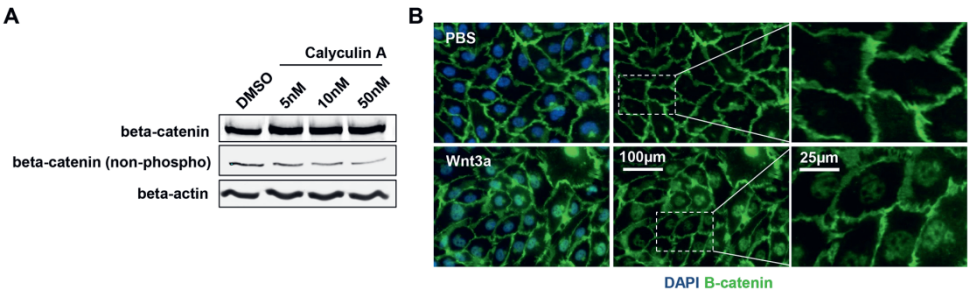

Supplemental Figure 3. Positive control experiments for β-catenin Western blot and immunofluorescent staining. (A) Representative Western blot of total β-catenin, non-phospho β-catenin, and β-actin levels in HUVECs after 30 min stimulation with DMSO or different concentrations of the phosphatase inhibitor Calyculin A (positive control for verification of phosphorylation status). **(B)** Representative immunofluorescent staining of β-catenin (green) in HUVECs after stimulation with PBS or recombinant Wnt3a. Scale bars represent 100 µm and 25 µm.

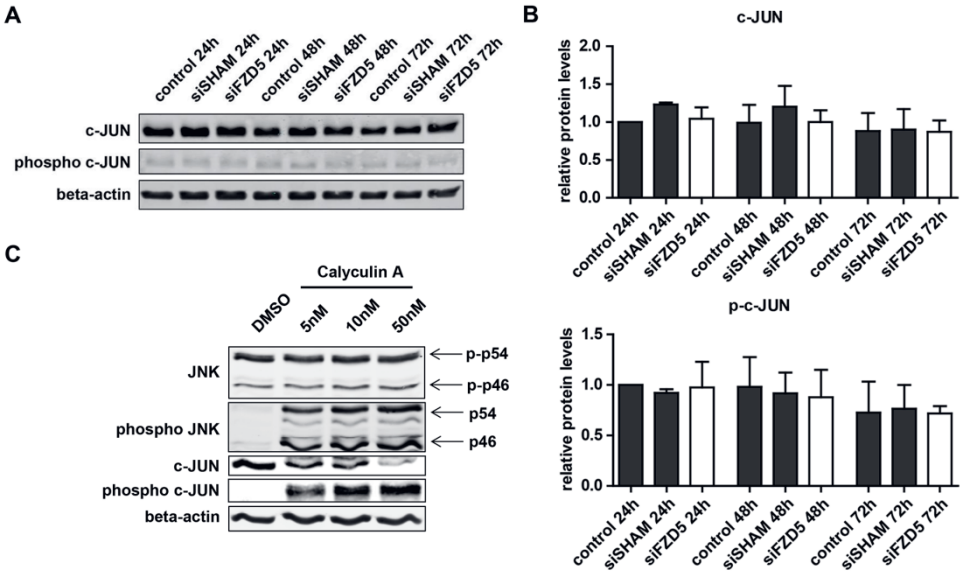

Supplemental Figure 4. Fzd5 knockdown did not affect c-JUN phosphorylation. (A) Representative Western blot of total c-JUN, phospho c-JUN and β-actin levels at different time points post-transfection. **(B)** Quantified results of c-JUN and phospho c-JUN Western blot. Shown are (phospho) c-JUN levels relative to β-actin loading control. N=3, no significance. **(C)** Representative Western blot of total JNK, phospho JNK, total c-JUN, phospho c-JUN and β-actin levels in HUVECs after 30 min stimulation with DMSO or different concentrations of the phosphatase inhibitor Calyculin A (positive control for verification of phosphorylation status).

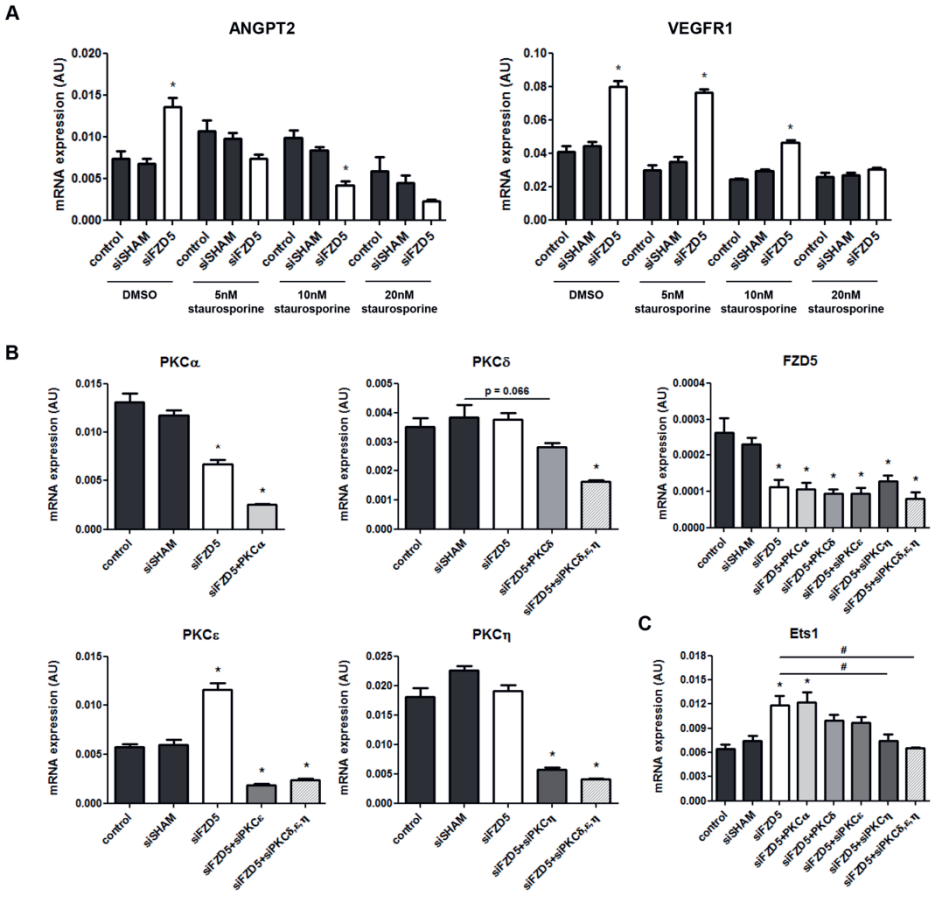

Supplemental Figure 5. Upregulation of Angpt2 and VEGFR1 in HUVECs with suppressed Fzd5 expression via novel PKC signaling. (A) QPCR results of Angpt2 and VEGFR1 in response to treatment to PKC inhibitor staurosporine (0-20nM), supplemented 48 hours post transfection to the different conditions. N=4, *P<0.05 compared to control and siSHAM condition within comparable conditions (two-way ANOVA followed by Bonferroni post hoc test). **(B)** QPCR results showing expression levels of conventional PKC isoform PKCα, novel PKC isoforms PKCδ, PKCε, and PKCη, Fzd5, and transcription factor Ets1 **(C)** in HUVECs after knockdown of Fzd5 alone, in combination with different PKC isoforms, and in combination with all novel PKC isoforms (PKCδ,ε,η), 48 hours post transfection. N=4, *P<0.05 compared to control and siSHAM condition, #P<0.05 as indicated in graph.

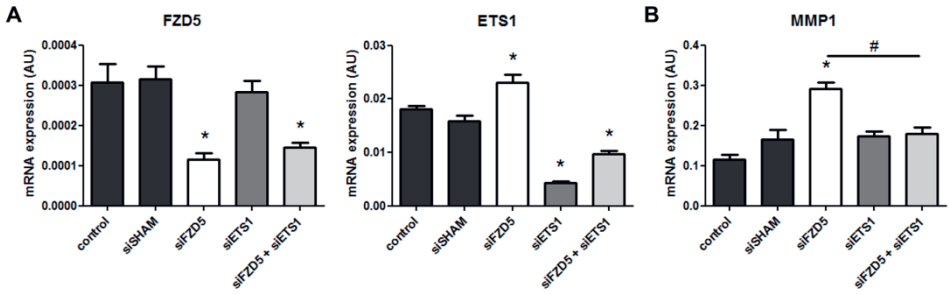

Supplemental Figure 6. Fzd5 and Ets1 knockdown validation and Ets1 dependent MMP1 expression in absence of Fzd5. qPCR results showing expression levels of Fzd5 and Ets1 **(A)**, and Ets1 target gene MMP1 **(B)** in HUVECs after knockdown of Fzd5, Ets1, and in a combined knockdown of Fzd5 and Ets1, 72 hours post transfection. N=4, *P<0.05 compared to control and siSHAM condition, #P<0.05 as indicated in graph.

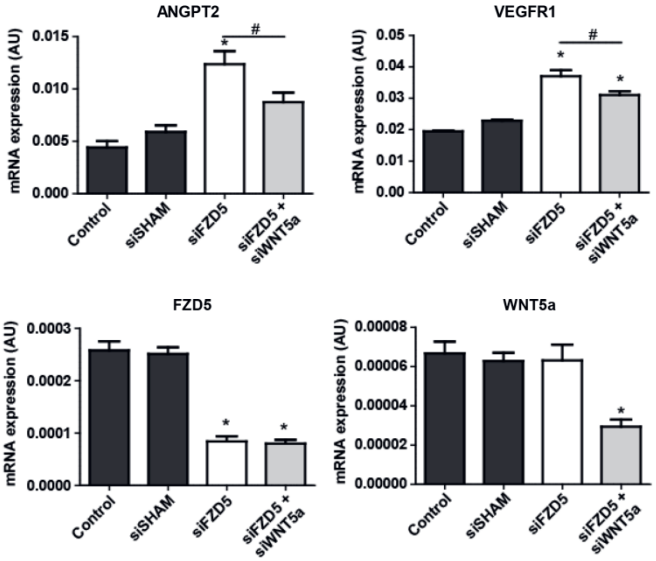

Supplemental Figure 7. Endogenous endothelial Wnt5a expression triggers Angpt2 and VEGFR1 upregulation in absence of Fzd5. qPCR results showing expression levels of Angpt2, VEGFR1, Fzd5 and Wnt5a in HUVECs after knockdown of Fzd5 alone or in combination with Wnt5a, 72 hours post transfection. N=11, *P<0.05 compared to control and siSHAM condition, #P<0.05 as indicated in graph.

Chapter 3

The complex mural cell: pericyte function in health and disease

Christian G. M. van Dijk*, Frederieke E. Nieuweboer*, Jia Yi Pei, Yan Juan Xu, Petra Burgisser, Elise van Mulligen, Hamid el Azzouzi, Dirk J. Duncker, Marianne C. Verhaar, Caroline Cheng

International Journal of Cardiology. 2015 Mar;190:75-89

* Authors contributed equally

Abstract

Pericytes are perivascular cells that can be distinguished from vascular smooth muscle cells by their specific morphology and expression of distinct molecular markers. Found in the microvascular beds distributed throughout the body, they are well-known for their regulation of a healthy vasculature. In this review, we examine the mechanism of pericyte support to vasomotion, and the known pathways that regulate pericyte response in angiogenesis and neovascular stabilization. We will also discuss the role of pericytes in vascular basement membrane and endothelial barrier function regulation.

In contrast, recent findings have indicated that pericyte dysfunction, characterized by changes in pericyte contractility or pericyte loss of microvascular coverage, plays an important role in onset and progression of vascular-related and fibrogenic diseases. From a therapeutic point of view, pericytes have recently been identified as a putative pool of endogenous mesenchymal stem cells that could be activated in response to tissue injury to contribute to the regenerative process on multiple levels. We will discuss the mechanisms via which pericytes are involved in disease onset and development in a number of pathophysiological conditions, as well as present the evidence that support a role for multipotent pericytes in tissue regeneration. The emerging field of pericyte research will not only contribute to the identification of new drug targets in pericyte dysfunction associated diseases, but may also boost the use of this cell type in future cell-based regenerative strategies.

Introduction

In 1873, Charles Rouget discovered a new cell type with a distinct perivascular morphology that wraps itself around blood capillaries [1]. Initially called Rouget cells and later renamed pericytes [2] they were formally described as cells with a prominent nucleus and limited cytoplasm. Pericytes are attached to the long axis of capillaries, embracing endothelial cells (ECs). Just like vascular smooth muscle cells (VSMCs) pericytes are called mural cells because of their perivascular basal membrane embedded position. In this review we discuss the biology of pericytes. We will summarize the markers that are currently used to identify pericyte cells, and we will discuss their basic physiological function. Furthermore the review will address the role of pericytes in diseases such as diabetic retinopathy and chronic kidney disease. In addition, we will also discuss the putative use of multipotent pericytes as therapeutic mediators in regenerative medicine.

Pericyte characteristics

Based on their perivascular position in the microvasculature, pericytes have often been considered the microvascular counterparts of VSMCs. Indeed, these two cell types are thought to be derived from the same lineage. Pericytes are found in the pre-capillary, capillary and post-capillary bed of many organs. However, coverage by pericytes is more extensive in post-capillary venules than in capillaries [3]. Similar to VSMCs, pericytes contain contractile filaments composed of vimentin and alpha-smooth muscle actin (αSMA), and are capable of vasomotion regulation. However, there are also a number of features that are more distinctive for pericytes rather than VSMCs. For example, pericytes can be primarily distinguished from VSMCs by their specific perivascular morphology. VSMCs typically maintain elongated and flattened nuclei. They also position themselves in a perpendicular fashion along the whole length of the vessel, encircling the whole endothelial surface. Layers of VSMCs are usually more dense and flat in the arterioles compared to the pre-capillary arterioles [4]. In contrast, pericytes are attached to the longitudinal axis of the capillaries. They typically maintain a rounded nuclear structure, and embrace the endothelial surface with multiple extensions.

Pericytes are also differently distributed over the vascular tree as compared to VSMCs. Pericytes are mainly localized in the microvasculature where they cover pre-capillary arterioles, capillaries, post-capillary venules, and collecting venules in a single layer of cells [5,6]. In contrast, in larger blood vessels that are exposed to high levels of hemodynamic stress, multiple dense layers of VSMCs and elastic fibers cover the endothelial tubule [7]. However, this distinction in distribution of pericytes and VSMCs is not absolute. In-between mural cell phenotypes that share characteristics with both pericytes and VSMCs have also been described in the coverage of medium to small sized blood vessels [8].

Compared to VSMCs, pericytes are typically embedded in a basal membrane (BM) that is seamlessly merged with the BM of the ECs [9]. This shared BM encompasses the majority of the pericyte-endothelial interface. Distinct places where the BM is interrupted. provide direct contact points between the two cell types. Connections that are created between pericytes and ECs are described as peg-and-socket structures. In these structures the pericytes form recognizable cytoplasmatic elongations (the so-called pegs) that are inserted in the invaginations of the endothelial membrane (the sockets). Peg-and-socket contacts are highly enriched in Connexin 43 mediated gap and (N-cadherin-based) adherence junctions [10]. Another regular type of pericyte-endothelial contact is the adhesion plaque. This structure also forms at sites where the BM is interrupted. Adhesion plaques anchor pericytes to the ECs via a matrix of fibronectin microfilament bundles that is connected to the cell's actin cytoskeleton via integrins [10]. It has been postulated that the direct transmission of biological and mechanical signals between pericytes and ECs predominantly takes place at these contact sites [6,9,10]. For example, Connexin 43 gap junctions in peg-and-socket contacts allow the exchange of ions and small molecules, whereas the adhesion plaques support transmission of contractile forces from pericytes to ECs [10,11]. Vice versa, shear stress forces can be transmitted from the endothelium to the underlying layer of pericytes. It has to be noted that although BM embedding is a regular feature of pericytes, it remains unclear to what extent mature pericytes are embedded in the BM. Several studies have reported incomplete or absent BM microvascular coverage [11]. The lack of a distinct BM surrounding immature blood vessels in embryonic or pathologic conditions where the BM is still being synthesized or has a high turnover rate, makes it impossible to apply these structural criteria in a generalizing manner. Luckily, in addition to their characteristic morphological and structural features, pericytes can also be identified by distinct molecular markers.

Pericyte identification markers

Increased interest in pericyte research has sparked the search for reliable specific markers for pericyte identification. Several reviews have composed comprehensive lists of markers that have previously been evaluated. We refer to these for a more extensive overview on this subject [6,11]. Here we will discuss the pericyte markers that have been most commonly used. A short summary of which markers for mural cells are currently used in the field and in which type of vascular structures marker expression can be detected is provided in Table 1.

Membrane bound markers for pericytes include platelet-derived growth factor receptor β (PDGFRβ), CD146, aminopeptidase A and N (CD13), endoglin, and neuron-glial 2 (NG2) [3,12-14]. Common cytosolic markers for pericyte identification include αSMA, non-muscle myosin, desmin, vimentin, and nestin.

Table 1. Cytosolic and membrane bound markers for the identification of mural cells.

Expressed in:	Pericytes	VSMCs	Arterioles	Capillaries	Venules	Remarks	References
Cytosolic markers							
Alpha-smooth muscle actin (αSMA)	+	+	+	-	+	Most frequently used and best characterized. Also a marker for VSMCs.	[3, 12-14, 18]
Non-muscle myosin	+	-	-	+	+	Present in relatively high concentration in capillary pericytes, absent in VSMCs.	[3, 12-14]
Tropomyosin	?	+	-	+	+	Part of the actin cytoskeleton.	[3, 12-14, 129]
Desmin	+	+	+	+	+	Useful marker in tissues other than skeletal muscle and heart tissue. Expressed on intermediate filament proteins in pericytes that are in direct contact with underlying endothelium. Also expressed by VSMCs.	[3, 4, 12, 14, 25, 87, 130]
Vimentin	+	+	+	+	+	Component of intermediate filaments.	[4, 18]
Nestin	+	+	+	+	+	An intermediate filament protein that is expressed mostly in nerve cells during early stages of development. In adulthood replaced by tissue specific intermediate filaments in mural cells.	[3, 12-14, 131]
Regulator of G protein signaling 5 (RGS5)	+	+	+	+	+	Tested in PDGFRβ - or PDGFβ deficient mice. Marker for developing pericytes independent of PDGFβ signaling.	[4, 17]
Membrane bound markers							
Platelet-derived growth factor receptor β (PDGFRβ)	+	+	+	+	+	Expressed by developing pericytes and precursor pericytes. Also a tyrosine kinase receptor important for pericyte function.	[13, 14, 24]

CD146	+	+	+	+	+	Transmembrane glycoprotein. EC antigen also expressed at the surface of pericytes and in larger blood vessel types.	[13, 14]
Aminopeptidase A and N (CD13)	+	+	+	+	+	Type II membrane zinc dependent metalloproteases.	[4, 131, 132]
Endoglin (CD105)	?	+	+	+	+	TGFβ1 co-receptor required for angiogenesis. Also a marker for ECs.	[3, 13-15, 87]
Neuron-glial 2 (NG2)	+	+	+	+	-	Broadly expressed in pericyte population, expressed during vascular morphogenesis. Also expressed by larger blood vessel types, and by oligodendrocytes.	[3, 13, 14 15, 87]

A new cytosolic marker that appears to be promising for specific pericyte detection is regulator of G protein signaling 5 (RGS5) [4,15]. RGS5 acts as a GTPase activating protein. RGS5 is postulated to play a role in proliferation and recruitment of VSMCs and pericytes during vascular maturation, vessel adaptation and wound healing [16]. RGS5 expression was detected in pericytes and VSMCs in large arteries and veins. It has been reported by Bondjers *et al*. that RGS5 expression is down regulated in PDGFβ knockout mouse embryos in comparison to wild types. This correlates with the typical phenotype of these knockout animals who have been shown to lack pericytes coverage of their vasculature [17]. Although a wide range of markers is currently available for pericyte detection, studies have still been hampered by the great heterogeneity in expression of pericyte markers. The use of a single target for pericyte identification has often led to misinterpretations. Marker expression is highly dependent on the type of tissue, and is often affected by local pericyte function and the pathogenic state of the organ. For example, pericytes that cover normal capillaries typically express desmin but not αSMA, whereas pericytes that cover venules are positive for both [12-14]. In contrast, mid-capillary pericytes supporting the blood-brain barrier and blood-retina barrier strongly express αSMA and myosin [3,18,19].

Pericyte marker expression also appears to be highly dynamic. For example, although capillary pericytes are mostly αSMA- pericytes, αSMA expression in capillary pericytes can be induced by endothelin-1 via receptor A (ET_A) and B (ET_B) signaling following traumatic brain injury. In contrast ET_A antagonists are responsible for a decrease of αSMA+ pericytes [20]. The αSMA expression levels correlate with the increase or decrease in vasoconstriction of the arteriole and capillary respectively. This suggests that αSMA expression is related to the role of pericytes in blood flow regulation in capillaries [20]. It has been postulated that

αSMA expression in capillaries is involved in the control of blood flow whereas mid-capillaries (αSMA negative) are non-contractile [5,21].

Further evidence for active regulation of pericyte marker expression is provided by studies of the transforming growth factor β (TGFβ) response of pericytes. Researchers demonstrated a causal relation between the differentiation to αSMA+, NG2+ and desmin+ pericytes and the release of TGFβ by ECs. When TGFβ release by ECs is inhibited, the differentiation of PDGFRβ+ perivascular cells into αSMA+ pericytes is decreased, but not the differentiation into NG2+ and desmin+ pericytes. Desmin+ pericytes are not induced in absence of ECs, indicating that the differentiation to desmin+ pericytes is dependent on cross-signaling between ECs and PDGFRβ+ perivascular cells [3,22]. These data suggest that marker expression levels are also indicative of pericyte maturity. Hughes *et al*. observed that during postnatal retinal vascular development, αSMA is expressed in VSMCs during early development and remains expressed in both mature VSMCs and mature pericytes. In contrast, juvenile pericytes do not express αSMA, but mainly express NG2 and desmin [23].

For vascular research focused on arterial biology and vascular growth, NG2 expression has often been considered as a more suitable pericyte marker than αSMA+. NG2 expression is restricted to arteriolar and capillary perivascular cells during vasculogenesis and angiogenesis [15,24]. The marker been reported to be absent on venular pericytes [3]. However, NG2 detection was successfully used together with αSMA to help distinguish three main subsets of human pericytes; identifying the capillary (NG2+ αSMA-), venule (NG2- αSMA+) and arteriole (NG2+ αSMA+) pericyte subsets [13,14,25]. Although expression level of αSMA varies between different tissues and pericyte activation status, it is important to note that the level of pericyte αSMA always remains intermediate between ECs and VSMC. Thus αSMA is still a suitable marker for pericyte detection and analysis when used in the right conditions or in combination of additional pericyte markers [21]. For example, Crisan and co-workers have successfully studied human pericytes defined as PDGFRβ+ CD146+ CD34- CD56- CD45- cells with various expression levels of NG2 and αSMA to help differentiate between pericyte subsets and activation state [13,14,25].

Pericyte function

As previously discussed, the morphology, biology, and density of pericytes vary greatly between different sites of the systemic vasculature. The ratio of pericytes/ECs ranges from 1:100 in the human skeletal muscles, to up to 1:3 and 1:1 as observed in the central nervous system and the retina, respectively [26]. Pericyte density appears to relate to organ function and correlates with the stringency of endothelial barrier function and rate of endothelial turnover. Tissues with the slowest EC turnover coincide with larger pericyte coverage.

Pericyte density also appear to relate to orthostatic blood pressure; e.g. larger pericyte coverage was observed in the lower body parts [4,27]. The highest pericyte coverage can be measured in the retina, and is possibly linked to tight endothelial barrier regulation [26,28]. Theoretically, higher pericyte numbers are needed in capillaries with high blood pressure levels to regulate the compensatory vasomotion response of the vascular wall [4,26]. Thus, density differences of pericytes appear to be associated with their distinct roles in endothelial barrier function, angiogenic response, and blood flow regulation in the microvasculature. We will discuss the different functions that have been attributed to pericytes in recent studies in the next section.

Contribution of pericytes to endothelial barrier function

Recent findings have revealed an important role for pericytes in endothelial barrier development and maintenance of integrity. Vascular permeability is highly diverse over the entire vascular tree and is tissue-specific. The most stringent endothelial barriers are found in the vasculature of the central nervous system (CNS), which include the retina. Here, the vascular bed forms the blood-brain-barrier (BBB). The BBB is a functional idiom representing the impermeability of the endothelial barrier to passive transport of circulatory cells, proteins and compounds. Like the BBB, the vascular endothelial barrier in the rest of the vasculature is mainly formed by direct cell-cell contact. The basal membrane does not contribute as a functional barrier against small molecule diffusion. Here we will further focus on the contribution of pericytes to the BBB, as most studies published so far on this subject are conducted in BBB models.

In the CNS, pericytes can be found in complex structures composed of microglia cells, neurons, ECs, and astrocyte endfeet that together form the so-called functional neurovascular unit (NVU) [29] (Figure 1). Although the role of astrocytes in BBB regulation in these NVUs is well documented, the involvement of NVU pericytes has also been reported. Daneman *et al*. showed that pericyte recruitment is necessary for BBB formation during embryogenesis a week before astrocytes are recruited. They also demonstrated that pericyte coverage was a determinant factor in vascular permeability [30]. Further *in vivo* evidence that support the involvement of pericytes in BBB was reported by Bell and co-workers. They showed that loss of pericyte coverage was correlated with BBB breakdown and accumulation of toxic serum proteins and macro-molecules in the adult brain [31]. Pericytes were further shown *in vitro* to regulate the BBB at the level of endothelial junctions. In pericyte co-cultures with ECs, the presence of pericytes increased the trans-endothelial electrical resistance. This is indicative of more robust cell-cell junction contacts in the endothelial monolayer [32-33].

Transport of molecules across the BBB is firmly regulated by tight junctions (TJ) and active transporter pathways [34], both vital for homeostasis regulation of the brain [34,35]. TJ complexes between the ECs consist of occludin, claudin, junctional adhesion molecules (JAM), and scaffold zonula occludens proteins [34]. Besides TJ, adherent junctions and gap junctions have also been shown to play an important role in the maintenance of the BBB [34] (Figure 1). In PDGFRβ+/- and homozygous mice with hypomorphic alleles of PDGFRβ that renders these animals pericyte deficient, TJ and adherent junction proteins were affected. Endothelial cell levels of TJ proteins like claudin-5, occludin, and zonula occludens-1, and levels of adherent junction protein like cadherin were shown to be significantly reduced in the microvasculature of the CNS. This coincided with BBB breakdown and vascular regression [31].

The exact mechanism via which pericytes can regulate the endothelial barrier remains to be further investigated. Several *in vitro* studies have indicated that paracrine signaling between pericytes and ECs mediated by TGFβ and angiopoietin 1 (Angpt1) contribute to endothelial barrier maintenance [36,37]. In addition, it has been reported that Wnt and hedgehog ligands secreted by pericytes could contribute to endothelial barrier formation. The Wnt ligands Wnt7a and Wnt7b can bind to the endothelial membrane receptor Frizzled 4 (Fzd4) and co-receptor LRP5/6, which leads to β-catenin accumulation and translocation to the nucleus. β-catenin induction of claudin-3 expression subsequently improves junction complex formation [38,39] (Figure 1). Furthermore, *in vivo* inactivation of these Wnt ligands, inhibition of the Fzd4 receptor or injection of inhibitors of Wnt/Fzd interactions results in vascular defects and BBB breakdown in the CNS but not in non-neuronal tissues [40]. Taken together, these studies point towards an essential role for pericytes in (BBB related) endothelial barrier function regulation.

Angiogenesis

Pericytes play an active role in new blood vessel formation and stabilization. The process of angiogenesis, which includes vascular sprouting, endothelial intussusception, and EC bridging or a combination of these processes, is complex and tightly regulated by multiple molecular pathways [41]. In Figure 2, the contribution of pericytes to the process of vascular sprouting is summarized. During the initial phase of vascular sprouting, angiogenic factors stimulate ECs to degrade the BM via secretion of matrix metalloproteinases (MMPs). Pericytes, when activated, can produce several MMPs like MMP2, MMP3 and MMP9 to support EC migration in the surrounding extracellular matrix (ECM) following a gradient of chemotactic factors [41]. Angpt2 driven detachment of pericyte from the ECs and degradation of the BM results in loosening of the EC junctions.

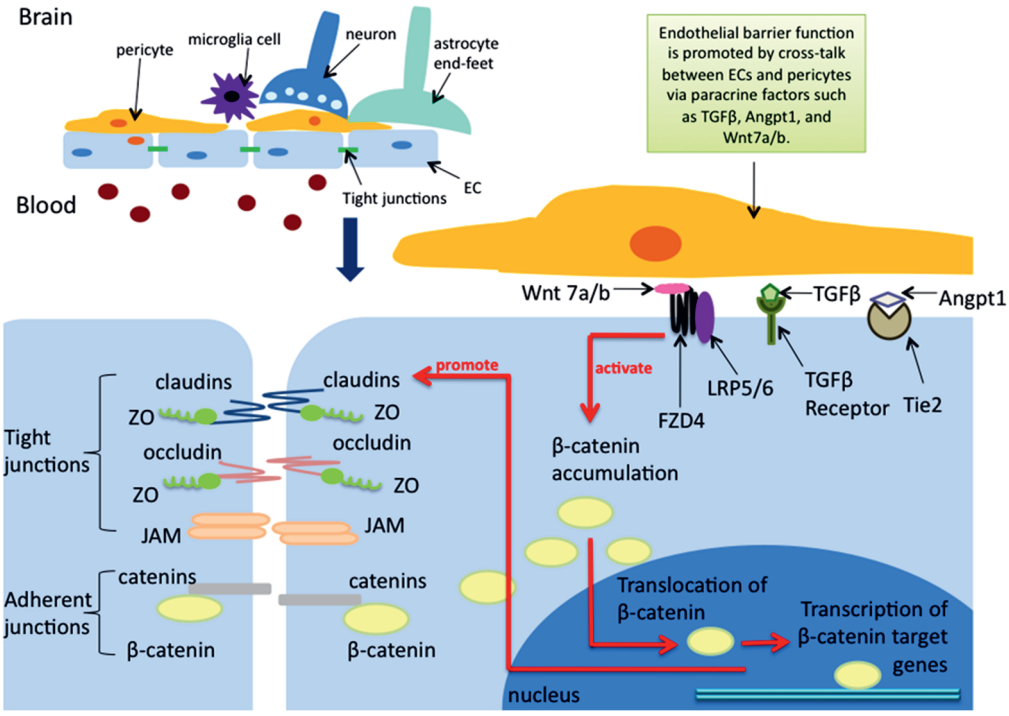

Figure 1. **Contribution of pericytes to the BBB.** In the CNS, pericytes can be found in complex structures composed of microglia cells, neurons, ECs, and astrocyte endfeet that together form the functional NVU. Pericytes recruitment and coverage is crucial for BBB formation and permeability, respectively. Like vascular endothelial barriers in the rest of the vasculature, the BBB is mainly formed by direct cell-cell contact composed by tight and adherent junction complexes between the ECs. By communicating with ECs via paracrine factors, like TGFβ and Angpt1, pericytes regulate BBB at the level of endothelial junctions, promoting the formation of tight junction and adherent junction complexes. Direct regulation of cell-junctions by pericytes has been demonstrated for Wnt ligands (Wnt7a and Wnt7b). These ligands are secreted by pericytes and bind to receptor Fzd4 and co-receptor LRP5/6 on ECs, which activates the accumulation of β-catenin, followed by β-catenin nuclear translocation. In the nucleus, β-catenin starts the transcription of target genes including claudin-3, subsequently improving junction complex formation.

EC detachment from the pre-existing vessel is led by so-called endothelial tip cells. These become activated by angiogenic factor stimulation and migrate outward into the ECM area [41]. Neighboring ECs in the vessel wall follow the tip cell to form stalk cells. These cells elongate the newly formed vascular sprout by cell proliferation. During this process, the vessel segment with stalk cells will also undergo active lumen formation [41]. Newly formed blood vessels are highly unstable with limited endothelial barrier integrity, and require further

maturation to prevent vascular rarefaction (disintegration of blood vessel). The ECs release chemokines, such as PDGFβ to recruit pericytes in order to initiate this vascular stabilization process [3,9]. Receptors for these ligands (such as PDGFRβ) are widely expressed on the surface of pericytes and drive the chemotactic response. The recruited pericytes are derived from cells that differentiate from surrounding mesenchymal precursors or are migrated from the mural wall of adjacent vessels [9]. Song *et al*. showed that PDGFRβ+ pericytes can also be recruited from the bone marrow in adult mice [22]. This pericyte coverage first contributes to the stability of new vessels by creating the BM in cooperation with ECs. Evidence for this is supplied by *In vitro* findings, in which co-culture of pericytes with ECs was shown to significantly increase the secretion of important BM components by pericytes and endothelial cells compared to monoculture conditions [42]. For a more detailed report on role of pericytes in BM turnover, please see further chapters. Recruited pericytes also release paracrine factors like TGFβ and Angpt1 that promote endothelial maturation and endothelial barrier formation [4,10,36,37]: TGFβ and Angpt1 secretion from the supporting pericytes suppresses EC growth and migratory response, resulting in a blood perfused and quiescent vessel [5,10]. Vice versa, TGFβ secreted by ECs triggers the TGFβ receptor 2 in pericytes, which inhibits pericyte proliferation and stimulates the production of contractile and ECM proteins [10]. Moreover, this signaling pathway facilitates pericyte attachment by upregulation of N-cadherin through Notch signaling [10]. The importance of PDGFβ signaling in pericyte recruitment and subsequent contribution to vascular stability is well demonstrated *in vivo* by Hellström *et al*. They showed that lack of pericyte support and prominent endothelial hyperplasia are prominent features in PDGFβ and PDGFRβ knockout mice [43].

Contractile function

Whereas VSMCs are important for vasodilatation and vasoconstriction in larger vessels, pericytes regulate the vascular diameter in the capillaries. A summary of contractile regulation of blood vessels by pericytes is presented in Figure 3. Subcellular structural pericyte marker proteins like αSMA, desmin, and vimentin contribute to the actin filament bundles located near the EC side, regulating cell contractility [44]. Pericytes located at the transition of arterioles to capillaries express a high concentration of contractile proteins, which suggests they might be acting as pre-capillary sphincters [5]. In addition, vasomotion response in pericytes can also contributes to increase of vessel wall stiffness, which serves to compensate for the elevated blood pressure levels. This process is partly mediated by calpain-induced remodeling of cytoskeletal proteins like talin, which increases the stiffness of the subcellular contractile structures of these perivascular cells [45].

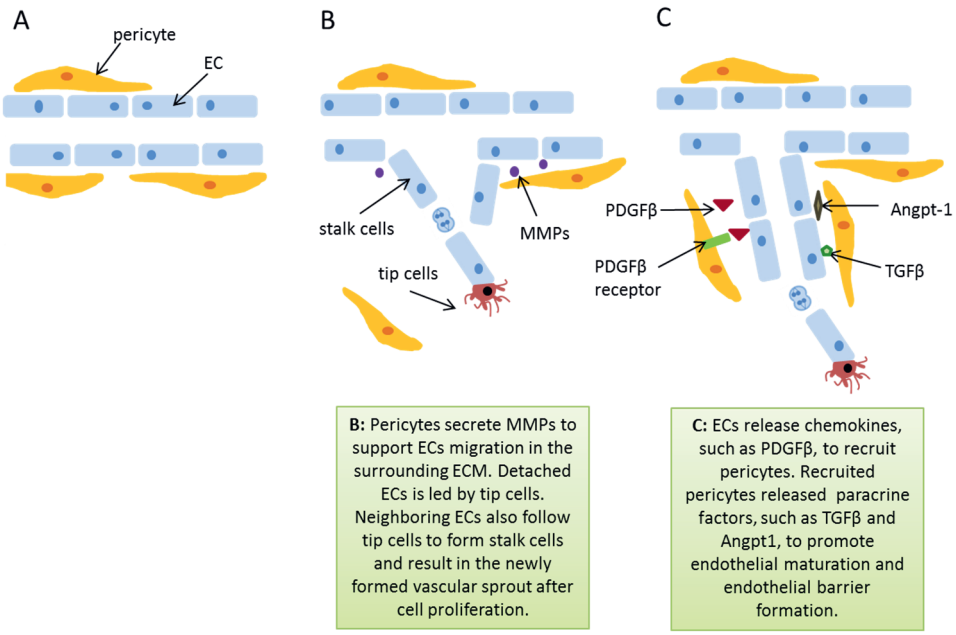

Figure 2. Pericytes in vascular sprouting. Pericytes play an active role in new blood vessel formation. **(A)** Before angiogenesis, pericytes are attached to the long axis of capillaries, embracing ECs. **(B)** During the initial phase of vascular sprouting, angiogenic factors stimulate ECs to degrade the BM via secretion of MMPs. Meanwhile, activated pericytes also produce several MMPs, including MMP2, MMP3 and MMP9, to support EC migration in the surrounding ECM. Angpt2 contributes to the detachment of pericytes from ECs. Detached EC from the pre-existing vessel is led by so-called endothelial tip cells, which become activated by stimulation of angiogenic factors. Neighboring EC follow the tip cell to form stalk cells, which elongate the newly formed vascular sprout by cell proliferation. **C)** Since newly formed blood vessels are highly unstable with limited endothelial barrier integrity, ECs release chemokines, like PDGFβ, to recruit pericytes and initiate the vascular stabilization process. Recruited pericytes further promote endothelial maturation and endothelial barrier formation by releasing paracrine factors, like Angpt1 and TGFβ, to suppress EC growth and migratory response. Vice versa, TGFβ secreted by ECs binds to TGFβ receptor 2 in pericytes, which inhibits pericyte proliferation and stimulates the production of contractile and BM/ECM proteins.

Various vasoactive circulatory ligands can influence the vessel diameter via activation of pericyte cell-surface receptors. Histamine, serotonin, angiotensin 2, endothelin-1, and α_2-adrenoceptors produce vasoconstriction. In contrast, nitric oxide, cholinergic agonists, and α_2-adrenoceptors produce vasodilation [46]. Like in VSMCs, the signal transduction pathways that are activated by these vasoactive ligands all converge to a rise in intracellular calcium, which initiates calcium-calmodulin mediated contraction. Hyperoxic conditions have also been

shown to induce pericyte contraction, whereas higher levels of carbon dioxide trigger pericyte relaxation [47,48]. These data are consistent with the concept that pericyte contractility plays a role in the regulation of the blood flow in the microvasculature.

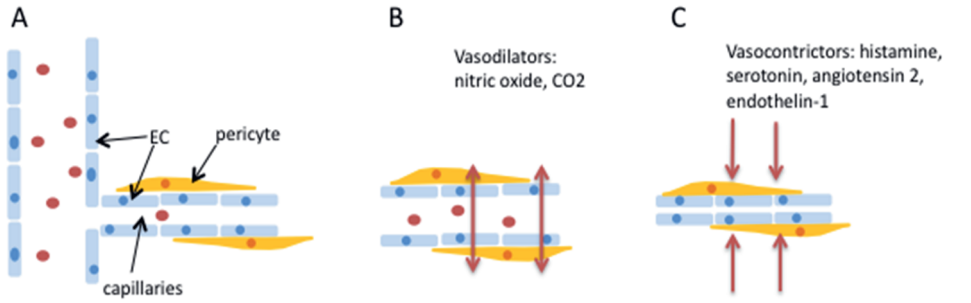

Figure 3. Vasomotion regulation by pericytes. Pericytes regulate the vascular diameter in the capillaries. In addition, pericytes located at the transition of arterioles to capillaries express a high concentration of contractile proteins, which suggests they might be acting as pre-capillary sphincters. Various vasoactive circulatory ligands can influence the vessel diameter via activation of pericyte cell-surface receptors. Histamine, serotonin, angiotensin 2, endothelin-1 and adrenergic agonists are known to be potent vasoconstrictors, whereas nitric oxide, CO2, and cholinergic agonists act as vasodilators.

Basement membrane formation

The basement membrane (BM) is defined as a thin, interwoven sheet of ECM located in blood vessels. It lies underneath the endothelium, and encases the pericytes, separating tissue compartments and facilitating vascular tubule stabilization [49] (Figure 4). It is mainly composed of the structural components laminin, collagen type IV, fibronectin and the proteins perlecan and nidogen 1 and 2 [50]. Laminin is essential for the organization and scaffolding of the BM. Type IV collagen enhances membrane stability and is one of the most important proteins for structural integrity of small vessels [29]. During the formation of the BM, both laminin and collagen type IV independently create three-dimensional networks that overlap and interact. BM-specific heparin sulphate proteoglycan, perlecan, and nidogen have a bridging function between the two networks. They bind to both laminin and collagen type IV structures and interact with each other, thus stabilizing the BM network [49].

Cell attachment to the BM occurs via cell surface glycolipids and transmembrane receptors binding to laminins [29]. While the composition of BM often remains similar between different types of tissues, the ratio between the components vary. Site-specific isoforms or other unique components can create structural and functional differences between BMs, which affect the dynamic interaction with the surrounding matrix or cellular ligands [49]. Concerning the latter, the BM is known to supply biological signals to vascular cells to regulate cell proliferation,

migration and differentiation. The BM itself has a high binding capacity and affinity for secreted growth factors as a result of the glycosylated nature of its components [49]. This may not only affect proliferation and activation of the attached vascular cells, but also provides a depot of chemotaxtic factors that may influence perivascular immune surveillance [49].

Although the BM is vital for physiological vascular function, degradation of the BM is sometimes required. BM degradation is an important initial step for sprouting tip cells that are invading the surrounding tissue during angiogenesis. The BM can also increase or decrease in thickness after receiving stress stimuli or in certain pathological conditions [29,51]. In response to changes in the signals supplied by the BM, migratory pericytes can stimulate ECs to produce MMPs. In fact, both pericytes and ECs are known to produce high amounts of MMPs during vascular expansion. BM components like collagen type IV and fibronectin can be proteolyzed by pericyte or EC release of MMP2 and MMP9. Release of MMP2 by pericytes and ECs can also cleave laminin [29]. The breakdown and alteration of BM leads to a decrease of EC anchorage, affecting the endothelial barrier function. It also facilitates the release of matrix-sequestered angiogenic factors [29].

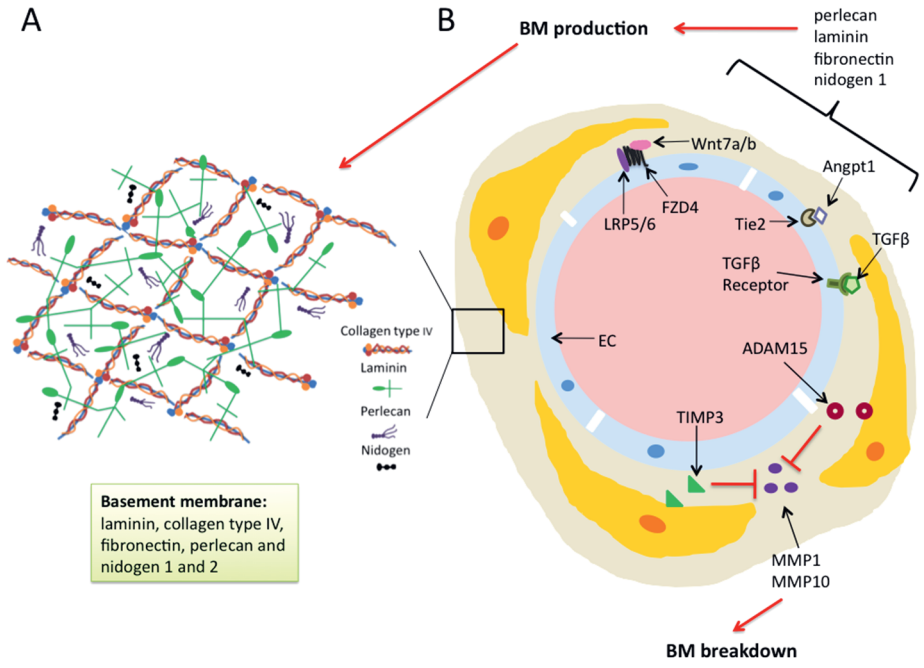

Figure 4. The role of pericytes in basement membrane regulation. The basement membrane is a thin, interwoven sheet of ECM surrounding blood vessels that provides an anchorage structure for the endothelium while encasing the pericytes. **(A)** It is mainly composed of the structural components laminin,

◄collagen type IV, fibronectin and the proteins perlecan and nidogen 1 and 2. **(B)** During angiogenesis as shown previously, BM degradation is an important initial step for sprouting tip cells that are invading the surrounding tissue. BM also supplies biological signals, which induce the MMPs production from ECs and pericytes. Released MMP2 and MMP9 actively breakdown BM components, like collagen type IV and fibronectin. This results in a decrease of EC anchorage, negatively affecting the endothelial barrier function. In contrast, during neovascular stabilization, recruited pericytes assemble along the EC tube abluminal surface, and produce TIMP3 and ADAM15. This inhibit further sprouting by protecting EC tubules from MMP1 and MMP10 dependent regression, thus stabilizing the newly deposited vascular BM. In addition, cross-talk between ECs and pericytes during neovessel stabilization as mediated by Wnt, TGFβ, and Angpt1 signaling stimulates production of BM components by both ECs and pericytes, contributing to BM assembly.

Previous studies have shown that both EC and pericytes are required for the formation of the BM. Whereas ECs have the ability to synthesize most of components of the BM, there is a lack of BM assembly when pericyte contact is absent [50]. Pericyte contact with ECs enhances the production and deposition of most BM proteins, including fibronectin, nidogen-1, perlecan and several laminin isoforms. Moreover, ECM binding integrins are also upregulated in pericytes-EC co-cultures compared to EC mono-cultures [42,50].

Pericytes have also been shown to synthesize tissue inhibitor of metalloproteinase (TIMP)3 and disintegrin and metallopeptidase domain 15 (ADAM-15) when they assemble along the EC tube abluminal surface. TIMP3 and ADAM-15 inhibit further sprouting by protecting EC tubules from MMP1 and MMP10 dependent regression, thus stabilizing the newly deposited vascular BM. TIMP2, synthesized by ECs when interacting with pericytes, suppresses angiogenesis by binding to the α3β1 integrin. This leads to dephosphorylation of pro-angiogenic receptor tyrosine kinases [50]. TIMP3 also binds vascular laminin isoforms in the BM, which is important during EC-pericyte co-assembly [50]. Thus, pericytes plays an important role in the creation and degradation of the BM.

Multipotency of vascular pericytes

Mesenchymal stem cells (MSCs) contribute to the body's regenerative capacity, as they are capable of differentiating into different types of functional cells. MSCs can be derived from bone marrow, umbilical cord blood (CBMSCs), adipose tissue and other tissues [52]. The morphological characteristics and surface markers of CBMSCs are similar to the bone-marrow derived MSC, although they differ in expression levels of CD44 and CD105 [52]. Furthermore, it has been reported that CBMSCs also express the pericyte markers CD146, NG2 and PDGFRβ and are negative for CD34 and CD45 [52].

Recently, the multipotency seen in MSCs has also been ascribed to vascular pericytes. Not only do pericytes exhibit surface markers of MSCs (CD44, CD73, CD90 and CD105) [13,25],

they also sustain similar differentiation capacities that are characteristic of the MSC phenotype [13]. Crisan *et al*. isolated human pericytes based on a combination of surface markers (CD146, NG2 and PDGFRβ) from multiple organs. They demonstrated that these cells, irrespective of the tissue of origin, (*i*) were skeletal myogenic, (*ii*) exhibited adipogenic, osteogenic and chondrogenic potential *in vitro*, and (*iii*) formed calcified tissue *in vivo* [13]. The chondrogenic and adipogenic potentials of pericytes were also reported in the study of Farrington-Rock *et al*. They showed that pericytes could fully differentiate into chondrocytes and are embedded in an ECM of sulphated proteoglycans and type II collagens when cultured in a chondrogenic medium [53]. When cultured in an adipogenic medium, the pericytes differentiated into adipocytes [53]. More evidence for the myogenic potential of pericytes was provided by Dellavalle and co-workers, who isolated pericytes from human skeletal muscle and transplanted these in dystrophic immunodeficient mice [54]. These pericyte-derived cells generated numerous myofibers and expressed human mini-dystrophin, providing proof that pericytes could act as myogenic precursors [54]. Finally, it has also been reported that during skin tissue regeneration, early differentiating pericytes can enhance the intrinsically low tissue-regenerative capacity of human epidermal cells independently of angiogenesis [55].

Other MSC-like behavior of pericytes was described in a study conducted by Davidoff and co-workers [56]. Previously it was demonstrated that nestin, aminopeptidase N and aminopeptidase A, are *in situ* markers that are commonly expressed by pericytes of the adult mouse brain. Nestin was used in the study of Davidoff to further characterize the progenitor cells of Leydig cells [56]. Leydig cells are responsible for testosterone production in testis, but are known to be derived from progenitors that resemble stem cells of the nervous system. Davidoff and co-workers demonstrated that during the tissue regenerative response that was induced by chemo-ablation, the progenitors of Leydig cells were predominantly derived from the perivascular pool of pericytes and VSMCs [56]. Other studies have described a pericyte-like cell population that form spontaneously in embryoid bodies that are cultivated from human pluripotent stem cells. These CD73+ CD90+ CD105+ CD31- multipotent precursors express the pericyte markers CD146, NG2 and PDGFRβ but not αSMA. In mature tissues, mesangial cells (the specialized pericytes in the kidney glomeruli) have been acknowledged to represent a glomerular MSC niche. These cells display pluripotency and can be reprogrammed to form pluripotent stem cells [57]. Together, these studies support the concept that a part of the MSC population find their origin in a subset of perivascular pericyte-like cells [13].

As previously discussed, a relatively small subset of pericytes in microvessels express most pericyte markers but not αSMA. Considering that one of the main tasks of this cell type is the active regulation of vasomotion by contractile function, the absence of αSMA in this particular pericyte subset appears unusual. It has been proposed that these αSMA negative cells could

represent a primitive element in the pericyte hierarchy, supporting the idea of a specialized subset within the pericyte pool with enhanced progenitor cell potential [52]. Although the exact hierarchical positioning of the pluripotent pericytes in the ancestry of MSCs is still a subject to debate, the presence of multipotency within the pericyte pool has been increasingly acknowledged by the scientific community. This led to the proposition made by Caplan and co-workers, that perhaps all MSCs are pericytes, although not all pericytes are MSCs [58].

It is postulated that perivascular located MSCs are able to function as a vascular pericyte and can be released from their position on the microvessel in response to injury. The well-documented regenerative contribution of MSCs following tissue injury includes (*i*) limiting tissue damage by inhibition of apoptosis, (*ii*) active reduction in scarring response, and (*iii*) stimulation of angiogenesis and mitosis of tissue-specific progenitor cells. Fittingly, initial studies that assessed the regenerative capacity of pericytes demonstrated similar contribution of this cell type to injury limitation and tissue healing (See discussion below in “Pericytes as therapeutic agents”). MSCs can also be activated to secrete immunomodulatory agents that inhibit the proliferative response of lymphocytes to limit chronic inflammation. In addition, transplantation studies using the MSCs have shown that this cell type stays relatively hidden from the recipient’s immune system. *Ex vivo* cultured naïve MSCs only have limited major histocompatibility complex class I expression and show no expression of co-stimulatory molecules that are both required for antigen presentation. Based on these qualities, MSCs have also been employed in regenerative therapy for their immunosuppressive properties to limit low grade inflammation [58].

Like MSCs, pericytes have been shown to contribute to immune modulation [59]. Several researchers have proposed that pericytes may act as putative precursor cells of macrophage-like cells [59]. Evidence that support this concept is supplied by studies that demonstrate that pericytes are capable of phagocytic activities by taking up small molecules by pinocytosis. In this way they contribute to removal of neurotoxic particles from the extracellular fluid compartment as part of the BBB. Furthermore, pericytes express different receptors with a wide ligand binding range. They also express Fc receptors for antibody-antigen complex formation, and class I and II major histocompatibility complex molecules for antigen presentation [59,60]. Additional studies are required to further explore this fascinating potential of pericytes in immune regulation.

Pericytes in vascular and fibrotic disease

As pericytes are an abundant cell type in the microvasculature, pericytes dysfunction can contribute to broad range of vascular related diseases. We will discuss the most well described pathological relations below.

Loss of EC-pericyte crosstalk in diabetic retinopathy

The contribution of pericyte dysfunction in diabetic retinopathy (DR) is well documented. DR is a common complication of diabetes mellitus. It is characterized by severe deterioration of the retinal microvasculature. This leads to a lack of vascular perfusion, increased permeability of the capillaries, pathological proliferation of retinal vessels, and eventually leading to blindness [61]. DR can be divided into the non-proliferative and proliferative phase [10,61]. In the initial non-proliferative phase, vessels suffer from micro-aneurysms and hemorrhaging, vessel destabilization, macular edema, BM thickening and vascular regression [62]. In contrast, the proliferative phase is characterized by extensive proliferation of abnormal vessels that are prone to rupture. This could ultimately lead to severe hemorrhaging and retinal detachment [10]. The exact stimulus that triggers the switch between non-proliferative and proliferative remains elusive. Previous findings suggest that vascular regression in the non-proliferative phase produces hypoxic conditions that drive the excessive growth response of the vasculature in the phase [10,61].

Although DR is mainly recognized as a disease initiated by a decline in function of ECs, it has been well-documented in animal studies that the pathogenic process starts with the loss of pericytes [61]. *In vivo* data have shown that the early disappearance of pericytes is quickly followed by the loss of ECs and capillary network collapse, leading to reduced blood flow in the retina. It has been postulated that this initial loss of pericytes is Angpt2 driven [63]. In contrast, Angpt1 has been associated with EC survival and stabilization of the vascular cell phenotype, thus introducing vessel homeostasis. Angpt2 can antagonize the effect of Angpt1 and even promote vessel regression when additional stimulation by VEGFA signaling is lacking. In normal conditions, the level of Angpt2 secreted by ECs is repressed by the binding of a transcription regulatory complex to a glucose sensitive GC box in the Angpt2 promoter [63,64]. In diabetic conditions, hyperglycemia inhibits this complex. Thus the glucose sensitive GC box in the Angpt2 promoter can induce the transcription of Angpt2 [63,64]. Indeed it has been reported that Angpt2 is 30-fold upregulated in the retina of diabetic rats. It is correlated with higher levels of pro-angiogenic and pro-fibrotic factors, such as MMP2, MMP9, VEGF, erythropoietin and TGFβ1 [65,66]. Treatment with Angpt1 in a DR rat model reduces endothelial injury and endothelial barrier breakdown in the retina in both new and established forms of the disease [67]. Evidence for involvement of Angpt2 in DR is also provided by studies in a transgenic mouse model in which human Angpt2 was overexpressed in the retina. These studies demonstrated that in non-diabetic conditions the transgenic animals spontaneously developed a degree of retinopathy that was very similar to the early phase of the disease in diabetic mice [68]. This predisposition to retinopathy was linked to the deleterious effects of high Angpt2 levels on retinal pericytes. Reduced pericyte coverage of the retinal vasculature

and a decrease in vascular density were discovered in these Angpt2 transgenic mice [69]. Other studies have supplied additional evidence and have shed light on the possible working mechanism by which Angpt-Tie2 may affect pericytes in DR: Angpt2 has been shown *in vivo* to mediate pericyte detachment and migration during DR onset [70]. *In vitro*, pericyte proliferation and survival was diminished by exposure to high glucose, but these adverse effects could be partially reversed by Angpt1 stimulation. In contrast, Angpt2 exposure significantly aggravated cell apoptosis [71].

PDGFβ/PDGFRβ signaling also appears to play an important role in the pericyte-mediated pathogenesis of DR. Loss of PDGFβ-mediated survival of vascular cells has been associated with hyperglycemia mediated vascular pathologies. Studies in PDGFβ full knockout mice report that PDGFβ deficiency causes severe pericyte depletion in the retinal capillaries during postnatal development [72]. Geraldes *et al*. identified a possible link between hyperglycemia and pericyte apoptosis that is mediated via the PDGFRβ signaling pathway [73]. High glucose levels activates PKCδ/p38α MAPK signaling, which induces expression of SHP-1. This protein tyrosine phosphatase mediates dephosphorylation of the PDGFRβ. This interferes with the downstream receptor signaling that mediates this vital survival signal, thus inducing pericyte apoptosis [73]. The importance of this interference pathway in DR was clearly demonstrated by studies in Prkcd (PKCδ) knockout mice. Results showed that PKCδ deficiency protected these animals against diabetes induced loss of PDGFRβ-signaling and prevented capillary network collapse in the retina [73]. These identified mechanisms in DR may provide an indication of how pericyte-linked patho-physiological processes in other disease conditions are mediated.

Loss of EC-pericyte crosstalk in BBB breakdown in CNS

Loss of pericyte coverage of the capillaries results in unstable vessels that cause the “classic” symptoms of the non-proliferative phase in DR and eventually leads to vasoregression. The various processes via which this loss of pericyte-EC contact contributes to the progression of other types of vascular disease have been further explored in studies that describe the role of the BBB in the CNS.

Several animal studies have already demonstrated that loss of pericyte coverage triggers the breakdown of the BBB and diminishes endothelial barrier function [31,74]. Pericytes contribute to a functional BBB by the release of high levels of Angpt1 and TGFβ1 [36,37]. Angpt1 derived from pericytes induces occludin expression in ECs via Tie2 receptor signaling [37]. Low occludin production in ECs is associated with less TJ formation and causes increased permeability [75]. Although some experiments provide evidence that occludin is not essential for TJ formation, decreased occludin levels are clearly shown to lead to BBB dysfunction in

disease [76]. Thus, a decline in TJ proteins as a result of a drop in pericyte-derived Angpt1 levels may contribute to the loss of BBB in several CNS diseases in which the contribution to disease via loss of pericyte-vascular contacts have been previously established. In line with this hypothesis, studies in the pathogenesis of stroke, multiple sclerosis, cerebral infection, epilepsy, Parkinson's disease and Alzheimer's disease have all identified defects in endothelial TJ assembly [38].

Furthermore, Dohgu *et al*. demonstrated that BBB function could also be directly regulated via pericyte derived TGFβ1 [36]. Transwell co-cultures of murine brain capillary ECs and rat brain derived pericytes results in less accumulation of soluble rhodamine marker in ECs compared to monocultures of ECs. This reflects increased activity of p-glycoprotein (P-gp) efflux pumps, which are widely distributed in the CNS vasculature and are vital for BBB homeostasis [34]. TGFβ1 stimulation of endothelial monolayers similarly increased P-gp pump activity. In contrast a TGFβ1 antagonist or TGFβ1 antibody could block the observed beneficial effect of pericyte co-culture. Based on these findings, the authors proposed that TGFβ1 signaling through MAPK increases the expression of TJ proteins and P-gp efflux in ECs, hence improving the BBB function [36]. In contrast, Shen *et al*. reported that TGFβ1 increases the paracellular permeability in brain derived ECs by enhancing tyrosine phosphorylation of VE-cadherin and claudin-5 [77]. Thus, the role of pericyte-derived TGFβ1 remains to be further elucidated in order to fully understand the exact contribution of this signaling pathway to the BBB in health and disease.

Dysfunction in pericyte contractility in response to an ischemic event in the brain microvasculature has also been reported to contribute to vascular disease progression. Yemischi *et al*. demonstrated in a mouse brain ischemia-reperfusion model that pericytes supporting the capillary network remained contracted despite the reflow of the occluded artery [78]. This is mediated by a rise in reactive oxygen species, which interacts with ion transport molecules. It alters intracellular Ca^{2+} levels that results in permanent contraction by calcium-activated phosphorylation of contractile proteins in pericytes [78,79]. Furthermore, Dore-Duffy *et al*. showed upregulation of endothelin-1 after traumatic brain injury [20]. This resulted in an upregulation of αSMA positive pericytes and a reduction of the vessel diameter due to pericyte contraction.

Pericyte dysfunction driven mechanisms of fibrosis – focus on chronic kidney disease

Recent studies have also identified a possible role for pericyte dysfunction in the onset of fibrosis, a chronic and progressive pathological process characterized by the deposition of collagen and other ECM components [80]. Fibrosis develops in response to tissue injury and is coincided with local chronic inflammation, leading to scar tissue formation. Following cell

damage, tissue repair takes place in two distinct phases. In the regenerative phase, injured cells are replaced by cells of the same type. This helps to sustain the original function of the affected organ. In contrast, during the following fibroplasia phase, damaged parenchymal tissue is replaced by connective tissue. This beneficial wound healing process becomes pathogenic when it is not fully controlled [80]. Excessive accumulation of ECM proteins results in disordered tissue organization and could further progress into organ failure [80]. It is generally accepted that myofibroblasts are the main regulatory cell type, responsible for the deposition of a fibrotic matrix. Myofibroblasts are characterized by the αSMA marker, the secretion of ECM proteins (mainly collagen type I and fibronectin), and high cell contractility. Myofibroblasts appear in spaces between functional cell clusters of the organ in response to fibrogenic stimuli [80,81]. Researchers from different fields have focused on unravelling the origin of myofibroblasts. Control of this putative progenitor population would allow the development of therapeutic strategies to target fibrosis in a broad range of diseases. Thus far, a number of cell types have been identified as candidates for the myofibroblast precursor cell, including epithelial and ECs undergoing epithelial-mesenchymal transition (EMT) and endothelial-mesenchymal transition (EndMT) [4].

Focusing on the kidney, Lin *et al*. have discovered a link between pericytes and kidney fibrosis [82]. Using transgenic mice expressing enhanced green fluorescent protein under the regulation of the coll1α1 promoter, they demonstrated that pericytes are the major source of collagen producing myofibroblasts in kidney fibrosis [82]. In addition, cell-fate tracing experiments *in vivo* using a Cre reporter system for heritable labeling of epithelial cells or renal stromal cells was previously conducted in a murine unilateral ureteric obstruction and an ischemia-reperfusion model [83]. The findings from that study provide evidence that renal myofibroblasts are not derived from EMT of epithelial cells. Instead, it suggests a pericyte origin for renal myofibroblasts [83]. Furthermore, Chen *et al*. demonstrated that PDGF receptor signaling is involved in pericyte differentiation into myofibroblasts [84].

Schrimpf *et al*. demonstrated that a disintegrin and metalloproteinase with thrombospondin motifs 1 (ADAMTS1) and TIMP3 levels are increased and decreased respectively during pericyte-myofibroblast transition [85]. ADAMTS1 is important in BM degradation whereas TIMP3 is the inhibitor of ADAMTS1. Degradation of BM by ADAMTS1 results in detachment of pericytes from the capillaries leading to subsequent vascular destabilization [85]. Furthermore, ADAMTS1 promotes growth of unstable vessels by VEGFR2 signaling due to a switch in VEGF isoform production. It has been postulated that ADAMTS1 blockade is beneficial for the kidney by attenuating pericyte detachment after injury, thereby promoting vessel stability and reducing fibrosis [85].

Renal pericytes align with the peritubular capillaries in the interstitium and play a vital role in the regulation of the vasa recta and medullary blood flow [86]. This contributes to the fine-tuning of the active re-absorption of solutes and water in the glomerular filtrate. Upon kidney injury, activated pericytes tend to detach from the capillaries of the peritubular vasculature and migrate into the interstitial space. There they proliferate and deposit ECM components [87]. The disappearance of pericytes from the vascular wall also leads to microvascular regression. Pericyte detachment thus may have a double impact on the progression of fibrosis. First of all by active transition into myofibroblasts, which leads to increased collagen type I deposition. Secondly, by inducing vascular regression and subsequent tissue hypoxia [87]. Microvascular rarefaction can be attenuated by targeting endothelium-pericyte crosstalk [88]. As demonstrated by Lin *et al*., systemic administration of the soluble domains of VEGFR2 and PDGFRβ to antagonize excessive PDGFRβ and VEGFR2 activation were able to limit the increase in collagen producing cells in mice subjected to progressive kidney injury. This was mainly attributed to the preservation of pericyte contact with the renal vasculature by blocking pericyte migration and proliferation [88].

Next to the pericytes covering the vascular network of the renal tubular system, specialized pericytes called mesangial cells can be found in the glomerular compartments. In the mature condition, mesangial cells form a dense core in the Bowman's capsule in which the capillaries are arranged in high density clusters. Mesangial cells have several functions in the glomeruli such as providing structural support for glomerular capillaries and generating matrix components. Furthermore, they control the turnover of their own mesangial ECM production in response to mechanical stress. For example, mesangial cells are also involved in the fine-tuning of the glomerular filtration process. Due to their contractile potency, they are able to regulate the capillary flow and define the filtration surface area in the glomeruli.

During kidney development, mesangial cells closely interact with vascular structures that invade the core. They guide the intussusceptive splitting of a single vascular loop into several glomerular capillaries, thus enhancing the capillary surface area for blood ultrafiltration [89]. Lack of mesangial cells in genetic animal models results in the replacement of the complex vascular clusters by simpler structures. In extreme cases this results in single dilated capillary loops, which severely diminished glomerular filtration capacities [90,91].

Mesangial cells are also linked to the onset of glomerulosclerosis, a pathological condition where functional glomerular tissue is replaced by ECM components, resulting in a significant decrease of glomerular function. This uncontrolled ECM replacement is characteristic of progressive renal disease caused by, for instance, diabetes [92]. It has been postulated that mesangial cells could be stimulated to overproduce ECM components like fibronectin, laminin, type I and type IV collagen, in response to TGFβ1 [93]. Furthermore, TGFβ decreases matrix

degradation by inhibition of matrix proteases [93]. Brunskill *et al*. demonstrated upregulation of thrombospondin in mesangial cells of db/db mice with an obese, diabetic, and diabetic nephropathy phenotype [94]. Thrombospondin is an important mediator in TGFβ signaling and thrombospondin null mice demonstrate a similar phenotype as TGFβ mutant mice [94]. Furthermore, the gene expression of ECM component type XII alpha 1 collagen is upregulated in mesangial cells that are derived from db/db mice with nephropathy compared to mesangial cells in wildtype counterparts [94]. Gene expression of the proteoglycan decorin is also upregulated in diabetic mesangial cells [94]. Decorin can interact with ECM molecules like collagen, and ECM-bound thrombospondin and TGFβ. Interestingly, decorin was able to reduce TGFβ induced fibrosis in several animal models, suggesting that overexpression of decorin has a protective function in diabetic mesangial cells [94]. Moreover, findings in studies focusing on fibrosis in the liver [95] or lung [96] have also suggested that pericytes may provide the progenitor cell population of myofibroblasts.

In contrast, LeBleu *et al*. demonstrated that NG2 and PDGFRβ positive pericytes do not appear to be the major source of αSMA positive myofibroblasts in kidney fibrosis [97]. In their study, myofibroblasts were shown to be derived from local fibroblast proliferation and recruited progenitor cells that originated from the bone marrow population. Although other studies suggest that EMT and EndMT are not involved in the differentiation of epithelial cells and ECs into myofibroblasts, LeBleu *et al*. demonstrated that epithelial cells and ECs could gain αSMA expression through EMT and EndMT and thereby contribute to myofibroblast accumulation [97].

Notwithstanding the controversy concerning the origin of myofibroblasts, recent data does indicate that there is a significant role for pericytes in the onset and development of fibrosis in chronic kidney disease. Further studies are needed to elucidate the contribution of pericytes to the progenitor pool of myofibroblasts in other organs with high pericyte densities.

Pericyte function in the heart

Myocardial distribution of pericytes

Previously, the presence of pericytes in the myocardial vasculature has been generally assumed but poorly characterized. Pericytes in the human coronary vasculature were only recently clearly demonstrated and more extensively studied in explanted hearts, using a range of isolation techniques in combination with detection by immunohistological staining of pericyte markers [98]. These studies indicated that the pericyte/EC ratio in the left ventricular myocardium lies between 1:2 to 1:3 [99]. Others have also demonstrated that a relatively large myocardial pericyte population reside in rodents. In rats, pericyte density appears to be correlated with age, with young (P12) animals containing pericyte numbers in the left ventricle

of $4.4X10^7/cm^3$ compared to $2.4X10^7/cm^3$ in older (P30) animals [100]. In line with this observation, our analysis in left ventricle tissue of the murine C57/bl6 strain revealed a dense pericyte coverage of cardiac capillary and arteriole structures, as identified by the immunostaining of the NG2 and PDGFRβ markers (Figure 5). Considering these numbers, and that there are reportedly a 3,3 fold less cardiomyocytes than endothelial cells per cm^3 of left ventricle area, this actually makes pericytes the second largest cell population in the myocardium [99]. Pericytes and endothelial cells in the myocardium are organized in vascular units. These units are interconnected and embedded in a dense ECM that extend from the BM of the microvascular network into the interstitial space between the cardiomyocytes. Within this ECM network, telocytes, a specialized form of interstitial stromal cells that are characterized by their extremely long and thin elongations (podomers), maintain contact between pericytes and myocardiocytes [101].

Notably, Nees and co-workers identified an extensive pericyte network in the heart macrovessels [99,102]. They showed that the larger myocardial arterioles and coronary arteries contain a concentric pericyte and BM layer that separates the endothelium from the elastic lamina and VSMCs [102]. In the larger venules and veins of myocardium, a sparse intermediate layer of pericytes also divides the endothelium from the underlying elastic and VSMC structures [101,102]. These new findings are intriguing and greatly extend our understanding of the role that pericytes play in maintaining vascular homeostasis in myocardial tissue. Furthermore, they also shed light on their putative contribution to cardiovascular disease.

Nees *et al*. and Juchem *et al*. have described significant differences in the barrier function in precapillary arterial and postcapillary venules derived from the heart [102,103]. They see less organized and leaky postcapillary venules whereas isolated precapillary arterioles are better organized and less leaky [102,103]. Based on what they have reported on the difference in pericyte coverage of myocardial venules and capillaries, this points towards active regulation of the endothelial barrier in cardiac tissue by pericytes. As discussed previously, pericyte-EC interaction is also important for the formation of the BM [42,50]. ECs and pericytes collectively contribute to the production of myocardial matrix, both expressing mRNA of types VI, IV and I collagen, as well as fibronectin [104]. Pericytes express significant higher levels of type IV collagen then ECs, indicating that they play a vital part in cardiac (micro)vascular stabilization by contributing to BM formation [104].

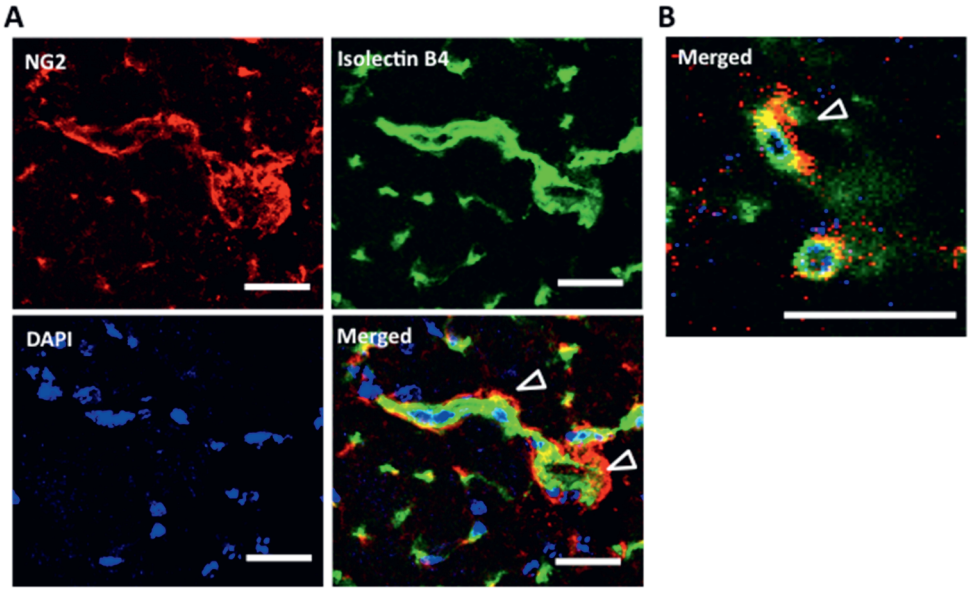

Figure 5. NG2 and PDGFRβ positive cells cover the microvasculature in left ventricle cardiac tissues of wild type C57/bl6 mice. (A) Confocal images of murine cardiac tissue stained for NG2 (red), Isolectin B4 (green), DAPI (blue), and the merged image. NG2+ pericytes (indicated by open arrow heads) cover the abluminal side of arterioles, identified by Isolectin B4 that distinguishes vascular ECs. **(B)** Higher magnification, merged, representative confocal image of capillaries in murine cardiac tissue in which Isolectin B4 staining (green) was used to identify ECs and PDGFRβ staining (red) was used for pericyte detection. The open arrowhead indicates the coverage of PDGFRβ+ pericytes of the smallest vascular structures. White scale bars = 20 μm.

Pericytes in cardiovascular disease and therapy

At the other end of the spectrum, loss of pericytes could lead to decreased support to the endothelial barrier and result in vascular disease. Notably, Juchem *et al*. described a prothrombotic feature of pericytes which could lead to coronary no-reflow [105]. Coronary no-reflow is the failure of cardiac microcirculatory reperfusion after often an ischemic event. In the vasculature, pericytes are the main producers of tissue factor, a key regulator in coagulation pathways [106]. Exposure of the cardiac microvasculature to inflammatory stimuli triggers the release of TF and activates the coagulation cascade, leading to fibrin crosslinking, thrombus formation and lumen occlusion. In addition, it has been implicated that pericyte constriction could contribute to coronary no-reflow morbidity by causing microvascular obstruction [107]. In patients with acute myocardial infarction, no-reflow was reported to be characterized by increase in endothelin-1 plasma levels [108]. This was associated with an increase in αSMA positive pericytes and a reduction of the vessel diameter due to pericyte

contraction [20]. These observations are similar to the ischemia-reperfusion model of Yemischi [79,107], implying that pericyte dysfunction as a result of an ischemic event is partly responsible for the no-reflow condition.

Although VSMCs are largely associated with atherosclerosis, pericytes were also detected in the intima [105,109]. Tigges and co-workers showed in a murine vascular injury model that during the stenosis response, NG2+ PDGFRB+ CD146+ pericytes are increased in the adventitia and migrate into the intima [110]. The strong link between pericyte dysfunction and fibrosis that has been so well documented in kidney fibrosis may provide a uniform hypothesis for pericyte-mediated fibrogenesis that may also apply to fibrosis in cardiac disease. For example, macrophages in inflamed myocardial tissue secrete galectin-3. This protein stimulates the proliferation of pericytes and secretion of procollagen 1, which can be cross-linked to form collagen and thus result in cardiac fibrosis [111]. More directly, cardiac pericyte may provide an interstitial pool of myofibroblast progenitors that upon activation by inflammatory and/or TGFβ stimulation undergo pericyte-myofibroblast transition. Indeed, a limited number of studies show that pericytes are associated with fibrosis in cardiac tissue [111,112]. For example, in fibrocalcific aortic valve disease, neovascularization in the aortic valve is strongly associated with disease onset and progression. Intriguingly, pericytes are often observed near these neovascular structures in stenotic valves [112]. It has been postulated that these pericytes may contribute to aortic valve fibrosis and calcification after myofibroblast transformation [112]. Currently, the role of cardiac pericytes in common cardiac disease entities like (diastolic) heart failure, cardiac outward remodeling and cardiac hypertrophy remains unclear and the subject certainly warrants further investigation.

The great potential that (cardiac) pericytes hold for treatment of cardiovascular disease has been demonstrated by Chen *et al*. Chen and his co-workers showed that pericytes derived from human skeletal muscle significantly improve cardiac function in NOD/SCID mice with acute infarcted hearts [14,113]. Injected pericytes were able to regenerate lost cardiac cells in the infarcted heart, and produced reverse ventricular remodeling, reduction of cardiac fibrosis, and stimulation of angiogenesis [113]. The researchers suggested that the decrease in fibrosis was attributed to MMP secretion from the injected pericytes. Moreover, pericytes were shown to reduce chronic inflammation mediated fibrosis by diminishing the monocyte/macrophage infiltration in the fibrotic myocardium [113]. In addition to the cardiovascular disease, other pioneers in the field have already successfully used pericytes as a source of therapeutic cells in treatment of a broad range of diseases. Other applications of pericytes in cell-based therapy are briefly discussed below.

Pericytes as therapeutic agents

Pericytes can be considered an abundant endogenous source of progenitor cells with great potential for clinical use. Moreover, pericytes can be harvested from more easily accessible tissue, including human placenta, umbilical cord and subcutaneous fat for applications in regenerative medicine. Cross-organ transplantation of pericytes has already yielded encouraging results in a number of animal studies [113,114]. A short summary of the use of pericytes as therapeutic agents is listed in Table 2.

Further support for considering pericytes in regenerative therapies is provided by studies that use pericytes derived from human pluripotent stem cells. Transplantation of these type of cells into immune deficient mice with hind limb ischemia, induced vascular regeneration and promoted muscle repair by active incorporation of pericytes into the damaged muscle and vasculature [114]. CBMSCs that express pericyte markers CD146 and αSMA have also been examined as a possible treatment in an animal model of chemotherapy induced acute renal failure. The infusion of pericyte-like CBMSCs enhanced therapeutic efficacy and restored kidney function compared to regular bone-marrow derived MSCs. However, it should be noted that these effects were mainly attributed to the paracrine actions of pericyte-like CBMSCs mediated by angiogenic and anti-apoptotic factors, whereas active replacement of damaged cells by incorporation of pericyte-like CBMSCs was limited [115,116].

The use of multipotent pericytes as a cell-based therapy in treatment of vascular and fibrosis related pathologies seems not only rational but also, based on the encouraging findings that are described in recent publications, highly feasible. For example, Mendel *et al*. evaluated adipose derived stem cells (ASCs) that express pericyte markers in a cell-based treatment for oxygen-induced retinopathy in mice [117]. Their data demonstrated that these pericyte-like ASCs could integrate as functional pericytes into the retinal capillary bed. They also protected the retina against vascular regression if the animals were treated with these cells before the onset of vascular destabilization. Similarly, ASC pericytes were shown to protect the retina against diabetes induced capillary loss in a murine model of DR [117]. It was postulated that pericytes derived from ASCs may be better able to sustain normal pericyte function in the hyperglycemic environment of the retina due to that they are more used to the hypoxic conditions in the adipose tissue than the local retinal pericytes [117]. Taken together, these findings demonstrate the great potency for ASC derived pericytes in stabilization of the retinal vasculature during the early non-proliferative phase of DR. In other CNS diseases such as stroke and Alzheimer's disease (AD) in which pericytes play an important role in pathogenesis, previous reports of successful use of MSCs in regenerative applications further support the notion that a strategy for pluripotent pericyte-based therapy should be further investigated.

Table 2. Pericytes used as therapeutic agents.

Disease model	Origin of pericytes	Outcome	References
Acute infarcted hearts in NOD/SCID mice	Human skeletal muscle derived pericytes	Reverse ventricular remodeling, reduction of cardiac fibrosis, reduction of chronic inflammation and induced host angiogenesis	[14, 113]
Hind limb ischemia in immune deficient mice	Human pluripotent stem cells (embryonic and induced)	Improves perfusion, blood vessel density and muscle regeneration	[114]
Acute renal failure in NOD/SCID mice	Human CBMSC	Promotes kidney regeneration and prolongs survival	[116]
Oxygen induced retinopathy in NOD/SCID mice	Human ASC	Differentiates to pericytes, protect against vascular dropout and accelerate vascular regrowth and recovery of the vasculature	[117]
Aβ induced murine model	Human bone marrow MSC	Increased activated microglia numbers, plaque formation reduction	[120]
Double transgenic murine model of AD	Human CBMSC	Reduced Aβ deposition and tau phosphorylation, prevent cognitive decline and memory impairment	[119]
Liver fibrosis induced mouse model	Mice bone marrow MSC + NO treatment	Reduction of fibrosis, increased liver function and improved MSC survival compared to MSC treatment only	[128]

For example, employing multipotent pericytes in the treatment of AD seems an attractive strategy on multiple levels.

AD is the most common cause of dementia in the elderly and is characterized by the accumulation of β-amyloid peptides (Aβ) in blood vessels or plaques within the brain, as well by the formation of neurofibrillary tangles, which can lead to neurodegeneration [118]. Researchers have previously demonstrated that tissue derived MSCs, bone marrow derived MSCs and CBMSCs are all able to increase Aβ clearance and improve cognitive impairment in AD mouse models [119-121]. This increase in Aβ clearance was facilitated by autophagosome activity and not by receptor-mediated transcytosis in the BBB, which normally mediates homeostasis in the brain and clearance of Aβ [34].

Although pericytes have not yet been assessed in AD therapy, we propose that this cell type is highly suitable for cell-based therapy in treatment of AD. Pericyte dysfunction in the CNS plays an important role in disease progression. Thus, not only are CNS pericytes involved in the maintenance of the BBB under physiological conditions, but healthy pericytes also contribute to clearance of Aβ by autophagy-mediated internalization of Aβ. The onset of AD

is also linked to degeneration of brain pericytes in response to Aβ accumulation, leading to capillary loss [122]. Bell *et al.* further demonstrated that pericyte deficient mice develop age-dependent cognitive deficiencies and neurodegeneration. These are caused by a combination of chronic cerebral hypoperfusion and BBB breakdown [31]. Replenishing the CNS pericyte pool could help restore BBB function, aid microvascular survival and regeneration, and could actively contribute to further Aβ clearance. In addition, *in vitro* data provide evidence that pluripotent pericytes can differentiate into neural cells [123]. CNS pericytes and neurons share pluripotent neural crest cells as their origin, supporting the hypothesis that the pluripotent CNS pericytes may harbor the potential of neurogenesis. In the study of Karow *et al.* pericyte-like cells derived from the human cerebral cortex can be differentiated into neural cells by retrovirus-mediated co-expression of the transcription factors Sox2 and Mash1 [123]. Mash1 plays an important role in the direct differentiation and commitment of somatic cells to neuronal cells, while Sox2 enhances Mash1 efficiency [123]. That non-CNS pericytes can be differentiated into neural cells was also shown by Montiel-Eulefi and co-workers. They obtained pericytes from aorta explants of rats and triggered these to undergo neural differentiation by trans retinoic acid activation [124]. Retinoic acid is known to promote neural lineage entry of embryonic cells, neural stem cells, bone-marrow MSCs, and ASCs with pericyte-specific markers [124]. When compared to MSCs, pericytes showed a greater neural potential even though they have less immune-modulatory capacity than MSCs.

As indicated earlier, multipotent pericytes have been successfully used in treatment of ischaemic hearts [113]. Similarly, pericytes or pericyte-like MSCs may also provide an efficient cell-based treatment of ischemic stroke. A decline in pericyte regulated vasomotion control and compromised BBB function [78] facilitate the microvascular pathogenesis that is so often the onset of any form of ischemic disease. Restoration of pericyte coverage of the microvasculature in the affected areas could improve capillary and BBB support, and promote reperfusion after stroke. Furthermore, the ability of pericytes to migrate within the brain to a perivascular location in response to stress or injury, and the capacity to differentiate into neuronal cells could actively contribute to neural tissue regeneration [125,126].

We have already discussed in this review the significant contribution of pericytes to the pathogenesis of fibrosis. Based on this notion, the use of therapeutic pericytes to combat the fibrotic component in different diseases seems a viable strategy. However, use of MSCs in treatment of fibrotic disease is still in its infancy and data are limited. Carvalho *et al.* have previously demonstrated that MSCs are not capable of reducing liver fibrosis and improving liver regeneration in rats with severe chronic liver disease [127]. More recent studies demonstrated that MSCs pre-treated with nitric oxide are capable to repair liver fibrosis [128]. Considering these reports, the use of pericytes to combat the fibrotic element of a disease

may still require further understanding of the role of MSCs and pericytes in the pathogenesis of fibrosis.

Conclusion and future directions

With the discovery of distinctive markers, together with a growing body of knowledge of how to conduct morphological characterization to identify pericytes, investigators have recently begun to unravel pericyte function. First studies have identified a vital role for this particular cell type in vascular homeostasis. In the last few years, researchers have also started to appreciate the impact pericyte dysfunction has in the onset and progression of a diverse range of diseases in which vascular degeneration plays a critical role. New evidence is also emerging that points towards a putative contribution of pericyte dysfunction to the etiology of fibrotic disease. Meanwhile, the importance of pericytes in the body's regenerative response is highlighted by an increasing number of reports. They demonstrate that this cell type shares similarities with MSCs or may be part of an intrinsic "vascular" MSC pool, and could function as multipotent cell in tissue healing. Although pericyte therapy is still in a very early phase, initial studies have already shown that these multifaceted pericytes represent a very promising regenerative approach in the treatment of ischemic and fibrotic disease. However, further studies are still required to fully understand pericyte function in health and disease and to enable us to further explore their regenerative potential. Indeed several important questions remain unanswered (See summary in Table 3). For example, since not all markers for pericyte identification are universally expressed on every pericyte in every perivascular location of the vascular tree, we still do not know whether (*i*) we can identify specific pericyte subpopulations; (ii) if there are differences in regenerative potency of these subsets; (*iii*) and if there are also differences in paracrine profile in response to growth factors and disease stimuli, or whether these subtypes differ in vascular stabilizing behavior. To answer these questions, the scientific community should focus on establishing a set of criteria to identify pericytes based on our knowledge so far. A subdivision of markers to be used based on pericyte localization in the vascular tree as suggested in Table 1 would already greatly help to demystify the complexity of pericyte identification. In relation to pericyte biology in the cardiovascular field, the presence of pericytes in coronary macrovessels is intriguing, and their contribution to ET1-mediated thrombogenesis and the no-reflow phenomenon and atherosclerosis should be further explored. The exact role of pericytes in the cardiac microvasculature in vascular dysfunction and fibrogenesis should be further investigated to help us understand the relation between pericyte dysfunction and common cardiac disease entities like (diastolic) heart failure and cardiac hypertrophy. To fully explore the therapeutic potential of pericytes, researchers should also focus on differentiating putative subsets of pericytes derived different organ origins for

cell-based therapy. The use of pericytes in treatment of fibrosis should also be further explored.

Increasing our understanding of this complex cell type will be critical for the development of new interventions to prevent pericyte dysfunction associated pathologies. It will also boost their therapeutic potential for use in future cell-based regenerative strategies.

Table 3. Questions on future directions.

Identification
Which pericyte specific markers are reliable to identify the various pericyte subpopulations?
How to define a set of characteristics to be used for pericyte identification?
Function and communication
Are there differences in signaling between endothelial cells and the many pericyte subtypes, and therefore difference in their function?
Disease
Will lack of pericytes or dysfunction of pericytes from various subtypes lead to differences in severity in the associated disease?
Since pericytes are abundantly presence in the body, are there other diseases in which pericytes play a prominent role?
Pericytes as therapeutic agent
Do different pericyte subtypes have different regenerative capabilities?
Do pericytes derived from different organs have different regenerative capacities?
Can *in vivo* restoration of pericyte signaling treat diseases that are associated with pericyte dysfunction?
Pericytes in the cardiac field
Since pericytes are the second cell type in the heart, do they play a significant role in heart failure, cardiac hypertrophy etc?
Could cardiac pericytes be used as a regenerative agent in heart disease?
On which aspects of pericyte function should we focus in the cardiac field?

References

1. Rouget C: Memoire sur le developement, la structure et les proprietes physiologiques des capillaries sanguins et lymphatiques. *Arch Physiol Norm Path* **1873**, 5:603-63.
2. Zimmermann K: Der feinere bau der blutkapillaren. *Z Anat Entwicklungsgesch* **1923**, 68:29-109.
3. Hall AP: Review of the pericyte during angiogenesis and its role in cancer and diabetic retinopathy. *Toxicol Pathol* **2006,** 34:763-75.
4. Armulik A, Genove G, Betsholtz C: Pericytes: developmental, physiological, and pathological perspectives, problems, and promises. *Dev Cell* **2011**, 21:193-215.
5. Allt G, Lawrenson JG: Pericytes: cell biology and pathology. *Cells Tissues Organs* **2001**, 169:1-11.
6. Armulik A, Abramsson A, Betsholtz C: Endothelial/pericyte interactions. *Circ Res* **2005**, 97:512-23.
7. Bergers G, Song S: The role of pericytes in blood-vessel formation and maintenance. *Neuro Oncol* **2005**, 7:452-64.
8. Andreeva ER, Pugach IM, Gordon D, Orekhov AN: Continuous subendothelial network formed by pericyte-like cells in human vascular bed. *Tissue Cell* **1998**, 30:127-35.
9. Gerhardt H, Betsholtz C: Endothelial-pericyte interactions in angiogenesis. *Cell Tissue Res* 2003, 314:15-23.
10. Winkler EA, Bell RD, Zlokovic BV: Central nervous system pericytes in health and disease. *Nat Neurosci* **2011**, 14:1398-405.
11. Diaz-Flores L, Gutierrez R, Madrid JF, Varela H, Valladares F, Acosta E, Martin-Vasallo P, Diaz-Flores L Jr: Pericytes. Morphofunction, interactions and pathology in a quiescent and activated mesenchymal cell niche. *Histol Histopathol* **2009**, 24:909-69.
12. Ribatti D, Nico B, Crivellato E: The role of pericytes in angiogenesis. *Int J Dev Biol* **2011**, 55:261-8.
13. Crisan M, Yap S, Casteilla L, Chen CW, Corselli M, Park TS, Andriolo G, Sun B, Zheng B, Zhang L, Norotte C, Teng PN, Traas J, Schugar R, Deasy BM, Badylak S, Buhring HJ, Giacobino JP, Lazzari L, Huard J, Peault B: A perivascular origin for mesenchymal stem cells in multiple human organs. *Cell Stem Cell* **2008**, 3:301-13.
14. Crisan M, Corselli M, Chen WC, Peault B: Perivascular cells for regenerative medicine. *J Cell Mol Med* **2012**, 16:2851-60.
15. Ozerdem U, Grako KA, hlin-Huppe K, Monosov E, Stallcup WB: NG2 proteoglycan is expressed exclusively by mural cells during vascular morphogenesis. *Dev Dyn* **2001**, 222:218-27.
16. Cho H, Kozasa T, Bondjers C, Betsholtz C, Kehrl JH: Pericyte-specific expression of Rgs5: implications for PDGF and EDG receptor signaling during vascular maturation. *FASEB J* **2003**, 17:440-2.
17. Bondjers C, Kalen M, Hellstrom M, Scheidl SJ, Abramsson A, Renner O, Lindahl P, Cho H, Kehrl J, Betsholtz C: Transcription profiling of platelet-derived growth factor-B-deficient mouse embryos identifies RGS5 as a novel marker for pericytes and vascular smooth muscle cells. *Am J Pathol* **2003**, 162:721-9.
18. Bandopadhyay R, Orte C, Lawrenson JG, Reid AR, De SS, Allt G: Contractile proteins in pericytes at the blood-brain and blood-retinal barriers. *J Neurocytol* **2001**, 30:35-44.
19. Joyce NC, Haire MF, Palade GE: Contractile proteins in pericytes. II. Immunocytochemical evidence for the presence of two isomyosins in graded concentrations. *J Cell Biol* **1985**, 100:1387-95.
20. Dore-Duffy P, Wang S, Mehedi A, Katyshev V, Cleary K, Tapper A, Reynolds C, Ding Y, Zhan P, Rafols J, Kreipke CW: Pericyte-mediated vasoconstriction underlies TBI-induced hypoperfusion. *Neurol Res* **2011**, 33:176-86.
21. Boado RJ, Pardridge WM: Differential expression of alpha-actin mRNA and immunoreactive protein in brain microvascular pericytes and smooth muscle cells. *J Neurosci Res* **1994**, 39:430-5.

22. Song S, Ewald AJ, Stallcup W, Werb Z, Bergers G: PDGFRbeta+ perivascular progenitor cells in tumours regulate pericyte differentiation and vascular survival. *Nat Cell Biol* **2005**, 7:870-9.
23. Hughes S, Gardiner T, Hu P, Baxter L, Rosinova E, Chan-Ling T: Altered pericyte-endothelial relations in the rat retina during aging: implications for vessel stability. *Neurobiol Aging* **2006**, 27:1838-47.
24. Ozerdem U, Stallcup WB: Early contribution of pericytes to angiogenic sprouting and tube formation. *Angiogenesis* **2003**, 6:241-9.
25. Crisan M, Corselli M, Chen CW, Peault B: Multilineage stem cells in the adult: a perivascular legacy? *Organogenesis* **2011**, 7:101-4.
26. Shepro D, Morel NM: Pericyte physiology. *FASEB J* **1993**, 7:1031-8.
27. Sims DE: Diversity within pericytes. *Clin Exp Pharmacol Physiol* **2000**, 27:842-6.
28. Chen Q, Anderson DR: Effect of CO2 on intracellular pH and contraction of retinal capillary pericytes. *Invest Ophthalmol Vis Sci* **1997**, 38:643-51.
29. Sa-Pereira I, Brites D, Brito MA: Neurovascular unit: a focus on pericytes. *Mol Neurobiol* **2012**, 45:327-47.
30. Daneman R, Zhou L, Kebede AA, Barres BA: Pericytes are required for blood-brain barrier integrity during embryogenesis. *Nature* **2010**, 468:562-6.
31. Bell RD, Winkler EA, Sagare AP, Singh I, LaRue B, Deane R, Zlokovic BV: Pericytes control key neurovascular functions and neuronal phenotype in the adult brain and during brain aging. *Neuron* **2010**, 68:409-27.
32. Al AA, Gassmann M, Ogunshola OO: Maintaining blood-brain barrier integrity: pericytes perform better than astrocytes during prolonged oxygen deprivation. *J Cell Physiol* **2009**, 218:612-22.
33. Nakagawa S, Deli MA, Kawaguchi H, Shimizudani T, Shimono T, Kittel A, Tanaka K, Niwa M: A new blood-brain barrier model using primary rat brain endothelial cells, pericytes and astrocytes. *Neurochem Int* **2009**, 54:253-63.
34. Zlokovic BV: The blood-brain barrier in health and chronic neurodegenerative disorders. *Neuron* **2008**, 57:178-201.
35. Zlokovic BV: Neurodegeneration and the neurovascular unit. *Nat Med* **2010**, 16:1370-1.
36. Dohgu S, Takata F, Yamauchi A, Nakagawa S, Egawa T, Naito M, Tsuruo T, Sawada Y, Niwa M, Kataoka Y: Brain pericytes contribute to the induction and up-regulation of blood-brain barrier functions through transforming growth factor-beta production. *Brain Res* **2005**, 1038:208-15.
37. Hori S, Ohtsuki S, Hosoya K, Nakashima E, Terasaki T: A pericyte-derived angiopoietin-1 multimeric complex induces occludin gene expression in brain capillary endothelial cells through Tie-2 activation in vitro. *J Neurochem* **2004**, 89:503-13.
38. Luissint AC, Artus C, Glacial F, Ganeshamoorthy K, Couraud PO: Tight junctions at the blood brain barrier: physiological architecture and disease-associated dysregulation. *Fluids Barriers CNS* **2012**, 9:23.
39. Liebner S, Corada M, Bangsow T, Babbage J, Taddei A, Czupalla CJ, Reis M, Felici A, Wolburg H, Fruttiger M, Taketo MM, von MH, Plate KH, Gerhardt H, Dejana E: Wnt/beta-catenin signaling controls development of the blood-brain barrier. *J Cell Biol* **2008**, 183:409-17.
40. Daneman R, Agalliu D, Zhou L, Kuhnert F, Kuo CJ, Barres BA: Wnt/beta-catenin signaling is required for CNS, but not non-CNS, angiogenesis. *Proc Natl Acad Sci U S A* **2009**, 106:641-6.
41. Carmeliet P, Jain RK: Molecular mechanisms and clinical applications of angiogenesis. *Nature* **2011**, 473:298-307.
42. Stratman AN, Malotte KM, Mahan RD, Davis MJ, Davis GE: Pericyte recruitment during vasculogenic tube assembly stimulates endothelial basement membrane matrix formation. *Blood* **2009**, 114:5091-101.
43. Hellstrom M, Gerhardt H, Kalen M, Li X, Eriksson U, Wolburg H, Betsholtz C: Lack of pericytes leads to endothelial hyperplasia and abnormal vascular morphogenesis. *J Cell Biol* **2001**, 153:543-53.

44. Dalkara T, Gursoy-Ozdemir Y, Yemisci M: Brain microvascular pericytes in health and disease. *Acta Neuropathol* **2011**, 122:1-9.
45. Kotecki M, Zeiger AS, Van Vliet KJ, Herman IM: Calpain- and talin-dependent control of microvascular pericyte contractility and cellular stiffness. *Microvasc Res* **2010**, 80:339-48.
46. Rucker HK, Wynder HJ, Thomas WE: Cellular mechanisms of CNS pericytes. *Brain Res Bull* **2000**, 51:363-9.
47. Kamouchi M, Ago T, Kitazono T: Brain pericytes: emerging concepts and functional roles in brain homeostasis. *Cell Mol Neurobiol* **2011**, 31:175-93.
48. Kamouchi M, Kitazono T, Ago T, Wakisaka M, Kuroda J, Nakamura K, Hagiwara N, Ooboshi H, Ibayashi S, Iida M: Hydrogen peroxide-induced Ca2+ responses in CNS pericytes. *Neurosci Lett* **2007**, 416:12-6.
49. Hallmann R, Horn N, Selg M, Wendler O, Pausch F, Sorokin LM: Expression and function of laminins in the embryonic and mature vasculature. *Physiol Rev* **2005**, 85:979-1000.
50. Stratman AN, Davis GE: Endothelial cell-pericyte interactions stimulate basement membrane matrix assembly: influence on vascular tube remodeling, maturation, and stabilization. *Microsc Microanal* **2012**, 18:68-80.
51. Dore-Duffy P, Cleary K: Morphology and properties of pericytes. *Methods Mol Biol* **2011**, 686:49-68.
52. Corselli M, Chen CW, Crisan M, Lazzari L, Peault B: Perivascular ancestors of adult multipotent stem cells. *Arterioscler Thromb Vasc Biol* **2010**, 30:1104-9.
53. Farrington-Rock C, Crofts NJ, Doherty MJ, Ashton BA, Griffin-Jones C, Canfield AE: Chondrogenic and adipogenic potential of microvascular pericytes. *Circulation* **2004**, 110:2226-32.
54. Dellavalle A, Sampaolesi M, Tonlorenzi R, Tagliafico E, Sacchetti B, Perani L, Innocenzi A, Galvez BG, Messina G, Morosetti R, Li S, Belicchi M, Peretti G, Chamberlain JS, Wright WE, Torrente Y, Ferrari S, Bianco P, Cossu G: Pericytes of human skeletal muscle are myogenic precursors distinct from satellite cells. *Nat Cell Biol* **2007**, 9:255-67.
55. Paquet-Fifield S, Schluter H, Li A, Aitken T, Gangatirkar P, Blashki D, Koelmeyer R, Pouliot N, Palatsides M, Ellis S, Brouard N, Zannettino A, Saunders N, Thompson N, Li J, Kaur P: A role for pericytes as microenvironmental regulators of human skin tissue regeneration. *J Clin Invest* **2009**, 119:2795-806.
56. Davidoff MS, Middendorff R, Enikolopov G, Riethmacher D, Holstein AF, Muller D: Progenitor cells of the testosterone-producing Leydig cells revealed. *J Cell Biol* **2004**, 167:935-44.
57. Song B, Niclis JC, Alikhan MA, Sakkal S, Sylvain A, Kerr PG, Laslett AL, Bernard CA, Ricardo SD: Generation of induced pluripotent stem cells from human kidney mesangial cells. *J Am Soc Nephrol* **2011**, 22:1213-20.
58. Caplan AI: Why are MSCs therapeutic? New data: new insight. *J Pathol* **2009**, 217(2):318-24.
59. Thomas WE: Brain macrophages: on the role of pericytes and perivascular cells. *Brain Res Brain Res Rev* **1999**, 31:42-57.
60. Balabanov R, Washington R, Wagnerova J, Dore-Duffy P: CNS microvascular pericytes express macrophage-like function, cell surface integrin alpha M, and macrophage marker ED-2. *Microvasc Res* **1996**, 52:127-42.
61. Hammes HP, Feng Y, Pfister F, Brownlee M: Diabetic retinopathy: targeting vasoregression. *Diabetes* **2011**, 60:9-16.
62. Frank RN: Diabetic retinopathy. *N Engl J Med* **2004**, 350:48-58.
63. Hammes HP, Lin J, Wagner P, Feng Y, vom HF, Krzizok T, Renner O, Breier G, Brownlee M, Deutsch U: Angiopoietin-2 causes pericyte dropout in the normal retina: evidence for involvement in diabetic retinopathy. *Diabetes* **2004**, 53:1104-10.
64. Yao D, Taguchi T, Matsumura T, Pestell R, Edelstein D, Giardino I, Suske G, Rabbani N, Thornalley PJ, Sarthy VP, Hammes HP, Brownlee M: High glucose increases angiopoietin-2 transcription in microvascular endothelial cells through methylglyoxal modification of mSin3A. *J Biol Chem* **2007**, 282:31038-45.

65. Loukovaara S, Robciuc A, Holopainen JM, Lehti K, Pessi T, Liinamaa J, Kukkonen KT, Jauhiainen M, Koli K, Keski-Oja J, Immonen I: Ang-2 upregulation correlates with increased levels of MMP-9, VEGF, EPO and TGFbeta1 in diabetic eyes undergoing vitrectomy. *Acta Ophthalmol* **2013**, 91:531-9.
66. Mohammad G, Siddiquei MM: Role of matrix metalloproteinase-2 and -9 in the development of diabetic retinopathy. *J Ocul Biol Dis Infor* **2012**, 5:1-8.
67. Joussen AM, Poulaki V, Tsujikawa A, Qin W, Qaum T, Xu Q, Moromizato Y, Bursell SE, Wiegand SJ, Rudge J, Ioffe E, Yancopoulos GD, Adamis AP: Suppression of diabetic retinopathy with angiopoietin-1. *Am J Pathol* **2002**, 160:1683-93.
68. Pfister F, Wang Y, Schreiter K, vom HF, Altvater K, Hoffmann S, Deutsch U, Hammes HP, Feng Y: Retinal overexpression of angiopoietin-2 mimics diabetic retinopathy and enhances vascular damages in hyperglycemia. *Acta Diabetol* **2010**, 47:59-64.
69. Feng Y, vom HF, Pfister F, Djokic S, Hoffmann S, Back W, Wagner P, Lin J, Deutsch U, Hammes HP: Impaired pericyte recruitment and abnormal retinal angiogenesis as a result of angiopoietin-2 overexpression. *Thromb Haemost* **2007**, 97:99-108.
70. Pfister F, Feng Y, vom HF, Hoffmann S, Molema G, Hillebrands JL, Shani M, Deutsch U, Hammes HP: Pericyte migration: a novel mechanism of pericyte loss in experimental diabetic retinopathy. *Diabetes* **2008**, 57:2495-502.
71. Cai J, Kehoe O, Smith GM, Hykin P, Boulton ME: The angiopoietin/Tie-2 system regulates pericyte survival and recruitment in diabetic retinopathy. *Invest Ophthalmol Vis Sci* **2008**, 49:2163-71.
72. Lindahl P, Johansson BR, Leveen P, Betsholtz C: Pericyte loss and microaneurysm formation in PDGF-B-deficient mice. *Science* **1997**, 277:242-5.
73. Geraldes P, Hiraoka-Yamamoto J, Matsumoto M, Clermont A, Leitges M, Marette A, Aiello LP, Kern TS, King GL: Activation of PKC-delta and SHP-1 by hyperglycemia causes vascular cell apoptosis and diabetic retinopathy. *Nat Med* **2009**, 15:1298-306.
74. Armulik A, Genove G, Mae M, Nisancioglu MH, Wallgard E, Niaudet C, He L, Norlin J, Lindblom P, Strittmatter K, Johansson BR, Betsholtz C: Pericytes regulate the blood-brain barrier. *Nature* **2010**, 468:557-61.
75. Hirase T, Staddon JM, Saitou M, ndo-Akatsuka Y, Itoh M, Furuse M, Fujimoto K, Tsukita S, Rubin LL: Occludin as a possible determinant of tight junction permeability in endothelial cells. *J Cell Sci* **1997**, 110:1603-13.
76. Persidsky Y, Ramirez SH, Haorah J, Kanmogne GD: Blood-brain barrier: structural components and function under physiologic and pathologic conditions. *J Neuroimmune Pharmacol* **2006**, 1:223-36.
77. Shen W, Li S, Chung SH, Zhu L, Stayt J, Su T, Couraud PO, Romero IA, Weksler B, Gillies MC: Tyrosine phosphorylation of VE-cadherin and claudin-5 is associated with TGF-beta1-induced permeability of centrally derived vascular endothelium. *Eur J Cell Biol* **2011**, 90:323-32.
78. Yemisci M, Gursoy-Ozdemir Y, Vural A, Can A, Topalkara K, Dalkara T: Pericyte contraction induced by oxidative-nitrative stress impairs capillary reflow despite successful opening of an occluded cerebral artery. *Nat Med* **2009**, 15:1031-7.
79. Aguilar HN, Mitchell BF: Physiological pathways and molecular mechanisms regulating uterine contractility. *Hum Reprod Update* **2010**, 16:725-44.
80. Wynn TA: Cellular and molecular mechanisms of fibrosis. *J Pathol* **2008**, 214:199-210.
81. Fligny C, Duffield JS: Activation of pericytes: recent insights into kidney fibrosis and microvascular rarefaction. *Curr Opin Rheumatol* **2013**, 25:78-86.
82. Lin SL, Kisseleva T, Brenner DA, Duffield JS: Pericytes and perivascular fibroblasts are the primary source of collagen-producing cells in obstructive fibrosis of the kidney. *Am J Pathol* **2008**, 173:1617-27.
83. Humphreys BD, Lin SL, Kobayashi A, Hudson TE, Nowlin BT, Bonventre JV, Valerius MT, McMahon AP, Duffield JS: Fate tracing reveals the pericyte and not epithelial origin of myofibroblasts in kidney fibrosis. *Am J Pathol* **2010**, 176:85-97.

84. Chen YT, Chang FC, Wu CF, Chou YH, Hsu HL, Chiang WC, Shen J, Chen YM, Wu KD, Tsai TJ, Duffield JS, Lin SL: Platelet-derived growth factor receptor signaling activates pericyte-myofibroblast transition in obstructive and post-ischemic kidney fibrosis. *Kidney Int* **2011**, 80:1170-81.
85. Schrimpf C, Xin C, Campanholle G, Gill SE, Stallcup W, Lin SL, Davis GE, Gharib SA, Humphreys BD, Duffield JS: Pericyte TIMP3 and ADAMTS1 modulate vascular stability after kidney injury. *J Am Soc Nephrol* **2012**, 23:868-83.
86. Kennedy-Lydon TM, Crawford C, Wildman SS, Peppiatt-Wildman CM: Renal pericytes: regulators of medullary blood flow. *Acta Physiol (Oxf)* **2013**, 207:212-25.
87. Smith SW, Chand S, Savage CO: Biology of the renal pericyte. *Nephrol Dial Transplant* **2012**, 27:2149-55.
88. Lin SL, Chang FC, Schrimpf C, Chen YT, Wu CF, Wu VC, Chiang WC, Kuhnert F, Kuo CJ, Chen YM, Wu KD, Tsai TJ, Duffield JS: Targeting endothelium-pericyte cross talk by inhibiting VEGF receptor signaling attenuates kidney microvascular rarefaction and fibrosis. *Am J Pathol* **2011**, 178:911-23.
89. Betsholtz C, Lindblom P, Bjarnegard M, Enge M, Gerhardt H, Lindahl P: Role of platelet-derived growth factor in mesangium development and vasculopathies: lessons from platelet-derived growth factor and platelet-derived growth factor receptor mutations in mice. *Curr Opin Nephrol Hypertens* **2004**, 13:45-52.
90. Leveen P, Pekny M, Gebre-Medhin S, Swolin B, Larsson E, Betsholtz C: Mice deficient for PDGF B show renal, cardiovascular, and hematological abnormalities. *Genes Dev* **1994**, 8:1875-87.
91. Soriano P. Abnormal kidney development and hematological disorders in PDGF beta-receptor mutant mice: *Genes Dev* **1994**, 8:1888-96.
92. Borza CM, Pozzi A: The role of cell-extracellular matrix interactions in glomerular injury. *Exp Cell Res* **2012**, 318:1001-10.
93. Ziyadeh FN: Mediators of diabetic renal disease: the case for tgf-Beta as the major mediator. *J Am Soc Nephrol* **2004**, 15:S55-S57.
94 Brunskill EW, Potter SS: Changes in the gene expression programs of renal mesangial cells during diabetic nephropathy. *BMC Nephrol* **2012**, 13:70.
95. Kisseleva T, Cong M, Paik Y, Scholten D, Jiang C, Benner C, Iwaisako K, Moore-Morris T, Scott B, Tsukamoto H, Evans SM, Dillmann W, Glass CK, Brenner DA: Myofibroblasts revert to an inactive phenotype during regression of liver fibrosis. *Proc Natl Acad Sci U S A* **2012**, 109:9448-53.
96. Rock JR, Barkauskas CE, Cronce MJ, Xue Y, Harris JR, Liang J, Noble PW, Hogan BL: Multiple stromal populations contribute to pulmonary fibrosis without evidence for epithelial to mesenchymal transition. *Proc Natl Acad Sci U S A* **2011**, 108:E1475-E1483.
97. LeBleu VS, Taduri G, O'Connell J, Teng Y, Cooke VG, Woda C, Sugimoto H, Kalluri R: Origin and function of myofibroblasts in kidney fibrosis. *Nat Med* **2013**, 19:1047-53.
98 Juchem G, Weiss D, Hagl C, Nees S: Pericytes in the human myocardium: Not only an anatomical "internet" coordinating coronary vessels, but also key functional players? Thorac cardiovasc Surg **2013**, 61: P22.
99. Nees S, Weiss DR, Senftl A, Knott M, Forch S, Schnurr M, Weyrich P, Juchem G: Isolation, bulk cultivation, and characterization of coronary microvascular pericytes: the second most frequent myocardial cell type in vitro. *Am J Physiol Heart Circ Physiol* **2012**, 302:H69-H84.
100. O'Farrell F, Coleman E, Kendrick S, Attwell D: Microanatomy of pericytes in the rat ventricular myocardium. Proc Physiol Soc **2012**, 27;C84.
101. Nees S, Weiss DR, Juchem G: Focus on cardiac pericytes. *Pflugers Arch* **2013**, 465:779-87.
102. Nees S, Juchem G, Eberhorn N, Thallmair M, Forch S, Knott M, Senftl A, Fischlein T, Reichart B, Weiss DR: Wall structures of myocardial precapillary arterioles and postcapillary venules reexamined and reconstructed in vitro for studies on barrier functions. *Am J Physiol Heart Circ Physiol* **2012**, 302:H51-H68.

103. Juchem G, Weiss DR, Knott M, Senftl A, Forch S, Fischlein T, Kreuzer E, Reichart B, Laufer S, Nees S: Regulation of coronary venular barrier function by blood borne inflammatory mediators and pharmacological tools: insights from novel microvascular wall models. *Am J Physiol Heart Circ Physiol* **2012**, 302:H567-H581.
104. He Q, Spiro MJ: Isolation of rat heart endothelial cells and pericytes: evaluation of their role in the formation of extracellular matrix components. *J Mol Cell Cardiol* **1995**, 27:1173-83.
105. Juchem G, Weiss DR, Gansera B, Kemkes BM, Mueller-Hoecker J, Nees S: Pericytes in the macrovascular intima: possible physiological and pathogenetic impact. *Am J Physiol Heart Circ Physiol* **2010**, 298:H754-H770.
106. Osterud B, Bjorklid E: Sources of tissue factor. *Semin Thromb Hemost* **2006**, 32:11-23.
107. O'Farrell FM, Attwell D: A role for pericytes in coronary no-reflow. *Nat Rev Cardiol* **2014**, 11:427-32.
108. Niccoli G, Lanza GA, Shaw S, Romagnoli E, Gioia D, Burzotta F, Trani C, Mazzari MA, Mongiardo R, De VM, Rebuzzi AG, Luscher TF, Crea F: Endothelin-1 and acute myocardial infarction: a no-reflow mediator after successful percutaneous myocardial revascularization. *Eur Heart J* **2006**, 27:1793-8.
109. Bostrom K, Watson KE, Horn S, Wortham C, Herman IM, Demer LL: Bone morphogenetic protein expression in human atherosclerotic lesions. *J Clin Invest* **1993**, 91:1800-9.
110. Tigges U, Komatsu M, Stallcup WB: Adventitial pericyte progenitor/mesenchymal stem cells participate in the restenotic response to arterial injury. *J Vasc Res* **2013**, 50:134-44.
111. McCullough PA, Olobatoke A, Vanhecke TE: Galectin-3: a novel blood test for the evaluation and management of patients with heart failure. *Rev Cardiovasc Med* **2011**, 12:200-10.
112. Weiss RM, Miller JD, Heistad DD: Fibrocalcific aortic valve disease: opportunity to understand disease mechanisms using mouse models. *Circ Res* **2013**, 113:209-22.
113. Chen CW, Okada M, Proto JD, Gao X, Sekiya N, Beckman SA, Corselli M, Crisan M, Saparov A, Tobita K, Peault B, Huard J: Human pericytes for ischemic heart repair. *Stem Cells* **2013**, 31:305-16.
114. Dar A, Domev H, Ben-Yosef O, Tzukerman M, Zeevi-Levin N, Novak A, Germanguz I, Amit M, Itskovitz-Eldor J: Multipotent vasculogenic pericytes from human pluripotent stem cells promote recovery of murine ischemic limb. *Circulation* **2012**, 125:87-99.
115. Corselli M, Chen CW, Sun B, Yap S, Rubin JP, Peault B: The tunica adventitia of human arteries and veins as a source of mesenchymal stem cells. *Stem Cells Dev* **2012**, 21:1299-308.
116. Morigi M, Rota C, Montemurro T, Montelatici E, Lo C, V, Imberti B, Abbate M, Zoja C, Cassis P, Longaretti L, Rebulla P, Introna M, Capelli C, Benigni A, Remuzzi G, Lazzari L: Life-sparing effect of human cord blood-mesenchymal stem cells in experimental acute kidney injury. *Stem Cells* **2010**, 28:513-22.
117. Mendel TA, Clabough EB, Kao DS, midova-Rice TN, Durham JT, Zotter BC, Seaman SA, Cronk SM, Rakoczy EP, Katz AJ, Herman IM, Peirce SM, Yates PA: Pericytes derived from adipose-derived stem cells protect against retinal vasculopathy. *PLoS One* **2013**, 8:e65691.
118. Pimentel-Coelho PM, Rivest S: The early contribution of cerebrovascular factors to the pathogenesis of Alzheimer's disease. *Eur J Neurosci* **2012**, 35:1917-37.
119. Lee HJ, Lee JK, Lee H, Carter JE, Chang JW, Oh W, Yang YS, Suh JG, Lee BH, Jin HK, Bae JS: Human umbilical cord blood-derived mesenchymal stem cells improve neuropathology and cognitive impairment in an Alzheimer's disease mouse model through modulation of neuroinflammation. *Neurobiol Aging* **2012**, 33:588-602.
120. Lee JK, Jin HK, Bae JS: Bone marrow-derived mesenchymal stem cells reduce brain amyloid-beta deposition and accelerate the activation of microglia in an acutely induced Alzheimer's disease mouse model. *Neurosci Lett* **2009**, 450:136-41.
121. Shin JY, Park HJ, Kim HN, Oh SH, Bae JS, Ha HJ, Lee PH: Mesenchymal stem cells enhance autophagy and increase beta-amyloid clearance in Alzheimer disease models. *Autophagy* **2014**, 10:32-44.
122. Verbeek MM, de Waal RM, Schipper JJ, Van Nostrand WE: Rapid degeneration of cultured human brain pericytes by amyloid beta protein. *J Neurochem* **1997**, 68:1135-41.

123. Karow M, Sanchez R, Schichor C, Masserdotti G, Ortega F, Heinrich C, Gascon S, Khan MA, Lie DC, Dellavalle A, Cossu G, Goldbrunner R, Gotz M, Berninger B: Reprogramming of pericyte-derived cells of the adult human brain into induced neuronal cells. *Cell Stem Cell* **2012**, 11:471-6.
124. Montiel-Eulefi E, Nery AA, Rodrigues LC, Sanchez R, Romero F, Ulrich H: Neural differentiation of rat aorta pericyte cells. *Cytometry A* **2012**, 81:65-71.
125. Dore-Duffy P, Katychev A, Wang X, Van BE: CNS microvascular pericytes exhibit multipotential stem cell activity. *J Cereb Blood Flow Metab* **2006**, 26:613-24.
126. Dore-Duffy P, Owen C, Balabanov R, Murphy S, Beaumont T, Rafols JA: Pericyte migration from the vascular wall in response to traumatic brain injury. *Microvasc Res* **2000**, 60:55-69.
127. Carvalho AB, Quintanilha LF, Dias JV, Paredes BD, Mannheimer EG, Carvalho FG, Asensi KD, Gutfilen B, Fonseca LM, Resende CM, Rezende GF, Takiya CM, de Carvalho AC, Goldenberg RC: Bone marrow multipotent mesenchymal stromal cells do not reduce fibrosis or improve function in a rat model of severe chronic liver injury. *Stem Cells* **2008**, 26:1307-14.
128. Ali G, Mohsin S, Khan M, Nasir GA, Shams S, Khan SN, Riazuddin S: Nitric oxide augments mesenchymal stem cell ability to repair liver fibrosis. *J Transl Med* **2012**, 10:75.
129. Joyce NC, Haire MF, Palade GE: Contractile proteins in pericytes. I. Immunoperoxidase localization of tropomyosin. *J Cell Biol* **1985**, 100:1379-86.
130. Morikawa S, Baluk P, Kaidoh T, Haskell A, Jain RK, McDonald DM: Abnormalities in pericytes on blood vessels and endothelial sprouts in tumors. *Am J Pathol* **2002**, 160:985-1000.
131. Alliot F, Rutin J, Leenen PJ, Pessac B: Pericytes and periendothelial cells of brain parenchyma vessels co-express aminopeptidase N, aminopeptidase A, and nestin. *J Neurosci Res* **1999**, 58:367-78.
132. Xueyong L, Shaozong C, Wangzhou L, Yuejun L, Xiaoxing L, Jing L, Yanli W, Jinqing L: Differentiation of the pericyte in wound healing: The precursor, the process, and the role of the vascular endothelial cell. *Wound Repair Regen* **2008**, 16:346-55.

Chapter 4

Transcriptome analysis reveals microvascular endothelial cell-dependent pericyte differentiation

Maarten M. Brandt, Christian G.M. van Dijk, Ranganath Maringanti, Ihsan Chrifi, Rafael Kramann, Marianne C. Verhaar, Dirk J. Duncker, Michal Mokry, Caroline Cheng

Scientific Reports, 2019 Oct ;9(1):15586

Abstract

Microvascular homeostasis is strictly regulated, requiring close interaction between endothelial cells and pericytes. Here, we aimed to improve our understanding on how microvascular crosstalk affects pericytes. Human-derived pericytes, cultured in absence, or presence of human endothelial cells, were studied by RNA sequencing. Compared with mono-cultured pericytes, a total of 6704 genes were differentially expressed in co-cultured pericytes. Direct endothelial contact induced transcriptome profiles associated with pericyte maturation, suppression of extracellular matrix production, proliferation, and morphological adaptation. *In vitro* studies confirmed enhanced pericyte proliferation mediated by endothelial-derived PDGFB and pericyte-derived HB-EGF and FGF2. Endothelial-induced PLXNA2 and ACTR3 upregulation also triggered pericyte morphological adaptation. Pathway analysis predicted a key role for TGFβ signaling in endothelial-induced pericyte differentiation, whereas the effect of signaling via gap- and adherens junctions was limited. We demonstrate that ECs have a major impact on the transcriptional profile of pericytes, regulating endothelial-induced maturation, proliferation, and suppression of ECM production.

Introduction

Complex organisms such as vertebrates rely on a well-functioning circulatory system to meet the body's oxygen and nutrient demand, and to remove waste products. The circulatory system is composed of blood vessels, lined by a single layer of endothelial cells (ECs) on the luminal side. These ECs are surrounded by a basement membrane which they share with mural cells. In the microvasculature, these mural cells consist of pericytes [1].

Maintaining microvascular homeostasis is a strictly regulated process, which requires close interplay between ECs and pericytes. Dysregulation of this comprehensive interaction is associated with the onset and progression of a variety of diseases [2]. Lack of pericytes compromises vascular integrity and causes leaky unstable vessels (e.g. in rapidly growing tumors) [3], as well as highly proliferative endothelium (e.g. in diabetic retinopathy) [4]. Moreover, pericytes have previously been linked to pathological organ fibrosis [5], though whether injury-induced stimulation, or loss of endothelial interaction drives this differentiation is poorly understood. Former studies on microvascular cross-talk provided valuable insights into the mechanisms involved in regulating in vascular homeostasis. For instance, Platelet Derived Growth Factor Subunit B (PDGFB) secretion by ECs was shown to modulate pericyte proliferation and migration towards the endothelium [4], whereas pericyte-derived Vascular Endothelial Growth Factor A (VEGFA) and Angiopoietin 1 secretion were reported to promote endothelial survival and maturation [6,7]. In addition to these paracrine interactions, ECs and pericytes also connect physically. At distinct places, the basement membrane separating the two cell types is interrupted, allowing the formation of direct connection sites called peg and socket contacts [8]. These contacts are highly enriched in gap- and adherens junctions, which provide a direct signaling route for ions, nutrients, metabolites, and secondary messengers [9]. Over the years, numerous studies have focused on the different aspects of signaling between these closely associated microvascular cells. However, since most emphasis was put on how pericytes affect endothelial behavior, only little is known about the consequence of this cross-talk for pericytes.

To gain a deeper understanding of the impact of vascular crosstalk on these critical, yet relatively underexposed, contributors of microvascular homeostasis, an RNA sequence-(RNAseq) based analysis was performed to compare the mRNA expression profiles of single cultured pericytes, with those of pericytes cultured in direct contact with endothelial cells. The results demonstrate that ECs have a major impact on the transcriptional profile of pericytes and provide functional evidence for endothelium-induced pericyte maturation, proliferation, and suppression of ECM expression.

Methods

Cell culture

Human dermal microvascular endothelial cells (HMVECs; Lonza) and human brain-derived pericytes (Sciencell) were cultured on 0.1% gelatin coated plates in EGM-2MV medium (EBM-2 medium supplemented with EGM-2MV bullet kit; Lonza) and DMEM (supplemented with 10% fetal calf serum (FCS); Lonza), respectively, in 5% CO_2 at 37 ˚C. HMVECs were transduced with a lentiviral green fluorescent protein (GFP) construct and pericytes with a lentiviral discosoma sp. red- (dsRED) construct. Experiments were performed with cells at passage 4-6. CDH2, CX43, HB-EGF, FGF2 and VEGFA, PLXN2A, ACTR3 knockdown in pericytes, and PDGFB knockdown in HMVECs was achieved by cell transfection with a pool containing 4 targeting short interference RNA- (siRNA) sequences (Dharmacon) in a final concentration of 100 nM. Control cells were transfected with a pool of 4 non-targeting siRNA sequences (Dharmacon) in a final concentration of 100 nM. Target sequences are listed in Supplemental Table 1.

Fluorescence-activated cell sorting

GFP-labeled HMVECs and dsRED-labeled pericytes were seeded in a confluent layer (4 million cells) on 10 cm dishes, either in co-culture at a 5:1 (HMVECs:pericytes) ratio, or in single culture (Figure 1A). Both single cultures and co-cultures were cultured on EBM supplemented with 5% FCS for 6 h, followed by 20 h on EBM supplemented with 0.5% FCS. For fluorescence activated cell sorting (FACS), cells were trypsinized, washed once in cold PBS and suspended in cold sterile filtered PBS containing 2% bovine serum albumin. GFP-labeled HMVECs and dsRED-labeled pericytes were separately sorted in cold FCS based on their fluorescent signal. Subsequently, cells were washed once in cold PBS, lysed in RNA lysis buffer and stored at -80 ˚C (Figure 1B).

RNA sequencing

RNA sequencing was done as previously described [10]. Briefly, sequencing libraries were made from poly-adenylated RNA using the Rapid Directional RNA-Seq Kit (NEXTflex) and sequenced on Illumina NextSeq500 to produce single-end 75 base long reads (Utrecht Sequencing Facility). Reads were aligned to the human reference genome GRCh37 using STAR version2.4.2a. Read groups were added to the compressed binary version of the sequence alignment file (*.bam) files using Picard's "AddOrReplaceReadGroups" tool (v1.98). The bam files were sorted with Sambamba v0.4.5, and transcript abundances were quantified with HTSeq-count version 0.6.1p117 using the union mode. Subsequently, reads per kilobase of transcript per million reads sequenced were calculated with edgeR's rpkm() function.

Differentially expressed genes in the transcriptome data were identified using the DESeq2 package with standard settings [11]. principle component analysis (PCA) was performed in R, using the plotPCA() command. Reads were normalized for sequencing depth and rlog transformed.

Quantitative PCR and Western blot analysis

RNA was reverse transcribed into cDNA using iScript cDNA synthesis kit (Bioline). Gene expression was assessed by qPCR using SensiFast SYBR & Fluorecein kit (Bioline) and primers as listed in Supplemental Table 2. Expression levels are relative to the housekeeping gene Ribosomal Phosphoprotein P0 (RPLP0) and RNA Polymerase II Subunit L (POLR2L). For assessment of protein levels, cells were lysed in cold NP-40 lysis buffer (150 mM NaCl, 1.0% NP-40, 50 mM Tris, pH 8.0) supplemented with 1 mM β-glycerolphosphate, 1 mM PMSF, 10 mM NaF, 1 mM NaOV, and protease inhibitor cocktail (Roche). Total protein concentration was quantified by Pierce® BCA Protein Assay Kit (Thermo Scientific) as a loading control. Lysates were denaturated in Laemmli buffer (60 mM Tris pH 6.8, 2% SDS, 10% glycerol, 5% β-mercaptoethanol, 0.01% bromophenol blue) at 90°C for 5 min followed by electrophoresis on a 10% SDS-PAGE gel (Biorad). Subsequently, proteins were transferred to a nitrocellulose membrane (Pierce) and incubated for 1 hour in PBS with 5% non-fat milk, followed by incubation with rabbit anti-CX43 and rabbit anti-N-cadherin (CST) according to manufacturer's description. Protein bands were visualized with the Li-Cor detection system (Westburg).

Immunofluorescent staining

Pericytes labeled with dsRED were seeded in a confluent layer (50.000 cells) in 96 wells plates in a 1:5 ratio, either with unlabeled HMVECs, or with unlabeled pericytes. After seeding, the cells were cultured on EBM supplemented with 5% FCS for 6h, followed by 20h on EBM supplemented with 0.5% FCS. After 20h in culture, cells were fixed for 20min in 2% paraformaldehyde and blocked for 60min in PBS containing 5% bovine serum albumin (Sigma) and 0.3% Triton X-100 (Sigma). Hereafter, 100µl PBS containing 1% BSA, 0.3% Triton X-100, and 1:400 rabbit anti-Ki67 antibody (CST) was added per well, followed by a 16h incubation at 4°C. After incubation with the primary antibody, Ki67 was stained with an Alexa Fluor 594-labeled secondary antibody (Invitrogen), dissolved (1:200) in PBS containing 1% BSA and 0.3% Triton X-100 for 2h at room temperature. Vectashield with DAPI (Brunschwig) was applied to the fixed cell cultures, followed by imaging using fluorescence microscopy. Analysis of Ki67 positive pericyte nuclei was averaged per individual experiment from at least 5 random image fields in ImageJ using the Cell Counter plugin.

Pathway analysis

RNAseq results were analyzed using QIAGEN's Ingenuity Pathway Analysis (IPA). IPA was used to study upstream regulators (growth factors and transcriptional regulators) of differentially expressed genes. P-values were calculated based on a right-tailed Fisher Exact Test, calculated by IPA.

Statistics

Data are presented as means ± SEM. Groups were compared by students t-test (two-tailed) or 1-way ANOVA followed by Tukey post hoc test when appropriate. Statistical significance was accepted when $p<0.05$.

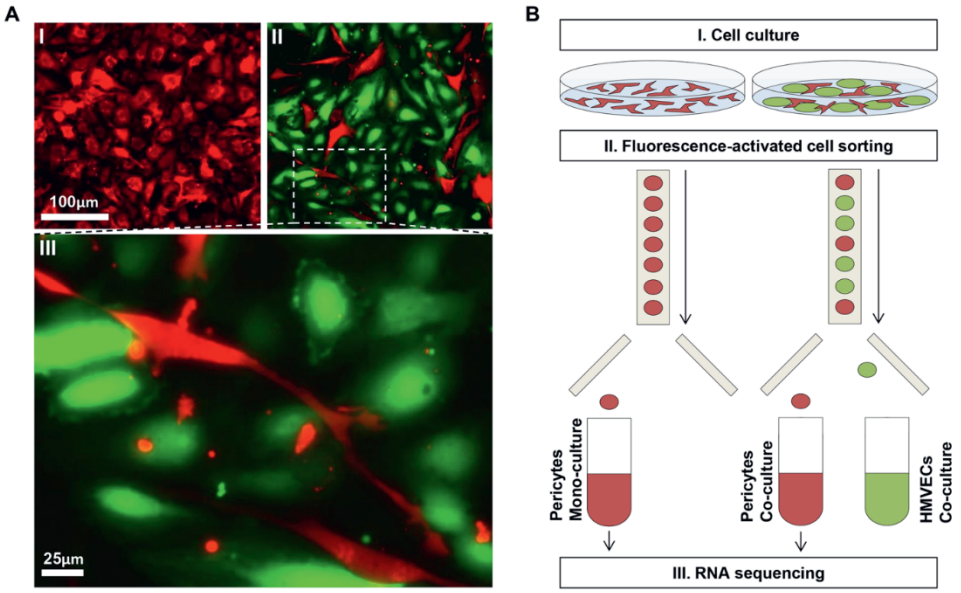

Figure 1. Expression profiles were generated from mono- and co-cultured pericytes via RNA sequencing. (A) Pericytes labeled with dsRED (red) were either cultured alone (I), or in direct contact with GFP-labeled HMVECs (green) (II). Magnified view of co-cultured cells clearly shows the elongated pericytes that appear to be in contact with multiple ECs (III). **(B)** Schematic overview of the experiments: Pericytes labeled with dsRED were cultured in a confluent layer, either alone, or in direct contact with GFP-labeled HMVECs for the duration of 20 hours (I). Hereafter, cells were trypsinized and sorted based on fluorescent signal (II), after which RNA was isolated from the pericytes for RNA sequencing (III).

Results

Endothelial cells markedly affect pericyte phenotype

To evaluate the impact of endothelial-pericyte interaction on pericyte behavior, dsRED labeled pericytes were cultured in a confluent layer either alone, or in the presence of GFP-labeled HMVECs, enabling direct contact between the two different cell types (Figure 1A). Twenty hours post seeding, cells were trypsinized and sorted based on fluorescent signal, after which RNA was isolated and processed for RNA sequencing (Figure 1B). A comparison of the transcription profile of single cultured pericytes and co-cultured pericytes in a PCA clearly illustrated the major effect of endothelial-pericyte crosstalk on pericytes (Figure 2A). In total, 6704 genes were differentially expressed (P adjusted <0.05; Figure 2B, Supplemental Table 3). Of these 6704 differentially expressed genes, 6081 were protein coding genes (almost one third of the estimated 19000 protein coding genes in the human genome) [12], suggesting that direct contact with ECs dramatically affects pericyte's transcriptomes.

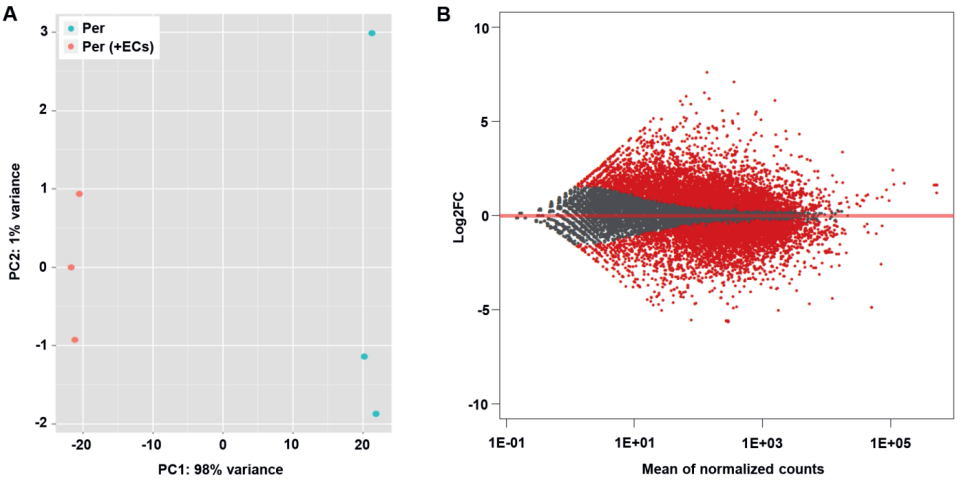

Figure 2. Endothelial cells have a major impact on the expression profile of pericytes. (A) PCA plot of expression profiles in single cultured pericytes (blue) and co-cultured pericytes (red), derived from 3 experimental replicates composed of single cultured and co-cultured pericytes. The x and y axes reflect the variance between the samples analyzed by RNAseq, in which most of the variance (98%) came from pericytes being cultured in absence or in presence of endothelial cells (x axis), and where likely the experimental variation had only a limited contribution (y axis). **(B)** Graphic display of differential gene expression (MA plot) in which log2FC is plotted against the mean of normalized counts. Red dots represent the 6.704 differentially expressed genes (P adjusted <0.05), grey dots represent non-differentially expressed genes.

Direct contact with endothelium stimulates pericyte maturation

A newly formed endothelial network is initially unstable and requires support from recruited pericytes. These pericytes either migrate from adjacent vessels or differentiate from local mesenchymal stem cells [13]. Comparing expression profiles from single cultured pericytes with pericytes co-cultured with ECs clearly illustrated the importance of interaction with ECs in this differentiation process. Expression of Glioma-associated oncogene 1 (GLI1), a zinc finger type transcription factor and downstream effector of the Hedgehog signaling pathway that has been reported to be expressed in pericyte-like progenitors [14], was significantly reduced in co-cultured pericytes (Figure 3A). In contrast, well-validated pericyte markers, including Chondroitin Sulfate Proteoglycan 4 (CSPG4/NG2), Alpha Smooth Muscle Actin 2 (ACTA2), Melanoma Cell Adhesion Molecule (CD146), and Nestin (NES), were highly upregulated after direct interaction with ECs (Figure 3B). Interestingly, Platelet Derived Growth Factor Receptor Beta (PDGFRβ), one of the most frequently used pericyte- and mesenchyme markers, was significantly downregulated in co-cultured pericytes (Figure 3B).

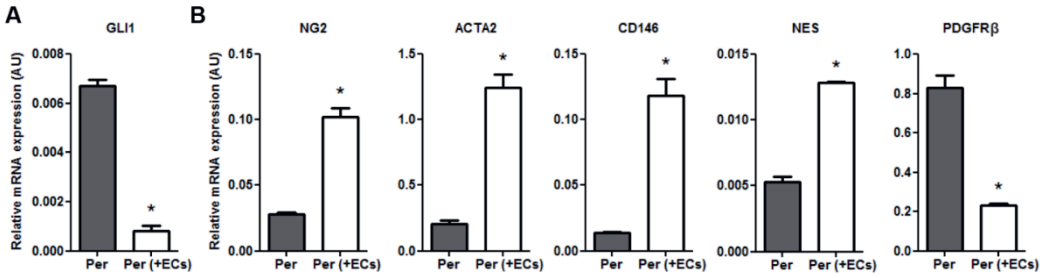

Figure 3. Direct contact with endothelium stimulates pericyte maturation. (A) QPCR results showing expression levels of mesenchymal transcription factor GLI1, and **(B)** pericyte markers NG2, ACTA2, CD146, NES, and PDGFRβ relative to RPLP0 and POLR2L in pericytes in monoculture (Per), and after 20h in co-culture with HMVECs (Per+ECs). N=3, *P<0.05 compared to pericytes in monoculture. GLI1: Glioma-associated oncogene 1, NG2: Chondroitin Sulfate Proteoglycan 4, ACTA2: Alpha Smooth Muscle Actin 2, CD146: Melanoma Cell Adhesion Molecule, NES: Nestin, PDGFRβ: Platelet Derived Growth Factor Receptor Beta.

Endothelial signaling stimulates pericyte proliferation and survival

Prior studies showed that pericyte-endothelial interaction had a profound positive effect on endothelial survival and maturation [15]. Interestingly, studying the upstream transcription factors of the differentially expressed genes using IPA led to the suggestion that direct interaction with ECs also stimulated pericyte proliferation and survival (Figure 4A), which corresponds with functional findings reported previously [16]. Expression levels of 330 Tumor

Protein 53- (TP53) dependent target genes in co-cultured pericytes (Supplemental Table 4), including BCL2 Binding Component 3 (BBC3), Tumor Protein P53 Inducible Nuclear Protein 1 (TP53INP1), and Growth Differentiation Factor 15 (GDF15), suggested suppressed activity of this pro-apoptotic and cell cycle inhibiting factor (Figure 4B). Vice versa, the activity of proliferation-stimulating transcription factors E2F1 and E2F3 appeared to be enhanced in co-cultured pericytes. Expression of 139 E2F target genes, including Cyclin Dependent Kinase 1 (CDK1), Retinoblastoma Transcriptional Corepressor Like 1 (RBL1), Proto-Oncogene C-Myc (MYC), Minichromosome Maintenance Complex Component 2 (MCM2), and Cyclin D1 (CCND1), was significantly enhanced after direct interaction with ECs (Figure 4C, Supplemental Table 5). To functionally validate the impact of endothelial contact on pericyte proliferation, we performed immunostaining for the proliferation (G1/S/G2M) marker Ki67 in dsRED-labeled pericytes, cultured in a confluent layer either with unlabeled HMVECs, or with unlabeled pericytes (Figure 4D). In line with the observed transcriptional adaptations in co-cultured pericytes, quantification of the percentage of Ki67-positive nuclei in dsRED-labeled pericytes clearly illustrated a significantly increased pericyte proliferation during co-culture with endothelium as compared with mono-cultured pericytes (Figure 4E). It was previously reported that pericyte proliferation could be stimulated by VEGFA [17], potentially via an autocrine signaling loop resulting from endothelium-induced upregulation of VEGFA expression in pericytes. In the present study however, a significant downregulation of VEGFA was observed in co-cultured pericytes, though expression was still higher than in co-cultured ECs (Figure 4F). To evaluate the involvement of pericyte-derived VEGFA in pericyte proliferation, as well as that of potent growth factors Heparin-binding EGF-like growth factor (HB-EGF) and fibroblast growth factor 2 (FGF2), which in contrast to VEGFA were upregulated in co-cultured pericytes, siRNA mediated knockdown was performed in dsRED-labeled pericytes followed by co-culture with ECs and Ki-67 immunostaining (Supplemental Figure 1A and 1C). Quantification of the percentage of Ki67-positive nuclei in dsRED-labeled pericytes revealed that knockdown of VEGFA had no effect on pericyte proliferation, whereas knockdown of HB-EGF and FGF2 significantly reduced the proliferative response of pericytes in co-culture with pericytes (Figure 4G). Similarly, endothelial knockdown of PDGFB, a well-known pericyte mitogen that was upregulated in co-cultured ECs (Supplemental Figure 1B and 1D), significantly reduced proliferation of pericytes in co-culture with ECs (Figure 4H).

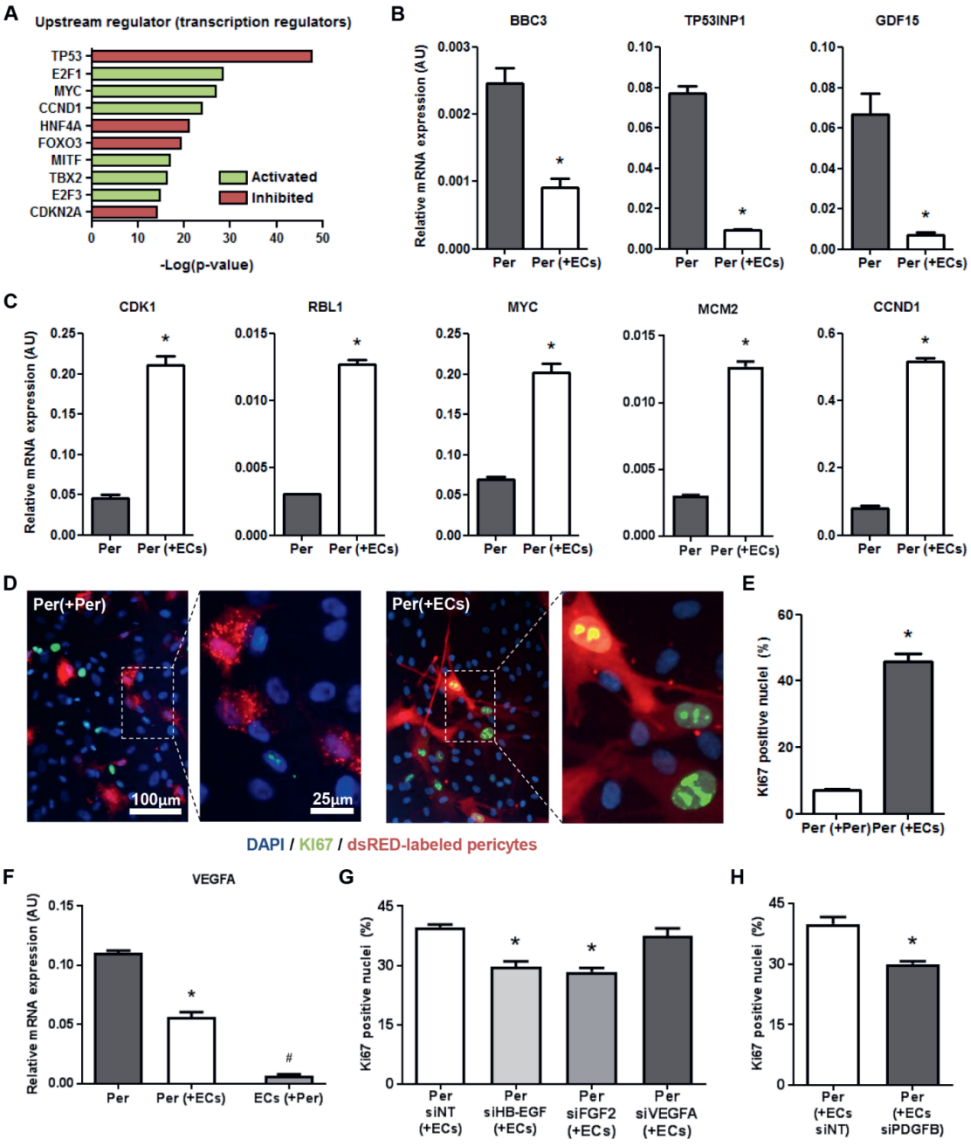

Figure 4. Endothelial signaling stimulates pericyte proliferation and survival. (A) IPA-derived prediction of activated or repressed transcription regulators in co-cultured pericytes compared with single cultured pericytes. Plotted is the –log(p-value) of overlap, in which green indicates predicted activation in co-culture versus predicted inhibition in red. **(B)** QPCR results showing expression levels of TP53 target genes BBC3, TP53INP1, and GDF15, as well as **(C)** E2F target genes CDK1, RBL1, MYC, MCM2 and CCND1 relative to RPLP0 and POLR2L in pericytes in monoculture (Per), and after 20h in co-culture with HMVECs (Per+ECs). N=3, *P<0.05 compared to pericytes in monoculture. **(D)** Immunofluorescent Ki67 (green), and DAPI (blue) staining in dsRED-labeled pericytes, either cultured with unlabeled HMVECs (left) or with unlabeled pericytes (right). **(E)** Bar graph shows the quantified results of the Ki67 staining.

◄Shown are the percentages of dsRED-labeled pericyte nuclei positive for the proliferation marker Ki67. N=3, *P<0.05 compared to dsRED-labeled pericytes in culture with unlabeled pericytes. **(F)** QPCR results showing expression levels of VEGFA in pericytes in monoculture (Per), and after 20h in co-culture in both pericytes (Per+ECs) and HMVECs (ECs+Per). N=3, *P<0.05 compared to pericytes in monoculture and ECs in co-culture, #P<0.05 compared to pericytes in mono- and co-culture. **(G)** Bar graph showing the percentage of Ki67 positive nuclei in dsRED-labeled pericytes after knockdown of HB-EGF, FGF2, and VEGFA in pericytes, and **(H)** PDGFB in ECs. N=4, *P<0.05 compared to siNT-treated condition. BBC3: BCL2 Binding Component 3, TP53INP1: Tumor Protein P53 Inducible Nuclear Protein 1, GDF15: Growth Differentiation Factor 15, CDK1: Cyclin Dependent Kinase 1, RBL1: RB Transcriptional Corepressor Like 1, MYC: MYC Proto-Oncogene, MCM2: Minichromosome Maintenance Complex Component 2, CCND1: Cyclin D1, VEGFA: Vascular Endothelial Growth Factor A, NT: non-targeting, HB-EGF: Heparin-binding EGF-like growth factor, FGF2: Fibroblast Growth Factor 2.

Direct endothelial contact triggers outgrowth of pericyte projections

Mature pericytes have a highly specialized morphology that is distinctly different from other microvascular cells. They align their nuclei with the endothelium and extent thin processes along and around the capillaries. These elongated projections allow individual pericytes to contact and communicate with multiple ECs and were recently shown to have an active role in maintaining normal cerebral microvascular lumen diameter [18]. These thin processes show morphological similarities with axons growing from neurons. Growing axons have a highly dynamic structure at the peripheral tip, called the growth cone, which senses the environment for attracting or repelling guiding cues. Following these cues, actin remodeling at the leading edge guides the growth cone, followed by a polymerizing and elongating bundle of microtubules [19]. Interestingly, an exceptionally high number of genes involved in this process was differentially expressed in co-cultured pericytes, as identified by IPA (Supplemental Table 6). Among these differentially expressed genes was a variety of different growth cone-guiding molecules, including Semaphorins (SEMA), Ephrins (EFN), Netrins (NTN), and their respective receptors (Figure 5A). Many Alpha and Beta Tubulins (TUBA and TUBB, respectively), composing the core of the growing projections, were upregulated in co-cultured pericytes (Figure 5B). Similarly, enhanced expression was observed for Cofilins (CFL) and all but one Actin Related Protein 2/3 Complex subunits (ARPC), which regulate actin polymerization required for growth cone dynamics (Figure 5B) [20]. To verify whether these transcriptional adaptations were associated with morphological changes that resemble outgrowth of pericyte projections, dsRED-labeled pericytes were again cultured in a confluent layer for the duration of 20h, either in combination with unlabeled HMVECs, or with unlabeled pericytes followed by fluorescent microscopy imaging. Interestingly, pericytes in direct contact with ECs had a completely different morphology, indeed forming extensive projections (Figure 5C). To study whether the differentially expressed growth cone-guiding molecules could in

fact be involved in the observed morphological adaptation in pericytes, a proof-of-principle approach was used in which Plexin A2 (PLXNA2) and Actin Related Protein 3 (ACTR3), both well expressed and highly upregulated in co-cultured pericytes (Supplemental Figure 2A), were knocked down (Supplemental Figure 2B). After culturing these siRNA-transfected pericytes in a confluent layer with HMVECs for the duration of 20h, the percentage of protrusion-forming pericytes was quantified using fluorescence microscopy. Knockdown of both PLXNA2 and ACTR3 significantly reduced the relative number of pericytes with projections (Figure 5D), substantiating the idea that direct interaction with ECs triggered a transcriptional response in pericytes necessary for morphological maturation.

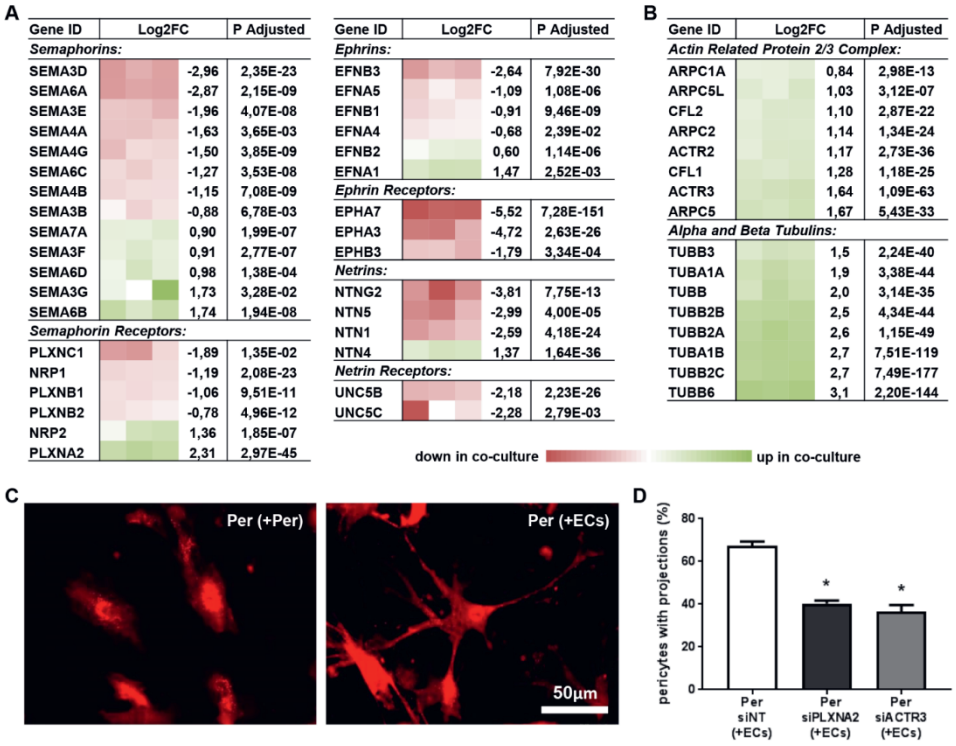

Figure 5. Direct endothelial contact triggers outgrowth of pericyte projections. (A) schematic presentation of RNAseq data for differentially expressed Semaphorins, Ephrins, Netrins, and their respective receptors, as well as **(B)** subunits of the Actin Related Protein 2/3 Complex and Tubulins, which were all listed by IPA in a group of 200 differentially expressed genes involved in projection outgrowth. Shown is a color-based representation of the log2FC in each of the 3 individual experiments (red is downregulated in co-culture, green is upregulated in co-culture), followed by the average log2FC and the adjusted p-value. **(C)** Representative fluorescence microscopy images of dsRED-labeled pericytes in co-culture with unlabeled pericytes (left), or with unlabeled HMVECs (right). **(D)** Bar graph showing the percentage of dsRED-labeled pericytes with outgrowth of projections after knockdown of

◄PLXNA2 and ACTR3 in pericytes. N=4, *P<0.05 compared to siNT-treated condition. NT: non-targeting, PLXNA2: Plexin A2, ACTR3: Actin Related Protein 3.

Endothelial interaction suppresses overall ECM production in pericytes

Recent studies showed that pericytes, detaching from the capillaries, not only leave the microvascular endothelium in a vulnerable position, but at the same time might undergo differentiation into ECM-producing cells themselves [5,21]. Whether this differentiation is a consequence of disrupted mutual cross-talk, or involves other extravascular signaling routes is not fully understood. Interestingly, expression of 24 collagen subtypes was significantly suppressed in pericytes co-cultured with endothelial cells, compared with mono-cultured pericytes (Figure 6A). Moreover, a variety of other ECM components, including Fibronectin 1 (FN1), and Alpha- and Beta Laminins (LAMA and LAMB, respectively) was transcriptionally downregulated in co-cultured pericytes (Figure 6A). This suppressed ECM expression in co-cultured pericytes might argue that differentiation into a fibrotic phenotype is indeed inhibited by direct interaction with ECs. Several studies have suggested that pericyte differentiation towards ECM producing cells depends on enhanced Transforming Growth Factor Beta (TGFβ) signaling [22,23]. However, in line with findings from many other studies (reviewed by Gaengel *et al*. [24]), our findings indicated that pericytes in contact with ECs have much higher activation of TGFβ signaling than pericytes lacking interaction with ECs. In fact, based on 315 differentially expressed genes, IPA considered TGFβ1 (overlap p-value 3.56E-34) as the most active upstream growth factor in co-cultured pericytes (Figure 6B, Supplemental Table 7). Other upregulated genes in co-cultured pericytes beside ACTA2, included Connective Tissue Growth Factor (CTGF), Smooth Muscle Protein 22 Alpha (TAGLN), and Plasminogen Activator Inhibitor 1 (SERPINE1), all of which are well-known TGFβ target genes (Figure 6C). These findings illustrate that, even in the presence of activated TGFβ signaling, ECM excretion by pericytes is suppressed when in contact with endothelium.

Destabilizing key gap- and adherens junctions has no effect on transcriptional adaptation

In the mature microvasculature, pericytes and ECs form direct connections called peg and socket interactions. These sites are enriched in CDH2 and CX43 adherens- and gap junctions, respectively, which provide a direct signaling route for ions, nutrients, metabolites, and secondary messengers, acting complementary to paracrine signaling routes (Figure 7A). This direct signaling was previously reported to play a key role in a particular aspect of endothelium-induced mural cell differentiation [25]. Interestingly in the present study, both CDH2 and CX43 were significantly upregulated in co-cultured pericytes, as validated by qPCR, suggesting enhanced requirement and thus signaling via these direct contacts in co-cultured pericytes (Figure 7B).

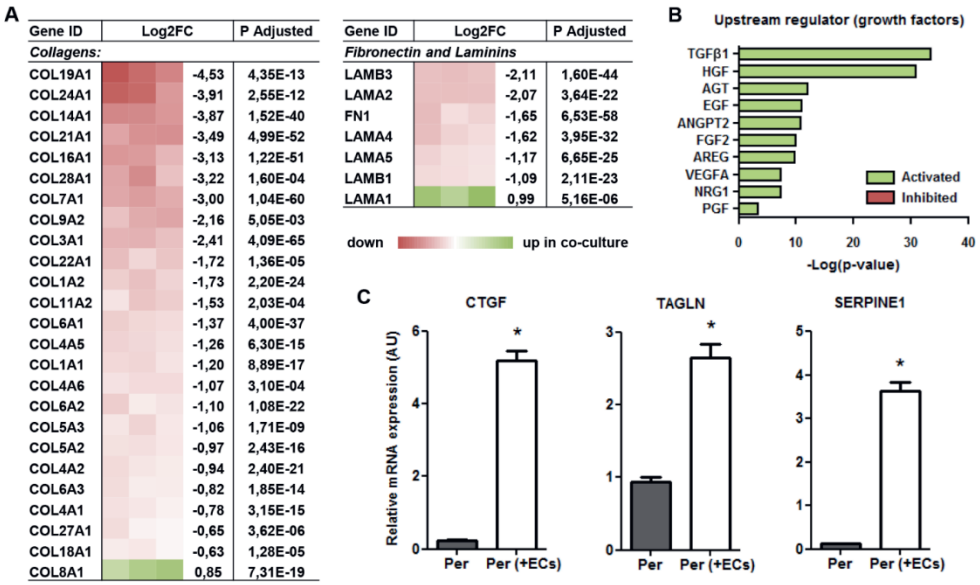

Figure 6. Endothelial interaction suppresses overall ECM production in pericytes. (A) Schematic presentation of RNAseq data for differentially expressed Collagens, Laminins, and Fibronectin. Shown is a color-based representation of the log2FC in each of the 3 individual experiments (red is downregulated in co-culture, green is upregulated in co-culture), followed by the average log2FC and the adjusted p-value. **(B)** IPA-derived prediction of the most activated or repressed growth factors in co-cultured pericytes compared with single cultured pericytes. Plotted is the –log(p-value) of overlap, in which green indicates predicted activation in co-culture versus predicted inhibition in red. **(C)** QPCR results showing expression levels of TGFβ target genes CTGF, TAGLN, and SERPINE1 relative to RPLP0 and POLR2L in pericytes in monoculture (Per), and after 20h in co-culture with HMVECs (Per+ECs). N=3, *P<0.05 compared to pericytes in monoculture. CTGF: Connective Tissue Growth Factor, TAGLN: Transgelin, SERPINE1: Plasminogen Activator Inhibitor 1.

This raised the question to what extent this signaling was mandatory for pericyte differentiation. To address this question, we took a similar approach as listed in Figure 1, but pericytes were now treated with non-targeting (NT) siRNA, CHD2-targeting siRNA, or CX43-targeting siRNA, to disrupt the main gap- and adherens junctions, followed by RNA sequencing. Knockdown efficiency was validated by Western blot for both CDH2 and CX43 (Figure 7C, full length blots in supplemental Figure 3A-B). Expression profiles of co-cultured pericytes treated with NT siRNA were compared with that of co-cultured pericytes with either CDH2- or CX43 knockdown. It was observed that, beside siRNA-mediated downregulation of CDH2 and CX43, only KRT8 was differentially expressed in co-cultured pericytes with suppressed CX43 expression compared with co-cultured pericytes treated with NT siRNA

(Log2FC: 0.54, adjusted p-value: 2.43E-02). KRT8 however was also upregulated in single cultured pericytes after CX43 knockdown (Log2FC: -0.52, adjusted p-value: 1.28E-02), indicating this was not related to destabilized interaction among ECs and pericytes. This also implicates that, in contrast to what has previously been reported, lack of CX43 expression thus did not block TGFβ-induced mural cell maturation. In co-cultured pericytes treated with CX43-targeting siRNA, an evident upregulation was still observed for known TGFβ target genes CTGF, ACTA2, TAGLN, and SERPINE1 (Figure 7D).

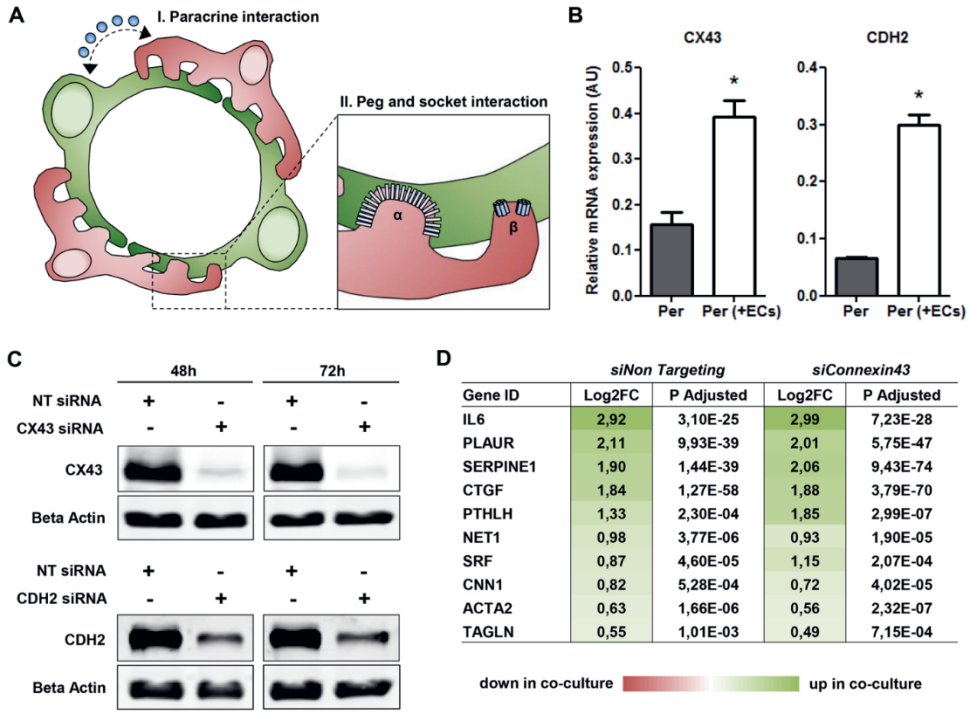

Gene ID	Log2FC	P Adjusted	Log2FC	P Adjusted
IL6	2,92	3,10E-25	2,99	7,23E-28
PLAUR	2,11	9,93E-39	2,01	5,75E-47
SERPINE1	1,90	1,44E-39	2,06	9,43E-74
CTGF	1,84	1,27E-58	1,88	3,79E-70
PTHLH	1,33	2,30E-04	1,85	2,99E-07
NET1	0,98	3,77E-06	0,93	1,90E-05
SRF	0,87	4,60E-05	1,15	2,07E-04
CNN1	0,82	5,28E-04	0,72	4,02E-05
ACTA2	0,63	1,66E-06	0,56	2,32E-07
TAGLN	0,55	1,01E-03	0,49	7,15E-04

Figure 7. Destabilizing key gap- and adherens junctions does not affect transcriptional adaptation. **(A)** Pericytes (red) and ECs (green) can either interact via paracrine interaction (I) or via direct interaction at peg and socket contacts (II). These contacts are enriched in adherens junction protein CDH (α) and gap junction protein CX43 (β). **(B)** QPCR results showing expression levels of CX43 and CDH2 relative to RPLP0 and POLR2L in pericytes in monoculture (Per), and after 20h in co-culture with HMVECs (Per+ECs). N=3, *P<0.05 compared to pericytes in monoculture. **(C)** Representative Western blots of CX43, CDH2, and β-actin levels in pericyte lysates at 48h and 72h post-transfection (full length blots in Supplemental Figure 3A-B). N=4. **(D)** Schematic presentation of RNAseq data for differentially expressed TGFβ target genes. Shown is a color-based representation of the log2FC (red is downregulated in co-culture, green is upregulated in co-culture), followed by the adjusted p-value. N=3. NT: non-targeting, CX43: Connexin 43, CDH2: N-Cadherin.

Discussion

The main findings of the current study are: (1) Interaction with ECs drives pericyte differentiation and maturation. (2) ECs stimulate pericyte proliferation and survival. (3) Direct endothelial contact stimulates the outgrowth of pericyte projections, and (4) represses overall ECM production in these perivascular cells. (5) Key gap- and adherens junctions genes CX43 and CDH2 do not appear to be involved in endothelium-induced differentiation of pericytes.

Pericytes have previously been described to be multipotent cells [26,27]. Thus, Crisan *et al*. reported that pericytes from multiple human organs, isolated using a combination of surface markers (including NG2, CD146, and PDGFRβ), were myogenic, osteogenic, chondrogenic, and adipogenic [28]. In light of these findings, it is not unexpected that direct interaction with ECs, resembling the physiological microvascular situation, triggers a defined adaptation in gene expression in these highly plastic cells when compared with single cultured pericytes. At the same time, these findings also align with studies showing that disease-induced loss of EC-pericyte interaction has a major impact on pericyte behavior. Among the differentially expressed genes in co-cultured pericytes there was a variety of well-known pericyte markers. The enhanced transcription of these markers was consistent with previous findings showing that endothelial contact with pericytes or mesenchymal progenitor cells plays a major role in their differentiation towards mature pericytes [14,29]. Remarkably, beside all upregulated pericyte markers, one of the most frequently used pericyte markers, PDGFRβ, was downregulated in pericytes after direct contact with ECs. PDGFRβ is a membrane-bound receptor with high affinity for PDGF subunits B and D [30]. PDGFB is abundantly expressed in ECs, and during vascular development endothelial-derived PDGFB triggers pericyte proliferation and migration towards a newly formed vessel to effectuate pericyte-induced vascular stabilization [31]. Noteworthy, PDGFRβ expression is highly dependent on cell cycle activation, in a way that actively dividing cells have suppressed expression of the receptor [32]. The transcription factor MYC, actively involved in cell cycle progression, was identified as a key repressor of the PDGFRβ promoter [33,34] Co-cultured pericytes were validated by Ki67 immunostaining to be actively proliferating, and not only was their expression of MYC upregulated almost threefold, analysis using IPA also suggested active transcriptional modulation by MYC in co-cultured pericytes (overlap p-value 1.03E-27). It is therefore likely that, among all the upregulated pericyte markers, the observed proliferative response in pericytes after direct contact with ECs triggers the – perhaps somewhat counterintuitive – suppression of PDGFRβ.

The enhanced proliferation in pericytes after contact with ECs supports the work of Tarallo *et al* [16]. Using cell culture inserts, on which pericytes and ECs were cultured on either side,

they found that ECs enhanced the number of pericytes, albeit after a relative long incubation of 8 days. Taking into consideration that TGFβ was confirmed by IPA to be the most active upstream growth factor inducing the observed transcriptional response, the increased proliferation was remarkable as TGFβ has been reported in multiple different studies to have an inhibiting effect on this process [35,36]. This implies that other mitogenic factors must have compensated for the TGFβ-induced proliferation stop. VEGFA was previously found to directly induce proliferation in pericytes [15]. However, in contrast to the findings of Darland *et al.*, who demonstrated that ECs induced VEGFA expression in pericytes [37], a significant downregulation of VEGFA was found in co-cultured pericytes in the present study. In combination with the significantly lower expression of VEGFA in ECs, it therefore seemed unlikely that the enhanced proliferation in co-cultured pericytes was VEGFA-dependent. Moreover, several other mitogens, that were either highly expressed in ECs or showed elevated transcription in pericytes after interaction with ECs, have been reported for pericytes, including the aforementioned PDGFB, FGF2 and HB-EGF [38-40]. Both FGF2 and HB-EGF were significantly upregulated in pericytes co-cultured with ECs, and based on the observed transcriptional response IPA also listed these factors among the most active upstream growth factors (overlap p-values 9.53E-11 and 1.02E-11, respectively). Interestingly, siRNA-mediated knockdown of HB-EGF and FGF2 in pericytes, as well as PDGFB in HMVECs, significantly reduced Ki67 positivity of co-cultured pericytes, whereas levels of Ki67 were not affected in VEGFA siRNA-treated pericytes. These findings substantiate that, beside paracrine stimulation with the well-documented endothelial-derived PDGFB, direct contact with ECs triggers the transcription of these particular growth factors that could stimulate pericyte proliferation in an autocrine fashion.

The endothelium-induced differentiation also involved morphological adaptations. Pericytes cultured in the absence of ECs had a somewhat bipolar elongated shape, whereas pericytes cultured in the presence of ECs were characterized by long and thin projections, a morphology that resembles the physiological shape of mature pericytes, which project finger-like extension around the capillary wall. The observed morphological differences were accompanied by transcriptional adaption of particular genes. Individually, these genes can be involved in various cellular processes. Upregulation of tubulin isoforms for instance, is also observed during distinct phases of the cell cycle and migration [41]. The ARP2/3 complex, in concert with CFLs, has been shown to be involved in the dynamics of lamellipodia growth [42], whereas many growth cone-guiding molecules have also been shown to be involved in vascular patterning, mostly affecting endothelial tip cell behavior. For example, signaling via the NRP receptor stimulates growth cone-collapse in the nervous systems in response to SEMAs [43], yet they appear to induce endothelial tip-cell extension and vessel sprouting in

the vascular system in response to VEGF [44]. Similarly, signaling of NTNs via UNC-5 Netrin Receptors (UNC5), downregulated in co-cultured pericytes, was shown to have a repulsive effect on endothelial branching [45,46], and Eph receptors and EFNs were reported to be involved in segregation of ECs with distinct arterial- or venous fates [47]. However, the fact that in co-cultured pericytes developing long cellular protrusions, 200 genes (overlap p-value 6.78E-13) associated with axonal guidance were differentially expressed, suggested that these signaling molecules may also have a profound effect on pericyte behavior. The hypothesized activation of growth cone-guiding in pericytes upon endothelial interaction was substantiated by the finding that siRNA-mediated downregulation of PLXNA2 and ACTR3, both upregulated in co-cultured pericytes, significantly reduced the relative number of pericytes with projections. The reduction of projection outgrowth after knockdown of ACTR3 was not unexpected considering its role in onset of actin filament formation [48]. However, PLXNs generally transduce the inhibitory effect of SEMAs on axon outgrowth [49], and consequently, loss of PLXNA2 was expected to actually stimulate outgrowth of pericyte projections. In ECs and U87MG glioblastoma cells, however, it was demonstrated that stimulation with SEMA3B and SEMA6A only in presence of PLXNA2 induced localized disassembly of the actin cytoskeleton and focal adhesion points, followed by cell contraction and the appearance of thin projections that remain attached to the substrate around the contracted cell [50], yielding a morphological resemblance with the co-cultured pericytes. To date, little is known about the growth cone-guiding signaling pathways in pericytes, yet the associated morphological changes may be of great importance for vascular integrity, as was recently shown in the adult mouse brain, where local ablation of pericytes provoked resident pericytes to extend the tips of their projections to cover the endothelium and to restore local vascular function [18].

The present study further provides evidence for an endothelium-induced suppression of overall ECM production in pericytes. This finding partially contrasts with the study of Stratman *et al*., in which basement membrane ECM expression was investigated in single-cultured and co-cultured human umbilical vein ECs and bovine pericytes in a collagen matrix [51]. Similar to our findings, they observed a defined downregulation of FN1 in pericytes cultured in the presence of ECs, yet a variety of other ECM molecules, including COL4A1 and COL4A2, demonstrated increased transcription levels in co-cultured pericytes. These apparent inconsistencies in transcriptional response are likely the result of differences in experimental approach, however, since we found that Glyceraldehyde-3-Phosphate Dehydrogenase, used by Stratman *et al*. as reference gene, was differentially expressed in co-cultured pericytes, it is difficult to draw definite conclusions. The findings on ECM expression do however appear to be in line with the many studies demonstrating that, upon organ injury, pericytes detach

and migrate from the endothelium and differentiate into ECM-producing cells [5,14,21,52]. The observed suppression of ECM production in co-cultured pericytes, however, went paradoxically along with enhanced TGFβ signaling. This enhanced TGFβ signaling itself is not unexpected, as several studies demonstrated that direct contact of pericytes with ECs triggers the activation of latent TGFβ, thereby inducing a swift activation of TGFβ-mediated signaling [53]. The paradox lies in the fact that TGFβ is well known for its role in transforming pericytes into ECM-producing fibroblasts [54]. These findings thus illustrate that, even in the presence of activated TGFβ signaling, ECM production by pericytes is suppressed when in contact with endothelium, implying that either the actual level of TGFβ determines healthy or pathological pericyte differentiation, or that a thus far unknown endothelial-derived cue must be counteracting TGFβ-induced differentiation of pericytes into fibrotic cells.

Beside secreted signaling molecules, such as VEGFA and PDGFB, ECs and pericytes also interact in a more direct physical manner via peg and socket contacts, which are enriched in CX43 and CDH2 [8,9]. In the present study, the expression of these molecules was suppressed in pericytes to assess if, and which, transcriptional adaptations in pericytes upon co-culture with ECs were regulated via these direct contacts. Unexpectedly, transcriptional comparison of co-cultured pericytes treated with NT siRNA and co-cultured pericytes with suppressed CX43 or CDH2 expression did not reveal significant differences. Hirschi *et al*. demonstrated that CX43 deficient mesenchymal cells lost their ability to activate latent TGFβ, and as a result were unable to differentiate into mature mural cells [25]. This is in contrast to our study where we did not observe any effect on TGFβ-mediated transcription in pericytes with suppressed CX43 expression. Our results suggest that endothelium-induced pericyte differentiation is not mediated by key gap- and adherens junctions CX43 and CDH2.

When exposing cells to a particular stimulus, a transcriptional response usually develops within hours. However, part of this response may depend on the formation of physical interactions that could require more than a few hours to develop. This led us to extent the incubation time to 20h, which is well beyond the moment at which we could optically perceive morphological adaptation in the form of protrusions from pericytes extending to multiple ECs. It is hard to determine if at that particular moment communication between both cell types used the full spectrum of interaction channels, but it was long enough to induce a considerable response and it enabled us to verify that the observed TGFβ-mediated differentiation did not depend on CX43 presence. Using a set of more than 200 brain mural cell-enriched genes, identified by He *et al*. [55], we also performed a gene set enrichment analysis (GSEA) on the RNAseq dataset to evaluate whether the presence of ECs pushed the pericytes into a phenotype resembling that of freshly isolated mature pericytes [56]. This GSEA illustrated that there was an enrichment of mature brain mural cell markers among the genes upregulated in

pericytes cultured in the presence of ECs (Supplemental Figure 4), substantiating the translatability of these findings, and further illustrating the endothelial-dependency of pericyte maturation.

In conclusion, the present study provides important evidence for pericyte differentiation upon interaction with ECs, by showing endothelium-induced pericyte maturation and proliferation, and suppression of ECM expression. However, functional gap- and adherens junctions do not appear to be involved in this process.

References

1. Armulik A, Genove G, Betsholtz C: Pericytes: developmental, physiological, and pathological perspectives, problems, and promises. *Dev Cell* **2011**, 21:193-215.
2. Carmeliet P: Angiogenesis in health and disease. *Nat Med* **2003**, 9:653-660.
3. Morikawa S, Baluk P, Kaidoh T, Haskell A, Jain RK, McDonald DM: Abnormalities in pericytes on blood vessels and endothelial sprouts in tumours. *Am J Pathol* **2002**, 160:985-1000.
4. Hellstrom M, Gerhardt H, Kalen M, Li X, Eriksson U, Wolburg H, Betsholtz C: Lack of pericytes leads to endothelial hyperplasia and abnormal vascular morphogenesis. *J Cell Biol* **2001**, 153:543-553.
5. Humphreys BD, Lin SL, Kobayashi A, Hudson TE, Nowlin BT, Bonventre JV, Valerius MT, McMahon AP, Duffield JS: Fate tracing reveals the pericyte and not epithelial origin of myofibroblasts in kidney fibrosis. *Am J Pathol* **2010**, 176:85-97.
6. Augustin HG, Koh GY, Thurston G, Alitalo K: Control of vascular morphogenesis and homeostasis through the angiopoietin-Tie system. *Nat Rev Mol Cell Biol* **2009**, 10:165-177.
7. Carmeliet P, Jain RK: Molecular mechanisms and clinical applications of angiogenesis. *Nature* **2011**, 473:298-307.
8. Allsopp G, Gamble HJ: An electron microscopic study of the pericytes of the developing capillaries in human fetal brain and muscle. *J Anat* **1979**, 128:155-168.
9. Winkler EA, Bell RD, Zlokovic BV: Central nervous system pericytes in health and disease. *Nat Neurosci* **2011**, 14:1398-1405.
10. Brandt MM, Meddens CA, Louzao-Martinez L, van den Dungen NAM, Lansu NR, Nieuwenhuis EES, Duncker DJ, Verhaar MC, Joles JA, Mokry M, Cheng C: Chromatin Conformation Links Distal Target Genes to CKD Loci. *J Am Soc Nephrol* **2018**, 29:462-476.
11. Love MI, Huber W, Anders S: Moderated estimation of fold change and dispersion for RNA-seq data with DESeq2. *Genome Biol* **2014**, 15:550.
12. Ezkurdia I, Juan D, Rodriguez JM, Frankish A, Diekhans M, Harrow J, Vazquez J, Valencia A, Tress ML: Multiple evidence strands suggest that there may be as few as 19,000 human protein-coding genes. *Hum Mol Genet* **2014**, 23:5866-5878.
13. Van Dijk CGM, Nieuweboer FE, Pei J, Xu YJ, Burgisser P, van Mulligen E, El Azzouzi H, Duncker DJ, Verhaar MC, Cheng C: The complex mural cell: pericyte function in health and disease. *Int J Cardiol* **2015**, 190:75-89.
14. Kramann R, Schneider RK, DiRocco DP, Machado F, Fleig S, Bondzie PA, Henderson JM, Ebert BL, Humphreys BD: Perivascular Gli1+ progenitors are key contributors to injury-induced organ fibrosis. *Cell Stem Cell* **2015**, 16:51-66.
15. Franco M, Roswall P, Cortez E, Hanahan D, Pietras K: Pericytes promote endothelial cell survival through induction of autocrine VEGF-A signaling and Bcl-w expression. *Blood* **2011**, 118:2906-2917.
16. Tarallo S, Beltramo E, Berrone E, Porta M: Human pericyte-endothelial cell interactions in co-culture models mimicking the diabetic retinal microvascular environment. *Acta Diabetol* **2012**, 49:S141-151.
17. Yamagishi S, Yonekura H, Yamamoto Y, Fujimori H, Sakurai S, Tanaka N, Yamamoto H: Vascular endothelial growth factor acts as a pericyte mitogen under hypoxic conditions. *Lab Invest* **1999**, 79:501-509.
18. Berthiaume AA, Grant GI, McDowell KP, Underly RG, Hartmann DA, Levy M, Bhat NR, Shih AY: Dynamic remodelling of pericytes in vivo maintains capillary coverage in the adult mouse brain. *Cell Rep* **2018**, 22:8-16.
19. Seiradake E, Jones EY, Klein R: Structural perspectives on axon guidance. *Annu Rev Cell Dev Biol* **2016**, 32:577-608.
20. Marsick BM, Flynn KC, Santiago-Medina M, Bamburg JR, Letourneau PC: Activation of ADF/cofilin mediates attractive growth cone turning toward nerve growth factor and netrin-1. *Dev Neurobiol* **2010**, 70:565-588.

21. Lin SL, Kisseleva T, Brenner DA, Duffield JS: Pericytes and perivascular fibroblasts are the primary source of collagen-producing cells in obstructive fibrosis of the kidney. *Am J Pathol* **2008**, 173:1617-1627.
22. Chen YT, Chang FC, Wu CF, Chou YH, Shu HL, Chiang WC, Shen J, Chen YM, Wu WD, Tsai TJ, Duffield JS, Lin SL: Platelet-derived growth factor receptor signalling activates pericyte-myofibroblast transition in obstructive and post-ischemic kidney fibrosis. *Kidney Int* **2011**, 80:1170-1181.
23. Sava P, Ramanathan A, Dobronyi A, Peng X, Sun H, Ledesma-Mendoza A, Herzog EL, Gonzalez AL: Human pericytes adopt myofibroblast properties in the microenvironment of the IPF lung. *JCI Insight* **2017**, 2:e96352.
24. Gaengel K, Genove G, Armulik A, Betsholtz C: Endothelial-mural cell signalling in vascular development and angiogenesis. *Arterioscler Thromb Vasc Biol* **2009**, 29:630-638.
25. Hirschi KK, Burt JM, Hirschi KD, Dai C: Gap junction communication mediates transforming growth factor-beta activation and endothelial-induced mural cell differentiation. *Circ Res* **2003**, 93:429-437.
26. Brighton CT, Lorich DG, Kupcha R, Reilly TM, Jones AR, Woodbury RA: The pericyte as a possible osteoblast progenitor cell. *Clin Orthop Relat Res* **1992**, 275:287-299.
27. Farrington-Rock C, Crofts NJ, Doherty MJ, Ashton BA, Griffin-Jones C, Canfield AE: Chondrogenic and adipogenic potential of microvascular pericytes. *Circulation* **2004**, 110:2226-2232.
28. Crisan M, Yap So, Casteilla L, Chen CW, Corselli M, Park TS, Andriolo G, Sun B, Zheng B, Zhang L, Norotte C, Teng PN, Traas J, Schugar R, Deasy BM, Badylak S, Buhring HJ, Giacobino JP, Lazzari L, Huard J, Peault B: A perivascular origin for mesenchymal stem cells in multiple human organs. *Cell Stem Cell* **2008**, 3:301-313.
29. Song S, Ewald AJ, Stallcup W, Werb Z, Bergers G: PDGFRbeta+ perivascular progenitor cells in tumours regulate pericyte differentiation and vascular survival. *Nat Cell Biol* **2005**, 7:870-879.
30. Betsholtz C: Biology of platelet-derived growth factors in development. *Birth Defects Res C Embryo Today* **2003**, 69:272-285.
31. Lindahl P, Johansson BR, Leveen P, Betsholtz C: Pericyte loss and microaneurysm formation in PDGF-B-deficient mice. *Science* **1997**, 277:242-245.
32. Vaziri C, Faller DV: Repression of platelet-derived growth factor beta-receptor expression by mitogenic growth factors and transforming oncogenes in murine 3T3 fibroblasts. *Mol Cell Biol* **1995**, 15:1244-1253.
33. Izumi H, Molander C, Penn LZ, Ishisaki A, Kohno K, Funa K: Mechanism for the transcriptional repression by c-Myc on PDGF beta-receptor. *J Cell Sci* **2001**, 114:1533-1544.
34. Mao DY, Barsyte-Lovejoy D, Ho CSW, Watson JD, Stojanova A, Penn LZ: Promoter-binding and repression of PDGFRB by c-Myc are separable activities. *Nucleic Acids Res* **2004**, 32:3462-3468.
35. Sieczkiewicz GJ, Herman IM: TGF-beta 1 signaling controls retinal pericyte contractile protein expression. *Microvasc Res* **2003**, 66:190-196.
36. Rustenhoven J, Aalderink M, Scotter EML, Oldfield RL, Bergin PS, Mee EW, Graham ES, Faull RLM, Curtis MA, Park TIH, Dragunow M: TGF-beta1 regulates human brain pericyte inflammatory processes involved in neurovasculature function. *J Neuroinflammation* **2016**, 13:37.
37. Darland DC, Massingham LJ, Smith SR, Piek E, Saint-Geneiz M, D'Amore PA: Pericyte production of cell-associated VEGF is differentiation-dependent and is associated with endothelial survival. *Dev Biol* **2003**, 264:275-288.
38. Papetti M, Shujath J, Riley KN, Herman IM: FGF-2 antagonizes the TGF-beta1-mediated induction of pericyte alpha-smooth muscle actin expression: a role for myf-5 and Smad-mediated signaling pathways. *Invest Ophthalmol Vis Sci* **2003**, 44:4994-5005.
39. Hosaka K, Yang Y, Nakamura M, Andersson P, Yang X, Zhang Y, Seki T, Scherzer M, Dubey O, Wang X, Cao Y: Dual roles of endothelial FGF-2-FGFR1-PDGF-BB and perivascular FGF-

2-FGFR2-PDGFRbeta signalling pathways in tumor vascular remodeling. *Cell Discov* **2018**, 4: 3.

40. Yu X, Radulescu A, Chen CL, James IO, Besner GE: Heparin-binding EGF-like growth factor protects pericytes from injury. *J Surg Res* **2012**, 172:165-176.
41. Parker AL, Kavallaris M, McCarroll JA: Microtubules and their role in cellular stress in cancer. *Front Oncol* **2014**, 4:153.
42. Wu C, Asokan SB, Berginski ME, Haynes EM, Sharpless NE, Griffith JD, Gomez SM, Bear JE: Arp2/3 is critical for lamellipodia and response to extracellular matrix cues but is dispensable for chemotaxis. *Cell* **2012**, 148:973-987.
43. Chen H, Bagri A, Zupicich JA, Zou Y, Stoeckli E, Pleasure SJ, Lowenstein DH, Skarnes WC, Chedotal A, Tessier-Lavigne M: Neuropilin-2 regulates the development of selective cranial and sensory nerves and hippocampal mossy fiber projections. *Neuron* **2000**, 25:43-56.
44. Gerhardt H, Ruhrberg C, Abramsson A, Fujisawa H, Shima D, Betsholtz C: Neuropilin-1 is required for endothelial tip cell guidance in the developing central nervous system. *Dev Dyn* **2004**, 231:503-509.
45. Leonardo ED, Hinck L, Masu M, Keino-Masu K, Ackerman SL, Tessier-Lavigne M: Vertebrate homologues of C. elegans UNC-5 are candidate netrin receptors. *Nature* **1997**, 386:833-838.
46. Lu X, Le Noble F, Yuan L, Jiang Q, De Lafarge B, Sugiyama D, Breant C, Claes F, De Smet F, Thomas JL, Autiero M, Carmeliet P, Tessier-Lavigne M, Eichmann A: The netrin receptor UNC5B mediates guidance events controlling morphogenesis of the vascular system. *Nature* **2004**, 432:179-186.
47. Herbert SP, Huisken J, Kim TN, Feldman ME, Houseman BT, Wang RA, Shokat KM, Stainier DYR: Arterial-venous segregation by selective cell sprouting: an alternative mode of blood vessel formation. *Science* **2009**, 326:294-298.
48. Pollard TD: Regulation of actin filament assembly by Arp2/3 complex and formins. *Annu Rev Biophys Biomol Struct* **2007**, 36:451-477.
49. Kong Y, Janssen BJC, Malinauskas T, Vangoor VR, Coles CH, Kaufmann R, Ni T, Gilbert RJC, Padilla-Parra S, Pasterkamp RJ, Jones EY: Structural Basis for Plexin Activation and Regulation. *Neuron* **2016**, 91:548-560.
50. Sabag AD, Smolkin T, Mumblat Y, Ueffing M, Kessler O, Gloeckner CJ, Neufeld G: The role of the plexin-A2 receptor in Sema3A and Sema3B signal transduction. *J Cell Sci* **2014**, 127:5240-5252.
51. Stratman AN, Malotte KM, Mahan RD, Davis MJ, Davis GE: Pericyte recruitment during vasculogenic tube assembly stimulates endothelial basement membrane matrix formation. *Blood* **2009**, 114:5091-5101.
52. Kramann R, Wongboonsin J, Chang-Panesso M, Machado FG, Humphreys BD: Gli1(+) Pericyte loss induces capillary rarefaction and proximal tubular injury. *J Am Soc Nephrol* **2017**, 28:776-784.
53. Sato Y, Tsuboi R, Lyons R, Moses H, Rifkin DB: Characterization of the activation of latent TGF-beta by co-cultures of endothelial cells and pericytes or smooth muscle cells: a self-regulating system. *J Cell Biol* **1990**, 111:757-763.
54. Wu CF, Chiang WC, Lai CF, Chang FC, Chen YT, Chou YH, Wu TH, Linn GR, Ling H, Wu KW, Tsai TJ, Chen YM, Duffield JS, Lin SL: Transforming growth factor beta-1 stimulates profibrotic epithelial signaling to activate pericyte-myofibroblast transition in obstructive kidney fibrosis. *Am J Pathol* **2013**, 182:118-131.
55. He L, Vanlandewijck M, Raschperger E, Mae MA, Jung B, Lebouvier T, Ando K, Hofmann J, Keller A, Betsholtz C: Analysis of the brain mural cell transcriptome. *Sci Rep* **2016**, 6:35108.
56. Subramanian A, Tamayo P, Mootha VK, Mukherjee S, Ebert BL, Gillette MA, Paulovich A, Pomeroy SL, Golub TR, Lander ES, Mesirov JP: Gene set enrichment analysis: a knowledge-based approach for interpreting genome-wide expression profiles. *Proc Natl Acad Sci U S A* **2005**, 102:15545-15550.

Supplemental Data

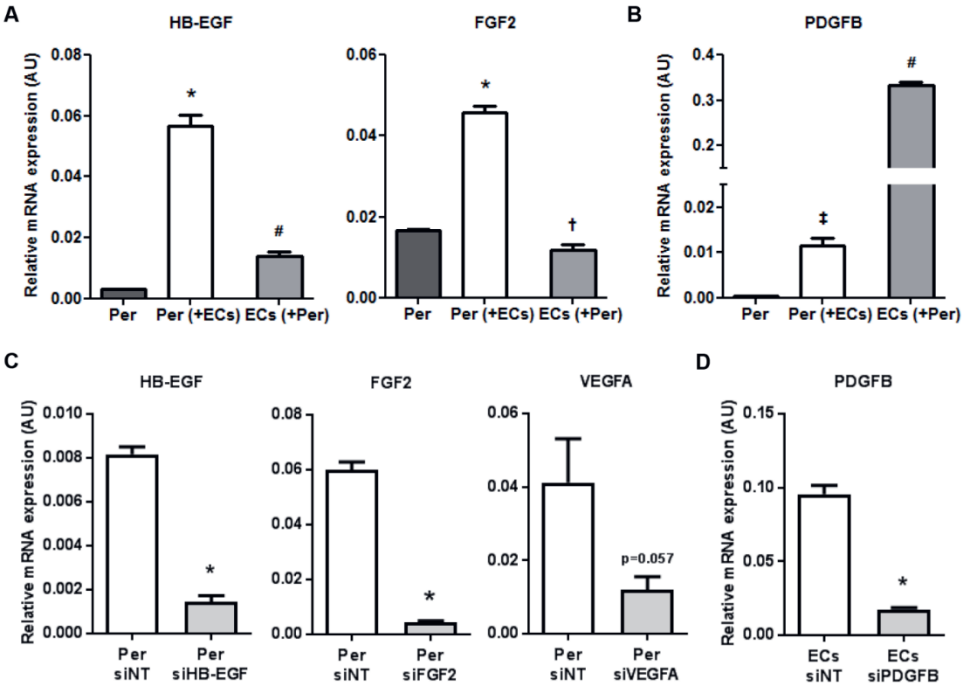

Supplemental Figure 1. Endothelial PDGFB, and pericyte HB-EGF and FGF2, are upregulated in co-cultured cells and were, like VEGFA, downregulated by siRNA. (A) QPCR results showing expression levels of HB-EGF, FGF2, and PDGFB relative to RPLP0 and POLR2L in mono- and co-cultured pericytes and co-cultured ECs. N=3, * P<0.05 compared to pericytes in monoculture and ECs in co-culture, # P<0.05 compared to pericytes in mono- and co-culture, ‡ P<0.05 compared to ECs in co-culture, † P<0.05 compared to pericytes in co-culture. **(C)** QPCR results showing expression levels of HB-EGF, FGF2 and VEGFA in pericytes, as well as **(D)** PDGFB in ECs relative to RPLP0 and POLR2L. N=3-4, * P<0.05 compared to siNT-treated control.

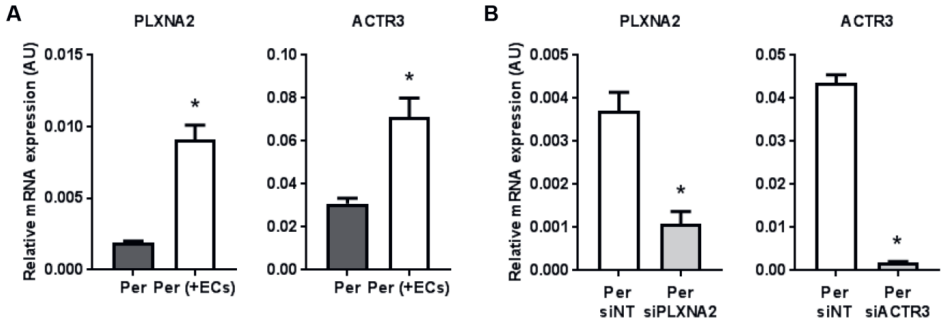

Supplemental Figure 2. PLXNA2 and ACTR3 are upregulated in co-cultured pericytes and were downregulated by siRNA. (A) QPCR results showing expression levels of PLXNA2 and ACTR3 relative to RPLP0 and POLR2L in mono- and co-cultured pericytes. N=3, * P<0.05 compared to pericytes in monoculture. **(B)** QPCR results showing expression levels of PLXNA2 and ACTR3 relative to RPLP0 and POLR2L in siRNA treated pericytes. N=3-4, * P<0.05 compared to siNT-treated control.

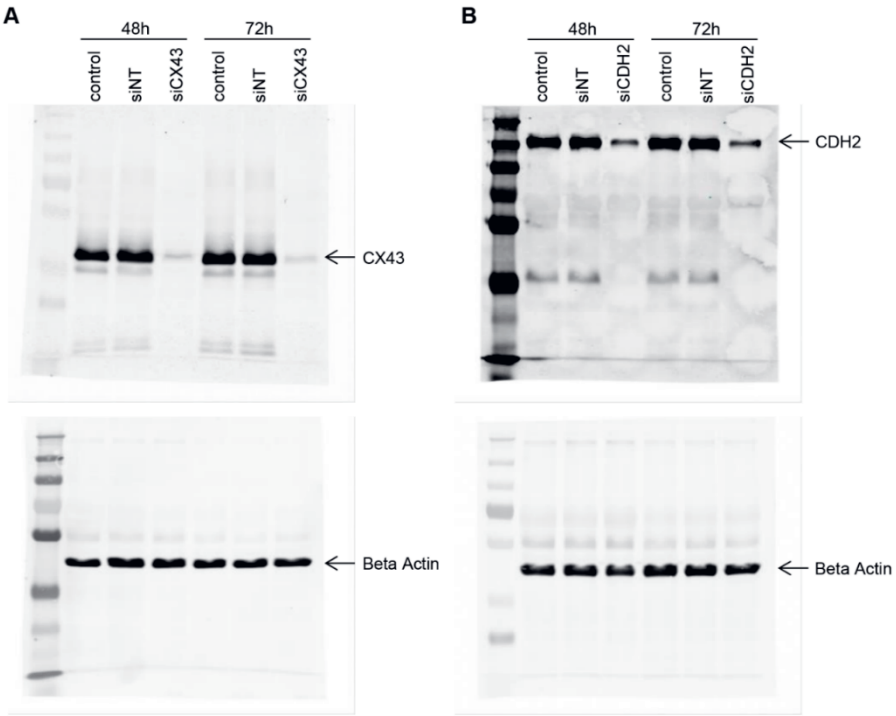

Supplemental Figure 3. Full length Western blots showing expression levels of CX43 and CDH2. (A) Full length Western blots of CX43 and β-actin in untreated controls, non-targeting siRNA treated- (siNT) and CX43-targeting siRNA treated pericyte, 48h and 72h post-transfection. **(B)** Full length Western blots of CDH2 and β-actin in untreated controls, non-targeting siRNA treated- (siNT) and CDH2-targeting siRNA treated pericyte, 48h and 72h post-transfection.

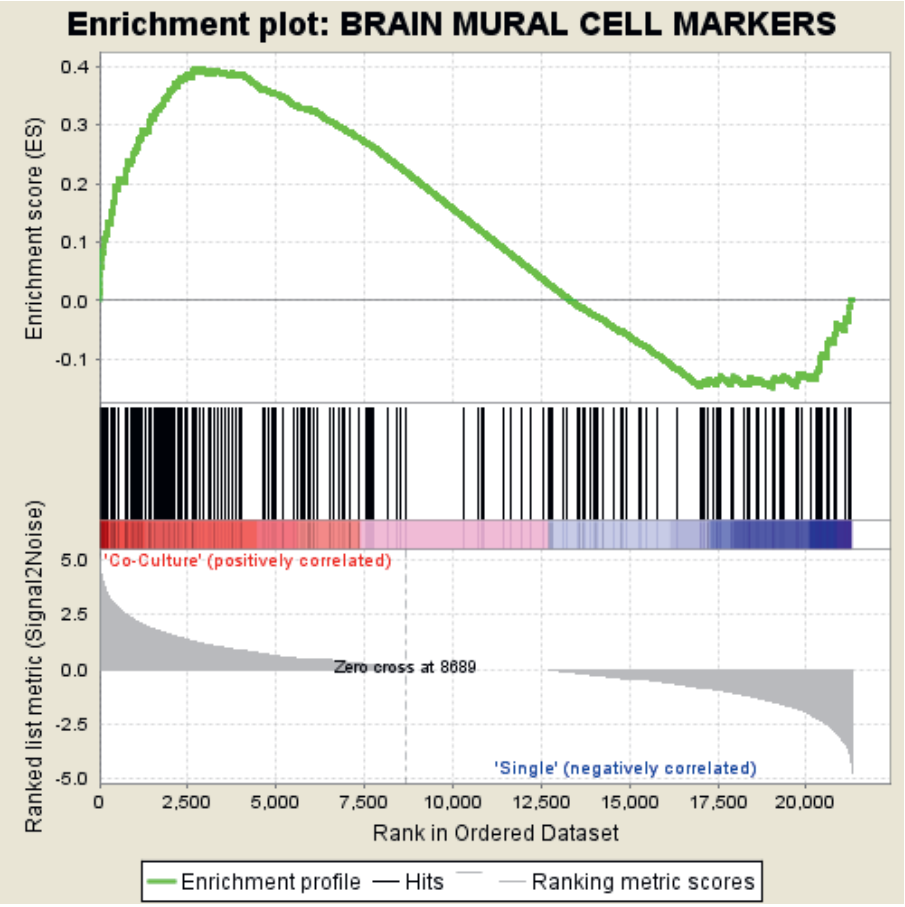

Supplemental Figure 4. **Gene set enrichment analysis (GSEA).** Enrichment analysis of markers from freshly isolated mature mural cells in the RNAseq dataset illustrates enrichment of these markers in genes upregulated in pericytes when cultured in presence of ECs. Normalized enrichment score: 1.146, nominal p-value: 0.119, FDR q value: 0.235 (q<0.25 is generally considered as significant in GSEA).

Supplemental Tables

Supplemental tables can be downloaded from:

https://www.nature.com/articles/s41598-019-51838-x

Or:

Chapter 5

A proteome comparison between human fetal and mature renal extracellular matrix identifies EMILIN1 as a regulator of renal epithelial cell adhesion

Laura Louzao-Martinez, Christian GM van Dijk, Yan Juan Xu, Amber Korn, Nicolaas J Bekker, Romi Brouwhuis, Maria Novella Nicesse, Jeroen AA Demmers, Marie-José TH Goumans, Rosalinde Masereeuw, Dirk J Duncker, Marianne C Verhaar, Caroline Cheng

Matrix Biology Plus, 2019 Nov;(4):100011

Abstract

Cell-based approaches using tissue engineering and regenerative medicine to replace damaged renal tissue with 3D constructs is a promising emerging therapy for kidney disease. Besides living cells, a template provided by a scaffold based on biomaterials and bioactive factors is needed for successful kidney engineering. Nature's own template for a scaffolding system is the extracellular matrix (ECM). Research has focused on mapping the mature renal ECM; however, the developing fetal ECM matches more the active environment required in 3D renal constructs. Here, we characterized the differences between the human fetal and mature renal ECM using spectrometry-based proteomics of decellularized tissue. We identified 99 different renal ECM proteins of which the majority forms an overlapping core, but also includes proteins enriched in either the fetal or mature ECM. Relative protein quantification showed a significant dominance of EMILIN1 in the fetal ECM. We functionally tested the role of EMILIN1 in the ECM using a novel methodology that permits the reliable anchorage of native cell-secreted ECM to glass coverslips. Depletion of EMILIN1 from the ECM layer using siRNA mediated knock-down technologies does not affect renal epithelial cell growth, but does promote migration. Lack of EMILIN1 in the ECM layer reduces the adhesion strength of renal epithelial cells, shown by a decrease in focal adhesion points and associated stress fibers. We showed in this study the importance of a human renal fetal and mature ECM catalogue for identifying promising ECM components that have high implementation potential in scaffolds for 3D renal constructs.

Introduction

In search of a potential treatment for kidney disease, current investigations focus on cell-based approaches using tissue engineering and regenerative medicine (TERM) to replace damaged renal tissue with engineered 3D structures. One promising TERM-based approach is the use of organoids. Renal organoids derived from induced pluripotent stem cells that model the morphology and segmentation of human fetal nephrons have been developed [1,2]. Human primary renal cells can also grow into 3D kidney-like constructs with tubular structures. When implanted into mice, these constructs survived and maintained their renal phenotypes for up to 6 weeks [3]. However, these techniques cannot fully recapitulate the complex organization of the kidney and cannot be grown on a large scale yet.

Besides cells, another basic component for kidney engineering is a template provided by a scaffolding system based on biomaterials and bioactive factors that create a microenvironment which facilitates cell-specific behavior. Nature's own template for a scaffolding system is the extracellular matrix (ECM), which is a collection of molecules deposited by surrounding cells, making it a tissue-specific 3D structure in which cells are embedded. The ECM not only gives structural support, it also contains biochemical cues that influence many biological processes, including cell migration, adhesion, proliferation and differentiation [4-7]. The matrices used to embed stem or primary renal cells are mostly collagen-based hydrogels or matrigel, which do not reflect the tissue-specific ECM of the kidney. Matrices containing renal-specific ECM cues could greatly advance TERM by promoting renal tissue formation. In order to create such a scaffolding system, the components of the human renal ECM first need to be fully characterized.

Proteomic techniques have been used to characterize the ECM composition in various tissues [8,9]. For the renal ECM, studies have focused on the human glomerular ECM and identified a highly connected network comprised of almost 200 different structural and regulatory ECM proteins [10-13]. Despite previous work, ECM proteome research until now only focused on mapping the mature renal ECM. In the fetal microenvironment, the ECM balance is shifted towards an active environment [14-17], which matches the need for tissue generation in 3D tissue constructs.

In this study, we characterized the differences between the developing fetal and the more static mature human renal ECM proteome. The resulting catalogue gives important insights into renal ECM structure and function and enables a detailed investigation of promising renal ECM molecules and their potential use for implementation in scaffolds.

Based on our proteome analysis, we identified Elastin Microfibril Interfacer 1 (EMILIN1) as an important component enriched in the fetal ECM. EMILIN1 is located in elastic fibers at the interface between elastin and the surrounding microfibrils [18]. The distinctive C-terminus

gC1q structure of EMILIN1 interacts with integrins, thereby connecting cells to elastic fibers [19,20]. Many cell types depend on this gC1q-integrin interaction for cell adhesion, migration and proliferation [21-24]. EMILIN1 is particularly abundant in the walls of blood and lymphatic vessels, where it is necessary for the formation of elastic fibers and anchoring filaments [25,26].

Despite studies implying that EMILIN1 is an important factor in maintaining cardiovascular health [26-29], the role of EMILIN1 in the kidney is unknown. Here, we have shown for the first time that EMILIN1 is an important regulator of renal cell migration and adhesion. These findings validate the importance of our human renal fetal and mature ECM catalogue for identifying promising ECM components with high potential for implementation in scaffolds for 3D kidney constructs.

Materials and Methods

Antibodies

Polyclonal antibodies used were against EMILIN1 (HPA002822; Sigma-Aldrich), fibrillin1 (HPA021057; Sigma-Aldrich) and collagen type IV (AB769; Merck Millipore). Monoclonal antibodies used were against Ki-67 (RM-9106-R7, ThermoFisher), paxillin (ab32084, Abcam), ZO-1 (610967; BD Biosciences) and β-actin (ab8226, Abcam). Rhodamine phalloidin conjugate was used for staining F-actin (R415; ThermoFischer). Secondary antibodies used for immunohistochemistry were goat-anti-rabbit Alexa Fluor 488 (A11034; ThermoFisher), donkey-anti-rabbit Alexa Fluor 568 (A10042; ThermoFisher), donkey-anti-goat Alexa Fluor 488 (A11055; ThermoFisher) and goat-anti-mouse Alexa Fluor 488 (A11029; ThermoFisher). Secondary antibodies used for Western blot were goat-anti-rabbit IRDye 800CW (926-32211; Li-cor Biosciences) and goat-anti-mouse IRDye 680RD (926-68070; Li-cor Biosciences).

Human samples

Normal human renal tissue from healthy adult donors was obtained from the Erasmus MC Tissue Bank (N=13; gender: 8 male, 5 female; age (mean ± SD): 55 ± 24 years). Normal human kidneys from healthy fetal donors were received from the department of Molecular Cell Biology from the Leiden UMC (N=13; age range: 18-24 weeks of pregnancy).

Cell culture

Primary aortic smooth muscle cells (aSMCs) were purchased from Lonza (CC-2571) and maintained in Smooth Muscle Growth Medium (CC-3182; Lonza). Primary Human Renal Proximal Tubular Epithelial Cells (HRPTECs) were purchased from ScienCell (#4100) and maintained in Epithelial Cell Medium (#4101; ScienCell). Immortalized Human Kidney [30]

(HK2) cells were maintained in RPMI-1640 medium with glutamine (61870010; ThermoFisher), supplemented with 10% (vol/vol) FCS (Biowest) and 100 Uml^{-1} PS (Gibco). All cells were cultured at 37ºC in a humidified atmosphere containing 5% CO2. Primary cell lines were used between passages 3 and 8.

Tissue decellularization and ECM homogenization

Tissue decellularization was used to reduce the complexity of samples by removing cellular components and thereby enriching for ECM proteins. Renal tissue was cut into 4 pieces of uniform thickness and one piece was fixed and saved for hematoxylin and eosin (H&E) staining to asses tissue morphology. The other pieces were decellularized overnight in 1% SDS under constant rotation. Next, a shorter decellularization step was performed for one hour with 1% Triton X-100 under constant rotation. Tissue was washed thoroughly in PBS for 2 hours under constant rotation to remove as much residual detergent as possible before proceeding with tissue lysis. One decellularized piece was fixed and saved for H&E staining to validate the removal of all cellular content and assess preservation of the ECM architecture. Tissue was homogenized in lysis buffer (10 mM Tris [pH 7.4], 100 mM NaCl, 0.1% SDS, 0.5% Na deoxycholate, 1% Triton X-100, 1 mM EGTA, 1 mM EDTA, 10% glycerol, 1 mM NaF, 1 mM Na orthovanadate, supplemented with a protein inhibitor cocktail (cOmplete, Mini Protease Inhibitor Tablets)) using an Ultra-Turrax (IKA) and lysed for an hour at 4°C under rotation. After homogenizing a second time, tissue lysates were centrifuged [10 min, 1000xg, 4°C] and supernatant was saved at -80°C until further processing.

MS data acquisition and analyses

ECM extracts were separated by SDS-PAGE. Three gels were loaded with a fetal and mature ECM extract of the same protein concentration, each containing 3-5 pooled kidney samples that were randomly selected (mixed age and gender). The separated samples were prepared for liquid chromatography-tandem mass spectrometry (LC-MS/MS) by the Proteomics Centre of the Erasmus MC as follows. 1D SDS-PAGE gel was visualized with a Coomassie staining and lanes were cut into 2-mm slices using an automatic gel slicer and subjected to in-gel reduction with dithiothreitol, alkylation with iodoacetamide and digestion with trypsin (Promega, sequencing grade), essentially as described previously [31]. Supernatants were stored in glass vials at -20°C until LC-MS. Nanoflow LC-MS/MS was performed on an 1100 series capillary LC system (Agilent Technologies) coupled to an LTQ-Orbitrap XL mass spectrometer (Thermo) operating in positive mode and equipped with a nanospray source, essentially as previously described [32]. Peptide mixtures were trapped on a ReproSil C18 reversed phase column (Dr Maisch GmbH; column dimensions 1.5 cm × 100 µm, packed in-

house) at a flow rate of 8 µl/min. Peptide separation was performed on ReproSil C18 reversed phase column (Dr Maisch GmbH; column dimensions 15 cm × 50 µm, packed in-house) using a linear gradient from 0 to 80% B (A = 0.1 % formic acid; B = 80% (v/v) acetonitrile, 0.1 % formic acid) in 70 min and at a constant flow rate of 200 nl/min using a splitter. The column eluent was directly sprayed into the ESI source of the mass spectrometer. Mass spectra were acquired in continuum mode; fragmentation of the peptides was performed in data-dependent mode.

Raw data files were analyzed using the MaxQuant software as described by Cox *et al* [33]. Proteins that were identified in at least two of the three fetal or mature replicates were used for further analysis. By cross-referencing with the Human Matrisome Project [8,9], we categorized the obtained proteins into ECM core and associated proteins. The label free quantification (LFQ) module was used to quantify the relative abundances of fetal and mature renal ECM proteins.

POMA-fibronectin coverslips preparation

Circular glass coverslips were cleaned to remove organic residues with a quick rinse in acetone and sonication in 50% methanol for 20 min and in chloroform for another 20 min. Coverslips were oxidized with piranha solution (70% sulphuric acid (99% w/v) and 30% hydrogen peroxide (35% w/v)) for 20 min and sonicated in chloroform for 10 min. To ensure complete removal of the piranha solution, coverslips were washed by sonication with ultrapure water for 5 min and with chloroform for another 5 min in an alternating fashion and repeated for at least 5 times 34]. Freshly oxidized coverslips were aminosilanized with a 2% (3-Aminopropyl)triethoxysilane (APTES, Sigma-Aldrich) solution in 95% ethanol for 10 min. Excess APTES was removed by 4 washings with 95% ethanol for 5 min. The APTES layer was cured at 120°C for 30 min [35,36]. In order to covalently bind fibronectin (FN), the coverslips were coated with a thin layer of 0.16% (w/v) poly(octadecene-alt-maleic anhydride (POMA; Sigma-Aldrich) solution in tetrahydrofuran (Sigma-Aldrich) using a spin-coater (Brewer Science) (1500 rpm s^{-1}, 30 sec, 4000 rpm). The polymer coating was cured at 120°C for 2 hours [35,36]. The POMA-coated coverslips were stored in the dark for up to 3 months. Heat activation of the anhydride moieties needed to be repeated if coverslips were stored for longer than 2 weeks. Prior to use in cell culture, the POMA-coated coverslips were sterilized under UV-light for 30 min. Lastly, the coverslips were coated with sterile 50 µg/ml fibronectin (FN; Roche) in PBS for 1 hour at 37°C to allow stable anchorage of cell secreted ECM. POMA-FN coverslips were rinsed twice with sterile PBS to remove excess FN and to achieve a homogeneous coating before seeding with cells [36].

Anchored cell-secreted ECM layer preparation

To create cell derived ECM layers anchored to POMA-FN coverslips, SMCs were seeded at 40,000 cells per cm^2. The cultures were decellularized at day 6 using warm 20 mM NH_4OH by gentle agitation for 15 min, which disrupts lipid interactions but preserves protein interactions. The resulting ECM layers were treated with 10% DNase I (Qiagen) for 10 min to remove DNA traces. Cell remnants were removed by washing thrice with ultrapure water and twice with PBS. The decellularized ECM layer was immediately re-seeded with renal cells or fixated for immunofluorescence analysis. The presence of nucleic acids was assessed with DAPI staining. After the decellularization procedure, cellular components such as DNA remnants were barely detected.

Immunofluorescence

Sucrose cryoprotected renal tissue was embedded in an OCT compound (TissueTek) and stored at -80°C. Frozen samples were cut into 7-µm-thick sections, fixated with acetone and stained with H&E or used for immunofluorescence stainings. Cells or ECM attached to coverslips were washed with PBS and fixed with 4% paraformaldehyde for 30 min. Blocking of tissue, cells or ECM occurred with 1% BSA/PBS for 30 min before incubation with primary and secondary antibodies for 1 hour at room temperature. Cells and tissue were also permeabilized with 0.5% Triton X-100/PBS for 30 min before antibody incubation. DAPI was used as a nuclear counterstaining. Images of fluorescent-labelled markers were obtained with a Leica TCS SP8 X microscope. For quantification of the total area, 3D images were obtained by scanning multiple XY planes in the Z direction. Serial pictures along the Z-axis were combined to create a stacked XY image that was further analyzed using ImageJ 1.47v. Single XY pictures were taken with the Olympus BX51 upright microscope.

Quantitative PCR

Total RNA was isolated from SMCs using the ISOLATE II RNA mini kit (Bioline) according to manufacturer's instructions and from human renal tissue using TRIzol. Briefly, tissue was homogenized in 1 mL TRIzol using an Ultra-Turrax (IKA) on ice. 200 µl chloroform was added per 1 mL TRIzol, mixed and incubated for 3 minutes at room temperature. The aqueous phase was separated from the phenol by centrifugation (15 min, 12,000xg, 4°C) and transferred to a new tube. RNA was precipitated by mixing the aqueous phase with 600 µl isopropanol and 1 µl of glycogen (5 mg/mL). After incubation for 10 minutes at room temperature, the precipitate was pelleted by centrifugation (10 min, 12,000xg, 4°C). The pellet was washed with 600 µl ice-cold 75% ethanol and pelleted again (5 min, 7,500xg, 4°C). The pellet was dried at room temperature and the RNA was precipitated over night at -20°C to increase yield by mixing the

pellet with 200 µl Nuclease-free water (Qiagen), 20 µl 3 M Sodium acetate and 600 µl 75% ice-cold ethanol. The precipitate was pelleted by centrifugation (30 min, 15,000xg, 4°C). The pellet was washed with 200 µl ice-cold 75% ethanol and pelleted again (5 min, 15,000xg, 4°C). The RNA pellet was dried at room temperature and dissolved in 50 µl Nuclease-free water (Qiagen). RNA concentrations were assessed with a nanodrop spectrophotometer. Total RNA was reverse-transcribed using the SensiFAST cDNA synthesis kit (Bioline) according to manufacturer's instructions. Gene expression was determined using quantitative real-time PCR (qPCR) by loading samples in duplicate on a CFX96 Real-Time PCR Detection System (Biorad). The primer sequences used are listed in Supplemental Table 2. Data was normalized for the expression of housekeeping gene *β-actin*.

Short interference RNA

EMILIN1 or *FBN1* knockdown in SMCs was achieved by using a mix of 4 complementary short interference RNA (siRNA) sequences directed against the mRNA of either *EMILIN1* or *FBN1* (ThermoScientific). As a negative control, cells were either untreated or transfected with a mix of 4 non-targeting siRNA (siSHAM) sequences (ThermoScientific). The siRNA sequences used are listed in Supplemental Table 3.

Western blot

SMCs received a PBS wash twice and were harvested in lysis buffer (50 mM Tris (pH 8.0), 1% NP-40, 150 mM NaCl, 0.1% SDS, 0.5% Na deoxycholate, supplemented with a protein inhibitor cocktail (cOmplete, Mini Protease Inhibitor Tablets)). The lysates were incubated on ice for 20 minutes, centrifuged [12 min, 13,000xg 4°C] and the supernatant was stored at -80°C until further processing. Total protein concentration was determined by using the Pierce® BCA Protein Assay Kit (Thermo Scientific). Lysates were denaturated in Laemmli buffer (60mM Tris (pH 6.8), 2% SDS, 10% glycerol, 5% β-mercaptoethanol, 0.01% bromophenol blue) at 90 °C for 5 minutes. Equal amounts of sample were separated by electrophoresis on a 10% SDS-PAGE gel and transferred onto a nitrocellulose membrane (Pierce) at 4ºC overnight. Membranes were blocked and probed with primary antibodies. Protein bands were visualized with Li-Cor secondary antibodies and detection system (Westburg) according to manufacturer`s instructions.

Live-cell tracking

POMA-FN coverslips were placed into a 6-wells plate containing a No. 0 coverslip glass bottom (P06G-0-20-F, MatTek) to allow live-cell tracking. SMCs were transfected with siRNA after 24 hours and coverslips were decellularized 6 days post-transfection. Before reseeding

with 3,700 HK2 cells per cm^2, HK2 cells were visualized for fluorescent tracking by incubating the cells for 15 min at 37°C in basal RMPI medium containing 4 µM CellTracker Blue CMAC dye (ThermoFisher). 24 hours post-seeding, single cell migration was tracked overnight at 37ºC in a humidified atmosphere containing 5% CO2 using a Leica SP8X confocal microscope. Per condition, three positions were selected and imaged every 15 min for 12 hours. Obtained videos were analyzed with ImageJ (v1.47) Manual Tracking and Chemotaxis Tool.

In vitro assays

Prior to all *in vitro* assays, SMCs were seeded on POMA-FN coverslips and transfected with siRNA after 24 hours. The coverslips were decellularized 6 days post-transfection and reseeded with renal cells.

Cell adhesion assay. Captured ECM was reseeded with 6,500 HRPTECs per cm^2 for testing initial binding to the ECM or 25,000 HK2 per cm^2 for measuring cell-ECM adhesion of a confluent monolayer. For testing initial binding, HRPTECs were left to adhere for 2 hours. HK2 were cultured to confluence (48 hours) on the captured ECM. Fixated cells were stained for either paxillin, a focal adhesion complex protein, or for ZO-1, a tight junction protein, and for F-actin.

PrestoBlue assay. Captured ECM was reseeded with 6,500 HRPTECs per cm^2. Cell viability was measured 24, 48 and 72 hours post-seeding using PrestoBlue Cell Viability Reagent (ThermoScientific) according to manufacturer's protocol.

Ki67 nuclear staining. Captured ECM was reseeded with 6,500 HRPTECs per cm^2. Cell proliferation was visualized 24, 48 and 72 hours post-seeding by immunofluorescence labelling with the proliferation marker ki67. The images were analyzed with ImageJ (v 1.47) to obtain the percentage of proliferating cells by dividing the amount of $ki67^+$ cells by the $DAPI^+$ count.

PicoGreen assay. Captured ECM was reseeded with 6,500 HRPTECs per cm^2. To quantify the amount of double stranded DNA, a Quant-iT™ PicoGreen™ dsDNA Assay (ThermoFisher) was performed 24, 48 and 72 hours post-seeding according to manufacturer's protocol.

RhoA activation assay

SMCs were seeded on POMA-FN coverslips and transfected with siRNA after 24 hours. The coverslips were decellularized 6 days post-transfection and reseeded with 25,000 HK2 per cm^2. The activation of the small G-protein RhoA was determined 48 hours post-seeding using the G-LISA RhoA Activation Assay Biochem Kit (Cytoskeleton, BK124) according to manufacturer's instructions. HK2 cells were serum starved overnight (in RPMI containing 0.2% FCS) and stimulated with full RPMI medium (containing the standard 20% FCS) for 1 min before starting the RhoA activation assay to modulate GTP-RhoA levels.

Statistical Analyses

Graphpad Prism (version 7.02) was used to perform the statistical analyses. To test if values came from a Gaussian distribution, either the D'Agostino-Pearson omnibus or Shapiro-Wilk normality test was used. The ordinary one-way ANOVA or unpaired t-test was used if the values were normally distributed. In case the values did not pass the normality test, either Kruskal-Wallis or the Mann-Whitney test was used as non-parametric tests. P-values <0.05 were considered significant. All measurements are shown as mean ± SEM.

Results

Enrichment of extracellular matrix proteins

We analyzed healthy kidney samples from adult and fetal human donors. The ECM was enriched in these samples by decellularization (Figure 1A). Cellular components were removed without disrupting the structure and morphology of the ECM (Figure 1B). The obtained ECM extracts were separated by SDS-PAGE and LC-MS/MS was used to characterize the differences between the fetal and mature renal ECM proteome (Figure 1A, Supplemental Figure 1A).

Comparison of the renal proteome: fetal versus mature

The obtained proteomic data were used to generate a catalogue of fetal and mature renal ECM proteins. Proteins that were identified in at least two replicates were included (Supplemental Figure 2A). By cross-referencing with the Human Matrisome Project [8,9], we categorized our data proteins into core ECM proteins, including collagens, glycoproteins and proteoglycans, and ECM-associated proteins, including ECM-affiliated proteins, regulators and secreted factors. Relative protein quantification showed a dominance of collagens and glycoproteins in both the fetal and mature ECM: 62% of the fetal and 64% of the mature signal consisted of collagens, whereas 33% of the fetal and 28% of the mature selection consisted of glycoproteins (Figure 2A).

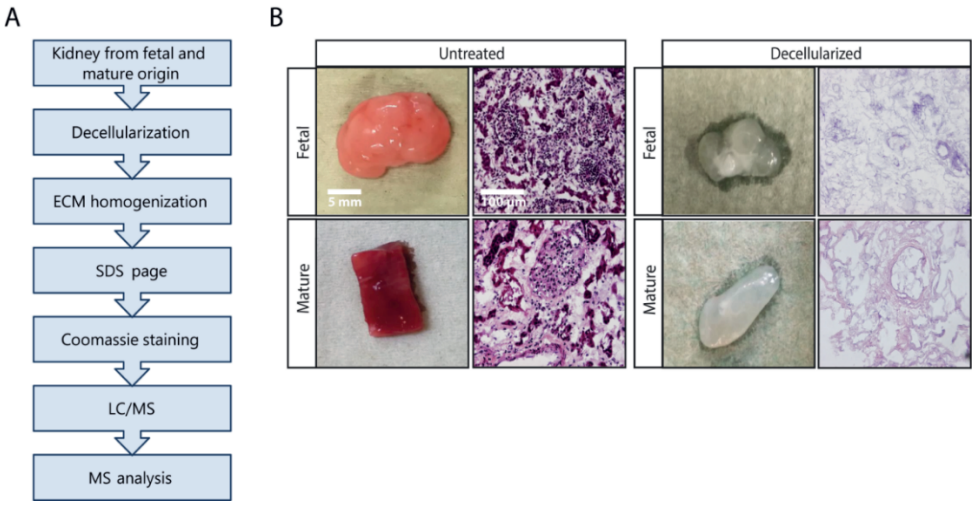

Figure 1. Isolation of renal fetal and mature extracellular matrix proteins. (A) Workflow for the isolation of the extracellular matrix (ECM) from healthy human fetal and mature renal tissue. **(B)** Macroscopic appearance of representative human fetal and mature renal samples before and after decellularization (left panels). Scale bar represents 5 mm. Hematoxylin and eosin staining (200x magnification) of human fetal and mature renal tissue before and after decellularization demonstrates the successful removal of cellular components (right panels). Scale bar represents 100 µm.

We identified 94 fetal and 76 mature renal ECM proteins, from which the majority could be classified as core ECM proteins (60 and 51, respectively). The most abundant signal came from core ECM proteins as well, with many collagens comprising more than 2% of the total ECM signal (Figure 2B, Supplemental Table 1). Four glycoproteins (EMILIN1, FGG, FBN1 and FBN2) and one proteoglycan (HSPG2) showed abundant signal, each comprising more than 2% of the total ECM signal (Figure 2B, Supplemental Table 1). We identified 23 proteins that were significantly enriched in the fetal renal ECM compared to the mature ECM. Only 6 ECM proteins were significantly enriched in the mature renal ECM. Among the 23 proteins significantly enriched in the fetal selection were the abundant glycoproteins EMILIN1, fibrillin1 (FBN1) and fibrillin2 (FBN2) (Figure 2C, Supplemental Table 1). Lennon and colleagues published the composition of the human glomerular ECM [10]. By cross-referencing their dataset with the Human Matrisome Project [8,9] and subsequently with our dataset, we further classified our list in either glomerular or tubulointerstitial ECM proteins (Supplemental Figure 3). By this means, we identified 55 glomerular ECM proteins, including 8 proteins detected exclusively in either the mature or fetal renal ECM. 29 glomerular ECM proteins were not detected by our MS analysis and were only found by Lennon *et al.* due to their extra glomeruli enrichment step prior to MS analysis [10]. Our remaining 54 ECM proteins could then be classified as mainly tubulointerstitial, including 19 proteins unique for the fetal renal ECM. One

tubulointerstitial ECM protein was found to be unique for the mature renal ECM. These findings show that the fetal and mature renal ECM are complex and share a central overlap, but are also characterized by unique ECM proteins.

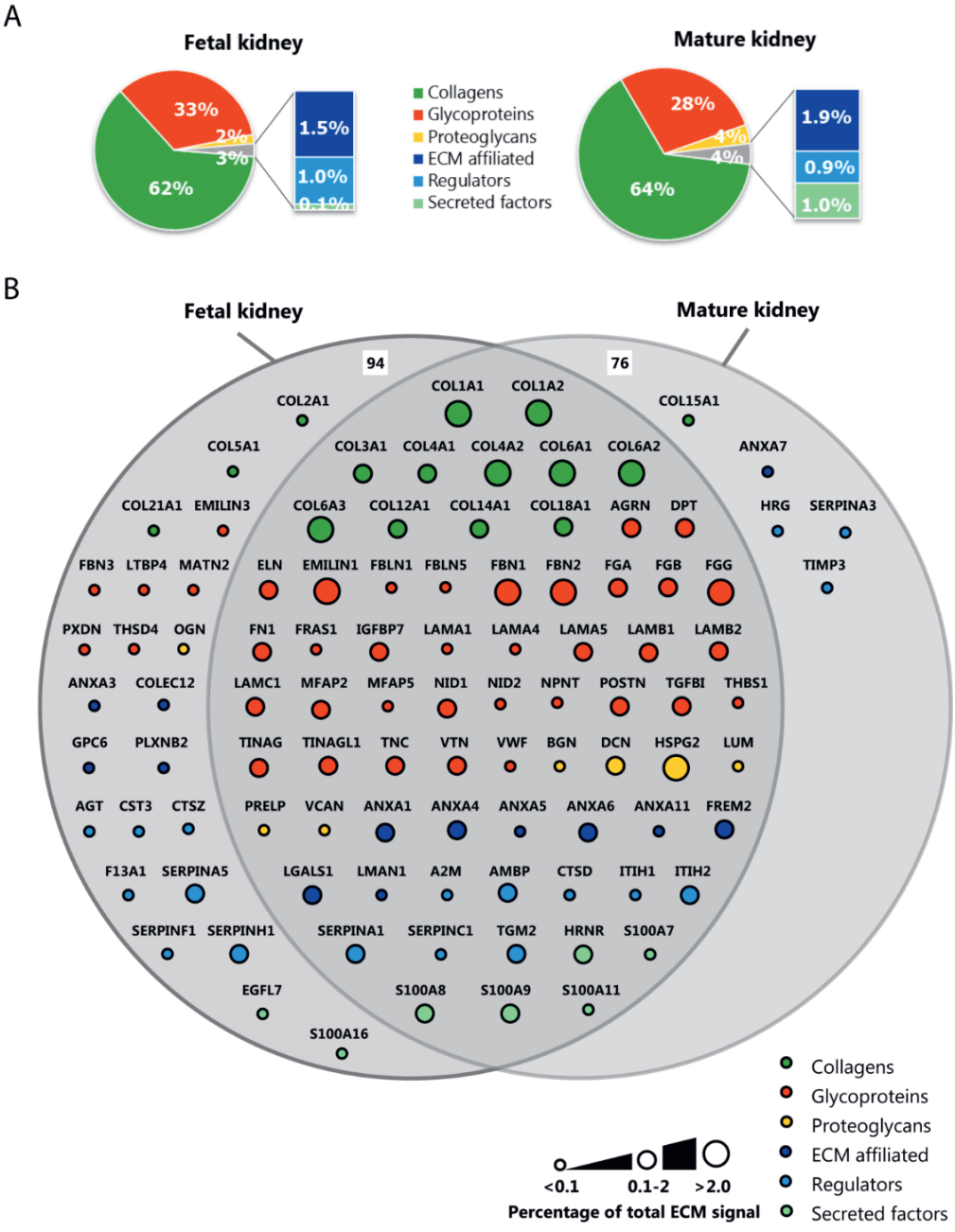

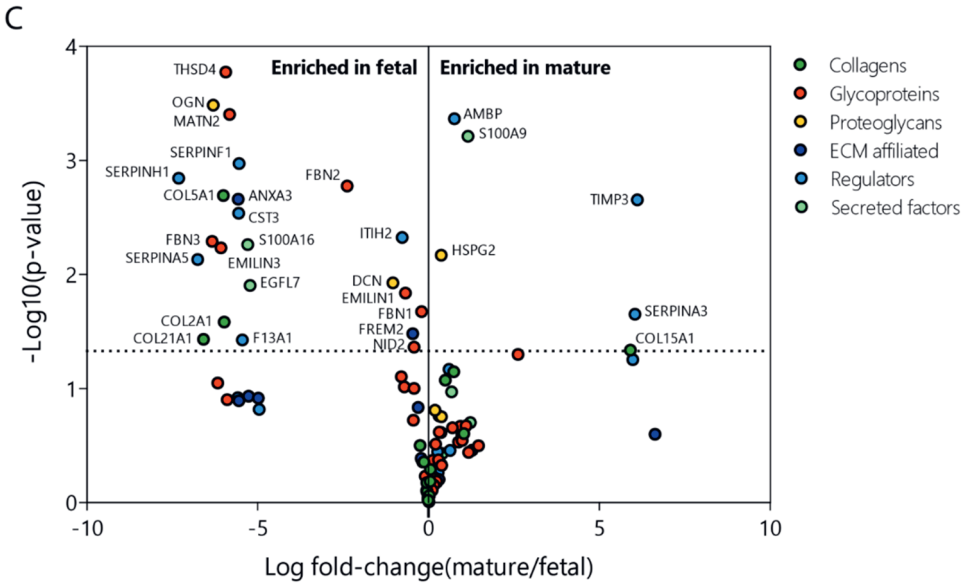

◄Figure 2. Defining the renal fetal and mature extracellular matrix proteome. Extracellular matrix (ECM) proteins identified by mass-spectrometry were classified as collagens, glycoproteins, proteoglycans, ECM affiliated, regulators or secreted factors and they were colored and arranged accordingly. **(A)** Pie charts summarizing the relative protein quantification for both the fetal (left) and mature (right) renal ECM proteome. **(B)** Euler-diagram visualizing the overlap and differences between the human fetal and mature renal ECM proteome. Each node represents a single protein and is labelled with the gene name. Node size is proportional to the abundance of the protein within the renal ECM proteome (less than 0.1%, between 0.1 and 2% or more than 2% of the total ECM signal in at least one dataset (fetal or mature)). **(C)** A volcano plot representation of the human fetal and mature ECM proteome showing the protein distribution between fetal and mature (log fold-change (mature/fetal), x-axis) and significance (P-value, y-axis) of all detected ECM proteins. Each circle represents a single protein. The horizontal dashed line indicates the threshold of statistical significance ($P<0.05$).

Validation of selected proteins within the renal extracellular matrix

EMILIN1 was found to be one of the glycoproteins with the most abundant signal in the renal ECM and significantly enriched in the fetal selection, making it an interesting ECM protein for further investigation. EMILIN1 is a component of elastic fibers and previous studies have implied that its main function is to bind integrins, thereby connecting cells to the ECM [23,24]. In the fetal renal ECM, the EMILIN1 signal comprises 6.8% of the total ECM signal, compared to only 1.5% of the mature ECM (Figure 3A, Supplemental Table 1). Protein verification was conducted using immunohistochemistry on non-decellularized renal tissue. Immunolocalization of EMILIN1 in mature and fetal human kidney showed localization mainly to the tubulointerstitial space (Figure 3B). In concordance with the proteomic analysis,

EMILIN1 was significantly enriched in the fetal kidney compared to the mature kidney (Figure 3C).

Another significantly abundant glycoprotein in the fetal renal ECM is FBN1, which is a major component of microfibrils that, together with elastins, form the elastic fibers [37]. The FBN1 signal comprises 11.1% of the fetal ECM signal, compared to 7.3% of the mature ECM (Supplemental Figure 4A, Supplemental Table 1). Immunolocalization of FBN1 showed localization to both the glomerular and tubulointerstitial space, leading to no differences in fluorescent signal between the fetal and mature kidney (Supplemental Figure 4B,C). mRNA levels on the other hand showed a significant increase of *FBN1* in the fetal kidney compared to the mature kidney (Supplemental Figure 4D). Elastic fiber components in general seem to be increased in the fetal kidney (Supplemental Table 1). Verification by gene expression analysis showed that indeed *MFAP2* was significantly increased in the fetal kidney compared to the adult kidney and the same trend was visible for *ELN* (Supplemental Figure 4E,F). Based on these results, EMILIN1 plays more likely a fundamental role within the fetal renal ECM.

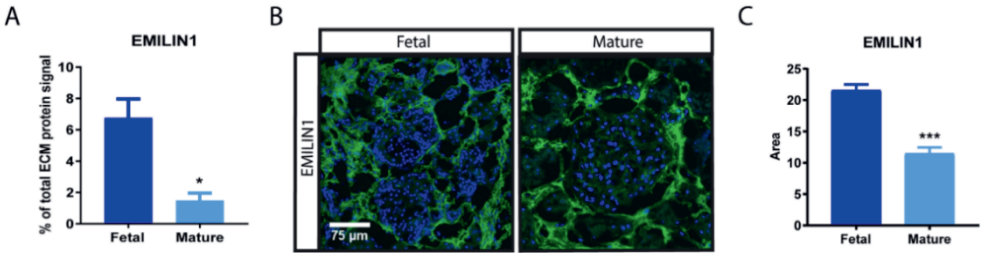

Figure 3. **Validation of selected ECM protein. (A)** EMILIN1 signal identified with mass-spectrometry (MS) within fetal and mature renal ECM extracts. N=3 MS analyses, each containing 3-5 kidney samples per group (fetal or mature). Shown is mean ± SEM; *P<0.05. **(B)** Representative fluorescence immunohistochemistry images (200x magnification) demonstrate the localization and amount of EMILIN1 (green) in fetal and mature renal tissue. Scale bar represents 75 µm. (C) Quantification of normalized EMILIN1 area in both fetal and mature renal samples. N≥25 fluorescent images, from N=3 samples. Shown is mean ± SEM; ***P<0.001.

Anchored cell-derived ECM can be modified by depleting specific ECM proteins

EMILIN1 was further investigated by using a method to reliably anchor native ECM through copolymer thin-film chemistry [31-33]. POMA was covalently coupled to aminosilanized glass coverslips [32]. Next, FN was covalently attached via its lysine sidechain to the reactive anhydride moieties [33] (Figure 4A). Immobilized FN allows the stable anchorage of the ECM via its binding domains to collagen, fibrin and heparin sulfate proteoglycans [31].

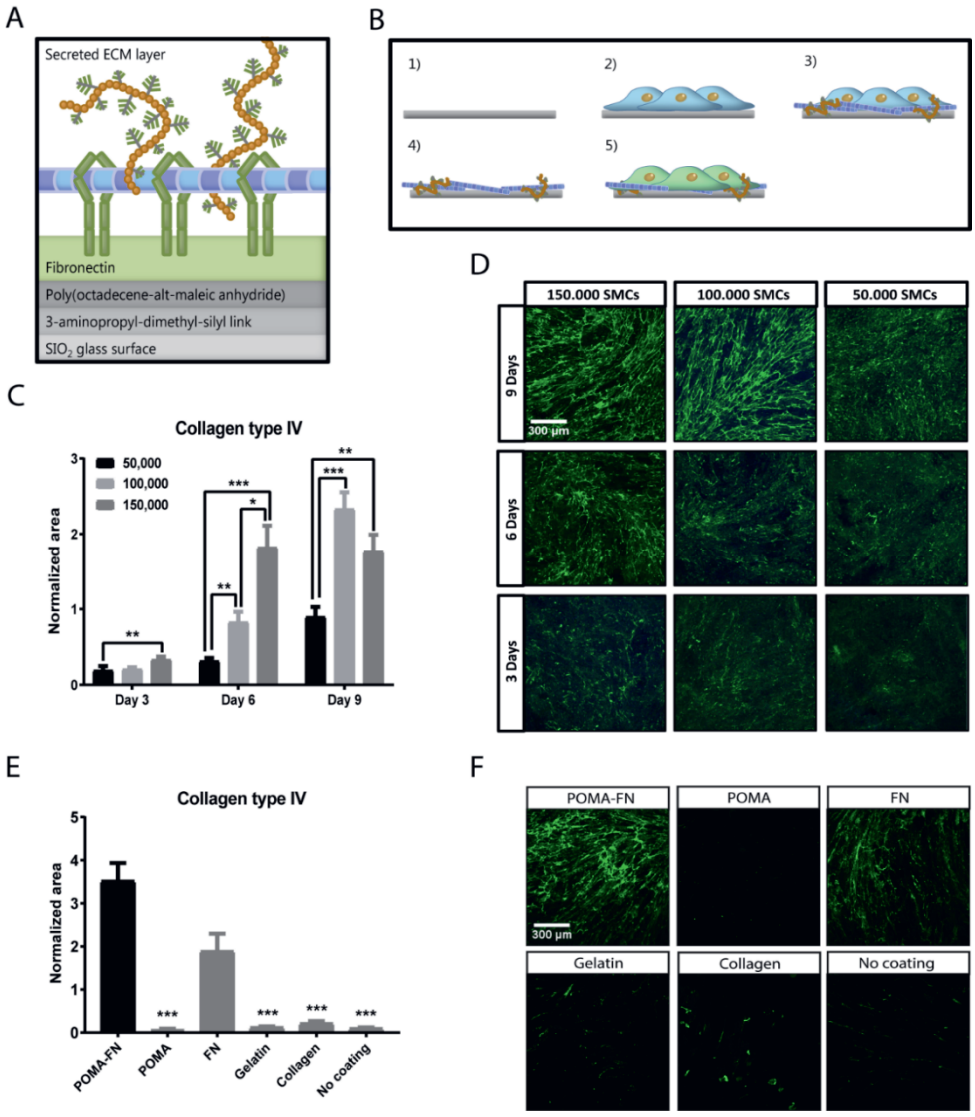

Figure 4. Reliable anchorage of native cell-secreted ECM to a glass surface. (A) Schematic overview of the chemical layers needed to reliably anchor cell-secreted ECM to a glass coverslip. Fibronectin (FN) is immobilized by a covalent linkage with poly(octadecene-alt-maleic anhydride (POMA) on an aminosilanized glass coverslip. Immobilized FN allows stable binding of cell-secreted ECM proteins. **(B)** Workflow for anchoring smooth muscle cell (SMC) ECM to glass coverslips: 1) FN is covalently immobilized on a POMA coverslip. 2) SMCs are grown to confluency. 3) During this culture time, the SMCs will deposit their own ECM. 4) The SMCs are removed by a decellularization process with NH_4OH, leaving the secreted ECM attached to the POMA-FN coverslip. 5) Evaluation of renal cell function on captured ECM. **(C)** Quantification of collagen type IV area deposited by 50,000, 100,000 or 150,000 SMCs

◄cultured for 3, 6 or 9 days on POMA-FN coverslips. Shown is mean ± SEM; **P<0.01, ***P<0.001. N≥23 fluorescent Z-stacks, from N=3 samples. **(D)** Representative immunofluorescence Z-stacks (100x magnification) of anchored collagen type IV on POMA-FN coverslips, deposited by 50,000, 100,000 or 150,000 SMCs cultured for 3, 6 or 9 days. Scale bar represents 300 µm. **(E)** Quantification of collagen type IV area deposited by 150,000 SMCs cultured for 6 days on coverslips coated with POMA-FN, POMA, FN, gelatin or collagen or no coating. Shown is mean ± SEM; ***P<0.001. N≥19 fluorescent Z-stacks, from N=4 samples. **(F)** Representative immunofluorescence Z-stacks (100x magnification) of anchored collagen type IV deposited by 150,000 SMCs cultured for 6 days on coverslips coated with POMA-FN, POMA, FN, gelatin or collagen or no coating. Scale bar represents 300 µm.

We cultured SMCs to confluency on POMA-FN coverslips to capture their secreted ECM (Figure 4B). SMCs were chosen as ECM production cells, since they expressed the highest amount of *EMILIN1* and *FBN1* compared to other cell types (Supplemental Figure 5A). A culture period of 6 days and a cell density of 150,000 was found to be the ideal combination between ECM deposition and time (Figure 4C,D). We verified the capacity of the POMA-FN coverslips to reliably anchor the SMC-secreted ECM by collagen type IV staining. When compared to a collagen or gelatin coating, solely a POMA layer, or no coating, the POMA-FN coverslips captured a significantly higher amount of homogeneously distributed ECM, with the rest exhibiting drastic delamination. With regards to a sole FN coating, almost double the amount of ECM was captured on POMA-FN coverslips (Figure 4E,F). SMCs did not grow to confluency on solely POMA or uncoated coverslips after 6 days of culture, as indicated by a significant decrease in F-actin area (Supplemental Figure 5B,D). However, no differences were found in collagen type IV production between SMCs grown on all coatings, as identified by intracellular staining (Supplemental Figure 5C,D). Thus, although production level of collagen type IV by SMCs remained unaffected by the type of coating, the POMA-FN coverslips captured the most intact and highest amount of ECM.

The next step was to deplete EMILIN1 from the anchored cell-secreted ECM. This was accomplished by using siRNA mediated silencing in the production cells. FBN1 was used as a second target to deplete from the ECM. QPCR analysis after 3, 6 and 9 days of culture showed efficient silencing of *EMILIN1* or *FBN1* expression in SMCs treated with a siRNA pool specific for *EMILIN1* (siEMILIN1) or *FBN1* (siFBN1), when compared to cells transfected with a pool of non-targeting siRNA sequences (siSHAM) (Figure 5A,B). The mRNA levels of other EMILIN/multimerin and fibrillin family members were not affected by either siEMILIN1 or siFBN1 when compared to siSHAM, indicating that the siRNA-mediated silencing was specific for *EMILIN1* and *FBN1* (Supplemental Figure 6A-H).

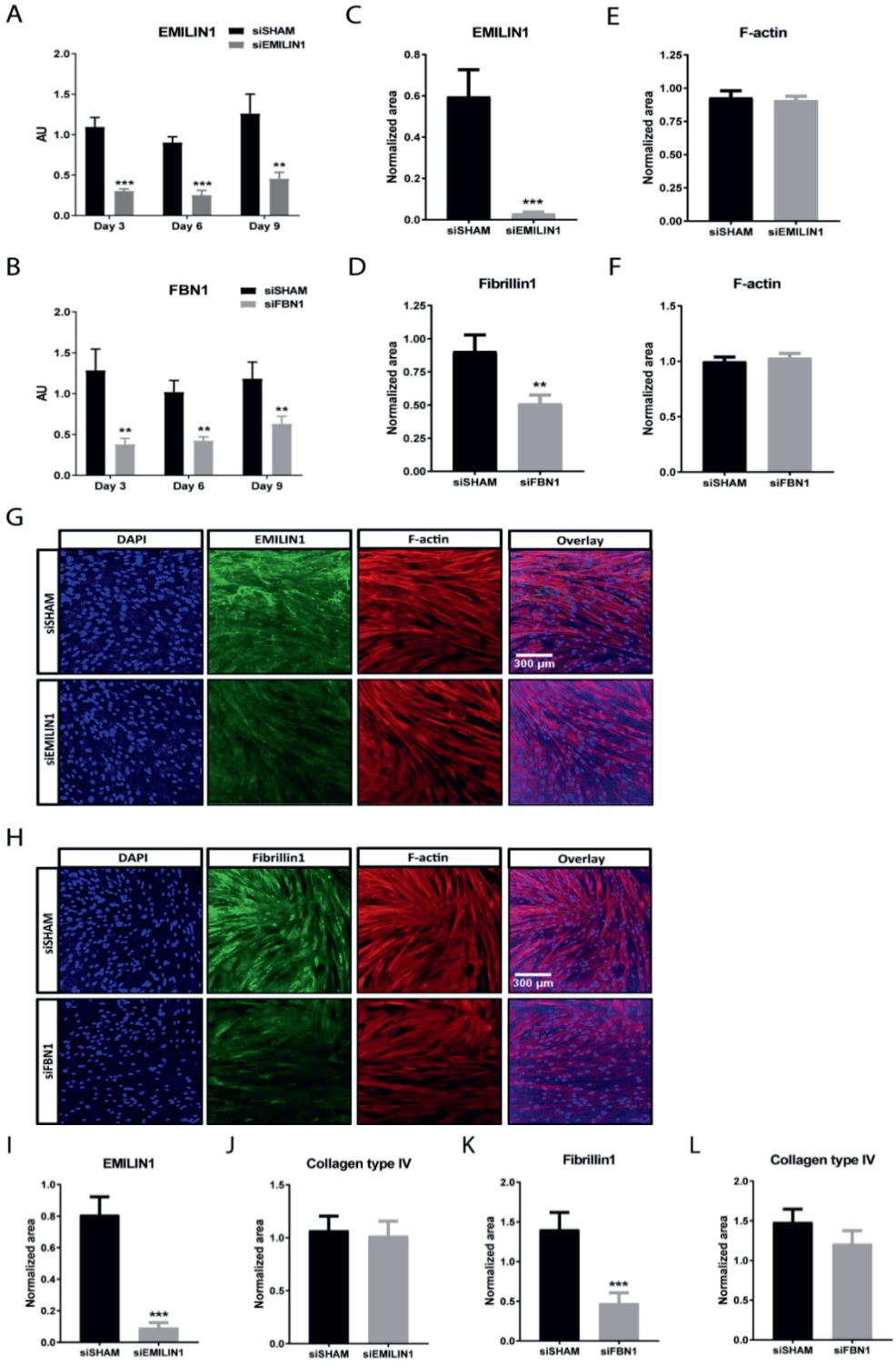
A
EMILIN1
siSHAM
siEMILIN1
AU
Day 3
Day 6
Day 9
B
FBN1
siSHAM
siFBN1
AU
Day 3
Day 6
Day 9
C
EMILIN1
Normalized area
siSHAM
siEMILIN1
D
Fibrillin1
Normalized area
siSHAM
siFBN1
E
F-actin
Normalized area
siSHAM
siEMILIN1
F
F-actin
Normalized area
siSHAM
siFBN1
G
DAPI
EMILIN1
F-actin
Overlay
siSHAM
siEMILIN1
300 µm
H
DAPI
Fibrillin1
F-actin
Overlay
siSHAM
siFBN1
300 µm
I
EMILIN1
Normalized area
siSHAM
siEMILIN1
J
Collagen type IV
Normalized area
siSHAM
siEMILIN1
K
Fibrillin1
Normalized area
siSHAM
siFBN1
L
Collagen type IV
Normalized area
siSHAM
siFBN1

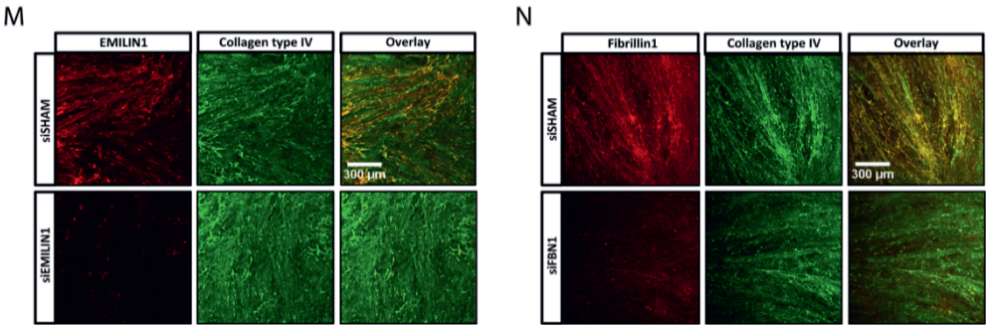

◄Figure 5. EMILIN1 and FBN1 targeting siRNAs induce significant silencing intracellular and on secreted ECM level. Quantitative polymerase chain reaction (qPCR) of *EMILIN1* **(A)** and *FBN1* **(B)** in smooth muscle cells (SMCs) transfected with EMILIN1-targeting siRNA (siEMILIN1), FBN1-targeting siRNA (siFBN1) or non-targeting siRNA (siSHAM), cultured for 3, 6 or 9 days on POMA-FN coverslips. Shown are target gene/housekeeping gene (*β-actin*) ratios (AU). Control (non-transfected SMCs) values are set to 1 (not shown). Shown is mean ± SEM. *P<0.05, **P<0.01, ***P<0.001. N≥5 qPCRs. Quantification of intracellular EMILIN1 **(C)**, Fibrillin1 **(D)** or F-actin **(E, F)** area in confluent SMCs transfected with siSHAM, siEMILIN1 or siFBN1 cultured for 6 days on POMA-FN coverslips. Control (non-transfected SMCs) values are set to 1 (not shown). Shown is mean ± SEM; **P<0.01, ***P<0.001. N≥29 fluorescent Z-stacks, from N=3 samples. Representative immunofluorescence Z-stacks (100x magnification) of SMCs transfected with siSHAM, siEMILIN1 **(G)** or siFBN1 **(H)** cultured for 6 days on POMA-FN coverslips and stained for F-actin (red), EMILIN1 or Fibrillin1 (green) and DAPI (blue). Scale bar represents 300 µm. Quantification of EMILIN1 **(I)**, Fibrillin1 **(J)** or collagen type IV **(K, L)** area in the extracellular matrix (ECM) deposited by SMCs transfected with siSHAM, siEMILIN1 or siFBN1 cultured for 6 days on POMA-FN coverslips. Control (non-transfected SMCs) values are set to 1 (not shown). Shown is mean ± SEM; **P<0.01, ***P<0.001. N≥29 fluorescent Z-stacks, from N=3 samples. Representative immunofluorescence Z-stacks (100x magnification) of the ECM deposited by SMCs transfected with siSHAM, siEMILIN1 **(M)** or siFBN1 **(N)** cultured for 6 days on POMA-FN coverslips and stained for collagen type IV (green) and EMILIN1 or Fibrillin1 (red). Scale bar represents 300 µm.

Importantly, genes encoding for major ECM components, such as *COL1A1*, *COL4A1*, *ELN* and *LAMA5* were also not affected by *EMILIN1* knockdown, implying that the absence of *EMILIN1* did not greatly affect ECM composition (Supplemental Figure 7A-D). Immunofluorescence confirmed a significant loss of EMILIN1 or FBN1 expression in siEMILIN1 or siFBN1 transfected SMCs when compared to siSHAM cells, with no variance in cellular F-actin area (Figure 5C-H). Western blot analysis for EMILIN1 verified the loss of protein expression (Supplemental Figure 8A,B). Additionally, their secreted ECM was significantly depleted of EMILIN1 or FBN1 and successfully anchored to the POMA-FN coverslips, with no difference in extracellular collagen type IV deposition (Figure 5I-N).

Depletion of EMILIN1 from the ECM promotes renal epithelial cell migration, but does not affect cell growth

Previous studies have shown that EMILIN1 is important for migration and growth of various cell types through the interaction of its gC1q domain with integrins [21-24]. Therefore, we studied the migration and growth of renal epithelial cells cultured on an ECM layer depleted of EMILIN1. Depletion of either EMILIN1 or FBN1 from the ECM did not affect proliferation, viability and DNA abundance of renal epithelial cells, when compared to cells cultured on siSHAM ECM (Figure 6A-C). Next, the migration capacity was assessed using live-cell tracking. A significant increase in velocity and distance covered by renal epithelial cells cultured on siEMILIN1 ECM was observed when compared to cells cultured on siSHAM ECM (Figure 6D-F,J-K). This positive effect was absent in renal epithelial cells cultured on siFBN1 ECM (Figure 6G-J,L), hinting towards a link between enhanced renal cell migration and disruption of gC1q-intergrin interaction.

EMILIN1 is important for binding of renal epithelial cells to the ECM and for focal adhesion assembly

Integrins form part of large dynamic protein complexes that connect the cell cytoskeleton to the ECM, called focal adhesion complexes. We assessed whether EMILIN1 in the ECM is required for assembly of focal adhesion complexes during the initial binding of renal epithelial cells to the ECM. Depletion of EMILIN1 from the ECM caused defects in the initial assembly of the focal adhesion-structural protein paxillin. Renal cells cultured for only 2 hours on siEMILIN1 ECM exhibited significantly decreased paxillin area when compared to cells cultured on siSHAM ECM, indicating a reduced spreading ability (Figure 7A,B). Cells cultured on siFBN1 ECM for 2 hours did not show a decrease in paxillin area (Supplemental Figure 9A,B), verifying that the putative effect is specific for EMILIN1 depletion. Next, we assessed the capacity of renal epithelial cells to form a tight monolayer when cultured on siEMILIN1 ECM. The tight junction protein ZO-1 was used to measure barrier formation. Intracellular staining revealed no changes in ZO-1 protein expression in renal cell cultured for 48 hours on siEMILIN1 ECM compared to siSHAM ECM, indicating that these cells are capable of creating a connected monolayer (Figure 7C). However, silencing of EMILIN1 in the ECM appeared to alter the junctional pattern of ZO-1 into a linear instead of zigzagged configuration (Figure 7E). A significant decrease in F-actin area was also observed in cells grown on siEMILIN1 ECM compared to siSHAM ECM (Figure 7D). Immunofluorescence visualization of F-actin revealed that formation of stress fibers was affected (Figure 7E).

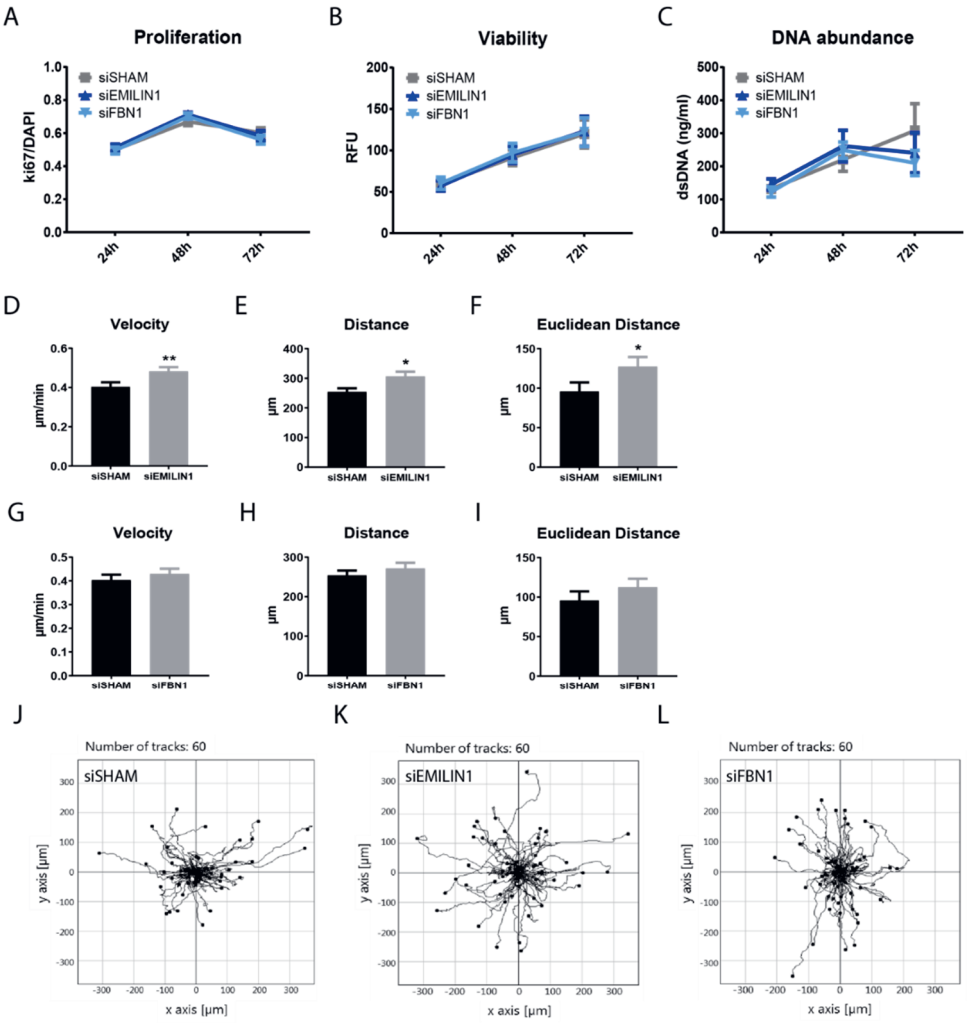

Figure 6. Effect of EMILIN1 or Fibrillin1 depletion from the extracellular matrix on renal epithelial cell growth and migration. (A) ki67/DAPI ratio as measure for cell proliferation at 24, 48 or 72 hours post seeding in HRPTECs cultured on siSHAM, siEMILIN1 and siFBN1 ECM. Shown is mean ± SEM. N≥26 fluorescent images, from N=3 samples. **(B)** Viability measurements using the PrestoBlue assay after 24, 48 or 72 hours post-seeding in HRPTECs on siSHAM, siEMILIN1 and siFBN1 ECM. Shown is mean ± SEM. N=6 assays. **(C)** DNA abundance measurements using the PicoGreen assay after 24, 48 or 72 hours post-seeding in HRPTECs on siSHAM, siEMILIN1 and siFBN1 ECM. Shown is mean ± SEM. N=5 assays. Quantified live-cell migration assay results showing velocity and covered and Euclidean distance of HK2 cells on either siEMILIN1 **(D-F)** and siFBN1 **(G-I)** ECM compared to cells on siSHAM ECM. The migration of HK2 cells on the ECM layer was tracked overnight with a confocal microscope. Shown is mean ± SEM; *P<0.05, **P<0.01. N=60 individual cells tracked, from N=4 assays. Migration plots showing multiple tracks of individual HK2 cells on siSHAM **(J)**, siEMILIN1 **(K)** and siFBN1 ECM **(L)**.

The assembly of focal adhesion complexes in confluent renal epithelial monolayers was impaired as well. Intracellular staining revealed that EMILIN1-depleted ECM significantly inhibited formation of paxillin points and stress fibers in confluent renal epithelial monolayers, since less paxillin co-localized with F-actin (Figure 7F,G). Cells cultured to confluency on FBN1-depleted ECM did not exhibit significantly less colocalization of paxillin with F-actin (Supplemental Figure 9C,D), verifying that the impairment of focal adhesion assembly is specific for EMILIN1 depletion. Actin cytoskeleton remodeling upon integrin mediated focal adhesion formation is regulated by RhoA signaling. Thus, we assessed the RhoA activity in renal epithelial cells grown on siEMILIN1 ECM for 48 hours when compared to cells grown on siSHAM ECM. In concordance with our previous results, EMILIN1 silencing in the ECM significantly reduced RhoA activation in renal cells (Figure 7H). All together, these findings indicate that EMILIN1 in the ECM is important for assembly of focal adhesion complexes and subsequent actin-cytoskeleton adaptation in renal epithelial cells.

Discussion

This study presents to date the first catalog that compares the human fetal and mature renal ECM. A total of 99 different ECM proteins was detected by proteomic analysis of which the majority form an overlapping core, but also includes many renal ECM proteins that are enriched in either the fetal or mature condition.

Using immunohistochemistry, we confirmed the identification of EMILIN1 and FBN1 as key proteins in renal ECM. EMILIN1 mainly localizes to the tubulointerstitial space, but is also classified as a structural glomerular protein by Lennon *et al* [10]. However, they solely focused on identifying glomerular proteins and did not analyze the remainder from their glomerular enrichment strategy. Immunolocalization of FBN1 showed its presence in both glomeruli and tubulointerstitial space, which is in concordance with Lennon *et al.*, who classified it as a glomerular basement membrane protein.

Our proteome comparison between the fetal and mature renal ECM has the potential to mark novel molecular players by which the renal ECM can influence cellular behavior. Percentile ranking by LFQ intensity proved effective at finding proteins enriched in the fetal ECM. One striking difference between the fetal and mature renal ECM proteome is the enrichment of elastic fiber components in the fetal ECM, including fibrillin1, MFAP2 and elastin. Particularly the glycoprotein EMILIN1 was abundant in the fetal ECM. Many other ECM proteins differ significantly between fetal and mature tissue, however most of them are present in low quantities in the renal ECM (<2%) and are therefore less likely to play a fundamental role (for example EMILIN3).

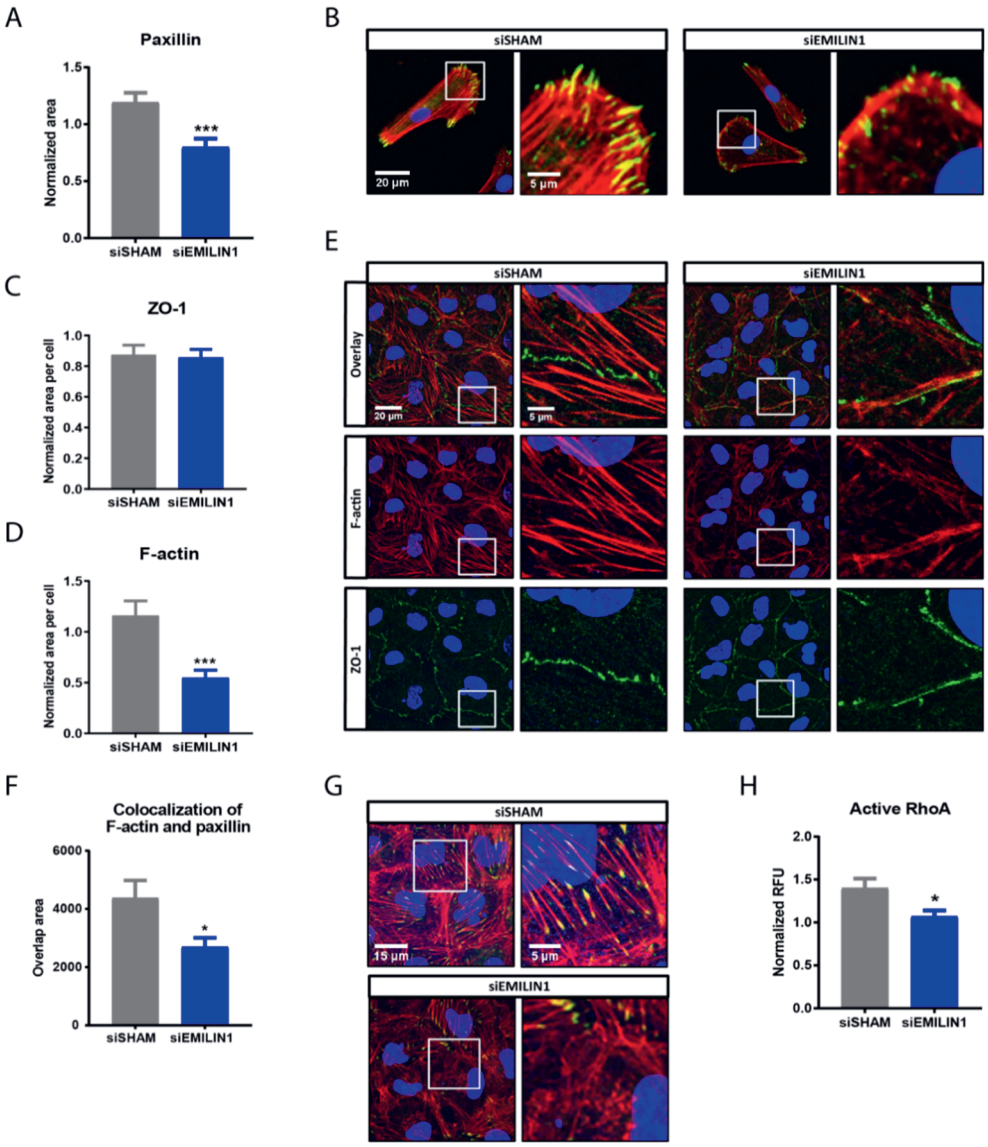

Figure 7. Depletion of EMILIN1 from the ECM layer reduces paxillin area and stress fibers in renal epithelial cells. (A) Quantified results showing the paxillin area in HRPTECs on siSHAM or siEMILIN1 ECM during initial binding to the ECM (cultured for 2 hours). Shown is mean ± SEM; ***P<0.001. N=30 fluorescent images, from N=3 samples. **(B)** Representative immunofluorescence images (400x magnification) of HRPTECs after 2 hours of binding on siSHAM or siEMILIN1 ECM and stained for paxillin (green), F-actin (red) and DAPI (blue). Scale bar represents 20 µm (overview image, left) and 5 µm (zoomed-in image, right). Quantified results showing the ZO-1 **(C)** and F-actin area **(D)** in HK2 cells cultured to confluency on siSHAM or siEMILIN1 ECM. Shown is mean ± SEM; ***P<0.001. N=20 fluorescent Z-stacks, from N=4 samples. **(E)** Representative immunofluorescence Z-stacks (630x magnification) of HK2 cells cultured to confluency (cultured for 48 hours) on siSHAM or siEMILIN1 ECM

◄and stained for ZO-1 (green), F-actin (red) and DAPI (blue). Scale bar represents 20 µm (overview image, left) and 5 µm (zoomed-in image, right). **(F)** Colocalization of paxillin and F-actin in HK2 cells cultured to confluency on siSHAM or siEMILIN1 ECM. Shown is mean ± SEM; *P<0.05. N≥25 fluorescent Z-stacks, from N≥5 samples. **(G)** Representative immunofluorescence Z-stacks (630x magnification) of HK2 cells cultured to confluency on siSHAM or siEMILIN1 ECM and stained for paxillin (green), F-actin (red) and DAPI (blue). Colocalization is displayed as yellow. Scale bar represents 15 µm (overview image, left) and 5 µm (zoomed-in image, right). **(H)** RhoA activation levels in HK2 cells cultured for 48 hours on siSHAM or siEMILIN1 ECM. Shown is mean ± SEM; *P<0.05. N=5 assays.

The importance of EMILIN1 has been previously studied using EMILIN$^{-/-}$ mice, which display several vascular defects, including impaired lymph drainage, increased leakage and elevated blood pressure associated with narrower vessels [26-29]. The latter is due to an increased presence of transforming growth factor β (TGFβ), since EMILIN1 prevents TGFβ processing [27-29]. In aortic valves, increased TGFβ signaling due to EMILIN1 deficiency causes elastic fiber fragmentation and subsequent aortic valve disease [38]. Both these mutant mice and aged mice exhibit ECM stiffness, fibrosis, increased collagen expression and cell adhesion and fibronectin alterations [39]. This suggests that loss of EMILIN1 and associated phenotype is linked to a mature state, which is in concordance with our proteomic data. Despite several studies described the function of EMILIN1, a possible renal function remains unclear.

Lack of EMILIN1 is associated with altered vascular and lymphatic cell anchorage, patterning and morphology [25,26]. Previous studies have reported that the gC1q domain of EMILIN1 is responsible for promoting cell adhesion [23,24,40]. Our study showed that renal epithelial cells exhibit a weaker adhesion pattern on EMILIN1-depleted ECM, indicated by fewer focal adhesion points. Focal adhesions provide linkage points between the cell cytoskeleton and the ECM, playing a central role in adhesion [41]. Renal epithelial cells grown on EMILIN1-depleted ECM exhibit a low number of actin stress fibers and less paxillin, a focal adhesion adaptor protein that localizes to large focal contacts at the tips of these fibers. More evidence for the role of EMILIN1 in renal cell adhesion comes from the activation of signaling molecule RhoA, that is recruited and activated upon integrin-ECM binding and leads to maturation of focal adhesions [41]. Less RhoA was activated in renal epithelial cells grown on EMILIN1-depleted ECM, indicating reduced stabilization of focal structures. Furthermore, the junctional pattern of ZO-1 in these renal cells appeared linear instead of zigzagged. High bioavailability of ZO-1 at tight junctions induces zigzag patterning and increases the overall permeability of epithelia [42]. Actin filaments terminate at tight junctions, thereby linking them with focal adhesions [43]. This suggests that defects in focal adhesion assembly by EMILIN1 depletion in the ECM can result in F-actin stress fiber dysregulation and subsequent reduction of

functional tight junctions, affecting renal epithelial barrier function. Indeed, previous studies showed that ZO-1 interaction with F-actin at tight junctions is important for epithelial polarization and formation of single lumens [44]. Altogether, our study indicates that EMILIN1 could be a promising candidate for implementation in renal scaffolds for the enhancement of cell attachment and barrier formation.

Our findings are not in line with previous studies, in which actin organization in cells attached to EMILIN1 was described to be organized along the cell periphery without any apparent focal contacts [24,40]. More in depth experiments have shown that in these cells, the gC1q domain of EMILIN1 promotes cell adhesion by interacting with α4/α9/β1 integrins [23,24,40]. The reported synovial sarcoma cells and T lymphocytes use α4β1 integrins for gC1q-mediated cell attachment, whereas lymphatic endothelial cells (LECs) and microvascular ECs attachment to EMILIN1 is mediated by α9β1 integrins [23,24]. These reports suggest that different cell types express a specific selection of integrins to react to environmental stimuli.

β1 is the most widely expressed renal integrin subunit and is responsible for interactions with the cell cytoskeleton via binding with several focal adhesion complex proteins [45,46]. Different α subunits have been demonstrated to be expressed by renal tissue, which all can form heterodimers with β1: α1, α2, α3, α5, α6, α8 and αv [45,46]. The renal cells used in our migration and confluent adhesion assays showed high expression of the integrin subunits α3, α5, αv, and β1, modest levels of α2, α4, α6 and non-detectable expression of α9 (data not shown). EMILIN1 may exerts its effect in renal cells through another αβ1 integrin heterodimer than the α4/α9/β1-gC1q interaction described, which might explain the distinct effect we found of EMILIN1 on renal epithelial cell adhesion strength.

The dynamic assembly and disassembly of focal adhesions play a central role in cell migration and proliferation. EMILIN1 also plays an important role in these processes: fibroblasts, keratinocytes and LECs obtained from EMILIN1$^{-/-}$ mice retain a high proliferation rate compared to wildtype cells [22,23]. This reduction in proliferation is associated with the gC1q–α9 integrin interaction, which also stimulates LEC migration [23]. Furthermore, the gC1q–α4 integrin interaction promotes haptotactic directional migration of trophoblasts [40], indicating that EMILIN1 can promote cell proliferation and migration by interacting with α4/α9/β1 integrins.

In contrast, the present study shows that EMILIN1-deficient ECM does not influence proliferation of renal epithelial cells and absence of EMILIN1 stimulates renal epithelial cell migration. Hence, the effect of EMILIN1 seems to be cell type specific. Indeed, Colombatti and colleagues indicated that the effect of EMILIN1 on cell adhesion and migration can be

either enhancing or reducing depending on the cell type investigated [47], which might be linked to different integrin expression profiles.

Strong adhesion through focal adhesion formation stabilized by stress fibers is considered to be unfavorable for cell detachment needed for migration [48]. In 1979, Couchman and Rees already made the observation that fibroblasts displayed little to no focal adhesions during the initial period of rapid migration. Focal adhesions and associated ventral stress fibers only developed when migration slowed down [49]. This observation implies that focal adhesion disassembly facilitates rapid migration. Indeed, we observed that renal epithelial cells migrate faster and cover more distance when less EMILIN1 is present in the ECM. Therefore, this rapid migration pattern is most likely stimulated by the reduction of focal adhesions and stress fibers seen in these renal cells as well.

The motility phenotype of cells also depends on which integrins are available on the cell membrane. For example, previous research has observed that the α4/α9/β1-gC1q interaction encourages a cellular phenotype that lacks stress fibers and promotes lamellipodia formation, thereby facilitating cell spreading [23,24,40]. The α4/α9 subfamily is a specific subset of α subunits based on evolutionary relationships, that share a high sequence similarity and ligand specificities [50]. In contrast, the present study showed that lack of EMILIN1 interaction stimulates cell migration. Renal cells express other α subunits in high quantities [45,46]; suggesting that they likely express subunits that stabilize focal adhesions. For example, the renal cells used in our migration assay highly express integrin subunits α5 and β1, which as a heterodimer is known to mediate stabilization of mature focal adhesions [51].

Apparent differences between the renal epithelial cell behavior seen in response to EMILIN1 in this study and the results of earlier studies may also be due to differences in study design. We cultured our renal cells on a complex ECM network depleted from a protein of interest from the beginning, rather than culturing on a coating of one specific ECM protein. It is inevitable that this rich ECM background from the start will have an influence on focal adhesion composition, mostly the integrin expression profile, and subsequent cell behavior. This environment mimics more the *in vivo* ECM complexity, even though it lacks a 3D configuration. Nevertheless, this 2D ECM model is a valuable resource for additional investigation and thereby aids in the search for promising ECM components to implement in 3D culture.

In conclusion, based on our proteome analysis we provide evidence for EMILIN1 as a promising candidate for implementation in renal scaffolds as a bioactive factor. Here, it would most likely stimulate an adhesive phenotype of the embedded renal cells. Matrices containing organ specific ECM cues to direct cell adhesion may ultimately allow the generation of whole 3D kidney constructs for implantation.

References

1. Takasato M, Er PX, Becroft M, Vanslambrouck JM, Stanley EG, Elefanty AG, Little MH: Directing human embryonic stem cell differentiation towards a renal lineage generates a self-organizing kidney. *Nature Cell Biology* **2014**, 16:118-26.
2. Takasato M, Er PX, Chiu HS, Maier B, Baillie GJ, Ferguson C, Parton RG, Wolvetang EJ, Roost MS, Chuva de Sousa Lopes SM, Little MH: Kidney organoids from human iPS cells contain multiple lineages and model human nephrogenesis. *Nature* **2015**, 526:564-8.
3. Guimaraes-Souza NK, Yamaleyeva LM, AbouShwareb T, Atala A, Yoo JJ: In vitro reconstitution of human kidney structures for renal cell therapy. *Nephrology, Dialysis, Transplantation* **2012**, 27:3082-90.
4. Flaim CJ, Chien S, Bhatia SN: An extracellular matrix microarray for probing cellular differentiation. *Nature Methods* **2015**, 2:119-25.
5. Plotnikov SV, Pasapera AM, Sabass B, Waterman CM: Force fluctuations within focal adhesions mediate ECM-rigidity sensing to guide directed cell migration. *Cell* **2012**, 151:1513-27.
6. Vorotnikova E, McIntosh D, Dewilde A, Zhang J, Reing JE, Zhang L, Cordero K, Bedelbaeva K, Gourevitch D, Heber-Katz E, Badylak SF, Braunhut SJ: Extracellular matrix-derived products modulate endothelial and progenitor cell migration and proliferation in vitro and stimulate regenerative healing in vivo. *Matrix Biology* **2010**, 29:690-700.
7. Van Genderen AM, Jansen J, Cheng C, Vermonden T, Masereeuw R: Renal tubular- and vascular basement membranes and their mimicry in engineering vascularized kidney tubules. *Advanced Healthcare Materials* **2018**, 7:e1800529.
8. Naba A, Clauser KR, Ding H, Whittaker CA, Carr SA, Hynes RO: The extracellular matrix: Tools and insights for the "omics" era. *Matrix Biology* **2016**, 49:10-24.
9. Naba A, Clauser KR, Hoersch S, Liu H, Carr SA, Hynes RO: The matrisome: in silico definition and in vivo characterization by proteomics of normal and tumor extracellular matrices. *Molecular & Cellular Proteomics* **2012**, 11:M111.014647.
10. Lennon R, Byron A, Humphries JD, Randles MJ, Carisey A, Murphy S, Knight D, Brenchley PE, Zent R, Humphries MJ: Global analysis reveals the complexity of the human glomerular extracellular matrix. *JASN* **2014**, 25:939-51.
11. Yoshida Y, Miyazaki K, Kamiie J, Sato M, Okuizumi S, Kenmochi A, Kamijo K, Nabetani T, Tsugita A, Xu B, Zhang Y, Yaoita E, Osawa T, Yamamoto T: Two-dimensional electrophoretic profiling of normal human kidney glomerulus proteome and construction of an extensible markup language (XML)-based database. *Proteomics* **2005**, 51083-96.
12. Cui Z, Yoshida Y, Xu B, Zhang Y, Nameta M, Magdeldin S, Makiguchi T, Ikoma T, Fujinaka H, Yaoita E, Yamamoto T: Profiling and annotation of human kidney glomerulus proteome. *Proteome Science* **2013**, 11:13.
13. Byron A, Randles MJ, Humphries JD, Mironov A, Hamidi H, Harris S, Mathieson PW, Saleem MA, Satchell SC, Zent R, Humphries MJ, Lennon R: Glomerular cell cross-talk influences composition and assembly of extracellular matrix. *JASN* **2014**, 25:953-66.
14. Virtanen I, Laitinen L, Korhonen M: Differential expression of laminin polypeptides in developing and adult human kidney. *Journal of Histochemistry and Cytochemistry* **1995**, 43:621-8.
15. Guinobert I, Viltard M, Piquemal D, Elalouf JM, Marti J, Lelievre-Pegorier M: Identification of differentially expressed genes between fetal and adult mouse kidney: candidate gene in kidney development. *Nephron Physiology* **2006**, 102:p81-91.
16. Upadhyay KK, Silverstein DM: Renal development: a complex process dependent on inductive interaction. *Current Pediatric Reviews* **2014**, 10:107-14.
17. Wang P, Chen Y, Yong J, Cui Y, Wang R, Wen L, Qiao J, Tang F: Dissecting the global dynamic molecular profiles of human fetal kidney development by single-cell RNA sequencing, *Cell Reports* **2018**, 24:3554-3567
18. Bressan GM, Daga-Gordini D, Colombatti A, Castellani I, Marigo V, Volpin D: Emilin, a component of elastic fibers preferentially located at the elastin-microfibrils interface. *The Journal of Cell Biology* **1993**, 121:201-12.

19. Colombatti A, Spessotto P, Doliana R, Mongiat M, Bressan GM, Esposito G: The EMILIN/Multimerin family. *Frontiers in Immunology* **2011**, 2:93.
20. Verdone G, Corazza A, Colebrooke SA, Cicero D, Eliseo T, Boyd J, Doliana R, Fogolari F, Viglino P, Colombatti A, Campbell ID, Esposito G: NMR-based homology model for the solution structure of the C-terminal globular domain of EMILIN1. *Journal of Biomolecular NMR* **2009**, 43:79-96.
21. Verdone G, Doliana R, Corazza A, Colebrooke SA, Spessotto P, Bot S, Bucciotti F, Capuano A, Silvestri A, Viglino P, Campbell ID, Colombatti A, Esposito G: The solution structure of EMILIN1 globular C1q domain reveals a disordered insertion necessary for interaction with the alpha4beta1 integrin. *The Journal of Biological Chemistry* **2008**, 283:18947-56.
22. Danussi C, Petrucco A, Wassermann B, Pivetta E, Modica TM, Del Bel Belluz L, Colombatti A, Spessotto P: EMILIN1-alpha4/alpha9 integrin interaction inhibits dermal fibroblast and keratinocyte proliferation. *The Journal of Cell Biology* **2011**, 195:131-45.
23. Danussi C, Del Bel Belluz L, Pivetta E, Modica TM, Muro A, Wassermann B, Doliana R, Sabatelli P, Colombatti A, Spessotto P: EMILIN1/alpha9beta1 integrin interaction is crucial in lymphatic valve formation and maintenance. *Molecular and Cellular Biology* **2013**, 33:4381-94.
24. Spessotto P, Cervi M, Mucignat MT, Mungiguerra G, Sartoretto I, Doliana R, Colombatti A: beta 1 Integrin-dependent cell adhesion to EMILIN-1 is mediated by the gC1q domain. *The Journal of Biological Chemistry* **2003**, 278:6160-7.
25. Zanetti M, Braghetta P, Sabatelli P, Mura I, Doliana R, Colombatti A, Volpin D, Bonaldo P, Bressan GM: EMILIN-1 deficiency induces elastogenesis and vascular cell defects. *Molecular and Cellular Biology* **2004**, 24:638-50.
26. Danussi C, Spessotto P, Petrucco A, Wassermann B, Sabatelli P, Montesi M, Doliana R, Bressan GM, Colombatti A: Emilin1 deficiency causes structural and functional defects of lymphatic vasculature. *Molecular and Cellular Biology* **2008**, 28:4026-39.
27. Raman M, Cobb MH: TGF-beta regulation by Emilin1: new links in the etiology of hypertension. *Cell* **2006**, 124:893-5.
28. Zacchigna L, Vecchione C, Notte A, Cordenonsi M, Dupont S, Maretto S, Cifelli G, Ferrari A, Maffei A, Fabbro C, Braghetta P, Marino G, Selvetella G, Aretini A, Colonnese C, Bettarini U, Russo G, Soligo S, Adorno M, Bonaldo P, Volpin D, Piccolo S, Lembo G, Bressan GM: Emilin1 links TGF-beta maturation to blood pressure homeostasis. *Cell* **2006**, 124:929-42.
29. Litteri G, Carnevale D, D'Urso A, Cifelli G, Braghetta P, Damato A, Bizzotto D, Landolfi A, Ros FD, Sabatelli P, Facchinello N, Maffei A, Volpin D, Colombatti A, Bressan GM, Lembo G: Vascular smooth muscle Emilin-1 is a regulator of arteriolar myogenic response and blood pressure. *Arteriosclerosis, Thrombosis, and Vascular Biology* **2012**, 32:2178-84.
30. Ryan MJ, Johnson G, Kirk J, Fuerstenberg SM, Zager RA, Torok-Storb B: HK-2: an immortalized proximal tubule epithelial cell line from normal adult human kidney. *Kidney International* **1994**, 45:48-57.
31. Wilm M, Shevchenko A, Houthaeve T, Breit S, Schweigerer L, Fotsis T, Mann M Femtomole sequencing of proteins from polyacrylamide gels by nano-electrospray mass spectrometry. *Nature* **1996**, 379:466-9.
32. Sap KA, Bezstarosti K, Dekkers DHW, Voets O, Demmers JAA: Quantitative proteomics reveals extensive changes in the ubiquitinome after perturbation of the proteasome by targeted dsRNA-mediated subunit knockdown in drosophila. *Journal of Proteome Research* **2017**, 16:2848-2862.
33. Cox J, Mann M: MaxQuant enables high peptide identification rates, individualized p.p.b.-range mass accuracies and proteome-wide protein quantification. *Nature Biotechnology* **2008**, 26:1367-72.
34. Labit H, Goldar A, Guilbaud G, Douarche C, Hyrien O, Marheineke K: A simple and optimized method of producing silanized surfaces for FISH and replication mapping on combed DNA fibers. *BioTechniques* **2008**, 45:649-658.

35. Prewitz MC, Seib FP, von Bonin M, Friedrichs J, Stissel A, Niehage C, Muller K, Anastassiadis K, Waskow C, Hoflack B, Bornhauser M, Werner C: Tightly anchored tissue-mimetic matrices as instructive stem cell microenvironments. *Nature Methods* **2013**, 10:788-94.
36. Pompe T, Salchert K, Alberti K, Zandstra P, Werner C: Immobilization of growth factors on solid supports for the modulation of stem cell fate. *Nature Protocols* **2010**, 5:1042-50.
37. Kielty CM, Sherratt MJ, Shuttleworth CA: Elastic fibres. *Journal of Cell Science* **2002**, 115:2817-28.
38. Munjal C, Opoka AM, Osinska H, James JF, Bressan GM, Hinton RB: TGF-beta mediates early angiogenesis and latent fibrosis in an Emilin1-deficient mouse model of aortic valve disease. *Disease Models & Mechanisms* **2014**, 7:987-96.
39. Angel PM, Narmoneva DA, Sewell-Loftin MK, Munjal C, Dupuis L, Landis BJ, Jegga A, Kern CB, Merryman WD, Baldwin HS, Bressan GM, Hinton RB: Proteomic Alterations Associated with Biomechanical Dysfunction are Early Processes in the Emilin1 Deficient Mouse Model of Aortic Valve Disease. *Annals of Biomedical Engineering* **2017**, 45:2548-2562.
40. Spessotto P, Bulla R, Danussi C, Radillo O, Cervi M, Monami G, Bossi F, Tedesco F, Doliana R, Colombatti A: EMILIN1 represents a major stromal element determining human trophoblast invasion of the uterine wall. *Journal of Cell Science* **2006**, 119:4574-84.
41. Parsons JT, Horwitz AR, Schwartz MA: Cell adhesion: integrating cytoskeletal dynamics and cellular tension. *Nature Reviews Molecular Cell Biology* **2010**, 11:633-43.
42. Tokuda S, Higashi T, Furuse M: ZO-1 knockout by TALEN-mediated gene targeting in MDCK cells: involvement of ZO-1 in the regulation of cytoskeleton and cell shape, *PloS ONE* **2014**, 9:e104994.
43. Itoh M, Nagafuchi A, Moroi S, Tsukita S: Involvement of ZO-1 in cadherin-based cell adhesion through its direct binding to alpha catenin and actin filaments, *The Journal of Cell Biology* **1997**, 138:181-92.
44. Odenwald MA, Choi W, Buckley A, Shashikanth N, Joseph NE, Wang Y, Warren MH, Buschmann MM, Pavlyuk R, Hildebrand J, Margolis B, Fanning AS, Turner JR: ZO-1 interactions with F-actin and occludin direct epithelial polarization and single lumen specification in 3D culture. *Journal of Cell Science* **2017**, 130:243-259.
45. Kreidberg JA, Symons JM: Integrins in kidney development, function, and disease, American journal of physiology. *Renal Physiology* **2000**, 279: F233-42.
46. Mathew S, Chen X, Pozzi A, Zent R: Integrins in renal development. *Pediatric Nephrology* **2012**, 27:891-900.
47. Colombatti A, Doliana R, Bot S, Canton A, Mongiat M, Mungiguerra G, Paron-Cilli S, Spessotto P: The EMILIN protein family. *Matrix Biology* **2000**, 19:289-301.
48. Palecek SP, Loftus JC, Ginsberg MH, Lauffenburger DA, Horwitz AF: Integrin-ligand binding properties govern cell migration speed through cell-substratum adhesiveness. *Nature* **1997**, 385:537-40.
49. J.R. Couchman, D.A. Rees, The behaviour of fibroblasts migrating from chick heart explants: changes in adhesion, locomotion and growth, and in the distribution of actomyosin and fibronectin. *Journal of Cell Science* **1979**, 39:149-65.
50. Hynes RO: Integrins: bidirectional, allosteric signaling machines, *Cell* **2002**, 110:673-87.
51. Laukaitis CM, Webb DJ, Donais K, Horwitz AF: Differential dynamics of alpha 5 integrin, paxillin, and alpha-actinin during formation and disassembly of adhesions in migrating cells. *The Journal of Cell Biology* **2001**, 153:1427-40.

Supplemental Data

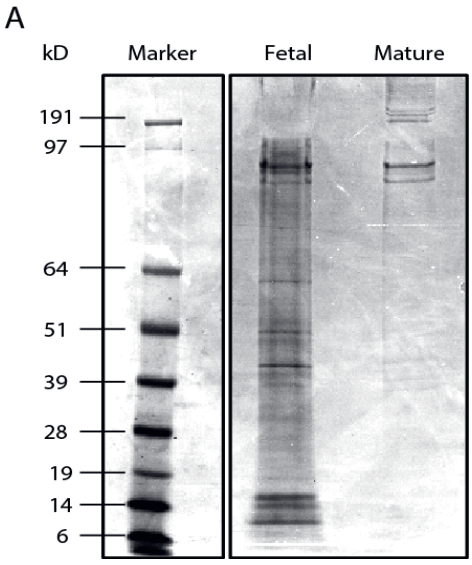

Supplemental Figure 1. (A) ECM extracts from human fetal and mature renal samples were separated by SDS-PAGE and visualized with a Coomassie staining, before further processing for MS analysis. Shown is a representative blot of 3 separate experiments, each containing 3-5 kidney samples per group (fetal or mature).

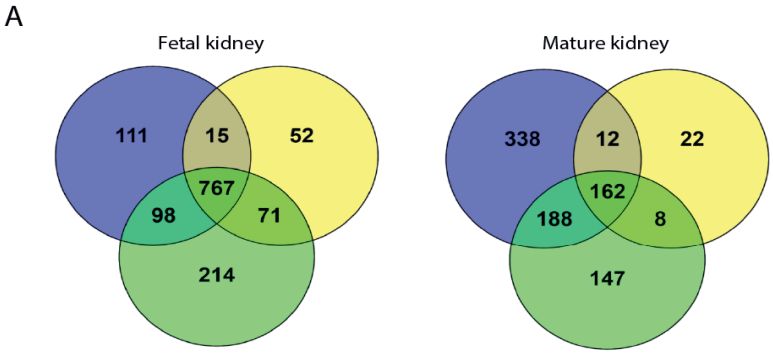

Supplemental Figure 2. (A) The Venn diagrams show the total amount and overlap of proteins identified in three separate mass-spectrometry analyses. Each analysis contained 3-5 kidney samples per group (fetal or mature).

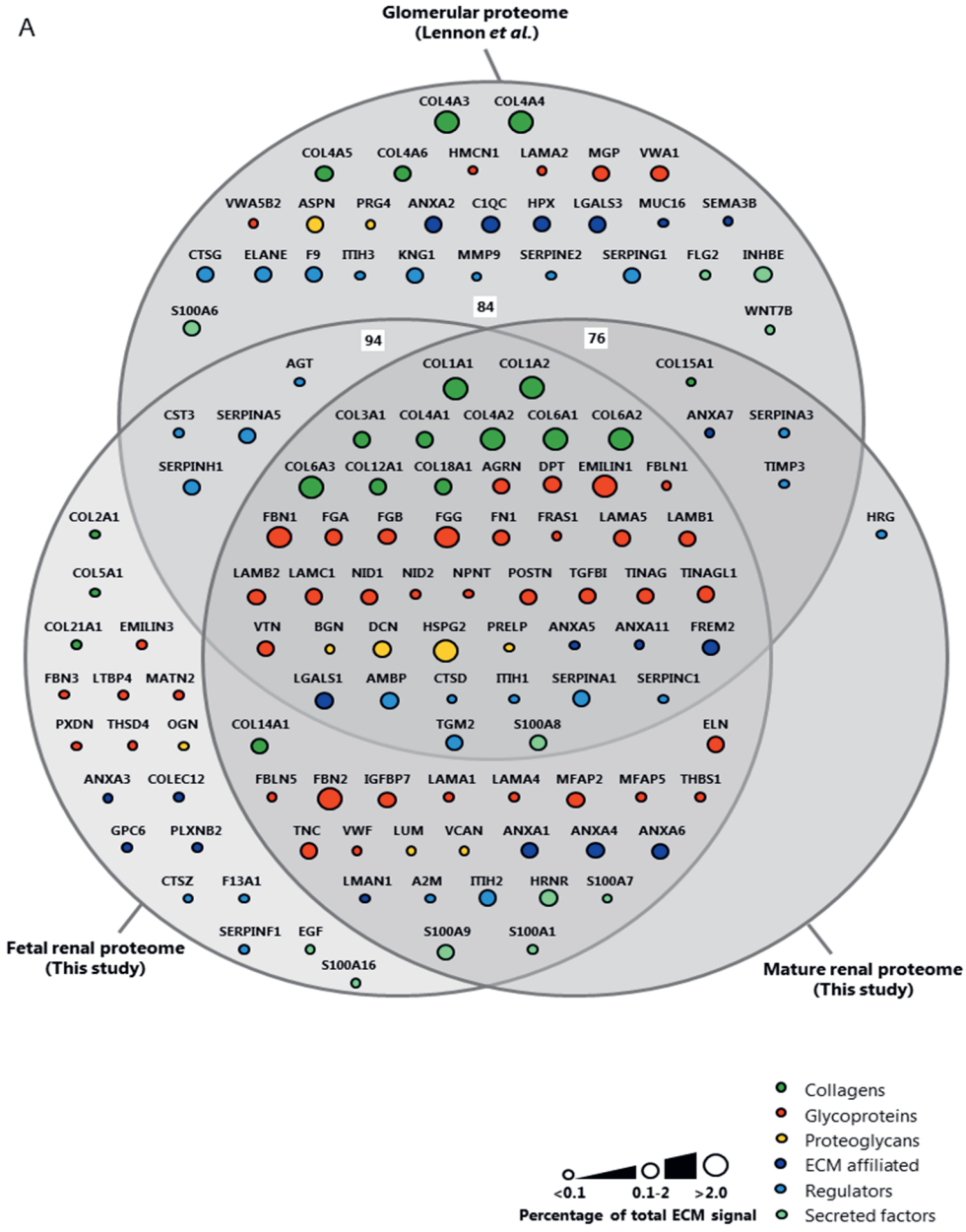

Supplemental Figure 3. (A) Euler-diagram visualizing the overlap and differences between the human fetal and mature renal ECM proteome found in this study and the glomerular proteome identified by Lennon *et al* [10]. Each node represents a single protein and is labeled with the gene name. Node size is proportional to the abundance of the protein within the renal ECM proteome (less than 0.1%, between 0.1 and 2% or more than 2% of the total ECM signal in at least one dataset (fetal or mature)).

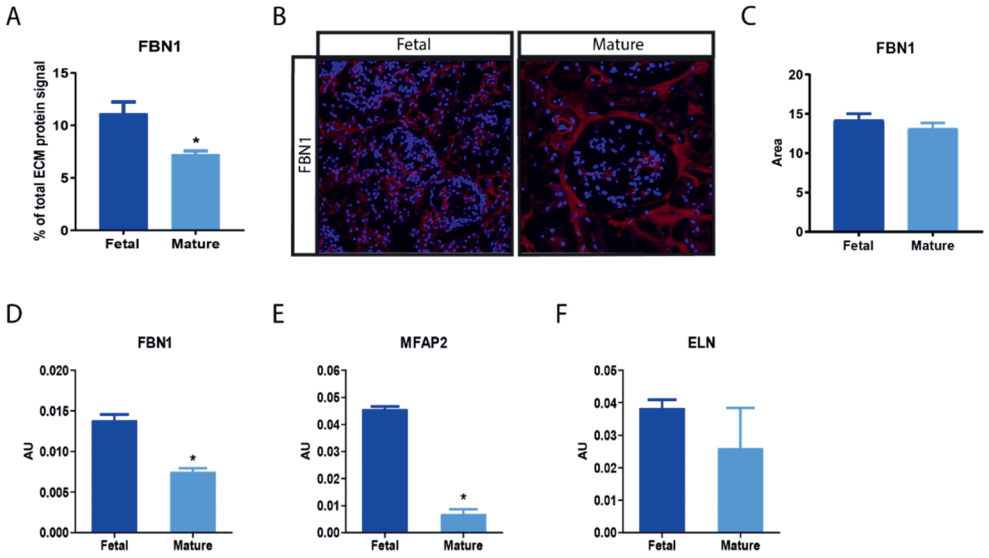

Supplemental Figure 4. (A) Bar graph showing FBN1 signal identified with mass-spectrometry (MS) within fetal and mature renal ECM extracts. N=3 MS analyses, each containing 3-5 kidney samples per group (fetal or mature). Shown is mean ± SEM; *P<0.05. **(B)** Representative fluorescence immunohistochemistry images (200x magnification) demonstrate the localization and amount of FBN1 (red) in fetal and mature renal tissue. **(C)** Quantification of normalized FBN1 area in both fetal and mature renal samples. N≥15 fluorescent images derived from N=3 samples. Shown is mean ± SEM. Quantitative polymerase chain reaction (qPCR) of *FBN1* **(D)**, *MFAP2* **(E)** and *ELN* **(F)** in human renal fetal and mature tissue. Shown is target gene/housekeeping gene (*β-actin*) ratio (AU). Shown is mean ± SEM. N≥4 qPCRs; *P<0.05.

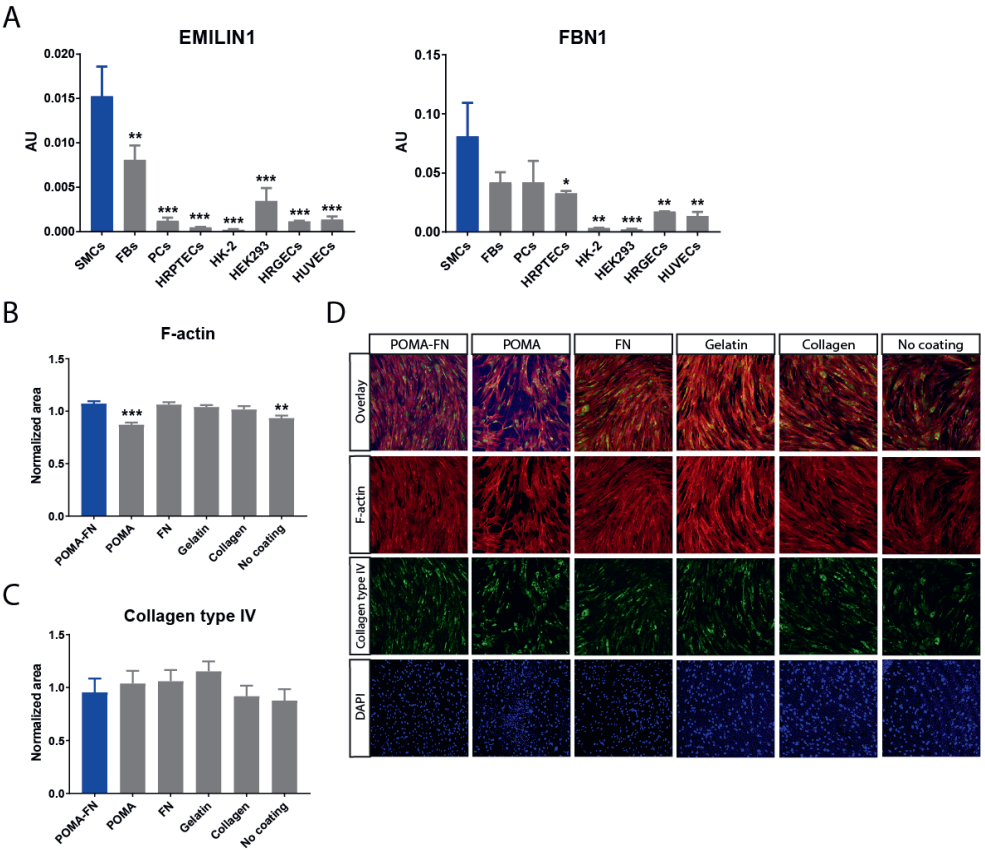

Supplemental Figure 5. (A) Quantitative polymerase chain reaction (qPCR) of *EMILIN1* (left) or *FBN1* (right) expression in the following cell types: HRPTECs, HK-2 cells, HK293 cells, HRGECs, HUVECs, PCs, SMCs and FBs. Shown are target gene/housekeeping gene (*β-actin*) ratio (AU), mean ± SEM. *P<0.05, **P<0.01, ***P<0.001; N≥5 qPCRs. Quantification of F-actin area **(B)** or collagen type IV area **(C)** of 150,000 SMCs cultured for 6 days on coverslips coated with POMA-FN, POMA, FN, gelatin or collagen or no coating. Shown is mean ± SEM; **P<0.01, ***P<0.001; N=15 fluorescent images derived from N=3 samples. **(D)** Representative immunofluorescence images (100x magnification) of 150,000 SMCs cultured for 6 days and stained for F-actin (red), collagen type IV (green) and DAPI (blue).

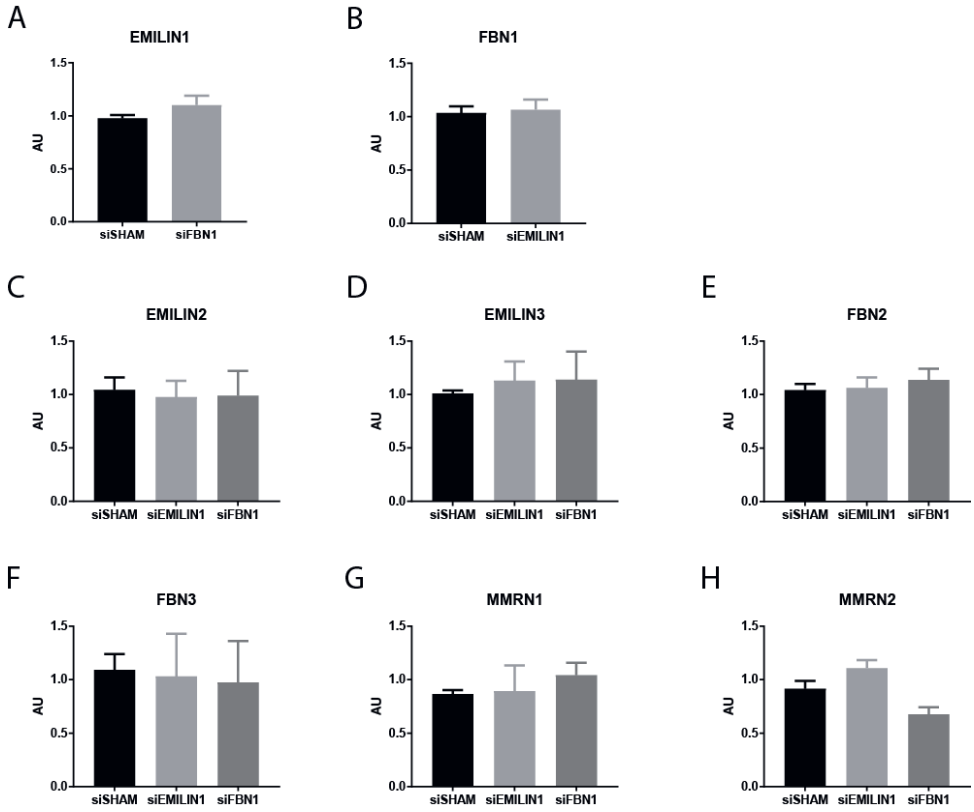

Supplemental Figure 6. Quantitative polymerase chain reaction (qPCR) of *EMILIN1* **(A)**, *FBN1* **(B)**, *EMILIN2* **(C)**, *EMILIN3* **(D)**, *FBN2* **(E)**, *FBN3* **(F)**, *MMRN1* **(G)** and *MMRN2* **(H)** expression in smooth muscle cells (SMCs) transfected with EMILIN1-targeting siRNA (siEMILIN1), FBN1-targeting siRNA (siFBN1) or non-targeting siRNA (siSHAM). Shown is target gene/housekeeping gene (*β-actin*) ratio (AU). Control values are set to 1 (not shown). Shown is mean ± SEM. N=3 qPCRs.

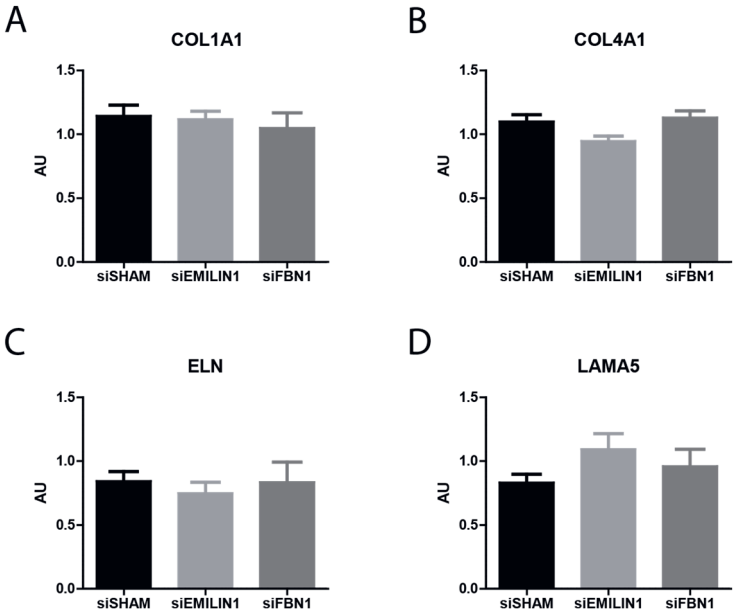

Supplemental Figure 7. Quantitative polymerase chain reaction (qPCR) of *COL1A1* **(A)**, *COL4A1* **(B)**, *ELN* **(C)** and *LAMA5* **(D)** expression in smooth muscle cells (SMCs) transfected with EMILIN1-targeting siRNA (siEMILIN1), FBN1-targeting siRNA (siFBN1) or non-targeting siRNA (siSHAM). Shown is target gene/housekeeping gene (*β-actin*) ratio (AU). Control values are set to 1 (not shown). Shown is mean ± SEM. N=5 qPCRs.

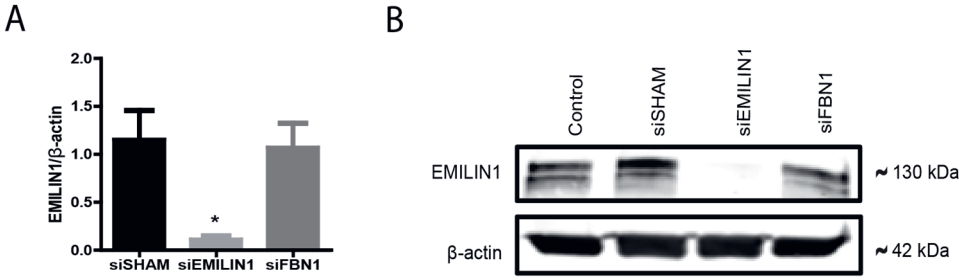

Supplemental Figure 8. (A) Western blot analysis of EMILIN1 expression in smooth muscle cells (SMCs) transfected with EMILIN1-targeting siRNA (siEMILIN1), FBN1-targeting siRNA (siFBN1) or non-targeting siRNA (siSHAM). Shown is EMILIN1/β-actin ratio. Control values are set to 1 (not shown). Shown is mean ± SEM. N=4 Western blots. *P<0.05 compared to siSHAM. **(B)** Representative Western blot of EMILIN1 and β-actin protein levels in siSHAM, siEMILIN1, siFBN1 and control SMCs.

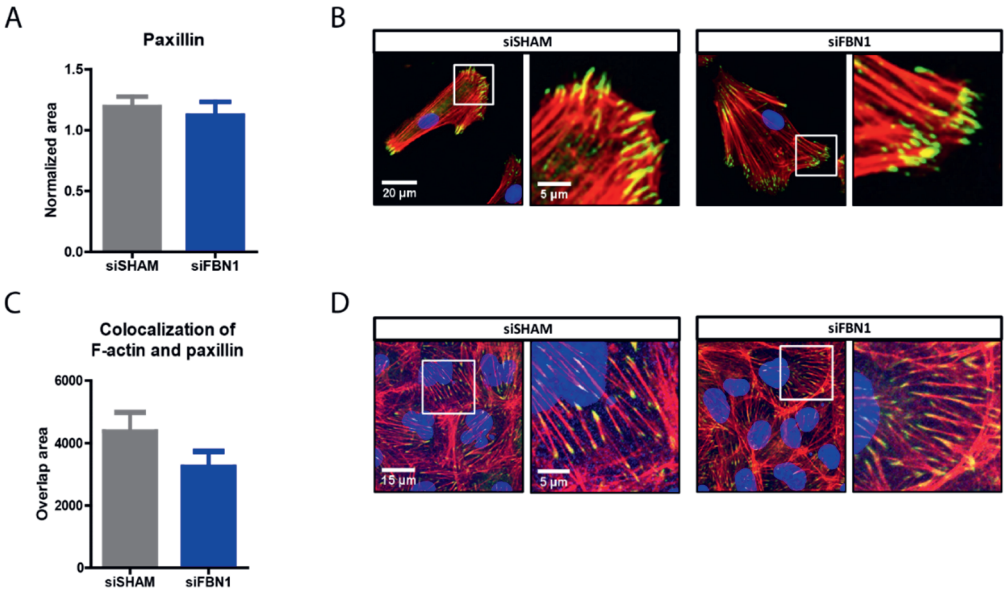

Supplemental Figure 9. (A) Quantified results showing the paxillin area in HRPTECs on siSHAM or siFBN1 ECM during initial binding to the ECM (cultured for 2 hours). Shown is mean ± SEM. N=30 fluorescent images derived from N=3 samples. **(B)** Representative immunofluorescence images (400x magnification) of HRPTECs after 2 hours of binding on siSHAM or siFBN1 ECM and stained for paxillin (green), F-actin (red) and DAPI (blue). Scale bar represents 20 µm (overview image, left) and 5 µm (zoomed-in image, right). **(C)** Colocalization of paxillin and F-actin in HK2 cells cultured to confluency on siSHAM or siFBN1 ECM. Shown is mean ± SEM. N≥15 fluorescent Z-stacks, from N≥3 samples. **(D)** Representative immunofluorescence Z-stacks (630x magnification) of HK2 cells cultured to confluency on siSHAM or sFBN1 ECM and stained for paxillin (green), F-actin (red) and DAPI (blue). Colocalization is displayed as yellow. Scale bar represents 15 µm (overview image, left) and 5 µm (zoomed-in image, right).

Supplemental Tables

Supplemental tables can be downloaded from:

https://www.sciencedirect.com/science/article/pii/S2590028519300109

Or:

Chapter 6

Extracellular matrix analysis of human renal arteries in both quiescent and active vascular state

Christian G.M. van Dijk, Laura Louzao-Martinez, Elise van Mulligen, Bart Boermans Jeroen A.A. Demmers, Thierry P.P. van den Bosch, Marie-José Goumans, Dirk J. Duncker, Marianne C. Verhaar, Caroline Cheng

International Journal of Molecular Sciences, 2020 May 30;21(11):3905

Abstract

In vascular tissue engineering strategies, the addition of vascular-specific extracellular matrix (ECM) components may better mimic the *in vivo* microenvironment and potentially enhance cell–matrix interactions and subsequent tissue growth. For this purpose, the exact composition of the human vascular ECM first needs to be fully characterized. Most research has focused on characterizing ECM components in mature vascular tissue; however, the developing fetal ECM matches the active environment required in vascular tissue engineering more closely. Consequently, we characterized the ECM protein composition of active (fetal) and quiescent (mature) renal arteries using a proteome analysis of decellularized tissue. The obtained human fetal renal artery ECM proteome dataset contains higher levels of 15 ECM proteins versus the mature renal artery ECM proteome, whereas 16 ECM proteins showed higher levels in the mature tissue compared to fetal. Elastic ECM proteins EMILIN1 and FBN1 are significantly enriched in fetal renal arteries and are mainly produced by cells of mesenchymal origin. We functionally tested the role of EMILIN1 and FBN1 by anchoring the ECM secreted by vascular smooth muscle cells (SMCs) to glass coverslips. This ECM layer was depleted from either EMILIN1 or FBN1 by using siRNA targeting of the SMCs. Cultured endothelial cells (ECs) on this modified ECM layer showed alterations on the transcriptome level of multiple pathways, especially the Rho GTPase controlled pathways. However, no significant alterations in adhesion, migration or proliferation were observed when ECs were cultured on EMILIN1- or FNB1-deficient ECM. To conclude, the proteome analysis identified unique ECM proteins involved in the embryonic development of renal arteries. Alterations in transcriptome levels of ECs cultured on EMILIN1- or FBN1-deficient ECM showed that these candidate proteins could affect the endothelial (regenerative) response.

Introduction

The human vasculature mainly consists of two different cell types that have their own specific function. Along with the endothelial cells (ECs) that actually compose the blood vessels, providing main blood barrier function, mural cells also play an important role in maintaining vascular homeostasis. From these, pericytes associate with capillaries to help maintain barrier function, whereas vascular smooth muscle cells (SMCs) are found predominantly on larger arteries for biomechanical strength and elasticity. These cells create their own dynamic microenvironment for protection and stability by synthesizing and secreting extracellular matrix (ECM) components, including constituents of the basement membrane [1,2]. This matrix microenvironment consists of many components, such as collagens, proteoglycans, and glycoproteins, and forms a reservoir for encapsulated growth factors [3,4]. Thus, ECM proteins do not only provide structural and organizational stability for the surrounding cells, they are also responsible for a wide variety of biochemical cues.

ECM remodeling is a critical step during vascular development. At the onset of angiogenesis, the basement membrane matrix is degraded to allow endothelial sprouting. As angiogenesis proceeds, the ECM is known to provide signals controlling EC migration, proliferation, survival, differentiation, shape, and invasion. Ultimately, through specific integrin-signaling pathways, the ECM controls the EC cytoskeleton to guide vascular morphogenesis towards a mature vascular network with functional lumens [5]. During this vascular response, different ECM cues are active. For example, ECs cultured on a collagen type I coating are stimulated to rearrange their cytoskeleton and cell junctions, inducing capillary morphogenesis. In contrast, culturing ECs on a laminin-1 coating inhibits this rearrangement [6]. These *in vitro* observations are in concordance with the laminin-rich basement membrane characteristics of *in vivo* mature vessels in a quiescent state [7]. This type of ECM component-driven response has also been described in (embryogenic) angiogenesis. Pro-angiogenic cues stimulate the breakdown of the vascular basement membrane (consisting mainly of laminins and collagen type IV) that exposes ECs to collagen type I, which is abundant between cells in tissues. This triggers EC proliferation and vascular sprouting, while formation of a new basement membrane during neovessel maturation brings the endothelium back into the quiescent state [5]. Mapping the differences in ECM composition during embryonic vessel development and comparing these with mature stable vessels could help to shed light on the effect of different ECM components on the regenerative capacity of vascular cells.

Applied technologies, such as vascular tissue engineering and regenerative medicine, could benefit from mimicking the vascular-specific ECM that is specifically active during development. At the moment, the regenerative cardiovascular research field uses multiple materials (synthetic and biological) to recreate functional grafts. For example, polymer

scaffolds are being used to mimic blood vessels and heart valves in combination *with ex vivo* or *in situ* tissue engineering (TE) [8,9]. For *in situ* TE in particular, achieving a balance between the biodegradability of a scaffold and how fast cells are attracted remains a significant challenge. The addition of vascular-specific ECM components to these scaffolds might better mimic the *in vivo* microenvironment and enhance cell–matrix interactions and subsequent cell survival and tissue growth. In order to create such a scaffold, the components of the human vascular ECM first need to be fully characterized.

Mass spectrometry-based approaches have been used to characterize ECM compositions of various tissues [3,10]. To unravel the vascular ECM, previous work mainly focused on mapping the ECM components in healthy, mature tissue in comparison with diseased tissue, rather than the changes in ECM during vascular development [11,12]. However, the fetal microenvironment is more dynamic and active compared to the matured ECM in order to cope with tissue morphogenesis and growth, which matches the environment needed in tissue scaffolds.

The aim of the present study was therefore to identify ECM components in vascular tissue during fetal development compared to the mature condition. By using proteomics, we created a catalogue of ECM proteins present in fetal renal arteries (in active, developmental state) and mature renal arteries (in stable, quiescent state). From this unique vascular ECM proteome, we selected two elastic components, Elastin Microfibril Interfacer 1 (EMILIN1) and fibrillin1 (FBN1), based on their abundance in the fetal renal artery, as candidates for further investigation. Both EMILIN1 and FBN1 are glycoproteins located at elastic fibers and microfibrils [13,14]. Next to structural functions, EMILIN1 is known as a ligand for integrins, connecting cells with the surrounding ECM [15,16]. Many cell types need this integrin–EMILIN1 interaction for adhesion, migration, and proliferation [17–20]. Deficiency of either EMILIN1 or FBN1 in mice leads to aortic valve disease and vascular abnormalities, respectively [21,22]. Mutations in the FBN1 gene cause Marfan syndrome, a genetic connective tissue disorder characterized by aortic aneurysms and dissections [23]. Furthermore, both EMILIN1 and FBN1 seem to play an important role in maintaining vascular homeostasis [24]. Therefore, we investigated the role of both ECM components in vascular regeneration.

Materials and Methods

Human tissue

Healthy, age- and sex-matched human fetal and mature renal artery tissue was used for ECM analysis by liquid chromatography tandem mass spectrometry (LC-MS/MS). Residual fetal renal arteries were obtained from the department of Molecular Cell Biology at the Leiden UMC.

Residual mature renal arteries were obtained from the Erasmus MC biobank for rest material used for diagnostics. All samples were fresh-frozen and stored at –80 °C prior to use. Sampling and handling and use of tissues were approved by the medical ethical committees of the Erasmus MC and Leiden UMC (project code 108017 (26-4-2019)).

Sample preparation

To enrich the ECM protein content, renal arteries were decellularized by several detergents. First, 1% SDS was used to decellularize the tissue for 12 h. Next, 1% Triton X-100 was used for 1 h. The samples were washed for 2 h with PBS to remove the detergents. All steps were performed at room temperature and under constant rotation. Frozen sections of decellularized and non-decellularized tissue were used for hematoxylin and eosin (HE) staining to confirm complete decellularization of the renal arteries while preserving the ECM architecture. Decellularized renal arteries were homogenized in lysis buffer (10 mM Tris (pH 7.4), 100 mM NaCl, 0.1% SDS, 0.5% sodium deoxycholate, 1% Triton X-100, 1 mM EGTA, 1 mM EDTA, 10% Glycerol, 1 mM NaF, 1 mM sodium orthovanadate, and a protease inhibitor cocktail (Roche, Mannheim, Germany)) using an Ultra-Turrax (IKA, Staufen, Germany). Lysates were placed on ice for 30 min and cell debris was pelleted via centrifugation (10 min, 1000× *g*, 4 °C). A pool of either 2 mature or 3 fetal renal arteries was considered as 1 sample for sufficient protein yield (Supplemental Table 6). Tissue lysates were separated by SDS-PAGE on an equally loaded pre-cast 4%–12% linear gradient gel (NuPAGE Bis-Tris Mini gels, Life Technologies, Bleiswijk, the Netherlands) and visualized with Coomassie Blue (Figure S1A). LC-MS/MS analysis was performed in triplicate.

LC-MS/MS analysis

SDS-PAGE-separated samples were prepared according previously used protocols for LC-MS/MS analysis by the Proteomics Centre of the Erasmus MC [24]. In short, proteins lanes were cut out of the gel, reduced with dithiothreitol, alkylated with iodoacetamide, and digested with trypsin, as described previously [25]. Supernatants were stored in glass vials at –20 °C until further measurements. An 1100 series capillary LC system (Agilent Technologies, Amstelveen, the Netherlands) was used for nanoflow LC-MS/MS coupled to an LTQ-Orbitrap XL mass spectrometer (Thermo, Landsmeer, the Netherlands) operating in positive mode and equipped with a nanospray source, as previously described [26]. Samples were trapped on a 1.5 cm × 100 µm in-house packed ReproSil C18 reversed phase column (Dr Maisch GmbH, Ammerbuch-Entringen, Germany) at a flow rate of 8 µL/min. Sequentially, samples were separated on a 15 cm × 50 µm in-house packed ReproSil C18 reversed phase column (Dr Maisch GmbH) by adding a linear gradient from 0%–80% solvent B in solvent A, where A

consisted of 0.1 % formic acid and B of 80% (*v*/*v*) acetonitrile and 0.1 % formic acid. Flow rate was set at 200 nL/min, and elution took place over 70 min. The eluent was sprayed by a nanospray device directly into the ESI source of the LTQ ion trap mass spectrometer. Mass spectra were acquired in continuum mode, and peptide fragmentation was performed in data-dependent mode. MS/MS spectra were extracted out of raw data files and were analyzed by using MaxQuant software, as previously described [27].

MS data analysis

First, analysis was done with proteins which were present in at least 2 fetal or 2 mature sample groups. Second, data from the Human Matrisome project [3,10] was used to filter ECM core and associated proteins from the generated datasets. Label-free quantification (LFQ) intensity was used to further specify the abundance of ECM components in the fetal and mature renal artery. Differences in the abundance of ECM components between fetal and mature tissue was showed as a percentage of the total ECM protein signal.

Immunohistochemistry

Protein validation was performed by immunohistochemistry on 7 µm thick frozen sections of non-decellularized tissue. Frozen sections were used for a standard hematoxylin and eosin staining and for a protein-specific staining using fluorescent secondary antibodies. Acetone-fixed sections were blocked with 1% BSA in PBS for 1 h. Polyclonal primary antibodies against EMILIN1 and FBN1 were diluted in 1% BSA/PBS (1:100 and 1:200, respectively; both Sigma Aldrich, Zwijndrecht, the Netherlands) and incubated for 1 h at room temperature. Sections were washed 3 times in PBS/T solution and incubated with Alexa Fluor 488 donkey anti-goat IgG (1:100; Life Technologies) and αSMA-Cy3 (1:500; Sigma) diluted in 1% BSA/PBS for 1 h at room temperature. After 3 times washing with PBS/T solution, sections were incubated with DAPI for 5 min, washed with PBS, and mounted. Stained sections were imaged using fluorescent microscopy (Olympus IX53, Olympus Leiderdorp, the Netherlands) and ImageJ (version 1.47) to analyze EMILIN1, FBN1, and αSMA positive area.

Cell culture

Human umbilical vein endothelial cells (HUVECs; Lonza, Basel, Switzerland) and HUVECs transfected with lentiviral green fluorescent protein (GFP) were cultured on gelatin-coated plates in endothelial growth medium (EBM-2 basal medium supplemented with EGM-2 bullit kit; Lonza) in 5% CO_2 at 37 °C. Human aorta smooth muscle cells (SMCs; Lonza) were cultured on gelatin-coated plates in smooth muscle growth medium (SMBM basal medium supplemented with SMGM bullet kit; Lonza) in 5% CO_2 at 37 °C. Experiments were performed

with cells between passage 3 and 6. Knockdown of the ECM components FBN1 and EMILIN1 were performed by their specific ON-TARGETplus SMARTpool siRNAs (Dharmacon, Horizon Discovery, Cambridge, United Kingdom) and DharmaFECT-1 (Dharmacon), with a final concentration of 200 nM. ON-TARGETplus Non-targeting pool (siSHAM; Dharmacon) was used as a negative control (Supplemental Table 7).

POMA slides for tight anchoring of ECM

To anchor secreted ECM proteins, coverslips were treated following the protocol as described by Labit *et al*. [28]. Briefly, contaminants on coverslips (ø18 mm; VWR, Amsterdam, the Netherlands) were removed by serially washing with acetone, methanol/water, and chloroform in combination with sonication. Coverslips were oxidized using piranha solution consisting of sulfuric acid (99.999%; Sigma) and hydrogen peroxide (35% wt. in H2O, Merck Millipore, Amsterdam, the Netherlands) in a ratio of 7:3, followed by salinization with a 2% (3-Aminopropyl)triethoxysilane (APTES, 99%; Sigma) solution in 95% ethanol. A poly(maleic anhydride-alt-1-octadecene) (POMA; Sigma) layer was applied by spin-coating at 4000 rpm for 30 s, using a 0.16% solution of POMA in tetrahydrofuran (Sigma). Polymerized coverslips were sterilized with UV-light and used immediately or stored in the dark at room temperature. Prior to cell culture, POMA-treated coverslips were coated with 50 µg/mL fibronectin (Roche) in PBS for 1 h at 37 °C, creating POMA-FN coverslips. SMCs were harvested and seeded onto POMA-FN at 150,000 cells per well. After transfection with siRNA, cells were cultured for six days in order to produce sufficient ECM. Decellularization was achieved by mild agitation in combination with warm 20 mM ammonium hydroxide. Light microscopy was used to confirm whether decellularization was complete. Coverslips were incubated with DNase (Qiagen, Venlo, the Netherlands) for 15 min at room temperature to remove DNA traces. Finally, decellularized ECM layers were washed in ultrapure water and PBS to remove cellular residues.

Immunocytochemistry

Prior to fixation, both control and decellularized ECM layers were washed in PBS twice. Samples were fixated with 4% paraformaldehyde (PFA), permeabilized with 0.1% Triton X-100, and blocked with 1% BSA in PBS. Samples were incubated for 1 h with collagen IV antibody (1:50, Millipore, Amsterdam, the Netherlands), EMILIN1 antibody (1:100; Sigma), or FBN1 antibody (1:200; Sigma). Samples were incubated with Alexa Fluor 488 donkey anti-goat IgG (1:100, Life Technologies) or Alexa Fluor 488 goat anti-rabbit IgG (1:100, Life Technologies), and Alexa Fluor 596 donkey anti-goat IgG (1:100; Life Technologies) or rhodamine-phalloidin (1:40; Life Technologies) in the dark for 1 h. Nuclei were counterstained

with DAPI (1:5000) for 15 min. Washing with 0.05% Tween in PBS occurred after every antibody incubation. Samples were mounted on object slides using Mowiol. Imaging was performed using a Leica SP8X confocal microscope (Leica Microsystems, Amsterdam, the Netherlands) and LAS X software. Z-stacks were made to capture all fluorescent signal (5 a 6 Z-stacks/coverslip). Projections of the z-stack images were analyzed with ImageJ to calculate the area of EMILIN1, FBN1, collagen type IV, and F-actin.

Quantitative PCR

RNA was isolated at indicated time points using the ISOLATE II RNA kit (Bioline, GC biotech, Waddinxveen, the Netherlands) and cDNA was made using the SensiFAST cDNA synthesis kit (Bioline) according to the manufacturer's protocol. qPCR was performed using FastStart Universal SYBR Green Master (Roche) according the following qPCR program: 8.5′ 95 °C, 38 cycles (15" 95 °C; 45" 60 °C) 1′ 95 °C, 1′ 65 °C, 62 cycles (10" 65 °C + 0.5 °C). Expression levels are relative to housekeeping gene β-actin. Primer sequences are listed in Supplemental Table 8.

Endothelial cell assays

HUVECs were reseeded with 35,000 cells per coverslips or indicated otherwise and cultured for various times on SMC-derived non-targeted, EMILIN1- or FBN1-deficient ECM coverslips in a 12-well plate. ECs were cultured in full EGM-2 medium or indicated otherwise, in 5% CO_2 at 37 °C.

RNA sequencing

RNA was isolated from HUVECs using the ISOLATE II RNA kit after 24 h culturing. RNA sequencing was done as previously described [29]. Briefly, sequencing libraries were made from poly-adenylated RNA using the Rapid Directional RNA-Seq Kit (NEXTflex, Perkin Elmer, Austin, Texas, United States) and sequenced on Illumina NextSeq500 to produce single-end 75-base long reads (Utrecht Sequencing Facility). Reads were aligned to the human reference genome GRCh37 using STAR version2.4.2a. Read groups were added to the BAM files with Picard's AddOrReplaceReadGroups (v1.98). The BAM files were sorted with Sambamba v0.4.5, and transcript abundances were quantified with HTSeq-count version 0.6.1p117 using the union mode. Subsequently, reads per kilobase of transcript per million reads sequenced were calculated with edgeR's rpkm() function. RNA-sequencing results were analyzed using Qiagen's Ingenuity Pathway Analysis (IPA). IPA was used to identify pathways that were altered by differentially expressed genes. P-values were calculated by IPA based on a right-tailed Fisher's Exact Test.

Proliferation assay

HUVECs were fixed with 4% PFA after 24, 48, and 72 h of culturing. Proliferation was assessed by staining with a Ki67 antibody (1:200; ThermoScientific, Landsmeer, the Netherlands) using the above-described immunocytochemistry protocol. Coverslips were imaged using a Leica DM 5500B microscope and images were quantified for $Ki67^+$ and $DAPI^+$ cells using ImageJ.

PicoGreen assay

HUVECs were isolated from the ECM coverslips after 24, 48, and 72 h culturing for dsDNA measurements using PicoGreen, according to the manufacturer's protocol (ThermoFisher, Landsmeer, the Netherlands).

PrestoBlue assay

Viability was measured using PrestoBlue Cell Viability Reagent (ThermoScientific) in the medium of HUVECs cultured on siRNA-treated ECM for 24, 48, and 72 h, according to the manufacturer's protocol.

Adhesion assay

After 2 and 24 h, HUVECs were fixed with 4% PFA. Adhesion was assessed by staining with a paxillin antibody (1:100; Abcam, Cambridge, United Kingdom) using the above-described immunocytochemistry protocol. Projection of the z-stack images were analyzed using ImageJ to calculate the area of paxillin, F-actin (phalloidin), and the co-localization of this focal adhesion protein with the cytoskeleton of the cells.

Migration assay

HUVECs-GFP (to visualize the cells) were seeded with 25,000 cells per coverslip and live-imaged overnight using a Leica SP8X confocal at 37 °C and humid atmosphere containing 5% CO_2. Single cell migration was imaged every 15 min at 10 positions in each condition, ending after 24 h of culturing. Obtained videos were analyzed using ImageJ Manual Tracking and Chemotaxis Tool.

RhoA GTPase activity assay

HUVECs were seeded with 200,000 cells per coverslip and starved overnight in bare EBM-2 medium and stimulated to activate RhoA for 5 min in full EGM-2 medium 24 h after seeding. Cells were lysed for GTPase activity using the G-Lisa RhoA Activation Assay Colorimetric Kit (Cytoskeleton, Denver, United States) according to the manufacturer's protocol.

Statistical analysis

All results were analyzed and presented using GraphPad Prism 6. All statistical comparisons were made by performing a Student's T-test or a one-way analysis of variance (ANOVA) followed by a Tukey's multiple comparison test. Error bars were visualized as standard error of the mean. *p*-values < 0.05 were considered statistically significant.

Results

Enrichment of ECM proteins in vascular tissue prior to LC-MS/MS

Healthy fetal and mature renal arteries were decellularized to enrich for ECM components (Figure 1A). The white appearance of the tissue after decellularization indicated loss of cells (Figure 1B). HE-staining confirmed complete decellularization, visualized by the absence of nuclei while maintaining the ECM architecture (Figure 1C,D). Proteins detected by LC-MS/MS in at least two pooled groups were used for further analysis (Supplemental Figure 1A,B). Detected fetal and mature proteins were categorized by cross-referencing with the Human Matrisome Project [3,10].

Of all proteins detected, 39% of the fetal and 35% of the mature samples were composed of matrisome components. The majority forms part of the matrisome core proteins, subdivided by glycoproteins, collagens, and proteoglycans. A quarter of the matrisome proteins detected were allocated to matrisome-associated proteins, such as ECM-affiliated proteins, ECM regulators, and growth factors. There was only a subtle difference between the number of detected proteins of fetal and mature human arteries (Table 1).

Matrisome protein expression differs between human fetal and mature renal arteries

Although there was almost no difference in the total number of different ECM proteins detected, relative protein quantification revealed a difference in protein abundance between fetal and mature samples. Mature renal arteries contained more proteoglycan signal compared to fetal tissue: 11.8% of the mature signal consisted of proteoglycans, compared to only 1.8% in the fetal selection. Furthermore, there was a dominance of collagens and glycoproteins in both the fetal and mature ECM over other matrisome components (Supplemental Figure 1C).

Seventy-nine proteins were identified in the fetal and 87 proteins were identified in the mature renal artery ECM pool, from which the majority formed an overlapping core. From this core, the most abundant signal came from collagens and glycoproteins, with many comprising ≥1% of the total signal (Supplemental Figure 2A). Fold-change of the LFQ intensity showed significant differences between fetal and mature ECM proteins (Figure S2B).

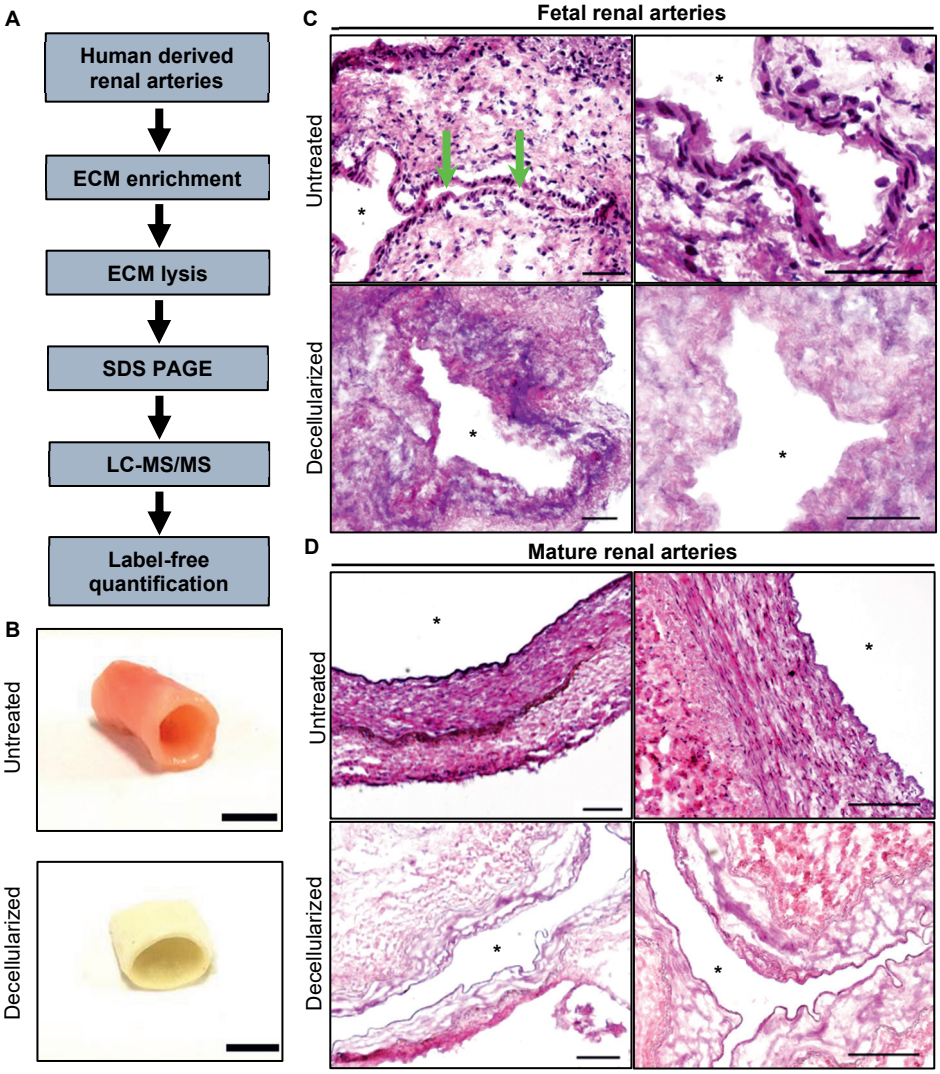

Figure 1. Proteomic workflow for extracellular matrix (ECM)-enriched vascular samples. (A) After decellularization of the human tissue, ECM-enriched samples were lysed and separated with SDS-PAGE prior to LC-MS/MS with label-free quantification. **(B)** Mature human renal arteries, before and after decellularization. Scale bar represents 1 cm. Hematoxylin and eosin staining for validation of decellularization procedure in **(C)** fetal human renal artery and (**D**) mature human renal artery. Black arrows indicate lumen. Open lumen is indicated with an asterix. Representative of 3 experiments. Scale bar represents 200 µm.

Table 1. Number of genes detected in the fetal and mature renal artery group, divided into matrisome (ECM) proteins and non-matrisome proteins. Within the group of matrisome proteins, different compartments are recognized as defined by the matrisome project: http://web.mit.edu/hyneslab/matrisome/. Core matrisome proteins comprise the building blocks of the ECM and include collagens, glycoproteins, and proteoglycans. In addition, matrisome-associated proteins are comprised of ECM binding proteins, which include ECM-affiliated proteins, ECM regulators, and secreted factors. Proteins were present in at least 2 out of 3 pools in both fetal and mature pooled samples.

Proteins detected	Fetal Renal Artery	Mature renal Artery
Total number of proteins detected	206	246
Matrisome proteins	79 (38.3% of total)	87 (35.4% of total)
Non-matrisome proteins	127 (61.7% of total)	159 (64.6% of total)
Matrisome core proteins	58 (73.4% of matrisome)	63 (73.3% of matrisome)
Glycoproteins	38 (65.6% of core)	39 (61.9% of core)
Collagens	14 (24.1% of core)	15 (23.8% of core)
Proteoglycans	6 (10.3% of core)	9 (14.3% of core)
Matrisome-associated proteins	21 (26.6% of matrisome)	23 (26.7% of matrisome)
ECM-affiliated	9 (42.9% of associated)	9 (39.1% of associated)
ECM regulators	7 (33.3% of associated)	10 (43.5% of associated)
Secreted factors	5 (23.8% of associated)	4 (17.4% of associated)

Sixteen proteins were significantly enriched in the mature renal artery ECM compared to the fetal ECM (Figure 2A), including collagen type IV (Figure 2B). Different subtypes of laminins were also significantly more abundant in the mature renal arteries compared to fetal renal arteries (Figure 2B). The proteoglycans HSPG2 and BGN were more abundant in the mature renal arteries as well. The growth factor TGFβ1, which is part of an important signaling pathway involved in both vascular development and vascular quiescence [30], was present in both fetal and mature renal arteries and represented approximately 1% of the total signal. The detection of proteoglycans and growth factors verifies that the used decellularization protocol is gentle enough to preserve low-abundance ECM proteins in the tissue. The full list of all detected fetal renal artery ECM proteins and their relative abundance to total protein composition compared to the mature tissue is available in Supplemental Table 1.

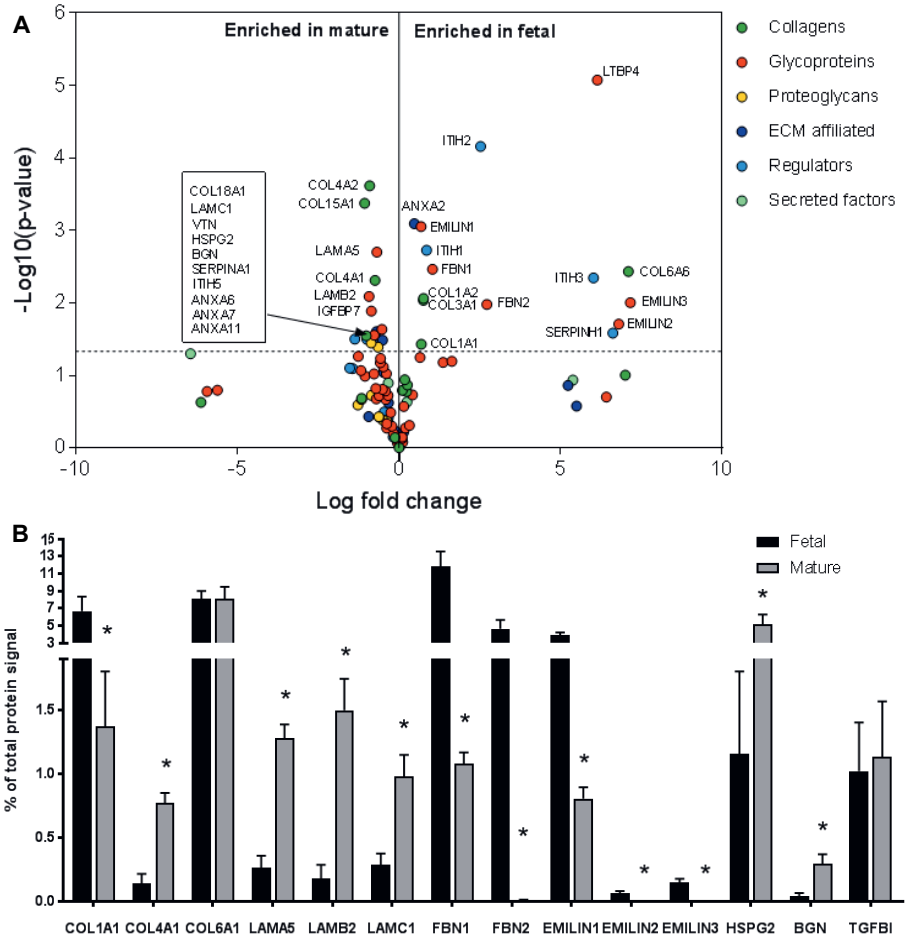

Figure 2. (A) Volcano plot represents the protein distribution of fetal and mature extracellular matrix (ECM) proteome fold-changes (x-axis, log fold-change) and significance (y-axis, −log P-value). Each circle represents a matrisome protein and each color a specific subset of the matrisome proteins. The horizontal line indicates P<0.05. **(B)** Bar graphs shows examples of ECM proteins identified with LC-MS/MS. Each protein signal is the percentage of the total protein signal. Data are shown as mean ± SEM, N=3, *P<0.05.

Glycoproteins EMILIN1 and FBN1 are enriched in fetal renal arteries and are produced by cells of the mesenchymal lineage

Elastic components EMILIN1 and FBN1 were significantly more abundant in the fetal renal arteries: 5% and 12% of the total signal were EMILIN1 and FBN1 respectively, compared to only 1% in the mature tissue (Figures 2A,B and Supplemental Figure 2B). Other EMILIN and FBN members had a higher fold-change in fetal renal arteries compared to mature (Figure S2B) but were less present in the tissue (Figures 2B and Supplemental Figure 2A). The high protein levels of EMILIN1 and FBN1 in fetal renal arteries hint towards an important role in vascular development and these were therefore selected for follow-up experiments. Candidate proteins EMILIN1 and FBN1 were verified on cross-sections of human fetal and mature renal arteries. Immunohistochemistry indeed showed the presence of the target proteins with dominance in the fetal tissue (Figure 3A–D).

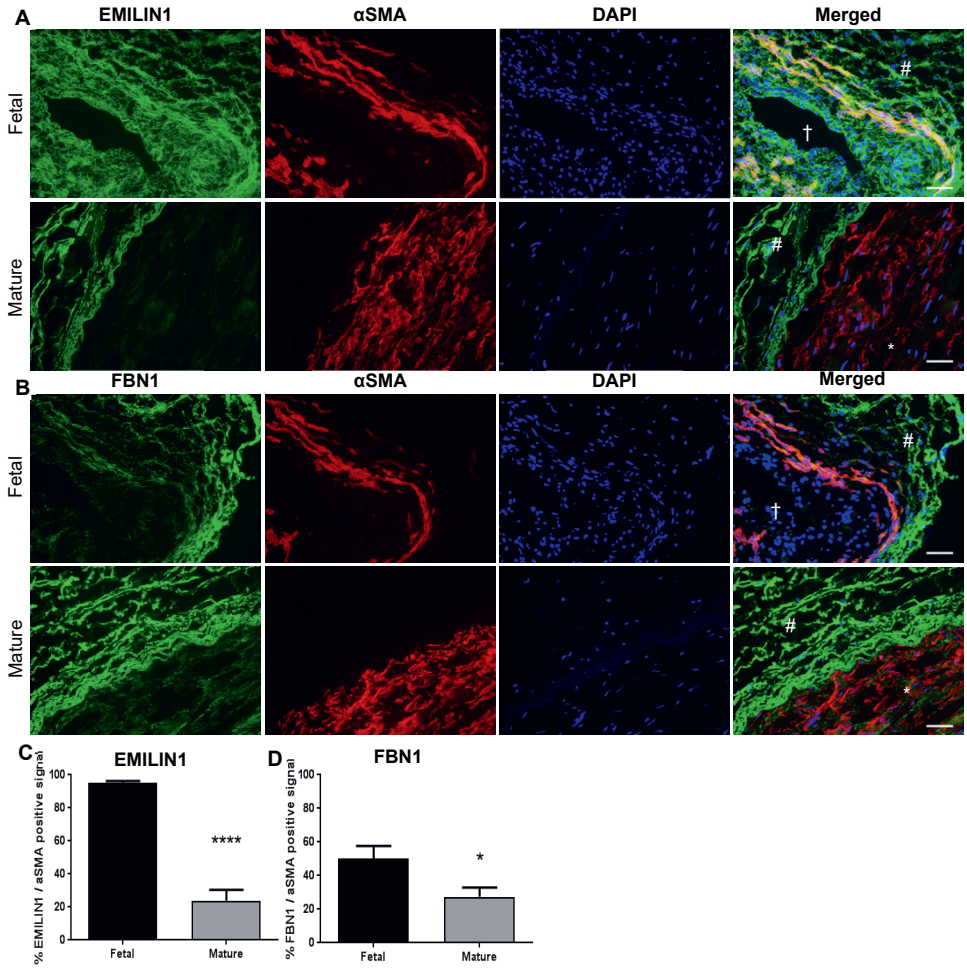

◄**Figure 3. (A)** Representative images demonstrate the distribution of EMILIN1 co-stained with smooth muscle actin (αSMA) in fetal and mature human renal arteries. Co-localization of αSMA and EMILIN1 in yellow. **(B)** Representative images demonstrate the distribution of FBN1 co-stained with αSMA in fetal and mature human renal arteries. Co-localization of αSMA and FBN1 in yellow. Scale bar represents 50 µm. Open lumen is indicated with a cross, tunica media layer is indicated with an asterix, and the tunica adventitia layer is indicated with a pound sign. **(C)** Quantification of EMILIN1 and αSMA positive signal in percentages in fetal and mature renal arteries. **(D)** Quantification of FBN1 and αSMA positive signal in percentages in fetal and mature renal arteries. Data are shown as mean ± SEM, N=4–5 fluorescent images for EMILIN1 and FBN1 respectively, in fetal samples. N=11–15 fluorescent images for EMILIN1 and FBN1 respectively, in mature samples. *P<0.05, ****P<0.0001 (Student's *t*-test).

EMILIN1 was present in all layers of the fetal renal artery, while in the mature renal artery, it is almost exclusively present in the adventitia. FBN1 was exclusively present in the adventitia of both fetal and mature renal arteries. EMILIN1 and FBN1 co-stained with alpha smooth muscle actin (αSMA) showed more overlap between this mesenchymal marker and the target proteins in the fetal renal artery (Figure 3A–D). Quantification of EMILIN1/FBN1 with αSMA demonstrated that almost 100% and 50% of all αSMA-positive cells were also positive for EMILIN1 and FNB1 respectively, in the fetal vascular tissues. This percentage of overlap declined in mature tissues, demonstrating that the candidate proteins were indeed expressed in fetal tissue by αSMA-positive cells. mRNA expression analysis confirmed a higher expression of *EMILIN1* and *FBN1* in SMCs and pericytes compared to ECs (Figure 4A). This suggests that cells from the mesenchymal lineage produce more EMILIN1 and FBN1 compared to ECs and thereby contribute to the ECM composition of the renal arteries.

ECM secreted by SMCs can be altered by depleting specific ECM components using siRNA

Elastic proteins EMILIN1 and FBN1 were abundantly present in fetal renal arteries, suggesting a pivotal role in vascular development. To study the effect of EMILIN1 and FBN1 on the ECM–ECs interaction, a pipeline for a loss of function assay on the ECM level was developed. SMCs *in vitro*, which produce large amounts of ECM containing EMILIN1 and FBN1, were grown on POMA-FN-modified glass coverslips and were treated with siRNA targeted against EMILIN1 or FBN1. After 6 days, the SMCs were removed, leaving only a coating of SMC-secreted ECM behind that is depleted from either EMILIN1 or FBN1. Anchorage of secreted ECM on coverslips coated with POMA-FN reached an optimum after 6 days of culture, compared with generally used coating methods (Supplemental Figure 3A–C). QPCR and immunocytochemistry analyses confirmed the knockdown of EMILIN1 or FBN1 in SMCs after 6 days of culturing (Figure 4B–E). After decellularization, the EMILIN1 amount in the anchored ECM was significantly lower compared to siSHAM-treated and untreated controls (Figure 4C,E). Secreted collagen type IV was stained as a reference in the decellularized conditions

and showed no difference in the amount of ECM anchored between control and siRNA conditions (Supplemental Figure 3D). Knockdown of FBN1 in SMCs showed similar results (Supplemental Figure 4A–C). Thus, using this unique approach, the expression and secretion of EMILIN1 and FBN1 by SMCs can be altered, creating an EMILIN1- or FBN1-depleted ECM layer that can be used in functional assays to study EC behavior.

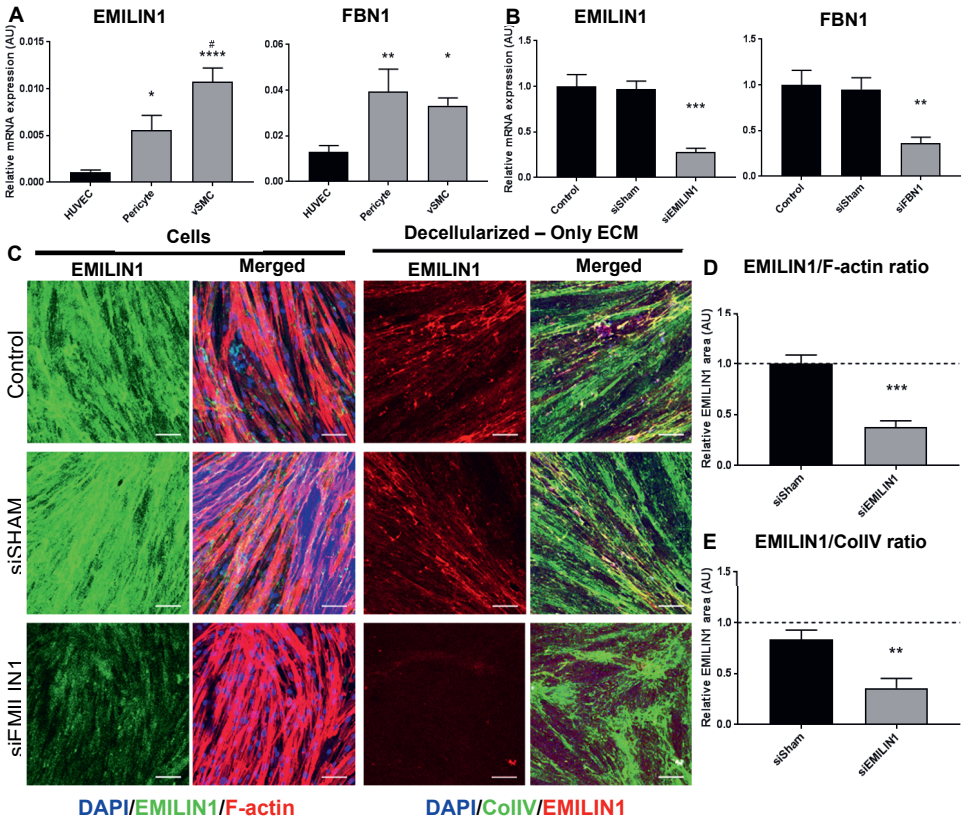

Figure 4. (**A**) qPCR analysis of EMILIN1 and FBN1 in different cell types of the vasculature, human umbilical vein endothelial cells (HUVECs; as endothelium source), pericytes and vascular smooth muscle cells (vSMC; hereafter referred as SMC). Data are shown as mean ± SEM corrected for β-actin (housekeeping gene). N≤10, *P<0.05, **P<0.01, ****P<0.0001 compared to HUVECs, #P<0.05 compared to pericytes (One-way analysis of variance (ANOVA), Tukey's post hoc test). (**B**) qPCR validation of EMILIN1 and FBN1 knockdown in SMC 6 days after siRNA transfection. Data are shown as mean ± SEM, N=7-9 for EMILIN1 and FBN1, respectively. **P<0.01, ***P<0.001 compared to siSHAM (Student's t-test). (**C**) Representative z-stacks of EMILIN1 on SMC cultured for 6 days after siRNA transfection and after decellularization. Scale bar represents 100 µm. (**D**) Quantification of EMILIN1 signal-corrected for the amount of F-actin in siRNA-treated SMC. Data are shown as mean ± SEM, N=5. (**E**) Quantification of EMILIN1 signal-corrected for the amount of collagen type IV present on SMC-derived ECM coverslips.

◄Data are shown as mean ± SEM, N=7, **P<0.01, ***P<0.0001 (Student's t-test). Non-treated SMC are set to one (dotted lines).

Loss of EMILIN1 or FBN1 in the ECM alters transcriptome of ECs that interacted with the depleted ECM

HUVECs were seeded on EMILIN1- or FBN1-depleted ECM for 24 h, after which the cells were lysed for RNA isolation and processed for RNA-sequencing. In total, 481 and 474 genes were found to be differentially expressed (P<0.05; Supplemental Figure 5A, Supplemental Tables 2, 3) for EMILIN1- and FBN1-depleted ECM respectively, compared to HUVECs seeded on ECM derived from SMC transfected with non-targeting siRNA (control condition). Multiple pathways were identified to be altered in HUVECs cultured on EMILIN1- or FBN1-deficient ECM (Supplemental Tables 4, 5). A cut-off for the z-score (>2 or <−2) was used to determine the most profound changes. This conical approach revealed the "regulation of actin-based motility by Rho" and "signaling by Rho family GTPases" pathways as a common theme that was decreased in ECs cultured on EMILIN1- or FBN1-deficient ECM, respectively (Supplemental Figure 5B).

Rho GTPase signaling coordinates cell proliferation by regulating cytoskeleton adaptations [31]. Therefore, *in vitro* functional assays on cell proliferation and viability were performed to investigate these altered pathways in ECs cultured on EMILIN1- or FBN1-deficient ECM. These assays showed that there was no significant effect of EMILIN1 or FBN1 depletion from the ECM on both EC proliferation and viability (Figure 5A–C).

Paxillin is a focal adhesion adaptor protein known to be critical for cytoskeleton rearrangements, especially for cell adhesion during migration [32]. According to the pathway analysis, "paxillin signaling" was decreased in HUVECs cultured on EMILIN1-deficient ECM (Supplemental Table 7). To further evaluate this, an adhesion assay was performed by staining for paxillin in HUVECs after 2 and 24 h of culturing on ECM-altered slides. There was no significant difference in paxillin area in ECs cultured on EMILIN1- or FBN1-depleted ECM (Figures 5D and Supplemental Figure 6A,B). Furthermore, these ECs did not show any difference on the actin cytoskeleton organization level, although according to the RNA-sequencing data, the pathway "regulation of actin-based motility by Rho" was altered (Figures 5D, Supplemental Figure 5B and 6A,B).

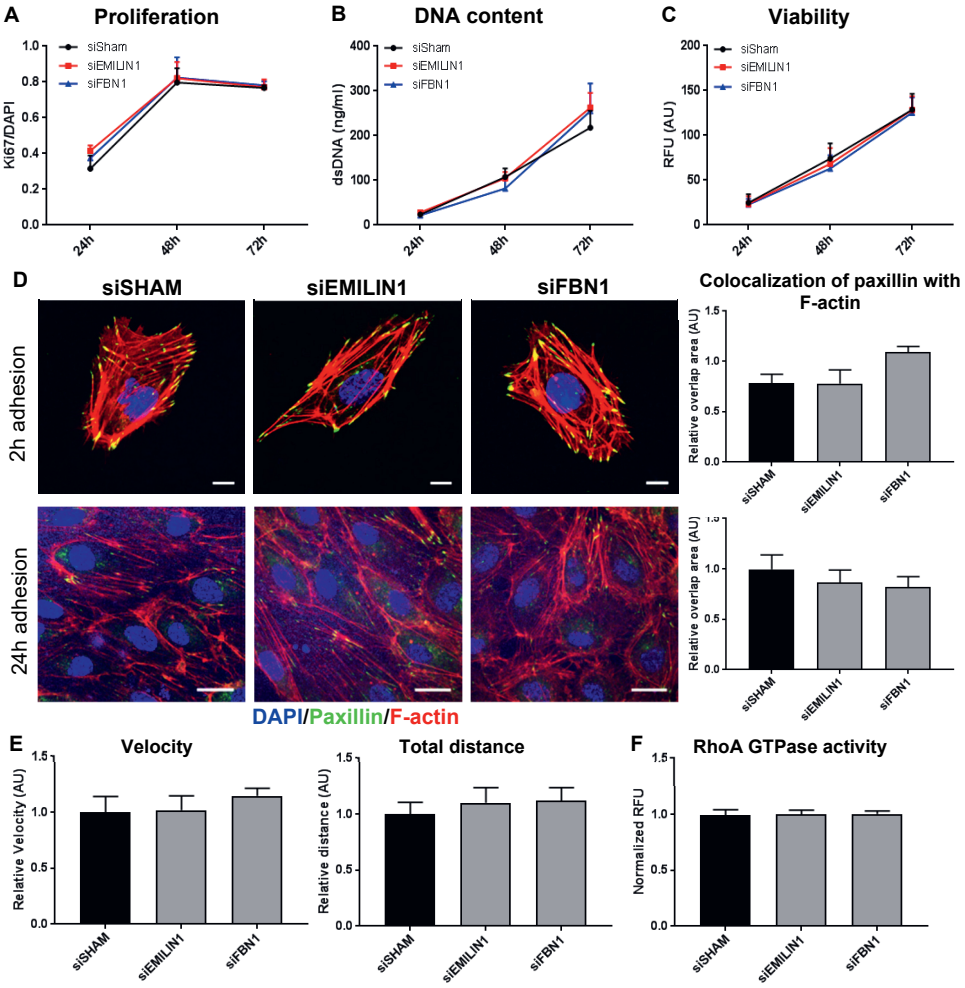

Figure 5. (**A**) Ki67-positive cells/DAPI ratio was used as measure for human umbilical vein endothelial cell (HUVEC) proliferation after 24, 48, and 72 h of culturing on siRNA-treated extracellular matrix (ECM). Shown are mean ± SEM, N=20 fluorescent images per assay, N=3 assays. (**B**) DNA content measurements with the PicoGreen assay was used as measure for HUVEC proliferation after 24, 48, and 72 h of culturing on siRNA-treated ECM. Data are shown as mean ± SEM, N=3. (**C**) HUVEC viability was measured with PrestoBlue after 24, 48, and 72 h of culturing on siRNA-treated ECM. Data are shown as mean ± SEM, N=3. (**D**) Representative z-stacks of HUVECs cultured on siRNA-treated ECM for 2 h (not confluent) to show initial binding to the ECM and 24 h (confluent) to show paxillin and F-actin changes. Scale bar represents 20 µm. Co-localization of paxillin and F-actin were quantified in both assays. Data are shown as mean ± SEM, N=10 fluorescent images per assay, N=4 assays. (**E**) Live cell migration assay results showing the velocity and total distance of HUVECs cultured on siRNA-treated ECM. Data are shown as mean ± SEM, N≈10 HUVECs per image, N=10 images per assay, N=6 assays. (**F**) RhoA activation measurements using the G-LISA RhoA GTPase activity assay in HUVECs cultured 24 h on siRNA-treated ECM. Data are shown as mean ± SEM, N=4.

Next, a cell migration assay was performed to investigate the motility capabilities of HUVECs cultured on EMILIN1- or FBN1-deficient ECM. Overnight migration and tracking of individual cells could not identify a significant effect of EMILIN1 and FBN1 depletion on the migratory capabilities of HUVECs (Figures 5E and Supplemental Figure 6C). Also, a RhoA GTPase activation assay showed no differences between HUVECs cultured on EMILIN- or FBN1-deficient ECM compared to control ECM (Figure 5F).

These findings indicate that depletion of EMILIN1 or FBN1 from the ECM only has a clear effect on the transcriptome response of ECs in the current setting, but does not influence their functional behavior with respect to adhesion, migration and proliferation.

Discussion

In this study, we characterized the ECM proteins present in fetal and mature renal arteries and focused on the impact of two elastic proteins on ECs: EMILIN1 and FBN1. Our major findings are: (1) Enriching the ECM in human vascular tissue by decellularization aids in the detection of ECM proteins using LC-MS/MS. (2) The ECM protein expression differs between fetal (growth-induced) and mature (quiescent) vascular tissue. (3) Next to 13 other proteins, elastic ECM proteins EMILIN1 and FBN1 are significantly enriched in fetal renal arteries and are mainly produced by cells of mesenchymal origin. (4) SMCs-secreted ECM can be altered and tightly anchored to POMA-FN coverslips, creating a platform to study EC–matrix interactions. (5) EMILIN1- and FBN1-deficient ECM provoked alterations in HUVECs via multiple pathways, especially Rho GTPase-controlled pathways. (6) However, EMILIN1 and FBN1 ECM components only play a minor role in EC behavior.

Our proteomic approach to unravel the differences between the fetal and mature vascular ECM has the potential to find interesting proteins that can influence EC behavior. Decellularization assured enrichment of ECM proteins before proteomic analysis. Not all cellular components were removed, but it guaranteed an enriched ECM fraction of 38% and 35% in fetal and mature conditions, respectively. Protein lysates of whole tissue contain only 5% ECM proteins of the total amount of proteins, confirming the necessity to enrich for ECM proteins. Detergents for decellularization can be very stringent, however fragile components of the ECM (proteoglycans, secreted factors) were still detectable.

Many ECM proteins were identified by cross-referencing with the Human Matrisome Project [3,10] and differences in protein abundance were observed between active (fetal) and quiescent (mature) vascular ECM. Overall, elastic proteins, such as members from the EMILIN/multimerin and fibrillin families, were more abundant in the fetal ECM compared to the mature ECM, while the reverse is observed for the laminin family. Although it was already known that the mature basement membrane is rich in laminin [5], the distribution of multiple

isoforms of laminin in the active and quiescent vascular ECM is now demonstrated by our dataset. Furthermore, this observation is in line with the hypothesis that a quiescent, more mature phenotype arises in ECs when cultured on a laminin coating compared to a collagen coating [6].

Multiple members of the EMILIN/multimerin and fibrillin families were significantly more abundant in the fetal renal artery ECM compared to the mature ECM, namely: EMILIN1, -2 and -3 and fibrillin1 and -2. Fibrillin2 is needed for the initial assembly of the aortic matrix during development and overlaps with fibrillin1 expression [33]. These findings indicates an important developmental role for fibrillin2. More proteins in our vascular ECM catalogue could represent interesting targets for further research, especially ECM interaction proteins such as members from the MAGP and LTBP families. Mutations in Microfibril-Associated Protein 5 (MFAP5), a member of the MGAP family, are linked to aortic aneurysms and dissections [34]. In concordance, double knockout of both MFAP2 and -5 in mice results in aortic dilation [35]. These studies indicate that MFAPs may contribute to maintaining large vessel integrity. Latent Transforming Growth Factor Beta Binding Proteins (LTBPs) attach to both fibrillins and latency-associated protein of TGFβ (LAP), thereby forming a TGFβ reservoir within the ECM [36,37]. LTBP (1–4)-null mice exhibit severe phenotypes, including defects in bone, lung, and cardiovascular development [38]. These are all examples of promising ECM proteins detected in this study that are known to be important during vascular development. These may be interesting candidates to improve the bioactivity of scaffolds in vascular grafts. Moreover, we also detected the majority of these elastic ECM proteins in a proteome screen of fetal versus mature renal tissue [24]. This suggests that elastic components of the ECM are not only important in vascular development, but also in renal development, and presumably in general embryonic development.

Due to their abundant presence in our vascular ECM catalogue compared to other family members, elastic proteins EMILIN1 and FBN1 were selected in this study to further elucidate their impact on EC fate. The role of EMILIN1 is extensively studied in EMILIN1-deficient mice, which display aortic valve malformations and hypertension [21,38]. EMILIN1 plays a pivotal role in mice blood vessel development and elastogenesis [39,40]. Most of the diseases accompanied by EMILIN1 deficiency are driven by TGFβ. In the vasculature, EMILIN1 functions as an antagonist in the processing steps of TGFβ and thereby regulates vascular tone and blood pressure [41–43]. EMILIN1 has multiple domains which exhibit different functions in the vasculature. The EMI domain is linked to hypertension and TGFβ processing [41], while adhesive functions of EMILIN1 are related to its gC1q domain. The gCq1 domain regulates cell migration and proliferation via a specific interaction with α4β1 integrin

[18,20,44]. Integrin α9β1 shows a similar interaction with the gC1q domain and plays a role in lymphatic EC migration and proliferation [18,19].

Similar to EMILIN1, FBN1 can mediate the adhesion and migration of several cell types, including ECs [45]. Endothelium dysfunction is an important contributor to Marfan syndrome, caused by mutations in the FBN1 gene. A heterozygous FBN1 mutation in mice accelerates vascular aging and eventually leads to aortic manifestations, resembling those of Marfan syndrome [22].

The data presented in this study focus on the role of EMILIN1 and FBN1 on ECs adhesion, migration, and proliferation. Although RNA-sequencing pointed towards a role of EMILIN1 and FBN1 in Rho-mediated cytoskeleton rearrangements, which is required for migration and proliferation, functional assays revealed that ECs are not altered in their capacity to divide and migrate when either EMILIN1 or FBN1 is depleted from the ECM. This is in contrast with the existing literature on the effect of EMILIN1 and FBN1 on proliferation and migration [24]. This discrepancy may be attributed to differences in study design and are potential limitations in this study. We cultured our cells on a complex ECM network depleted from either EMILIN1 or FBN1 from the beginning, rather than using protein fragments of EMILIN1 or FBN1 as coating, which is a strategy often used in other EMILIN1 or FBN1 *in vitro* studies [17,19,46,47]. A possible combination of both EMILIN1- and FBN1-deficient ECM may demonstrate a synergistic effect. Furthermore, although both candidate proteins are prominently present in the fetal ECM, they are potentially less effective compared to family members or other candidate proteins such as the LTBP and MFAP family. Further studies should explore the (synergistic) effects of other interesting proteins in vascular development. The environment created by our protocol resembles the complex ECM *in vivo* more closely, however this approach might not be ideal to pick up small behavioral changes. Conversely, our recent study shows that renal cells cultured using the exact same 2D ECM coating approach do respond to depletion of EMILIN1 by reducing their adhesive strength and subsequently adopting a more migratory phenotype [24]. It is therefore possible that the lack of response as observed in this study, is cell type-specific, and that ECs are perhaps less reliant on both candidate proteins compared to renal cells for adapting their cell behavior to ECM [24]. It is possible that the HUVECs used in our study express an integrin profile that is less sensitive to changes in EMILIN1 or FBN1 level. HUVECs have been used as the golden standard in vascular research since the late 1970s [48] and are considered to be a robust cell model with a high proliferation rate. Using a different and more sensitive type of EC instead, for example human microvascular endothelial cells (HMVECs) or endothelial colony-forming cells (ECFCs), might prove to be more suitable to test EC behavior. For example, in line with this hypothesis, it has been shown that EMILIN1 can regulate the proliferation of HMVECs and acts as a guiding

molecule during their migration by interacting with α9 integrins actively expressed by these cells [19].

In conclusion, the addition of EMILIN1 or FBN1 to scaffolds for cell seeding of HUVECs most likely will not have an effect on their adhesive, migratory and proliferative behavior. Nevertheless, EMILIN1 or FBN1 might still be an interesting candidate for implementing in scaffolds containing other (vascular) cell types, as studies have clearly identified these elastic proteins as regulators of cell adhesion and migration. The presented ECM protein catalogue could help in identifying valuable target proteins for the next phase of vascular tissue engineering.

References

1. Stratman AN, Malotte KM, Mahan RD, Davis MJ, Davis GE: Pericyte recruitment during vasculogenic tube assembly stimulates endothelial basement membrane matrix formation. *Blood* **2009**, 114:5091–5101.
2. Stratman AN, Davis GE: Endothelial cell-pericyte interactions stimulate basement membrane matrix assembly, influence on vascular tube remodeling, maturation, and stabilization. *Microsc Microanal* **2012**, 18**:**68-80002E.
3. Naba A, Clauser KR, Hoersch S, Liu H, Carr SA, Hynes RO: The matrisome, in silico definition and in vivo characterization by proteomics of normal and tumor extracellular matrices. *Mol Cell Proteom* **2012**, 11:M111.014647
4. Hynes RO, Naba A: Overview of the matrisome--an inventory of extracellular matrix constituents and functions. *Cold Spring Harb Perspect Biol* **2012**, 4:a004903.
5. Davis GE, Senger DR: Endothelial extracellular matrix, biosynthesis, remodeling, and functions during vascular morphogenesis and neovessel stabilization. *Circ Res* **2005**, 97:1093–1107.
6. Liu Y, Senger DR: Matrix-specific activation of Src and Rho initiates capillary morphogenesis of endothelial cells. *FASEB J* **2004**, 18:457–468.
7. Hallmann R, Horn N, Selg M, Wendler O, Pausch F, Sorokin LM: Expression and function of laminins in the embryonic and mature vasculature. *Physiol Rev* **2005**, 85:979–1000.
8. Thottappillil N, Nair PD: Scaffolds in vascular regeneration, current status. *Vasc Health Risk Manag* **2015**, 11:79–91.
9. Bouten CVC, Smits A, Baaijens FPT: Can We Grow Valves Inside the Heart? Perspective on Material-based In Situ Heart Valve Tissue Engineering. *Front Cardiovasc Med* **2018**, 5:54.
10. Naba A, Clauser KR, Ding H, Whittaker CA, Carr SA, Hynes RO: The extracellular matrix, Tools and insights for the “omics” era. *Matrix Biol* **2016**, 49:10–24.
11. Barallobre-Barreiro J, Oklu R, Lynch M, Fava M, Baig F, Yin X, Barwari T, Potier DN, Albadawi H, Jahangiri M, Porter KE, Watkins MT, Misra S, Stoughton J, Mayr M: Extracellular matrix remodelling in response to venous hypertension, proteomics of human varicose veins. *Cardiovasc Res* **2016**, 110:419–430.
12. Mustafa DA, Dekker LJ, Stingl C, Kremer A, Stoop M, Sillevis Smitt PA, Kros JM, Luider TM: A proteome comparison between physiological angiogenesis and angiogenesis in glioblastoma. *Mol Cell Proteom* **2012**, 11:M111.008466.
13. Bressan GM, Daga-Gordini D, Colombatti A, Castellani I, Marigo V, Volpin D: Emilin, a component of elastic fibers preferentially located at the elastin-microfibrils interface. *J Cell Biol* **1993**, 121:201–212.
14. Kielty CM, Sherratt MJ, Shuttleworth CA: Elastic fibres. *J Cell Sci* **2002**, 115:2817–2828.
15. Colombatti A, Spessotto P, Doliana R, Mongiat M, Bressan GM, Esposito G, The EMILIN/Multimerin family. *Front Immunol* **2011**, 2:93.
16. Verdone G, Corazza A, Colebrooke SA, Cicero D, Eliseo T, Boyd J, Doliana R, Fogolari F, Viglino P, Colombatti A, Campbell ID, Esposito G: NMR-based homology model for the solution structure of the C-terminal globular domain of EMILIN1. *J Biomol NMR* **2009**, 43:79–96.
17. Verdone G, Doliana R, Corazza A, Colebrooke SA, Spessotto P, Bot S, Bucciotti F, Capuano A, Silvestri A, Viglino P, Campbell ID, Colombatti A, Esposito G: The solution structure of EMILIN1 globular C1q domain reveals a disordered insertion necessary for interaction with the alpha4beta1 integrin. *J Biol Chem* **2008**, 283:18947–18956.
18. Danussi C, Petrucco A, Wassermann B, Pivetta E, Modica TM, Del Bel Belluz L, Colombatti A, Spessotto P: EMILIN1-alpha4/alpha9 integrin interaction inhibits dermal fibroblast and keratinocyte proliferation. *J Cell Bio.* **2011**, 195:131–145.
19. Danussi C, Del Bel Belluz L, Pivetta E, Modica TM, Muro A, Wassermann B, Doliana R, Sabatelli P, Colombatti A, Spessotto P: EMILIN1/alpha9beta1 integrin interaction is crucial in lymphatic valve formation and maintenance. *Mol Cell Biol* **2013**, 33:4381–4394.

20. Spessotto P, Cervi M, Mucignat MT, Mungiguerra G, Sartoretto I, Doliana R, Colombatti A: Beta 1 Integrin-dependent cell adhesion to EMILIN-1 is mediated by the gC1q domain. *J Biol Chem* **2003**, 278:6160–6167.
21. Angel PM, Narmoneva DA, Sewell-Loftin MK, Munjal C, Dupuis L, Landis BJ, Jegga A, Kern CB, Merryman WD, Baldwin HS, Bressan GM, Hinton RB: Proteomic Alterations Associated with Biomechanical Dysfunction are Early Processes in the Emilin1 Deficient Mouse Model of Aortic Valve Disease. *Ann Biomed Eng* **2017**, 45:2548–2562.
22. Mariko B, Pezet M, Escoubet B, Bouillot S, Andrieu JP, Starcher B, Quaglino D, Jacob MP, Huber P, Ramirez F, Faury G: Fibrillin-1 genetic deficiency leads to pathological ageing of arteries in mice. *J Pathol* **2011**, 224:33–44.
23. Sakai LY, Keene DR, Renard M, De Backer J: FBN1, The disease-causing gene for Marfan syndrome and other genetic disorders. *Gene* **2016**, 591:279–291.
24. Louzao-Martinez L, van Dijk CGM, Xu YJ, Korn A, Bekker NJ, Brouwhuis R, Nicese MN, Demmers JAA, Goumans MJTH, Masereeuw R, Duncker DJ, Verhaar MC, Cheng C: A proteome comparison between human fetal and mature renal extracellular matrix identifies EMILIN1 as a regulator of renal epithelial cell adhesion. *Matrix Biol Plus* **2019**, 4:100011.
25. Wilm M, Shevchenko A, Houthaeve T, Breit S, Schweigerer L, Fotsis T, Mann M: Femtomole sequencing of proteins from polyacrylamide gels by nano-electrospray mass spectrometry. *Nature* **1996**, 379:466–469.
26. Sap KA, Bezstarosti K, Dekkers DHW, Voets O, Demmers JAA: Quantitative Proteomics Reveals Extensive Changes in the Ubiquitinome after Perturbation of the Proteasome by Targeted dsRNA-Mediated Subunit Knockdown in Drosophila. *J Proteome Res* **2017**, 16:2848–2862.
27. Cox J, Mann M: MaxQuant enables high peptide identification rates, individualized p.p.b.-range mass accuracies and proteome-wide protein quantification. *Nat Biotechnol* **2008**, 26:1367–1372.
28. Labit H, Goldar A, Guilbaud G, Douarche C, Hyrien O, Marheineke K: A simple and optimized method of producing silanized surfaces for FISH and replication mapping on combed DNA fibers. *Biotechniques* **2008**, 45:649–648.
29. Brandt MM, Meddens CA, Louzao-Martinez L, van den Dungen NAM, Lansu NR, Nieuwenhuis EES, Duncker DJ, Verhaar MC, Joles JA, Mokry M, Cheng C: Chromatin Conformation Links Distal Target Genes to CKD Loci. *J Am Soc Nephrol* **2018**, 29:462–476.
30. Goumans MJ, Liu Z, ten Dijke P: TGF-beta signaling in vascular biology and dysfunction. *Cell Res* **2009**, 19:116–127.
31. Provenzano PP, Keely PJ: Mechanical signaling through the cytoskeleton regulates cell proliferation by coordinated focal adhesion and Rho GTPase signaling. *J Cell Sci* **2011**, 124:1195–1205.
32. Hu YL, Lu S, Szeto KW, Sun J, Wang Y, Lasheras JC, Chien S: FAK and paxillin dynamics at focal adhesions in the protrusions of migrating cells. *Sci Rep* **2014**, 4:6024.
33. Carta L, Pereira L, Arteaga-Solis E, Lee-Arteaga SY, Lenart B, Starcher B, Merkel CA, Sukoyan M, Kerkis A, Hazeki N, Keene DR, Sakai LY, Ramirez F: Fibrillins 1 and 2 perform partially overlapping functions during aortic development. *J Biol Chem* **2006**, 281:8016–8023.
34. Barbier M, Gross MS, Aubart M, Hanna N, Kessler K, Guo DC, Tosolini L, Ho-Tin-Noe B, Regalado E, Varret M, Abifadel M, Milleron O, Odent S, Dupuis-Girod S, Faivre L, Edouard T, Dulac Y, Busa T, Gouya L, Milewicz DM, Jondeau G, Boileau C: MFAP5 loss-of-function mutations underscore the involvement of matrix alteration in the pathogenesis of familial thoracic aortic aneurysms and dissections. *Am J Hum Genet* **2014**, 95:736–743.
35. Combs MD, Knutsen RH, Broekelmann TJ, Toennies HM, Brett TJ Miller CA, Kober DL, Craft CS, Atkinson JJ, Shipley JM, Trask BC, Mecham RP: Microfibril-associated glycoprotein 2 (MAGP2) loss of function has pleiotropic effects in vivo. *J Biol Chem* **2013**, 288:28869–28880.
36. Nakajima Y, Miyazono K, Kato M, Takase M, Yamagishi T, Nakamura H: Extracellular fibrillar structure of latent TGF beta binding protein-1, role in TGF beta-dependent endothelial-

mesenchymal transformation during endocardial cushion tissue formation in mouse embryonic heart. *J Cell Biol* **1997**, 136:193–204.

37. Rifkin DB, Rifkin WJ, Zilberberg L: LTBPs in biology and medicine, LTBP diseases. *Matrix Biol* **2018**, 71:90–99.
38. Litteri G, Carnevale D, D'Urso A, Cifelli G, Braghetta P, Damato A, Bizzotto D, Landolfi A, Ros FD, Sabatelli P, Facchinello N, Maffei A, Volpin D, Colombatti A, Bressan GM, Lembo G: Vascular smooth muscle Emilin-1 is a regulator of arteriolar myogenic response and blood pressure. *Arter Thromb Vasc Biol* **2012**, 32:2178–2184.
39. Braghetta P, Ferrari A, de Gemmis P, Zanetti M, Volpin D, Bonaldo P, Bressan GM: Expression of the EMILIN-1 gene during mouse development. *Matrix Biol* **2002**, 21:603–609.
40. Zanetti M, Braghetta P, Sabatelli P, Mura I, Doliana R, Colombatti A, Volpin D, Bonaldo P, Bressan GM: EMILIN-1 deficiency induces elastogenesis and vascular cell defects. *Mol Cell Biol* **2004**, 24:638–650.
41. Zacchigna L, Vecchione C, Notte A, Cordenonsi M, Dupont S, Maretto S, Cifelli G, Ferrari A, Maffei A, Fabbro C, Braghetta P, Marino G, Selvetella G, Aretini A, Colonnese C, Bettarini U, Russo G, Soligo S, Adorno M, Bonaldo P, Volpin D, Piccolo, Lembo G, Bressan GM: Emilin1 links TGF-beta maturation to blood pressure homeostasis. *Cell* **2006**, 124:929–942.
42. Raman M, Cobb MH: TGF-beta regulation by Emilin1, new links in the etiology of hypertension. *Cell* **2006**, 124:893–895.
43. Carnevale D, Facchinello N, Iodice D, Bizzotto D, Perrotta M, De Stefani D, Pallante F, Carnevale L, Ricciardi F, Cifelli G, Da Ros F, Casaburo M, Fardella S, Bonaldo P, Innocenzi G, Rizzuto R, Braghetta P, Lembo G, Bressan GM: Loss of EMILIN-1 enhances arteriolar myogenic tone through TGF-beta (transforming growth factor-beta)-dependent transactivation of EGFR (epidermal growth factor receptor) and is relevant for hypertension in mice and humans. *Arter Thromb Vasc Biol* **2018**, 38:2484–2497.
44. Spessotto P, Bulla R, Danussi C, Radillo O, Cervi M, Monami G, Bossi F, Tedesco F, Doliana R, Colombatti A: EMILIN1 represents a major stromal element determining human trophoblast invasion of the uterine wall. *J Cell Sci* **2006**, 119:4574–4584.
45. Mariko B, Ghandour Z, Raveaud S, Quentin M, Usson Y, Verdetti J, Huber P, Kielty C, Faury G: Microfibrils and fibrillin-1 induce integrin-mediated signaling, proliferation and migration in human endothelial cells. *Am J Physiol Cell Physiol* **2010**, 299:C977–C987.
46. Cheng A, Cain SA, Tian P, Baldwin AK, Uppanan P, Kielty CM, Kimber SJ: Recombinant extracellular matrix protein fragments support human embryonic stem cell chondrogenesis. *Tissue Eng Part A* **2018**, 24:968–978.
47. Hajian H, Wise SG, Bax DV, Kondyurin A, Waterhouse A, Dunn LL, Kielty CM, Yu Y, Weiss AS, Bilek MM, Bannon PG, Ng MKC: Immobilisation of a fibrillin-1 fragment enhances the biocompatibility of PTFE. *Colloids Surf B Biointerfaces* **2014**, 116:544–552.
48. Sacks T, Moldow CF, Craddock PR, Bowers TK, Jacob HS: Oxygen radicals mediate endothelial cell damage by complement-stimulated granulocytes. An in vitro model of immune vascular damage. *J Clin Invest* **1978**, 61:1161–1167.

Supplemental Data

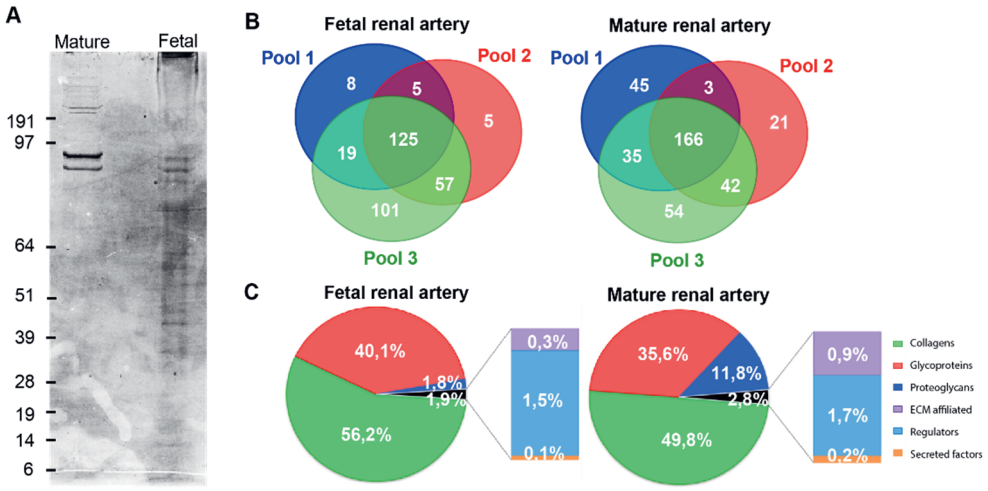

Supplemental Figure 1. (A) Extracellular matrix (ECM) lysates from human fetal and mature renal arteries were separated by SDS-PAGE and stained with Coomassie Blue prior to LC-MS/MS analysis. Shown is a representative blot of 3 experiments containing pooled renal arteries samples (fetal or mature). **(B)** Venn diagrams showing the total amount and overlap of proteins identified in the three pools of either fetal and mature samples by LC-MS/MS. Proteins identified in at least 2 pools samples were used for further analysis. **(C)** Pie charts showing the distribution of the six matrisome classes in percentages of the LFQ intensity compared to LFQ intensity of the total matrisome present in fetal and mature renal arteries.

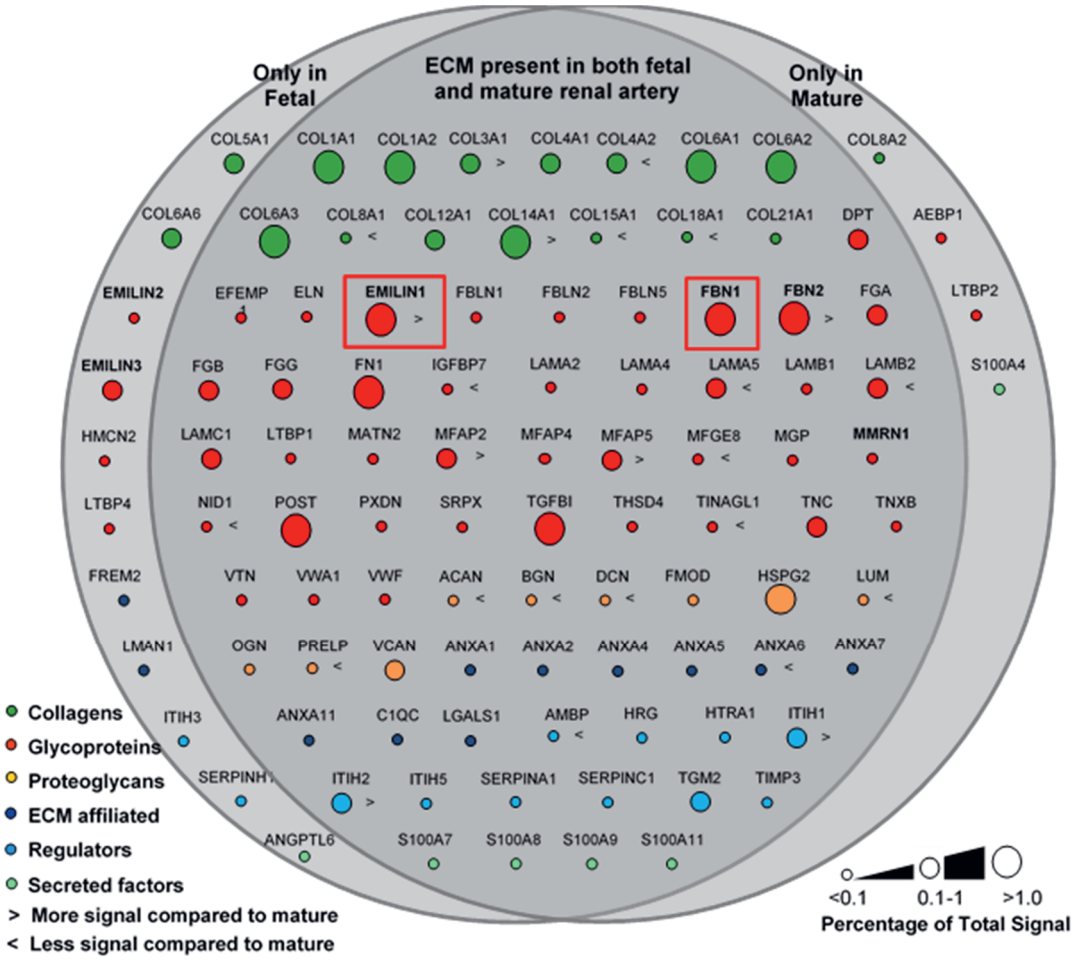

Supplemental Figure 2. (**A**) Euler-diagram visualizing the overlap and differences between the human fetal and mature renal artery proteome. Each node represents an ECM protein labeled with the gene name. Node size represents protein abundance in percentages of the total protein signal. Proteins of interest EMILIN1 and FBN1 are highlighted in bold and with a red box, their family members highlighted in bold. Shown are the means of all pooled samples (N=3).

B

Protein ID	Log FC	P-value
Glycoproteins		
EMILIN3	4,15	0,010
EMILIN2	3,77	0,020
FBN2	3,57	0,011
MFAP2	3,15	0,064
LTBP4	3,15	0,000
HMCN2	2,36	0,199
MFAP5	2,19	0,066
PXDN	1,93	0,057
THSD4	1,18	0,186
FBN1	1,03	0,003
MMRN1	1,01	0,490
ELN	0,91	0,503
EMILIN1	0,69	0,001
POSTN	0,17	0,269
VWF	0,12	0,535
FGA	0,02	0,631
TGFBI	-0,04	0,858
FBLN5	-0,07	0,782
TNXB	-0,14	0,533
FGG	-0,31	0,190
FGB	-0,36	0,165
FN1	-0,46	0,077
LAMC1	-0,57	0,023
TNC	-0,63	0,215
LAMA2	-0,68	0,467
MATN2	-0,71	0,834
LAMA5	-0,77	0,002
LAMA4	-0,83	0,746
LAMB1	-0,91	0,715
LAMB2	-1,12	0,008
LTBP1	-1,17	0,327
SRPX	-1,20	0,211
EFEMP1	-1,31	0,059
FBLN2	-1,39	0,095
FBLN1	-1,42	0,156
VWA1	-1,44	0,095
VTN	-1,68	0,028
MFAP4	-1,76	0,103
AEBP1	-1,85	0,161
DPT	-1,86	0,191
NID1	-1,96	0,067
IGFBP7	-1,97	0,013
LTBP2	-2,06	0,167
MGP	-2,47	0,152
MFGE8	-2,91	0,055
TINAGL1	-3,19	0,086

Protein ID	Log FC	P-value
Collagens		
COL6A6	4,09	0,004
COL5A1	3,91	0,099
COL3A1	1,94	0,009
COL1A2	0,78	0,009
COL1A1	0,69	0,037
COL14A1	0,28	0,136
COL12A1	0,21	0,168
COL6A3	0,19	0,115
COL6A2	0,10	0,162
COL6A1	0,01	0,995
COL21A1	-0,09	0,724
COL15A1	-1,97	0,000
COL4A1	-2,01	0,005
COL8A2	-2,14	0,237
COL4A2	-2,23	0,000
COL8A1	-2,78	0,208
COL18A1	-3,25	0,028
Proteoglycans		
OGN	-1,28	0,417
ACAN	-1,69	0,188
BGN	-1,95	0,036
DCN	-2,05	0,257
PRELP	-2,83	0,216
Secreted Factors		
ANGPTL6	1,71	0,116
S100A7	0,90	0,959
S100A8	0,25	0,233
S100A11	-1,07	0,128
S100A9	-1,30	0,194
S100A4	-3,38	0,050

Protein ID	Log FC	P-value
ECM Affliated		
FREM2	1,70	0,267
LMAN1	1,60	0,138
ANXA2	0,48	0,001
ANXA5	-0,12	0,599
ANXA1	-0,49	0,091
LGALS1	-0,97	0,614
C1QC	-1,20	0,371
ANXA4	-1,22	0,240
ANXA11	-1,48	0,038
ANXA6	-1,71	0,033
ANXA7	-2,18	0,025
LUM	-0,24	0,417
VCAN	-0,34	0,374
HSPG2	-0,83	0,041
FMOD	-0,91	0,379
ECM Regulators		
SERPINH1	3,59	0,026
ITIH2	3,26	0,000
ITIH3	3,01	0,005
ITIH1	0,88	0,002
HRG	-0,22	0,391
TIMP3	-0,33	0,320
TGM2	-0,60	0,088
SERPINC1	-0,90	0,711
ITIH5	-2,49	0,032
SERPINA1	-2,53	0,032
HTRA1	-2,84	0,081
AMBP	-3,26	0,080

Supplemental Figure 2 Continued. (**B**) Heat map of fetal vs mature fold change. Fold changes were calculated by the LFQ intensity percentages in fetal compared to mature renal artery. Both core and associated matrisome proteins are included in the heat map. Proteins of interest EMILIN1 and FBN1 are highlighted in bold and with a red box, their family members highlighted in bold. Sample size N=3. Student t-test was used for statistical analysis.

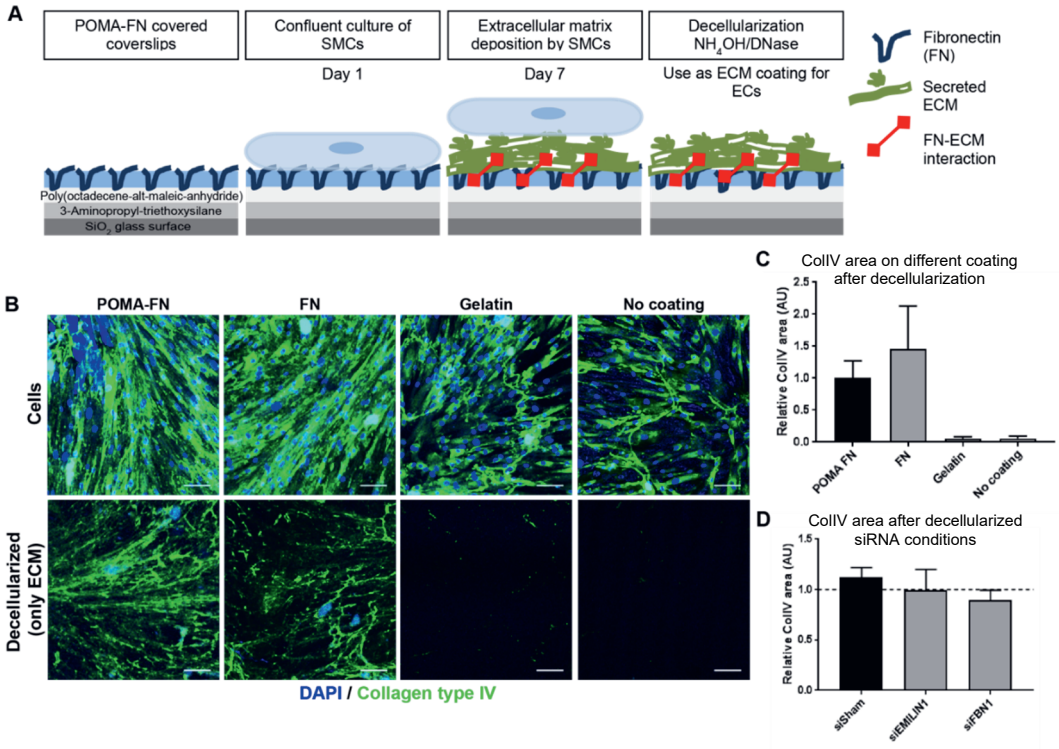

Supplemental Figure 3. (**A**) Timeline for the production of smooth muscle cell (SMC) derived extracellular matrix (ECM) on poly(octadecene-alt-maleic) anhydride-fibronectin (POMA-FN) treated coverslips. First, coverslips were oxidized using piranha solution to link silane to the aminosilane (APTES) group. POMA binds to APTES that can covalently bond fibronectin (FN). Over time, SMCs deposit ECM, which covalently bonds to FN, anchoring the secreted ECM. Ammoniumhydroxide (NH_4OH) and DNase remove all traces of the SMCs, leaving only a cell-derived ECM coating attached to glass coverslips that can be used for functional assays. (**B**) Representative images of SMCs cultured 6 days on coverslips with a coating of POMA-FN, FN, gelatin or without a coating. All cells are positively stained for collagen type IV. After decellularization, deposited collagen type IV remained anchored only on POMA-FN and FN treated coverslips. Scale bar represents 100 µm. (**C**) Quantification of collagen type IV area deposited by SMC on coverslips with different coatings (POMA-FN, FN, gelatin or no coating). Shown is mean ± SEM, N=4-5. (**D**) Quantification of collagen type IV area deposited by SMC treated by different siRNA (siSHAM, siEMILIN1, siFBN1). Shown is mean ± SEM, N=5-7. Non-treated SMCs are set to one (dotted line).

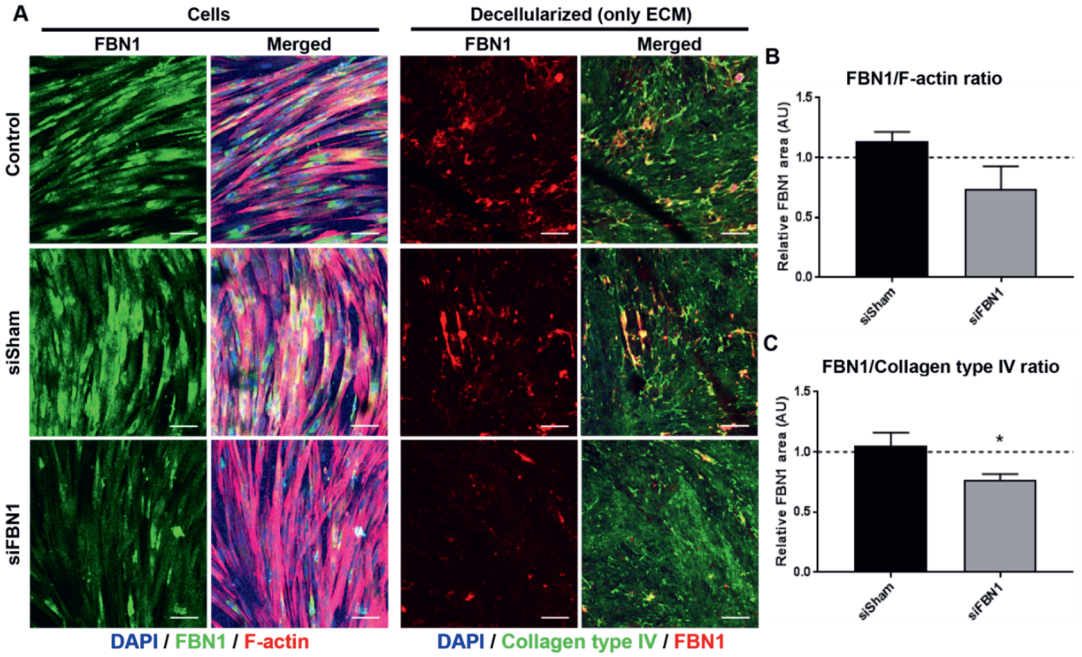

Supplemental Figure 4. (**A**) Representative Z-stacks of smooth muscle cell (SMCs) cultured for 6 days after siRNA transfection and after decellularization. Stained for FBN1 and either F-actin (cells) or collagen type IV (ECM). Scale bar represents 100 µm. (**B**) Quantification of FBN1 signal corrected for the amount of F-actin in siRNA treated SMCs. Shown is mean ± SEM, N=4. (**C**) Quantification of FBN1 signal corrected for the amount of collagen type IV present in SMC-derived ECM. Shown is mean ± SEM, N=5, *P<0.05. Non-treated SMC are set to one (dotted lines).

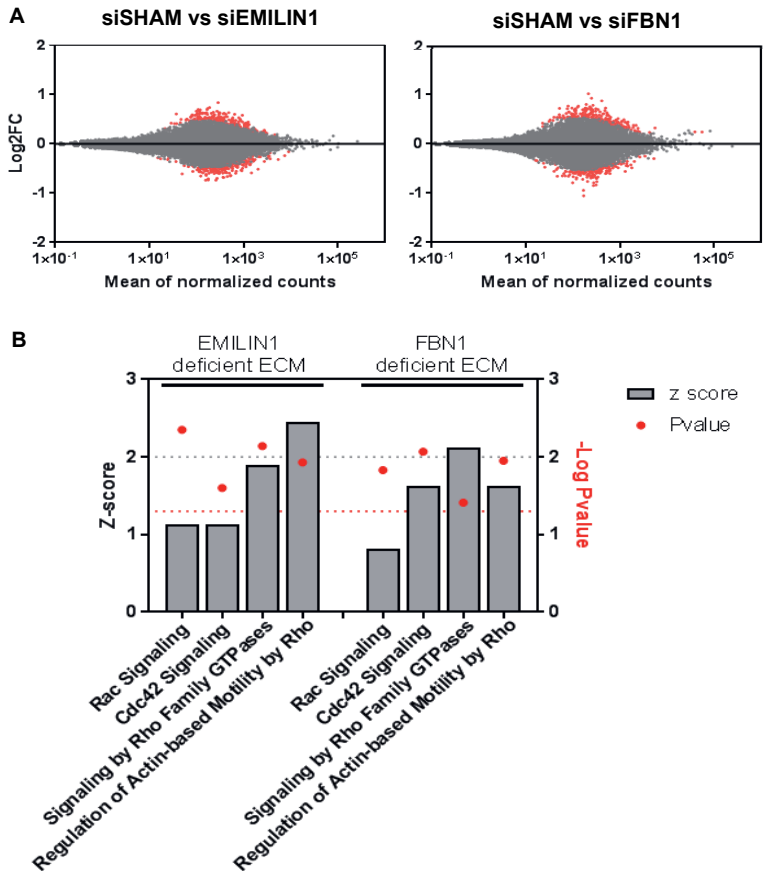

Supplemental Figure 5. (**A**) Visualization of differential gene expression in which Log2 fold change (FC) is plotted against the mean of normalized counts (MA-plot) in human umbilical vein endothelial cells (HUVECs) cultured on siSHAM extracellular matrix (ECM) vs. either EMILIN1-deficient or FBN1-deficient ECM. Gray dots represent non-differentially expressed genes, red dots represent differentially expressed genes ($P<0.05$, 481 and 474 genes for siEMILIN1 and siFBN1, respectively). RNA sequencing was performed on 3 samples per condition. (**B**) Z-score and P-value of pathways of the Rho GTPase family in HUVECs cultured on EMILIN1 or FBN1 deficient ECM.

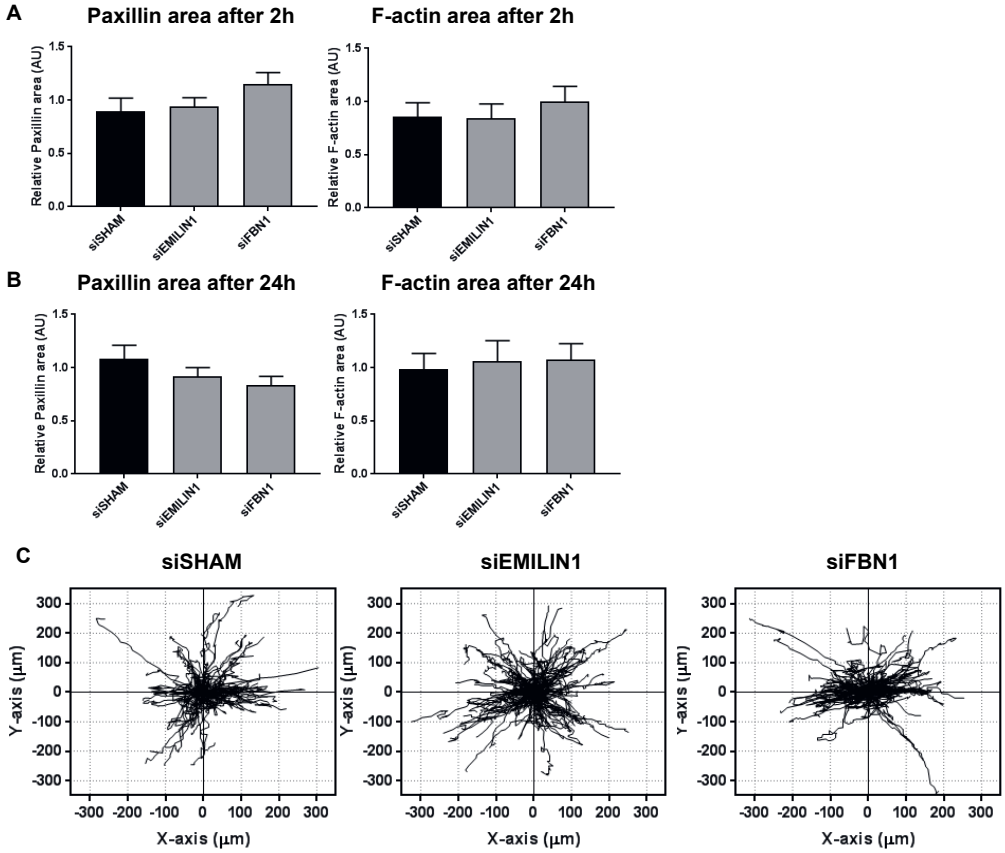

Supplemental Figure 6. (**A**) Paxillin area and F-actin area in HUVECs after 2 hours (not confluent) adhesion or after 24 hours (**B**) (confluent) adhesion on siRNA-treated ECM (siSHAM, siEMILIN1, siFBN1). Shown is mean ± SEM, N=4. (**C**) Representative migration plots showing tracks of individual HUVECs on siRNA treated ECM (siSHAM, siEMILIN1, siFBN1). Migration of HUVECs was traced overnight with confocal microscopy. N=<90 individual tracks per assay, N=4 assays.

Supplemental Tables

Supplemental tables can be downloaded from:

https://www.mdpi.com/1422-0067/21/11/3905

Or:

Chapter 7

Matrix metalloproteinases and tissue inhibitors of metalloproteinases in extracellular matrix remodeling during left ventricular diastolic dysfunction and heart failure with preserved ejection fraction: a systematic review and met-analysis

Merle M. Krebber*, Christian G.M. van Dijk*, Robin W.M. Vernooij, Maarten M. Brandt, Craig A. Emter, Christoph D. Rau, Joost O. Fledderus, Dirk J. Duncker, Marianne C. Verhaar, Caroline Cheng, Jaap A. Joles

International Journal of Molecular Science. 2020 Sep;21(18):e6742

* Authors contributed equally

Abstract

Matrix metalloproteinases (MMPs) and tissue inhibitors of metalloproteinases (TIMPs) are pivotal regulators of extracellular matrix (ECM) composition and could, due to their dynamic activity, function as prognostic tools for fibrosis and cardiac function in left ventricular diastolic dysfunction (LVDD) and heart failure with preserved ejection fraction (HFpEF). We conducted a systematic review on experimental animal models of LVDD and HFpEF published in MEDLINE or Embase. Twenty-three studies were included with a total of 36 comparisons that reported established LVDD, quantification of cardiac fibrosis and cardiac MMP or TIMP expression or activity. LVDD/HFpEF models were divided based on underlying pathology: hemodynamic overload (17 comparisons), metabolic alteration (16 comparisons) or ageing (3 comparisons). Meta-analysis showed that echocardiographic parameters were not consistently altered in LVDD/HFpEF with invasive hemodynamic measurements better representing LVDD. Increased myocardial fibrotic area indicated comparable characteristics between hemodynamic and metabolic models. Regarding MMPs and TIMPs; MMP2 and MMP9 activity and protein and TIMP1 protein levels were mainly enhanced in hemodynamic models. In most cases only mRNA was assessed and there were no correlations between cardiac tissue and plasma levels. Female gender, a known risk factor for LVDD and HFpEF, was underrepresented. Novel studies should detail relevant model characteristics and focus on MMP and TIMP protein expression and activity to identify predictive circulating markers in cardiac ECM remodeling.

Introduction

Left ventricular diastolic dysfunction (LVDD) is an early common alteration in many cardiovascular diseases (CVDs) and highly prevalent in the general population, with reported incidence ranging from 3% to 39% [1,2]. LVDD leads to elevated LV filling pressures which result from increased chamber stiffness, reduced restoring forces and impaired left atrial (LA) function and LV relaxation [3–5]. Clinically, LVDD can remain latent or be accompanied by heart failure (HF) symptoms and deteriorate into HF with preserved ejection fraction (HFpEF) [6,7]. In contrast to HF with reduced ejection fraction (HFrEF) where the LV ejection fraction (LVEF) is <40%, subclinical LVDD and HFpEF patients show a LVEF >50% [8]. It is estimated that around 50% of HF patients suffer from HFpEF, with a two-times higher prevalence in women [9,10], indicating sex-based differences in disease etiology [11–13]. Evidence from clinical studies supports the concept that HFrEF and HFpEF have a different pathophysiology [14]. LVDD appears to be a chronic systemic syndrome resulting from CVD co-morbidities [15] which include hypertension and chronic kidney disease (CKD) [16,17], diabetes [18], obesity and metabolic syndrome [19,20] and ageing [21].

LVDD and HFpEF are characterized by systemic inflammation, endothelial (microvascular) dysfunction, impaired intracellular cardiomyocyte calcium handling, cardiac hypertrophy and interstitial fibrosis [22,23]. Fibrosis is a fundamental process in cardiac remodeling and central in development and progression of HF [24]. Following injury, resident cardiac fibroblasts and infiltrating immune cells control extracellular matrix (ECM) composition primarily by secretion of matrix metalloproteinase (MMPs) and tissue inhibitors of metalloproteinases (TIMPs), the inhibitors of MMP proteolytic function [25,26]. Both MMPs and TIMPs can directly impact ECM turnover and homeostasis. Alterations in cardiac expression levels of MMPs and TIMPs have been found in patients with different types of heart disease [27], including idiopathic dilated cardiomyopathy [28,29]. While it was initially thought that MMP activity would limit cardiac fibrosis through ECM protein degradation, new insights have shown that MMPs and TIMPs can directly induce ECM deposition and ECM remodeling based on the type of micro-environment [30]. However, causal data on the role of MMPs and TIMPs in initiation and progression of cardiac fibrosis in LVDD/HFpEF cardiac micro-environment is still lacking.

Despite diagnostic advances, therapeutic approaches known to benefit HFrEF patients have not proven as clinically efficacious for LVDD and HFpEF patients. HFpEF management primarily consists of treatment of co-morbidities, blood pressure control and diuretic treatment but overall, there is poor control of symptoms [31,32]. The use of animal models with specific HFpEF-associated co-morbidities may lead to better understanding of cell-cell and cell-ECM interactions that drive dynamic ECM remodeling. MMPs and TIMPs may have additive value to improve clinical specificity and/or predictive value for LVDD/HFpEF. Circulating levels of

MMPs and TIMPs have both been used as prognostic tools in clinical studies [33–35] and as potential therapeutic targets [36].

In this systematic review, our aim was to report cardiac MMP and TIMP expression or activity in relation to both LVDD/HFpEF and fibrosis in adequately controlled animal models, e.g., established diastolic dysfunction in absence of systolic dysfunction. Besides providing insights into overall ECM dynamics and patterns of fibrosis, this information may be further used to critically assess (a combination of) novel interesting MMPs and TIMPs as prognostic tools in future studies.

Materials and Methods

We registered the systematic review protocol in PROSPERO (CRD4202018315) on 27th of May 2020.

Literature search

A systematic search MEDLINE and Embase was conducted from database inception up to March 2020. Medical Subject Headings (MeSH) terms and free text terms in title and abstract were used to identify all possible studies regarding HFpEF and LVDD with measured (diastolic) heart function, fibrosis and MMP or TIMP measurements. The search syntax can be found in Supplemental Table 8.

Study selection

Titles and abstracts were evaluated independently by two researchers (C.G.M.v.D. and M.M.K.). Duplicates, non-English, editorials, poster presentations, letters or abstracts only were excluded prior to full text assessment. Consequently, all articles deemed eligible in the title and abstract screening phase were reviewed in the full-text screening phase, independently and in duplicate. The two reviewers resolved disagreements by discussion and, if needed, by third-party adjudication. Only animal studies focusing on stable HFpEF or LVDD and not progressive models leading to HFrEF were included. Inclusion and exclusion criteria for all different animal models and cardiac parameters were predefined and listed below:

Pathologies eligible for inclusion: (1) amyloid (non-hereditary) cardiomyopathy, (2) hypertrophic cardiomyopathy independent of coronary artery disease (CAD) and myocardial infarction (MI), (3) all models of trans-aortic constriction (TAC) in absence of effects on ejection fraction (EF) and fractional shortening (FS), e.g., 2-kidney-1-clip (2K1C) and abdominal-aortic banding, (4) aortic stenosis in absence of CAD or MI, (5) atrial fibrillation in exercise in absence of CAD or MI, (6) pulmonary hypertension, (7) chronic (e.g., osmotic pump-induced) angiotensin II (AngII), (8) chronic (e.g., osmotic pump-induced) deoxycorticosterone acetate (DOCA)-salt, (9) chronically induced isoproterenol, (10) mitral (non-hereditary) regurgitation,

(11) arterio-venous fistula (AVF), (12) natural ageing and (13) (genetic) models not restricted to rodents described by Valero-Muñoz *et al*. [11].

Pathologies that were excluded: (1) stenotic or hypertensive models where the underlying cause is based on systemic atherosclerosis and/or atherosclerotic coronary artery disease (CAD) since CAD is seen as a macrovascular disease and onset mechanisms may deviate from true LVDD and HFpEF, (2) unstable HFpEF of LVDD models that eventually progress into HFrEF (e.g., early phase MI), (3) trained ischemia models such as ischemia-reperfusion (I/R), (4) genetic models of dilated cardiomyopathy (DCM), (5) Homocysteine-enriched diets, (6) exclusion criteria in accordance with HELPFUL protocol [6]. (7) LVDD in combination with HFrEF was also excluded [11] as well as (8) animals with localized genetic alterations prior to introduction of diastolic heart failure.

Studies that met the criteria were further assessed and only included if; (1) HFpEF or LVDD was confirmed with at least one parameter of diastolic function in accordance with the American Society of Echocardiography and the European Association of Cardiovascular Imaging (ASE/EACVI) guidelines [4], (2) fibrosis was confirmed at mRNA or protein (e.g., Western Blot (WB) or immunohistochemistry (IHC)) level, and (3) MMP and/or TIMP activity was confirmed at protein level, preferentially using gelatin zymography. Changes in levels of fibrosis and MMP/TIMP (over time) measured using mRNA were also included. After this final round, all articles that met the criteria were well cross-referenced to ascertain that all relevant articles were included.

Quality assessment

Methodological quality assessment of the included studies was performed by a risk of bias tool adapted from Papazova *et al*. [37]. We separated animal characteristics in specified questions addressing each detail. Furthermore, we divided the blinded assessor for the histological (fibrosis) outcome and echocardiography. Studies were labeled as positive (yes), negative (either partially addressed or not mentioned (N.M.)) or not applicable (N.A.).

Data extraction

Using standardized piloted data-extraction forms, pair of reviewers independently extracted data on study characteristics including species, strain, sex, age, weight, number of animals and experimental model. The total duration of the experiment was reported as end time point. Cardiac parameters from either echocardiography, invasive hemodynamics or tissue Doppler were extracted for (1) diastolic function and, when applicable, (2) systolic function. Fibrotic outcomes and MMP and/or TIMP outcomes were extracted from all parameters measured. Studies that only showed representative images of a staining or WB related to fibrosis or

collagen or zymography but no quantitative data were excluded. For each outcome, the sample size and standard deviation (SD) or standard error (SEM) were extracted. When the sample size was described as a range, the lowest number of replicates was used. When data was not present in text or tables, graphical data was extracted using WebPlotDigitizer (https://automeris.io/WebPlotDigitizer/) by one researcher (C.G.M.v.D.) and validated using PlotDigitizer (http://plotdigitizer.sourceforge.net/) by a second researcher (M.M.K.).

Data analysis

SEM of all extracted data was transformed to SD. Extracted data of cardiac outcome, fibrotic outcome and MMP/TIMP outcome were converted to their effect size and displayed as standardized mean differences (SMD), defined as the between-group difference in mean values divided by the pooled SD, with their corresponding 95% confidence interval using Review Manager (version 5.3.5). Studies were divided based on underlying pathophysiology; ageing, hemodynamic alterations and metabolic alterations.

We examined the heterogeneity by visually inspecting forest plots for the presence of heterogeneity and the tau^2 and I^2 statistics as a measure of between-study heterogeneity. The I^2 described a percentage of variation across the studies attributable to heterogeneity with values of <25%, 25-75%, and >75% interpreted as, respectively, low, moderate, and high between-trial heterogeneity. We used standard inverse-variance random-effect meta-analysis to combine outcome data across studies on predetermined parameters [38] in Review Manager (Version 5.3.5). This systematic review followed the PRISMA guidelines (Supplemental Table 9).

Results

Study population selection and overall characteristics

Our systematic search resulted in 4868 articles. As described in the Materials and Methods section 4.2, we applied stringent inclusion and exclusion criteria, in order to only cover those phenotypically well-characterized models of HFpEF with established echocardiographic diastolic dysfunction in absence of systolic dysfunction. Studies moreover had to include quantification of fibrosis in cardiac tissue and quantification of at least one cardiac MMP or TIMP. In total, 254 manuscripts were screened on full-text, and 239 articles were excluded per exclusion criteria, of which 28 included systolic dysfunction. Eight articles were added after cross-referencing. Finally, data was extracted from 23 articles (Figure 1**)**. We observed a large variety in overall study characteristics (Supplemental Table 1). The majority of studies used rodents: either mice (12 articles) [39-50] or rats (6 articles) [51-56]. Other species included swine (n=3) [57-59], rabbit (n=1) [60] and guinea pig (n=1) [61]. All but one of the studies

employing mice used a C57BL/6 strain or adapted strains with a C57BL/6 background. Rat models showed more heterogeneity; Wistar (Han), spontaneously-hypertensive (SHR), Dahl salt-sensitive (SS) and ZSF1. All three swine models were a different strain. Eighteen articles reported the animal's sex, while the remainder did not specify the sex or, in one case, used both sexes. Only few of the included articles (5/23) focused on female animals. Various articles studied more than one underlying co-morbidity for LVDD/HFpEF. For example, Brandt *et al*. studied LVDD in male lean and obese rats with and without deoxycorticosterone acetate (DOCA)-induced hypertension. They showed significant changes in LVDD in three relevant comparisons, e.g. lean vs. obese (metabolic alteration), lean + DOCA vs. obese + DOCA (metabolic alteration) and obese vs. obese + DOCA (hemodynamic alteration) (Supplemental Table 1) [51]. LVDD was primarily examined using (tissue Doppler) echocardiography E/A ratio (15/23), followed by changes in peak E-wave velocity (8/23), E/e' ratio (6/23) or isovolumic relaxation time (IVRT, 7/23). Invasive hemodynamic measurements end diastolic pressure (EDP) (11/23), minimum derivative of pressure over time (dP/dt_{min}) (7/23),

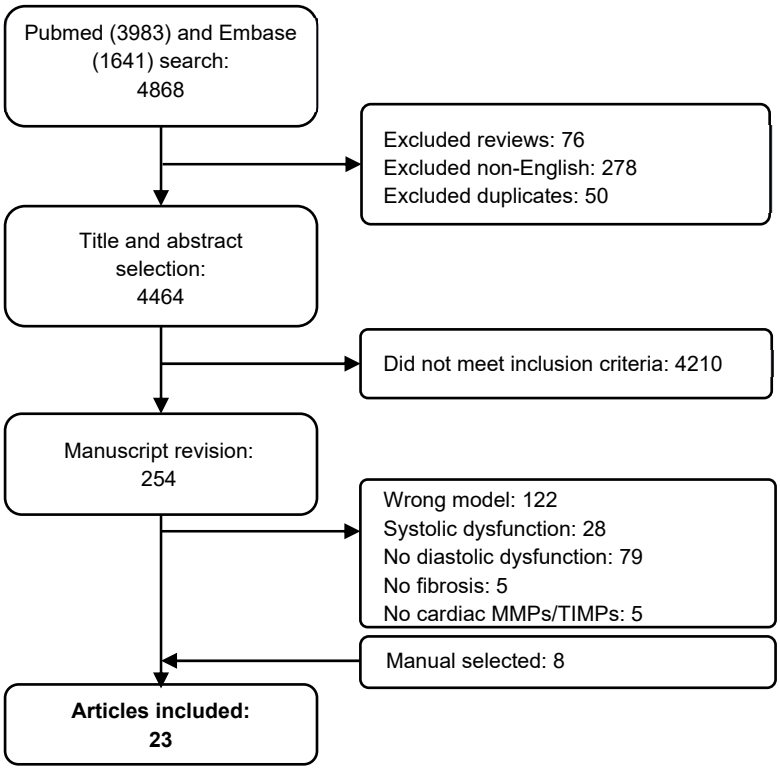

Figure 1. Flow chart of study selection. All articles are included and excluded according to the selection criteria defined in the Materials and Method section.

time constant of relaxation Tau (6/23) and end diastolic pressure volume relationship (EDPVR) (5/23) were reported less frequently (Supplemental Figure 1A). Moreover, two studies included strain measurements using speckle tracking echocardiography. Due to the low number of studies, no meta-analysis was performed. Quantification of fibrosis primarily focused on protein; collagen content using IHC staining, mainly Sirius Red (SR) (12/23) or hydroxyproline assay (Supplemental Figure 1B,C). MMP tissue activity by gelatinase assay was measured in about half of the articles (11/23) (Supplemental Figure 2A). These 11 articles assessed MMP2, or variants, while MMP9 was quantified 5 times (Supplemental Figure 2B). MMP tissue protein levels were primarily quantified by WB, and focused on MMP9 (4/23) (Supplemental Figure 2C). Most articles reported mRNA expression of MMP9 (13/23), MMP2 (12/23), or TIMP1 (12/23) (Supplemental Figure 2D). Extracted data of all studies can be found in Supplemental Table 2 (cardiac outcomes), Supplemental Table 3 (fibrotic outcomes), and Supplemental Table 4 (MMP and TIMP outcome).

Table 1. Summarizing table of meta-analysis.

	Cardiac diastolic parameters								Fibrotic outcome					
	E/A	E/e'	IVRT	E wave	Tau	dP/dt_{min}	EDPVR	EDP	Fibrosis	Collagen content	Col1 protein	Col3 protein	Col1 mRNA	Col3 mRNA
Hemodynamic	=	↑	=	=	↑	=	↑	=	↑	=	↑	=	↑	↑
Metabolic	=	↑	=	=	↑	↓	↑	=	↑	=	=	=	↑	↑
Pooled effect	=	↑*	=	=	↑	↓	↑	↑	↑	↑	↑	=	↑	↑

	MMP and TIMP outcome																	
	MMP2 activity	MMP9 activity	MMP2 protein	MMP9 protein	TIMP1 protein	TIMP2 protein	MMP2 mRNA	MMP8 mRNA	MMP9 mRNA	MMP11 mRNA	MMP12 mRNA	MMP13 mRNA	MMP14 mRNA	MMP15 mRNA	TIMP1 mRNA	TIMP2 mRNA	TIMP3 mRNA	TIMP4 mRNA
Hemodynamic	↑	↑	↑	↑	=	↑	↑	=	=	=	=	=	=	=	↑	=	=	=
Metabolic	=	=	↓	↑	=	=	=	=	=	=	=	N/A	=	=	=	=	=	↓
Pooled effect	↑	↑	=*	↑*	=	=	=*	=	=	=	=	=	=	↓	↑	=	=	=*

◄↑, effect is higher in LVDD/HFpEF; ↓, effect is lower in LVDD/HFpEF; =, no significant effect; *, significant subgroup difference. Col, collagen; dP/dt_{min}, minimum rate of pressure change; E/A, ratio between peak early diastolic transmitral velocity (E) and late (atrial) transmitral flow velocity (A); E wave, peak early diastolic transmitral velocity; E/e', ratio between peak early diastolic transmitral velocity (E) and early diastolic mitral annular velocity (e'); EDP, end diastolic pressure; EDPVR, end diastolic pressure volume relationship; IVRT, isovolumetric relaxation time; MMP, matrix metalloproteinase; N/A, not available; Tau, time constant of ventricular relaxation; TIMP, tissue inhibitor of metalloproteinase.

Quality assessment of the studies

The majority of studies reported the animal details such as strain, sex and age adequately (Supplemental Figure 3). Noteworthy, only 40% of the studies reported random allocation or stratification of the animals. Baseline characteristics regarding echocardiographic parameters and blinded data processing and analysis were reported infrequently.

Meta-analysis on diastolic function and fibrosis in models of LVDD/HFpEF

Concerning diastolic function, all included studies showed similar EF, FS and/or peak derivative of pressure over time (dP/dt_{max}) in the experimental model and control, as defined in the exclusion criteria. Studies were first divided based on underlying pathophysiology; ageing (3 comparisons), hemodynamic alterations (17 comparisons) and metabolic alterations (16 comparisons) (Supplemental Table 1). Due to the low number of comparisons; i.e. three, all in mice, no meta-analysis was performed for ageing. All relevant directional changes, standard mean differences (SMDs) and confidence intervals (CIs) resulting from meta-analysis are available in Table 1 and Supplemental Table 5 respectively.

Pooled analysis of E/e' (Figure 2A) but not E/A (Figure 2B) ratios showed an overall increase in LVDD/HFpEF. There was no pooled effect on E-wave or IVRT. E/e' alone moreover significantly increased in both models with metabolic alterations having a higher E/e' ratio (subgroup difference p=0.03). For E/A, E-wave and IVRT, there were no subgroup differences. Invasive hemodynamic measurements represented by EDP showed an increased pressure in HFpEF, EDPVR increased in slope and Tau showed a prolonged relaxation duration (Figure 3A). dP/dt_{min} (Figure 3B) showed overall reduced maximal rate of fall of LV pressure. Subgroup analysis revealed that EDPVR and Tau increased in both hemodynamic and metabolic models, without subgroup differences (p=0.89 and p=0.76). EDP remained unchanged in subgroup analysis and was similar in both models. dP/dt_{min} decreased in metabolic models, without subgroup differences (p=0.39). Thus hemodynamic and metabolic models generally display similar changes in cardiodynamics (Table 1).

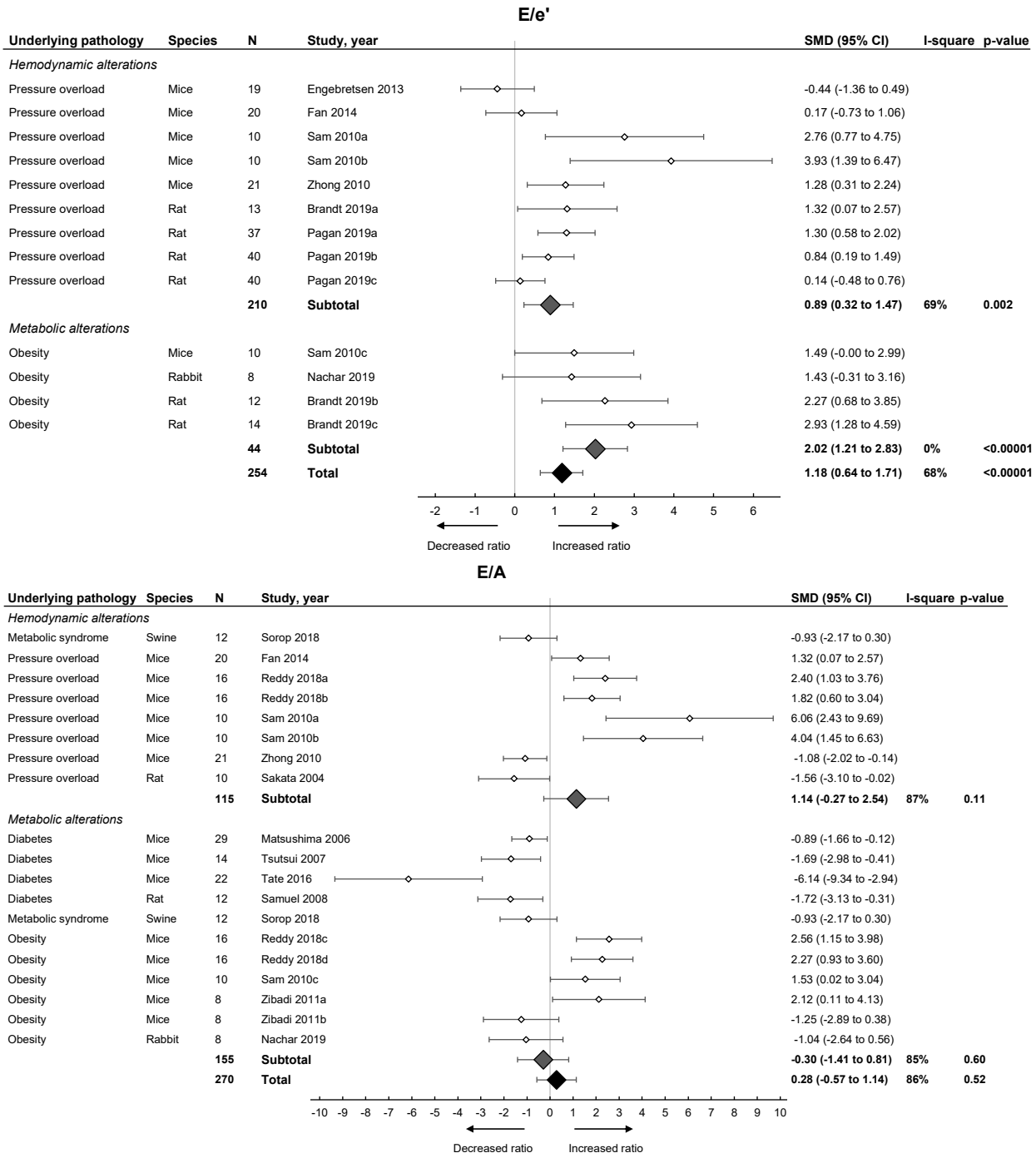

Figure 2. The effect of LVDD/HFpEF on cardiac parameters E/e' (**panel A**) and E/A (**panel B**). Forrest plot; the right side shows an increased effect in LVDD/HFpEF animals, the left side shows a decreased effect in LVDD/HFpEF animals. Data are presented as SMDs with 95% CI. Arrows indicate increased and

◄decreased E/e' ratio **(A)**, and increased and decreased E/A ratio **(B)** respectively. Only the first author of each study is shown, multiple comparisons within one study are shown with a, b, c or d and correspond with the study overview (supplemental table 1). CI, confidence interval; E/A, ratio between peak early diastolic transmitral velocity (E) and late (atrial) transmitral flow velocity (A); E/e', ratio between peak early diastolic transmitral velocity (E) and early diastolic mitral annular velocity (e'); I^2, measurement of heterogeneity; N, cumulative sample size; SMD, standardized mean difference.

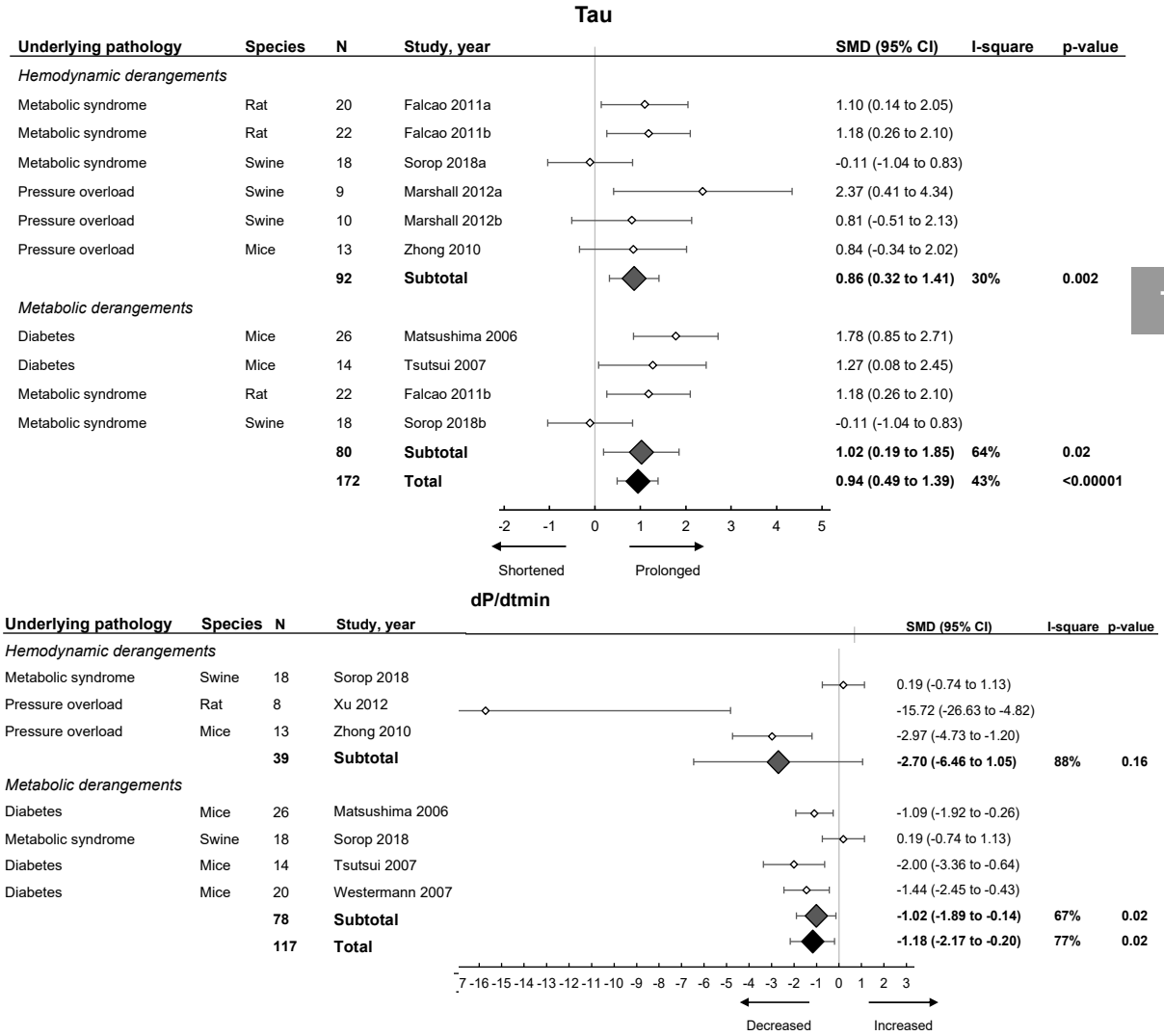

Figure 3. The effect of LVDD/HFpEF on cardiac parameters Tau (**panel A**) and dP/dt_{min} (**panel B**). Forrest plot; the right side shows an increased effect in LVDD/HFpEF animals, the left side shows a decreased effect in LVDD/HFpEF animals. Data are presented as SMDs with 95% CI. Arrows indicate shortened and prolonged time constant of relaxation Tau **(A)**, and decreased and increased rate of pressure change dP/dt_{min} **(B)** respectively. Only the first author of each study is shown, multiple comparisons within one

◄study are shown with a, b, c or d and correspond with the study overview (supplemental table 1). CI, confidence interval; I^2, measurement of heterogeneity; N, cumulative sample size; SMD, standardized mean difference; dP/dt_{min}, minimum rate of pressure change; Tau, time constant of ventricular relaxation.

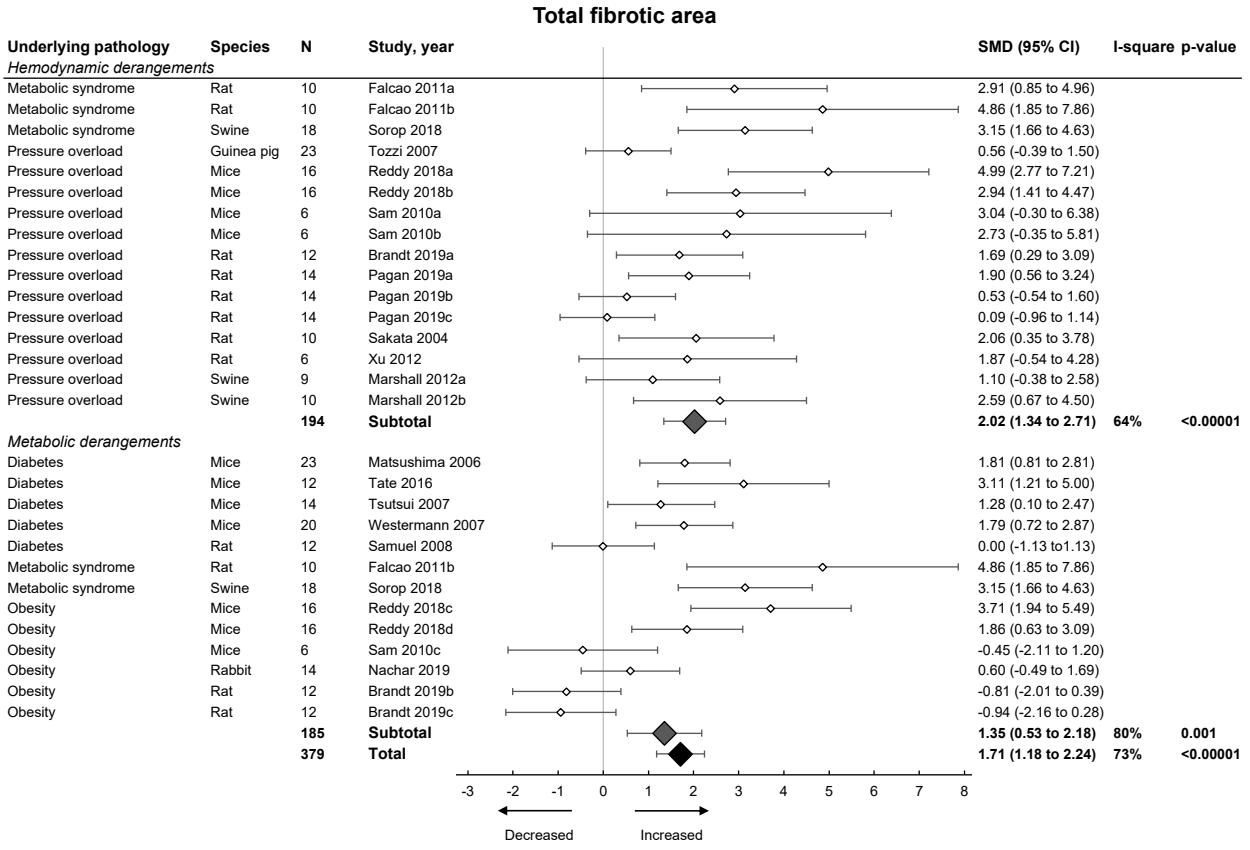

Figure 4. The effect of LVDD/HFpEF on total fibrotic area. Forrest plot; the right side shows an increased effect in LVDD/HFpEF animals, the left side shows a decreased effect in LVDD/HFpEF animals. Data are presented as SMDs with 95% CI. Arrows indicate increased and decreased fibrotic percentage area respectively. Only the first author of each study is shown, multiple comparisons within one study are shown with a, b, c or d and correspond with the study overview (supplemental table 1). CI, confidence interval; I^2, measurement of heterogeneity; N, cumulative sample size; SMD, standardized mean difference.

Collagen type I

Underlying pathology	Species	N	Study, year	SMD (95% CI)	I-square	p-value
Hemodynamic derangements						
Metabolic syndrome	Swine	9	Olver 2019	1.44 (-0.15 to 3.02)		
Pressure overload	Mice	24	Engebretsen 2013	1.90 (0.90 to 2.89)		
Pressure overload	Mice	10	Fan 2014	1.55 (0.03 to 3.07)		
Pressure overload	Mice	12	Reddy 2018a	5.78 (2.74 to 8.82)		
Pressure overload	Mice	12	Reddy 2018b	1.79 (0.36 to 3.22)		
Pressure overload	Mice	12	Zhong 2010	1.70 (0.40 to 2.99)		
Pressure overload	Rat	10	Brandt 2019a	2.32 (0.52 to 4.13)		
Pressure overload	Rat	6	Xu 2012	3.64 (-0.22 to 7.50)		
Pressure overload	Swine	9	Marshall 2012a	0.80 (-0.60 to 2.21)		
Pressure overload	Swine	10	Marshall 2012b	0.10 (-1.15 to 1.34)		
		114	**Subtotal**	**1.65 (0.99 to 2.31)**	**45%**	**<0.00001**
Metabolic derangements						
Metabolic syndrome	Swine	9	Olver 2019	1.44 (-0.15 to 3.02)		
Obesity	Rat	10	Brandt 2019b	0.69 (-0.61 to 1.98)		
Obesity	Rat	10	Brandt 2019c	-1.07 (-2.45 to 0.31)		
Obesity	Rabbit	14	Nachar 2019	0.99 (-0.16 to 2.13)		
Obesity	Mice	12	Reddy 2018c	2.24 (0.66 to 3.81)		
Obesity	Mice	12	Reddy 2018d	2.15 (0.61 to 3.70)		
Obesity	Mice	8	Zibadi 2011a	1.18 (-0.43 to 2.78)		
Obesity	Mice	8	Zibadi 2011b	2.73 (0.40 to 5.06)		
		83	**Subtotal**	**1.17 (0.37 to 1.97)**	**56%**	**0.004**
		197	**Total**	**1.43 (0.92 to 1.94)**	**50%**	**<0.00001**

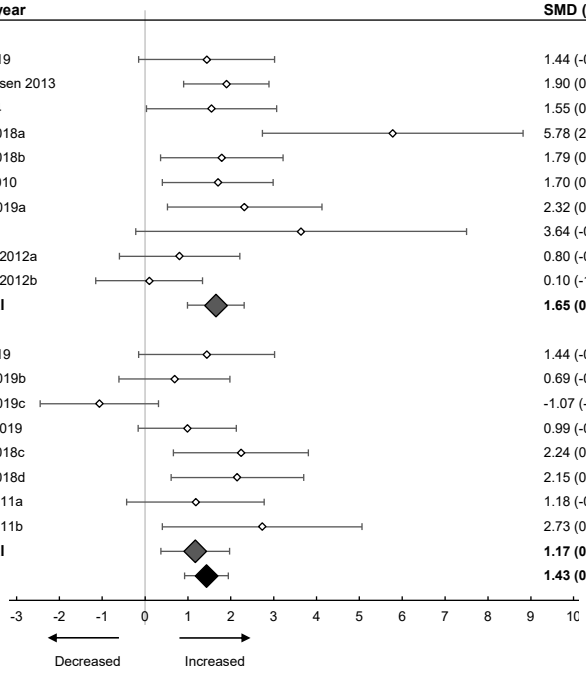

Collagen type III

Underlying pathology	Species	N	Study, year	SMD (95% CI)	I-square	p-value
Hemodynamic derangements						
Metabolic syndrome	Swine	9	Olver 2019	-0.30 (-1.63 to 1.03)		
Pressure overload	Mice	24	Engebretsen 2013	1.23 (0.34 to 2.12)		
Pressure overload	Mice	10	Fan 2014	1.90 (0.26 to 3.54)		
Pressure overload	Mice	12	Reddy 2018a	5.57 (2.63 to 8.52)		
Pressure overload	Mice	12	Reddy 2018b	3.19 (1.26 to 5.11)		
Pressure overload	Mice	12	Zhong 2010	3.83 (1.85 to 5.81)		
Pressure overload	Rat	10	Brandt 2019a	2.78 (0.78 to 4.77)		
Pressure overload	Rat	6	Xu 2012	2.52 (-0.39 to 5.44)		
Pressure overload	Swine	9	Marshall 2012a	0.50 (-0.85 to 1.85)		
Pressure overload	Swine	10	Marshall 2012b	-1.00 (-2.37 to 0.36)		
		114	**Subtotal**	**1.75 (0.68 to 2.83)**	**77%**	**0.001**
Metabolic derangements						
Diabetes	Mice	12	Tate 2016	1.67 (0.27 to 3.06)		
Metabolic syndrome	Swine	9	Olver 2019	-0.30 (-1.63 to 1.03)		
Obesity	Mice	12	Reddy 2018c	0.67 (-0.51 to 1.85)		
Obesity	Mice	12	Reddy 2018d	2.21 (0.65 to 3.78)		
Obesity	Mice	8	Zibadi 2011a	1.64 (-0.15 to 3.42)		
Obesity	Mice	8	Zibadi 2011b	1.12 (-0.47 to 2.71)		
Obesity	Rabbit	14	Nachar 2019	0.92 (-0.21 to 2.05)		
Obesity	Rat	10	Brandt 2019b	0.50 (-0.77 to 1.77)		
Obesity	Rat	10	Brandt 2019c	-1.53 (-3.04 to -0.02)		
		95	**Subtotal**	**0.73 (0.05 to 1.42)**	**54%**	**0.04**
		209	**Total**	**1.19 (0.56 to 1.82)**	**70%**	**0.0002**

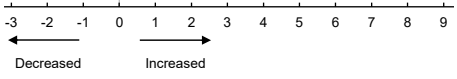

◄**Figure 5.** The effect of LVDD/HFpEF on collagen type 1 (**panel A**) and collagen type 3 (**panel B**) mRNA levels. Forrest plot; the right side shows an increased effect in LVDD/HFpEF animals, the left side shows a decreased effect in LVDD/HFpEF animals. Data are presented as SMDs with 95% CI. Arrows indicate increased and decreased Collagen type 1 **(A)**, and increased and decreased type 3 **(B)** mRNA expression respectively. Only the first author of each study is shown, multiple comparisons within one study are shown with a, b, c or d and correspond with the study overview (supplemental table 1). CI, confidence interval; COL1, collagen type 1; COL3, collagen type 3; I^2, measurement of heterogeneity; N, cumulative sample size; SMD, standardized mean difference.

Subsequently, we focused on fibrosis. An overview of meta-analyses outcomes for fibrosis can be found in Table 1 and Supplemental Table 6. Note the relative paucity of data on collagen protein as compared to mRNA levels (Supplemental Table 6). Meta-analysis on positive percentage area as assessed by IHC showed a pooled increase (Figure 4). Both hemodynamic and metabolic models were associated with an increase, without subgroup differences (p=0.22), resulting from increased collagen type I expression (mRNA and protein) and increased collagen type III on mRNA but not protein level (Figure 5A,B).

Meta-analysis on MMPs and TIMPs in pooled models of LVDD/HFpEF

We then investigated the pooled effects of LVDD/HFpEF on MMP and TIMP expression and activity. An overview of meta-analyses outcomes for all MMPs and TIMPs can be found in Table 1 and Supplemental Table 7. Note the paucity of data on MMP and TIMP protein as well as MMP zymography as compared to mRNA levels (Supplemental Table 7). For mRNA expression, MMP2, -8, -9, -11, -12, -14, -15 and TIMP1, -2, -3, -4 were investigated. We found no pooled changes in MMP or TIMP expression in LVDD/HFpEF, except for decreased MMP15 and increased TIMP1 expression. Protein levels of MMP2, -9, TIMP1 and -2 were subsequently analyzed. Pooled MMP2, TIMP1 and TIMP2 protein expressions were similar but MMP9 increased. LVDD/HFpEF increased zymographic activity of MMP2 and MMP9 (Figure 6A,B).

Meta-analysis on MMPs and TIMPs in models involving hemodynamic and metabolic alterations

Hemodynamic models showed no changes in MMP2, -8 -9, -14, -15, TIMP2, -3 and -4 mRNA and TIMP1 protein expression, but MMP2 and TIMP1 protein expression increased. MMP2 and MMP9 protein expression also increased but were only measured in one study [42]. TIMP2 protein and MMP2 and MMP9 zymographic activity increased (Figure 6; Table 1; Supplemental Table 7).

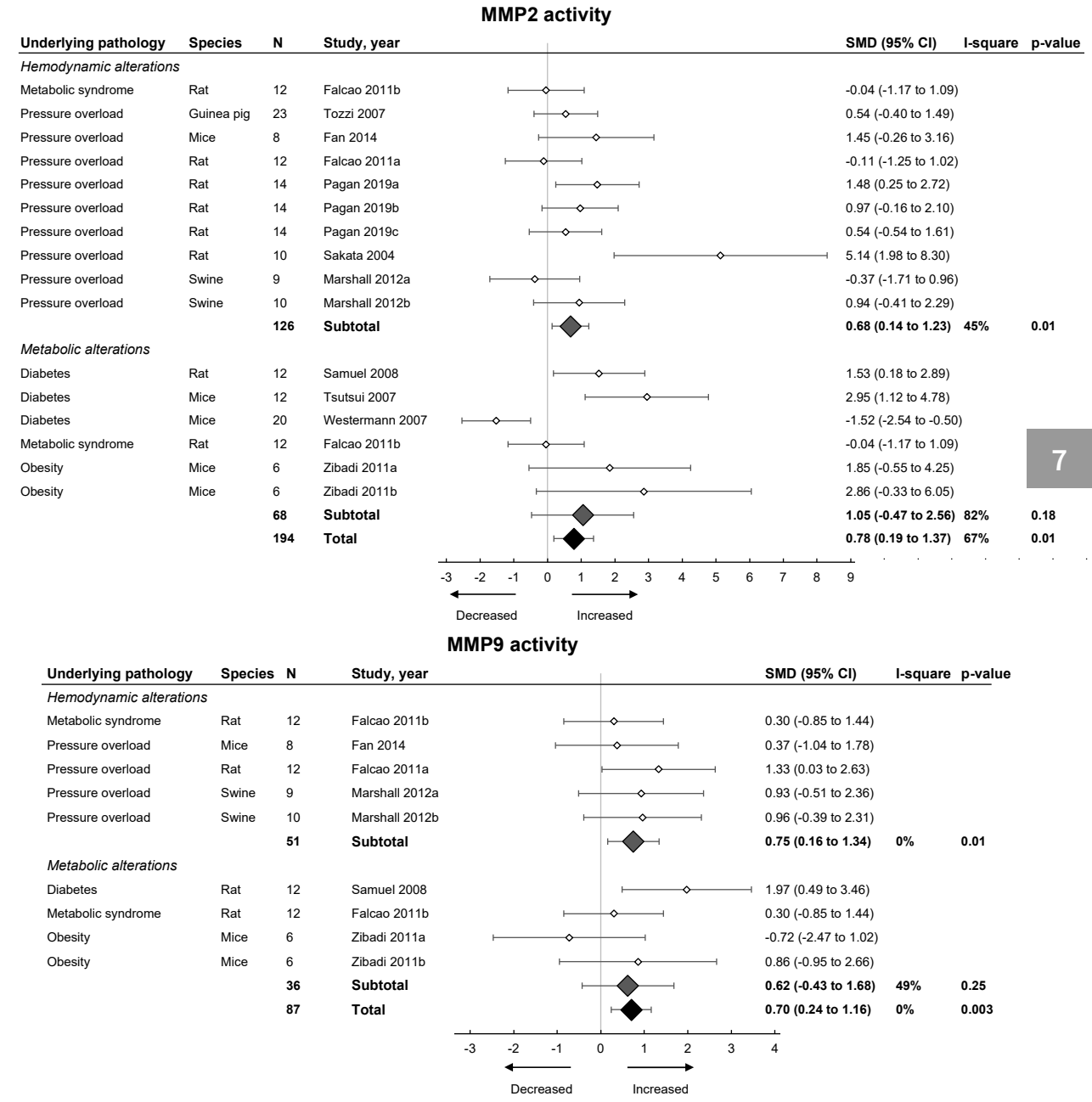

Figure 6. The effect of LVDD/HFpEF on MMP2 (**panel A**) and MMP9 (**panel B**) activity. Forrest plot; the right side shows an increased effect in LVDD/HFpEF animals, the left side shows a decreased effect in LVDD/HFpEF animals. Data are presented as SMDs with 95% CI. Arrows indicate increased and decreased MMP2 **(A)**, and increased and decreased MMP9 **(B)** enzyme activity respectively. Only the first author of each study is shown, multiple comparisons within one study are shown with a, b, c or d and

◄correspond with the study overview (supplemental table 1). CI, confidence interval; I^2, measurement of heterogeneity; MMP, matrix metalloproteinase; N, cumulative sample size; SMD, standardized mean difference; TIMP, tissue inhibitor of metalloproteinase.

Metabolic models showed no changes in MMP2, -8, -9, -11, -14, -15, TIMP1, -2 and -3 mRNA expression. There was a decrease in TIMP4 mRNA. MMP2 protein was only measured in 1 study and decreased while TIMP1 and TIMP2 protein remained unchanged [42]. MMP9 protein levels increased. Both MMP2 and MMP9 zymographic activity were similar in metabolic models versus controls (Figure 6; Table 1; Supplemental Table 7)

Descriptive effect on models involving ageing (all in mice)

Chiao *et al*. [39] but not Ma *et al*. [40] showed increased fibrotic percentage area. However, both studies reported decreased collagen I and/or collagen III mRNA. Thus, cardiac fibrosis in ageing, at least in mice, in contrast to the induced hemodynamic and metabolic models, was not due to increased collagen synthesis. Ageing was associated with decreased MMP8 and MMP9 [39] and MMP28 protein [40]. There were no changes in other MMPs or TIMPs.

Discussion

Due to the high morbidity and mortality associated with HFpEF [62] there is an urgent need for additive and predictive circulating markers and early detection of changes in structural and functional cardiac parameters. In our systematic review concerning animal models of LVDD/HFpEF and cardiac fibrosis in relation to MMPs and TIMPs, we aimed to identify patterns associating ECM dynamics with LVDD and HFpEF pathology. We included 23 studies with a large range of study characteristics and our assessment indicated relatively low quality with respect to random allocation and blinded assessment of results. The relative heterogeneity of study characteristics partially reflects clinical findings since HFpEF is a multifactorial disease and an overarching pathology resulting from a variety of underlying CVD co-morbidities [31]. Overall, there was a sex-based bias towards male gender and bias towards pressure overload and metabolic models of LVDD/HFpEF. Our main findings show that echocardiographic measurements of LVDD/HFpEF, including E/A, E-wave and IVRT, do not consistently relate with accepted phenotypic criteria of the current established experimental models of LVDD/HFpEF. Invasive hemodynamic measurements such as Tau, EDP, EDPVR and dP/dt_{min}, on the other hand, seem to associate more closely with the phenotype. Regarding cardiac expression of MMPs and TIMPs, it appears highly unlikely that the presence or activity of a single MMP or TIMP may hold the key to diagnosing or even treating a multifactorial disease such as HFpEF. We identified MMP15 and increased TIMP1

mRNA and MMP9 protein expression in LVDD/HFpEF. Increased MMP2 and MMP9 zymographic activity both associated with pooled LVDD/HFpEF.

Echocardiography and tissue Doppler parameters of LVDD and HFpEF

For our study inclusion, we selected and prioritized cardiac parameters in accordance with the current ASE/EACVI guidelines [4]. While LV cardiac pressure catheterization is the gold standard for evaluating EDPVR, dP/dt_{min} and Tau, in the clinic both LVDD and HFpEF are primarily diagnosed using echocardiography [3,63,64]. Assessing LA strain by speckle tracking echocardiography has recently also emerged as a relevant non-invasive clinical alternative, circumventing the time-consuming measurements associated with tissue Doppler [64–66]. In clinical practice, measurements in patients with normal EF currently include e' and E/e' ratio to estimate LV filling pressure. The interpretation of the E-wave, A-wave and e' however depend on strictly defined thresholds; decreased E/A ratio (<0.8) reflects the compensatory increase in late atrial filling when the LV fails to relax, primarily linked to alterations in early LVDD [3,5]. To the best of our knowledge, such thresholds have not been clearly set for experimental animals. In the current study, E/A ratios were still the most frequently used to assess diastolic function. However, our meta-analysis on pooled effects showed that this ratio is not consistently altered. This may be partially explained by the fact that this ratio is highly afterload-dependent [67,68] and the majority of our models involved a hypertensive background (20/36 comparisons). Previously it was found that E/A ratios in murine models of HFpEF were difficult to measure due to high heart rates [69]. In general, anesthetic agents influence diastolic function in healthy mice [70]. Among others, inhaled anesthetics reduce afterload beneficially [71] but changes may be less evident in HF models [72]. Almost half of the included studies (11/23) performed echocardiography or tissue Doppler under isoflurane (analogues) and it remains pivotal for obtaining accurate measurements. The general impact of anesthetics on perioperative LVDD and HFpEF remains unclear [73].

Given the pooled and separate effect of hemodynamic models on increased E/e' ratio but lack of effect on E/A and E-wave, e' seems to represent the most reliable change in LVDD/HFpEF. Indeed, Zhong *et al*. [45], Pagan *et al.* [53] and Sam *et al*. [44] show a decreased e' (3/5 comparisons). Clinically, e' also has the highest reproducibility and a consistent association with CVD outcomes [64].

Invasive hemodynamics were less frequently applied in the included articles, probably due to practical constraints, especially in small animals. In pooled data, we did find prolonged Tau and decreased dP/dt_{min}, which were both identified in metabolic alterations, in accordance with literature [77,75].

Influence of fibrosis on development and progression of LVDD and HFpEF

The cardiac ECM mainly comprises fibrillar collagen, specifically collagen type I and III (85–90% to 5–11%, respectively) [25]. Myocardial stiffness in patients with HFpEF is associated with increased collagen type I expression and cross-linking [76]. Besides cardiac (myo) fibroblasts, other cardiac cell types contribute to excess ECM accumulation by either ECM secretion [77] or differentiation to myofibroblasts [78,79]. Animal models have shown that cardiac fibroblasts are activated early in development of LVDD, leading to collagen deposition and activation of the cardiac renin-angiotensin-aldosterone system (RAAS), driving inflammatory processes and TGF-β signaling [80]. Our meta-analysis showed that HFpEF is associated with an overall increase in positive fibrotic area. Both hemodynamic and metabolic alterations associated with increased fibrotic area. Transcriptome analysis on lateral LV wall biopsies of HFpEF patients indeed showed upregulation of collagen 1α1 and collagen 3α1, among others [81].

MMP and TIMP activity in LVDD and HFpEF

Several clinical studies have previously tried to improve LVDD and HFpEF diagnosis by incorporating plasma markers of collagen turnover [82–84]. The majority of our included studies investigating the relation between HFpEF and MMPs focused on MMP2, MMP9 and TIMP1 mRNA expression. Our overall meta-analysis showed increased MMP2 and MMP9 activity, MMP9 protein, TIMP1 gene expression and decreased MMP15 gene expression. RNA-sequencing of atrium of high-salt fed rats however showed increased MMP15 levels [85] emphasizing the need to further study this MMP in both hemodynamic and metabolic models of HFpEF. In general, increases in plasma levels of MMP2, MMP9 [82] and TIMP1 [86] have been found in HFpEF patients with a hypertensive background. A transcriptomic study on lateral LV wall biopsies of HFpEF previously showed a decreased MMP15 gene expression [81]. MMP gene expression may be determined by different external factors and may be cell type and ECM-specific [87,88]. Moreover, both MMPs and TIMPs are heavily regulated at mRNA, protein and activity levels. Interpreting MMP and TIMP activity in LVDD/HFpEF solely based on mRNA levels therefore is not directly translatable to clinical settings. While previous studies have confirmed that a ratio of 1:1 exists for the breakdown product of collagen type I, procollagen type I C-terminal propeptide (PICP), in the bloodstream versus (cardiac) collagen type I production, this seems to be less established for cardiac MMP and TIMP activity versus their circulating levels. Zhang *et al*. employed a rodent model of aortic stenosis-induced pressure overload and while they did not report MMP or TIMP cardiac tissue mRNA or protein levels, 8 weeks after induction of pressure overload, MMP1, MMP2, MMP9 and TIMP1 protein levels were significantly increased in the circulation compared to time-matched controls [89].

In streptozotocin (STZ)-induced diabetic minipigs, both pro- and active MMP2 and MMP9 zymography in the LV decreased compared to control animals [90]. This finding was in accordance with decreased serum protein levels of MMP2 and MMP9. Protein levels as measured by WB and IHC of these MMPs, however, showed no changes in expression while mRNA levels for MMP9 even increased in diabetic animals [90]. These data also indicate dissimilarities between mRNA and protein expression and MMP tissue enzymatic activity. Changes in active MMPs seem to most closely resemble serum values.

Differences in MMP and TIMP expression and activity may also be relevant in relation to underlying co-morbidities and severity of HFpEF. While our meta-analysis had a low power concerning subgroup analysis, we did identify higher MMP2 and MMP9 protein in hemodynamic and lower TIMP4 gene expression in metabolic alterations. Sakamuri *et al*. previously studied high-fat diet changes in TIMP4 knock-out (KO) mice compared to wild-type. TIMP4 KO mice showed reduced cardiac fibrosis and systemic protection from dyslipidemia, indicating a protective mechanism in the context of metabolic changes [91]. In chronic HF settings, epigenetic changes could be a relevant mode of action. In a mouse model of aorta-vena cava fistula, methylation of the TIMP4 promotor was shown. TIMP4 directly regulates MMP9 and indeed MMP9 protein was upregulated in the mouse model [92], in accordance with our findings; MMP9 protein showed significant upregulation in hemodynamic compared to metabolic models. No conclusions on MMP2 protein in metabolic alterations could be drawn, since they were only assessed in one study [44]. Similar results were found by Ahmed *et al*., where MMP-9 levels were elevated in hypertensive patients with LVH and HFpEF and hypertensive LVH patients but not in hypertensive controls [93]. Contrarily, MMP2 levels decreased in hypertensive LVH patients without HFpEF [93]. Assessing circulating MMP and TIMP levels in relation to HFpEF could aid physicians in determining whether a certain co-morbidity primarily drives disease progression in a particular patient. Note that the chosen end-point of experimental studies will certainly influence fibrotic progression. Thus, even within the pathology of LVDD and HFpEF, severity may directly relate to MMP and TIMP dynamics and ECM turnover.

Study limitations

We retrieved 23 relevant studies via our systematic search, complemented by cross-referencing. In order to exclusively include models with well-established phenotypic characterization, we applied stringent inclusion criteria. These included established echocardiographic measurements of diastolic function in absence of systolic dysfunction, combined with quantification of fibrosis and cardiac tissue quantification of at least one MMP or TIMP, and only in pre-determined experimental models known to represent co-morbidities

in human HFpEF. Inclusion of stable LVDD/HFpEF models came at the cost of the relatively low power of our meta-analysis. Our broad search strategy was performed in two biomedical databases, leading to a large number of references. Several papers did not explicitly mention either LVDD/HFpEF or MMP/TIMP expression while focusing on disease development or only retrieved MMPs/TIMPs by applying an mRNA-sequencing protocol. Consequently, these studies could not be identified by our search, but we have resolved this by cross-reference searching.

Several studies including relevant co-morbidities were excluded based on a decrease in systolic function. While a threshold to discern HFrEF from HFpEF is routine in clinical practice [4], this does not automatically hold true for experimental models. We therefore excluded all studies (28/239) showing significant differences in systolic function, e.g., EF, FS or dP/dt_{max}, compared to controls. On the other hand, clinical diagnosis of LVDD or HFpEF is described in detailed guidelines and depends on specific alterations in cardiac parameters that are not well-defined in animal models. We therefore included all studies that showed a significant difference in at least one measured clinically relevant diastolic parameter, e.g., E/e', E/A, Tau and dP/dt_{min}, compared to control, irrespective of the direction of the change. We also identified significant heterogeneity (>75%) between several comparisons. This can be largely explained by differences in study design, cardiac, fibrotic and MMP and TIMP outcome as well as the differences between underlying pathology, animal species and strains. Creating a division between hemodynamic and metabolic-driven pathologies allowed us to analyze both overall data and individual underlying pathologies, in line with the heterogeneity of co-morbidities found in HFpEF patients [94,95]. By including more than one comparison for several studies, controls may be over-analyzed which could affect the pooled outcome but to lesser extent the subgroups. Moreover, most studies did not specify which part of the myocardium was used for fibrotic or MMP/TIMP analysis, probably accounting for some of the differences in outcome.

Conclusions

Our study shows that when MMPs and TIMPs are studied in relation to LVDD/HFpEF, cardiac mRNA expression is still most frequently measured while this does not seem to resemble cardiac ECM dynamics in these experimental models. Since post-transcriptional and post-translational activation of both MMPs and TIMPs takes place, future studies should focus on MMP and TIMP protein levels and enzyme activity. Changes in active MMPs seem to most closely resemble serum values. Besides increased enzymatic activity of MMP2 and MMP9 and TIMP1 mRNA, we propose MMP15 as an interesting novel candidate in HFpEF-driven cardiac fibrosis, as MMP15 mRNA was downregulated in HFpEF compared to controls.

Ideally, a combination of tissue and plasma concentration should be measured to correlate MMP and TIMP dynamics for a better clinical translatability. Furthermore, MMP and TIMP protein expression and enzymatic activity may differ in underlying co-morbidities associated with LVDD/HFpEF; we identified TIMP4 mRNA as a relevant candidate since it was downregulated in metabolic compared to hemodynamic models.

Besides these conclusions related to MMPs and TIMPs, a number of general recommendations related to experimental LVDD/HFpEF studies can be put forward. These are listed below.

Recommendations for future studies on LVDD/HFpEF:

We recommend future studies to focus on experimental LVDD/HFpEF models in which female gender is separately represented, on models that include pure volume overload and atrial fibrillation and on models of ageing and ageing in combination with either hemodynamic or metabolic models.

Perform adequate hemodynamic and metabolic phenotyping to more clearly discern differences between LVDD/HFpEF associated sub-groups. Focus should be on measuring invasive hemodynamic parameters instead of, or in addition to, (speckle tracking) echocardiography, since these appear to be more reliable across species and will decrease the translation bias to the clinic. Include a systolic parameter, in addition to establishing diastolic dysfunction, to ascertain pure LVDD/HFpEF. Lastly, we recommend a focus on spatiotemporal patterns of diastolic dysfunction and fibrosis, to ascertain whether clinical stages of LVDD/HFpEF are translatable to experimental models.

References

1. Kloch-Badelek M, Kuznetsova T, Sakiewicz W, Tikhonoff V, Ryabikov A, Gonzalez A, Lopez B, Thijs L, Jin Y, Malyutina S, Stolarz-Skrzypek K, Casiglia E, Diez J, Narkiewicz K, Kawecka-Jaszcz K, Staessen JA, European Project On Genes in Hypertension: Prevalence of left ventricular diastolic dysfunction in European populations based on cross-validated diagnostic thresholds. *Cardiovasc Ultrasound* **2012**, *10***:** 10.
2. Rasmussen-Torvik LJ, Colangelo, LA, Lima JAC, Jacobs DR, Rodriguez CJ, Gidding SS, Lloyd-Jones DM, Shah SJ: Prevalence and Predictors of Diastolic Dysfunction According to Different Classification Criteria: The Coronary Artery Risk Development in Young in Adults Study. *Am J Epidemiol* **2017**, *185***:** 1221-1227.
3. Palmiero P, Zito A, Maiello M, Cameli M, Modesti PA, Muiesan ML, Novo S, Saba PS, Scicchitano P, Pedrinelli R, Ciccone MM: Left ventricular diastolic function in hypertension: methodological considerations and clinical implications. *J Clin Med Res* **2015**, *7***:** 137-44.
4. Nagueh SF, Smiseth OA, Appleton CP, Byrd BF 3rd, Dokainish H, Edvardsen T, Flachskampf FA, Gillebert TC, Klein AL, Lancellotti P, Marino P, Oh JK, Alexandru Popescu B, Waggoner AD, Houston T, Oslo N, Phoenix A, Nashville T, Hamilton OC, Uppsala S, Ghent Liege B, Cleveland O, Novara I, Rochester M, Bucharest R, St. Louis M: Recommendations for the Evaluation of Left Ventricular Diastolic Function by Echocardiography: An Update from the American Society of Echocardiography and the European Association of Cardiovascular Imaging. *Eur Heart J Cardiovasc Imaging* **2016**, *17***:** 1321-1360.
5. Mitter SS, Shah SJ, Thomas JD: A Test in Context: E/A and E/e' to Assess Diastolic Dysfunction and LV Filling Pressure. *J Am Coll Cardiol* **2017**, *69***:** 1451-1464.
6. Valstar GB, Bots SH, Groepenhoff F, Gohar A, Rutten FH, Leiner T, Cramer MJM, Teske AJ, Suciadi LP, Menken R, Pasterkamp G, Asselbergs FW, Hofstra L, Bots ML, den Ruijter HM: Discovery of biomarkers for the presence and progression of left ventricular diastolic dysfunction and HEart faiLure with Preserved ejection Fraction in patients at risk for cardiovascular disease: rationale and design of the HELPFul case-cohort study in a Dutch cardiology outpatient clinic. *BMJ Open* **2019**, *9***:** e028408.
7. Guan Z, Liu S, Wang Y, Meng P, Zheng X, Jia D, Yang J, Ma C: Left ventricular systolic dysfunction potentially contributes to the symptoms in heart failure with preserved ejection fraction. *Echocardiography* **2019**, *36***:** 1825-1833.
8. Senni M, Paulus WJ, Gavazzi A, Fraser AG, Diez J, Solomon SD, Smiseth OA, Guazzi M, Lam CS, Maggioni AP, Tschope C, Metra M, Hummel SL, Edelmann F, Ambrosio G, Stewart Coats AJ, Filippatos GS, Gheorghiade M, Anker SD, Levy D, Pfeffer MA, Stough WG, Pieske BM: New strategies for heart failure with preserved ejection fraction: the importance of targeted therapies for heart failure phenotypes. *Eur Heart J* **2014**, *35***:** 2797-815.
9. Bhatia RS, Tu JV, Lee DS, Austin PC, Fang J, Haouzi A, Gong Y, Liu PP: Outcome of heart failure with preserved ejection fraction in a population-based study. *N Engl J Med* **2006**, *355***:** 260-269.
10. Devereux RB, Roman MJ, Liu JE, Welty TK, Lee EL, Rodeheffer R, Fabsitz RR, Howard BV: Congestive heart failure despite normal left ventricular systolic function in a population-based sample: the strong heart study. *Am J Cardiol* **2000**, *86***:** 1090-1096.
11. Valero-Munoz M, Backman W, Sam F: Murine Models of Heart Failure with Preserved Ejection Fraction: a "Fishing Expedition". *JACC Basic Transl Sci* **2017**, *2***:** 770-789.
12. Scantlebury DC, Borlaug BA: Why are women more likely than men to develop heart failure with preserved ejection fraction? *Curr Opin Cardiol* **2011**, *26***:** 562-8.
13. Dewan P, Rorth R, Raparelli V, Campbell RT, Shen L, Jhund PS, Petrie MC, Anand IS, Carson PE, Desai AS, Granger CB, Kober L, Komajda M, McKelvie RS, O'Meara E, Pfeffer MA, Pitt B, Solomon SD, Swedberg K, Zile MR, McMurray JJV: Sex-Related Differences in Heart Failure With Preserved Ejection Fraction. *Circ Heart Fail* **2019**, *12***:** e006539.
14. Borlaug BA, Redfield MM: Diastolic and systolic heart failure are distinct phenotypes within the heart failure spectrum. *Circulation* **2011**, *123***:** 2006-13; discussion 2014.

15. Chamberlain AM, St Sauver JL, Gerber Y, Manemann SM, Boyd CM, Dunlay SM, Rocca WA, Finney Rutten LJ, Jiang R, Weston SA, Roger VL: Multimorbidity in heart failure: a community perspective. *Am J Med* **2015**, *128***:** 38-45.
16. Swierblewska E, Wolf J, Kunicka K, Graff B, Polonis K, Hoffmann M, Chrostowska M, Szyndler A, Bandosz P, Graff B, Narkiewicz K: Prevalence and distribution of left ventricular diastolic dysfunction in treated patients with long-lasting hypertension. *Blood Press* **2018**, *27***:** 376-384.
17. van de Wouw J, Broekhuizen M, Sorop O, Joles JA, Verhaar MC, Duncker DJ, Danser AHJ, Merkus D: Chronic Kidney Disease as a Risk Factor for Heart Failure With Preserved Ejection Fraction: A Focus on Microcirculatory Factors and Therapeutic Targets. *Front Physiol* **2019**, *10***:** 1108.
18. Bouthoorn S, Valstar GB, Gohar A, den Ruijter HM, Reitsma HB, Hoes AW, Rutten FH: The prevalence of left ventricular diastolic dysfunction and heart failure with preserved ejection fraction in men and women with type 2 diabetes: A systematic review and meta-analysis. *Diab Vasc Dis Res* **2018**, *15***:** 477-493.
19. Russo C, Jin Z, Homma S, Rundek T, Elkind MS, Sacco RL, Di Tullio MR: Effect of obesity and overweight on left ventricular diastolic function: a community-based study in an elderly cohort. *J Am Coll Cardiol* **2011**, *57***:** 1368-74.
20. Savji N, Meijers WC, Bartz TM, Bhambhani V, Cushman M, Nayor M, Kizer JR, Sarma A, Blaha MJ, Gansevoort RT, Gardin JM, Hillege HL, Ji F, Kop WJ, Lau ES, Lee DS, Sadreyev R, van Gilst WH, Wang TJ, Zanni MV, Vasan RS, Allen NB, Psaty BM, van der Harst P, Levy D, Larson M, Shah SJ, de Boer RA, Gottdiener JS, Ho JE: The Association of Obesity and Cardiometabolic Traits With Incident HFpEF and HFrEF. *JACC Heart Fail* **2018**, *6***:** 701-709.
21. van Riet EE, Hoes AW, Wagenaar KP, Limburg A, Landman MA, Rutten FH: Epidemiology of heart failure: the prevalence of heart failure and ventricular dysfunction in older adults over time. A systematic review. *Eur J Heart Fail* **2016**, *18***:** 242-52.
22. Mohammed SF, Hussain S, Mirzoyev SA, Edwards WD, Maleszewski JJ, Redfield MM: Coronary microvascular rarefaction and myocardial fibrosis in heart failure with preserved ejection fraction. *Circulation* **2015**, *131***:** 550-9.
23. Mocan M, Mocan Hognogi LD, Anton FP, Chiorescu RM, Goidescu CM, Stoia MA, Farcas AD: Biomarkers of Inflammation in Left Ventricular Diastolic Dysfunction. *Dis Markers* **2019**, *2019***:** 7583690.
24. de Boer RA, De Keulenaer G, Bauersachs J, Brutsaert D, Cleland JG, Diez J, Du XJ, Ford P, Heinzel FR, Lipson KE, McDonagh T, Lopez-Andres N, Lunde IG, Lyon AR, Pollesello P, Prasad SK, Tocchetti CG, Mayr M, Sluijter JPG, Thum T, Tschope C, Zannad F, Zimmermann WH, Ruschitzka F, Filippatos G, Lindsey ML, Maack C, Heymans S: Towards better definition, quantification and treatment of fibrosis in heart failure. A scientific roadmap by the Committee of Translational Research of the Heart Failure Association (HFA) of the European Society of Cardiology. *Eur J Heart Fail* **2019**, *21***:** 272-285.
25. Frangogiannis NG: The extracellular matrix in myocardial injury, repair, and remodeling. *J Clin Invest* **2017**, *127***:** 1600-1612.
26. Li YY, McTiernan CF, Feldman AM: Proinflammatory cytokines regulate tissue inhibitors of metalloproteinases and disintegrin metalloproteinase in cardiac cells. *Cardiovascular Research* **1999**, *42***:** 162-172.
27. Fan D, Takawale A, Lee J, Kassiri Z: Cardiac fibroblasts, fibrosis and extracellular matrix remodeling in heart disease. *Fibrogenesis Tissue Repair* **2012**, 5:
28. Reinhardt D, Sigusch HH, Hensse J, Tyagi SC, Körfer R, Figulla HR: Cardiac remodelling in end stage heart failure: upregulation of matrix metalloproteinase (MMP) irrespective of the underlying disease, and evidence for a direct inhibitory effect of ACE inhibitors on MMP. *Heart* **2002**, 88: 525-530.
29. Antonov IB, Kozlov KL, Pal'tseva EM, Polyakova OV, Lin'kova NS: Matrix Metalloproteinases MMP-1 and MMP-9 and Their Inhibitor TIMP-1 as Markers of Dilated Cardiomyopathy in Patients of Different Age. *Bull Exp Biol Med* **2018**, 164: 550-553

30. Ngu JM, Teng G, Meijndert HC, Mewhort HE, Turnbull JD, Stetler-Stevenson WG, Fedak PW: Human cardiac fibroblast extracellular matrix remodeling: dual effects of tissue inhibitor of metalloproteinase-2. *Cardiovasc Pathol* **2014**, *23***:** 335-43
31. Pfeffer MA, Shah AM, Borlaug BA: Heart Failure With Preserved Ejection Fraction In Perspective. *Circ Res* **2019**, *124***:** 1598-1617.
32. Sava RI, Pepine CJ, March KL: Immune Dysregulation in HFpEF: A Target for Mesenchymal Stem/Stromal Cell Therapy. *J Clin Med* **2020**, *9***:**
33. Zachariah JP, Colan SD, Lang P, Triedman JK, Alexander ME, Walsh EP, Berul CI, Cecchin F: Circulating matrix metalloproteinases in adolescents with hypertrophic cardiomyopathy and ventricular arrhythmia. *Circ Heart Fail* **2012**, *5***:** 462-6.
34. Eiros R, Romero-Gonzalez G, Gavira JJ, Beloqui O, Colina I, Fortun Landecho M, Lopez B, Gonzalez A, Diez J, Ravassa S: Does Chronic Kidney Disease Facilitate Malignant Myocardial Fibrosis in Heart Failure with Preserved Ejection Fraction of Hypertensive Origin? *J Clin Med* **2020**, *9***:**
35. Agrinier N, Thilly N, Boivin JM, Dousset B, Alla F, Zannad F: Prognostic value of serum PIIINP, MMP1 and TIMP1 levels in hypertensive patients: a community-based prospective cohort study. *Fundam Clin Pharmacol* **2013**, *27***:** 572-80.
36. DeLeon-Pennell KY, Meschiari CA, Jung M, Lindsey ML: Matrix Metalloproteinases in Myocardial Infarction and Heart Failure. *Prog Mol Biol Transl Sci* **2017**, *147***:** 75-100.
37. Papazova DA, Oosterhuis NR, Gremmels H, van Koppen A, Joles JA, Verhaar MC: Cell-based therapies for experimental chronic kidney disease: a systematic review and meta-analysis. *Dis Model Mech* **2015**, *8***:** 281-93.
38. DerSimonian R, Laird N: Meta-analysis in Clinical Trials. *Controlled Clinical Trials* **1986**, *7***:** 177-188.
39. Chiao YA, Ramirez TA, Zamilpa R, Okoronkwo SM, Dai Q, Zhang J, Jin YF, Lindsey ML: Matrix metalloproteinase-9 deletion attenuates myocardial fibrosis and diastolic dysfunction in ageing mice. *Cardiovasc Res* **2012**, *96***:** 444-55.
40. Ma Y, Chiao YA, Zhang J, Manicone AM, Jin YF, Lindsey ML: Matrix metalloproteinase-28 deletion amplifies inflammatory and extracellular matrix responses to cardiac aging. *Microsc Microanal* **2012**, *18***:** 81-90.
41. Engebretsen KV, Lunde IG, Strand ME, Waehre A, Sjaastad I, Marstein HS, Skrbic B, Dahl CP, Askevold ET, Christensen G, Bjornstad JL, Tonnessen T: Lumican is increased in experimental and clinical heart failure, and its production by cardiac fibroblasts is induced by mechanical and proinflammatory stimuli. *FEBS J* **2013**, *280***:** 2382-98.
42. Fan D, Takawale A, Basu R, Patel V, Lee J, Kandalam V, Wang X, Oudit GY, Kassiri Z: Differential role of TIMP2 and TIMP3 in cardiac hypertrophy, fibrosis, and diastolic dysfunction. *Cardiovasc Res* **2014**, *103***:** 268-80.
43. Reddy SS, Agarwal H, Barthwal MK: Cilostazol ameliorates heart failure with preserved ejection fraction and diastolic dysfunction in obese and non-obese hypertensive mice. *J Mol Cell Cardiol* **2018**, *123***:** 46-57.
44. Sam F, Duhaney TA, Sato K, Wilson RM, Ohashi K, Sono-Romanelli S, Higuchi A, De Silva DS, Qin F, Walsh K, Ouchi N: Adiponectin deficiency, diastolic dysfunction, and diastolic heart failure. *Endocrinology* **2010**, *151***:** 322-31.
45. Zhong J, Basu R, Guo D, Chow FL, Byrns S, Schuster M, Loibner H, Wang XH, Penninger, JM, Kassiri Z, Oudit GY: Angiotensin-converting enzyme 2 suppresses pathological hypertrophy, myocardial fibrosis, and cardiac dysfunction. *Circulation* **2010**, *122***:** 717-28,
46. Westermann D, Rutschow S, Jager S, Linderer A, Anker S, Riad A, Unger T, Schultheiss HP, Pauschinger M, Tschope C: Contributions of inflammation and cardiac matrix metalloproteinase activity to cardiac failure in diabetic cardiomyopathy: the role of angiotensin type 1 receptor antagonism. *Diabetes* **2007**, *56***:** 641-6.
47. Tate M, Robinson E, Green BD, McDermott BJ, Grieve DJ: Exendin-4 attenuates adverse cardiac remodelling in streptozocin-induced diabetes via specific actions on infiltrating macrophages. *Basic Res Cardiol* **2016**, *111***:** 1.

48. Matsushima S, Kinugawa S, Ide T, Matsusaka H, Inoue N, Ohta Y, Yokota T, Sunagawa K, Tsutsui H: Overexpression of glutathione peroxidase attenuates myocardial remodeling and preserves diastolic function in diabetic heart. *Am J Physiol Heart Circ Physiol* **2006**, *291***:** H2237-45.
49. Tsutsui H, Matsushima S, Kinugawa S, Ide T, Inoue N, Ohta Y, Yokota T, Hamaguchi S, Sunagawa K: Angiotensin II type 1 receptor blocker attenuates myocardial remodeling and preserves diastolic function in diabetic heart. *Hypertens Res* **2007**, *30***:** 439-449.
50. Zibadi S, Cordova F, Slack EH, Watson RR, Larson DF: Leptin's regulation of obesity-induced cardiac extracellular matrix remodeling. *Cardiovasc Toxicol* **2011**, *11***:** 325-33.
51. Brandt MM, Nguyen ITN, Krebber MM, van de Wouw J, Mokry M, Cramer MJ, Duncker DJ, Verhaar MC, Joles JA, Cheng C: Limited synergy of obesity and hypertension, prevalent risk factors in onset and progression of heart failure with preserved ejection fraction. *J Cell Mol Med* **2019**, *23***:** 6666-6678.
52. Falcao-Pires I, Palladini G, Goncalves N, van der Velden J, Moreira-Goncalves D, Miranda-Silva D, Salinaro F, Paulus WJ, Niessen HW, Perlini S, Leite-Moreira AF: Distinct mechanisms for diastolic dysfunction in diabetes mellitus and chronic pressure-overload. *Basic Res Cardiol* **2011**, *106***:** 801-14.
53. Pagan LU, Damatto RL, Gomes MJ, Lima ARR, Cezar MDM, Damatto FC, Reyes DRA, Caldonazo TMM, Polegato BF, Okoshi MP, Okoshi K: Low-intensity aerobic exercise improves cardiac remodelling of adult spontaneously hypertensive rats. *J Cell Mol Med* **2019**, *23***:** 6504-6507.
54. Sakata Y, Yamamoto K, Mano T, Nishikawa N, Yoshida J, Hori M, Miwa T, Masuyama T: Activation of matrix metalloproteinases precedes left ventricular remodeling in hypertensive heart failure rats: its inhibition as a primary effect of Angiotensin-converting enzyme inhibitor. *Circulation* **2004**, *109***:** 2143-9.
55. Xu X, Ding F, Pang J, Gao X, Xu RK, Hao W, Cao JM, Chen C: Chronic administration of hexarelin attenuates cardiac fibrosis in the spontaneously hypertensive rat. *Am J Physiol Heart Circ Physiol* **2012**, *303***:** H703-11.
56. Samuel CS, Hewitson TD, Zhang Y, Kelly DJ: Relaxin ameliorates fibrosis in experimental diabetic cardiomyopathy. *Endocrinology* **2008**, *149***:** 3286-93.
57. Marshall KD, Muller BN, Krenz M, Hanft LM, McDonald KS, Dellsperger KC, Emter CA: Heart failure with preserved ejection fraction: chronic low-intensity interval exercise training preserves myocardial O_2 balance and diastolic function. *J Appl Physiol (1985)* **2013**, *114***:** 131-47.
58. Olver TD, Edwards JC, Jurrissen TJ, Veteto AB, Jones JL, Gao C, Rau C, Warren CM, Klutho PJ, Alex L, Ferreira-Nichols SC, Ivey JR, Thorne PK, McDonald KS, Krenz M, Baines CP, Solaro RJ, Wang Y, Ford DA, Domeier TL, Padilla J, Rector RS, Emter CA: Western Diet-Fed, Aortic-Banded Ossabaw Swine: A Preclinical Model of Cardio-Metabolic Heart Failure. *JACC Basic Transl Sci* **2019**, *4***:** 404-421.
59. Sorop O, Heinonen I, van Kranenburg M, van de Wouw J, de Beer VJ, Nguyen ITN, Octavia Y, van Duin RWB, Stam K, van Geuns RJ, Wielopolski PA, Krestin GP, van den Meiracker AH, Verjans R, van Bilsen M, Danser AHJ, Paulus WJ, Cheng C, Linke WA, Joles JA, Verhaar MC, van der Velden J, Merkus D, Duncker DJ: Multiple common comorbidities produce left ventricular diastolic dysfunction associated with coronary microvascular dysfunction, oxidative stress, and myocardial stiffening. *Cardiovasc Res* **2018**, *114***:** 954-964.
60. Nachar W, Merlet N, Maafi F, Shi Y, Mihalache-Avram T, Mecteau M, Ferron M, Rheaume E, Tardif JC: Cardiac inflammation and diastolic dysfunction in hypercholesterolemic rabbits. *PLoS One* **2019**, *14***:** e0220707.
61. Tozzi R, Palladini G, Fallarini S, Nano R, Gatti C, Presotto C, Schiavone A, Micheletti R, Ferrari P, Fogari R, Perlini S: Matrix metalloprotease activity is enhanced in the compensated but not in the decompensated phase of pressure overload hypertrophy. *Am J Hypertens* **2007**, *20***:** 663-9.
62. Ferrari R, Bohm M, Cleland JG, Paulus WJ, Pieske B, Rapezzi C, Tavazzi L: Heart failure with preserved ejection fraction: uncertainties and dilemmas. *Eur J Heart Fail* **2015**, *17***:** 665-71.

63. Thomas L, Marwick TH, Popescu BA, Donal E, Badano LP: Left Atrial Structure and Function, and Left Ventricular Diastolic Dysfunction: JACC State-of-the-Art Review. *J Am Coll Cardiol* **2019**, *73***:** 1961-1977.
64. Nagueh SF: Left Ventricular Diastolic Function: Understanding Pathophysiology, Diagnosis, and Prognosis With Echocardiography. *JACC Cardiovasc Imaging* **2020**, *13***:** 228-244.
65. Wang J, Khoury DS, Yue Y, Torre-Amione G, Nagueh SF: Preserved left ventricular twist and circumferential deformation, but depressed longitudinal and radial deformation in patients with diastolic heart failure. *Eur Heart J* **2008**, *29***:** 1283-9.
66. Choudhury A, Magoon R, Malik V, Kapoor PM, Ramakrishnan S: Studying diastology with speckle tracking echocardiography: The essentials. *Ann Card Anaesth* **2017**, *20***:** S57-S60.
67. Mottram PM, Marwick TH: Assessment of diastolic function: what the general cardiologist needs to know. *Heart* **2005**, *91***:** 681-95.
68. Garcia MJ, Thomas JD, Klein AL: New Doppler echocardiographic applications for the study of diastolic function. *Journal of the American College of Cardiology* **1998**, *32***:** 865-875.
69. Schnelle M, Catibog N, Zhang M, Nabeebaccus AA, Anderson G, Richards DA, Sawyer G, Zhang X, Toischer K, Hasenfuss G, Monaghan MJ, Shah AM: Echocardiographic evaluation of diastolic function in mouse models of heart disease. *J Mol Cell Cardiol* **2018**, *114***:** 20-28.
70. Schaefer A, Meyer GP, Brand B, Hilfiker-Kleiner D, Drexler H, Klein G: Effects of Anesthesia on Diastolic Function in Mice Assessed by Echocardiography. *Echocardiography* **2005**, *22***:** 665-670.
71. Heerdt PM, Gandhi CD, Dickstein ML: Disparity of isoflurane effects on left and right ventricular afterload and hydraulic power generation in swine. *Anesth Analg* **1998**, *87***:** 511-521.
72. Hettrick DA, Pagal PS, Kersten JR, Lowe D, Warltier DC: The effects of isoflurane and halothane on left ventricular afterload in dogs with dilated cardiomyopathy. *Anesth Analg* **1997**, *85***:** 979-986.
73. Shillcutt SK, Chacon MM, Brakke TR, Roberts EK, Schulte TE, Markin N: Heart Failure With Preserved Ejection Fraction: A Perioperative Review. *J Cardiothorac Vasc Anesth* **2017**, *31***:** 1820-1830.
74. Penicka M, Bartunek J, Trakalova H, Hrabakova H, Maruskova M, Karasek J, Kocka V: Heart failure with preserved ejection fraction in outpatients with unexplained dyspnea: a pressure-volume loop analysis. *J Am Coll Cardiol* **2010**, *55***:** 1701-10.
75. Runte KE, Bell SP, Selby DE, Haussler TN, Ashikaga T, LeWinter MM, Palmer BM, Meyer M: Relaxation and the Role of Calcium in Isolated Contracting Myocardium From Patients With Hypertensive Heart Disease and Heart Failure With Preserved Ejection Fraction. *Circ Heart Fail* **2017**, *10***:**
76. Kasner M, Westermann D, Lopez B, Gaub R, Escher F, Kuhl U, Schultheiss HP, Tschope C: Diastolic tissue Doppler indexes correlate with the degree of collagen expression and cross-linking in heart failure and normal ejection fraction. *J Am Coll Cardiol* **2011**, *57***:** 977-85.
77. van Dijk CGM, Oosterhuis NR, Xu YJ, Brandt M, Paulus WJ, van Heerebeek L, Duncker DJ, Verhaar MC, Fontoura D, Lourenco AP, Leite-Moreira AF, Falcao-Pires I, Joles JA, Cheng C: Distinct Endothelial Cell Responses in the Heart and Kidney Microvasculature Characterize the Progression of Heart Failure With Preserved Ejection Fraction in the Obese ZSF1 Rat With Cardiorenal Metabolic Syndrome. *Circ Heart Fail* **2016**, *9***:** e002760.
78. She G, Ren YJ, Wang Y, Hou MC, Wang HF, Gou W, Lai BC, Lei T, Du XJ, Deng XL: KCa3.1 Channels Promote Cardiac Fibrosis Through Mediating Inflammation and Differentiation of Monocytes Into Myofibroblasts in Angiotensin II -Treated Rats. *J Am Heart Assoc* **2019**, *8***:** e010418.
79. Santiago JJ, Dangerfield AL, Rattan SG, Bathe KL, Cunnington RH, Raizman JE, Bedosky KM, Freed DH, Kardami E, Dixon IM: Cardiac fibroblast to myofibroblast differentiation in vivo and in vitro: expression of focal adhesion components in neonatal and adult rat ventricular myofibroblasts. *Dev Dyn* **2010**, *239***:** 1573-84.
80. Rosenkranz S: TGF-beta1 and angiotensin networking in cardiac remodeling. *Cardiovasc Res* **2004**, *63***:** 423-32.

81. Das S, Frisk C, Eriksson MJ, Walentinsson A, Corbascio M, Hage C, Kumar C, Asp M, Lundeberg J, Maret E, Persson H, Linde C, Persson B: Transcriptomics of cardiac biopsies reveals differences in patients with or without diagnostic parameters for heart failure with preserved ejection fraction. *Sci Rep* **2019**, *9***:** 3179.
82. Martos R, Baugh J, Ledwidge M, O'Loughlin C, Murphy NF, Conlon C, Patle A, Donnelly SC, McDonald K: Diagnosis of heart failure with preserved ejection fraction: improved accuracy with the use of markers of collagen turnover. *Eur J Heart Fail* **2009**, *11***:** 191-7.
83. Zile MR, Desantis SM, Baicu CF, Stroud RE, Thompson SB, McClure CD, Mehurg SM, Spinale FG: Plasma biomarkers that reflect determinants of matrix composition identify the presence of left ventricular hypertrophy and diastolic heart failure. *Circ Heart Fail* **2011**, *4***:** 246-56.
84. Müller-Brunotte R, Kahan T, López B, Edner M, González A, Díez J, Malmqvist K: Myocardial fibrosis and diastolic dysfunction in patients with hypertension: results from the Swedish Irbesartan Left Ventricular Hypertrophy Investigation versus Atenolol (SILVHIA). *Journal of Hypertension* **2007**, *25***:** 1958-1966.
85. Xu H, Qing T, Shen Y, Huang J, Liu Y, Zhen T, Xing K, Zhu S, Luo M: RNA-seq analyses the effect of high-salt diet in hypertension. *Gene* **2018**, 677: 245-250.
86. Lindsay MM, Maxwell P, Dunn FG: TIMP-1: a marker of left ventricular diastolic dysfunction and fibrosis in hypertension. *Hypertension* **2002**, *40***:** 136-41.
87. Moore L, Fan D, Basu R, Kandalam V, Kassiri Z: Tissue inhibitor of metalloproteinases (TIMPs) in heart failure. *Heart Fail Rev* **2012**, *17***:** 693-706.
88. Gaffney J, Solomonov I, Zehorai E, Sagi I: Multilevel regulation of matrix metalloproteinases in tissue homeostasis indicates their molecular specificity in vivo. *Matrix Biol* **2015**, *44-46***:** 191-9.
89. Zhang Y, Shao L, Ma A, Guan G, Wang J, Wang Y, Tian G: Telmisartan delays myocardial fibrosis in rats with hypertensive left ventricular hypertrophy by TGF-beta1/Smad signal pathway. *Hypertens Res* **2014**, *37***:** 43-9.
90. Lu L, Zhang Q, Pu LJ, Peng WH, Yan XX, Wang LJ, Chen QJ, Zhu ZB, Michel JB, Shen WF: Dysregulation of matrix metalloproteinases and their tissue inhibitors is related to abnormality of left ventricular geometry and function in streptozotocin-induced diabetic minipigs. *Int J Exp Pathol* **2008**, *89***:** 125-37.
91. Sakamuri SVP, Watts R, Takawale A, Wang X, Hernandez-Anzaldo S, Bahitman W, Fernandez-Patron C, Lehner R, Kassiri Z: Absence of Tissue Inhibitor of Metalloproteinase-4 (TIMP4) ameliorates high fat diet-induced obesity in mice due to defective lipid absorption. *Sci Rep* **2017**, 7:
92. Chaturvedi P, Tyagi SC: Epigenetic silencing of TIMP4 in heart failure. *J Cell Mol Med* **2016**, 20: 2089-2101.
93. Ahmed SH, Clark LL, Pennington WR, Webb CS, Bonnema DD, Leonardi AH, McClure CD, Spinale FG, Zile MR: Matrix metalloproteinases/tissue inhibitors of metalloproteinases: relationship between changes in proteolytic determinants of matrix composition and structural, functional, and clinical manifestations of hypertensive heart disease. *Circulation* **2006**, *113***:** 2089-96.
94. Uijl A, Koudstaal S, Vaartjes I, Boer JMA, Verschuren WMM, van der Schouw YT, Asselbergs FW, Hoes AW, Sluijs I: Risk for Heart Failure: The Opportunity for Prevention With the American Heart Association's Life's Simple 7. *JACC Heart Fail* **2019**, 7: 637-647.
95. Davison BA, Takagi K, Senger S, Koch G, Metra M, Kimmoun A, Mebazaa A, Voors AA, Nielsen OW, Chioncel O, Pang PS, Greenberg BH, Maggioni AP, Cohen-Solal A, Ertl G, Sato N, Teerlink JR, Filippatos G, Ponikowski P, Gayat E, Edwards C, Cotter G: Mega-trials in heart failure: effects of dilution in examination of new therapies. *Eur J Heart Fail* **2020**, ejhf.1780

Supplemental Data

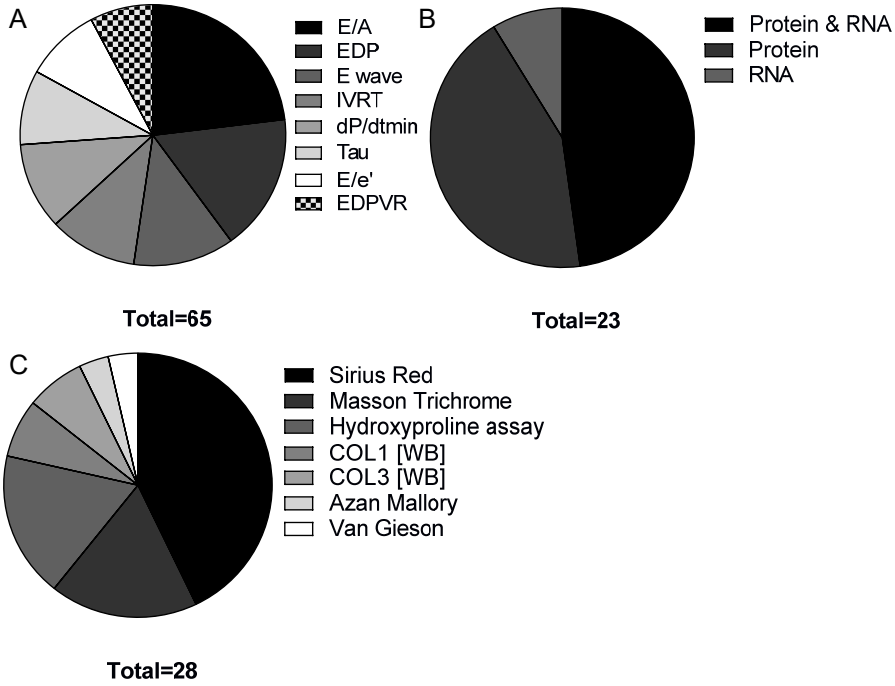

Supplemental Figure 1. Study characteristics of cardiac and fibrotic outcomes. **(A)** Diastolic parameters measured in number of studies. **(B)** Total number of studies measuring fibrotic outcomes, subdivided in protein analysis (histological staining, WB and collagen content assays) and mRNA analysis (qPCR analysis). **(C)** Different protein targets analyzed for fibrotic outcomes. COL1, Collagen type 1; COL3, Collagen type 3; dP/dt_{min}, minimum rate of pressure change; E wave, peak early diastolic transmitral velocity; E/A, ratio between peak early diastolic transmitral velocity (E) and late (atrial) transmitral flow velocity (A); E/e', ratio between peak early diastolic transmitral velocity (E) and early diastolic mitral annular velocity (e'); EDP, end diastolic pressure; EDPVR, end diastolic pressure volume relationship; IVRT, isovolumetric relaxation time; Tau, time constant of ventricular relaxation; WB, western blot.

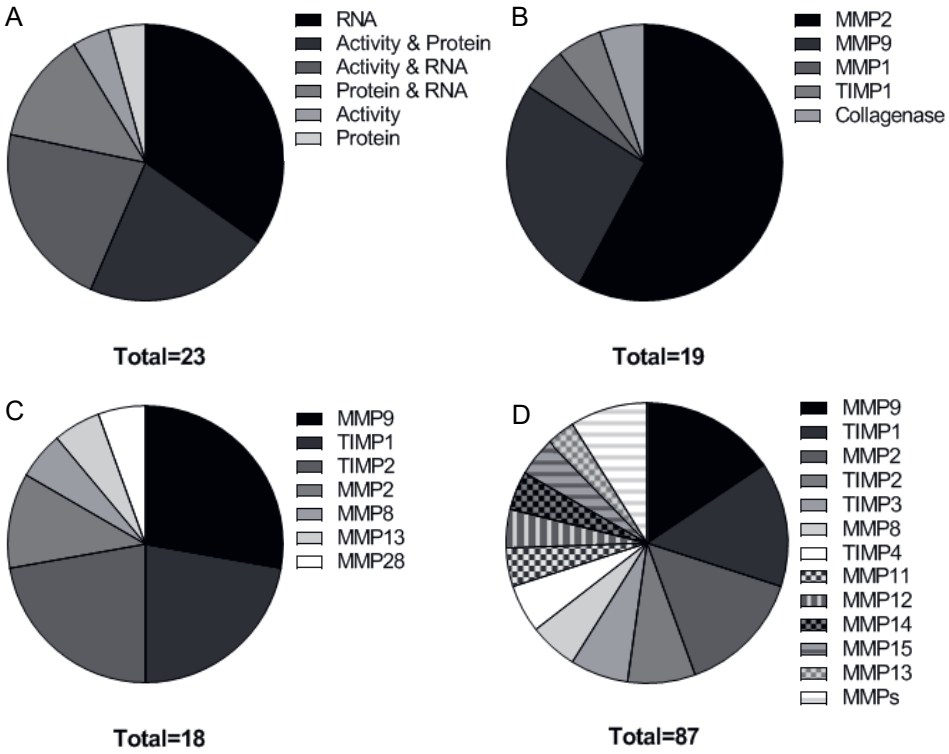

Supplemental Figure 2. Study characteristics of MMPs and TIMPs. **(A)** Total number of studies measuring MMP and TIMP outcomes, subdivided in MMP activity, protein analysis (WB, ELISA), mRNA expression (qPCR, mRNA sequencing) or a combination of measurements. **(B)** Different MMPs and TIMP1 targets analyzed for their enzymatic activity. **(C)** Different MMP and TIMP targets analyzed for their protein expression. **(D)** Different MMPs and TIMPs targets analyzed for their mRNA expression. Multiple MMP family members were clustered in the part named 'MMPs'. These MMP family members were not measured often and can be found back in Supplemental Table 4. MMP, matrix metalloproteinase; TIMP, tissue inhibitor of metalloproteinase.

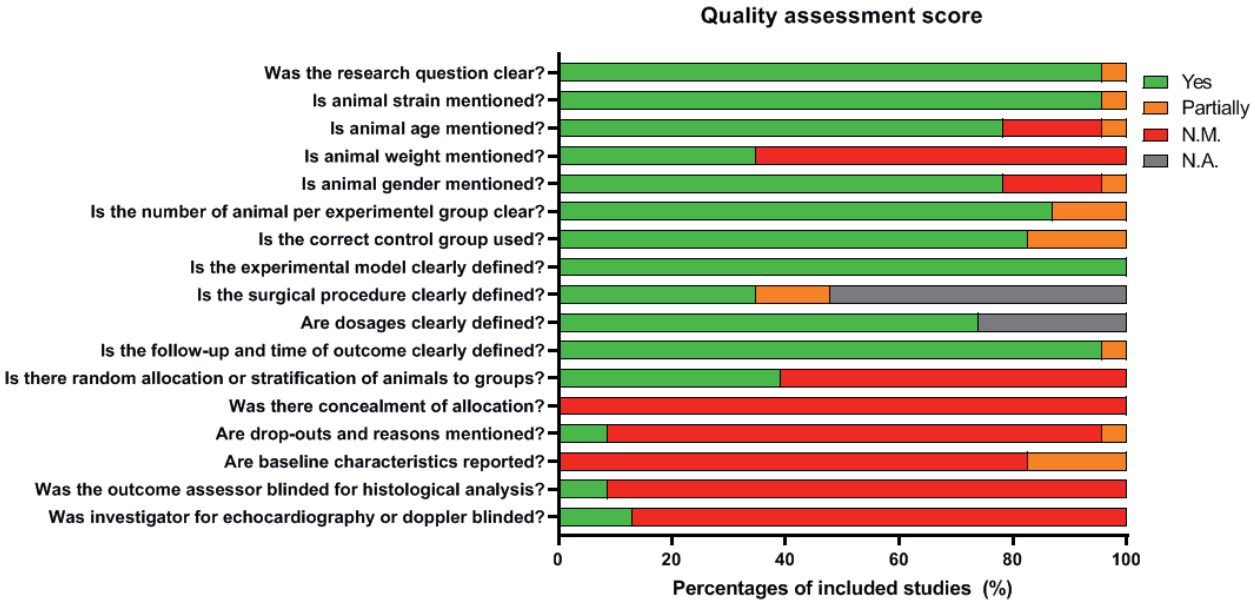

Supplemental Figure 3. Quality assessment score. Shown is the quality assessment score (Risk of Bias tool) for the 23 included studies. This is an adapted version from Papazova *et al*., 2015 [37].

Supplemental Tables

Supplemental tables can be downloaded from:

https://www.mdpi.com/1422-0067/21/18/6742

Or:

Chapter 8

Distinct endothelial cell responses in the heart and kidney microvasculature characterize the progression of heart failure with preserved ejection fraction in the obese ZSF1 rat with cardio-renal metabolic syndrome

Christian G.M. van Dijk*, Nynke R. Oosterhuis*, Yan Juan Xu*, Maarten Brandt, Walter J. Paulus, Loek van Heerebeek, Dirk J. Duncker, Marianne C. Verhaar, Dulce Fontoura, André P Lourenço, Adelino F. Leite-Moreira, Inês Falcão-Pires, Jaap A. Joles, Caroline Cheng

Circulation Heart Failure. 2016 Apr;9(4):e002760

* Authors contributed equally

Abstract

The combination of cardiac and renal disease driven by metabolic risk factors, referred to as cardio-renal metabolic syndrome (CRMS), is increasingly recognized as a critical pathological entity. The contribution of (micro)vascular injury to CRMS is considered to be substantial. However, mechanistic studies are hampered by lack of *in vivo* models that mimic the natural onset of the disease. Here we evaluated the coronary and renal microvasculature during CRMS development in obese diabetic Zucker fatty/Spontaneously hypertensive heart failure F1 hybrid (ZSF1) rats.

Echocardiographic, urine and blood evaluations were conducted in three groups (Wistar-Kyoto; lean ZSF1; obese ZSF1) at 20 and 25 weeks of age. Immunohistological evaluation of renal and cardiac tissues was conducted at both time points. At 20 and 25 weeks, obese ZSF1 rats showed higher body weight, significant left ventricular (LV) hypertrophy, and impaired diastolic function compared to all other groups. Indices of systolic function did not differ between groups. Obese ZSF1 rats developed hyperproliferative vascular foci in the sub-endocardium, which lacked microvascular organization and were predilection sites of inflammation and fibrosis. In the kidney, obese ZSF1 animals showed regression of the peritubular and glomerular microvasculature, accompanied by tubulo-interstitial damage, glomerulosclerosis, and proteinuria.

The obese ZSF1 rat strain is a suitable *in vivo* model for CRMS, sharing characteristics with the human syndrome during the earliest onset of disease. In these rats, CRMS induces microvascular fibrotic responses in heart and kidneys, associated with functional impairment of both organs.

Introduction

Cardio-renal syndrome (CRS) represents the interdependent relation between the heart and kidneys during disease onset and progression. This important link between cardiac and renal pathophysiology is demonstrated by the high prevalence of chronic kidney disease (CKD) in heart failure patients and vice versa, while dysfunction in both organs is strongly associated with increased morbidity and mortality [1]. Recent findings have highlighted the connection between metabolic risk factors and CRS:

Metabolic syndrome is a multitude of risk factors that includes high blood pressure, hyperglycemia, obesity and dyslipidemia from which at least 3 occur together, thereby functioning as a synergistic complex of risk factors that drastically increase the risk of cardiovascular disease [2]. This syndrome is growing ever more prevalent, affecting ~20% of adults in the aging Western population [3]. A significant amount of evidence clearly shows a strong relation between metabolic syndrome and onset and progression of cardiovascular disease [4,5]. In regard to renal disease, a clear association between metabolic syndrome and renal dysfunction has also been described [4,6]. Thus, metabolic risk factors appear to be the driving force behind cardiovascular and CKD disease, and hence CRS. Similarly, the association between all individual components of metabolic syndrome and CRS development is now well established and is increasingly recognized as a separate disease-entity termed CRMS [1,6,7].

At present, rodent CRS models typically involve renal ablation and coronary ligation, either alone or in combination to directly induce diastolic and systolic dysfunction [8]. An *in vivo* model that utilizes metabolic triggers may be more relevant for studies that focus on onset and early progression of CRS. Here we propose the obese diabetic Zucker fatty/Spontaneously hypertensive heart failure F1 hybrid (ZSF1) rat strain as a model for CRMS [9]. Recently, we have reported that obese ZSF1 (ZSF1 Ob) rats develop HFpEF between week 10 and 20 of natural aging [9]. The ZSF1 strain also autonomously develops renal disease, making it suitable for studying CKD in relation to metabolic triggers [10,11]. HFpEF development in ZSF1 Ob rats was characterized by progressive left ventricle (LV) diastolic dysfunction, concentric LV remodeling, and hypertrophy [12]. This was preceded by insulin resistance, glycosuria and proteinuria [9]. This phenotype is consistent with CRMS in humans, which is defined by the presence of metabolic syndrome in addition to insulin resistance, microalbuminurina and/or reduced renal function [13]. Therefore, these data indicate that the obese ZSF1 strain may be used as an *in vivo* model of CRS early progression against a well-defined background of metabolic injury, thus providing a model to study CRMS. ZSF1 Ob rats also suffer from increased vascular stiffness and lack of NO response, consistent with endothelial dysfunction [14]. Persistent nitrosative/oxidative stress and

inflammation have been observed in the coronary microvascular bed of HFpEF patients [15,16]. Vascular oxidative stress leading to endothelial dysfunction and inflammation has been proposed as one of the key pathways in HFpEF [17] and CRS [18-20], and is strongly linked to metabolic risk factors [19,21]. However, details of the cardiac and renal microvasculature response in CRMS remain to be investigated. Consequently, we studied the microvascular changes in the heart and kidney during progression of HFpEF and renal dysfunction in ZSF1 Ob rats.

Materials and Methods

Ethics

All animal studies were carried out in accordance with the Council of Europe Convention (Directive (2010/63/EU) for the protection of vertebrate animals used for experimental and other scientific purposes with the approval of the National and Local Animal Care Committee of Faculty of Medicine of Porto. Animal experiments were performed according to ARRIVE guidelines.

Animal model

Nine week old male Wistar Kyoto (WKY, n=12), ZSF1 Lean (ZSF1 Ln, n=10) and ZSF1 Obese rats (ZSF1 Ob, n=12) were obtained from Charles River (Barcelona, Spain) and housed in a light, temperature and humidity controlled environment following a 12 hour light-dark cycle with free access to water and standard diet (Purina diet #5008). Phenotypic evaluation was conducted after 1 week of acclimatization, consisting of metabolic and echocardiography studies. Weight gain was monitored every third day. In weeks 18 and 24, phenotypic evaluation was repeated. Cardiac hemodynamic measurements followed by euthanasia were performed at 20^{th} and 25^{th} week. Heart and kidneys were excised, weighed, fixed in formaldehyde and embedded in paraffin for further analysis.

Echocardiography evaluation

Rats were anaesthetized by inhalation of sevoflurane (8 and 2.5–3% for induction and maintenance respectively; Penlon Sigma Delta), mechanically ventilated while homeostasis was maintained by anesthetic monitoring. After applying echocardiography gel a linear 15MHz probe (Sequoia 15L8W) was positioned on the thorax. Systolic and diastolic wall thickness and cavity dimensions were recorded in M-mode and 2D echocardiography, at the level just above the papillary muscles in the parasternal short axis view. The long axis diastolic dimensions of the left ventricle and transverse aortic root diameter were recorded by 2D and M-mode echocardiography respectively, in the parasternal long axis view. Aortic flow velocity

was recorded by pulsed-wave Doppler above the aortic valve. Mitral flow velocity tracings were obtained with pulsed-wave Doppler above the mitral leaflets, peak systolic tissue velocity and E' were measured with tissue Doppler at the medial mitral annulus and lateral mitral annulus, respectively, and left atrial dimensions were measured at their maximum, by 2D echocardiography in the four chamber view. Acquisitions were conducted while suspending mechanical ventilation and recordings were averaged from three consecutive heartbeats (Siemens Acuson Sequoia C512). Left ventricular (LV) mass and volumes were calculated by the 2D area-length method and M-mode. For evaluation of diastolic function, peak velocity of early (E) and late (A) mitral inflow and the ratio of E over E' were measured as an indicator of LV filling pressure. Myocardial performance index was retrieved from the mitral flow pattern. Volumes and masses were indexed for body surface area as defined by 9.1*body weight $(BW)^{2/3}$.

Measurement of biochemical variables

Plasma samples were treated with chloroform to remove lipids which interfere with plasma analysis. Chloroform and plasma (1:1) were centrifuged at 1000 x g for 30 min. Supernatant was transferred to a new tube a new tube and centrifuged at 10000 x g for 45 min. Supernatant was transferred to a new tube and used for creatinine and urea analysis. Plasma and urine creatinine were enzymatically measured (DiaSys PAP FS; DiaSys Diagnostic Systems, Holzheim, Germany). Plasma urea was enzymatically measured (DiaSys Urea CT FS; Diasys Diagnostic systems). Total protein excretion was measured using Bradford method (BioRad Laboratories, Veenendaal, Netherlands). Thiobarbituric Acid Reactive Substances (TBARS) as indicators for the level of systemic oxidative stress were measured colorimetrically (Cayman Chemical, Ann Arbor, MI).

Hemodynamic evaluation

Animals were sedated with 100 µg.kg-1 and 5 mg.kg-1 intraperitoneal fentanyl and midazolam, respectively, followed by anesthesia (8 and 2.5-3% sevoflurane for induction and maintenance, respectively; Penlon Sigma Delta), endothracheal intubation, and mechanical ventilation (TOPO, Kent scientific). Fluid replacement with warm Ringer's lactate at 32 $mL.kg^{-1}.h^{-1}$ (Ne-1000, New Era Pump Systems) was administered through a peripheral dorsal foot vein catheter (24G) and animals were maintained at 38ºC on a heating pad. A flowmeter probe was transiently placed in the ascending aorta for cardiac output (CO) calibration (2.5PS, Transonic). A pressure-volume catheter (SPR-847 Millar Instruments) was inserted in the left ventricle (LV) apex and placed along the LV long axis. 3-0 silk threads were placed around the inferior vena cava to enable transient occlusions. Parallel conductance was determined

by 40 µl 10% hypertonic saline injection and slope factor α was derived by simultaneous measurement of CO by a flowmeter placed around the ascending aorta (TS420, Transonic). After a stabilization period of 30 min, recordings were obtained at suspended end-expiration. Transient 5-7 cycle occlusions of the inferior vena cava occlusions were performed to obtain load independent indexes of LV chamber stiffness by fitting an exponential function to the end-diastolic pressure-volume relationship (EDPVR) as previously described [9]. Single beat occlusions of the ascending aorta were performed to assess diastolic response to isovolumic afterload as reported [22]. Three separate acquisitions were obtained and averaged in each animal. Data with arrhythmia, hear rate changes higher than 2% or evidence of incomplete afterload elevations were excluded. Resting periods were allowed between each intervention. Signals were continuously acquired (MPVS 300, Millar Instruments), recorded at 1000 Hz (ML889 PowerLab 16/30, ADinstruments), and analyzed (PVAN 3.5, Millar Instruments). To account for large differences in body weight between groups, volumes were indexed for body surface area as estimated by 9.1*body weight in grams$^{3/4}$. Upon completion of experiments, blood (4mL) was collected for volume calibration (910-1048, Millar instruments) and storage. Finally the anesthetized animals were euthanized by exsanguination.

Right ventricle (RV) and LV + interventricular septum (IVS) were weighed after dissection, and tibia length (TL) was measured. Samples were snap-frozen and stored at -80ºC or processed for histology. Weights were normalized to TL.

Renal and cardiac immunohistochemistry

Three to five µm sections were sliced from formaldehyde-fixed, paraffin-embedded kidneys and hearts. For the analysis of the kidneys, tubule-interstitial (TI) damage and glomerulosclerosis (GS) were scored on Periodic-acid Schiff (PAS) stained sections in a blinded manner. TI damage was scored on a scale of 1-5 in at least 10 different non-overlapping fields per animal. Scored variables include the amount of per-tubular inflammatory infiltrate, interstitial fibrosis, tubular atrophy and tubular dilatation. GS was scored on at least 30 separate glomeruli by quadrants, on a scale of 0 to 4, with 0 meaning no quadrant affect and 4 meaning that the whole glomerulus was affected. Scored variables for GS were matrix expansion, sclerosis, adhesion of Bowman's capsule and dilation. For both TI and GS a total damage score was calculated.

Peritubular and glomerular endothelium was stained with a primary antibody for JG12 (mouse anti-JG12, BMS1104, 1:200, Bender Medsystems GmbH, Vienne, Austria). Deparaffinized sections were subjected to heat-induced antigen retrieval by incubation with citrate/HCl buffer (pH 6.0) at 100ºC for 20 min. As a secondary antibody brightvision-HRP (ImmunoLogic, Duiven, Netherlands) was used. Positive cells were visualized with Vector Nova Red (Vector Laboratories, Burlingame, CA) and counterstained with hematoxylin. Sections were scanned

using an Aperio ScanScope XT (Aperio Technologies, Vista, CA) and analyzed using Adobe Photoshop (Adobe Systems, San Jose, CA) and ImageJ software. Ten tubular fields and 30 glomeruli were selected and the percentage of JG12+ area was calculated, to correct JG12+ area for glomerular size.

For the analysis of the heart, deparaffinized cardiac sections were subjected to heat-induced antigen retrieval with antigen retriever 2100 (Aptum Biologics Ltd, UK) with citrate/HCl buffer (pH 6.0) for 20 min. After a brief wash with PBS, sections were blocked with superblock (Life Technologies, Netherlands) for 1 hour before incubation with the following primary antibodies at 4ºC overnight. The following antibodies were used; rabbit anti-NG2 (1:100, Abcam ab5320), rabbit anti-PDGFRβ (1:100, Abcam ab32570), biotin labelled anti-Lectin (1:200, Sigma-Aldrich L-3759), mouse anti-JG12 (1:100, eBioscience BMS1104), Rabbit anti-Ki67 (1:100, Thermo Scientific RM-9106), goat anti-Collagen IV (1:50, Millipore AB769), rabbit anti-Fibronectin (1:100, Sigma Aldrich F3648), mouse anti-CD68 (1:100, Abcam ab31630), and mouse anti-CD3 (1:100, Dako M7254). Appropriate secondary antibodies (Invitrogen, Netherlands) were used for visualization under fluorescent microscope. Nuclei were counterstained with DAPI (1 µg/ml, Sigma-Aldrich).

Images were taken by Olympus BX53 microscope. The numbers of NG2+ or PDGFRβ+ foci were counted for the whole heart section by microscope examination. For quantification of Lectin staining, pictures from the left ventricle were randomly obtained from lectin stained heart sections (four in the endocardium, four near the epicardium). Images were analyzed using ImageJ v1.49) by quantification of the percentage of the lectin+ area per image area.

Immunofluorescence cell staining

Human umbilical vein endothelial cells (HUVECs), pericytes and vascular smooth muscle cells (VSMCs) were seeded on sterile glass cover slips and cultured in EGM2 (Lonza), DMEM (Gibco, #41965), and SmGM-2 (Lonza) medium respectively for four days at 37ºC. Cells were first washed with PBS and then fixed with cold methanol for 10 min. Cells were blocked with Super blot (ScyTek Laboratories #AAA125) for 1 hour at room temperature. After that, cells were incubated with rabbit anti-NG2 (1:100, Abcam ab5320) or rabbit anti-PDGFRβ (1:100, Abcam ab32570) antibodies overnight at 4ºC. After washing with PBS, this was followed by incubation with AlexaFluor 488-conjgated goat anti rabbit secondary antibody for 1 hour at room temperature. Nuclei were counterstained with DAPI. Images were taken with the same setting by Olympus BX53 microscope with 20x objective.

QPCR analysis

Total RNA of HUVECs, pericytes, VSMCS and fibroblasts was isolated using RNAeasy kit (Qiagen) and treated with DNAse to remove genomic DNA contamination. cDNAs were generated using iScript cDNA synthesis kit (Bio-Rad) according to manufacturer's instructions. Quantitative PCR was performed on the BioRad CFX96 RT system using SYBR Green, and mRNA expression levels were normalized to the housekeeping gene β-actin. The PCR primers used are as follows: β-actin forward: 5'-TCCCTGGAGAAGAGCTACGA-3', β-actin reverse: 5'-AGCACTGTGTTGGCGTACAG-3', COL4a1 forward: 5'-ACGGGGGAAAACATAAGACC-3', COL4a1 reverse: 5'-TGGCGCACTTCTAAACTCCT-3', COL4a2 forward: 5'-TTATGCACTGCCTAAAGAGGAGC-3', COL4a2 reverse: 5'-CCCTTAACTCCGTAGAAACCAAG-3'.

Statistics

Groups were compared by two-way ANOVA for repeated measurements, followed by Student–Newman–Keuls (SNK) post-hoc test using SigmaPlot 12.3 (Systat Software Inc., San Jose, CA). Data are presented as mean ± standard deviation (SD). $P<0.05$ was considered significant.

Results

HFpEF progression in ZSF1 Ob animals

ZSF1 Ob rats had LV hypertrophy, as shown by increased echocardiographic indices of LV mass and LV posterior wall thickness at end-diastole (dLVPW) versus WKY and ZSF1 Ln at 25 weeks, and increase in LV + interventricular septum (IVS) weight/ tibial length (TL) versus WKY and ZSF1 Ln at 20 and 25 weeks (Table 1 and 2). Echocardiographic data showed preserved systolic function in all groups as assessed by ejection fraction (EF), fractional shortening (FS) and cardiac index (CI) at 20 or 25 weeks (Table 2). In contrast, ZSF1 Ob presented increased ratio of E to early diastolic TD mitral annulus velocity (E'), significant increase in E/E'/end diastolic volume (EDV) ratio, and increase of left atrial area (LAA) (Table 2), indicative of impaired diastolic function. Hemodynamic evaluation showed significant increase in Tau, end diastolic pressure (EDP), and end diastolic pressure volume relationship β1 (EDPVR β1) in ZSF1 Ob rats at 25 weeks versus WKY and ZSF1 Ln animals at 20 and 25 weeks (Supplemental Table 1). Furthermore, right ventricular (RV) weight/TL, and lung weight/TL were increased in ZSF1 Ob at 25 weeks versus WKY and ZSF1 Ln at 20 and 25 weeks (Table 1). Systolic, diastolic and mean blood pressure levels were increased in the ZSF1 Ob at 25 weeks versus WKY and ZSF1 Ln at 25 weeks (Supplemental Table 2).

Table 1. Morphometrics of WKY, ZSF1 lean and ZSF1 obese rats.

	WKY 20wks	ZSF1 ln 20wks	ZSF1 ob 20wks	WKY 25wks	ZSF1 ln 25wks	ZSF1 ob 25wks
body weight (g)	360 ± 31	410 ± 26	595 ± 31*	368 ± 24	469 ± 23†‡	633 ± 36*†
TL (mm)	39.4 ± 0.8	41.9 ± 0.9§	40.1 ± 1.3	38.8 ± 0.5	40.9 ± 0.8§	39.2 ± 1.0
LV+IVS weight/TL (mg/mm)	30.1 ± 3.9	28.2 ± 1.0	36.4 ± 2.5*	32.6 ± 4.0	35.0 ± 3.3†	37.4 ± 2.2‡
RV weight/TL (mg/mm)	3.4 ± 1.1	2.7 ± 0.4	4.1 ± 0.6#	3.1 ± 0.8	3.6 ± 0.5	4.8 ± 1.2*
lung weight/TL (mg/mm)	34.9 ± 5.3	40.6 ± 7.8	55.1 ± 5.2*	45.4 ± 6.1†	48.8 ± 3.3†	64.7 ± 3.0*†

Two-way ANOVA with Student–Newman–Keuls post hoc test. n=5-6 animals per group. Values are mean ± SD. IVS indicates interventricular septum; LV, left ventricle; RV, right ventricle; TL, tibial length; and WKY, Wistar Kyoto. *P<0.05 vs. WKY and ZSF1 Ln 20 or 25; †P<0.05 vs. week 20; ‡P<0.05 vs. WKY 20 or 25; §P<0.05 vs. WKY and ZSF1 Ob 20 or 25; #P<0.05 vs. ZSF1 Ln.

Table 2. Echocardiographic data for WKY, ZSF1 lean and ZSF1 obese rat.

	WKY 20wks	ZSF1 ln 20wks	ZSF1 ob 20wks	WKY 25wks	ZSF1 ln 25wks	ZSF1 ob 25wks
Heart rate (bpm)	299 ± 18	337 ± 5	309 ± 24	298 ± 55	301 ± 33	282 ± 24
dLVPW (mm)	1.40 ± 0.00	1.45 ± 0.07	1.47 ± 0.11	1.11 ± 0.05*	1.25 ± 0.15*†	1.46 ± 0.11‡
LV mass (mg)	483 ± 93	628 ± 14	797 ± 35†	386 ± 81	604 ± 142†	976 ± 201*‡
FS (%)	35.4 ± 3.7	41.2 ± 4.4	37.9 ± 1.8	36.2 ± 7.4	34.8 ± 6.1	35.4 ± 5.3
EF (%)	70.8 ± 4.8	77.3 ± 4.7	73.3 ± 2.1	71.0 ± 9.0	69.2 ± 7.9	69.7 ± 6.6
S (mm/s)	45 ± 3	59 ± 6†	58 ± 4†	48 ± 7	54 ± 4	52 ± 4
CI (µl/min/cm^2)	212 ± 30	187 ± 50	215 ± 19	172 ± 32	178 ± 11	220 ± 40
MPI (Tei)	0.60 ± 0.01	0.59 ± 0.01	0.62 ± 0.02	0.64 ± 0.03	0.62 ± 0.05	0.60 ± 0.04
E/A	1.79 ± 0.42	1.40 ± 0.08	1.33 ± 0.15†	1.68 ± 0.24	1.56 ± 0.13	1.30 ± 0.19‡
E/e'	12.7 ± 0.05	11.9 ± 2.3	16.7 ± 0.9‡	12.2 ± 1.6	11.9 ± 2.1	14.3 ± 1.4*
E/e'/EDV (log^2)	22.9 ± 4.7	13.2 ± 1.6	11.4 ± 0.6†	21.4 ± 9.9	12.5 ± 5.0†	9.0 ± 2.5†
LAA (mm^2)	2.48 ± 0.08	2.81 ± 0.30	3.51 ± 0.06‡	2.25 ± 0.14	2.70 ± 0.30†	3.71 ± 0.13‡
EDVI (µl/cm^2)	1.30 ± 0.17	1.87 ± 0.17	2.35 ± 0.22	1.37 ± 0.41	1.87 ± 0.46	2.45 ± 0.49

Two-way ANOVA with Student–Newman–Keuls post hoc test. n=2 to 4 animals per group at 20 weeks; n=5 to 6 animals per group at 25 weeks. Values are mean ± SD. CI indicates cardiac index; dLVPW, left ventricular posterior wall measured in diastole; E/A, ratio between peak E and A waves of pulsed-wave Doppler mitral flow velocity; EDVI, end-diastolic volume indexed for body surface area; E/e′, ratio between peak E-wave velocity of pulsed-wave Doppler mitral flow and peak e′-wave velocity of tissue Doppler at the lateral mitral annulus; EF, ejection fraction; EVD; end-diastolic volume; FS, fractional shortening; HR, heart rate; LAA, left atrial area; MPI, myocardial performance or Tei index; S, peak systolic tissue Doppler velocity at the mitral annulus; and WKY, Wistar Kyoto. *P<0.05 vs week 20; †P<0.05 vs WKY 20 or 25; ‡P<0.05 vs WKY and ZSF1 Ln 20 or 25.

ZSF1 Ob animals develop multiple sub-endocardial micro-structures of high cell density that are enriched in lectin+ ECs

Hematoxylin/eosin examination of heart cross-sections revealed no major differences in tissue morphology between WKY and ZSF1 Ln at 20 or 25 weeks. However, multiple areas with high cell density were observed at sub-endocardial locations of ZSF1 Ob rats at both time points, which were absent in WKY and ZSF1 Ln (Figure 1AI-II versus 1BI-II). High magnification assessment identified these ZSF1 Ob specific areas as irregular star-shaped foci composed of more than 50 mononuclear cells, located in the interstitial space between the cardiomyocytes (Figure 1C-G). Erythrocytes were detected in the extravascular space (Figure 1D,F), or in the lumen of capillary-like arrangements (Figure 1D,H), suggesting that these foci may contain vascular cells. Lectin+ ECs were organized in a well-structured

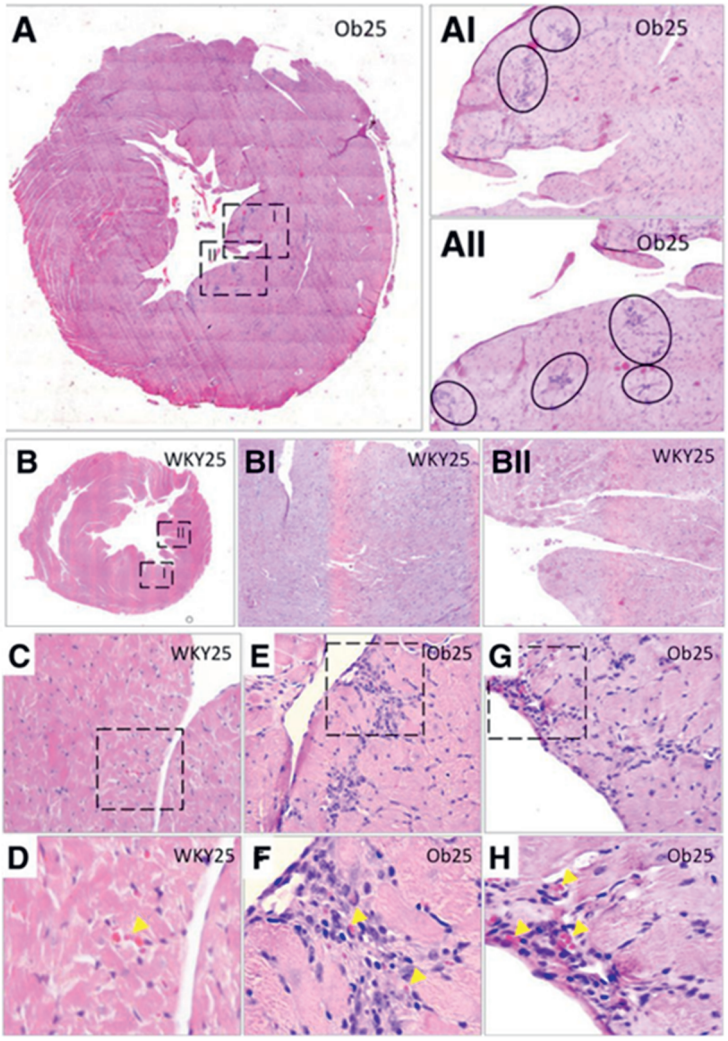

◄Figure 1. High cell density sub-endocardial foci develop specifically in the LVs of ZSF1 Ob rats, but not in ZSF1 Ln and WKY rats. Representative hematoxylin/eosin stained cross-sections of the heart LVs of ZSF1 Ob and WKY at 25 weeks. **(A)** Low magnification micrograph of the whole heart section of ZSF1 Ob. **(AI-II)** Higher magnification micrographs, high cell density sub-endocardial foci marked by black circles. **(B)** Low magnification figure of heart section of WKY. **(BI-II)** Higher magnification figures showing the absence of high cell density sub-endocardial foci. **(C)** High magnification figure showing typical morphology at the LV sub-endocardial location in WKY. **(D)** High magnification detail. Erythrocytes in the microcapillary bed are indicated by arrowhead. **(E, G)** High magnification examples showing foci morphology in ZSF1 Ob rats. (**F, H)** High magnification details with erythrocytes indicated by arrowheads.

micro-capillary network in both WKY and ZSF1 Ln at 20 and 25 weeks (Figure 2A,B). Similarly, a well-organized micro-capillary network was observed in ZSF1 Ob at both 20 and 25 weeks in the areas outside the foci (Figure 2A,B). Quantification of lectin staining showed a significant increase in capillary area in ZSF1 Ob at 20 weeks of age compared to WKY and ZSF1 Ln (9.3 ± 1.0 versus 4.7 ± 1.1 and 5.8 ± 1.0 respectively; $P<0.01$), whereas at 25 weeks, capillary areas normalized between groups, mainly due to the increase in WKY and ZSF1 Ln (Figure 2C). The sub-endocardial foci in ZSF1 Ob also stained positive for lectin, indicating that most of the accumulated cells were endothelial cells (Figure 2D,E). In contrast to the coherent lectin+ capillary structures that were found outside the foci, the bulk of lectin+ ECs inside these foci showed a distinct lack of vascular morphology with only limited luminal and monolayer organization (See inserts in Figure 2D,E).

ZSF1 Ob specific sub-endocardial foci are enriched in NG2+ and PDGFRβ+ pericytes that form disorganized vascular clusters with lectin+ and JG12+ ECs

Pericytes are vascular mural cells that are typically found in the capillary bed. They are vital for microvascular survival and regulation of blood flow [23]. Immunostaining for NG2 identified vascular pericytes located in the sub-endocardial foci, further validating their vascular identity. In the WKY and ZSF1 Ln, NG2+ pericytes were detected at their characteristic peri-EC localization, as shown by lectin double staining (Representative cross-section of WKY at 25 weeks is shown in Figure 3A). In contrast, in ZSF1 Ob, the number of NG2+ pericytes was markedly increased in the regions outside the foci (Figure 3A). In the sub-cardiac foci, NG2+ pericytes were also observed in close distance to lectin+ ECs (Figure 3A,B). Although some coverage of vascular structures could be recognized, the majority of the NG2+ pericytes form atypical multi-layered clusters mixed with lectin+ ECs (Figure 3B).

To further validate the vascular content of the ZSF1 Ob foci, pericytes were stained with a second vascular mural cell marker PDGFRβ in combination with a second EC marker, JG12.

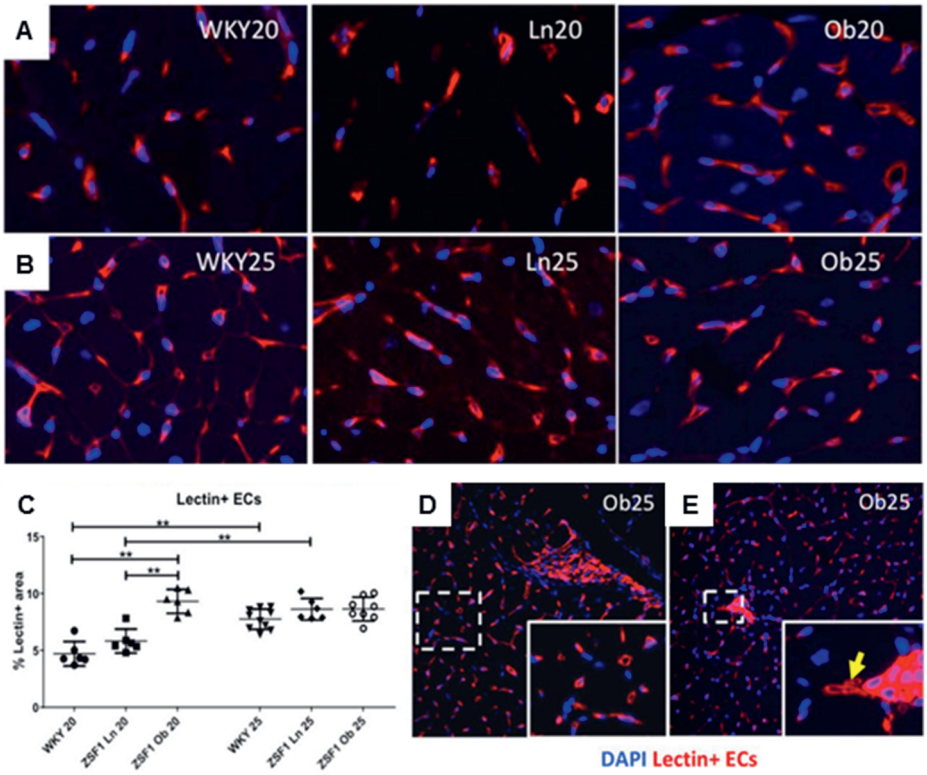

Figure 2. Sub-endocardial foci in ZSF1 Ob rats are enriched with lectin+ EC. Representative cross-sections of the LVs of WKY, ZSF1 Ln, and ZSF1 Ob at **(A)** 20 and **(B)** 25 weeks, stained for lectin+ endothelium, imaged by confocal microscopy (red signal). Cell nuclei are stained with DAPI (blue signal). **(C)** Quantification of percentage of lectin+ endothelial area in WKY, ZSF1 Ln, and Ob at 20 and 25 weeks. Mean ± SD. *P<0.05. High magnification detail panels showing the microcapillary structures in ZSF1 Ob **(D)** outside and **(E)** inside the sub-endocardial foci. Arrow indicates vascular structures with open lumen.

Immunostaining experiments using cultured human vascular cells demonstrate that NG2 and PDGFRβ are suitable markers for mural cells, in particular pericytes, being minimally expressed by endothelial cells (Supplemental Figure 1A). PDGFRβ+ pericytes were detected in WKY and ZSF1 Ln at peri-EC localization (Figure 3C). In the ZSF1 Ob, PDGFRβ+ pericytes accumulated in the foci and were atypically organized with limited perivascular coverage (Figure 3C,D). In the capillary network directly surrounding these foci, an increase in PDGFRβ+ pericytes was observed as compared to the capillary network in WKY and ZSF1 Ln (Figure 3E,F). The number of vascular foci increased by 9-and 20-fold in ZSF1 Ob versus WKY, and by 4-and 27-fold in ZSF1 Ob versus ZSF1 Ln, at 20 and 25 weeks respectively, when quantified using the NG2+ signal (P<0.001; Figure 3G, left graph). Similarly, quantification of foci using the PDGFRβ+ signal showed increases of 7-and 25-fold in ZSF1

Ob versus WKY, and of 4-and 29-fold in ZSF1 Ob versus ZSF1 Ln, at 20 and 25 weeks respectively (P<0.001; Figure 3G, right graph). The number of foci also increased in ZSF1 Ob over time based on both NG2 and PDGFRβ methods of quantification (P<0.001; Figure 3G). Combined, these data identify the sub-endocardial structures as vascular cells enriched foci that specifically develop in ZSF1 Ob rats.

Increased endothelial cell proliferative activity, fibrosis and AGTR1 expression in the vascular foci of ZSF1 Ob animals

The large number of vascular cells in the foci point towards increased endothelial cell proliferation. We used a combination of lectin and Ki67 staining to assess the number of proliferating endothelial cells. In ZSF1 Ob foci, lectin+ ECs were enriched in nuclear Ki67 signals as compared to the surrounding tissue that displayed a regular organization of microvascular network (Figure 4A,C). These results were verified using a second JG12/Ki67 staining combination, which demonstrated a similar preferential signal of Ki67 in JG12+ ECs located in the foci (Figure 4B,D).

Fibrogenic activity in these pericytes enriched foci was investigated by histological Periodic acid-Schiff (PAS) examination, a staining method that is often used to detect extracellular deposition of (vascular) basal membrane glycoproteins. Extracellular fibril-like PAS+ structures were detected in between vascular cells located in the foci, pointing towards active glycoprotein deposition (WKY cross-section compared to ZSF1 Ob foci at 25 weeks; Figure 5A-F).

Double staining for lectin+ ECs and fibronectin showed limited deposition of these early fibrosis-associated extra cellular matrix (ECM) components in the regular capillary network of WKY and ZSF1 Ln (Figure 5G). In contrast, fibronectin deposition was increased in the sub-endocardial foci of ZSF1 Ob, and in the vascular network surrounding the foci (Figure 5G,H). Double staining for PDGFRβ+ pericytes and collagen IV, a vascular basal membrane component predominantly produced by vascular cells, showed robust collagen IV deposition in the regular capillary network of WKY and ZSF1 Ln (Figure 5I). Similarly, collagen IV was detected in the PDGFRβ+ foci and direct surrounding capillaries of ZSF1 Ob rats (Figure 5I,J).

Activation of the Renin-Angiotensin-Aldosterone System (RAAS) may contribute to CRMS and HFpEF development in the ZSF1 Ob animals. Immunostaining for AGTR1, the Angiotensin II receptor most associated with cardiac hypertrophy, VSMC hyperproliferation, and vascular constriction, showed increased expression of AGTR1 by cardiomyocytes and interstitial perivascular cells in ZSF1 Ob versus WKY and ZSF1 Ln controls in areas outside the vascular foci (Figure 5K,L). AGTR1 was highly expressed by both by lectin+ ECs and perivascular cells in the ZSF1 Ob specific vascular foci (Figure 5M).

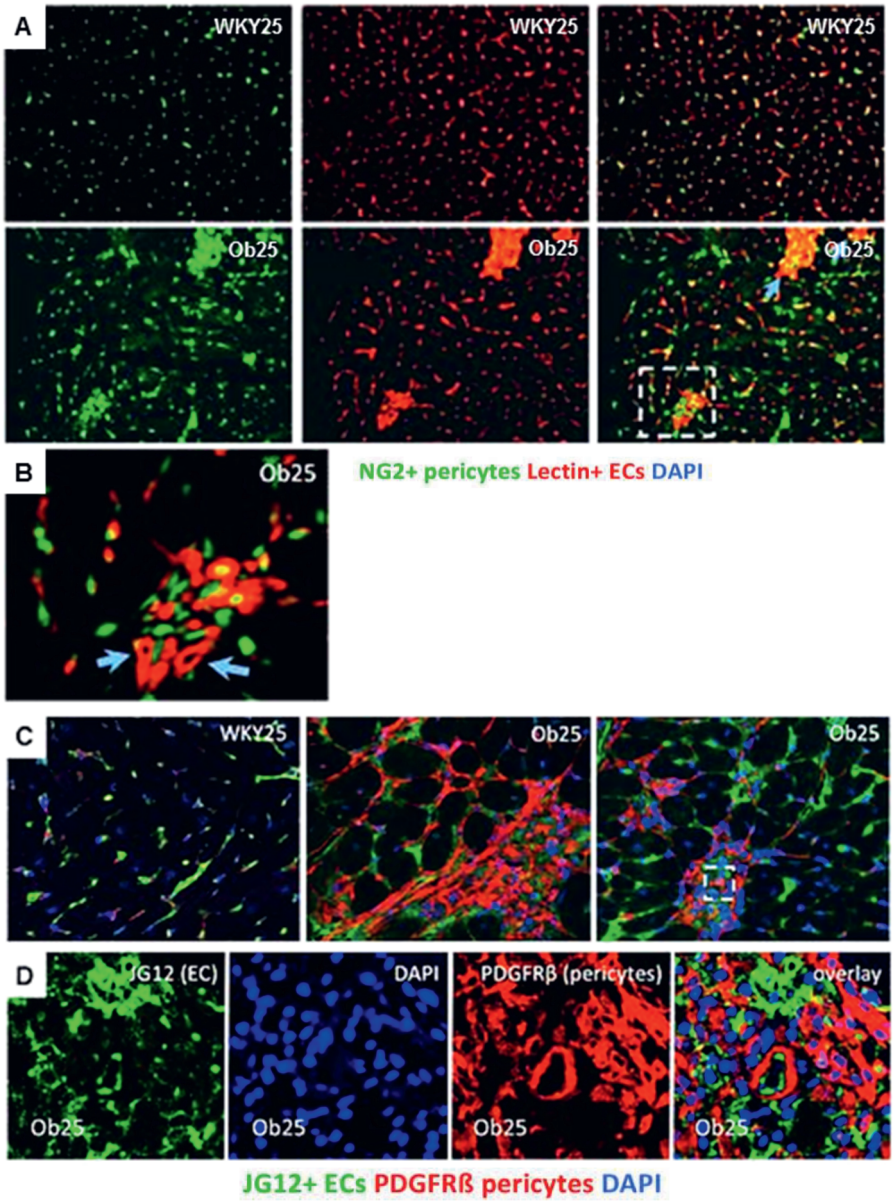

Figure 3. Sub-endocardial foci in ZSF1 Ob rats are also enriched with NG2+ and PDGFRβ+ pericytes. (A) Representative cross-sections of the LVs of WKY and ZSF1 Ob at 25 weeks, stained for NG2+ pericytes (green signal) and lectin+ endothelium (red signal), imaged by confocal microscopy.

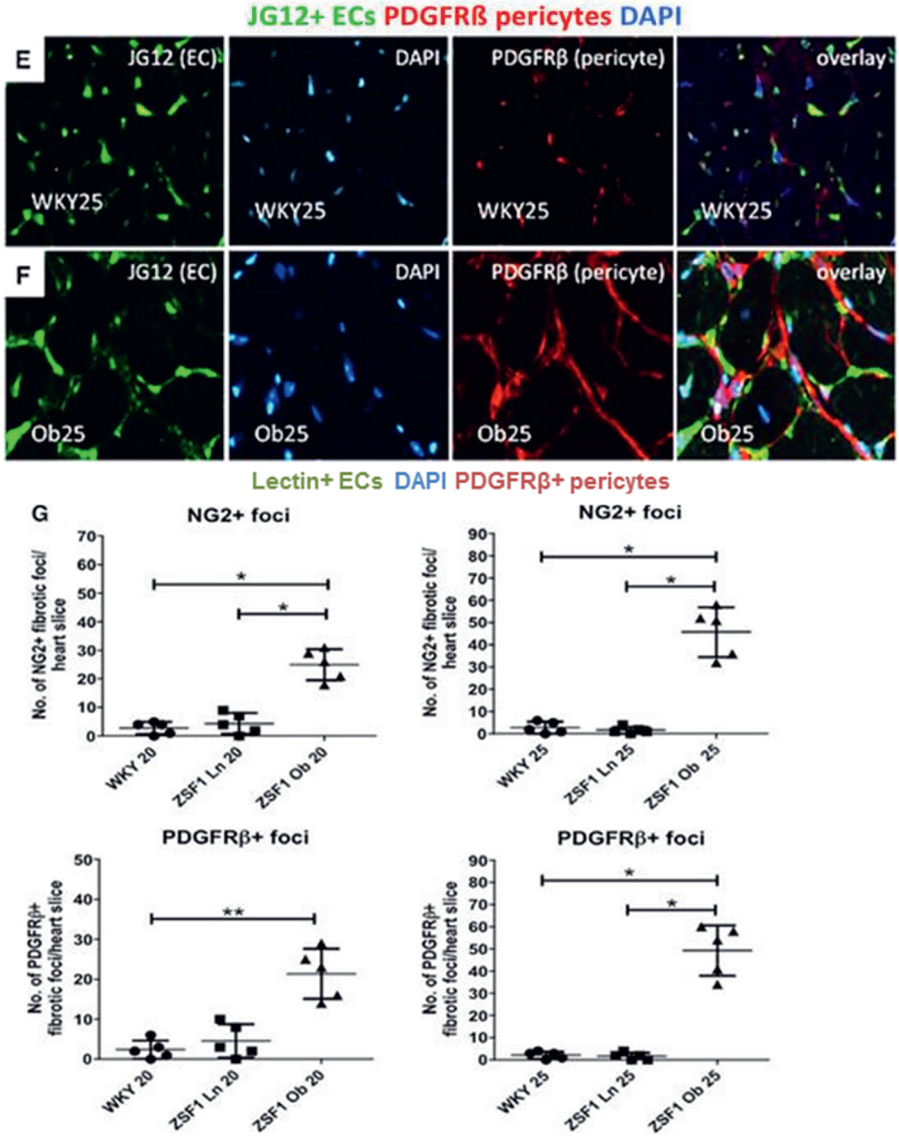

◄**(B)** High magnification detail showing disorganized clusters of lectin+ ECs and NG2+ pericytes in the sub-endocardial foci of ZSF1 Ob. Arrows indicate Lectin+ vascular structures with open lumens. **(C)** Representative cross-sections of the LVs of WKY and ZSF1 Ob at 25 weeks, stained for JG12+ endothelium (green signal), and PDGFRβ+ pericytes/mural cells (red signal), imaged by confocal microscopy. Cell nuclei are stained with DAPI (blue signal). High magnification detail panels showing **(D)** clusters of disorganized JG12+ ECs and PDGFRβ+ pericytes/mural cells in sub-endocardial foci of ZSF1 Ob, **(E)** typical organization of the microcapillary bed at the sub-endocardial location of WKY, **(F)** increase of PDGFRβ+ pericytes/mural cells coverage of the JG12+ microcapillary bed directly surrounding the sub-endocardial foci of ZSF1 Ob. **(G)** Quantification of the number of sub-endocardial foci per heart cross-section, determined by NG2 and PDGFRβ+ staining in WKY, ZSF1 Ln and Ob at 20 and 25 weeks of age. Mean ± SD. ***P<0.001.

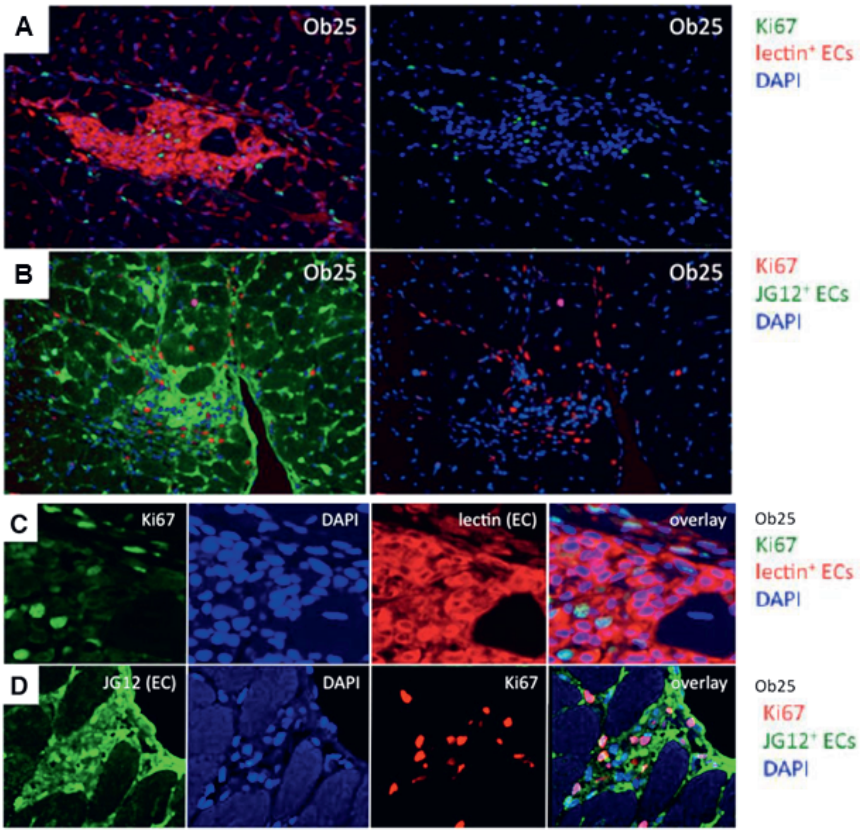

Figure 4. Sub-endocardial foci in ZSF1 Ob rats are sites of increased endothelial cell proliferation. Representative images of sub-endocardial foci of ZSF1 Ob at 25 weeks, stained for **(A)** lectin+ endothelium (red signal) and Ki67 cell proliferation marker (green signal), and **(B)** JG12+ endothelium (green signal), and Ki67 (red signal), followed by confocal imaging. Cell nuclei are stained with DAPI (blue signal). High magnification detail panels showing **(C)** lectin-Ki67 staining and **(D)** JG12-Ki67 staining.

The vascular foci of ZSF1 Ob animals are preferred recruitment sites for circulatory immune cells

To assess whether inflammatory cells contribute to the fibrogenic process, double staining for lectin+ ECs and CD3+ T cells was conducted. Perivascular CD3+ T cells were absent in the microvascular bed of WKY and ZSF1 Ln (Figure 6A). In contrast, perivascular CD3+ T cells were detected in limited numbers in ZSF1 Ob in the vascular foci, whereas the remaining capillary network showed no CD3+ T cell recruitment. Similarly, double staining for lectin+ ECs and ED1+ macrophages showed an absence of perivascular macrophages in WKY and ZSF1 Ln capillary networks, whereas in ZSF1 Ob, ED1+ macrophages accumulated in the sub-endocardial foci, indicating active recruitment of circulating immune cells at these sites (Figure 6B).

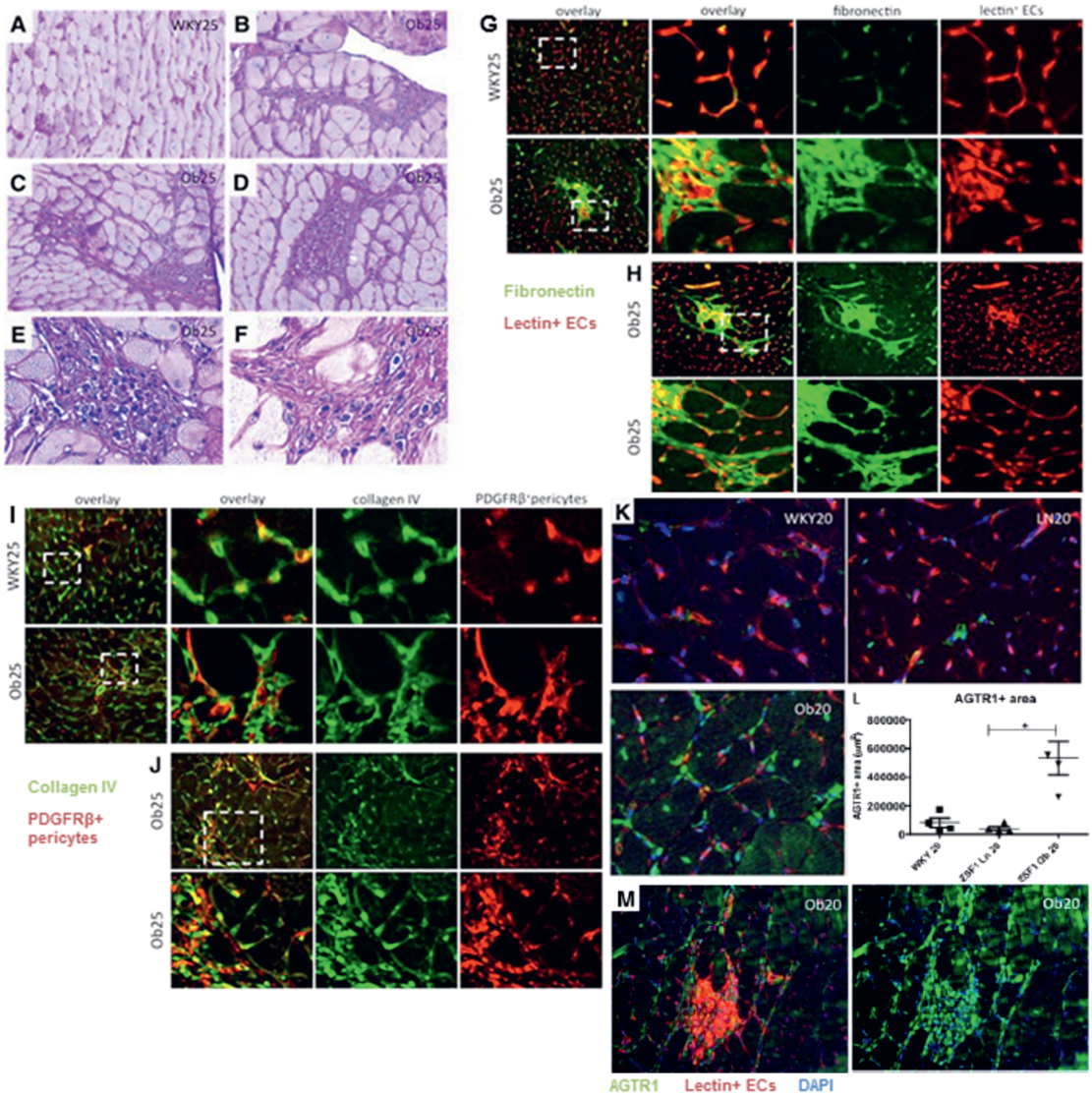

Figure 5. Onset of fibrosis at the sub-endocardial foci of ZSF1 Ob rats. Representative PAS stained cross-sections of the LVs of WKY and ZSF1 Ob at 25 weeks. **(A)** ECM glycoprotein deposition in the interstitial space between cardiomyocytes in WKY. **(B-D)** Accumulation of ECM glycoprotein in sub-endocardial foci of ZSF1 Ob. **(E, F)** High magnification detail showing PAS signal distribution in sub-endocardial foci of ZSF1 Ob. **(G)** Representative cross-sections of the LVs of WKY and ZSF1 Ob at 25 weeks, stained for ECM fibronectin (green signal) and lectin+ endothelium (red signal) at low magnification (left panel in each row), and at high magnification (remaining panels). **(H)** Representative example of overlap between fibronectin and lectin+ endothelial distribution in sub-endocardial foci of ZSF1 Ob at low (upper panels) and high magnification (lower panels). **(I)** Cross-sections of the LVs of WKY and ZSF1 Ob at 25 weeks, stained for vascular basal membrane collagen IV (green signal) and

◄PDGFRβ+ pericytes/mural cells (red signal) at low magnification (left panel in each row), and at high magnification (remaining panels). **(J)** Representative example of overlap between fibronectin and lectin+endothelial distribution in sub-endocardial foci of ZSF1 Ob at low (upper panels) and high magnification (lower panels). Increased expression of AGTR1 by cardiomyocytes and sub-endothelial foci of ZSF1 Ob rats. Representative figures of the LVs of WKY, ZSF1 Ln and ZSF1 Ob at 20 weeks, double stained for **(K)** lectin+ endothelium (red signal), AGTR1+ cells (green signal), and cell nuclei (blue signal). **(L)** Quantified results depicting the AGTR1+ areas in the WKY and ZSF1 Ln and Ob groups at 20 weeks. Mean ± SD. **P<0.01. **(M)** Representative example of overlap between AGTR1 (green signal) and lectin+ endothelial (red signal) distribution in sub-endocardial foci of ZSF1 Ob. Cell nuclei are stained with DAPI (blue signal).

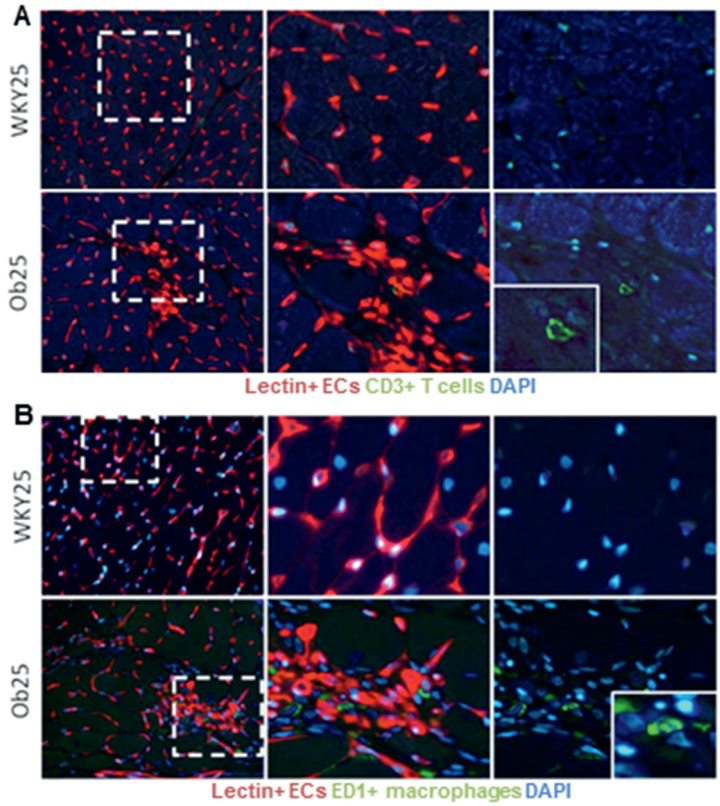

Figure 6. Recruitment of circulatory immune cells at sub-endocardial foci of ZSF1 Ob rats. (A) Representative figures of the LVs of WKY and ZSF1 Ob at 25 weeks, double stained for **(A)** lectin+ endothelium (red signal) and CD3+ T cells (green signal), and **(B)** lectin+ endothelium (red signal) and ED1+ macrophages (green signal) at low magnification (left panel in each row), and at higher magnification (remaining panels). Cell nuclei are stained with DAPI (blue signal).

Renal function declines in ZSF1 Ob rats

Compared to WKY, plasma urea was not affected in ZSF1 Ln and Ob at 20 and 25 weeks. At 20 and 25 weeks respectively, a 9-and 38-fold increase in protein/creatinine ratio was observed in ZSF1 Ob compared to WKY (P<0.001; Table 3). Similarly, at 20 and 25 weeks, a 6-and 37-fold increase in protein/creatinine ratio was observed in ZSF1 Ob compared to ZSF1 Ln (P<0.001; Table 3). Oxidative stress, measured by thiobarbituric acid reactive substance (TBARS), was increased in ZSF1 Ob compared to WKY and ZSF1 Ln at both time points (P<0.001; Table 3). No differences in protein/creatinine and TBARS/creatinine ratio were observed between WKY and ZSF1 Ln. Calculated per body weight (per 100 g), creatinine clearance was significantly reduced in ZSF1 Ob rats (1.2 ± 0.1 ml/min/100g versus 0.7 ± 0.1 ml/min/100g for ZSF1 Ln and ZSF1 Ob, P<0.05, based on Student's T-test).

Table 3. Biochemical variables for WKY, ZSF1 lean and ZSF1 obese rats.

	WKY 20wks	ZSF1 ln 20wks	ZSF1 ob 20wks	WKY 25wks	ZSF1 ln 25wks	ZSF1 ob 25wks
Plasma						
Creatinine (µmol/L)	36.1 ± 1.9	28.3 ± 8.9	21.1 ± 5.5*	34.2 ± 8.7	36.0 ± 8.5	22.4 ± 7.6†
Urea (mmol/L)	4.1 ± 0.2	5.3 ± 0.7*	6.3 ± 1.0*	7.3 ± 1.1‡	6.7 ± 0.5‡	5.9 ± 0.7*
Urine						
Protein/creatinine ratio	119 ± 17	181 ± 9	1086 ± 871†	126 ± 8	130 ± 5	4774 ± 239†
TBARS/creatinine ratio	4.1 ± 0.2	3.8 ± 0.6	19.3 ± 15.1†	3.0 ± 0.1	2.3 ± 0.1	49.7 ± 8.5†

Two-way ANOVA with Student–Newman–Keuls post hoc test. Plasma sample size; N=3 to 6 animals per group at 20 weeks. N=5 to 6 animals per group at 25 weeks. Urine plasma size; N=2 to 4 animals per group at 20 weeks. N=4 animals per group at 25 weeks. Values are mean ± SD. TBARS indicates thiobarbituric acid reactive substance; and WKY, Wistar Kyoto. ‡P<0.05 vs week 20; *P<0.05 vs WKY 20 or 25; †P<0.05 vs WKY and ZSF1 Ln 20 or 25.

ZSF1 Ob rats show degradation of renal endothelium and develop progressive glomerulosclerosis

The highest chronic tubulo-interstitial (TI) damage and glomerulosclerosis (GS) scores were measured in ZSF1 Ob compared to WKY and ZSF1 Ln at 20 and 25 weeks (Figure 7A,B). Compared to WKY, GS was increased in ZSF1 Ln (11 ± 5 versus 23 ± 5 and 13 ± 5 versus 24 ± 5, P<0.05). With age GS increased in ZSF1 Ob (39 ± 10 versus 53 ± 14, P<0.01). Peritubular and glomerular endothelia were visualized on JG12 stained slides (Figure 8A). Compared to WKY and ZSF1 Ln, the percentage of peritubular and glomerular endothelium decreased in ZSF1 Ob (Figure 8B,C).

Discussion

The main findings of the current study are: (1) The obese ZSF1 rat strain is a suitable *in vivo* model for CRMS, sharing characteristics with the human syndrome during the earliest onset of disease. (2) In obese ZSF1 rats, CRMS induces microvascular fibrotic responses in heart and kidneys, associated with functional impairment of both organs.

ZSF1 Ob rats as a suitable model for CRMS – metabolic syndrome as a trigger for chronic cardio-renal syndrome

Humans with metabolic derangements such as obesity, hypertension, hyperglycemia, and dyslipidemia – all recognized as important risk factors for chronic kidney and cardiovascular disease [24,25] – often present with preclinical diastolic dysfunction [26], diastolic heart failure, or heart failure with preserved ejection fraction (HFpEF) [27,28]. In current and previous reports, we could validate that the ZSF1 Ob animals share these characteristics with metabolic syndrome patients [2]: ZSF1 Ob rats are obese (65% and 45% increase compared to WKY and ZSF1 Ln respectively, Table 1), hypertensive (46% and 19% increase in mean blood pressure compared to WKY and ZSF1 Ln, Supplemental Table 2), and show elevated fasting plasma glucose levels (65% and 45% increase compared to WKY and ZSF1 Ln respectively [9]), whereas other studies have reported hypertriglyceridemia (increase of more than 25-fold) and hypercholesterolemia (increase of more than 5-fold) in ZSF1 Ob versus ZSF1 Ln [10,29]. Furthermore, CRMS in humans is defined by the presence of metabolic syndrome in addition to insulin resistance, microalbuminurina and/or reduced renal function [13].

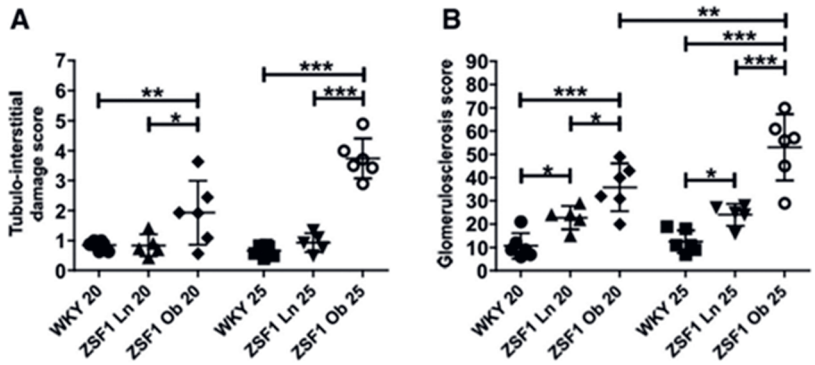

Figure 7. Increase in tubulo-interstitial damage and glomerulosclerosis in the kidneys of ZSF1 Ob rats compared to WKY and ZSF1 Ln rats. Tubulo-interstitial damage **(A)** and glomerulosclerosis **(B)** scores for WKY and ZSF1 Ln and ZSF1 Ob at 20 and 25 weeks. Mean ± SD. *P<0.05, **P<0.01, ***P<0.001.

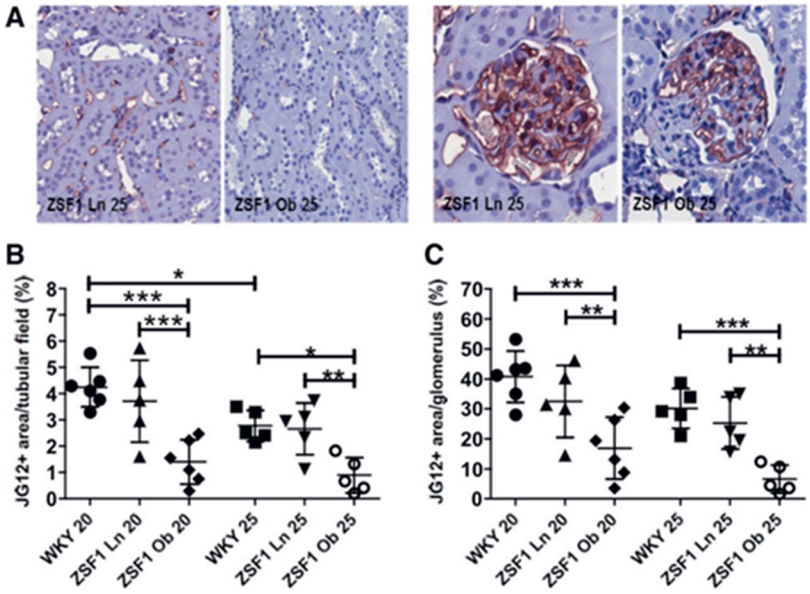

Figure 8. Rarefaction of the peritubular and glomerular vasculature in ZSF1 Ob rats. (A) Representative images of JG12-stained sections for ZSF1 Ln and ZSF1 Ob. Quantified results depicting the percentage of JG12+ endothelial area in the **(B)** peritubular and **(C)** glomerular vasculature determined in WKY and ZSF1 at 20 and 25 weeks. Mean ± SD. *P<0.05, **P<0.01, ***P<0.001.

Current and previous findings demonstrate that ZSF1 Ob develops proteinuria from 10 weeks onwards [9] whereas early signs of HFpEF were detected from 14 weeks onwards. Similarly at 10 weeks, increased oral glucose tolerance and insulin resistance, glycosuria and significant weight gain can be detected [9]. These observations indicate that the presentation of metabolic risk factors accompanies the onset of renal dysfunction (signified by proteinuria) and precedes HFpEF development in ZSF1 Ob rats, which is consistent with a pathophysiological course of CRMS in ZSF1 Ob in which metabolic and renal complications induce cardiac dysfunction [18]. Based on these combined data, we therefore propose ZSF1 Ob as a small animal model for metabolic syndrome induced CRS (and thus CRMS), in which the combined metabolic risk factors act together to trigger early onset and progression of CKD and HF, creating the downward spiral of disease progression that is so typical for patients with chronic CRS [10].

Microvascular fibrotic changes in ZSF1 Ob rats

CRMS was first suggested as a disease entity in 2004 [30]. Already in this first publication a relation with endothelial dysfunction was proposed [30]. Endothelial injury is implicated in CRS [20], whereas in HFpEF patients, vascular changes represented by endothelial dysfunction

have been reported [31]. A direct link between heart failure, vascular activation, metabolic comorbidities, and CKD was presented by Shestakova *et al.*, who demonstrated a correlation between endothelial dysfunction and the hallmarks of HF in CRS patients with DM type 1 [19]. In line with these studies, our data show changes in the coronary microvascular bed of ZSF1 Ob rats: Endothelial and mural cells form atypical vascular patches of cells, with remarkable increases in proliferation rate. Not only do these structures lack functional organization, they also appear to act as origin sites of fibrosis, for we could demonstrate enriched deposition of fibrosis associated ECM components such as fibronectin and collagen type IV in these vascular foci.

In CRS rat models that use subnephrectomy (SNX) in combination with coronary ligation to initiate ischemic heart disease, a decrease in LV microvascular density was reported to be associated with systolic dysfunction [32,33]. Other clinical and experimental studies provide evidence that coronary microvascular rarefaction in diastolic and hypertrophic heart failure promotes tissue hypoxia, cell death, and fibrosis, all contributing to the progression from compensated hypertrophy to contractile dysfunction [34,35]. In adults, vascular proliferation is part of the compensatory and repair response to local hypoxia and tissue damage in which endothelial cells proliferate and migrate into the ischemic injury site during macrophage influx and phagocytosis of necrotic tissue. As repair proceeds, dead tissue is replaced by granulation tissue, characterized by the deposition of a provisional matrix enriched in glycoproteins and fibronectin [36,37]. The vascular foci that developed in ZSF1 Ob rats resembled this process of scar formation, with excessive endothelial cell proliferation, fibronectin deposition and local recruitment of macrophages.

Vascular cells in the foci contribute to the formation of granulation matrix, demonstrated by deposition of the typical vascular basal membrane component collagen type IV. Collagen type IV is predominantly produced by pericytes and not by fibroblasts, as shown by qPCR using *in vitro* human primary vascular cell types (Supplemental Figure 1B).

Extensive myocardial fibrosis is one of the hallmarks of CRMS. Previously, we reported that at 20 weeks, cardiac hypertrophy was increased in ZSF1 Ob versus ZSF1 Ln and WKY, but overall levels of myocardial fibrosis remained comparable between groups [9]. In contrast, glomerulosclerosis score in the kidneys (shown in Figure 8B) was significantly increased in ZSF1 Ob versus the other 2 groups. Thus, the effect of metabolic risk factors on kidney fibrosis seems to precede the effects on fibrosis in the myocardium in the ZSF1 Ob animals. In this study, we could demonstrate that onset of fibrosis is present in the sub-endocardial vascular foci at 20 and 25 weeks in ZSF1 Ob rats. This was accompanied by vascular inflammation, yet another hallmark of CRMS.

On the basis of our observations to date, we hypothesize that the hyperproliferative vascular reaction in ZSF1 Ob heart is part of a destructive response that leads to replacement of functional vascular structures by fibrotic tissue with semi and non-functional microvascular clusters, which may ultimately deteriorate into large fibrotic areas that are completely devoid of vascular support, in line with the previously reported vascular rarefaction phenotype. Additional studies are planned to further elucidate this highly dynamic process and to validate if microvascular hyperproliferation of pre-existing vessels indeed precedes fibrogenesis and vascular rarefaction in CRMS.

Potential impact of current findings on the field of CRMS research

Chronic CRS type 2, which is initiated by chronic cardiac dysfunction (such as congestive HF), and type 4, initiated by chronic renal dysfunction (resulting in LV hypertrophy and diastolic HF), are currently under-recognized syndromes in the cardiovascular research community in comparison to acute CRS types. This is largely due to the lack of a suitable animal model to mimic the human condition. However the population of patients with chronic types of CRS is substantial: In adult patients with congestive HF it has been reported that 31% of NYHA III and 39% of NYHA IV patients suffer from renal dysfunction [38]. Recent findings presented in the PREVEND study also showed that early onset of renal dysfunction, indicated by albuminuria, is a strong predictor for new onset of HFpEF, but not HFrEF [39]. Others have also demonstrated that the prevalence of LV hypertrophy is significantly increased in CKD patients from mild renal impairment onwards [40]. These findings are consistent with the concept that the synergy between renal and cardiac dysfunction is a driving factor in the early disease onset of HFpEF. An improved understanding of the disease mechanism of, in particular, chronic CRS would greatly aid in the development of new diagnostic and treatment options that are specifically targeted to this large subgroup of cardiac and renal patients.

The ZSF1 Ob strain presents a suitable model to investigate the contribution of different disease pathways to CRMS, as the disease course resembles the onset phase of chronic CRS within the first 10-25 weeks of the animals' lifespan. In particular, studies that investigate the relation between metabolic risk factors and endothelial dysfunction could shed further light on the contribution of vascular injury to HF in chronic CRMS.

Limitations of the current study

The ZSF1 Ob model described in the current paper is not suitable for studying type 1 and type 3 CRS, as these forms require acute cardiac and renal failure to adequately mimic the human conditions, and may involve different disease mechanisms compared to the chronic forms (See review of disease etiologies of CRS subtypes) [18]. A more suitable model for acute CRS

would be surgical induction methods for myocardial infarction such as coronary ligation, and SNX for severe renal dysfunction. Previous studies have indicated that a dual injury model to heart and kidneys is needed to produce a more robust acceleration of renal failure and heart failure with reduced ejection fraction, that are typical for acute CRS [41,42]. However, the causal relation between metabolic risk factors and chronic CRS can be better studied in the ZSF1 Ob model, as this would best imitate the natural course of the disease in chronic CRS patients. The addition of ZSF1 Ob to our arsenal of animal models for CRS will greatly expand our means to adequately study mechanisms in the earliest phases of disease.

In addition to the proposed mechanism of vascular fibrosis mediated CRMS, other disease mechanisms could trigger CRS, including low cardiac output leading to impaired renal perfusion, which vice versa leads to kidney-mediated RAAS and sympathetic activation. Initial renal dysfunction could also induce chronic CRS via RAA and sympathetic activation, in addition to Na^+ and H_2O overload, hypertension, accumulation of uremic toxins and Ca and Phosphate abnormalities that all contribute to cardiovascular complications. Furthermore, renal impairment and subsequent dysregulation of erythropoietin contributes to anemia, which further aggravate hypoxia in both organs [18]. In this study, we have not specifically assessed the contribution of these mechanisms to CRS development in the ZSF1 Ob model. However, cardiac output represented by the indexed cardiac output (CI, in Table 2) is similar between the 3 groups at both time points assessed. In addition, ZSF1 Ob animals are indeed hypertensive, and expression of AGTR1, the main receptor for RAAS mediated effects on the cardiovascular system, was increased in LV sections of the ZSF1 Ob group, particularly at the vascular foci. Further systematic evaluation will help identify for which specific pathological mechanisms of chronic CRS the ZSF1 Ob strain is a suitable research model.

In conclusion, this study demonstrates that the ZSF1 Ob rat strain is a suitable *in vivo* model for CRMS, sharing many characteristics with the human CRS during the earliest onset of the disease, as triggered and mediated by metabolic risk factors. Further studies in the classic pathways of CRMS using this ZSF1 Ob model will enhance our understanding of the contribution of microvascular and metabolic changes during the onset of CRMS.

References

1. Forman DE, Butler J, Wang Y, Abraham WT, O'Connor CM, Gottlieb SS, Loh E, Massie BM, Rich MW, Stevenson LW, Young JB, Krumholz HM: Incidence, predictors at admission, and impact of worsening renal function among patients hospitalized with heart failure. *J Am Coll Cardiol* **2004**, 43:61-7.
2. Grundy SM, Brewer HB, Jr., Cleeman JI, Smith SC, Jr., Lenfant C, American Heart A, National Heart L, Blood I: Definition of metabolic syndrome: Report of the National Heart, Lung, and Blood Institute/American Heart Association conference on scientific issues related to definition. *Circulation* **2004**, 109:433-8.
3. Raimundo M, Lopes JA: Metabolic syndrome, chronic kidney disease, and cardiovascular disease: a dynamic and life-threatening triad. Cardiol Res Pract. **2011**, 2011:747861.
4. Galassi A, Reynolds K, He J: Metabolic syndrome and risk of cardiovascular disease: a meta-analysis. *Am J Med* **2006**, 119:812-9.
5. Gami AS, Witt BJ, Howard DE, Erwin PJ, Gami LA, Somers VK, Montori VM: Metabolic syndrome and risk of incident cardiovascular events and death: a systematic review and meta-analysis of longitudinal studies. *J Am Coll Cardiol* **2007**, 49:403-14.
6. Kurella M, Lo JC, Chertow GM: Metabolic syndrome and the risk for chronic kidney disease among nondiabetic adults. *J Am Soc Nephrol* **2005**, 16:2134-40.
7. Whaley-Connell A, Pavey BS, McCullough PA, Saab G, Li S, McFarlane SI, Chen SC, Vassalotti JA, Collins AJ, Bakris G, Sowers JR, Investigators K: Dysglycemia predicts cardiovascular and kidney disease in the Kidney Early Evaluation Program. *J Clin Hypertens* **2010**, 12:51-8.
8. Bongartz LG, Braam B, Gaillard CA, Cramer MJ, Goldschmeding R, Verhaar MC, Doevendans PA, Joles JA: Target organ cross talk in cardiorenal syndrome: animal models. *Am J Physiol Renal Physiol* **2012**, 303:F1253-63.
9. Hamdani N, Franssen C, Lourenco A, Falcao-Pires I, Fontoura D, Leite S, Plettig L, Lopez B, Ottenheijm CA, Becher PM, Gonzalez A, Tschope C, Diez J, Linke WA, Leite-Moreira AF, Paulus WJ: Myocardial titin hypophosphorylation importantly contributes to heart failure with preserved ejection fraction in a rat metabolic risk model. *Circ Heart Fail* **2013**, 6:1239-49.
10. Bilan VP, Salah EM, Bastacky S, Jones HB, Mayers RM, Zinker B, Poucher SM, Tofovic SP: Diabetic nephropathy and long-term treatment effects of rosiglitazone and enalapril in obese ZSF1 rats. *J Endocrinol* **2011**, 210:293-308.
11. Griffin KA, Abu-Naser M, Abu-Amarah I, Picken M, Williamson GA, Bidani AK: Dynamic blood pressure load and nephropathy in the ZSF1 (fa/fa cp) model of type 2 diabetes. *Am J Physiol Renal Physiol* **2007**, 293:F1605-13.
12. Leite S, Oliveira-Pinto J, Tavares-Silva M, Abdellatif M, Fontoura D, Falcao-Pires I, Leite-Moreira AF, Lourenco AP: Echocardiography and invasive hemodynamics during stress testing for diagnosis of heart failure with preserved ejection fraction: an experimental study. *Am J Physiol Heart Circ Physiol* **2015**, 308:H1556-63
13. Sowers JR, Whaley-Connell A, Hayden MR: The role of overweight and obesity in the cardiorenal syndrome. *Cardiorenal Med* **2011**, 1:5-12.
14. LourenÇo AP, Falcão-Pires I, Cerqueira R, Fontoura DM, D, Hamdani N, Paulus W, Leite-Moreira AF: The obese Zsf1 rat as a new model of heart failure with preserved ejection fraction accompanying the metabolic syndrome. *Circulation* **2012**, 126.
15. Westermann D, Lindner D, Kasner M, Zietsch C, Savvatis K, Escher F, von Schlippenbach J, Skurk C, Steendijk P, Riad A, Poller W, Schultheiss HP, Tschope C: Cardiac inflammation contributes to changes in the extracellular matrix in patients with heart failure and normal ejection fraction. *Circ Heart Fail* **2011**, 4:44-52.
16. Van Heerebeek L, Hamdani N, Falcao-Pires I, Leite-Moreira AF, Begieneman MP, Bronzwaer JG, van der Velden J, Stienen GJ, Laarman GJ, Somsen A, Verheugt FW, Niessen HW, Paulus WJ: Low myocardial protein kinase G activity in heart failure with preserved ejection fraction. *Circulation* **2012**, 126:830-9.

17. Paulus WJ, Tschope C: A novel paradigm for heart failure with preserved ejection fraction: comorbidities drive myocardial dysfunction and remodeling through coronary microvascular endothelial inflammation. *J Am Coll Cardiol* **2013**, 62:263-71.
18. Ronco C, Haapio M, House AA, Anavekar N, Bellomo R: Cardiorenal syndrome. *J Am Coll Cardiol* **2008**, 52:1527-39.
19. Shestakova MV, Jarek-Martynowa IR, Ivanishina NS, Kuharenko SS, Yadrihinskaya MN, Aleksandrov AA, Dedov, II: Role of endothelial dysfunction in the development of cardiorenal syndrome in patients with type 1 diabetes mellitus. *Diabetes Res Clin Pract* **2005**, 68:S65-72.
20. Hatamizadeh P, Fonarow GC, Budoff MJ, Darabian S, Kovesdy CP, Kalantar-Zadeh K: Cardiorenal syndrome: pathophysiology and potential targets for clinical management. *Nat Rev Nephrol* **2013**, 9:99-111.
21. Karnib HH, Ziyadeh FN: The cardiorenal syndrome in diabetes mellitus. *Diabetes Res Clin Pract* **2010**, 89:201-8.
22. Leite-Moreira AF, Correia-Pinto J. Load as an acute determinant of end-diastolic pressurevolume relation. *Am J Physiol Heart Circ Physiol* **2001**, 280:H51-9.
23. Van Dijk CGM, Nieuweboer FE, Pei JY, Xu YJ, Burgisser P, van Mulligen E, El Azzouzi H, Duncker DJ, Verhaar MC, Cheng C: The complex mural cell: Pericyte function in health and disease. *Int J Cardiol* **2015**, 190:75-89.
24. Hall JE, Crook ED, Jones DW, Wofford MR, Dubbert PM: Mechanisms of obesity-associated cardiovascular and renal disease. *Am J Med Sci* **2002**, 324:127-37.
25. Cohen JB, Cohen DL: Cardiovascular and renal effects of weight reduction in obesity and the metabolic syndrome. *Curr Hypertens Rep* **2015**, 17:34.
26. Correa de Sa DD, Hodge DO, Slusser JP, Redfield MM, Simari RD, Burnett JC, Chen HH: Progression of preclinical diastolic dysfunction to the development of symptoms. *Heart* **2010**, 96:528-32.
27. Afshinnia F, Spitalewitz S, Chou SY, Gunsburg DZ, Chadow HL: Left ventricular geometry and renal function in hypertensive patients with diastolic heart failure. *Am J Kidney Dis* **2007**, 49:227-36.
28. Ahmed A, Rich MW, Sanders PW, Perry GJ, Bakris GL, Zile MR, Love TE, Aban IB, Shlipak MG: Chronic kidney disease associated mortality in diastolic versus systolic heart failure: a propensity matched study. *Am J Cardiol* **2007**, 99:393-8.
29. Tofovic SP, Kusaka H, Kost CK, Jr., Bastacky S: Renal function and structure in diabetic, hypertensive, obese ZDFxSHHF-hybrid rats. *Ren Fail* **2000**, 22:387-406.
30. El-Atat FA, Stas SN, McFarlane SI, Sowers JR: The relationship between hyperinsulinemia, hypertension and progressive renal disease. *J Am Soc Nephrol* **2004**, 15:2816-27.
31. Akiyama E, Sugiyama S, Matsuzawa Y, Konishi M, Suzuki H, Nozaki T, Ohba K, Matsubara J, Maeda H, Horibata Y, Sakamoto K, Sugamura K, Yamamuro M, Sumida H, Kaikita K, Iwashita S, Matsui K, Kimura K, Umemura S, Ogawa H: Incremental prognostic significance of peripheral endothelial dysfunction in patients with heart failure with normal left ventricular ejection fraction. *J Am Coll Cardiol* **2012**, 60:1778-86.
32. Windt WA, Henning RH, Kluppel AC, Xu Y, de Zeeuw D, van Dokkum RP: Myocardial infarction does not further impair renal damage in 5/6 nephrectomized rats. *Nephrol Dial Transplant* **2008**, 23:3103-10.
33. Dikow R, Schmidt U, Kihm LP, Schaier M, Schwenger V, Gross ML, Katus HA, Zeier M, Hardt SE: Uremia aggravates left ventricular remodeling after myocardial infarction. *Am J Nephrol* **2010**, 32:13-22.
34. Mohammed SF, Hussain S, Mirzoyev SA, Edwards WD, Maleszewski JJ, Redfield MM: Coronary microvascular rarefaction and myocardial fibrosis in heart failure with preserved ejection fraction. *Circulation* **2015**, 131:550-9.
35. Oka T, Akazawa H, Naito AT, Komuro I: Angiogenesis and cardiac hypertrophy: maintenance of cardiac function and causative roles in heart failure. Circ Res **2014**, 114:565-71.
36. Frangogiannis NG, Smith CW, Entman ML: The inflammatory response in myocardial infarction. *Cardiovasc Res* **2002**, 53:31-47.

37. Virag JI, Murry CE: Myofibroblast and endothelial cell proliferation during murine myocardial infarct repair. *Am J Pathol* **2003**, 163:2433-40.
38. McAlister FA, Ezekowitz J, Tonelli M, Armstrong PW: Renal insufficiency and heart failure: prognostic and therapeutic implications from a prospective cohort study. *Circulation* **2004**, 109:1004-9.
39. Brouwers FP, de Boer RA, van der Harst P, Voors AA, Gansevoort RT, Bakker SJ, Hillege HL, van Veldhuisen DJ, van Gilst WH: Incidence and epidemiology of new onset heart failure with preserved vs. reduced ejection fraction in a community-based cohort: 11-year follow-up of PREVEND. *Eur Heart J* **2013**, 34:1424-31.
40. Greaves K, Chen R, Ge L, Wei M, Tong B, Cai N, Senior R, Hemingway H: Mild to moderate renal impairment is associated with increased left ventricular mass. *Int J Cardiol* **2008**, 124:384-6.
41. Van Dokkum RP, Eijkelkamp WB, Kluppel AC, Henning RH, van Goor H, Citgez M, Windt WA, van Veldhuisen DJ, de Graeff PA, de Zeeuw D: Myocardial infarction enhances progressive renal damage in an experimental model for cardio-renal interaction. *J Am Soc Nephrol* **2004**, 15:3103-10.
42. Bongartz LG, Joles JA, Verhaar MC, Cramer MJ, Goldschmeding R, Tilburgs C, Gaillard CA, Doevendans PA, Braam B: Subtotal nephrectomy plus coronary ligation leads to more pronounced damage in both organs than either nephrectomy or coronary ligation. *Am J Physiol Heart Circ Physiol* **2012**, 302:H845-54.

Supplemental Data

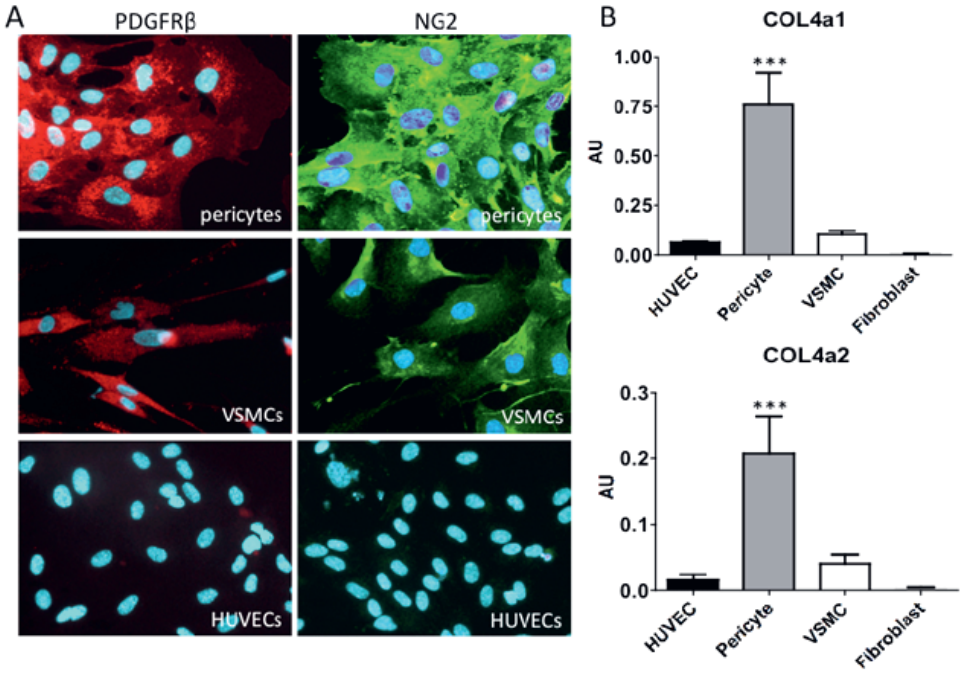

Supplemental Figure 1. NG2, PDGFRβ, and COL4 expression in human vascular cell types. (A) Representative immunofluorescent staining of mural cells derived from human origin (pericytes and VSMCs) and HUVECs. NG2 (red), PDGFRβ (green), and nuclei (blue). 20X magnification. **(B)** QPCR analysis of COL4a1 and COL4a2 expression levels in human derived vascular cells and fibroblasts. N=3, Mean ± SD. ***P<0.001 versus all.

Supplemental Tables

Supplemental tables can be downloaded from:

https://www.ahajournals.org/doi/10.1161/CIRCHEARTFAILURE.115.002760?url_ver=Z39.88-2003&rfr_id=ori:rid:crossref.org&rfr_dat=cr_pub%20%200pubmed

Or:

Chapter 9

A new microfluidic model that allows monitoring of complex vascular structures and cell interactions in a 3D biological matrix

Christian G.M. van Dijk, Maarten M. Brandt, Nikolaos Poulis, Jonas Anten, Matthijs van der Moolen, Liana Kramer, Erik F.G.A. Homburg, Laura Louzao-Martinez, Jiayi Pei, Merle M. Krebber, Bas W.M. van Balkom, Petra de Graaf, Dirk J. Duncker, Marianne C. Verhaar, Regina Luttge, Caroline Cheng

Lab on a Chip, 2020 May;20(10):1827-1844

Abstract

Microfluidic organ-on-a-chip designs are used to mimic human tissues, including the vasculature. Here we present a novel microfluidic device that allows the interaction of endothelial cells (ECs) with pericytes and the extracellular matrix (ECM) in full bio-matrix encased 3D vessel structures (neovessels) that can be subjected to continuous, unidirectional flow and perfusion with circulating immune cells.

We designed a in a polydimethylsiloxane (PDMS) device with a reservoir for a 3D fibrinogen gel with pericytes. Open channels were created for ECs to form a monolayer. Controlled, continuous, and unidirectional flow was introduced via a pump system while the design facilitated 3D confocal imaging.

In this vessel-on-a-chip system, ECs interact with pericytes to create a human cell derived blood vessel which maintains a perfusable lumen for up to 7 days. Dextran diffusion verified endothelial barrier function while demonstrating the beneficial role of supporting pericytes. Increased permeability after thrombin stimulation, showed the capacity of the neovessels to show natural vascular response. Perfusion of neovessels with circulating THP-1 cells demonstrated this system as a valuable platform for assessing interaction between the endothelium and immune cells in response to TNFα.

In conclusion: We created a novel vascular microfluidic device that facilitates the fabrication of an array of parallel soft-channel structures in ECM gel that develop into biologically functional neovessels without hard-scaffold support. This model provides a unique tool to conduct live *in vitro* imaging of the human vasculature during perfusion with circulating cells to mimic (disease) environments in a highly systematic but freely configurable manner.

Introduction

Current vascular research focuses on the understanding of fundamental and disease-driven processes for therapeutical purposes and regenerative aims. A broad variety of *in vitro* assays are available in the field, with each designed to study a specific aspect of vascular biology [1]. Endothelial barrier homeostasis is vital for vascular performance and is often assessed in *in vitro* setups [2]. Junction proteins such as vascular endothelial cadherin (VE-cadherin) and zonula occludens 1 (ZO-1) facilitate barrier function [2,3], and are widely studied in multiple settings, including disease-associated inflammation. During inflammation, VE-cadherin junctions are disrupted by leukocytes, thereby increasing barrier permeability [4] and facilitating diapedesis of these circulating cells [5-7]. Leukocyte extravasation during inflammation requires complex interactions between multiple vascular cell types and the surrounding extracellular matrix (ECM), and are mainly assessed *in vitro* in parallel flow chambers, which allow perfusion of circulating cells over a confluent endothelial monolayer with employment of syringe pumps to control the flow hemodynamics [8,9]. These *in vitro* models offer easily accessible, and (sometimes) high throughput solutions for live confocal monitoring. However, although they provide excellent *in vitro* platforms to study basic vascular mechanisms, the high biological and biomechanical complexity of the natural vasculature give rise to many technical challenges that remain to be addressed. For example, perfusable channels may not mimic the natural vessel geometry [10,11] or are not fully 3D ECM encapsulated due to limitations to the mechanical strength of the available (hydro) gels [12,13]. Co-culture of all relevant vascular cell types may also not be possible in certain setups, and lack of e.g. mural cells (pericytes and smooth muscle cells) support may hamper native vascular function *in vivo* [14-16]. On the other hand, animal models which do provide the required complex vascular environment, may also be practically and logistically challenging, are less suitable for high throughput screening, and may be limited in human relevance. The development of novel, more improved *in vitro* systems that combine the complexity of the native vasculature and allow direct monitoring of the cells in a physiologically relevant setting would greatly enhance the current insights into vascular and circulating cell behavior in healthy and different disease conditions.

Microfluidic technology that allows controlled pre-fabrication of perfusable micro-channels in the microvascular range could provide a low cost, high through put-based, quantifiable solution that captures the human microenvironment for in depth mechanistic studies [17]. Moreover, human based microfluidic systems have the ability to bridge the gap between non-complex *in vitro* models and complex, non-human *in vivo* techniques. In the last decade, this technology has been widely applied to successfully mimic human tissues, including the

vasculature [18]. Some examples of advanced microfluidic “vessel-on-a-chip” systems include the assay presented by Lam *et al.* which consists of a set of polydimethylsiloxane (PDMS) channels from which the largest one functions as a central angiogenesis chamber with endothelial colony-forming-cell derived endothelial cells (ECFC ECs), connected to adjacent stromal cell chambers and channels with oxygen scavenging compounds [19]. Basic PDMS designs often require micro-vessel formation by sprouting (from adjacent chambers) or self-assembly in an ECM environment in the angiogenic chamber. Here, the additional PDMS channels introduce spatial and temporal variants in local oxygen levels to mimic physiological conditions [19]. By adding more relevant cell types, such as astrocytes and epidermal cells to the vascular cells in the angiogenesis chamber or adjacent chambers, the blood brain barrier and the vascularized skin microenvironment could be replicated more accurately in a variety of comparable PDMS channels based microfluidic systems [20-23]. Similar devices have been presented with micro-channels which are partially in contact with 3D ECM gels from which the shared surfaces are lined with human ECs to mimic blood vessels [22,24-26]. Other studies have used channels that are cast in full collagen type I gel to mimic the lymphatic vessels or to study skin cell interaction with blood vessels [27-29].

Despite development of these highly advanced systems, several challenges in blood vessel-on-a-chip design remain, such as optimization of a protocol that would allow addition of mural cells to the endothelial monolayer [14-16,19,27,30,31]. Vascular-supporting cells, particularly pericytes that are present in the native microvasculature, play a significant role in establishing vascular homeostasis and maintaining the barrier function [32,33]. Pericyte deficiency in specific murine knockdown lines results in significant loss of endothelial barrier function, causing vascular leakage, and reduced vascular growth [34-36]. Inclusion of perivascular cells into the vessel-on-a-chip system is therefore a crucial requirement to fully emulate the functional human microvasculature.

The use of micro-channels fully cast in PDMS with the (endothelial) cells directly cultured on a PDMS surface [12,13,37,38] also provides another challenge; PDMS has different properties than native ECM in context of stiffness and bio-stimulation of (endothelial) cells, and limits the natural interaction between mural cells and ECs [39,40]. However, PDMS does provide the right amount of mechanical stiffness to support physiologically relevant levels of flow in small caliber channels (<1000 µm) without compromising the channel geometry, which is often an encountered issue with perfusion of hydrogel-based channels. Most current models also do not use mechanically applied flow, but a passive low flow system based on volume differences in the in- and outlet reservoirs to circumvent these problems in hydrogel based channels [41-43]. The development of a novel vessel-on-a-chip system with controlled,

unidirectional, continuous flow at levels that more closely mimic the physiological condition would greatly aid in the study of typical circulating immune cell behavior during interactions with the vasculature such as rolling, adhesion and extravasation [5,6].

Here we present a new advanced *in vitro* microfluidics model that more closely mimics the *in vivo* vasculature by: (1) Creating a mechanically controlled perfusion system with multiple tubular micro-channels that are completely enclosed in 3D ECM without direct contact of seeded cells with the PDMS casing or any other hard-material scaffolding. (2) Seeding these channels with human-derived GFP-labeled ECs and dsRED-labeled pericytes, and thereby recreating a blood vessel with a confluent endothelium and mural cell support providing optimized endothelial barrier function. (3) Controlling perfusion with circulating immune cells through these neovessels to provide a platform for interaction studies of circulating cells with the activated endothelium. This new system is designed to allow spatiotemporal visualization of the multiple steps in leukocyte adhesion *in vitro* using confocal microscopy with the possibility of live imaging. It can be used to enhance our understanding of the mechanisms of vascular inflammation processes in various diseases.

Materials and Methods

Cell culture

Human umbilical vein endothelial cells (HUVECs; Lonza) were cultured in EGM-2 (EBM-2 supplemented with single quots; Lonza). Human brain derived pericytes (ScienCell) were cultured in DMEM (Gibco) with additional 10% FBS (GE healthcare). All media was supplemented with 100 U/ml penicillin/streptomycin (Gibco). Cells were cultured on fresh gelatin (Sigma-Aldrich) coated dishes until passage 8 and harvested using trypsin (Gibco). Lentivirus green fluorescent protein- (GFP) transduced HUVECs and lentivirus discosoma sp. Red fluorescent protein- (dsRED) transduced pericytes (both under the human EF1a promoter) were used until passage 8. GFP-transduced HUVECs and dsRED-transduced pericytes show bright fluorescence in their cytoplasm. Dead cells will not express any fluorescent signal. THP-1 cells were kept in suspension culture using RPMI (Gibco) with the addition of 10% FBS (GE healthcare) and 1% penicillin/streptomycin (Gibco) until passage 23. All cells and experiments were incubated at 37°C with 5% CO_2.

Microfluidic device manufacturing

A microfluidic device mold was designed in NX version 10.0 and milled with a Roland MDX-40a benchtop CNC Mill from polymethylmethacrylate (PMMA). Twenty seven G needles (BD Bioscience) were glued into 21G needles (BD Bioscience, New Jersey/United States) with

metal-metal epoxy glue (Bison). PMMA mold and needles were cleaned and assembled to form the microfluidic mold. Sylgard 184 elastomer polydimethylsiloxane (PDMS; Dow Corning) was prepared in a 1:10 curing agent to base ratio, stirred and placed in a vacuum dissector until all air was removed. PDMS was poured into the PMMA-based microfluidic device mold and placed in a 65°C oven for at least 2 hours. After peeling off the PDMS from the mold, a glass coverslip was assembled to the PDMS device. Both, the PDMS component and the glass coverslips (22x22 mm) (Paul Marienfield, GmbH & Co) were tape cleaned for dust and the bonding surface was treated with corona discharge (SpotTEC, Tantec) prior to assembly. Furthermore, the bonded microfluidic devices were put in 65^{o}C for 30 min with additional weights to reinforce covalent bonds. Freshly formed covalent bonds between glass and PDMS results in a leakage-free microfluidic device. The reservoir is 5 mm by 17 mm by 1.7 mm in a PDMS device of 21 mm by 41 mm. Needles for molding the ECM gel channels were located at a distance of 0.75 mm of the bottom.

Fibrinogen gel creation and channel molding

Supplemental Figure 1 illustrates the work flow overview. PDMS devices were sterilized with UV for 30 min. Five sterile 26G needles (450 µm in diameter, BD bioscience) were inserted in the ports of the PDMS and function as the molds for casting the channels. Fibrinogen (7.5 mg/ml; Millipore) was dissolved in EGM-2 (Lonza). Vacuum was applied to remove air bubbles in the ECM containing. Next, a pericyte pellet was resuspended in the fibrinogen solution to a concentration of 5X10^{5} cells/ml which was injected into the reservoir of the sterile PDMS microfluidic device via a syringe and 30G needle (BD Bioscience). A 30G needle on the opposite site of the reservoir acts as outlet for air (Supplemental Figure 1). Devices with ECM gel and pericytes were placed in an incubator and turned over every 30 min for 2 hours, before leaving in the incubator overnight for further crosslinking. Needles were removed after 24 hours subsequently forming channels in the ECM gel (indicated in all further experiments as day 0). HUVECs were concentrated to a 12x10^{6} cells/ml suspension in EGM-2 and seeded into the formed channels. The PDMS device was turned over every 30 min to evenly seed the top and bottom of the channels. After 2 hours, the microfluidic device was submerged in EGM-2 (static condition) for three days to ensure the HUVECs formed a monolayer in the channel. Based on the reservoir volume and channel volume (all 5 channels combined) and the previously described cell concentrations, the estimate ratio between pericyte and HUVECs is 1:4.2 (12560 pericytes vs 52800 HUVECs) per microfluidic device. All experiments were conducted 3 days after seeding HUVECs in the channels after visual validation of successful endothelial monolayer formation.

Perfusion set up

The Ibidi perfusion sets (black; Ibidi) were fitted with an additional PE-50 (Becton Dickinson) with inner diameter of 0.5 mm in order to match the specifications of the inlets of the PDMS mold. All perfusion sets were sterilized with 70% ethanol and UV radiation for one hour. The connection of the perfusion set with the microfluidic device was made with the PE-50 tubing and needles. Sterile 26G needles were inserted before the perfusion in the PDMS. The points of the needles reach the start of the HUVECS channel in order to keep residual PDMS from closing the channel and disturbing the flow. The setup was placed in an incubator and flow speed was adjusted using the Ibidi pump software. Perfusion with THP-1 cells was performed with a combination of culturing media, in ratio 1:1 of EGM-2 and RPMI (further referred as perfusion medium). THP-1 cells ($5X10^5$ cells/ml in total) were stained with CellTracker Deep Red Dye (Thermo Fisher) according to manufacturer's manual and used for perfusion. Cells were kept in perfusion medium after staining. Tumor necrosis factor (TNFα 10 ng/ml; rhTNFα, R&D systems) or control (PBS) in perfusion medium was added to the THP-1 perfusion.

In-channel immunofluorescent staining

Immunofluorescent staining was performed at specific time points. The PDMS device was fixated by submersion in PFA 4%. 1% BSA (bovine serum albumin), primary antibody (Anti-VE-Cadherin (CD144) clone BV9, Millipore), secondary antibody (Alexa Fluor® 568, Invitrogen Life Technologies) and DAPI were applied with caution using a 30G needle. After each injection step, a wash step was performed 3 times by submerging the channels in PBS. VE-cadherin primary antibody targets extracellular parts of VE-cadherin and was incubated overnight at 4^{o}C before incubation with the secondary antibody for 1h at room temperature.

RNA isolation and qPCR

RNA from the cells in the microfluidic device was isolated in 2 ways, either as a pool of HUVECs and pericyte RNA (1), or per individual cell type (2). For condition 1: The PDMS casing was cut open to gain access to the reservoir. The full reservoir (ECM gel including pericytes and HUVECs) was lysed using RLY lysis buffer for RNA isolation. For condition 2: RLY lysis buffer was flushed into the channel using a syringe and needle in the inlet and outlet of the microfluidic device. Lysate from all channels was combined for RNA isolation to form the HUVECs specific fraction. The remaining gel with pericytes in the microfluidic device was lysed, creating a separate pericyte fraction. RNA was isolated using ISOLATE II RNA kit (Bioline) with DNAse and cDNA was made using SensiFAST cDNA synthesis kit (Bioline) according manufactures protocol. qPCR was performed using FastStart Universal SYBR Green Master (Roche) following the qPCR program: 8,5' 95 ºC, 38 cycles (15" 95 ºC; 45" 60

ºC) 1’ 95 ºC, 1’ 65 ºC, 62 cycles (10” 65 ºC + 0,5 ºC). Gene expression levels were normalized to β-actin (Supplemental Table 1).

Dextran diffusion assay

Dextran Rhodamine B 70 kDa (10 nM in PBS; Sigma-Aldrich) was used to address endothelial barrier function. Dextran was initially applied to the cell seeded channels of the microfluidic device in the presence or absence of human recombinant thrombin (0.5 and 1 U/ml; hThrombin, R&D systems).

Imaging

Imaging of the microfluidic device was performed with a Leica TCS SP8X confocal microscope. Due to the dimensional properties of the channels, images were made with 10x or 20x magnification for both z-stack mode (42 focus sections per z-stack, 12 µm step size) and tile scan mode (3x2 tile). Average confocal time for each channel was 45 min using these settings. Images shown are projections of these tile scan/z-stack images unless indicated otherwise. Image analysis was performed with Leica LASX software and ImageJ. Longitudinal cross sections, 3D reconstructions, and GIF movies of the channels in the microfluidic device were generated with Leica LASX software. Dextran diffusion assays and channel width measurements were performed with an inverted microscope (Olympus IX53). Immediately after dextran injection, the channels were imaged every 10 min. Image analysis and quantification was performed using ImageJ and Graphpad Prism software (version 7.02). Dextran permeability coefficient was calculated according to the method published by Price and Tien [44].

Statistics

All data shown in bar graphs are presented as means +/- SEM. Groups were compared by students t-test or one-way ANOVA followed by Tukey post hoc test when appropriate. $P<0.05$ was accepted as statistically significant.

Results

Microfluidics device design, production, and use

The microfluidic device is composed of an open reservoir made of PDMS walls and a bottom that is sealed with a coverslip. This reservoir is filled with ECM gel (fibrinogen in the present study) and is connected to 5 inlets and 5 outlets in the PDMS walls that can be linked to tubing for monitored perfusion.

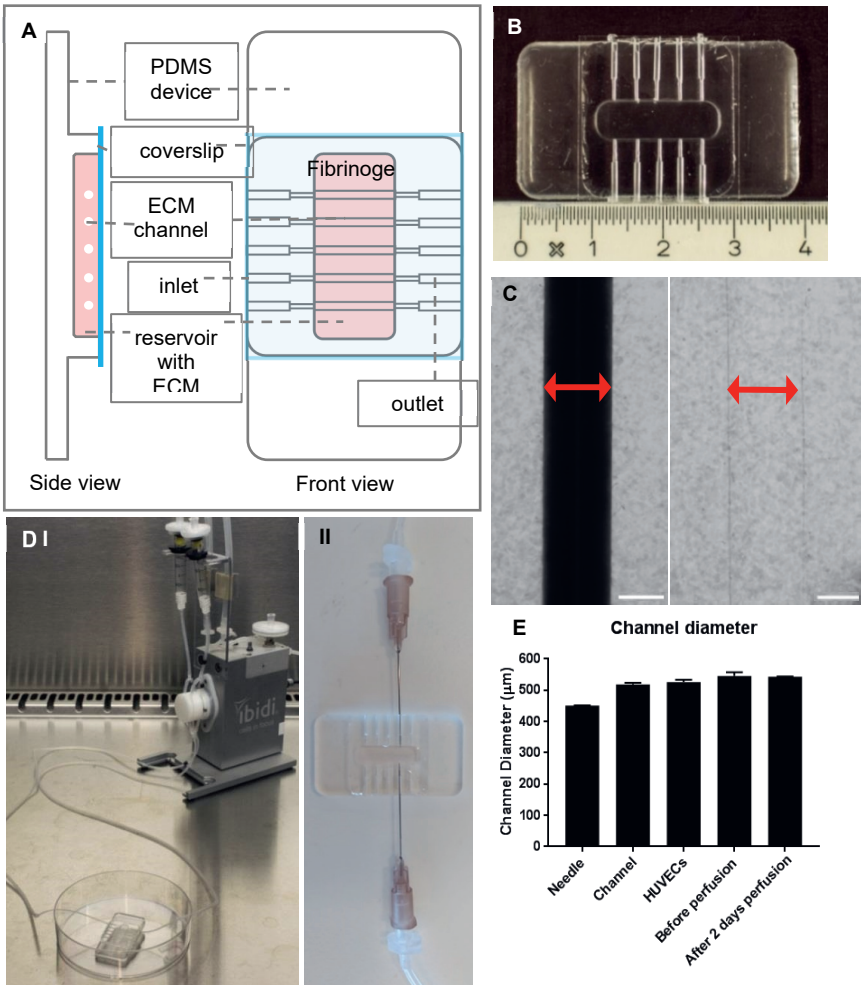

Figure 1. Microfluidics device design, production, and use. (A) Overview of the design of the microfluidics device. **(B)** Prototype of the microfluidics device. **(C)** Micrographs show on the left hand side the needle embedded in the fibrinogen gel, and on the right hand side the ECM channel left behind in the cross-linked fibrinogen matrix after removal of the needle. Diameter of the channel is indicated by a red bar. **(D; I and II)** Setup of the microfluidics system connected to the Ibidi perfusion pump via needles and tubing. **(E)** Bar graph showing the ECM channel diameter in the presence of the needle, after removal of the needle (channel), after seeding with HUVECs in the channel (HUVECs), before perfusion (3 days after seeding) and after 2 days of perfusion (40 µl/ml). N=3. Scale bar = 250 µm.

These connectors narrow down to 450 µm diameter sections towards the reservoir. The schematic device design is shown in Figure 1A and prototype replicated PDMS device is shown in Figure 1B. A fibrinogen gel mixed with (dsRED-labeled) pericytes is injected through the PDMS into the reservoir to form the ECM gel. The reservoir offers the possibility to cast different types of ECM gels, with or without additional cells, to mimic the microenvironment. In total, five 26 gauge needles are inserted through the inlets and outlets to act as molds during the casting of the fibrinogen gel to create 450 µm diameter channels in the 3D ECM. After gel cross-linking, the needles are extracted, leaving behind the open channel structures (Figure 1C). The five individual ECM channels are aligned with the PDMS inlets and outlets, creating a closed leakage-free system that allows flow perfusion of the ECM channels using tubing connected to the Ibidi pump system (Figure 1D i and ii). The channels are seeded with GFP-labeled HUVECs to create the endothelial monolayer lining of the blood vessels. A schematic overview of the workflow, including a time line (ECM casting; day -1, EC seeding; day 0, maturation of the channel and start experiment; day 3), is shown in Supplemental Figure 1. Quantification of channel diameter shows a limited ~60 µm (~12%) increase in channel diameter immediately after needle removal (Figure 1E). Other procedures, such as seeding of the channels with HUVECs, prolonged static culture and flow perfusion did not further influence the channel diameter. Using this setup, the device offers a biocompatible, homogenous, isotropic, and optically transparent setting that is suitable for direct observation of the ECM channels by (fluorescence) microscopy in real-time. The distance from the center of the ECM channel to the cover glass is 0.9 µm, which places the entire channel within the working distance of a high-resolution lens on standard confocal microscopes. This arrangement allows direct monitoring and recording of dynamic interactions of vascular and circulating cells in the 3D blood vessel structure.

Bio-engineering of a mechanical flow perfused blood vessel in the fibrinogen matrix environment of the microfluidic device

The human blood vessel is composed of a confluent monolayer of ECs supported by mural cells such as pericytes. To evaluate ECs and pericytes behavior, we co-seeded the microfluidic system with both cell types. GFP-labeled HUVECs directly seeded into the ECM channels of the device developed confluent monolayers in 3 days time under static conditions (Figure 2A, view from bottom side of vessel wall). Monitoring the same channels from day 1 to day 3 reveals a steady increase of ECs till full coverage at day 3. Meanwhile dsRED-labeled pericytes, homogeneously seeded in the fibrinogen matrix, were increasingly recruited to the neovessel over time (Supplemental Figure 2A).

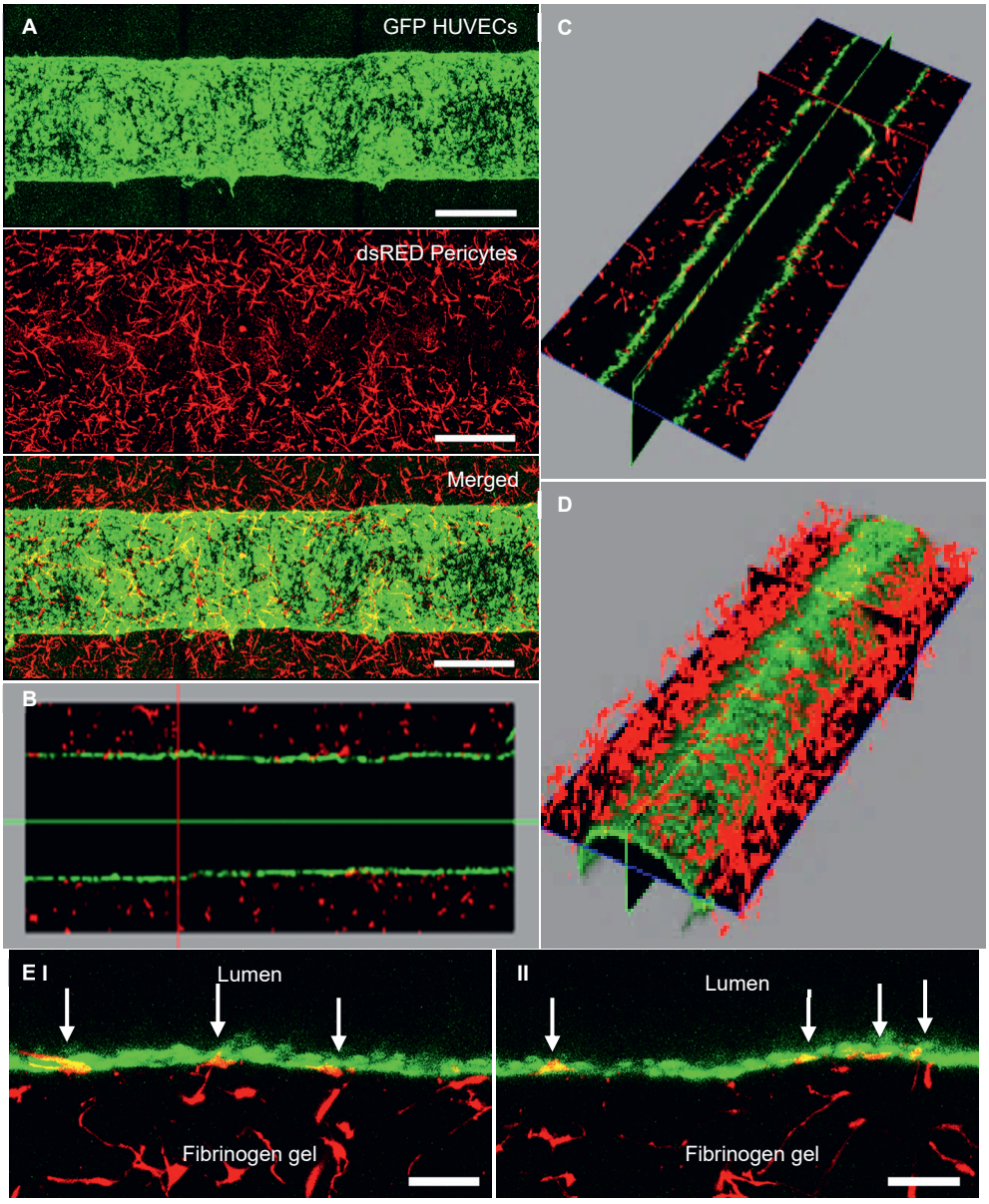

Figure 2. A complex neovessel with open lumen is formed in the ECM channels after 3 days of static co-culture after cell seeding. (A) Confocal micrograph of the endothelial monolayer formed by GFP-labeled HUVECs (green) with perivascular coverage by dsRED-labeled pericytes (red) of the artificial neovessel. Scale bar = 500 µm. **(B)** Longitudinal cross section of the vessel. **(C)** Composite display of longitudinal cross section micrographs. **(D)** 3D reconstruction of half a wall of the neovessel. **(E; I and II)** High magnification views of the vessel wall. Pericytes are localized in direct contact with ECs, indicated by white arrows. Scale bar = 250 µm.

In contrast, in conditions in which only HUVECs-GFP were seeded in the channels without pericytes in the ECM, ECs coverage of the channels remained poor with the cells showing difficulties to maintain a confluent monolayer (Supplemental Figure 2B). The neovessel structures created by co-culture of HUVECs and pericytes maintained an open lumen as shown in the longitudinal and composite views (Figure 2B,C; Supplemental Figure 2C, Supplemental Movie 1). At day 3, some dsRED-labeled pericytes made direct contact with the endothelial monolayer, as shown in the 3D composite (Figure 2D) and high magnification (Figure 2E i and ii) views. Flow perfusion was introduced in the microfluidics device by connecting the inlets and outlets with tubing in a closed system connected to an Ibidi pump. The ECM channels were first perfused with medium at 20 µl/minute and incubated at 5% CO_2 at 37˚C to allow the ECs monolayer to adjust from a static condition to flow.

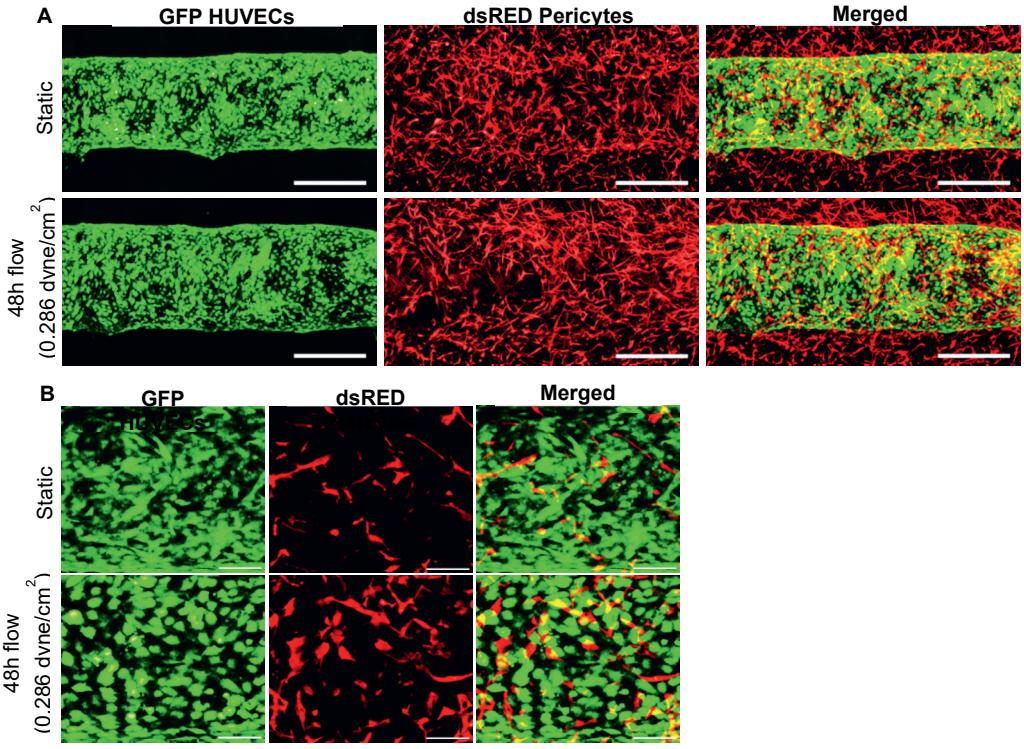

Figure 3. Flow perfusion of the neovessels in the microfluidics device. (A) Micrographs show the monolayer of GFP-labeled HUVECs and perivascular coverage of dsRED-labeled pericytes of the neovessels after 5 days of static culture (upper row) and after 3 days of static culture + 2 days of flow perfusion (0.286 dyne/cm^2, 40 µl/ml, lower row). Scale bar = 500 µm. **(B)** high magnification images of static culture (upper row) and perfused (lower row) neovessels. Scale bar = 100 µm.

Experiments to evaluate the sprouting capacity of the established neovessel also showed pericyte coverage of the emerging endothelial sprouts (Supplemental Figure 2D, Supplemental Movie 2).

After 24h, the flow rate was increased to 40 µl/min, which yields an estimated shear rate of 38.3 sec^{-1} or a wall shear stress of 0.286 $dyne/cm^2$. This is close to, or within the range of, the levels previously used in microfluidic studies that focus on leukocyte-endothelium interaction under controlled flow [45-47]. After 2 days of controlled continuous perfusion at 40 µl/min, the endothelial coverage of the seeded ECM channels remained fully confluent and perivascular pericyte coverage of the neovessel remained intact (Figure 3A,B).

To assess in more detail if prolonged culture and/or flow improves the number of recruited pericytes to the direct neovessel ECM surroundings and subsequent promote neovessel coverage, quantification of the dsRED signal was conducted in co-cultures at 4- and 5-days post seeding. A steady increase of pericyte area per standardized image view was observed when comparing day 4 and 5 with day 3 post seeding under static conditions (Figure 4A,B). No additional effect on pericyte area in the neovessel surrounding ECM was observed when flow was applied at day 4 (Figure 4B). The increased coverage over time was not attributed to adaptations in cell morphology and subsequent increase per individual pericyte cell surface area, but is associated with an increase in total pericyte number (Supplemental Figure 2E). This increase in the amount of pericytes stabilized after 7 days of static co-culture (data not shown).

The time-dependent increase in local accumulation of pericytes was more pronounced closer to the endothelial wall (Figure 4C). To analyze pericyte distribution, different segments were defined, ranging from 0-200, 200-400, 400-600 µm from the vessel wall into the ECM gel, with 0 assigned to the location nearest to the vessel wall. Quantification of pericyte+ areas in each segment showed that there are more pericytes present within the segments closest to the neovessel after 5 days of static culture (Figure 4D,E). This typical distribution pattern persists after prolonged incubation (e.g. day 9) of the microfluidic device (data not shown). Prolonged co-culture of pericytes with ECs in the microfluidic system did not diminish the pericyte phenotype, as shown by assessment of expression levels of typical pericyte markers PDGFRβ and NG2 over a period of 7 days, in whole neovessels and ECM lysates. At 7 days post seeding, a significant increase in mRNA levels of both pericytes markers was observed compared to earlier time points (Figure 4F).

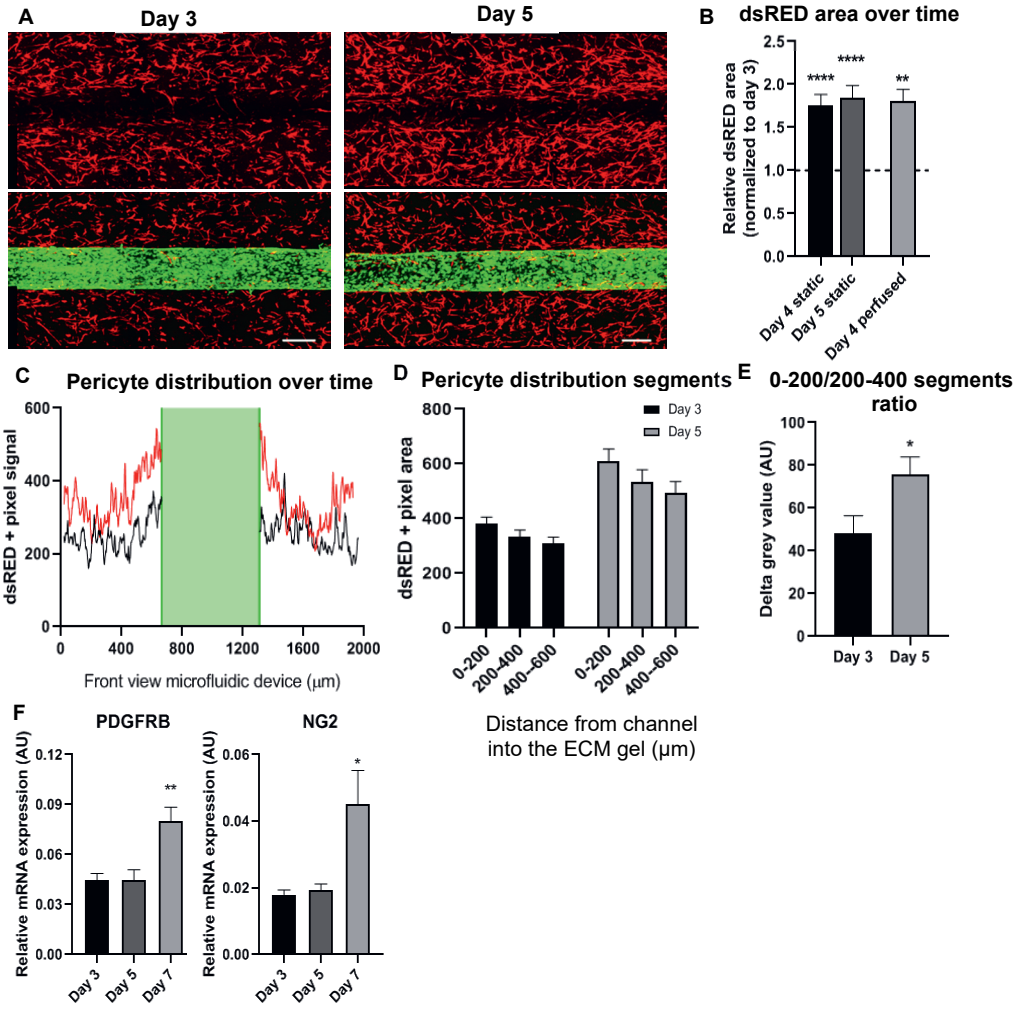

Figure 4. Pericyte characteristics over time. (A) Representative projection of dsRED pericytes (upper picture) and merged with GFP endothelial cells (green; lower picture) signals at day 3 and day 5 of culture under static conditions. Scale bar = 250 µm. **(B)** Increase of pericyte dsRED area over time and after flow: total dsRED area per image view are displayed for day 4 (N=6) and day 5 (N=14) under static conditions and 1 day after perfusion (day 4; N=5). Day 4 and 5 (both static) and day 4 perfusion (1 day of perfusion) are normalized to their starting point, day 3 (dotted line). **P<0.01, ****P<0.0001. **(C)** Representative view of changes in pericyte distribution over time. Average dsRED signal (grey value) of day 3 (black line) and day 5 (red line) quantified in a cross section perpendicular to the neovessel. The green area represents the neovessel area. Beside the higher signal of pericytes at day 5 (due to increase in numbers), the distribution of the pericytes is more shifted to the vicinity of the neovessel compared to day 3. **(D)** Changes in pericyte distribution over time in different locations in close and distant proximity of the neovessel. To analyze pericyte distribution, different segments were defined ranging from 0-200, 200-400, 400-600 from the neovessel wall into the ECM gel, with 0 nearest to the vessel wall. The graph shows the average

◄pericyte area (grey value dsRED) of the different segments at day 3 and day 5. Pericyte area at day 5 is increased compared to day 3, due to increase in pericyte numbers. **(E)** Significant increase in pericyte recruitment towards the vessel wall over time. To analyze the changes in pericyte recruitment towards the 0 baseline location (vessel wall), changes in pericyte area in segment 0-200 and 200-400 were assessed as calculated by the delta of area values in segments 0-200 vs 200-400 at day 3 (black bar graph) compared to day 5 (grey bar graph). N=6, *P<0.05. **(F)** mRNA levels for well-known pericyte markers PDGFRβ and NG2 over time. Both genes were significantly upregulated at day 7 compared to earlier time points. N=5, *P<0.05, **P<0.01.

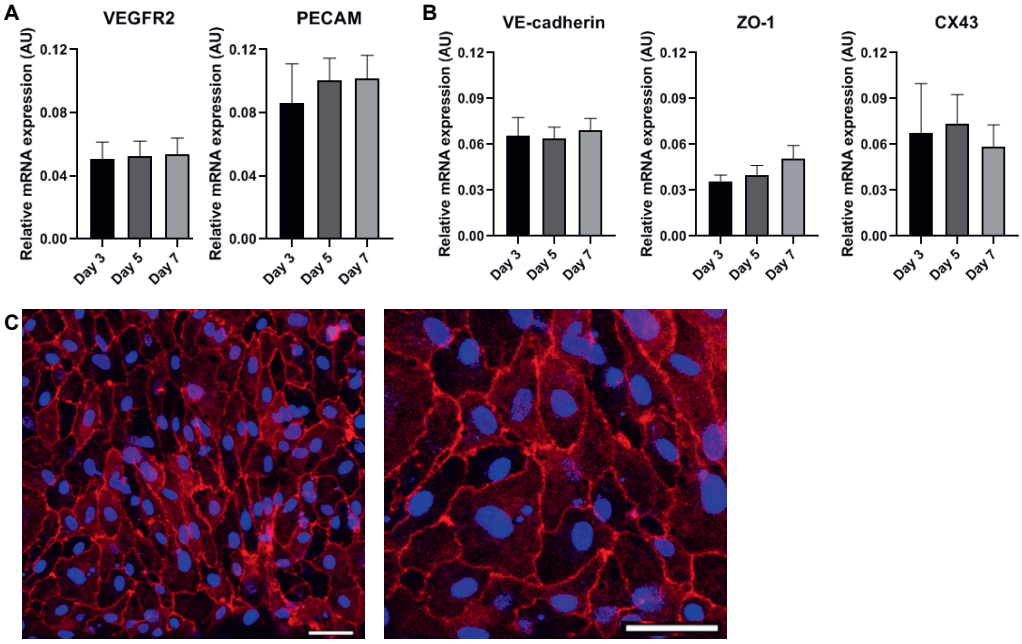

Figure 5. Endothelial characteristics over time. (A) Stable mRNA levels of well-known endothelial cells markers VEGFR2 and PECAM over time. **(B)** Stable mRNA levels of junction markers VE-cadherin, ZO-1 and CX43 over time. All graphs are N=5, except ZO-1 (N=4). **(C)** VE-cadherin staining of the endothelial monolayer of the neovessel. VE-cadherin junctions (red) are clearly visible between the endothelial cells. DAPI signal (blue) stains cell nuclei. High magnification image (right) shows the VE-cadherin junctions between endothelial cells and DAPI+ nuclei. Scale bar = 50 µm.

Similarly, prolonged co-culture in the device did not diminish the EC phenotype, as shown by stable mRNA levels of typical endothelial markers VEGFR2 and PECAM (Figure 5A). Likewise mRNA levels of adherens junction VE-cadherin, tight junction ZO-1 and gap junction connexin 43 (CX43) remained constant during the 7 days of co-culture (Figure 5B). To specifically evaluate the expression of cell junction markers by ECs that comprise the monolayer in the

neovessels, separate lysates for RNA isolation of ECs in the channels and pericytes in the gel were harvested. ECs and pericytes enrichment of the harvested fractions was validated by qPCR evaluation of ECs and pericytes markers (Supplemental Figure 3A). The ECs enriched fraction showed a trend (P=0.099) of higher VE-cadherin expression compared to 2D mono cultured ECs and comparable expression levels to ECs co-cultured with pericytes in a trans-well setup (Supplemental Figure 3B). Fluorescent immunostaining of VE-cadherin of the neovessels in static co-culture conditions showed well-established adherens junctions in the endothelial monolayer (Figure 5C), indicating successful establishment of an intact endothelial barrier.

Assessment of endothelial barrier function

An important function of the endothelium *in vivo* is to form an active, regulatory barrier between the vessel lumen and the surrounding tissue for relatively large sized plasma proteins and circulating cells. Therefore, we assessed the endothelial barrier function of the established ECs monolayer in the ECM channels by monitoring the trans-endothelial diffusion of rhodamine labeled 70 kDa dextran during static culture conditions at 3 days post seeding in the microfluidic device. ECM channels without coverage of HUVECs and pericytes showed dextran leakage into the ECM environment at 1 min after onset of dextran injection. Fluorescent dextran signal was increased after 30 min. Similarly, coverage of ECM channels with HUVECs only produced considerable dextran leakage at 1 and 30 min post perfusion time points. In contrast, coverage of ECM channels with HUVECs and pericytes clearly reduced dextran leakage at 1 and 30 min after onset of dextran perfusion compared to the other two conditions (Figure 6A). The fluorescent area of the dextran rhodamine signal that has penetrated into the surrounding ECM was quantified per cross-sectional location and displayed in bell-curve graphs for 1 and 30 min measurements. The slopes for the 1 and 30 min bell-curves of the ’HUVECs + pericytes’ condition were considerably steeper than the slopes of the ’no cells‘ and ’HUVECs single‘ conditions, indicating that dextran rhodamine signal was more maintained within the ECM channel when the device was seeded with both HUVECs and pericytes (Figure 6B). Quantification of the area under the bell-curve (AUC), showed a significant increase in dextran area inside the channel for ‘HUVECs + pericytes‘ versus ’HUVECs single‘ or ’no cells‘ conditions at 30 min after onset of dextran perfusion (Figure 6C). In line with these findings, the AUC shows a significant increase in dextran area outside of the channel for ‘no cells’ and ‘HUVECs single’ versus ’HUVECs + pericytes‘ conditions at 30 min after onset of dextran perfusion (Figure 6D). The calculated permeability coefficients derived from these data similarly shows a reduction in dextran leakage between ’HUVECs + pericytes’ compared to ‘HUVECs single’ (2.62×10^{-7} cm/s +/- 2.45×10^{-7} cm/s

versus 3.12 x 10^{-6} cm/s +/- 4.26 x 10^{-7} cm/s; P=0.002) and 'HUVECs + pericytes' versus 'no cells' (2.62 x 10^{-7} cm/s +/- 2.45 x 10^{-7} cm/s versus 4.21 x 10^{-6} cm/s +/- 4.7 x 10^{-8} cm/s; P<=0.001) conditions.

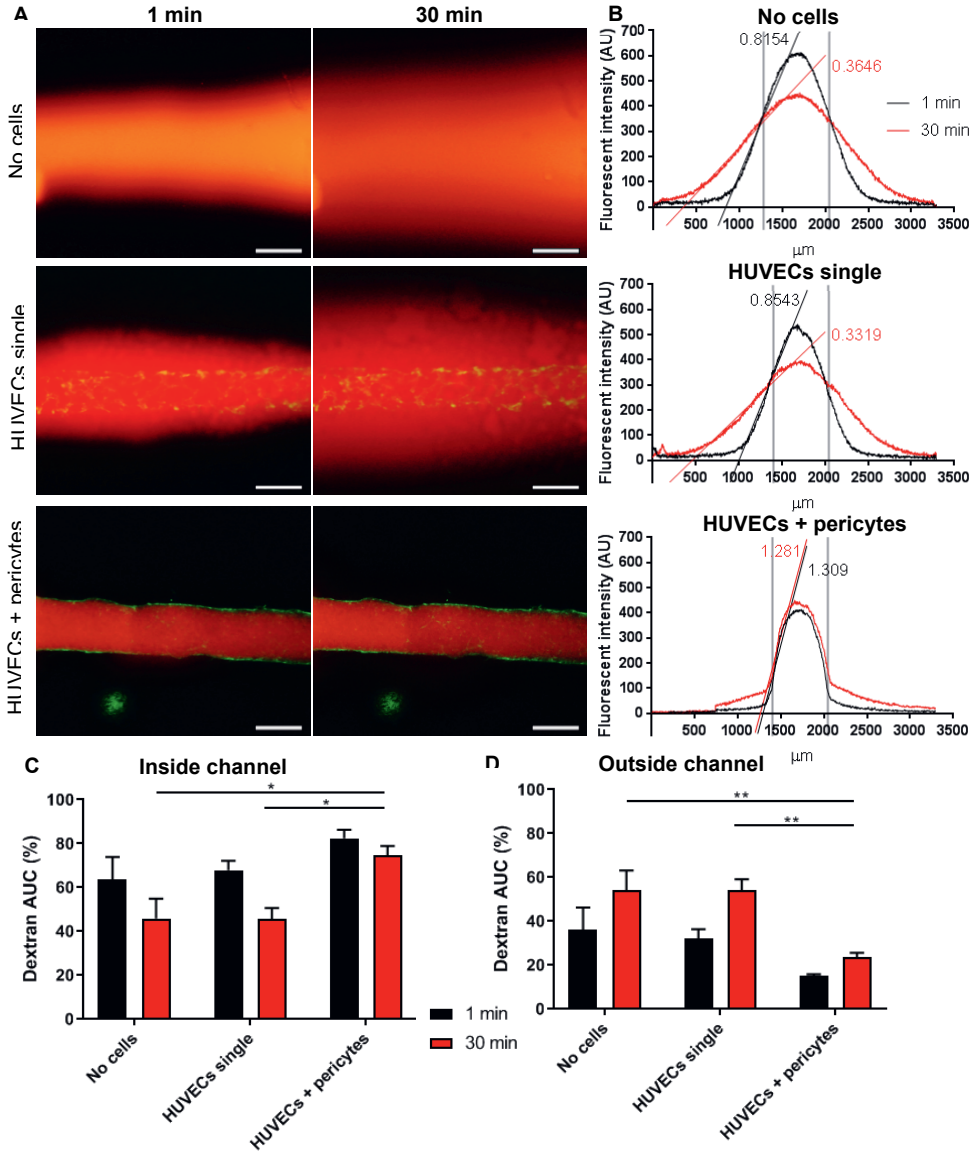

Figure 6. Assessment of the endothelial barrier function of neovessels in the microfluidics device. **(A)** Micrographs show 70 kDa dextran rhodamine diffusion out of the vessel lumens at 1 minute and 30 minutes post dextran infusion into ECM in channels without cells (upper row), ECM channels seeded with single GFP-labeled HUVECs (mid row), and neovessels composed of GFP-labeled HUVECs and

◄pericytes seeded in the ECM channels (lower row). Scale bar = 500 µm. **(B)** Cross-diameter bell-curve distribution of the fluorescent intensity of dextran rhodamine over the ECM compartment and channels for the different groups (without cells, with only GFP-labeled HUVECs, and with GFP-labeled HUVECs + pericytes), at 1 and 30 minutes post dextran rhodamine infusion. Slopes of the shoulders of the bell-curves are indicated in the graph. Quantified fluorescent intensity is shown on the Y-axes. Cross section location is shown on X-axes. The channel area is indicated by the grey lines in the graphs. **(C)** Bar graphs show the quantified data of dextran rhodamine+ area under the curve (AUC) inside the ECM channel of the different groups (without cells, with only GFP-labeled HUVECs, and with GFP-labeled HUVECs + pericytes), at 1 and 30 minutes post dextran rhodamine infusion, in percentage of total curve area. N=4, *P<0.05. **(D)** Bar graphs show the quantified data of dextran rhodamine+ AUC outside of the ECM channels of the different groups (without cells, with only GFP-labeled HUVECs, and with GFP-labeled HUVECs + pericytes), at 1 and 30 minutes post dextran rhodamine infusion, in percentage of total curve area. N=4 (1 channel from 4 different microfluidic devices), **P<0.001.

The fluorescent area of the dextran rhodamine signal that has penetrated into the surrounding ECM was again quantified per cross-sectional location and displayed in bell-curve graphs for different doses of Thrombin at different time points. Bell-curves of 0.5 U and 1 U thrombin addition to dextran at 1 minute, 30 min and 60 min after onset of dextran injection show a different distribution compared to control conditions (Figure 7A). Quantification of the AUC shows a significant increase in dextran area outside the channel in the ECM in thrombin versus control conditions at the 30 and 60 min time points (Figure 7B). However, the calculated permeability coefficient did not show a significant difference.
In addition, thrombin treated endothelial channels stained for VE-cadherin showed small disruptions of the adherens junction versus non-treated controls (Figure 7C). These data show that the newly developed platform can be used to monitor and quantify vascular leakage over time and detect inflammatory cytokine induced alterations in endothelial barrier function.

Assessment of monocyte-endothelial interaction

One important aspect for a vessel-on-a-chip system to replicate for disease studies is the interaction between ECs and circulating (immune) cells. We assessed the interaction of circulating monocytes (THP-1) and the vascular wall in the presence and absence of pro-inflammatory cytokine TNFα. Flow perfusion was introduced as described above, but now with the addition of THP-1 cells in the perfusion medium. The perfusion medium was a mix of EGM-2 and RPMI medium to meet both ECs and THP-1 cells requirements. THP-1 cells were visualized with CellTracker deep red in combination with GFP-labeled HUVECs and dsRED-labeled pericytes. Confocal microscopy showed live perfusion of THP-1 cells through the endothelial channel (Supplemental Figure 4A,B; Supplemental Movie 3).

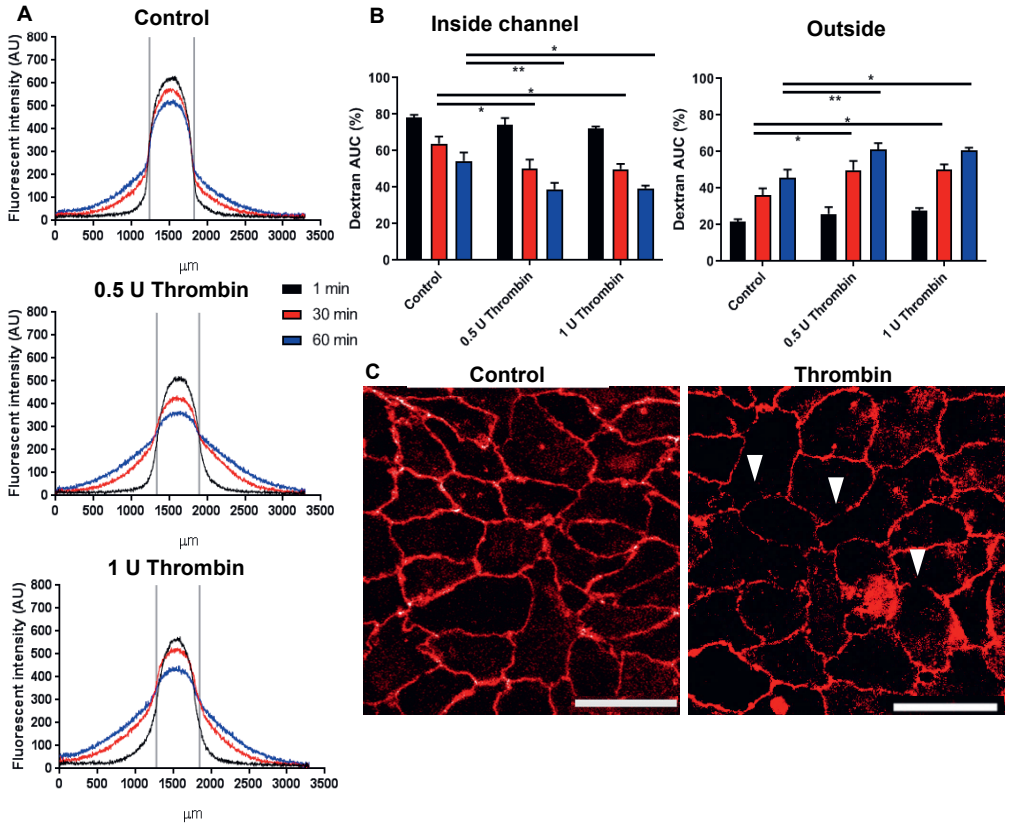

Figure 7. Endothelial barrier function in the microfluidics device is responsive to thrombin stimulation. (A) Cross-diameter bell-curve distribution of the fluorescent intensity of dextran rhodamine over the ECM compartment and neovessels for the different groups (control, 0.5 U and 1 U thrombin), at 1, 30 and 60 minutes post dextran rhodamine infusion. Quantified fluorescent intensity is shown on the Y-axes. Cross section location is shown on X-axes. ECM channel area is indicated with grey lines in the graph. **(B)** Bar graphs show the quantified data of dextran rhodamine+ area under the curve (AUC) inside (top graph) or outside vessel (lower graph) areas of the different groups (control, 0.5 U and 1 U thrombin), at 1, 30 and 60 minutes post dextran rhodamine infusion. N=4 (1 channel from 4 different microfluidic devices), *P<0.05, **P<0.001. **(C)** VE-cadherin staining of the endothelial monolayer of the neovessels with and without thrombin stimulation. The control condition shows the clear line patterns of the VE-cadherin junctions between the endothelial cells (left). Thrombin stimulation results in small interruptions between the VE-cadherin junctions (white arrowheads). Scale bar = 50 µm.

A limited number of THP-1 cells attached to the endothelial wall under earlier described flow conditions (Figure 8A). Addition of TNFα in the perfusion medium significantly increase attachment of THP-1 cells in these neovessels (Figure 8B,C). Quantification of Z-stack images showed increased co-localization of THP-1 cells and ECs with TNFα stimulation (Figure 8D). TNFα did not influence THP-1 proliferation (data not shown). In addition, a trend (P=0.07) is observed demonstrating an increase in percentage THP-1 area co-localized with pericyte area in TNFα conditions (Figure 8E). TNFα did not influence total HUVECs or pericyte area, nor did it affect co-localization of HUVECs with pericytes (Supplemental Figure 4C,E). Binding of THP-1 cells to these neovessels in pro-inflammatory conditions illustrates that this *in vitro* microfluidic model emulates *in vivo* properties of the vasculature during inflammation.

Discussion

In this study, we designed, manufactured, and validated a novel microfluidic vessel-on-a-chip system that replicates complex, and most importantly, functional neovessel structures in a full 3D ECM environment. The most important findings of the present study are: 1) The ECM channels provide an excellent base to seed ECs to form tissue-engineered neovessels with relevant morphology and an open lumen supported by perivascular pericytes in a full 3D ECM microenvironment. 2) The endothelial monolayer inside the channels is maintained when exposed to controlled, unidirectional, continuous flow when perfused for up to 48 hours. 3) The created device provides an easily accessible platform for live confocal imaging of interaction between vascular cells, and (4) both pericytes and ECs contribute to a viable and functional neovessel. 5) The presence of pericytes in the microfluidic system is essential to maintain the endothelial barrier function of the tissue-engineered vessel, as monitored and quantified by using fluorescent labeled dextran perfusion. 6) Endothelial barrier function in the device is responsive to biological stimuli such as thrombin, making it a suitable platform for testing endothelial barrier function to different biological factors and pharmaceutical compounds. Furthermore, 7) circulating monocytes interact with the endothelial wall in response to the pro-inflammatory cytokine TNFα, demonstrating that the system is suitable for testing circulating leukocytes attachment to the endothelium during inflammation.

The low-cost and high throughput capacity of microfluidic technology could bridge the gap between *in vitro* and *in vivo* methods. We designed a microfluidic device that can easily be manufactured using standard PDMS casting techniques and can be used for live confocal imaging.

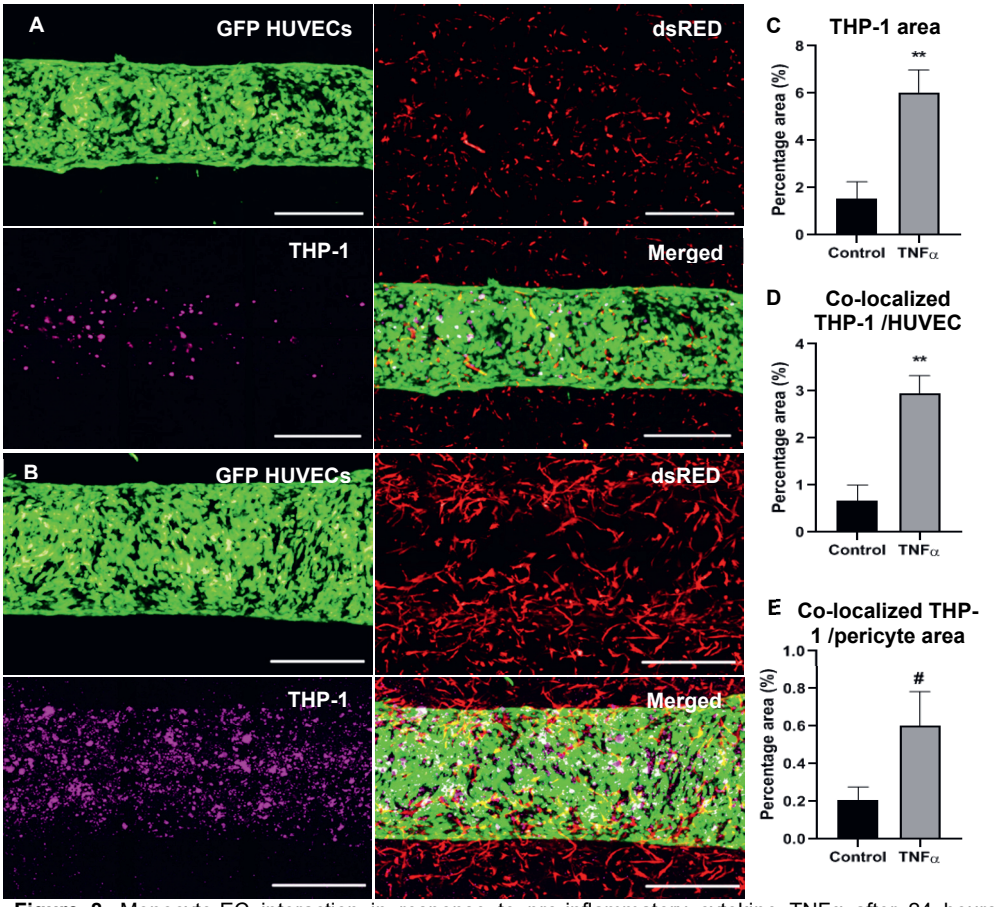

Figure 8. Monocyte-EC interaction in response to pro-inflammatory cytokine TNFα after 24 hours perfusion. **(A)** Vessel wall shown after perfusion with medium with THP-1 cells (magenta) for 24 hours, shown are attached THP-1 cells. HUVECs are shown in green, pericytes in red. **(B)** Vessel wall after perfusion with THP-1 (magenta) for 24 hours in presence of TNFα. Scale bar = 500 µm. **(C)** THP-1 positive area shown in percentage of the total image area (displayed on Y-axes) is significantly increased in response to TNFα stimulation. **(D)** THP-1 positive area co-localizing with ECs is significantly increased in TNFα conditions. **(E)** THP-1 positive area co-localizing with pericytes shows a trend (#P=0.0701) of increase when TNFα present. N=6 (1 channel from 6 different microfluidic devices), **P<0.001.

The PDMS devices are highly reproducible due to the casting method and easy to handle during culturing and setup. This device enables the co-cultivation of multiple vascular cell types in a 3D fashion with ECM interactions, thereby mimicking the *in vivo* situation. Our current microfluidic platform supports two important readout parameters for the assessment of vascular function:

(1) Endothelial barrier function: Our tissue-engineered vessel supported by pericytes establishes a functional monolayer which can be quantified using fluorescent labelled dextran diffusion. This method is often used in microfluidic systems to quantify vascular barrier function [48,49]. The calculated permeability coefficients of 2.62×10^{-7} cm/s and 3.12×10^{-6} cm/s for pericytes + ECs and only ECs conditions in our microfluidic system fall within the broad range reported by previous studies [49-51]. This level of permeability is higher than the levels observed *in vivo* models, yet lower compared to other *in vitro* models as indicated by Lee and colleagues [51]. In line with our data, Kim *et al.* observed a reduction in permeability when ECs were co-cultured with pericytes in their vessel-on-a-chip system [52]. Similarly Campisi *et al.* observed a reduction in permeability when pericytes were added to an iPSC derived endothelial culture in their blood brain barrier system [21], with permeability further reduced when the authors used a combination of pericytes, iPSC ECs, and astrocytes [21]. Alimperti *et al.* also demonstrated the supportive role of bone marrow stromal cells in endothelial barrier function when these cells were co-cultured at different ratios with ECs, illustrating that pericytes are not the only dedicated cell types for vasculature support [53].
Furthermore, our microfluidic model also responds to thrombin-induced ECs barrier changes: Thrombin stimulation disrupts VE-cadherin binding between ECs, thus decreasing the number of intact adherens junctions and impairing vascular barrier function [54-56]. Our data demonstrates that quantification of alterations in endothelial barrier function in response to thrombin is possible within a short time frame (1 hour) by assessment of dextran diffusion and VE-cadherin disturbance, which is line with a limited number of microfluidics systems that in their design offer a similar possibility to test endothelial barrier changes to thrombin [53,57].

(2) Interaction with circulating immune cells under flow: Circulating monocytes that show limited interaction with blood vessels during healthy conditions engage profoundly with the endothelium during inflammation, with leukocyte-rolling, -adhesion and -diapedesis mounting to an efficient first immune response at the inflammation site in response to multiple pro-inflammatory cytokines such as TNFα [58-65]. Our novel vessel-on-a-chip system allows pump-controlled, continuous, unidirectional perfusion of the tissue-engineered vessel with circulating cells, such as THP-1 cells, thus permitting live assessment of interaction of these cells with the endothelium in response to e.g. TNFα stimulation. Increased attachment of THP-1 cells to the vessel wall was observed in presence of TNFα after 24 hours, making the model suitable for studying immunological responses of the inflamed vasculature. TNFα levels vary greatly in different inflammatory diseases. For example, rheumatoid arthritis patients show a modest rise to 17.9 pg/ml compared to patients with severe bone fractures (0.1 ng/ml) [66,67]. Other groups found different TNFα levels in pre-eclamptic women (210 pg/ml vs 1.93 pg/ml),

clearly demonstrating the marked variation of TNFα levels reported in serum, even within the same disease, which could be due to differences in detection method or cohort group [68]. The concentration of TNFα used *in vitro* is usually much higher (range in ng per ml) compared to the serum TNFα levels measured *in vivo* during inflammation-related diseases, with the latter normally measured in the pg per ml range. The TNFα concentration that was used in the present study is well in line with other *in vitro* assays which assess monocyte adhesion and interaction with the ECs under flow in more traditional fluid-chamber settings [11,65,69]. In the present study, a trend ($p=0.07$) towards increased pericyte/THP-1 co-localization was observed when THP-1 were flowed in the presence of TNFα compared to control. Recent studies identified pericytes as important regulators in leukocytes extravasation [70,71]. $NG2^+$ subsets of pericytes constitutively express ICAM-1 on their membrane, whereas $NG2^-$ pericytes express ICAM-1 after TNFα stimulation [71]. Proebstl *et al.* showed that the occurrence of enlarged gaps between adjacent pericytes in response to inflammatory cytokines facilitates transmigration of leukocytes by binding to ICAM-1 expressing pericytes [71]. Ayres-Sander *et al.* confirmed the beneficial role of pericytes in trans-endothelial migration of neutrophils [72].

Current model vs existing state-of-the-art microfluidic models

The scientific community increasingly demands more complex 3D models that provide a more complete recapitulation of different vascular biological aspects. Currently, most research groups create their own microfluidic models using novel bio-fabrication methods with each model tailored to their specific research questions and needs.

When comparing our model to current state-of-the-art vessel-on-a-chip systems, our model provides some answers to previously encountered challenges in platform design, particularly in terms of vascular biology and constant flow regulation and perfusion. The advanced system presented by Takahashi *et al*. demonstrated a tubular channel seeded with HUVECs in a full collagen type I hydrogel environment in the absence of flow and mural cell incorporation [14]. The paper by *Tan et al*. presented a tubular channel seeded with human ECs in a full ECM environment with inclusion of vascular smooth muscle cells [73]. The use of other bio-fabrication techniques such as those developed by Jia *et al*. allows coaxial 3D printing to create a hollow tube composed of a bio-ink gel consisting of mainly gelatin-methacryloyl (GelMA) and 4-arm poly(ethylene glycol)-tetra-acrylate (PEGTA) in which a mixture of human mesenchymal cells and HUVECs are fully encapsulated in the tube wall [74]. These types of approaches successfully create a tubular structure with both ECs and mural cells. However, the organization of the cells remains an issue as high density GelMA is known to limit cell

migration [75] and the formation of the distinct layers requires the ability of the cells suspended in the GelMA mix to self-organize into these layers. Similarly, Kolesky *et al.* also created a channel system in a full GelMA environment seeded with a monolayer of endothelial cells that could support endothelial barrier function [31]. However, although they combined this vascular network with other tissue cell types, mural cells were not incorporated and the system was not tested with pump-controlled, continuous flow.

In summary, the most recent studies reporting on vascular regeneration and vascular tissue on a chip all focus on improving different aspects ranging from how to increase complexity and biological function to assessment of different bio-fabrication methods for vascular structures. The majority of the published vascular microfluidic models share common features concerning bio-fabrication method, flow, 3D environment, ECM and types of cells used in culture. Most studies focus on a specific research question using a dedicated microfluidic model with predefined characteristics to test their hypothesis and thus, all have their own merits and limitations. For our vessel-on–a-chip system, we focus mainly on recreating a system with a biological environment that not only sustains vascular cells, but also supports a vascular response that mimics the natural conditions, including the capacity of the cytokine-activated endothelium to interact with circulating immune cells. Our system thereby offers a valuable complementary model to existing platforms, which are more orientated towards assessing e.g. sprouting capacity and interaction with tissue specific cells. Follow up studies using this new model can provide valuable new insights in the immune cell-mediated pathogenesis of vascular disease. For example, current research in the pericyte field has demonstrated the involvement of pericytes in tissue fibrogenesis: upon activation by macrophage derived Amphiregulin (an epidermal growth factor receptor (EGFR) ligand), pericytes transdifferentiate into myofibroblasts in a TGFβ dependent manner [76]. Yet, certain subtypes of pericytes, such as CD73+ pericytes in the kidney, have been shown to suppress inflammation and prevent progressive renal fibrosis [77]. Furthermore, the presented model provides a suitable platform to allow in depth analysis of the contribution of different subtypes of pericytes in relation to inflammation control and fibrogenesis in multiple diseases including chronic kidney disease.

For diastolic heart failure, we have recently identified a possible role for the pericytes that support the cardiac microvascular bed in disease onset or progression. Characterized by increased stiffness in the left ventricle with decreased compliance and impaired relaxation, research of the pathogenesis of diastolic heart failure points towards a disease pathway with which involves endothelial dysfunction, vascular rarefaction, inflammation and fibrosis that negatively influences myocyte performance and promotes cardiac wall stiffening. Most

significantly, we have recently shown in a rat model of diastolic heart failure, that cardiac fibrosis initiates in microvascular foci, which are characterized by a disorganization of hyper proliferative endothelial cells and pericytes. These foci are hotbeds of inflammation and deposition of fibrosis-associated ECM components [78]. In addition, rise in TGFβ levels and TGFβ pathway activation plays a central role in pathogenesis of this disease. Despite these obvious links with inflammation and fibrosis, the role of pericytes has not been studied in diastolic heart failure.

Limitations of the study

In the current model, human brain-derived pericytes were used for mural cell support of the endothelial monolayer. Although human brain-derived pericytes are considered a specialized phenotype of perivascular cells, they are often used to conduct microvascular research [21,79-82]. Cross check with multiple GEO datasets of freshly isolated murine mural cells [82] with *in vitro* cultured iPSC derived pericytes [83] (GSE124579) and placental pericytes [84] (GSE117469) with our own dataset of *in vitro* brain derived pericytes showed many similarities [85]. Overlap of all genes with positive reads produces a list of 137 genes that includes prominent and well defined pericytes markers such as ACTA2, PDGFRβ, NG2 (CSPG4), TAGLN, CD248, MYH11, DES, ZIC1 and MCAM [85]. The most prominent pericyte markers PDGFRβ and NG2 were also expressed in the top tertile of the total RNA signal. These findings show that human brain-derived pericytes share a large number of common markers with pericytes derived from other sources.

The diameter of the current neovessels may be considered too large to mimic micro-vessels. One of the main aims of this study was to design and create a vessel-on-a-chip system that has the capacity to mimic circulating cell interaction with the vasculature *in vivo* during an inflammatory response. *In vivo*, leukocyte activation and subsequent rolling and adhesion to the vessel luminal surface mainly takes place in the post-capillary venules where shear rate and shear stress levels are intrinsically low [86,87]. These venules may range in 10-100 μm in diameter. In relation to this, pericytes are not only present in the capillaries, but also provide support to vessels with larger diameters, including pre- and post-arterioles, capillaries and venules (<100 μm) as reviewed in multiple publications [33,88]. Our present system supports neovessels with a diameter of 500 μm, which may be considered too large. For any vessel-on-a-chip system that focusses on faithfully recreating native biomechanical conditions, it remains very challenging to create vessels in the capillary range that can sustain prolonged physiologically relevant flow without damaging the integrity of the vessel structure or compromising on the stiffness of the supporting ECM or hydrogel. Thus far, several studies

have reported the use of fully soft material encased channels with a diameter ranging between 360 and 800 µm, which permit perfusion [15,16,30,89]. Similar to our system, these previously reported setups were limited in their ability to further reduce the diameter to the desired range due to limitations in the biomechanical properties of the encasing ECM or hydrogel. Studies that have achieved flowed channels within the capillary range have their own disadvantages as most of the time, they can only sustain perfusion using low levels (bi-directional and non-continuous) of gravitational flow without the active control of mechanical pump systems [41-43]. Despite the discrepancy in size between venules and the neovessels in our current system, many traits in the natural behavior of pericytes and ECs during their interaction, such as pericyte recruitment and effect on the establishment of the endothelial barrier, could still be successfully demonstrated in our platform.

Channel size reduction may be achieved in future studies using the top-down subtractive 3D printing strategy, based on printing the predefined channels with a soluble material, such as carbohydrate glass [87] and Pluronic F127 [31] before casting or 3D printing the hydrogel, followed by channel creation by dissolving the sacrificial materials. This approach allows creation of channels in a range of 1000 to 50 µm, although perfusion with physiological flow without disruption of the hydrogel wall will still remain an issue. Relatively high circumferential stretch (>110%) as a result of flow may cause channel expansion and disruption of cell-cell junctions in the endothelium thus compromising barrier function and vessel integrity. In the living body, the native micro-vessels are surrounded by tissue cells that provide additional mechanical support. An increase in hydrogel strength, so stretch remain limited under physiological flow levels, may provide the answer to gel encapsulated systems like ours. However, it has to be taken into consideration that the desired properties of an optimal hydrogel for the perfused vascular system require a delicate balance between what is supportive of biological function (such as maintaining migratory ability of mural cells through the hydrogel for self-organization) and providing mechanical strength and elasticity to counter act the circumferential stretch.

When considering the microvasculature, the shear stress level of 0.286 dyne/cm^2 is low compared to the levels reported by e.g. Koutsiaris *et al.* who calculated wall shear stress in the human eye [86]. Based on the diameter of the smallest human conjunctival capillaries, the wall shear stress was ~95 dyne/cm^2, whereas 2.8 dyne/cm^2 was calculated for the post-capillary venules [86]. Shear stress levels differ largely between organs and tissues and also varies considerably within the same tissue depending on the location in the capillary bed [91]. For example, the shear stress in glomerular capillaries ranges between 1 and 95 dyne/cm^2

[92], whereas shear stress in the capillaries of the highly vascularized placenta is calculated to be ~0.5 dyne/cm^2 [93]. Furthermore, shear stress is often calculated based on the following equation: $\tau w = 4\mu Q/\pi r3$, in which shear stress at the luminal wall (τw) depends on flow rate (Q), fluid viscosity (μ), and inner radius the vessel (r). It has been suggested that although this is a correct assumption for larger straight vessels segments with limited bifurcations, an alternative formula should be used to calculated wall shear stress in capillaries of the microvascular bed: $\tau w = \Delta Pd/4L$, with wall shear stress (τw) calculated from the pressure difference across the capillary (ΔP), and the inner diameter (d) and length (L) of the capillary [94]. By using this method for wall shear stress calculations, Cho *et al.* calculated that in murine mesentery capillaries, based on the pressure gradients reported [95], wall shear stress in a micro-vessel was 0.16 dyne/cm^2 [94]. Our calculated wall shear stress (0.286 dyne/cm^2) is similar compared to the study of Osaki *et al* [16]. Systems that use unmonitored gravitational flow have severely limited control over flow speed, as it will decline with exhaustion of the source reservoir, and are therefore unsuitable for studies with circulating cells which require controlled unidirectional flow with a consistent flow rate [15,43,49]. Some *in vitro* systems use Ibidi slides and pumps or other designs to perfuse immune cells in a blood vessel mimicking environment. In these systems, slide seeded ECs are perfused with neutrophils or other circulating cells with a shear stress between 0.5 and 1 dyne/cm^2 [11,65,69,96]. These shear stress levels are close to the range of shear stress in our current microfluidic model.

Conclusions

In conclusion, we designed, fabricated and tested a novel vasculature microfluidic device to mimic complex vasculature tissue. Our vessel-on-a-chip can be easily produced and (live) monitored using a standard confocal microscope setup. This model enables the co-culture of multiple (vascular) cell types in a 3D ECM environment while being perfused with relevant microvascular flow levels. The high flexibility of this model allows researchers to study specific interactions between different cell types and cell-ECM interaction, in a background of different stimuli to mimic specific (disease) environments. Our current microfluidic device provides a unique tool to conduct *in vitro* analysis of the human microvasculature during the inflammation process of a multitude of different relevant human diseases.

References

1. Chang WG, Niklason LE: A short discourse on vascular tissue engineering. *NPJ. Regen. Med* **2017**, 2:7.
2. Dejana E, Orsenigo F, Lampugnani MG: The role of adherens junctions and VE-cadherin in the control of vascular permeability. *J. Cell Sci* **2008**, 121:2115-2122.
3. Tornavaca O, Chia M, Dufton N, Almagro O, Conway DE, Randi AM, Schwartz MA, Matter K, Balda MS: ZO-1 controls endothelial adherens junctions, cell-cell tension, angiogenesis, and barrier formation. *J. Cell Biol* **2015**, 208:821-838.
4. Allport JR, Muller WA, Luscinskdas FW: Monocytes induce reversible focal changes in vascular endothelial cadherin complex during transendothelial migration under flow. *J. Cell Biol* **2000**, 148:203-216.
5. Vestweber D: How leukocytes cross the vascular endothelium. *Nat. Rev. Immunol* **2015**, 15:692-704.
6. Schnoor M, Alcaide P, Voisin MB, van Buul JD: Crossing the vascular wall: common and unique mechanisms exploited by different leukocyte subsets during extravasation. *Mediators. Inflamm* **2015**:946509.
7. Leick M, Azcutia V, Newton G, Luscinskas FW: Leukocyte recruitment in inflammation: basic concepts and new mechanistic insights based on new models and microscopic imaging technologies. *Cell Tissue Res* **2014**, 355(3):647-656.
8. Lawrence M, McIntire L, Eskin S: Effect of flow on polymorphonuclear leukocyte/endothelial cell adhesion. *Blood* **1987**, 70(5):1284-1290.
9. Abbitt KB, Nash GB: Characteristics of leucocyte adhesion directly observed in flowing whole blood *in vitro. British Journal of Haematology* **2001**, 112:55-63.
10. Huang R, Zheng W, Liu W, Zhang W, Long Y, Jiang X: Investigation of tumor cell behaviors on a vascular microenvironment-mimicking microfluidic chip. *Sci Rep* **2015**, 5:17768.
11. Ganguly A, Zhang H, Sharma R, Parsons S, Patel KD: Isolation of human umbilical vein endothelial cells and their use in the study of neutrophil transmigration under flow conditions. *J Vis Exp* **2012,** 66:e4032.
12. Sato, M, Sasaki N, Ato M, Hirakawa S, Sato K, Sato K: Microcirculation-on-a-chip: a microfluidic platform for assaying blood- and lymphatic-vessel permeability. *Plos One* **2015**, 10:e0137301.
13. Song JW, Cavnar SP, Walker AC, Luker KE, Gupta M, Tung YC, Luker GD, Takayama S: Microfluidic endothelium for studying the intravascular adhesion of metastatic breast cancer cells. *PLoS. One* **2009**, 4:e5756.
14. Takahashi H, Kato K, Ueyama K, Kobayashi M, Baik G, Yukawa, Y, Suehiro JI, Matsunaga YT: Visualizing dynamics of angiogenic sprouting from a three-dimensional microvasculature model using stage-top optical coherence tomography. *Sci Rep* **2017**, 7:42426.
15. Nguyen DH, Stapleton SC, Yang MT, Cha SS, Choi CK, Galie PA, Chen CS: Biomimetic model to reconstitute angiogenic sprouting morphogenesis in vitro. *Proc. Natl. Acad. Sci. U. S. A* **2013**, 110:6712-6717.
16. Osaki T, Kakegawa T, Kageyama T, Enomoto J, Nittami T, Fukuda J: Acceleration of vascular sprouting from fabricated perfusable vascular-like structures. *PLoS. One* **2015**, 10:e0123735.
17. Tehranirokh, M, Kouzani AZ, Francis PS, Kanwar JR: Microfluidic devices for cell cultivation and proliferation. *Biomicrofluidics* **2013,** 7:51502.
18. Wong KH, Chang JM, Kamm RD, Tien J: Microfluidic models of vascular functions. *Annu. Rev. Biomed. Eng* **2012**, 14:205-230.
19. Lam SF, Shirure S, Chu YE, Soetikno AG, George SC: Microfluidic device to attain high spatial and temporal control of oxygen. *Plos One* **2018**, 13:e0209574.
20. Shin Y, Choi SH, Kim E, Bylykbashi E, Kim JA, Chung S, Kim DY, Kamm RD, Tanzi RE: Blood-brain barrier dysfunction in a 3D in vitro model of Alzheimer's disease. *Adv Sci (Weinh)* **2019**, 6:1900962.
21. Campisi, M, Shin Y, Osaki T, Hajal C, Chiono V, Kamm RD: 3D self-organized microvascular model of the human blood-brain barrier with endothelial cells, pericytes and astrocytes. *Biomaterials* **2018**, 180:117-129.

22. Bang S, Lee SR, Ko J, Son K, Tahk D, Ahn J, Im C, Jeon NL: A low permeability microfluidic blood-brain barrier platform with direct contact between perfusable vascular network and astrocytes. *Sci. Rep* **2017**, 7:8083.
23. Lee S, Chung M, Jeon NL: 3D brain angiogenesis model to reconstitute maturation of functional human blood-brain barrier *in vitro*. *Biotech Bioeng* **2018**, 117.
24. Kim S, Kim W, Lim S Jeon JS: Vasculature-on-a-chip for in vitro disease models. *Bioengineering* **2017**, 4.
25. Kurokawa, YK, Yin RT, Shang MR, Shirure S, Moya ML, George SC: Human induced pluripotent stem cell-derived endothelial cells for three-dimensional microphysiological systems. *Tissue Eng Part C Methods* **2017**, 23:474-484.
26. Yamamoto K, Tanimura K, Watanabe M, Sano H, Uwamori H, Mabuchi Y, Matsuzaki Y, Chung S, Kamm RD, Tanishita K, Sudo R: Construction of continuous capillary networks stabilized by pericyte-like perivascular cells. *Tissue Eng Part A* **2019**, 25:499-510.
27. Osaki T, Serrano JC, Kamm RD: Cooperative effects of vascular angiogenesis and lymphangiogenesis. *Regen Eng Transl Med* **2018**, 4:120-132.
28. Thompson RL, Margolis EA, Ryan TJ, Coisman BJ, Price GM, Wong KHK, Tien J: Design principles for lymphatic drainage of fluid and solutes from collagen scaffolds. *J Biomed Mater Res A* **2018**, 106:106-114.
29. Jusoh N, Ko J, Jeon NL: Microfluidics-based skin irritation test using in vitro 3D angiogenesis platform. *APL Bioeng* **2019**, 3:036101.
30. Kim JA, Kim HN, Im SK, Chung S, Kang JY, Choi N: Collagen-based brain microvasculature model in vitro using three-dimensional printed template. *Biomicrofluidics* **2015**, 9:024115.
31. Kolesky DB, Truby RL, Gladman AS, Busbee TA, Homan KA, Lewis JA: 3D bioprinting of vascularized, heterogeneous cell-laden tissue constructs. *Adv Mater* **2014**, 26:3124-3130.
32. Armulik A, Genove G, Betsholtz C: Pericytes: developmental, physiological, and pathological perspectives, problems, and promises. *Dev Cell* **2011**, 21:193-215.
33. Van Dijk CGM, Nieuweboer FE, Pei JY, Xu YJ, Burgisser P, van Mulligen E, El Azzouzzi H, Duncker DJ, Verhaar MC, Cheng C: The complex mural cell: pericyte function in health and disease. *Int. J. Cardiol* **2015**, 190:75-89.
34. Lindahl P, Johansson BR, Leveen P, Betsholtz C: Pericyte loss and microaneurysm formation in PDGF-B-deficient mice. *Science* **1997**, 277:242-245.
35. Winkler EA, Bell RD, Zlokovic BV: Pericyte-specific expression of PDGF beta receptor in mouse models with normal and deficient PDGF beta receptor signaling. *Mol. Neurodegener* **2010**, 5:32.
36. Bjarnegard M, Enge M, Norlin J, Gustafsdottir S, Fredriksson S, Abramsson A, Takemoto M, Gustafsson E, Fassler R, Betsholtz C: Endothelium-specific ablation of PDGFB leads to pericyte loss and glomerular, cardiac and placental abnormalities. *Development* **2004**, 131:1847-1857.
37. Chaw KC, Manimaran M, Tay EH, Swaminathan S: Multi-step microfluidic device for studying cancer metastasis. *Lab Chip* **2007**, 7:1041-1047.
38. Zhang Q, Liu T, Qin J: A microfluidic-based device for study of transendothelial invasion of tumor aggregates in realtime. *Lab Chip* **2012**, 12:2837-2842.
39. Kolahi KS, Donjacour A, Liu X, Lin W, Simbulan RK, Bloise E, Maltepe E, Rinaudo P: Effect of substrate stiffness on early mouse embryo development. *Plos One* **2012**, 7:e41717.
40. Hassanisaber, H, Jafari L, Campeau MA, Drevelle O, Lauzon MA, Langelier E, Faucheux N, Rouleau L: The effect of substrate bulk stiffness on focal and fibrillar adhesion formation in human abdominal aortic endothelial cells. *Mater Sci Eng C Mater Biol Appl* **2019**, 98:572-583.
41. Chen MB, Whisler JA, Frose J, Yu C, Shin Y, Kamm RD: On-chip human microvasculature assay for visualization and quantification of tumor cell extravasation dynamics. *Nat Protoc* **2017**, 12:865-880.
42. Kim S, Chung M, Ahn J, Lee S, Jeon NL: Interstitial flow regulates the angiogenic response and phenotype of endothelial cells in a 3D culture model. *Lab Chip* **2016**, 16:4189-4199.

43. Van Duinen V, van de Heuvel A, Trietsch SJ, Lanz HL, van Gils JM, van Zonneveld AJ, Vulto P, Hankemeier T: 96 perfusable blood vessels to study vascular permeability in vitro. *Sci. Rep* **2017**, 7:18071.
44. Price GM, Tien J: Methods for forming human microvascular tubes in vitro and measuring their macromolecular permeability. *Biological Microarrays* **2011**, 671:281-293.
45. Lamberti G, Prabhakarpandian B, Garson C, Smith A, Pant K, Wang B, Kiani MF: Bioinspired microfluidic assay for in vitro modeling of leukocyte-endothelium interactions. *Anal Chem* **2014**, 86:8344-8351.
46. Lawrence MB, Kansas GS, Kunkel EJ, Ley K: Threshold levels of fluid shear promote leukocyte adhesion through selectins (CD62L,P,E). *The Journal of Cell Biology* **1997**, 136:717-727.
47. Simon SI, Hu Y, Vestweber D, Smith CW: Neutrophil tethering on E-selectin activates beta 2 integrin binding to ICAM-1 through a mitogen-activated protein kinase signal transduction pathway. *J Immunol* **2000**, 164:4348-4358.
48. Zervantonakis IK, Hughes-Alford SK, Charest JL, Condeelis JS, Gertler FB, Kamm RD: Three-dimensional microfluidic model for tumor cell intravasation and endothelial barrier function. *Proc. Natl. Acad. Sci. U. S. A* **2012**, 109:13515-13520.
49. Zheng Y, Cheng J, Craven M, Choi NW, Totorica S, Diaz-Santana A, Kermani P, Hempstead B, Fischbach-Teschl C, Lopez JA, Stroock AD: In vitro microvessels for the study of angiogenesis and thrombosis. *Proc. Natl. Acad. Sci. U. S. A* **2012**, 109:9342-9347.
50. Kim S, Lee H, Chung M, Jeon NL: Engineering of functional, perfusable 3D microvascular networks on a chip. *Lab Chip* **2013**, 13:1489-1500.
51. Lee H, Kim S, Chung M, Kim JH, Jeon NL: A bioengineered array of 3D microvessels for vascular permeability assay. *Microvasc Res* **2014**, 91:90-98.
52. Kim J, Chung M, Kim S, Jo DH, Kim JH, Jeon NL: Engineering of a biomimetic pericyte-covered 3D microvascular network. *Plos One* **2015**, 10:e0133880.
53. Alimperti S, Mirabella T, Bajaj V, Polacheck W, Pirone DM, Duffield J, Eyckmans J, Assoian RK, Chen CS: Three-dimensional biomimetic vascular model reveals a RhoA, Rac1, and N-cadherin balance in mural cell-endothelial cell-regulated barrier function. *Proc Natl Acad Sci U S A* **2017**, 114:8758-8763.
54. Huveneers S, Oldenburg J, Spanjaard E, van der Krogt G, Grigoriev I, Akhmanova A, Rehmann H, de Rooij RJ: Vinculin associates with endothelial VE-cadherin junctions to control force-dependent remodeling. *J. Cell Biol* **2012**, 196:641-652.
55. Van Nieuw Amerongen GP, van Delft S, Vermeer MA, Collard JG, van Hinsbergh VW: Activation of RhoA by thrombin in endothelial hyperpermeability: role of Rho kinase and protein tyrosine kinases. *Circ. Res* **2000**, 87:335-340.
56. Wojciak-Stothard B, Potempa S, Eichholtz T, Ridley AJ: Rho and Rac but not Cdc42 regulate endothelial cell permeability. *J. Cell Sci* **2001**, 114:1343-1355.
57. Chrobak KM, Potter DR, Tien J: Formation of perfused, functional microvascular tubes in vitro. *Microvasc Res* **2006**, 71:185-196
58. Choi JS, Choi YS, Park SH, Kang JS, Kang YH: Flavones mitigate tumor necrosis factor-alpha-induced adhesion molecule upregulation in cultured human endothelial cells: role of nuclear factor-kappa B. *J. Nutr* **2004**, 134:1013-1019.
59. Bosteen MH, Tritsaris K, Hansen AJ, Dissing S: IL-17A potentiates TNFalpha-induced secretion from human endothelial cells and alters barrier functions controlling neutrophils rights of passage. *Pflugers Arch* **2014**, 466:961-972.
60. Zhang H, Park Y, Wu J, Cheng X, Lee S, Yang J, Dellsperger KC, Zhang C: Role of TNF-alpha in vascular dysfunction. *Clin. Sci. (Lond)* **2009**, 116:219-230.
61. Sprague AH, Khalil RA: Inflammatory cytokines in vascular dysfunction and vascular disease. *Biochem. Pharmacol* **2009**, 78:539-552.
62. Nakada MT, Tam SH, Woulfe DS, Casper KA, Swerlick RA, Ghrayeb J: Neutralization of TNF by the antibody cA2 reveals differential regulation of adhesion molecule expression on TNF-activated endothelial cells. *Cell Adhes. Commun* **1998**, 5:491-503.

63. Clark PR, Manes TD, Pber JS, Kluger MS: Increased ICAM-1 expression causes endothelial cell leakiness, cytoskeletal reorganization and junctional alterations. *J. Invest Dermatol* **2007**, 127:762-774.
64. Bian T, Li H, Zhou Q, Ni C, Zhang Y, Yan F: Human beta-defensin 3 reduces TNF-alpha-induced inflammation and monocyte adhesion in human umbilical vein endothelial cells. *Mediators Inflamm* **2017**, 2017:8529542.
65. Oberoi R, Schuett J, Schuett H, Koch AK, Luchtefeld M, Grote K, Schieffer B: Targeting Tumor Necrosis Factor-alpha with Adalimumab: effects on endothelial activation and monocyte adhesion. *Plos One* **2016**, 11:e0160145.
66. Thilagar S, Thevagarajan R, Sudhakar U, Suresh S, Saketharaman P, Ahamed N: Comparison of serum tumor necrosis factor-alpha levels in rheumatoid arthritis individuals with and without chronic periodontitis: A biochemical study. *J Indian Soc Periodontol* **2018**, 22:116-121.
67. Pape HC, Schmidt RE, Rice J, van Griensven M, das Gupta R, Krettek C, Tscherne H: Biochemical changes after trauma and skeletal surgery of the lower extremity: Quantification of the operative burden. *Crit Care Med* **2000**, 28:3441-8.
68. Haider S, Knofler M: Human tumor necrosis factor: physiological and pathological roles in placenta and endometrium. *Placenta* **2009**, 30:111-123.
69. Munir H, Rainger GE, Nash GB, McGettrick H: Analyzing the effects of stromal cells on the recruitment of leukocytes from flow. *J Vis Exp* **2015***,* 95:e52480.
70. Stark K, Eckart A, Haidari S, Timiceriu A, Lorenz M, von Bruhl ML, Cartner F, Khandoga AG, Legate KR, Pless R, Hepper I, Lauber K, Walzog B, Massber S: Capillary and arteriolar pericytes attract innate leukocytes exiting through venules and 'instruct' them with pattern-recognition and motility programs. *Nat. Immunol* **2013**, 14:41-51.
71. Proebstl D, Voisin MB, Woodfin A, Whiteford J, DÁcquisto F, Jones GE, Rowe D, Nourshargh S: Pericytes support neutrophil subendothelial cell crawling and breaching of venular walls in vivo. *J. Exp. Med* **2012**, 209:1219-1234.
72. Ayres-Sander CE, Lauridsen H, Maier CL, Sava P, Pober JS, Gonzalez AL: Transendothelial migration enables subsequent transmigration of neutrophils through underlying pericytes. *PLoS. One* **2013**, 8:e60025.
73. Tan A, Fujisawa K, Yukawa Y, Matsunaga YT: Bottom-up fabrication of artery-mimicking tubular co-cultures in collagen-based microchannel scaffolds. *Biomater Sci* **2016**, 4:1503-1514.
74. Jia W, Gungor-Ozkerim PS, Zhang YS, Yue K, Zhu K, Liu W, Pi Q, Byambaa B, Dokmeci MR, Shin SR, Khademhosseini A: Direct 3D bioprinting of perfusable vascular constructs using a blend bioink. *Biomaterials* **2016**, 106:58-68.
75. Pepelanova I, Kruppa K, Scheper T, Lavrentieva A: Gelatin-Methacryloyl (GelMA) hydrogels with defined degree of functionalization as a versatile toolkit for 3D cell culture and extrusion bioprinting. *Bioengineering (Basel)* **2018**, 5:55.
76. Minutti CM, Modak RV, Macdonald F, Li F, Smyth DJ, Dorward DA, Blair N, Husovsky C, Muir A, Ciampazolias E, Dobie R, Maizels RM, Kendall TJ, Griggs DW, Kopf M, Henderson NC, Zaiss DM: A macrophage-pericyte axis directs tissue restoration via Amphiregulin-induced transforming growth factor beta activation. *Immunity* **2019**, 50;645-654.
77. Perry HM, Görldt N, Sung SJ, Huang L, Rudnicka P, Encamacion IM, Bajwa A, Tanaka S, Poudel N, Yao J, Rosin DL, Schrade J, Okusa MD: Perivascular CD73 $^{+}$ cells attenuate inflammation and interstitial fibrosis in the kidney microenvironment. *Am J Physiol Renal Physiol* **2019**, 317:F658-F669.
78. Van Dijk CGM, Oosterhuis NR, Xu YJ, Brandt MM, Paulus WJ, van Heerebeek L, Duncker DJ, Verhaar MC, Fontoura D, Lourenco AP, Leite-Moreira AF, Falcão-Pires I, Joles JA, Cheng C: Distinct endothelial cell responses in the heart and kidney microvasculature characterize the progression of heart failure with preserved ejection fraction in the obese ZSF1 rat with cardiorenal metabolic syndrome. *Circulation Heart Failure* **2016**, 9:e002760.
79. Brandt MM, van Dijk CGM, Chrifi I, Kool HM, Burgisser PE, Louzao-Martinez L, Pei J, Rottier J, Verhaar MC, Duncker DJ, Cheng C: Endothelial loss of Fzd5 stimulates PKC/Ets1-mediated transcription of Angpt2 and Flt1. *Angiogenesis* **2018**, 21:805-821.

80. Chrifi I, Louzao-Martinez L, Brandt MM, van Dijk CGM, Burgisser PE, Zhu C, Kros JM, Verhaar MC, Duncker DJ, Cheng C: CMTM4 regulates angiogenesis by promoting cell surface recycling of VE-cadherin to endothelial adherens junctions. *Angiogenesis* **2018**, 22:75-93.
81. Vanlandewijck M, Lebouvier T, Andaloussi Mae M, Nahar K, Hornemann S, Kenkel D, Cunha SI, Lennartsson J, Boss A, Heldin CH, Keller A, Betsholtz C: Functional characterization of germline mutations in PDGFB and PDGFRB in primary familial brain calcification. *Plos One* **2015**, 10:e0143407.
82. He L, Vanlandewijck M, Raschperger E, Andaloussi Mae M, Jung B, Lebouvier T, Ando K, Hofmann J, Keller A, Betsholtz C: Analysis of the brain mural cell transcriptome. *Scientific reports* **2016**, 6:35108.
83. Stebbins MJ, Gastfriend BD, Canfield SG, Lee MS, Richards D, Faubion MG, Li WJ, Daneman R, Palecek SP, Shusta EV: Human pluripotent stem cell-derived brain pericyte-like cells induce blood-brain barrier properties. *Science Advances* **2019**, 5:Eaau7375.
84. Wimmer RA, Leopoldi A, Aichinger M, Wick N, Hantusch B, Novatchkova M, Taubenschmid J, Hammerkle M, Esk C, Bagley JA, Lindenhofer D, Cheng G, Boehm M, Aug CA, Yang F, Fu B, Zuber J, Knoblich JA, Kerjaschki D, Penninger JM: Human blood vessel organoids as a model of diabetic vasculopathy. *Nature Letter* **2019**, 565:505-510.
85. Brandt MM, van Dijk CGM, Maringanti R, Chrifi I, Kramann R, Verhaar MC, Duncker DJ, Mokry M, Cheng C: Transcriptome analysis reveals microvascular endothelial cell-dependent pericyte differentiation. *Sci Rep* **2019**, 9:15586.
86. Koutsiaris AG, Tachmitzi SV, Batis N, Kotoula MG, Karabatsas CH, Tsironi E, Chatzoulis DZ.: Volume flow and wall shear stress quantification in the human conjunctival capillaries and post-capillary venules *in vivo*. *Biorheology* **2007**, 44:375-386.
87. Miller JS, Stevens KR, Yang MT, Baker BM, Nguyen DHT, Cohen CM, Toro E, Cheng AA, Galie PA, Yu X, Chaturvedi R, Bhatia SN, Chen CS: Rapid casting of patterned vascular networks for perfusable engineered three-dimensional tissues. *Nature Materials* **2012**, 11:768-774.
88. Girard JP, Springer TA: High endothelial venules (HEVs): specialized endothelium for lymphocyte migration. *Immunology Today* **1995**, 16:449-57.
89. Diaz-Flores L, Gutierrez R, Madrid JF, Varela H, Valladares F, Acosta E, Martin-Vasallo P, Diaz-Flores JL: Pericytes. Morphofunction, interactions and pathology in a quiescent and activated mesenchymal cell niche. *Histology and Histopathology* **2009**, 24:909-969.
90. Herland A, van der Meer AD, FitzGerald EA, Park TE, Sleeboom JJ, Ingber DE: Distinct contributions of astrocytes and pericytes to neuroinflammation identified in a 3D human blood-brain barrier on a chip. *PLoS. One* **2016**, 11:e0150360.
91. Cheng C, Helderman F, Tempel D, Segers D, Hierck B, Poelmann R, van Tol A, Duncker DJ, Robbers-Visser D, Ursem NT, van Haperen R, Wentzel JJ, Gijsen F, van der Steen AF, de Crom R, Krams R: Large variations in absolute wall shear stress levels within one species and between species. *Atherosclerosis* **2007**, 195:225-235.
92. Ballermann BJ, Dardik A, Eng E, Liu A: Shear stress and the endothelium. *Kidney Int Suppl* **1998**, 67:S100-108.
93. Tun WM, Yap CH, Saw SN, James JL, Clark AR: Differences in placental capillary shear stress in fetal growth restriction may affect endothelial cell function and vascular network formation. *Sci Rep* **2019**, 9:9876.
94. Cho YI, Cho DJ: Hemorheology and microvascular disorders. *Korean Circ J* **2011**, 41:287-295.
95. Pries AR, Secomb TW, Gaehtgens P: Structure and hemodynamics of microvascular networks: heterogeneity and correlations. *American Physiology Society* **1995**, 269:1713-22.
96. Shaw SK, Ma S, Kim MB, Rao RM, Hartman CU, Frojo RM, Yang L, Jones T, Liu Y, Nusrat A, Parkos CA, Luscinskas FW: Coordinated redistribution of leukocyte LFA-1 and endothelial cell ICAM-1 accompany neutrophil transmigration. *J Exp Med* **2004**, 200:1571-1580.

Supplemental Data

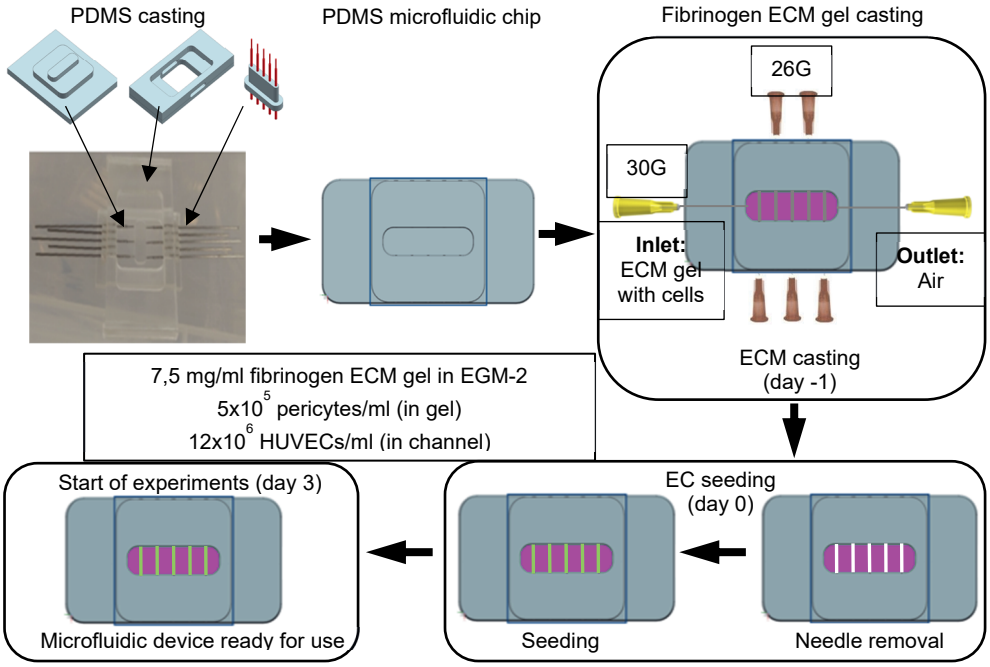

Supplemental Figure 1. Schematic overview of the work flow. Shown are step by step illustrations of the process to create a biological functional microfluidic device. PDMS microfluidic device are produced, sealed with a coverslip and sterilized with UV prior to use. Five 26G needles are placed in the pre-made channels of the PDMS microfluidic device and act as mold for the channels. Fibrinogen gel is dissolved in EGM-2 medium (7.5 mg/ml) and put under a vacuum to remove air bubbles. A pellet of pericytes ($5x10^5$/ml) is resuspended in the fibrinogen solution. The ECM/cell mix is injected in the reservoir using a syringe and 30G needle. A 30G needle on the opposite site of the reservoir acts as outlet for air. The casted microfluidic device is turned over every 30 min for 2 hours to ensure a homogenous distribution of the pericytes. After overnight polymerization of the ECM, 26G needles are removed, leaving a hollow, tube shaped channel (indicated as day 0). A suspension of HUVECs ($12x10^6$/ml) is injected in the channels and the microfluidic device is turned over every 30 min for 2 hours to ensure homogenous seeding of the HUVECs at the surface of the channel. The microfluidic device is placed in a dish with medium (EGM-2) for further maturation of the vessel-on-a-chip. At day 3, experiments as described in this study are started (indicated as day 3 in the results).

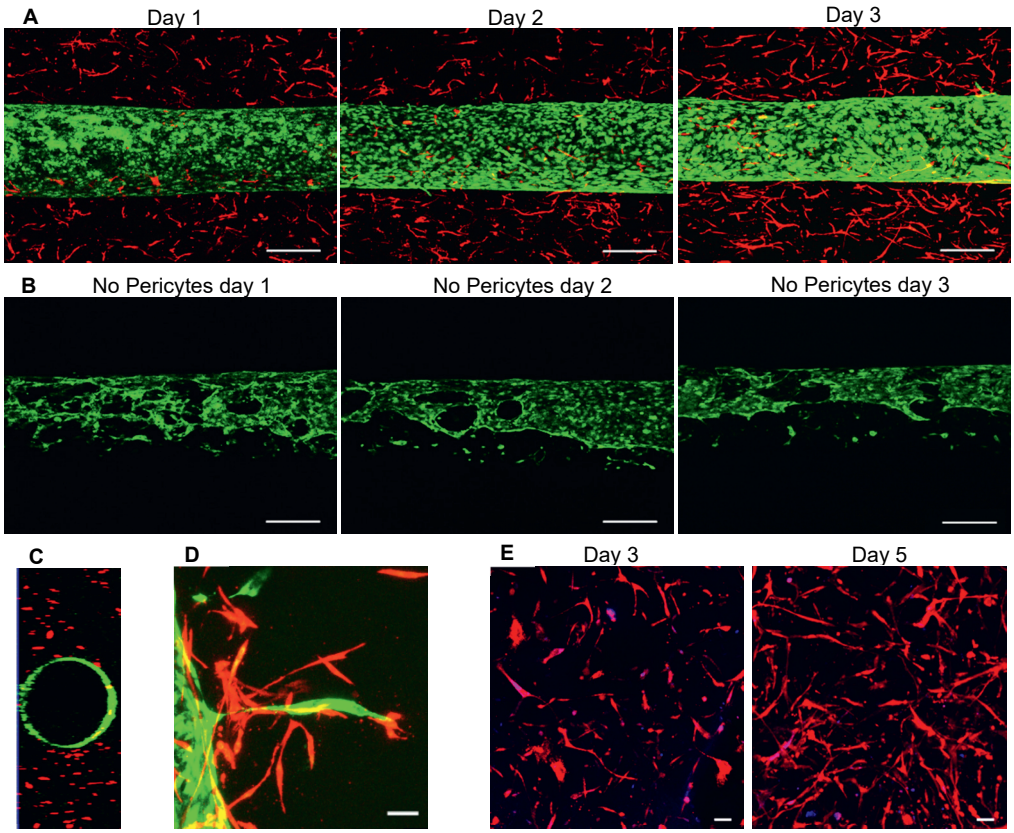

Supplemental Figure 2. Endothelial channel development. (A) Merged images of an endothelial channel during development. HUVEC (green) do not form a full monolayer and pericytes (red) do not cover and stabilize the neovessel until day 3. Scale bar = 250 µm. **(B)** Endothelial channel development over time without pericytes in the ECM gel. Scale bar = 250 µm. **(C)** Cross section of the microfluidic fluidic device. The ECs (green) form a round, open lumen with pericytes (red) in the surrounding ECM gel. **(D)** High magnification image of an endothelial sprout (green) supported by pericytes (red). Pilot experiments shows the sprouting capacity of ECs towards a gradient with pro-angiogenic factors. Pericytes are attracted and support the newly formed vessel. Scale bar = 50 µm. **(E)** Morphology of pericytes do not change in time. To assess if dsRED area (red) is a valid method to quantify pericyte proliferation, pericytes are stained with DAPI (blue, overlap magenta). No changes in pericytes morphology was observed in time. Scale bar = 50 µm.

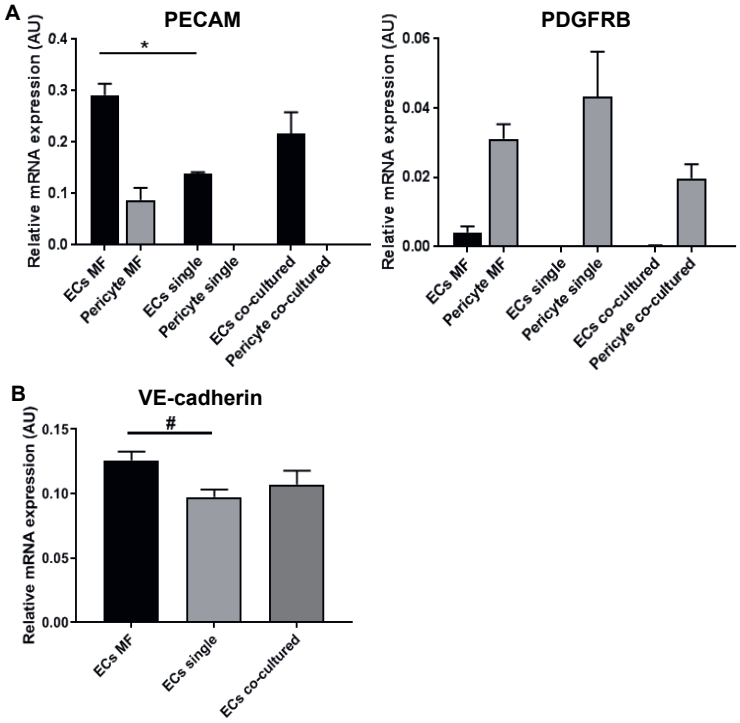

Supplemental Figure 3. Specific cell fractions can be isolated for mRNA isolation. (A) mRNA expression levels of endothelial specific PECAM and pericyte specific PDGFRβ. Cells lysed in the ECs fraction show more PECAM expression compared to single and co-cultured ECs. Cells lysed in the pericyte fraction show similar PDGFRβ expression compared to single and co-cultured pericytes. N=3, *P<0.05. **(B)** mRNA expression levels of VE-cadherin in ECs cultured in the microfluidic channel (ECs MF), single cultured ECs (ECs single) and ECs co-cultured with pericytes in a transwell system (ECs co-cultured). N=3, # P=0.0985. mRNA levels are normalized to β-actin. MF: microfluidic device.

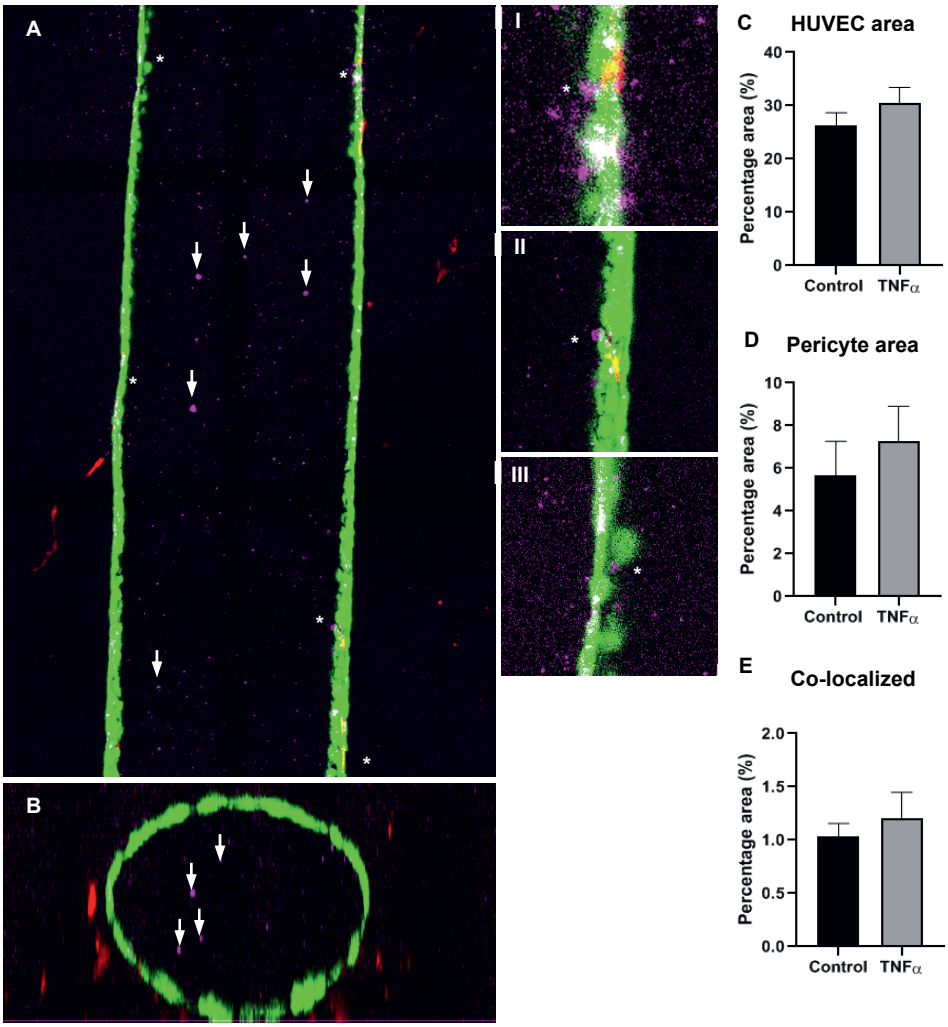

Supplemental Figure 4. Flowing the tissue-engineered channels with circulatory THP-1 cells. (A) Projection of the mid-section of the neovessel shows attachment of THP-1 cells to the vessel wall (asterisks) and suspended THP-1 (magenta) in the lumen (indicated with arrows). High magnifications images of THP-1 attachment (asterisks) are shown in I, II and III. **(B)** Projection of multiple cross sectional Z stacks shows suspended THP-1 in the lumen during flowing (arrows). There is no influence of TNFα on **(C)** total HUVEC nor **(D)** pericyte area, as shown in the bar graphs in percentage of co-localized area of total image area. **(E)** Percentage co-localization area of HUVECs with pericyte is not changed in the presence of TNFα. N=6.

Supplemental Table 1. Primer sequences used for qPCR.

Target gene	Sense primer sequence	Antisense primer sequence
β-actin	TCCCTGGAGAAGAGCTACGA	AGCACTGTGTTGGCGTACAG
VEGFR2	TCTCTGCCTACCTCACCTGT	GCTCTTTCGCTTACTGTTCTGC
PECAM	GATGTCAGCACCACCTCTCAG	GAAGTGTATTGGGGCCTTTTC
PDGFRβ	GAGGAATCCCTCACCCTCTC	GGGTATATGGCCTTGCTTCA
NG2	CTGTCCTTCCCAGTGACCAT	GGAGCCTGAACCACCTCATA
VE-cadherin	TTGGAACCAGATGCACATTAT	TCTTGCGACTCACGCTTGAC
ZO-1	ATTTTGTCCGCTCAGCCTGTT	GCCAGCTTTTCTCTGGCAAC
CX43	TGGATTCAGCTTGAGTGCTG	GGTCGCTCTTTCCCTTAACC

Supplemental movies can be downloaded from:

https://pubs.rsc.org/en/content/articlelanding/2020/LC/D0LC00059K#!divAbstract

Or:

Supplemental Movie 1. GIF movie of a longitudinal, composite view of the endothelial (green) channel supported by the ECM containing pericytes (red). The channel shows an open lumen.

Supplemental Movie 2. GIF movie of endothelial sprout (green), starting from the tissue-engineered blood vessel wall into the ECM supported by pericytes (red).

Supplemental Movie 3. Small movie of circulating THP-1 (blue) in the endothelial channel (green borders) embedded in the pericytes (magenta) supported ECM. Movie is made at a specific z-position almost halfway the endothelial channel.

Chapter 10

General discussion

Fundamental research regarding vascular molecular pathways, vascular cell and extracellular matrix (ECM) interaction, and interactions between the multiple vascular cells in health and disease is essential for the development and optimization of regenerative strategies. In this thesis we aimed to improve our knowledge of mechanisms that regulate vascular development and stabilization in healthy and diseased conditions. In more detail, we focused on pericyte/endothelial cell (EC) interaction and the contribution of ECM to vascular development and stabilization. The findings described in this thesis could be implemented to develop and improve new and current therapies to stimulate vascular development and regeneration.

Endothelial Fzd5 signaling and its potential in regenerative strategies

In **Chapter 2** we demonstrated that Frizzled 5 (Fzd5) knockdown in ECs using siRNA hampers angiogenesis in an *in vitro* co-culture model of vessel formation. Furthermore, siFzd5 treated ECs upregulate angiopoietin 2 (Angpt2) and vascular endothelial growth factor receptor 1 (VEGFR1) levels, both well-known factors involved in angiogenesis. Angpt2 functions as a Angpt1 antagonist by binding to the Tie2 receptor. This leads to pericyte detachment and destabilization of the capillary and is essential for angiogenesis. However, when there is a lack of pro-angiogenic signals such as Angpt1, elevated Angpt2/Angpt1 ratios lead to vascular regression [1]. Similarly, VEGFR1 is known as a soluble decoy receptor for pro-angiogenic vascular endothelial growth factor A (VEGFA). Although the binding affinity of VEGFA to VEGFR1 is high, soluble VEGFR1 will not trigger downstream factors [2,3], acting as an antagonist of VEGFA signaling. Our findings thus suggest that the Fzd5 pathway may be an interesting target for regenerative strategies. Care should be taken to consider during which step of the angiogenic process drug targeting of the Fzd5 should be implemented. Early intervention in the Wnt signaling pathway by Fzd5 blockade may not be successful as this will increase Angpt2 and VEGFR1 levels, resulting in destabilized capillaries while pro-angiogenic VEGFA is neutralized. Once capillaries are formed, drug stimulation of the Fzd5 pathway by Wnt5a will decrease Angpt2 and VEGFR1 levels, resulting in more stable capillaries by pericyte recruitment and a more mature microvascular bed. Thus Fzd5 agonists may be used as therapeutic target once capillary maturation stays absent. This approach may be an ideal strategy in diseases associated with microvascular dysfunction such as heart failure with preserved ejection fraction, in which this may prevent microvascular destabilization and decline.

Previously, an animal study has demonstrated the therapeutic potential of Wnt-Fzd pathway targeting; antagonists of Wnt3a and Wnt5a were shown to reduce myocardial infarct size, preserve cardiac function and survival of the peri-infarct capillaries in a murine myocardial infarction [4]. Besides drug based therapy directly targeting the diseased cardiovascular

tissue, circulating monocytes could provide an additional compartment for drug targeting. Arderiu *et al*. demonstrated interaction of monocyte derived Wnt5a with endothelial Fzd5 [5]. This resulted in angiogenic stimulation and monolayer repair via Fzd5 activation [5], indicating that monocyte activation of the Fzd5 may help stabilize newly formed capillaries. Wnt5a is upregulated in the serum of diabetic patients, sepsis patients, and atherosclerosis patients and is also highly expressed in macrophage rich atherosclerotic plaques [6,7]. However, Skaria *et al*. described endothelial barrier impairment after Wnt5a/Ryk signaling suggesting that macrophage derived Wnt5a during inflammation could cause vascular leakage [8]. Together this indicates that targeting the Wnt-Fzd pathway may not be such an easy straight-forward strategy and will require consideration of multiple factors. Nevertheless, considering the therapeutic potential of the Wnt-Fzd pathway, future studies should focus on controlling this pathway to improve vessel stabilization in vascular regeneration strategies.

Pericyte/endothelium interactions and maturation are key for regenerative vascular strategies

The pericytes within a shared basement membrane (BM) with ECs facilitate well-orchestrated pericyte/EC crosstalk via direct contact (for example via peg and socket interactions) as well as paracrine contact [9,10]. To improve our insights in pericyte/EC interactions, we studied the transcriptome of pericytes cultured in absence and in presence of microvascular ECs. In **Chapter 4** we describe pericyte mRNA upregulation by EC interaction of well-validated pericyte markers such as neural glial antigen 2 (NG2) and α smooth muscle actin 2 (ACTA2) as compared to pericytes cultured in absence of ECs, highlighting the essential role of this type of interaction in pericyte maturation. Direct endothelial contact also represses overall ECM production by pericytes, induce transforming growth factor β (TGFβ) signaling and trigger growth of long cellular protrusions. Stratman *et al.* showed that pericyte/ECs interaction is essential for BM formation [11,12]. Our data indicate, that pericytes cultured in presence of EC have a limited contribution to BM formation. However, pericytes still contribute to this process by stimulating endothelial ECM production of the BM. This is in line with earlier findings that pericytes in direct contact of ECs are more mature whereas pericytes without endothelial contact shift to Gli+, progenitor pericytes which are involved in renal fibrosis [13]. Whereas ECM production in co-cultured pericytes is reduced, TGFβ signaling is increased, a critical pathway in pericyte differentiation towards ECM producing fibroblasts [14]. These findings implies that the TGFβ signaling and ECM production is tightly regulated and orchestrated by ECs contact.

Although the pericytes and ECs were cultured in direct contact, downregulation of key gap- and adherens junctions genes connexin-43 (CX43) and N-cadherin (CDH2) with siRNA, did not reveal any differences in pericytes co-cultured with ECs compared to pericytes in absence

of ECs. This suggest that, although highly present in peg and socket junctions, CX43 and CDH2 are not involved in endothelium induced pericyte differentiation Instead our data imply a major role for paracrine signaling in this process, but this needs to be further evaluated. Paracrine signaling between ECs and pericytes provides a potential avenue for therapeutic applications by the use of secreted endothelial derived extracellular vesicles (EVs) [15,16]. Paracrine EV signaling could contribute to pericyte maturation and differentiation as the content of EVs may include some of the content of the endothelial cellular cytoplasm, including multiple cytokines and growth factors [16]. EVs derived from ECs can potentially be used for *in situ* generative strategies. For example, injections of a high dosage endothelial derived EVs at peri-infarct sites in the myocardium may aid in pericyte maturation which, in turn, might promote endothelial barrier function and BM formation, subsequently resulting in preservation of the cardiac vasculature.

Combined, our findings and that of others indicate that pericytes play a key role in capillary stabilization and that their interaction with ECs contributes to vascular homeostasis. This is mainly due to their versatile function, as reviewed in **Chapter 3**. Studies focusing on vascular regeneration, including *in vitro* vascular models, are still limited in the use of pericytes. There are studies that include the use of mesenchymal stem cells (MSCs) as supporting cells for vasculogenesis [17-19]. Although these studies did demonstrate the beneficial effects of MSCs on the establishment of a vascular bed, most studies do not distinguish between pericytes and MSCs. **Chapter 4** demonstrated that the phenotype and transcriptome of pericytes without EC interaction partly overlap with that of MSCs [20-23]. Researchers may consider the use of MSCs as a source for pericyte progenitor cell in vascular regeneration. Moreover, tissue specific pericytes harbor specific functions in different organs, including vitamin A storage in the liver and renin production in the kidney [24]. Advanced vascular regeneration strategies should consider the use of tissue specific pericytes to sustain these important functions in addition to their aim to stabilize the neovasculature. In our view, a combination of multipotent cell derived pericytes, ECs and tissue specific cells provide a more optimal environment to study tissue specific pericytes in *in vitro* vascular regeneration strategies.

ECM components in tissue engineering strategies

Basic biological ECM gels such as collagen type I, fibrin and alginate or more complex biological ECM gels such as Matrigel, are widely used in vascular tissue engineering (TE) strategies [25]. Moreover, synthetic monomer such as polyethylene glycol (PEG) and polycaprolactone (PCL) are progressively used in TE to mimic mechanical ECM properties [26-28]. Lately, hybrid ECM gels in which synthetic “scaffold” components with higher

mechanical strength are combined with soft hydrogels are now also widely used. For example, coating of PCL scaffolds with collagen or fibrin will provide both mechanical strength and cell adhesion sites and therefore offer more optimal conditions for tissue growth [29-31]. The hybrid approach is a strategy that is suitable for 3D printing of vascularized constructs, in which the researchers aim to design bio-inks with desirable biological and mechanical characteristics for tissue printing. The gelatin methacrylate (GelMA) that is often used in *in vitro* and *in vivo* vascularization strategies [32,33] is a promising candidate for the choice of hydrogel 3D printing applications. The degree of crosslinking of the methacrylate groups in GelMA that define material stiffness can be accurately controlled, making GelMA an ideal 3D bioink for various applications including vascular biofabrication [34-36]. For the biofunctionalization of the bio-ink, decellularized ECM derived from various organs has been successfully used as additive in 3D printing [37,38]. Thus, incorporation of promising (tissue specific) proteins or functional peptide domains in general such as integrin binding RGD motifs that promote cell attachment [39], stromal cell derived factor 1 (SDF1α) to attract monocytes [40] or VEGF [41] in ECM gels, scaffolds or grafts, may improve vascular TE strategies. The results described in **Chapter 5 and 6** demonstrate a possible beneficial role of elastin microfibril interfacer 1 (EMILIN1) in renal epithelial cell adhesion and in lesser extent a role in EC behavior. This difference in cell adhesion is attributed to the gC1q domain of EMILIN1 that interacts with integrins α4/α9/β1 [42-45] suggesting that the effect of EMILIN1 is integrin mediated. As different cell types express different integrin subunits, the contribution of EMILIN1 to cell adhesion capacity thus may be cell type dependent. Literature ascribes distinct integrins to renal tissue, except α4 and α9 [46,47]. Although integrin subunits α4 and α9 can interact with ligands on ECs [48], the endothelium has little to no expression of these integrin subunits. The findings described in **Chapter 5 and 6** suggest that effect of renal epithelial cells and ECs cultured on EMILIN1 deficient ECM is mediated via other integrin subunits instead of α4/α9/β1. Nevertheless, addition of EMILIN1 to ECM gels in renal or vascular TE applications may benefit cellular behavior, and the use of the specific EMILIN1 gC1q domain as an additive to ECM gels could be useful in vascular regeneration strategies. The proteomic approach described in these chapters in which mature, quiescent tissue is compared with fetal, developing tissue could help identify candidates involved in specific tissue development for potential TE strategies. **Chapter 5 and 6** describes a list of proteins that are more abundantly present in renal and vascular tissue during development, including fibrillin (FBN), EMILIN, latent TGFβ binding protein (LTBP) and microfibrillar associated protein (MFAP). From these, other members of their protein family could also be interesting candidates. All of them are involved in TGFβ bioavailability and therefore can impact the TGFβ signaling pathway [49-53]. TGFβ signaling pathway is involved in numerous developmental

processes including vascular development [49]. Control of this key signaling pathway could be beneficial for vascular TE strategies [54]. A combination of these ECM proteins may be used to regulate the bioavailability of TGFβ on different levels. For example, EMILIN1 can antagonize pro-TGFβ by preventing furin convertases in the Golgi complex, thereby preventing TGFβ maturation and secretion [49,55]. Further down the TGFβ processing cascade, the secreted latent TGFβ complex that is normally formed by successful furin cleavage of pro-TGFβ, will bind to LTPBs, which in turn require binding to FBN1. Proteases including matrix metalloproteinase 2 (MMP2) can then finally cleave the latent complex and release the mature and active TGFβ [49]. Application of EMILIN1 in vascular regeneration strategies will aid in regulating early TGFβ processing, whereas further combining FBN1 and LTBPs ensures local latent TGFβ binding. Furthermore, the application of MFAP proteins in ECM or hydrogels may also aid in binding activated TGFβ for fine-tune the release of TGFβ [53,56]. MFAP competes with FBN1 for binding with the latent TGFβ complex, thereby blocking further the downstream cascade and reducing levels of active TGFβ [53,56]. Depending on the requirements, a combination of these ECM proteins can be used in ECM/hydrogel based therapies to adjust the TGFβ availability.

Vascular human measurement models

The development of efficient, state-of-the-art human measurement models to study disease conditions and potential interventions is essential to improve the clinical translation of obtained research results to therapeutic applications in patients. The fundamental findings discussed previously can be applied in the development of vascular human measurement models. Similar, relevant *in vivo* models mimicking human (patho)physiological conditions including (multiple) co-morbidities are essential for a deeper understanding on the role of the vasculature in the onset, development and progression of several diseases. The findings in these advanced animal models can be implemented in human measurement models as well. Here, we emphasize the development and validation of two models that focus on vascular development and stabilization. In more detail, we discuss the development of an *in vitro* vascular microfluidic model to study cell-cell and cell-ECM interactions and the validation of vascular dysfunction in an *in vivo* model of cardiorenal metabolic syndrome (CRMS).

Novel microfluidics model for complex vascular structures and interactions

Vascular microfluidic models have the ability to mimic the (micro)vasculature in an *in vitro* model by combining multiple vascular characteristics. However, many vascular microfluidic models focus mainly on ECs and lack key interactions with the ECM and other cell types that constitute the *in vivo* vascular microenvironment. The vessel-on-a-chip model demonstrated

in **Chapter 9** is an example of a more advanced *in vitro* model to study vascular interactions which combines 3D geometry, ECM and mural cell support, an established vascular barrier, hemodynamic stimulation and circulating immune cell interaction with the endothelial monolayer in one single model. A logical next step in *in vitro* modeling would be to combine tissue specific cells and the vasculature to study cell-cell interactions in a vascularized, tissue specific microenvironment for use in drug screening and disease modelling. For example, the different functional regions of a nephron can be mimicked *in vitro,* like the glomerulus (filtration) and the tubulointerstitial segment (secretion and reabsorption) [57,58]. The microfluidic vascular model in **Chapter 9** can easily be adapted for such a purpose.

Additional improvements could be implemented in the current microfluidic model to better mimic the vasculature. Besides the previously discussed use of tissue specific pericytes and tailored ECM compositions for the ECM compartment, novel *in vitro* culturing techniques such as the culture of vascular organoids generated from human induced pluripotent stem cells (iPSCs) could provide a patient-derived cell source for the vascular human measurement model, resulting in a tailored platform for personalized drug screening. The regenerative potential of iPSCs is already widely reviewed [59], including for use in the generation of musculoskeletal [60] and cardiac tissues [61]. iPSCs are also increasingly used to generate vascular cells [62-64]. Furthermore, organoid cultures are developed as models for multiple organs such as intestine [65], liver [66,67] and kidney [68]. These advanced 3D cultures provide ECM support and more complex micro-tissue organization consisting of multiple cell types, thus providing a multicellular microenvironment that can be used for drug screening and disease research. An ideal source of vascular cells for our model could be provided by the iPSCs derived vascular organoids described by Wimmer ***et al***. [69,70], which contain both ECs and mural cells organized in a micro capillary bed. These vascular organoids may be used as a direct platform for drug screening, or as a cell source for therapeutic TE strategies including *ex vivo* cellularization of polymer based vascular scaffolds. Additionally, genetic modulation of the iPSC derived ECs and pericytes (and smooth muscle cells) could recreate subpopulations of vascular cells that are phenotypically more similar to their equivalent subtypes in arteries, capillaries or veins, thus expanding their potential use as in vascular TE strategies as well as providing an opportunity to study these EC and mural cell subtypes in human measurement models.

On top of selecting the right source of vascular cells, biomechanical cues are essential for vascular cell behavior. ECs are exposed to shear stress and cyclic stretch as a result of direct contact with circulating blood. This flow induced mechanical stimulation is essential for endothelial and mural cell function [71-73]. The currently most advanced *in vitro* models provide shear stress and limited stretch, using dedicated pump systems [74] rather than

gravitational flow [75]. When mimicking tubular structures such as the vasculature in combination with kidney tubules, the tissue geometry also provides important mechanical cues. For example, bone marrow stromal cell alignment and migration is guided by the curvature of the substrate in a curvature with a cylindrical diameter smaller than 1000 µm which overrules the effect of contact guidance alignment [76]. Moreover, the tubular curvature contributes to kidney epithelial cell polarization, morphology and orientation [77], emphasizing the importance of this mechanical cue for *in vitro* modeling and regenerative strategies. Other mechanical cues are provided by matrix stiffness. Cellular response to soft or rigid ECM plays an important role in cell fate. Fibrotic diseases are characterized by an altered ECM composition and increased ECM stiffness due to excessive collagen type I deposition and increased collagen cross-linking by the lysyl oxidase family [78]. Human measurement models that aim to mimic fibrotic diseases *in vitro* should therefore implement ECM stiffening as part of the disease modeling. Advanced *in vitro* models could incorporate techniques that are typically used for therapeutic strategies such as bioprinting and electrospun PCL vascular grafts to improve the representation of their systems to the human disease specific microenvironment. Vice versa, advanced *in vitro* models can be exploited to assess and improve vascular grafts before testing in animal models in regenerative strategies.

ECM regulators as marker of fibrosis in diastolic dysfunction

Matrix metalloproteinases (MMPs) and their inhibitors, tissue inhibitors of metalloproteinases (TIMPs) are dynamic ECM regulators responsible for controlling matrix protein degradation and are often used as markers of matrix degradation to monitor fibrosis progression [79-82]. However, there are discrepancies between secreted MMP and TIMP protein measured in blood plasma and the physical dynamic levels in the affected tissue. Left ventricular diastolic dysfunction (LVDD) and heart failure with preserved ejection fraction (HFpEF) are increasingly recognized as major cardiac pathologies, characterized with progressive cardiac fibrosis. Mapping the MMP and TIMP dynamics could provide a potential prognostic tool to monitor fibrosis development. Moreover, identification of spatiotemporal patterns of diastolic dysfunction and fibrosis could map different clinical stages of LVDD/HFpEF which could improve current experimental *in vivo* models. **Chapter 7** describes a systematic review and a subsequent meta-analysis of MMPs and TIMPs in animal models with LVDD to provide insights into overall ECM dynamics. Besides increased enzymatic activity of MMP2 and MMP9 and TIMP1 mRNA, MMP15 is proposed as an interesting novel candidate in HFpEF-driven cardiac fibrosis, as MMP15 mRNA was downregulated in HFpEF compared to controls. TIMP4 was also identified as a relevant candidate since it was downregulated in metabolic compared to hemodynamic models. In **Chapter 7** we report a lack of animal studies accurately validating

diastolic dysfunction while systolic function remains preserved using echocardiography and hemodynamic measurements. The number of studies included in our systematic review was not sufficient to correlate multiple cardiac or fibrotic parameters with MMP or TIMP levels. Nevertheless, this systematic review provided recommendations for future studies that are necessary to improve the translation to different clinical stages of LVDD/HFpEF. This includes experimental LVDD/HFpEF models that focus on gender differences and models that not only focus on metabolic or hemodynamic alterations but also include other underlying pathologies of diastolic dysfunction such as volume overload, atrial fibrillation and ageing. Since post-transcriptional and post-translational activation of both MMPs and TIMPs takes place, future studies should focus on MMP and TIMP protein levels and enzyme activity. Ideally, a combination of tissue and plasma concentration should be measured to correlate MMP and TIMP dynamics for a better clinical translatability.

In addition, MMPs and TIMPs assessment and implementation *in vitro* could improve human measurement models. Their prognostic value to monitor fibrosis progression could be extended to monitor the balance between regenerative and pathologic ECM production in *in vitro* applications. Moreover, controlling MMPs and TIMPs protein levels or substrate cleavage sites could regulate ECM degradation and subsequently have impact on the matrix stiffness. Besides the formation of functional ECM fragments including TGFβ, MMP cleavage of ECM substrates could modify a migratory track in a (synthetic) ECM environment, paving the way for e.g. vascular cells during microvascular bed formation.

ZSF1 rats as in vivo HFpEF model to study vascular dysfunction

In **Chapter 8**, we describe the obese Zucker spontaneously hypertensive fatty (ZSF1) rat strain as suitable *in vivo* model to study HFpEF. Via metabolic alterations and hypertension induced pressure overload, these rats develop CRMS and HFpEF over time. At the age of 25 weeks, obese ZSF1 rats have an increased body weight and elevated plasma glucose levels. Left ventricle mass, atria and lung weight was increased which is in line with human HFpEF characteristics [83]. Diastolic dysfunction was validated by elevated E/e' ratio while the ejection fraction remains preserved. Obese ZSF1 rats demonstrated a decline in renal function characterized by proteinuria, capillary rarefaction, glomerular sclerosis and tubulointerstitial fibrosis. **Chapter 8** also demonstrated the presence of hyperproliferative cardiac microvascular foci. These fibrotic foci are enriched with ECs and pericytes. Platelet derived growth factor receptor β (PDGFRβ) positive pericytes are also positive for BM protein collagen type IV. The development of CRMS induces microvascular fibrotic responses in both heart and kidneys which is associated with the decline of organ function. Therefore, the obese ZSF1 rat model allows the study of natural HFpEF onset, development and progression on a

background of validated human co-morbidities. Brandt *et al.* demonstrated that there is limited synergy between co-morbidities of HFpEF by decoupling obesity and hypertension in this rat model [84]. The differences in obesity and hypertension induced cardiac remodeling prioritize the characterization of co-morbidity specific alterations.

These *in vivo* observations could be implemented in human measurement model to improve translation regenerative strategies. The previously discussed vascular microfluidic device can be adapted including a microvascular bed to study the capillary dysfunction in the presence of CRMS co-morbidities. Pump controlled artificial hypertension, addition of glucose and triglycerides in the circulating medium and addition of ED1+ macrophages can be combined to mimic hyperproliferative cardiac foci to assess vascular dysfunction in more detail and subsequent potential therapeutic interventions. For example, a study using ZSF1 rats revealed that the fatty acid β oxidation (FAO) pathway in obese ZSF1 rat hearts is activated compared to their controls using RNA sequencing [84]. FAO is upregulated in quiescent ECs for vascular protection against oxidative stress exposure [85], which failed in obese ZSF1 rat hearts. We could study the effect of FAO in quiescent ECs under CRMS conditions using the adapted vascular microfluidic model. This could give new leads to use the FAO pathway as therapeutic target for vascular protection in patients with CRMS co-morbidities.

Concluding remarks and future perspectives

The studies described in this thesis provide fundamental insights in vascular cell and ECM interactions and improve our understanding of vascular development and stabilization in health and disease. Targeting specific sections of the vasculature e.g. cell types and ECM harbor potential therapeutic capacities and implementation of the here discussed results will impact the development of vascular regenerative and TE strategies, including the design of novel, innovative vascular human measurement models. Implementation of fundamental findings will contribute to more clinically relevant *in vitro* models that include all biological and biomechanical characteristics to mimic the complex vasculature and test potential therapeutic interventions. Since combining multiple characteristics can be technically challenging, we opt to use advanced human measurement models that will answer a specific part of the research question and, if necessary, benefit from multiple advanced models. The combination of vascular human measurement models and vascular TE strategies will significantly improve the translation of research data to clinical applications. Besides exclusive vascular therapeutic applications, the field of TE will benefit from the here described and future vascular research since larger, tissue specific TE constructs rely on a functional circulatory system to increase the therapeutic possibilities of using TE.

References

1. Lobov IB, Brooks PC, Lang RA: Angiopoietin-2 displays VEGF-dependent modulation of capillary structure and endothelial cell survival in vivo. *PNAS* **2002,** 99:11205-11210
2. Shibuya M: Vascular endothelial growth factor receptor-1 (VEGFR-1/Flt-1): a dual regulator for angiogenesis. *Angiogenesis* **2006,** 9:225-230; discussion 231
3. Zygmunt T, Gay CM, Blondelle J, Singh MK, Flaherty KM, Means PC, Herwig L, Krudewig A, Belting HG, Affolter M, Epstein JA, Torres-Vazquez J: Semaphorin-PlexinD1 signaling limits angiogenic potential via the VEGF decoy receptor sFlt1. *Dev Cell* **2011,** 21:301-314
4. Laeremans H, Hackeng TM, van Zandvoort MA, Thijssen VL, Janssen BJ, Ottenheijm HC, Smits JF, Blankesteijn WM: Blocking of frizzled signaling with a homologous peptide fragment of wnt3a/wnt5a reduces infarct expansion and prevents the development of heart failure after myocardial infarction. *Circulation* **2011,** 124:1626-1635
5. Arderiu G, Espinosa S, Pena E, Aledo R, Badimon L: Monocyte-secreted Wnt5a interacts with FZD5 in microvascular endothelial cells and induces angiogenesis through tissue factor signaling. *J Mol Cell Biol* **2014,** 6:380-393
6. Foulquier S, Daskalopoulos EP, Lluri G, Hermans KCM, Deb A, Blankesteijn WM: WNT Signaling in Cardiac and Vascular Disease. *Pharmacol Rev* **2018,** 70:68-141
7. Pereira C, Schaer DJ, Bachli EB, Kurrer MO, Schoedon G: Wnt5A/CaMKII signaling contributes to the inflammatory response of macrophages and is a target for the antiinflammatory action of activated protein C and interleukin-10. *Arterioscler Thromb Vasc Biol* **2008,** 28:504-510
8. Skaria T, Bachli E, Schoedon G: Wnt5A/Ryk signaling critically affects barrier function in human vascular endothelial cells. *Cell Adh Migr* **2017,** 11:24-38
9. Armulik A, Abramsson A, Betsholtz C: Endothelial/pericyte interactions. *Circ Res* **2005,** 97:512-523
10. Armulik A, Genove G, Betsholtz C: Pericytes: developmental, physiological, and pathological perspectives, problems, and promises. *Dev Cell* **2011,** 21:193-215
11. Stratman AN, Davis GE: Endothelial cell-pericyte interactions stimulate basement membrane matrix assembly: influence on vascular tube remodeling, maturation, and stabilization. *Microsc Microanal* **2012,** 18:68-80
12. Stratman AN, Malotte KM, Mahan RD, Davis MJ, Davis GE: Pericyte recruitment during vasculogenic tube assembly stimulates endothelial basement membrane matrix formation. *Blood* **2009,** 114:5091-5101
13. Kramann R, Wongboonsin J, Chang-Panesso M, Machado FG, Humphreys BD: Gli1(+) Pericyte Loss Induces Capillary Rarefaction and Proximal Tubular Injury. *J Am Soc Nephrol* **2017,** 28:776-784
14. Wu CF, Chiang WC, Lai CF, Chang FC, Chen YT, Chou YH, Wu TH, Linn GR, Ling H, Wu KD, Tsai TJ, Chen YM, Duffield JS, Lin SL: Transforming growth factor beta-1 stimulates profibrotic epithelial signaling to activate pericyte-myofibroblast transition in obstructive kidney fibrosis. *Am J Pathol* **2013,** 182:118-131
15. De Jong OG, Van Balkom BW, Schiffelers RM, Bouten CV, Verhaar MC: Extracellular vesicles: potential roles in regenerative medicine. *Front Immunol* **2014,** 5:608
16. De Jong OG, Verhaar MC, Chen Y, Vader P, Gremmels H, Posthuma G, Schiffelers RM, Gucek M, van Balkom BW: Cellular stress conditions are reflected in the protein and RNA content of endothelial cell-derived exosomes. *J Extracell Vesicles* **2012,** 1:
17. Pennings I, van Dijk LA, van Huuksloot J, Fledderus JO, Schepers K, Braat AK, Hsiao EC, Barruet E, Morales BM, Verhaar MC, Rosenberg A, Gawlitta D: Effect of donor variation on osteogenesis and vasculogenesis in hydrogel cocultures. *J Tissue Eng Regen Med* **2019,** 13:433-445
18. Au P, Tam J, Fukumura D, Jain RK: Bone marrow-derived mesenchymal stem cells facilitate engineering of long-lasting functional vasculature. *Blood* **2008,** 111:4551-4558
19. Tao H, Han Z, Han ZC, Li Z: Proangiogenic Features of Mesenchymal Stem Cells and Their Therapeutic Applications. *Stem Cells Int* **2016,** 2016:1314709
20. Caplan AI: All MSCs are pericytes? *Cell Stem Cell* **2008,** 3:229-230
21. Corselli M, Chen CW, Crisan M, Lazzari L, Peault B: Perivascular ancestors of adult multipotent stem cells. *Arterioscler Thromb Vasc Biol* **2010,** 30:1104-1109
22. Nehls V, Drenckhahn D: Heterogeneity of microvascular pericytes for smooth muscle type alpha-actin. *The Journal of Cell Biology* **1991,** 113:147-144
23. Thomas H, Cowin AJ, Mills SJ: The Importance of Pericytes in Healing: Wounds and other Pathologies. *Int J Mol Sci* **2017,** 18:

24. Meijer EM, van Dijk CGM, Kramann R, Verhaar MC, Cheng C: Implementation of pericytes in vascular regeneration strategies. *Tissue Eng Part B Rev* **2020,**
25. Malafaya PB, Silva GA, Reis RL: Natural-origin polymers as carriers and scaffolds for biomolecules and cell delivery in tissue engineering applications. *Adv Drug Deliv Rev* **2007,** 59:207-233
26. Slaughter BV, Khurshid SS, Fisher OZ, Khademhosseini A, Peppas NA: Hydrogels in regenerative medicine. *Adv Mater* **2009,** 21:3307-3329
27. Lin CC, Anseth KS: PEG hydrogels for the controlled release of biomolecules in regenerative medicine. *Pharm Res* **2009,** 26:631-643
28. Aljohani W, Ullah MW, Zhang X, Yang G: Bioprinting and its applications in tissue engineering and regenerative medicine. *Int J Biol Macromol* **2018,** 107:261-275
29. Pennings I, van Haaften EE, Jungst T, Bulsink JA, Rosenberg A, Groll J, Bouten CVC, Kurniawan NA, Smits A, Gawlitta D: Layer-specific cell differentiation in bi-layered vascular grafts under flow perfusion. *Biofabrication* **2019,** 12:015009
30. Coakley DN, Shaikh FM, O'Sullivan K, Kavanagh EG, Grace PA, Walsh SR, McGloughlin TM: Comparing the endothelialisation of extracellular matrix bioscaffolds with coated synthetic vascular graft materials. *Int J Surg* **2016,** 25:31-37
31. Rentsch C, Rentsch B, Heinemann S, Bernhardt R, Bischoff B, Forster Y, Scharnweber D, Rammelt S: ECM inspired coating of embroidered 3D scaffolds enhances calvaria bone regeneration. *Biomed Res Int* **2014,** 2014:217078
32. Chen YC, Lin RZ, Qi H, Yang Y, Bae H, Melero-Martin JM, Khademhosseini A: Functional Human Vascular Network Generated in Photocrosslinkable Gelatin Methacrylate Hydrogels. *Adv Funct Mater* **2012,** 22:2027-2039
33. Klotz BJ, Oosterhoff LA, Utomo L, Lim KS, Vallmajo-Martin Q, Clevers H, Woodfield TBF, Rosenberg A, Malda J, Ehrbar M, Spee B, Gawlitta D: A Versatile Biosynthetic Hydrogel Platform for Engineering of Tissue Analogues. *Adv Healthc Mater* **2019,** 8:e1900979
34. Levato R, Visser J, Planell JA, Engel E, Malda J, Mateos-Timoneda MA: Biofabrication of tissue constructs by 3D bioprinting of cell-laden microcarriers. *Biofabrication* **2014,** 6:035020
35. Thomas A, Orellano I, Lam T, Noichl B, Geiger MA, Amler AK, Kreuder AE, Palmer C, Duda G, Lauster R, Kloke L: Vascular bioprinting with enzymatically degradable bioinks via multi-material projection-based stereolithography. *Acta Biomater* **2020,** 117:121-132
36. Leucht A, Volz AC, Rogal J, Borchers K, Kluger PJ: Advanced gelatin-based vascularization bioinks for extrusion-based bioprinting of vascularized bone equivalents. *Sci Rep* **2020,** 10:5330
37. Hoch AI, Mittal V, Mitra D, Vollmer N, Zikry CA, Leach JK: Cell-secreted matrices perpetuate the bone-forming phenotype of differentiated mesenchymal stem cells. *Biomaterials* **2016,** 74:178-187
38. Pati F, Jang J, Ha DH, Won Kim S, Rhie JW, Shim JH, Kim DH, Cho DW: Printing three-dimensional tissue analogues with decellularized extracellular matrix bioink. *Nat Commun* **2014,** 5:3935
39. Zhao J, Santino F, Giacomini D, Gentilucci L: Integrin-Targeting Peptides for the Design of Functional Cell-Responsive Biomaterials. *Biomedicines* **2020,** 8:
40. Muylaert DE, van Almen GC, Talacua H, Fledderus JO, Kluin J, Hendrikse SI, van Dongen JL, Sijbesma E, Bosman AW, Mes T, Thakkar SH, Smits AI, Bouten CV, Dankers PY, Verhaar MC: Early in-situ cellularization of a supramolecular vascular graft is modified by synthetic stromal cell-derived factor-1alpha derived peptides. *Biomaterials* **2016,** 76:187-195
41. Byambaa B, Annabi N, Yue K, Trujillo-de Santiago G, Alvarez MM, Jia W, Kazemzadeh-Narbat M, Shin SR, Tamayol A, Khademhosseini A: Bioprinted Osteogenic and Vasculogenic Patterns for Engineering 3D Bone Tissue. *Adv Healthc Mater* **2017,** 6:
42. Verdone G, Doliana R, Corazza A, Colebrooke SA, Spessotto P, Bot S, Bucciotti F, Capuano A, Silvestri A, Viglino P, Campbell ID, Colombatti A, Esposito G: The solution structure of EMILIN1 globular C1q domain reveals a disordered insertion necessary for interaction with the alpha4beta1 integrin. *J Biol Chem* **2008,** 283:18947-18956
43. Danussi C, Del Bel Belluz L, Pivetta E, Modica TM, Muro A, Wassermann B, Doliana R, Sabatelli P, Colombatti A, Spessotto P: EMILIN1/alpha9beta1 integrin interaction is crucial in lymphatic valve formation and maintenance. *Mol Cell Biol* **2013,** 33:4381-4394
44. Danussi C, Petrucco A, Wassermann B, Pivetta E, Modica TM, Del Bel Belluz L, Colombatti A, Spessotto P: EMILIN1-alpha4/alpha9 integrin interaction inhibits dermal fibroblast and keratinocyte proliferation. *J Cell Biol* **2011,** 195:131-145

45. Spessotto P, Cervi M, Mucignat MT, Mungiguerra G, Sartoretto I, Doliana R, Colombatti A: beta 1 Integrin-dependent cell adhesion to EMILIN-1 is mediated by the gC1q domain. *J Biol Chem* **2003,** 278:6160-6167
46. Kreidberg JA, Symons JM: Integrins in kidney development, function, and disease. *Am J Physiol Renal Physiol* **2000,** 279:F233-F242
47. Mathew S, Chen X, Pozzi A, Zent R: Integrins in renal development. *Pediatr Nephrol* **2012,** 27:891-900
48. Silva R, D'Amico G, Hodivala-Dilke KM, Reynolds LE: Integrins: the keys to unlocking angiogenesis. *Arterioscler Thromb Vasc Biol* **2008,** 28:1703-1713
49. ten Dijke P, Arthur HM: Extracellular control of TGFbeta signalling in vascular development and disease. *Nat Rev Mol Cell Biol* **2007,** 8:857-869
50. Wu D, Shen YH, Russell L, Coselli JS, LeMaire SA: Molecular mechanisms of thoracic aortic dissection. *J Surg Res* **2013,** 184:907-924
51. Rifkin DB, Rifkin WJ, Zilberberg L: LTBPs in biology and medicine: LTBP diseases. *Matrix Biol* **2018,** 71-72:90-99
52. Godwin ARF, Singh M, Lockhart-Cairns MP, Alanazi YF, Cain SA, Baldock C: The role of fibrillin and microfibril binding proteins in elastin and elastic fibre assembly. *Matrix Biol* **2019,** 84:17-30
53. Craft CS, Broekelmann TJ, Mecham RP: Microfibril-associated glycoproteins MAGP-1 and MAGP-2 in disease. *Matrix Biol* **2018,** 71-72:100-111
54. Kwak EA, Lee NY: Synergetic roles of TGF-beta signaling in tissue engineering. *Cytokine* **2019,** 115:60-63
55. Zacchigna L, Vecchione C, Notte A, Cordenonsi M, Dupont S, Maretto S, Cifelli G, Ferrari A, Maffei A, Fabbro C, Braghetta P, Marino G, Selvetella G, Aretini A, Colonnese C, Bettarini U, Russo G, Soligo S, Adorno M, Bonaldo P, Volpin D, Piccolo S, Lembo G, Bressan GM: Emilin1 links TGF-beta maturation to blood pressure homeostasis. *Cell* **2006,** 124:929-942
56. Mecham RP, Gibson MA: The microfibril-associated glycoproteins (MAGPs) and the microfibrillar niche. *Matrix Biol* **2015,** 47:13-33
57. Homan KA, Kolesky DB, Skylar-Scott MA, Herrmann J, Obuobi H, Moisan A, Lewis JA: Bioprinting of 3D Convoluted Renal Proximal Tubules on Perfusable Chips. *Sci Rep* **2016,** 6:34845
58. Lin NYC, Homan KA, Robinson SS, Kolesky DB, Duarte N, Moisan A, Lewis JA: Renal reabsorption in 3D vascularized proximal tubule models. *Proc Natl Acad Sci U S A* **2019,** 116:5399-5404
59. Liu G, David BT, Trawczynski M, Fessler RG: Advances in Pluripotent Stem Cells: History, Mechanisms, Technologies, and Applications. *Stem Cell Rev Rep* **2020,** 16:3-32
60. Sanjurjo-Rodriguez C, Castro-Vinuelas R, Pineiro-Ramil M, Rodriguez-Fernandez S, Fuentes-Boquete I, Blanco FJ, Diaz-Prado S: Versatility of Induced Pluripotent Stem Cells (iPSCs) for Improving the Knowledge on Musculoskeletal Diseases. *Int J Mol Sci* **2020,** 21:
61. Kadota S, Tanaka Y, Shiba Y: Heart regeneration using pluripotent stem cells. *J Cardiol* **2020,** 76:459-463
62. Klein D: iPSCs-based generation of vascular cells: reprogramming approaches and applications. *Cell Mol Life Sci* **2018,** 75:1411-1433
63. Williams IM, Wu JC: Generation of Endothelial Cells From Human Pluripotent Stem Cells. *Arteriosclerosis, Thrombosis, and Vascular Biology* **2019,** 39:1317-1329
64. Clayton ZE, Sadeghipour S, Patel S: Generating induced pluripotent stem cell derived endothelial cells and induced endothelial cells for cardiovascular disease modelling and therapeutic angiogenesis. *Int J Cardiol* **2015,** 197:116-122
65. Sato T, Vries RG, Snippert HJ, van de Wetering M, Barker N, Stange DE, van Es JH, Abo A, Kujala P, Peters PJ, Clevers H: Single Lgr5 stem cells build crypt-villus structures in vitro without a mesenchymal niche. *Nature* **2009,** 459:262-265
66. Huch M, Dorrell C, Boj SF, van Es JH, Li VS, van de Wetering M, Sato T, Hamer K, Sasaki N, Finegold MJ, Haft A, Vries RG, Grompe M, Clevers H: In vitro expansion of single Lgr5+ liver stem cells induced by Wnt-driven regeneration. *Nature* **2013,** 494:247-250
67. Huch M, Gehart H, van Boxtel R, Hamer K, Blokzijl F, Verstegen MM, Ellis E, van Wenum M, Fuchs SA, de Ligt J, van de Wetering M, Sasaki N, Boers SJ, Kemperman H, de Jonge J, Ijzermans JN, Nieuwenhuis EE, Hoekstra R, Strom S, Vries RR, van der Laan LJ, Cuppen E, Clevers H: Long-term culture of genome-stable bipotent stem cells from adult human liver. *Cell* **2015,** 160:299-312
68. Schutgens F, Rookmaaker MB, Margaritis T, Rios A, Ammerlaan C, Jansen J, Gijzen L, Vormann M, Vonk A, Viveen M, Yengej FY, Derakhshan S, de Winter-de Groot KM, Artegiani B, van Boxtel R, Cuppen E, Hendrickx APA, van den Heuvel-Eibrink MM, Heitzer E, Lanz H,

Beekman J, Murk JL, Masereeuw R, Holstege F, Drost J, Verhaar MC, Clevers H: Tubuloids derived from human adult kidney and urine for personalized disease modeling. *Nat Biotechnol* **2019,** 37:303-313

69. Wimmer RA, Leopoldi A, Aichinger M, Kerjaschki D, Penninger JM: Generation of blood vessel organoids from human pluripotent stem cells. *Nat Protoc* **2019,** 14:3082-3100
70. Wimmer RA, Leopoldi A, Aichinger M, Wick N, Hantusch B, Novatchkova M, Taubenschmid J, Hammerle M, Esk C, Bagley JA, Lindenhofer D, Chen G, Boehm M, Agu CA, Yang F, Fu B, Zuber J, Knoblich JA, Kerjaschki D, Penninger JM: Human blood vessel organoids as a model of diabetic vasculopathy. *Nature* **2019,** 565:505-510
71. Ballermann BJ, Dardik A, Eng E, Liu A: Shear stress and the endothelium. *Kidney Int Suppl* **1998,** 67:S100-108
72. Lu D, Kassab GS: Role of shear stress and stretch in vascular mechanobiology. *J R Soc Interface* **2011,** 8:1379-1385
73. Dekker RJ, van Soest S, Fontijn RD, Salamanca S, de Groot PG, VanBavel E, Pannekoek H, Horrevoets AJ: Prolonged fluid shear stress induces a distinct set of endothelial cell genes, most specifically lung Kruppel-like factor (KLF2). *Blood* **2002,** 100:1689-1698
74. Herland A, van der Meer AD, FitzGerald EA, Park TE, Sleeboom JJ, Ingber DE: Distinct Contributions of Astrocytes and Pericytes to Neuroinflammation Identified in a 3D Human Blood-Brain Barrier on a Chip. *PLoS One* **2016,** 11:e0150360
75. van Duinen V, van den Heuvel A, Trietsch SJ, Lanz HL, van Gils JM, van Zonneveld AJ, Vulto P, Hankemeier T: 96 perfusable blood vessels to study vascular permeability in vitro. *Sci Rep* **2017,** 7:18071
76. Werner M, Kurniawan NA, Korus G, Bouten CVC, Petersen A: Mesoscale substrate curvature overrules nanoscale contact guidance to direct bone marrow stromal cell migration. *J R Soc Interface* **2018,** 15:
77. Yu SM, Oh JM, Lee J, Lee-Kwon W, Jung W, Amblard F, Granick S, Cho YK: Substrate curvature affects the shape, orientation, and polarization of renal epithelial cells. *Acta Biomater* **2018,** 77:311-321
78. Wells RG: Tissue mechanics and fibrosis. *Biochim Biophys Acta* **2013,** 1832:884-890
79. Lindsay MM, Maxwell P, Dunn FG: TIMP-1: a marker of left ventricular diastolic dysfunction and fibrosis in hypertension. *Hypertension* **2002,** 40:136-141
80. Moore L, Fan D, Basu R, Kandalam V, Kassiri Z: Tissue inhibitor of metalloproteinases (TIMPs) in heart failure. *Heart Failure Reviews* **2011,** 17:693-706
81. Ngu JM, Teng G, Meijndert HC, Mewhort HE, Turnbull JD, Stetler-Stevenson WG, Fedak PW: Human cardiac fibroblast extracellular matrix remodeling: dual effects of tissue inhibitor of metalloproteinase-2. *Cardiovasc Pathol* **2014,** 23:335-343
82. DeLeon-Pennell KY, Meschiari CA, Jung M, Lindsey ML: Matrix Metalloproteinases in Myocardial Infarction and Heart Failure. *Prog Mol Biol Transl Sci* **2017,** 147:75-100
83. Shah SJ, Katz DH, Deo RC: Phenotypic spectrum of heart failure with preserved ejection fraction. *Heart Fail Clin* **2014,** 10:407-418
84. Brandt MM, Nguyen ITN, Krebber MM, van de Wouw J, Mokry M, Cramer MJ, Duncker DJ, Verhaar MC, Joles JA, Cheng C: Limited synergy of obesity and hypertension, prevalent risk factors in onset and progression of heart failure with preserved ejection fraction. *J Cell Mol Med* **2019,** 23:6666-6678
85. Kalucka J, Bierhansl L, Conchinha NV, Missiaen R, Elia I, Bruning U, Scheinok S, Treps L, Cantelmo AR, Dubois C, de Zeeuw P, Goveia J, Zecchin A, Taverna F, Morales-Rodriguez F, Brajic A, Conradi LC, Schoors S, Harjes U, Vriens K, Pilz GA, Chen R, Cubbon R, Thienpont B, Cruys B, Wong BW, Ghesquiere B, Dewerchin M, De Bock K, Sagaert X, Jessberger S, Jones EAV, Gallez B, Lambrechts D, Mazzone M, Eelen G, Li X, Fendt SM, Carmeliet P: Quiescent Endothelial Cells Upregulate Fatty Acid beta-Oxidation for Vasculoprotection via Redox Homeostasis. *Cell Metab* **2018,** 28:881-894 e813

Appendix

Nederlandse samenvatting

Alle cellen in het menselijk lichaam hebben zuurstof en voedingsstoffen nodig om te overleven en te functioneren. Daarnaast moeten ook afvalstoffen van deze cellen worden verwijderd. Weefsels en organen bestaan uit miljoenen cellen waardoor diffusie van zuurstof en voedingsstoffen niet volstaat. Daarom is het menselijk lichaam afhankelijk van een gespecialiseerd vaatnetwerk, het cardiovasculaire systeem. Dit netwerk van bloedvaten, met het hart als pomp, bereikt alle cellen in het lichaam. Bloedvaten zijn gespecialiseerd om bloed te transporteren maar ook om de interactie aan te gaan met circulerende immuuncellen.

Bloedvaten zijn grofweg te verdelen in drie typen; (slag)aders, capillairen en venen. De gemeenschappelijke factor van deze vaten is de binnenste laag van endotheelcellen. Deze cellen vormen een barrière tussen het circulerende bloed en het omliggende weefsel. Deze laag wordt ondersteund door extracellulaire matrix (ECM) eiwitten en ondersteunde cellen zoals gladde spiercellen (SMCs) of pericyten. Aders en slagaders bestaan uit meerdere lagen SMCs om de druk van het pompende hart op te vangen. In deze vaten stroomt het bloed onder hoge druk en vertakt naar een netwerk van kleine capillairen. Endotheelcellen in de capillairen worden ondersteund door pericyten en hier vindt de daadwerkelijk uitwisseling plaats van zuurstof en voedingstoffen naar het omliggende weefsel. Alle kleine vertakkingen bundelen zich weer samen in de venen, grotere (veneuze) vaten met ondersteunde SMCs, waardoor het bloed met een lage druk terug naar het hart stroomt om vervolgens weer een nieuwe cyclus te beginnen.

Het vasculaire netwerk ontwikkelt zich al in embryonale fase. De basis wordt gelegd door vasculogenese, de ontwikkeling van capillairen uit zogenoemde angioblasten. Deze kleine bloedvaten kunnen zich ontwikkelen naar grotere aders of venen. Door een proces genaamd angiogenese worden er nieuwe capillairen gevormd uit reeds bestaande capillairen. Dit strak gecontroleerde proces zorgt voor het constant remodeleren van het vasculaire netwerk, wat essentieel is voor ontwikkeling en groei, maar ook voor wondheling (regeneratie) en pathologische aandoeningen zoals tumorformatie. Angiogenese is een complex proces waar duidelijk wordt dat cellulaire interacties en interacties met de ECM essentieel zijn in vaat -homeostase, -ontwikkeling en -regeneratie.

Hier ligt dan ook een belangrijk punt in een relatief nieuw onderzoeksgebied; regeneratieve geneeskunde en tissue engineering (TE). Dit snel ontwikkelende onderzoeksgebied heeft een potentieel grote therapeutische impact om weefsels en organen te herstellen of te vervangen. Onderdeel hiervan is de constante ontwikkelingen van innovatieve biomaterialen; biologische of synthetische materialen die in het lichaam een specifieke functie kunnen overnemen zoals protheses. Door middel van biomaterialen, weefselspecifieke cellen en nieuwste technieken

zoals 3D printen, kunnen delen van weefsels en organen worden nagemaakt en gebruikt worden als therapie. Een van de grootste valkuilen in de regeneratieve geneeskunde op dit moment is het creëren van een functioneel vaatbed zodat alle cellen van zuurstof worden voorzien en kunnen functioneren. Daarnaast kunnen regeneratieve technieken gebruikt worden om bloedvaten na te bootsen in het laboratorium, in zogenoemde *in vitro* modellen die zo natuurgetrouw zijn als mogelijk. Dit soort modellen geeft wetenschappers de kans om de ontwikkeling van bloedvaten in ziekte en gezondheid te bestuderen en de complexe interacties te ontrafelen. Omdat het cardiovasculaire systeem erg complex is, is fundamenteel onderzoek belangrijk om bestaande en nieuwe, vasculaire therapeutische en regeneratieve strategieën te verbeteren. Daarom is het doel van deze thesis om complexe interacties tussen vasculaire cellen en de ECM te onderzoeken tijdens ontwikkeling en ziekte om *in vitro* bloedvat modellen te ontwikkelen en te verbeteren voor implementatie in regeneratieve strategieën.

Het bestuderen van angiogenese processen en interacties tussen vasculaire cellen is essentieel voor therapeutische microvasculaire strategieën. Om een beter inzicht te krijgen in moleculaire processen, wordt in **hoofdstuk 2** de rol van Frizzled 5 (Fzd5) in angiogenese onderzocht. Deze endotheel receptor speelt een belangrijke rol in de ontwikkeling van het vaatnetwerk, alleen de manier waarop was nog niet bekend. Onze studie laat zien dat een verlaging van de Fzd5 receptor leidt tot minder proliferatie, migratie en vaatformatie van endotheelcellen. Daarnaast leidt een verlaging van Fzd5 tot de verhoogde aanmaak van vascular endothelial growth factor receptor 1 en angiopoietin-1. Deze uitgescheiden factoren zorgen voor een verminderde gevoeligheid voor pro-angiogenese factoren en een verminderde vaatstabilisatie door het loskomen van pericyten.

Naast vaatstabilisatie, beschikken pericyten over meerdere, belangrijke functies voor het microvasculaire netwerk. In **hoofdstuk 3** worden deze functies in gezondheid en ziekte verder uiteengezet. Het beter begrijpen van de essentiële interactie tussen endotheelcellen en pericyten is dan ook van belang voor vaat gerelateerde regeneratieve toepassingen. Daarnaast wordt in **hoofdstuk 3** dieper ingegaan op de diverse rol van pericyten in de regeneratieve geneeskunde.

Om de belangrijke interactie tussen pericyten en endotheelcellen verder uit te diepen, beschrijft **hoofdstuk 4** de genexpressie van pericyten in aan- en afwezigheid van endotheelcellen. Deze studie toont aan dat pericyten in interactie met endotheelcellen differentiëren en prolifereren. Daarnaast hebben pericyten een verhoogde genexpressie van ECM eiwitten als er geen interactie is met endotheelcellen. Dit is in lijn met de huidige hypothese dat pericyten zich losmaken van het endotheel om vervolgens een rol te spelen in

fibrogenese, de pathologische aanmaak van ECM eiwitten. Dit zorgt tevens voor verminderde vaatstabilisatie.

Naast de interactie tussen vasculaire cellen, is ook de interactie van cellen met het omliggend en ondersteunend ECM belangrijk. ECM eiwitten zorgen voor belangrijke biochemische signalen waar cellen op reageren, bijvoorbeeld door proliferatie, migratie en adhesie. Cellen hechten aan ECM eiwitten via integrin receptoren die vervolgens een cascade aan interne signalen aanstuurt. Hierdoor reageren cellen op de stijfheid, geometrie en typen ECM eiwit. De ECM is erg dynamisch doordat het constant wordt afgebroken en weer opgebouwd, hierdoor ontstaat constante remodelering van het ECM en daarmee het weefsel. Dit proces begint al gedurende embryogenese en speelt een leven lang een rol. Omdat ECM een belangrijke rol heeft in ontwikkeling en homeostase maar ook gedurende ziekte (fibrose bijvoorbeeld), is het belangrijk om de ECM compositie van weefsels in kaart te brengen, zodat het nuttig kan worden gebruikt in de regeneratieve geneeskunde. Hierbij is onze hypothese dat (1) de ECM compositie van weefsel in ontwikkeling (foetaal) anders is vergeleken met weefsel in homeostase (matuur), en dat (2) de ECM componenten die in veelvoud aanwezig zijn gedurende ontwikkeling een belangrijke rol kunnen spelen in regeneratieve geneeskunde. In dit proefschrift beschrijven wij de ECM eiwit compositie van nier (**hoofdstuk 5**) en renale nier arterie (**hoofdstuk 6**) in gezond foetaal en matuur humaan weefsel. Elastische ECM componenten komen veelvuldig voor in foetale nieren en nier arteriën terwijl andere ECM componenten zoals laminin meer voorkomen in matuur weefsel. **Hoofdstuk 5** beschrijft hoe niercellen hechten en migreren op een oppervlakte van ECM componenten in de aanwezig- en afwezigheid van EMILIN1, een elastisch ECM eiwit dat veel voorkomt in foetaal nier weefsel. Niercellen laten minder adhesie punten zien en migreren meer op een ECM oppervlakte met minder EMILIN1. **Hoofdstuk 6** beschrijft een zelfde aanpak met endotheelcellen op een ECM oppervlakte in de aanwezig- en afwezigheid van EMILIN1. In tegenstelling tot renale cellen, laten endotheelcellen geen verschil zien in adhesie punten en migratie op een ECM oppervlakte met minder EMILIN1. Dit suggereert dat het effect van EMILIN1 op het gedrag van cellen afhankelijk is van het celtype. Zowel adhesie als migratie van cellen is belangrijk in TE toepassingen, en de beschreven studies laten zien dat EMILIN1 wel een rol kan spelen in renale TE strategieën, en in mindere mate in vasculaire TE strategieën. Daarnaast laat **hoofdstuk 5** zien dat renale TE toepassingen kunnen worden verrijkt met EMILIN1 om of adhesie of migratie te stimuleren, en niet beide tegelijk. De fundamentele bevindingen uit zowel **hoofdstuk 5** als **6** laten zien dat het ontrafelen van de ECM compositie belangrijk is en kan bijdragen aan het identificeren van ECM eiwitten die een belangrijke rol kunnen spelen in regeneratieve toepassingen.

ECM wordt voortdurend geremodelleerd door het afzetten van nieuwe ECM componenten en door het afbreken daarvan. Matrix metalloproteinases (MMPs) en hun remmers, tissue inhibitors of metalloproteinases (TIMPs) zijn dynamische ECM regulatoren en verantwoordelijk voor ECM afbraak. Het meten van zowel MMP en TIMP levels is een goede afmeting van ECM eiwit afbraak en opbouw en kan daardoor gebruikt worden om de ECM opbouw in fibrose te monitoren gedurende ziekte progressie. Om de lokale MMP en TIMP levels in kaart te brengen in hart weefsel, beschrijft **hoofdstuk 7** een systematische literatuur review en een daaropvolgende meta-analyse van diermodellen met diastolische dysfunctie. De belangrijkste bevinding van **hoofdstuk 7** is het gebrek aan dierstudies die op de juiste manier diastolische dysfunctie meten. Daarnaast bestuderen de meeste studies MMPs en TIMPs op genexpressie niveau in plaats van het meer informatieve eiwit expressie of eiwit activiteit. Het aantal geïncludeerde studies was uiteindelijk niet toereikend om een correlatie te maken tussen verschillende hart of fibrose parameters en MMP of TIMP levels. **Hoofdstuk 7** geeft belangrijke aanbevelingen voor toekomstige dierstudies die nodig zijn om de translatie naar de kliniek te verbeteren. Dit is nodig om dier modellen maar ook *in vitro* modellen te blijven verbeteren zodat de kloof tussen dier en mens en *in vitro* modellen en mens wordt verkleind, wat ten gunste komt van regeneratieve geneeskunde.

Diastolische dysfunctie is een kenmerkend probleem in hartfalen met een gepreserveerde ejectie fractie (HFpEF). Dit type hartfalen is verschillend van hartfalen met een verminderde ejectie fractie (HFrEF) al zijn beide geassocieerd met meerdere comorbiditeiten zoals obesitas, diabetes en hoge bloeddruk. Door veelvuldig onderzoek in goed gevalideerde diermodellen van HFrEF zijn er goede therapieën ontwikkeld voor deze ziekte. Helaas werken deze behandelingen niet voor HFpEF patiënten. Het ontstaan en het ontwikkelen van HFpEF wordt nog niet volledig begrepen en de huidige behandelingen richten zich daardoor vooral op de comorbiditeiten. De met HFpEF geassocieerde comorbiditeiten zijn ook schadelijk voor de nierfunctie. Een verslechterde nierfunctie is ook een risicofactor voor hartfalen door de belangrijke tweezijdige interactie tussen het hart en de nieren. Dit noemt men ook wel het cardio-renale metabolisch syndroom (CRMS) en classificeert HFpEF niet alleen als diastolisch hartfalen, maar als een systemisch syndroom dat zowel hart als nieren aantast. Daarnaast is HFpEF geassocieerd met microvasculaire dysfunctie en fibrose in het hart. Door het gebrek aan goed gevalideerde diermodellen blijft fundamenteel onderzoek naar HFpEF achter. Omdat HFpEF een systemische ziekte is met verschillende comorbiditeiten en risicofactoren moeten diermodellen dit CRMS ook nabootsen. **Hoofdstuk 8** beschrijft de validatie van de obese ZSF1 rat als model voor CRMS en HFpEF. Deze rattenstam is obese en heeft een hoge bloeddruk waardoor ze spontaan CRMS en HFpEF ontwikkelen in 25 weken tijd. **Hoofdstuk 8** laat zien dat deze dieren inderdaad diastolische dysfunctie

ontwikkelen. Daarnaast hebben deze ratten verhoogde glucose levels in het bloed en een verminderde nierfunctie door fibrose. Verder zijn er geconcentreerde microvasculaire plekken in het hart die prolifereren. Deze fibrotische plekken zijn kenmerkend door de vele endotheelcellen en pericyten. Deze studie laat zien dat de obese ZSF1 rat een gevalideerd model is om het ontstaan en de ontwikkeling van HFpEF te bestuderen op een achtergrond van meerdere risicofactoren.

Microfluidic modellen zijn kleine kanalen omgeven door glas of polymeren die samen de mogelijkheid hebben om een specifieke biochemische en biomechanische omgeving na te bootsen en te controleren. Daarom zijn microfluidic modellen uitermate geschikt om meerdere eigenschappen van bloedvaten te combineren en na te bootsen in een *in vitro* model. Dit soort *in vitro* modellen kunnen ook meerdere TE strategieën zoals bioprinten combineren en valideren, en daarmee een weefselspecifieke omgeving nabootsen. Zoals hierboven uitgelegd, is de interactie tussen de cellen van de vasculaire netwerk en ECM essentieel in vaat -homeostase en -ontwikkeling en daarom is het belangrijk om deze karakteristieken te combineren in een *in vitro* model. Huidige microfluidic modellen die het vasculaire netwerk nabootsen, focussen voornamelijk op endotheelcellen en missen daardoor belangrijke andere interacties. **Hoofdstuk 9** beschrijft een geavanceerd microfluidic systeem dat het vasculaire netwerk nabootst en gebruikt kan worden om vasculaire interacties te bestuderen. Het hier gepresenteerde model omschrijft een model met een reservoir voor ECM gel waar pericyten in zitten. Naalden vormen een kanaal in deze ECM gel dat dient als vorm voor endotheelcellen. Zodra de endotheelcellen hierin worden gezaaid, nemen ze een circulaire, 3D vorm aan en vormen ze een monolaag en dus een artificieel bloedvat, met een open lumen dat geperfuseerd kan worden met medium. Hierdoor worden de endotheelcellen blootgesteld aan biomechanische stimulatie. Het artificiële bloedvat behoudt de belangrijke vasculaire barrière functie. Circulerende immuuncellen die worden toegevoegd aan het medium kunnen tevens een interactie met de wand van het bloedvat aan gaan wanneer er omstandigheden worden geïntroduceerd die een ontsteking nabootsen.

Conclusie en toekomstige perspectieven

De studies die in deze thesis worden beschreven hebben als doel om meer fundamentele inzichten te verkrijgen in vasculaire cellen en ECM interactie, bloedvat ontwikkeling en vaatstabilisatie in zowel gezondheid als ziekte. De fundamentele bevindingen hier beschreven, kunnen worden geïmplementeerd in verschillende regeneratieve en TE strategieën waaronder het ontwerpen van nieuwe, efficiënte vasculaire *in vitro* modellen. Deze modellen zijn hierdoor meer klinisch relevant doordat ze alle biologische en biomechanische karakteristieke van het complexe vasculaire netwerk nabootsen en mogelijkheden biedt om

potentiele interventies te testen. De combinatie van al deze vasculaire eigenschappen kan een technische uitdaging worden. Wij stellen voor om geavanceerde *in vitro* modellen te gebruiken dat een specifieke onderdeel van je onderzoeksvraag kan beantwoorden en waar nodig, gebruik te maken van meerdere geavanceerde modellen. De combinatie van humane *in vitro* modellen en vasculaire TE strategieën verbetert de translatie van research data naar klinische toepassingen. Naast alle mogelijke vasculaire therapeutische toepassingen zal het gehele TE onderzoeksgebied kunnen profiteren van het hier beschreven en toekomstig vasculaire onderzoek, omdat grote, weefselspecifieke TE constructen en therapeutische toepassingen allen afhankelijk zijn van een functioneel vasculair netwerk.

Curriculum Vitae

Christian Gerardus Marinus van Dijk was born on February 4th, 1988 in Oosterhout, Noord-Brabant, The Netherlands. After finishing his HAVO education at Mgr. Frencken College in Oosterhout in 2006, he continued his studies at Avans Hogeschool Breda. As part of this Bachelor Biomedical Laboratory Research, he performed two internships at TNO Rijswijk, CBRN Protection under the supervision of dr. Marloes Joosen. After receiving his bachelor of Applied Sciences in 2010, Christian continued his education in Leiden. During the Master Biomedical Science, he followed his first internship at the department of Hematology at the University of Medical Center Leiden under the supervision of dr. Marieke Griffioen and Judith van der Griendt. Christian finished his last Master internship at the department of Experimental Cardiology at the Erasmus Medical Center Rotterdam under the supervision of dr. Caroline Cheng and Maarten Brandt. Immediately after this internship, Christian continued to work as research technician in the group of dr. Caroline Cheng and helped with the transition of the lab and current lab techniques to the department of Nephrology and Hypertension at the University Medical Center Utrecht. After obtaining his Master of Science degree in 2014, he continued his career later that year as PhD candidate in the same department under the supervision of Prof. dr. Marianne Verhaar and dr. Caroline Cheng. The results of this PhD period are presented in this thesis.

List of Publications

Meijer EM, **van Dijk CGM**, Kramann R, Verhaar MC, Cheng C. *Implementation of pericytes in vascular regeneration strategies.*
Tissue Engineering Part B – 2021 Jan:

Krebber MM, **van Dijk CGM**, Vernooij RWM, Brandt MM, Emter GA, Rau CD, Fledderus JO, Duncker DJ, Verhaar MC, Cheng C, Joles JA. *Matrix metalloproteinases and tissue inhibitors of metalloproteinases in extracellular matrix remodeling during left ventricular diastolic dysfunction and heart failure with preserved ejection fraction: a systematic review and meta-analysis.*
International Journal of Molecular Science – 2020 Oct: 21(18):e6742

Pei J, Harakalova M, Treibel TA, Lumbers RT, Boukens BJ, Efimov IR, van Dinter JT, González A, López B, El Azzouzi H, van den Dungen N, **van Dijk CGM**, Krebber MM, den Ruiter H, Pasterkamp G, Duncker DJ, Nieuwenhuis EES, de Weger R, Huibers MM, Vink A, Moore JH, Moon JC, Verhaar MC, Kararigas G, Mokry M, Asselbergs FW, Cheng C. *Histone acetylome signatures reveal the epigenomic reorganization in remodeled non-failing human hearts.*
Clinical Epigenetics – 2020 Jul: 12(1):106

Van Dijk CGM, Louzao-Martinez L, van Mulligen E, Boermans B, Demmers JAA, van den Bosch TPP, Goumans MJTH, Duncker DJ, Verhaar MC, Cheng C. *Extracellular matrix analysis of human renal arteries in both quiescent and active vascular state.*
International Journal of Molecular Science - 2020 May: 21(11):3905

Van Dijk CGM, Brandt MM, Poulis N, Anten J, van der Moolen M, Kramer L, Homburg EFGA, Louzao-Martinez L, Pei J, Krebber MM, van Balkom BWM, de Graaf P, Duncker DJ, Verhaar MC, Luttge R, Cheng C. *A new microfluidic model that allows monitoring of complex vascular structures and cell interactions in a 3D biological matrix.*
Lab on a Chip – 2020 May: 20(10):1827-1844

Louzao-Martinez L, **van Dijk CGM**, Xu YJ, Korn A, Bekker NJ, Brouwhuis R, Nicese MN, Demmers JAA, Goumans MJTH, Masereeuw R, Duncker DJ, Verhaar MC, Cheng C. *A proteome comparison between human feta land mature renal extracellular matrix identifies EMILIN1 as a regulator of renal epithelial cell adhesion.*
Matrix Biology Plus - 2019 Nov: (4):100011

Brandt MM, **van Dijk CGM**, Maringanti R, Chrifi I, Kramann R, Verhaar MC, Duncker DJ, Mokry M, Cheng C. *Transcriptome analysis reveals microvascular endothelial cell-dependent pericyte differentiation.*
Scientific Reports - 2019 Oct: 9(1):15586

Chrifi I, Louzao-Martinez L, Brandt MM, **Van Dijk CGM**, Bürgisser PE, Zhu C, Kros JM, Verhaar MC, Duncker DJ, Cheng C. *CMTM4 regulates angiogenesis by promoting cell surface recycling of VE-cadherin to endothelial adherens junctions.*
Angiogenesis - 2019 Feb: 22(1):75-93

Brandt MM, **van Dijk CGM**, Chrifi I, Kool HM, Bürgisser PE, Louzao-Martinez L, Pei J, Rottier RJ, Verhaar MC, Duncker DJ, Cheng C. *Endothelial loss of Fzd5 stimulates PKC/Ets1-mediated transcription of Angpt2 and Flt1.*
Angiogenesis - 2018 Nov: 21(4):805-821

Chrifi I, Hermkens D, Brandt MM, **Van Dijk CGM**, Bürgisser PE, Haasdijk R, Pei J, van de Kamp EHM, Zhu C, Blonden L, Kros JM, Duncker DJ, Duckers HJ, Cheng C. *Cgnl1, an endothelial junction complex protein, regulates GTPase mediated angiogenesis.*
Cardiovascular Research - 2017 Dec: 113(14):1776-1788

Chrifi I, Louzao-Martinez L, Brandt M, **Van Dijk CGM**, Bürgisser P, Zhu C, Kros JM, Duncker DJ, Cheng C. *CMTM3 (CKLF-Like Marvel Transmembrane Domain 3) Mediates Angiogenesis by Regulating Cell Surface Availability of VE-Cadherin in Endothelial Adherens Junctions.*
Arteriosclerosis Thrombosis Vascular Biology - 2017 Jun: 37(6):1098-1114

Haasdijk RA, Den Dekker WK, Cheng C, Tempel D, Szulcek R, Bos FL, Hermkens DM, Chrifi I, Brandt MM, **Van Dijk C**, Xu YJ, Van De Kamp EH, Blonden LA, Van Bezu J, Sluimer JC, Biessen EA, Van Nieuw Amerongen GP, Duckers HJ. *THSD1 preserves vascular integrity and protects against intraplaque haemorrhaging in ApoE-/- mice.*
Cardiovascular Research - 2016 May: 110(1):129-39

Van Dijk CG, Oosterhuis NR, Xu YJ, Brandt M, Paulus WJ, van Heerebeek L, Duncker DJ, Verhaar MC, Fontoura D, Lourenço AP, Leite-Moreira AF, Falcão-Pires I, Joles JA, Cheng C. *Distinct Endothelial Cell Responses in the Heart and Kidney Microvasculature Characterize the Progression of Heart Failure With Preserved Ejection Fraction in the Obese ZSF1 Rat With Cardiorenal Metabolic Syndrome.*
Circulation Heart Failure - 2016 Apr: 9(4):e002760

Van Dijk CG, Nieuweboer FE, Pei JY, Xu YJ, Bürgisser P, van Mulligen E, el Azzouzi H, Duncker DJ, Verhaar MC, Cheng C. *The complex mural cell: pericyte function in health and disease.*
International Journal of Cardiology - 2015 Mar: 190:75-89

Dankwoord

Eindelijk. Klaar. Mijn proefschrift is eindelijk klaar en dat heb ik aan een hoop mensen te danken. Dit proefschrift is mede tot stand gekomen door de hulp van mijn collega's, maar ook door vrienden en familie. Zonder jullie had ik niet de motivatie om dit af te maken en mij te ontwikkelen in de wetenschap. Ik ben jullie erg dankbaar!

Prof. dr. Marianne Verhaar. Beste Marianne, dank je voor de mogelijkheid om te promoveren bij de afdeling Nefrologie en Hypertensie. Je advies en informatie gedurende mijn promotie waren erg waardevol.

Dr. Caroline Cheng. Beste Caroline, dank je wel voor de fijne begeleiding. Als master student kwam ik terecht in jouw onderzoeksgroep in het Erasmus en al snel had je vertrouwen in mij. Als analist in jouw groep kreeg ik de kans om jouw lab in Utrecht verder op te zetten. Dit liep vloeiend over in mijn PhD traject en was dan ook gelijk een fijne start. Onder jouw vleugels kon ik mezelf verder ontwikkelen als onderzoeker. Ik ben je erg dankbaar voor de tijd en moeite die je in mijn ontwikkeling hebt gestopt en het vertrouwen dat je me hebt gegeven.

Ook wil ik graag de leden van mijn promotiecommissie bedanken. Prof. dr. Masereeuw, prof. dr. Sluijter, prof. dr. Malda, prof. dr. Bouten, prof. dr. Kramann, dank jullie voor het kritisch lezen van dit proefschrift.

Mijn paranimfen, Maarten en Paul. Tof dat jullie tijdens mijn verdediging naast me staan, het is een hele eer (voor jullie). Maarten, dit hele traject is voor mij bij jou begonnen. Ik kan me geen betere stage begeleider bedenken. Ik heb veel van je geleerd gedurende mijn stage, en daarna als collega's. We hebben heel wat gesprekken gevoerd bij de koffieautomaat, carpoolend in de auto, en met een bak droogijs op de stoep bij het Erasmus of het RMCU. Dit was zowel wetenschappelijk gerelateerd als over het leven en de belangrijkste bijzaak daarvan; voetbal (jammer dat je er niks van snapt). Het was dan ook altijd gezellig en waardevol. Jouw wetenschappelijke aanpak heeft mij ook zeker gevormd gedurende afgelopen periode. Je hebt me ook laten zien dat promoveren en het gezinsleven te combineren is. Hopelijk blijven we de komende jaren nog aan leuke en mooie projecten verder werken!
Paul, jouw kennis van, nou, eigenlijk alles is soms gewoon bizar. Met al je kennis en interesse in lab technieken en onderzoek, ook van andere groepen op de wereld, ben je een aanwinst

voor het lab. Het is altijd fijn om met je te sparren over lopende projecten en over het leven onder het genot van koffie of een biertje.

Er zijn heel wat collega's te bedanken. Laten we beginnen met de groep van Caroline. Ihsane, wat begon als lab partner op het HBO, online soccer manager spelen en samen Turkse pizza's eten bij Hizmet is gegroeid naar een mooie vriendschap. Je tipte mij dat ik bij de afdeling waar je werkte wel kon afstuderen. Zo geschiedde. Bedankt voor alle leuke en waardevolle (wetenschappelijke) gesprekken. Ik heb veel van je geleerd gedurende mijn promotie en ik ben dan ook blij dat ik je weer directe collega kan noemen. Afgelopen jaar was weer als vanouds! Laura, bedankt voor de goede samenwerking met meerdere projecten en fijne gesprekken. Succes met je carrière! Jiayi, thanks for the nice collaborations and talks. Good luck with your further career. Merle, we zijn zo ongeveer tegelijk begonnen. Waar we elkaar eerst weinig spraken, zijn we meer naar elkaar toegegroeid op weg naar het einde van onze PhDs. Fijn dat we in ons laatste jaar PhD samen naar de promotie konden toewerken. Ik koester de fijne samenwerking met de systematic review. Elana, bedankt voor je energieke input hier op het lab. Het is fijn om met je te werken aan je projecten. Op naar een mooi boekje! Ranga, I enjoyed our talks. Good luck with your projects! The newest members of Caroline's group, Runa and Ijsbrand. Unfortunately we did not work that much together (yet), hopefully the future brings nice collaborations. Good luck!

Ondertussen ben ik al wat jaren werkzaam bij Nefrologie en Hypertensie, en heb ik met veel mensen mogen samenwerken. Petra dB, Krista, Melanie, Diënty, Juan, Adele, dank je voor de fijne samenwerkingen en het delen van jullie kennis. En natuurlijk voor de gezellige momenten buiten het lab om! Petra dG, Bas, Joost, Rachel, Robin, Silvia en Jaap, bedankt voor jullie kritische blik op mijn projecten. Het is altijd fijn om jullie mening en suggesties te horen. Tobias, bedankt voor alle waardevolle gesprekken. Het was fijn om samen te werken aan verschillende projecten. Van jouw kritische blik op onderzoek kan iedereen wat leren! Ik ben blij dat we de (zelf gemalen) koffie-momenten op het RM hebben ingeruild voor bier drinken in Utrecht. Succes met je carrière in de kliniek.

In het lab ben ik altijd goed opgevangen door de PhD studenten die er al zaten en nu al lang klaar zijn. Bedankt Gisela, Dimitri, Nynke, Diana, Olivier, Hendrik, Tim, Frans, Glenn, Tonja en Femke voor de fijne gesprekken en hulp. Dit is ook zeker het geval voor de nu zittende generatie PhD studenten; Isabel, Murillo en Vivian, bedankt!

Ik heb het RM ervaren als een leuke, sociale groep, waarin werkgebied of expertise er niet toe doet. Loes, bedankt voor de leuke gesprekken in de celkweek. Debby, Guy en Frank, bedankt voor de fijne gesprekken en input tijdens de VTE meetings. Renee, Alain, Corina, Iris, Christian, en alle andere collega's van de Cardiologie, bedankt, het was altijd fijn om 5 groen te delen. In het bijzonder met Tom. Tom, bedankt voor de leuke en leerzame gesprekken. Mooi om te zien hoe je als arts het lab op kwam en vervolgens eerder klaar bent dan ik. Hopelijk kun je nu een pipet vasthouden! Al het goeds in je toekomstige carrière in de kliniek. Dat we nog maar vaak een biertje drinken (uiteraard met Paul, Elana en Pieters!).

Rotterdam, waar het allemaal begon met een stage en waar ik later altijd welkom was voor andere projecten, meetings en borrels. Prof. dr. Dirk Duncker, Beste Dirk, dank je voor de fijne samenwerking gedurende meerdere studies. Ook wil je graag bedanken voor de mogelijkheid om als gast onderdeel te zijn van jouw groep in het Erasmus MC. Ik heb me altijd welkom gevoeld op de 23e. Esther en Lau, bedankt voor het delen van jullie kennis en het runnen van het lab. Tijdens mijn stage ben ik goed opgevangen door de toenmalige PhD studenten; Remco, Dennie, Renate en Wijnand, bedankt! Als ik gedurende mijn PhD weer in Rotterdam was te vinden was dat met name in kamer Ee2369. Oana, Jens, Ruben en Jarno (ok, andere kamer), bedankt voor de leuke gesprekken en gezelligheid. Vincent, Richard, Andre, ik heb krom gelegen bij het maken van de vele promotie filmpjes, bedankt! Ook de rest van de Cardio groep, bedankt voor de fijne gesprekken tijdens meetings en bij de koffieautomaat.

Gedurende mijn PhD traject heb ik heel wat studenten mogen begeleiden. Elise, Christy, Erma, Bart, Jonas, Angela, Nikos, Matthijs, Liana, Romi, Alice, Neal en Maite, bedankt voor jullie inzet. Jullie hebben veel werk verzet en daardoor mooie data voor papers gegenereerd. Veel succes met jullie carrières, hopelijk komen we elkaar nog eens tegen!

Lieve Casa vrienden, wat begon met ouderwets spammen op het forum van Virgo is uitgegroeid tot hechte vriendschap. Pieter en Nicky, Stefano en Michelle, Lonneke en Jack, Nelleke en Martijn, Loos, Mandy, Devin, Glenn, bedankt voor alle mooie momenten en feesten samen. Het was mooi om te zien hoe we samen langzaam ons wilde studentenleven achter ons lieten en serieus en oud werden. Behalve Loos en Def dan..(jaloers). Ik ben blij dat we als groep nog steeds mooie momenten beleven en steeds hechter worden!

Lieve Beertjes, de studiegenoten van Avans. Renier en Sabine met Sebas, Sanne en Frank, Lizanne en Michael, Martijn en Lisanne met Thomas, Roel, Arjan, Ihsane, al zien we elkaar niet veel meer en is onbeperkt spareribs eten ook verleden tijd, het is mooi dat we een hecht

groepje vrienden blijven. Beertjes, bedankt voor de leuke tripjes, sinterkerst en de beste verjaardagen ooit.

Fab en Ronnie met Max en Kay, Eef en Joëll, bedankt voor de leuke momenten. Op naar nog veel meer! Bram, van toffe feestjes naar serieuze koffie gesprekken op het werk, bedankt voor de mooie en leuke momenten. Renate en Jeroen met Liva en Novi, Ilona en Remco met Mila en Tobi, Yvonne en Wessel met Ole en Jade, bedankt voor de leuke avondjes en nu de drukke, chaotische kinderfeestjes en middagen. De AC leden van Judolub Made, bedankt voor de mooie weekenden in de Biesbosch en op kamp. Dit was altijd een welkome afwisseling!

Sander en Kevin, de drie musketiers. Macho's, jullie zijn mijn oudste vrienden en al zien we elkaar niet meer zo vaak, we staan altijd voor elkaar klaar. Sander, mooi om te zien hoe wij vanaf ons 4de jaar al bevriend zijn en op het Frencken Kevin hebben ontmoet. Vele stapavonden, vakanties en autosport gerelateerde evenementen verder zijn we nu volwassen gasten met een gezin. Jengamasters Sander en Patricia met Niels en Cas, Kevin en Kelly met Veerle, en uiteraard Kuno, bedankt voor het lachen en jullie steun afgelopen jaren. Misschien hebben jullie na het lezen van dit boekje eindelijk een idee wat ik afgelopen jaren allemaal heb gedaan.

Lieve familie van Dijk en Segeren. Bedankt voor alle leuke momenten samen en jullie interesse in mijn promotie onderzoek. Op naar nog vele mooie feestdagen, verjaardagen, familieweekenden en momenten samen!

Uiteraard kan ik ook mijn schoonfamilie niet vergeten; Jacqueline en Ron, Alex en Lisa, Michael. Bedankt voor jullie steun en interesse in mijn werk afgelopen jaren. Jullie waren/zijn altijd een fijne en makkelijke uitval basis voor Stefanie en de kinderen als ik weer tot laat aan het werk was. Ondanks drie verhuizingen afgelopen jaar wonen jullie gelukkig nog steeds dichtbij! Als ik de schoonfamilie bedank, kan ik de fijne gesprekken met Theo niet vergeten.

Lieve papa en mama, dank jullie voor alle steun. Wie had dit jaren geleden kunnen bedenken. Ik niet in ieder geval. Jullie hebben me altijd vrij gelaten in mijn keuzes en interesse getoond in alles wat ik deed. Ik heb bewondering voor hoe jullie beide een druk werkleven met een druk gezinsleven en een tal van hobby's konden combineren (ook dankzij Loes!). En al zijn jullie nu minder druk met werken, opa en oma zijn is ook doorwerken. Ook zijn wij en onze vrienden altijd welkom bij jullie. Door dit alles zijn jullie nog altijd mijn voorbeeld!

Lieve (schoon)broertjes en (schoon)zusjes. Irene en Bart met Bobby, Jens en Robin, ik ben trots op jullie. Allemaal een druk en leuk leven, maar wel altijd tijd om met het hele gezin samen te zijn.

Tot slot, Lieve Stefanie, wat hebben we het fijn samen. Je hebt me altijd gesteund tijdens mijn promotie. Het scheelt gelukkig dat je weet wat op het lab werken inhoud als ik weer laat thuis kwam. Een huis kopen, je carrière switch, kinderen krijgen, samen kunnen we alles aan. Je bent een geweldige moeder voor Juna en Ruben. Onze kleine draakjes, wat zijn de clichés waar! Het is fantastisch om samen met deze lieve kinderen een gezin te vormen. Ik hou van jullie!